SANDIA REPORT
SAND2019-9189
Printed August 2019

Sandia National Laboratories

Pool Fire and Fireball Experiments in Support of the US DOE/DOT/TC Crude Oil Characterization Research Study

Anay Luketa, Thomas Blanchat, David Lord, Joseph Hogge, Alvaro Cruz-Cabrera, and Ray Allen

Prepared by
Sandia National Laboratories
Albuquerque, New Mexico
87185 and Livermore,
California 94550

Issued by Sandia National Laboratories, operated for the United States Department of Energy by National Technology & Engineering Solutions of Sandia, LLC.

Available to DOE and DOE contractors from
U.S. Department of Energy
Office of Scientific and Technical Information
P.O. Box 62
Oak Ridge, TN 37831

Telephone: (865) 576-8401
Facsimile: (865) 576-5728
E-Mail: reports@osti.gov
Online ordering: http://www.osti.gov/scitech

Available to the public from
U.S. Department of Commerce
National Technical Information Service
5301 Shawnee Rd
Alexandria, VA 22312

Telephone: (800) 553-6847
Facsimile: (703) 605-6900
E-Mail: orders@ntis.gov
Online order: https://classic.ntis.gov/help/order-methods/

ABSTRACT

This report describes an experimental study of physical, chemical, and combustion characteristics of selected North American crude oils, and how these associate with thermal hazard distances resulting from pool fires and fireballs. The emergence of large volumes of tight oils within the North American Transportation system over the last decade coupled with several high-profile train accidents involving crude oils, has raised questions about the role of oil properties in general, and tight oils in particular, in affecting the severity of hazard outcomes in related crude oil fires.

The objective of the pool fire experiments is to measure parameters necessary for hazard evaluation, namely, burn rate, surface emissive power, flame height, and heat flux to an engulfed object. To carry out this objective, a series of 2-m diameter indoor and 5-m diameter outdoor experiments were performed. The objective of the fireball experiments is to measure parameters required for hazard evaluation which include fireball maximum diameter, height at maximum diameter, duration, and surface emissive power using 400-gallons of crude oil per test. The crude oil samples used for the experiments were obtained from several U.S. locations, including "tight" oils from the Bakken region of North Dakota and Permian region of Texas, and a conventionally produced oil from the U.S. Strategic Petroleum Reserve stockpile. These samples spanned a measurable range of vapor pressure ($VPCR_x(T)$) and light ends content representative of U.S. domestic conventional and tight crudes.

The results indicate that all the oils tested here have comparable thermal hazard distances and the measured properties are consistent with other alkane-based hydrocarbon liquids. The similarity of pool fire and fireball burn characteristics pertinent to thermal hazard outcomes of the three oils studied indicate that vapor pressure is not a statistically significant factor in affecting these outcomes. Thus, the results from this work do not support creating a distinction for crude oils based on vapor pressure with regards to these combustion events.

ACKNOWLEDGEMENTS

The authors would like to thank the sponsors of this project which includes the U.S. Department of Energy (US DOE), the U.S. Department of Transportation (US DOT), and Transport Canada.

The authors would like to express deep gratitude to the many people who supported this large project for their substantial efforts in overcoming numerous obstacles and challenges. The technologist team of the Fire Science and Technology department, particularly the test conductors, provided outstanding support. This team included Sylvia Gomez, Brandon Servantes, and Shane Adee who supervised supporting technologists which include Scott Jordan, Randy Foster, Donald McManaway, Dawn Settecerri, Bryan Koenig, Jerry Koenig, Christopher Steele, and Chuck Hanks. Tremendous support was also provided by Rich Ivey and Wes Kuhns on arming and firing operations, and by Venner Saul in the explosive design. Photometric support was provided by Michael Montoya, Ryan Flanagan, and Anthony Tanbakuchi. Video support was provided by Richard Simpson, Mark Olona, and Jason Everett. Test tank design support was provided by Michael Teague and Richard Streit. Sampling operations were conducted by Louis Ory (contracted from Intertek), with additional support from Walt Gill, Kelly Urvanejo, Dann Jernigan, and Liz Carson. Assistance from those involved in environment compliance and safety includes Dennis Peek, Susan Lacy, Rick Anderson, Georgia Fernandez, Stan Laktasic, Kathleen Pass, Ben Martinez, Joanna Eckstein, Anita Reiser, John Kay, Doug Vetter, Penny Avery, Evan Fahy, John Hostak, Robert Griffith, Pasqual Vallejos, and Michael Vigil. The emergency support team included Christopher Mullaney, Margaret Mora, John Ledet, Ricky Romero, Carol Bonney, and the Kirtland Airforce Fire Department. Weather forecasting was provided by Gina Deola. The business support team included Andrae Griffin, Matt Brigance, Tracy Woolever, and Ken Street. The management team comprised Karen Rogers, Erik Webb, Doug Cotter, Carlos Lopez, Nancy Brodsky, Randy Watkins, Steven Samuels, Mary Clare Stoddard, and Tara Olivier.

Finally, the authors greatly appreciate the reviews by the fire subject matter experts Elizabeth Weckman, Ph.D. and Michael Gollner, Ph.D., as well as the sampling and characterization subject matter experts Robert Falkiner, M.Sc. P. Eng and Kesavalu Bagawandoss, Ph.D., J.D.

The contributing roles of the authors have been the following:

Anay Luketa - principal author, investigator, test director, and analyst
Tom Blanchat – initial investigator and test director (retired July 2016)
Dave Lord – project manager and sampling and analysis lead
Alvaro Cruz-Cabrera – lead photometric experimentalist
Joe Hogge – analysis of oil compositional data
Ray Allen – oil operations consultant

CONTENTS

LIST OF FIGURES

LIST OF TABLES

EXECUTIVE SUMMARY

This report describes an experimental study of physical, chemical, and combustion characteristics of selected North American crude oils, and how these associate with thermal hazard distances that may be realized in transportation accidents involving crude oil fires. This report is part of a series describing the Crude Oil Characterization Research Study, which was sponsored by the U.S. Department of Energy, U.S. Department of Transportation, and Transport Canada. Prior reports in this series include a scoping document[1], literature survey[2], and technical report[3] on completed experimental work.

For the current report, series of 2-m and 5-m diameter pool fires and 400-gallon fireballs were conducted using three different crude oils that exhibited measurable differences in physical properties. Two light (gravity ≥ 33°API) "tight" oils from modern unconventional production and one stabilized (degassed) medium (gravity between 28-33°API) sour oil from historical conventional production were tested. One tight oil was obtained from a Bakken terminal in North Dakota (Tight 1 - Bakken), and a second was obtained from a production facility sales point in the Texas Permian that handles tight shale production (Tight 2 - TX Shale). The third oil, the stabilized medium sour conventional (SPR), was obtained from the U.S. Strategic Petroleum Reserve.

Property testing of the oils associated with combustion testing indicated that the samples spanned a measurable range of vapor pressure and light ends content representative of U.S. domestic conventional and tight crudes. Vapor pressure of the test crudes as measured by $VPCR_4$(100°F) ranged from ~4-10 psia for pool fire experiments, and from ~2-10 psia for fireball tests. Mass % of light components in the test crudes ranged from ~2-6% for pool fire experiments and from ~1-6% for fireball tests. Light components quantified in this study included fixed gases N_2, CO_2 and light hydrocarbons from methane through pentane, expressed more succinctly as "mass % < C6" in tables and figures shown herein. The test oils (Tight 1 – Bakken, Tight 2 – TX Shale) that were maintained in closed, pressurized storage over the 1+ year while at the Sandia facility retained light component composition and vapor pressure properties that were consistent with those measured at the time of collection from the supply chain, within the resolution of the analytical methods used here. The test oil (SPR) that was maintained in open, unpressurized storage over the 1+ year while at the Sandia facility experienced gradual decreases in VPCR and light ends content during storage time, consistent with expectations for a slowly "weathering" oil. The final sample of weathered SPR showed nearly 70% reduction in light components and VPCR relative to when it was obtained at the beginning of the project. Properties of each test oil were measured upon loading in the field and then again in close association with each combustion test at Sandia so that fuel properties were well-defined for each specific test.

The main conclusions from this study are the following:

General:

- The similarity of pool fire and fireball burn characteristics pertinent to thermal hazard outcomes of the three oils studied indicate that vapor pressure is not a statistically significant

[1] See https://www.energy.gov/fe/articles/crude-oil-characteristics-research
[2] See https://www.osti.gov/biblio/1177758-literature-survey-crude-oil-properties-relevant-handling-fire-safety-transport
[3] See https://www.osti.gov/biblio/1458999-doe-dot-crude-oil-characterization-research-study-task-test-report-evaluating-crude-oil-sampling-analysis-methods-revision-winter-sampling

factor in affecting these outcomes. Thus, the results from this work do not support creating a distinction for crude oils based on vapor pressure with regards to these combustion events.

- Based on comparison to combustion data from public literature on common liquid fuels (primarily commercial grade propane and butane), the results of this study are considered to be pertinent to crude oils and most hydrocarbon liquids that exceed the vapor pressures of the crude oils tested here.

Pool Fires:

- The experimental results indicate that measured values of surface emissive power and flame height among the oils tested are within 1 % and 24% of each other, respectively, with standard deviation ranges overlapping. The burn rate for the Tight 1 (Bakken) oil is about a factor of 1.5 higher than that for other tested oils.
- The predicted thermal hazard distances are similar among the oils tested for contained pool fires and are within 14% of each other, with standard deviation ranges overlapping. Distances were evaluated using the measured parameters, an integral model, and the injury criterion of 2nd degree burns after 30-second exposure to a radiant heat flux of 5 kW/m^2 for both a 5-m and a 50-m diameter contained pool fire. A 50-m pool diameter is representative of a 114-m^3 (30,000-gallon) release. Predicted thermal hazard distances are for comparison purposes only and not intended to be applied to railcar accidents.
- The predicted thermal hazard distances using the measured parameters and a 2nd degree burn criterion for an uncontained or spreading pool resulting from a 114-m^3 (30,000-gallon) release indicate that the Tight 1 (Bakken) oil results in lower distances compared to the other oils by 16%-27%.
- Historic accidents have demonstrated that hazards can exceed the distances calculated in this work due to damage of numerous railcars leading to significant amounts of oil contributing to a fire which can then propagate to surrounding fuels sources, such as wooden structures, vegetation, and other hydrocarbons.
- The measurements of burn rate, flame height, surface emissive power, and heat flux to an engulfed object are consistent with other alkane-based liquid hydrocarbons for all oils tested.

Fireballs:

- The experimental results indicate that the average surface emissive at maximum power for the two tight oils are about 30% higher than the SPR oil.
- The maximum fireball diameters measured were similar among the three oils (~62-65 m).
- The Tight 1 (Bakken) oil had a 10% lower height at fireball extinction than the other oils.
- The times to fireball extinction were similar among the oils (~10-11 s).
- The predicted thermal hazard distance using the injury criterion of 2nd degree burns after 30-second exposure to a thermal dose level of 240 $(kW/m^2)^{4/3}s$ was evaluated for a 400-gallon release for all oils tested. The results indicate the distances for the tight oils are similar but are about 20-30% higher than the distance predicted for the SPR oil.

- Predicted thermal hazard distances, for a 30,000-gallon release, among the crude oils differ by about 12% with the range of uncertainties overlapping. Thus, the predicted thermal hazard distances among the oils are comparable.
- The observed measurements of diameter, duration, and surface emissive power for the tested crude oils are consistent with experiments performed by other researchers testing similar volumes for propane, butane, gasoline, and diesel as fuels.
- The maximum average surface emissive power for all oils are below the Center for Chemical Process Safety (CCPS) recommendation[4] to use a value of 350 kW/m^2 for thermal hazard evaluation. It is anticipated that the oils will not exceed this value for larger releases. The CCPS is a non-regulatory organization within AIChE that addresses process safety of hazardous materials. They gather input from manufacturers, government agencies, consultants, academia and insurers to provide recommendations on process safety.

[4] *Guidelines for Vapor Cloud Explosion, Pressure Vessel Burst, BLEVE and Flash Fire Hazards* (Center for Process Safety). American Institute of Chemical Engineers, 2011

ACRONYMS AND DEFINITIONS

Abbreviation	Definition
ε	emissivity
ANSI	American National Standards Institute
API	American Petroleum Institute (oil & gas trade association)
ASTM	American Society for Testing and Materials (standards organization)
BKN	Bakken oil
BLEVE	boiling liquid expanding vapor explosion
DHA	detailed hydrocarbon analysis
DFT	directional flame thermometer
EOS	equation of state
FLAME	Fire Laboratory for Accreditation of Models and Experiments
FPA	focal plane array
FPS	frames per second
GPA	Gas Processor's Association (standards organization)
GC	gas chromatograph
InSb	indium antimonide
IR	infrared radiation
LWIR	long wave infrared (7-14 μm)
MWIR	mid wave infrared (3-5 μm)
ND-X	Neutral density filter (X is attenuation by a factor or 10x)
NUC	nonlinear uniformity correction
NV	narrow view
PSV	pressure safety valve
PVT	pressure-volume-temperature
RH	relative humidity

Abbreviation	Definition
RVP	Reid Vapor Pressure
RVPE	Reid Vapor Pressure Equivalent (per ASTM D6377-16 section X1)
SEP	surface emissive power
SNL	Sandia National Laboratories
SPR	Crude oil sample obtained from the Strategic Petroleum Reserve Site
TC	thermocouple
TDU	Thermal dose unit
TTC	Thermal Test Complex
Tx or τ	Transmission
TX Sh	Texas shale oil
UOP	Universal Oil Products (standards organization)
US DOE	U.S. Department of Energy
US DOT	U.S. Department of Transportation
USSPR	U.S. Strategic Petroleum Reserve Program
WV	wide view
VFD	Variable frequency drive (description of pump)
VPCRx	vapor pressure of crude oil at vapor-liquid volume ratio x, ASTM D6377

This page left blank

1. INTRODUCTION

This report describes an experimental study of physical, chemical, and combustion characteristics of selected North American crude oils, and how these associate with thermal hazard distances that may be realized in rail transportation accidents involving crude oil fires. This report is part of a series documenting the Crude Oil Characterization Research Study, which was sponsored by the U.S. Department of Energy, U.S. Department of Transportation, and Transport Canada. The first report in this series [1] outlined the current state of knowledge around crude oil flammability in the context of transportation safety, and identified gaps that needed to be addressed. From there, a sampling & analysis plan [2] was developed to close some of these gaps through scientific study. Two subsequent reports [3, 4] documented findings in what is called Task 2, identifying commercially available crude oil sampling and analysis methods suitable for use in later phases of the study. The current report documents Task 3, which subjected selected crude oils from the North American transportation system to property and combustion analyses under controlled conditions to understand possible relationships and associated hazard potential if these oils caught fire in an accident. An additional research effort, called Task 4 in the abovementioned sampling & analysis plan [2], was proposed to leverage sampling & analysis methods established in Task 2 to gather a comprehensive oil property data set across several crude types, production regions, and supply chain stages.

Task 3 obtained crude oils from different points in the North American transportation system that exhibited distinct, measurable differences in physical properties (vapor pressure, composition, density), and determined how these same oils behaved in controlled pool fire and fireball test configurations, since these are the most likely combustion events resulting from railcar accidents. Of particular interest were differences, if any, between "tight" oils, which represented about half of U.S. production in 2017 [5], and others, to include oils produced from conventional reservoirs. "Tight" oils are produced from relatively impermeable reservoir rock that must be stimulated by hydraulic fracturing to increase permeability to a level that supports oil production rates that are economically feasible. Oils from conventional reservoirs are produced from formations that have the right combination of permeability and fluid characteristics to permit the oil to flow naturally to the wellbore. The emergence of large volumes of tight oils within the North American transportation system over the last decade coupled with several high-profile train accidents involving crude oils, have raised questions about the role of oil properties in affecting the severity of outcomes in related crude oil fires.

1.1. Overview of Test Oils

Three crude oils were tested in Task 3: two light "tight" oils from unconventional production and one stabilized medium sour from conventional production. One tight oil was obtained from a Bakken terminal in North Dakota (Tight 1 - Bakken), and a second was obtained from a production facility sales point in the Texas Permian that handles tight shale production (Tight 2 - TX Shale). The third oil was obtained from the U.S. Strategic Petroleum Reserve (USSPR). The SPR oil was additionally stabilized[5] at the USSPR facility to reduce its vapor pressure to meet U.S. SPR program performance requirements and was also weathered at Sandia during months of unpressurized storage. These crudes were selected to span a measurable range of vapor pressure and light ends content that may be observed among domestic conventional and tight, unconventional crudes.

The range of vapor pressures ($VPCR_4$(100°F) by ASTM-D6377) and light components (mass % < C6 by GPA 2103-M) for the three oils as tested in association with the fireballs, 5-m pool fires, and 2-m

[5] See section F.2.1.2 for additional information on the stabilized SPR sample.

pool fires are given in Table 1-1. The Bakken exhibited both the highest $VPCR_4$ and Mass% < C6 among the three samples, with the TX Shale in the middle, and the SPR lowest. Additional detail on sample acquisition and property analysis is given in the appendices to this report.

Table 1-1. Average vapor pressures and < C6 content for crude oil samples tested.

Oil Type	$VPCR_4$(100°F), psia	< C6 Content, mass%
Fireballs		
Tight 1 (Bakken)	9.6 ± 0.6	6.21 ± 0.04
Tight 2 (TX Shale)	7.8 ± 0.6	4.20 ± 0.05
SPR	1.9 ± 0.6	1.40 ± 0.02
5-m Diameter Pool Fires		
Tight 1 (Bakken)	10.2 ± 0.6	5.99 [1]
Tight 2 (TX Shale)	8.5 ± 0.6	4.03 ± 0.07
SPR	3.6 ± 0.6	2.07 [1]
SPR-hot	4.6 ± 0.6	3.09 [1]
2-m Diameter Pool Fires		
SPR-hot	4.9 ± 0.6	3.18
SPR-cold	5.7 ± 0.6	3.70 [1]

[1] Insufficient data to estimate the uncertainty

An important feature of the test series is maintaining the composition and volatility characteristics representative of the of the oil as obtained from the supply chain by taking care to fully purge air from all sampling and storage systems. Allowing the oil samples uncontrolled exposure to the atmosphere during loading, transport, and storage over the months required to complete the testing would have resulted in a convergence to a very stable, weathered state that (i) may not represent the properties applicable to hydrocarbon fluids that are loaded into railcars or pipelines on their way from the production facility to the refinery, and (ii) possibly result in small or indistinct differences in properties, particularly vapor pressure, among test fluids that were once distinct when they entered the transportation supply chain. Additional care was taken to assure that only single-phase liquid oil was loaded into and out of the Sandia tankers. To achieve this, the system pressure was maintained at least 20 psi above the bubblepoint pressure of the oil, at system temperature, during all fuel transfer processes. This extra care in handling contrasts with typical pool fire testing in which the fuel is simply pumped from a tank into a pan, with no concern of the above requirements. The SPR oil was handled differently than the tight oils; it was transported and maintained in a standard unpressurized crude oil hauler for a combination of logistical and technical reasons that are described in the appendix. The end result was that the SPR source oil started at a lower vapor pressure than the tight oils and was further allowed to "weather" during the testing sequence. The SPR oil thus served as the low vapor pressure end-member while the two tight oils served as the higher vapor pressure samples of the test oil set.

1.2. Pool Fire Testing

The objective of the pool fire tests is to compare combustion characteristics with regards to burn rate, surface emissive power, flame height, and heat flux to an engulfed object. These parameters are

necessary for hazard evaluation. Two indoor tests with a pool diameter of 2-m and four outdoor tests with a pool diameter of 5-m were conducted. Since most accident scenarios result in pool diameters on the order of 10s of meters, a pool diameter of 5-m should be on the lower bound of accident scenario scales. As will be explained in section 3.1.2, obtaining combustion parameters from a 5-m pool will provide for conservative estimates of thermal hazard distances. Further discussion of hazard distances in the context of accident scenarios are also discussed in this section.

The test matrix for the pool fire tests is provided in Table 1-2. Data acquisition instrumentation is provided in Table 1-3 and includes radiometers, cameras, gas samplers, liquid level sensors, and thick wall calorimeters.

Table 1-2: Pool Fire Test Matrix

2-m diameter pool fires*		
Test	**Fuel Temperature, °C**	**Oil Description**
1	6.9 ± 0.4	SPR
2	59.5 ± 4.5	SPR
5-m diameter pool fires*		
Test	**Fuel Temperature, °C**	**Oil Description**
3	54 ± 2.7	SPR
4	27 ± 0.0	SPR
5	22 ± 2.7	Tight 1 (Bakken)
6	20 ± 1.1	Tight 2 (Tx Shale)

*For both 2-m and 5-m pools, a Jet-A fuel test was performed for system checks

Table 1-3: Pool Fire Instrumentation

Parameter	**Method**
Plume surface emissive power	Spectral imaging radiometer
Heat flux to engulfed objects	Thick wall calorimeter with inverse analysis
Burn rate	Flow meter/constant level
Flame height	Video image analysis
Heat release rate*	Oxygen consumption calorimetry

*2-m pool diameters only.

1.3. Fireball Testing

The objective of the fireball tests is to compare parameters required for hazard evaluation which include fireball maximum diameter, height at maximum diameter, duration, and surface emissive power. The experiments involved creating fireballs by releasing and igniting the oil as a vapor/atomized mixture from a heated, pressurized 1000-gallon vessel, containing 400-gallons of oil. The thermodynamic state was chosen to maximize the probability that the entire mass of the oil contributes to the fireball. To facilitate the design of the vessel and ensure quality data, a preliminary set of experiments with a smaller 100-gallon vessel was initially performed. The pressure vessel was designed to 1) allow control of the oil's temperature and pressure, 2) prevent air contact within the vessel, and 3) control time of release. The test matrix for the fireball tests is provided in Table 1-4. Measurements include fireball diameter, height, duration, external heat flux, and surface emissive power. Data acquisition instrumentation is provided in Table 1-5.

Table 1-4: Fireball Test Matrix

Test	Vessel Size* (gallons)	Oil Description
1	100	Water
2	100	50/50 mix Jet-A and gasoline
3	100	Jet-A
4	1000	Tight 1 (Bakken)
5	1000	Tight 2 (Tx Shale)
6	1000	SPR

*40 gallons and 400 gallons of oil released from 100-gallon and 1000-gallon tanks, respectively.

Table 1-5: Fireball Test Instrumentation

Parameter	Method
Plume surface emissive power	Spectral imaging radiometers
Heat flux to nearby objects	Narrow and wide-angle radiometers
Fireball geometry and duration	Spectral imaging radiometers

As shown in Table 1-6, approximately 3,900 gallons of oil was required for the tests. Because it is necessary to provide each burn test with oil that has the same properties exhibited when the oil was loaded at the acquisition site, each large sample was collected and maintained at "sample source pressure", with exception of the SPR oil, to prevent any losses of light ends. To ensure consistent oil quality during the time between sample acquisition and burn testing, analytical samples were collected at the sample source during tanker truck loading, and again from the storage container just prior to a test suite. The same test methods and conditions were used to ensure consistent oil quality.

Table 1-6: Gallons of crude oil required for tests

Test Description	Gallons per Test	Number of Tests	Total Gallons
2-meter pool fire	150	2	300
5-meter pool fire	600	4	2,400
400-gallon fireball	400	3	1,200
Total – all tests		9	3,900*

*Three different crude oils make up this total.

Note that the original test matrix for the pool fires included performing small and large-scale tests for all oils. Since oil contained within a rail car experiences seasonal changes in temperature, the pool fires included testing all oils at two different fuel feed temperatures. However, testing with 2-m and 5-m pool fires using the SPR oil revealed that fuel feed temperature doesn't significantly affect pertinent combustion properties. The small-scale 2-m pool fire tests were not conducted for all oils since they were used as scoping tests. Thus, tests involving temperature variation for the remaining oils were not performed. The original fireball test matrix included conducting small and large-scale tests for all oils, however, it was decided that the small-scale tests were not necessary for all the oils, rather they were used as scoping tests for proof of concept for the large-scale tests.

Description of the testing facilities, as well as details regarding test infrastructure, measurements, instrumentation, test procedures, crude oil procurement, and test descriptions are provided in the appendices. The following sections provide a summary of experimental results and discussion thereof, with a focus on hazard analysis and comparison to other fuels.

2. SUMMARY OF EXPERIMENTAL RESULTS

2.1. Pool Fires

Table 2-1 provides a summary of the results for the pool fire experiments. Averages were determined from data that displayed a steady-state. Table 2-2 provides averaged atmospheric conditions during the 5-m diameter pool fire experiments.

Table 2-1: Summary of results for pool fire experiments

Oil	Fuel Supply Temperature (°C)	Average Burn rate (mm/min)	Average Flame Height (m)	Average Surface Emissive Power (kW/m^2)	Average heat flux to calorimeter (kW/m^2)
2-m diameter indoor pool fires					
SPR	6.9 ±0.35	2.12 ±0.01	5.0 ±2.0	47.4 ±17.7*	74.3 ±2.6
SPR	59.5 ±4.5	1.95 ±0.02	2.9 ±1.6**	48.1 ±13.7*	103.2 ±5.9***
5-m diameter outdoor pool fires					
SPR	54 ±2.7	3.0 ±0.5	5.6 ±3.1	na†	89.6 ±34.4
SPR	27 ±0.0	2.7 ±0.1	4.9 ±3.1	78.2 ±13.4	90.0 ±33.8
Tight 1 (Bakken)	22 ±2.7	4.6 ±0.1	4.5 ±3.9	77.4 ±12.7	70.5 ±25.8
Tight 2 (Tx Shale)	20 ±1.1	2.7 ±0.3††	5.5 ±3.9	77.2 ±9.9	78.3 ±18.0

*from narrow-angle radiometers with focal diameter of about 0.8 m

** pan lip increased from 4" to 12" (see section A.1.2.5)

*** averaged over all thermocouples and over time. Calorimeter was about 0.5" lower in elevation within flame for the 'hot' fuel test.

†IR cameras not used for this test

††estimated (see section A.2.4.7)

Table 2-2: Atmospheric conditions for 5-m diameter pool fire experiments

Oil	Average wind speed (m/s) (mph)	Average wind direction (deg)	Average temperature (°C)	Average relative humidity (%)
SPR	1.5 (3.3)	121	5.6	34
SPR	2.7 (6.1)	229	19.4	53
Tight 1 (Bakken)	3.6 (8.1)	204	13.3	20
Tight 2 (Tx Shale)	3.1 (7.0)	280	7.5	36

Figure 2-1 through Figure 2-3 provide the measured average surface emissive power versus $VPCR_{0.2}$(100°F), $VPCR_4$(100°F) (psia) and mass% of whole oil <C6 content for both the 2-m and 5-m diameter pool fire tests, respectively. $VPCR_{0.2}$ and $VPCR_4$ are both measures of equilibrium crude oil vapor pressure (absolute) at 100°F by standard method ASTM D6377. The subscripts 0.2 and 4 represent vapor to liquid volume ratio, so that the V/L = 0.2 system has a much smaller ($1/20^{th}$) vapor space than the V/L = 4.0 system for the same starting liquid volume. V/L is important to vapor pressure of a multicomponent fluid like crude oil because lighter components will preferentially partition into the vapor space, leaving higher concentrations of heavier components in the liquid phase. This effect increases as vapor volume over a given liquid volume is increased. Hence, higher V/L conditions for a starting liquid oil lead to lower VPCR at a given temperature. Practical applications of VPCR for transportation often see V/L lower than measured here (1% is referenced

in ANSI/API [6]). Previous work under the Crude Oil Characterization Research Study [4] was unable to generate reproducible measures of ASTM D6377 $VPCR_x(100°F)$ for vapor/liquid ratios V/L = 0.02 and 0.05. Reasonable agreement was found in the same report between ASTM D6377 $VPCR_{0.2}$ and the bubble point pressure for crude oils as determined by the baseline vapor pressure measurement system used for managing vapor pressure for the U.S. Strategic Petroleum Reserve stockpile. As such, V/L = 0.2 is presented here as a representative measure of crude oil bubble point pressure and the lowest measurable V/L that the authors could validate against another measurement method. The caveat of using $VPCR_{0.2}$ is that the measurement uncertainty is larger than for $VPCR_4$ so that confidence level is not as high that the oil property values (independent variable) are significantly different (i.e., error bars overlap) when relating to the burn properties (dependent variable). VPCR at both V/L = 0.2 and 4.0 are presented here. The average surface emissive power is not affected by wind conditions and thus is provided here for conciseness since it does not require additional discussion for interpretation of the results. As Figure 2-1 through Figure 2-3 indicate, average surface emissive power for a given pool fire diameter (2 m or 5 m) was nearly constant for all three oils, so no variation with oil properties $VPCR_{0.2}$, $VPCR_4$, or mass% whole oil < C6 was observed for the crude oils tested here. Additional parameters provided in Appendix G are plotted as a function of $VPCR_{0.2}(100°F)$ (psia), $VPCR_4(100°F)$ (psia), API gravity, content <C6 (wt%), and heat of combustion (MJ/kg). Some additional context for where these properties sit in a larger view of the U.S. supply are given in Appendix F, where the test oils used here are compared to lower 48 US production on the basis of API gravity (see section F.3.2) and $VPCR_x(100°F)$ (see section F.4.2).

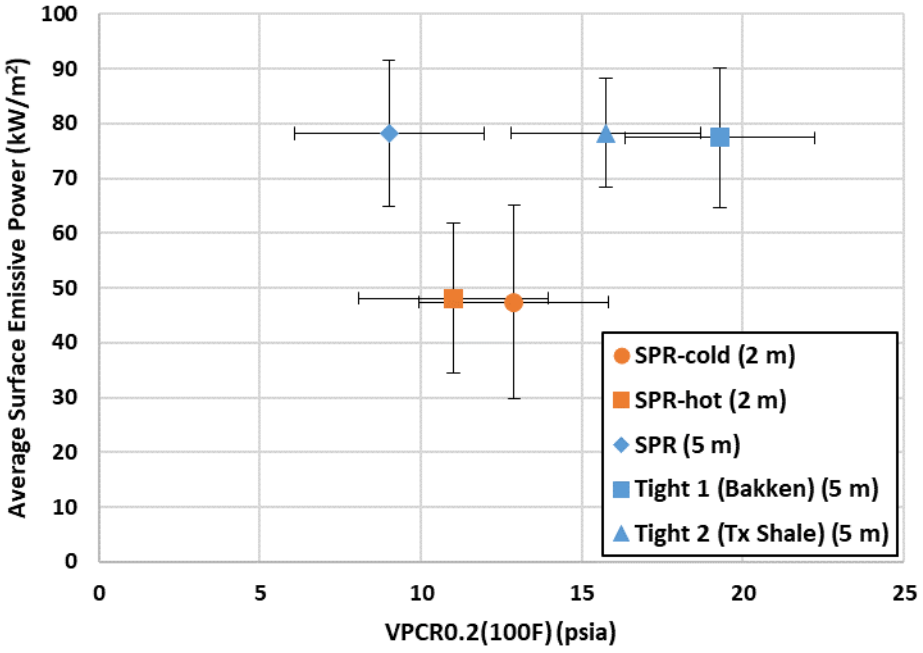

Figure 2-1. $VPCR_{0.2}(100°F)$ (psia) vs. average surface emissive power for the pool fire tests.

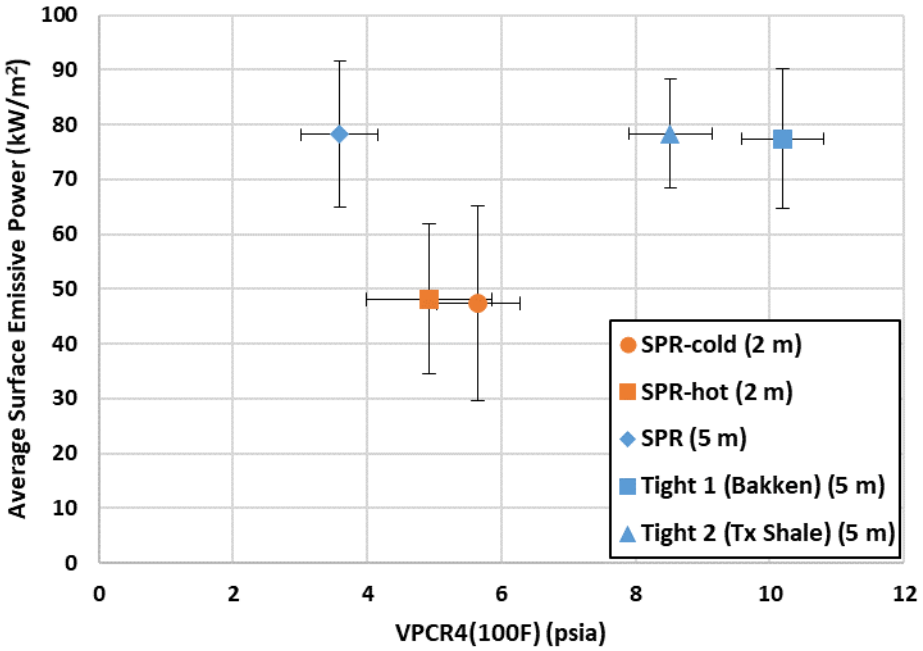

Figure 2-2. $VPCR_4$(100°F) (psia) vs. average surface emissive power for the pool fire tests.

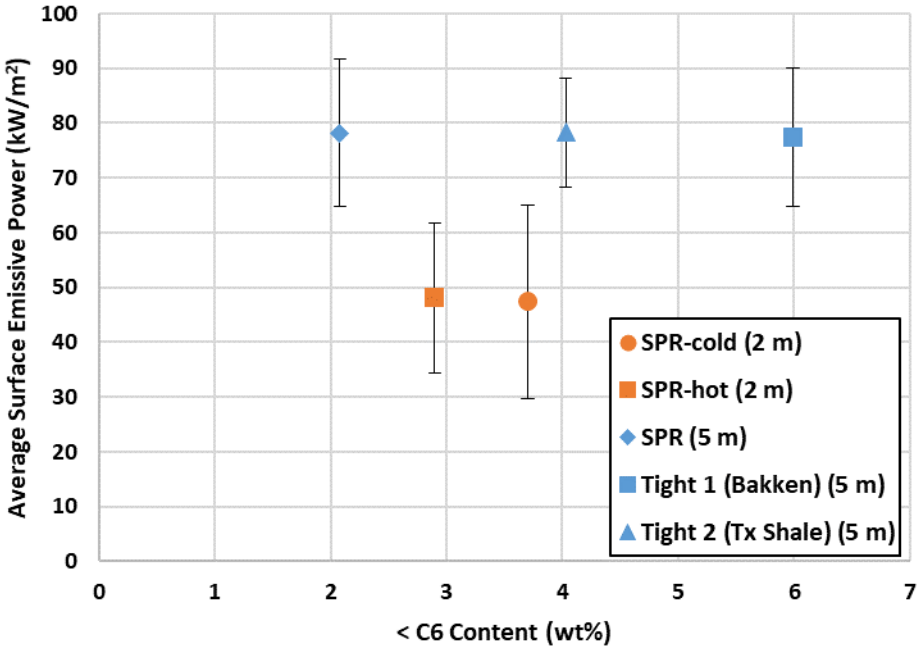

Figure 2-3. <C6 content (mass%) vs. average surface emissive power for the pool fire tests.

2.2. Fireballs

Table 2-3 and Table 2-4 provide a summary of results and conditions for the fireball experiments, respectively.

Table 2-3: Summary of results for fireball experiments.

Fuel	Mass (kg)	Diameter* (m)	Height*† (m)	Duration** (s)	Average Surface Emissive Power*** (kW/m^2)	Maximum Power**† (MW)	Energy**† (MJ)
Jet-A	116	23 ±1	15 ±1	3.2 ±0.2	287 ±17	117 ±14	162 ±19
Tight 1 (Bakken)	1229	58 ±4	55 ±4	10.0 ±1	293 ±22	764 ±119	1823 ±285
Tight 2 (Tx Shale)	1269	54 ±4	52 ±4	10.0 ±1	295 ±22	686 ±107	1515 ±236
SPR	1303	61 ±4	81 ±5	11.0 ±1	225 ±14	665 ±82	1491 ±184

*effective diameter based on projected area measurements at time of maximum power

*† distance from ground to fireball center at time of maximum power

**time until visible thermal radiation ceases

***spatially averaged and at time of maximum power

**† average of X6900 IR cameras over 3.3 seconds

Table 2-4: Conditions of fireball experiments

Fuel	Release Pressure (psig)	Release Temperature (°C)	Wind Speed (m/s)	Wind direction
Jet-A	275	370	<2	East
Tight 1 (Bakken)	250	275	<1.3	Calm
Tight 2 (Tx Shale)	250	300	2	South-east
SPR	168	293	<1.3	Calm

Figure 2-4 through Figure 2-6 present the measured average surface emissive at maximum power versus oil properties $VPCR_{0.2}$ (100°F), $VPCR_4$(100°F) (psia) and whole oil mass % <C6 content for the fireball tests, respectively. The average surface emissive power at maximum power for the higher vapor pressure and light ends content tight oils was about 30% greater than for the lower vapor pressure SPR oil. Implications of these differences are discussed in detail in Section 3. Additional parameters provided in Appendix G are plotted as a function of $VPCR_{0.2}$(100°F) (psia), $VPCR_4$(100°F) (psia), API gravity, content <C6 (wt%), and heat of combustion.

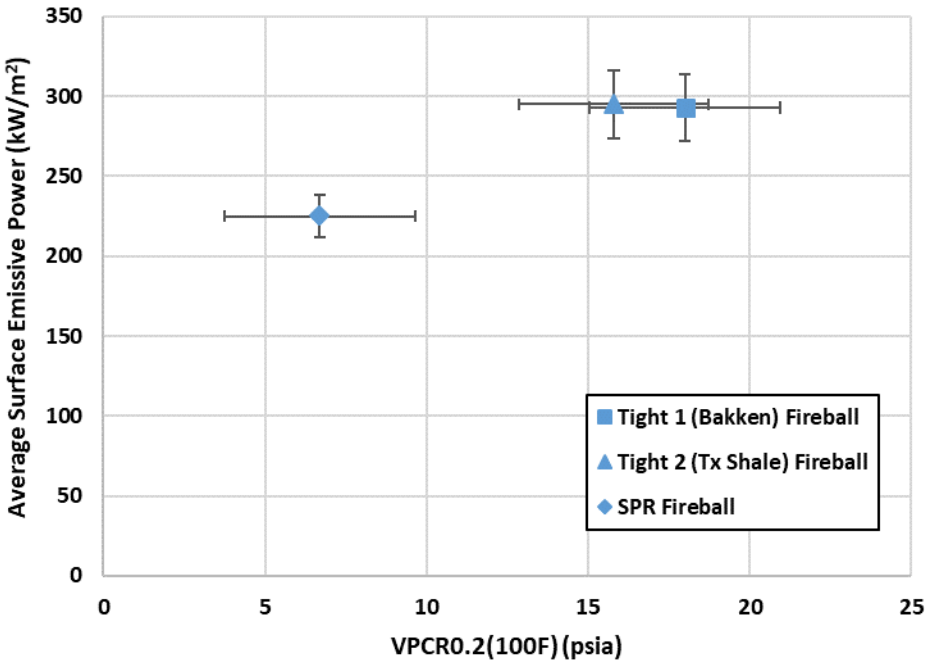

Figure 2-4. $VPCR_{0.2}$(100°F) (psia) vs. average surface emissive power at maximum power, fireball tests.

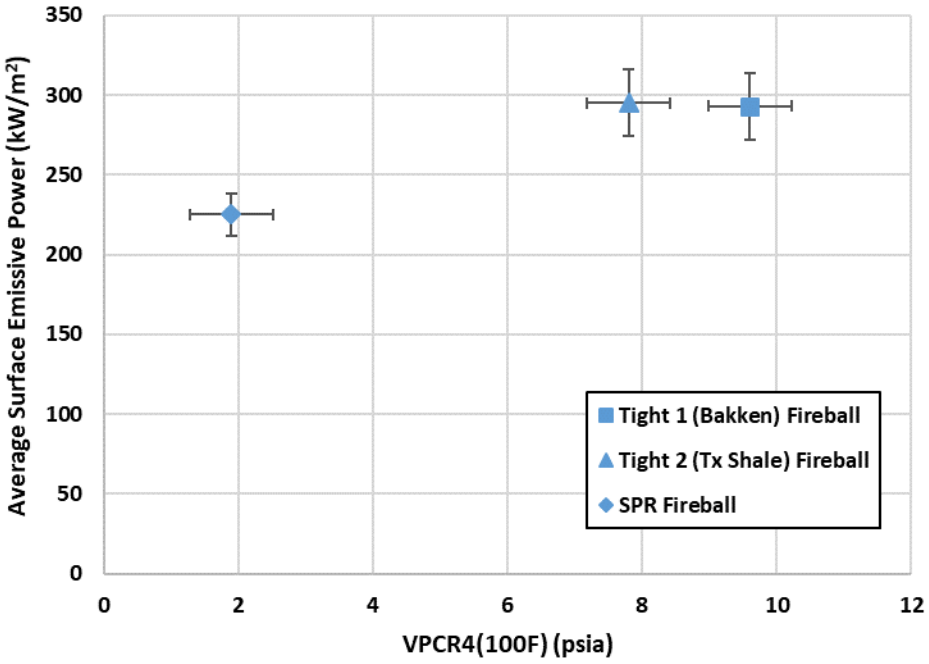

Figure 2-5. $VPCR_4$(100°F) (psia), vs. average surface emissive power at maximum power, fireball tests.

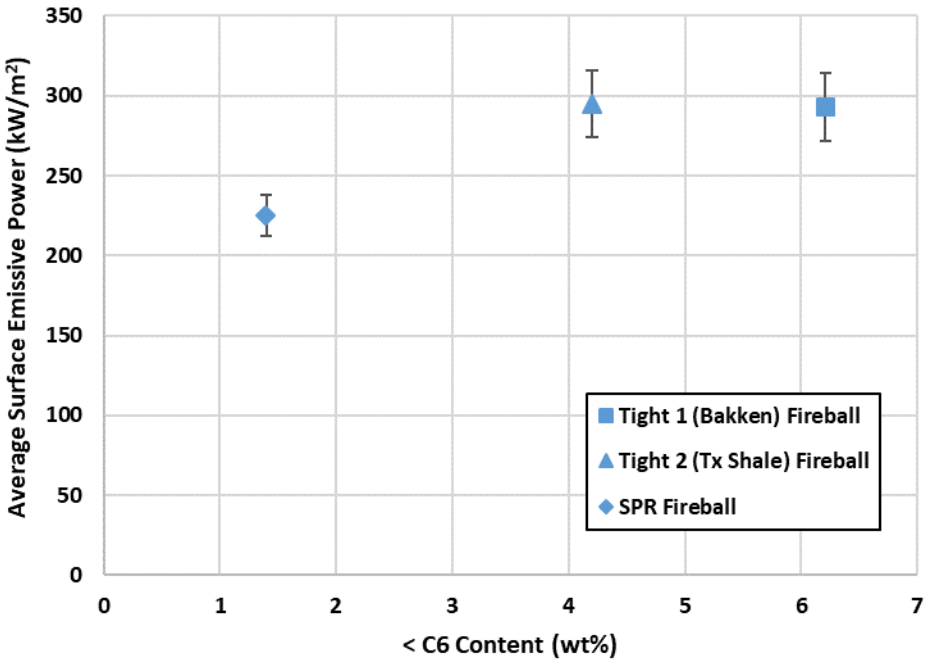

Figure 2-6. <C6 content (mass%) vs. average surface emissive power at maximum power, fireball tests.

3. COMPARATIVE EVALUATION

The following presents a comparison of thermal hazard distances among the oils using the collected data, along with discussion of the input parameters, a description of the model used for the evaluation, and the results and discussion of this comparison. Also provided is discussion of how the experimental results compare to other hydrocarbons and implications to thermal hazard distances. Following this, fireballs are similarly addressed, with comparison of thermal hazards distances, comparison to other fuels, and discussion thereof.

3.1. Pool Fires

Thermal hazard distances demark regions of thermal injury and damage from radiant heat exposure from a fire. Before presenting comparative results of the thermal hazard distances for pool fires, discussion of the parameters is warranted for contextual understanding. Since these tests were conducted in the outdoors, the effect of atmospheric conditions will be discussed first, followed by discussion of the parameters.

The atmospheric quantities that affect thermal hazard distances are wind speed, wind direction, temperature, and humidity. Wind affects a pool fire in many ways. Wind-driven pool fires will tilt in the downward wind direction, and the base dimension of the flame will extend in the downwind dimension, also termed flame drag, while the upwind and crosswind dimensions remain relatively unchanged. The extent of drag depends on the pan lip height above the fuel surface where increasing pan height results in reduced drag. The effect of flame tilt and drag is to create an elliptical pool which can result in either increasing or decreasing the thermal hazard distances in the downwind direction depending upon the degree of tilt and the distance from the fire. Also, the angle of the wind is important with regards to impacting downwind infrastructure if it results in flame impingement.

Wind can also alter the burn rate, with increasing wind speeds tending to result in increasing burn rates. Figure 3-1 shows data collected at SNL for jet fuel (JP-8) pool fires indicating the potential impact of wind speed on the burn rate. If the wind speed reaches a sufficiently high level, it can lead to extinguishment where the time scale of chemical reaction cannot keep up with the mixing time scale of the fuel and oxidant. Note that the effect of wind as a function of fuel type and pool diameter has not been fully mapped. Thus, a universal correlation or comprehensive database of correlations does not currently exist in the fire science community.

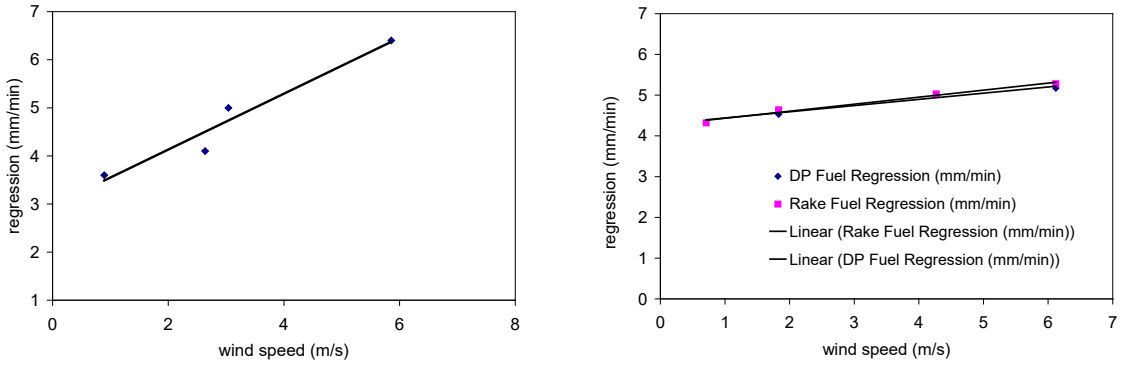

Figure 3-1: Regression rates as a function of wind speed for: (left) 18.9 m JP-8 pool fire, 4000 gallons, China Lake [7] and (right) 7.9 m JP-8 pool fire, 2200 gallons, SNL[8].

In addition to affecting burn rate, wind speed can affect flame height. Based on empirically derived correlations, the flame height can be reduced by up to half from quiescent conditions depending on pool size and wind speed.

Other atmospheric factors include atmospheric temperature and humidity which can affect thermal hazard distances by means of the transmissivity which is a measure of the attenuation of radiation by absorption and scattering through the atmosphere. The transmissivity will decrease with increasing levels of relative humidity and atmospheric temperature. As illustration of this,

Figure 3-2 shows the difference in transmissivity between two extreme temperature and relative humidity conditions using a formula developed by Wayne [9]. The temperature and relative humidity condition of 269 K (25°F) and 10% provides transmissivity values that are from 20% to 60% higher along the path length compared to a condition with a temperature of 310 K (98°F) and 100% relative humidity. Thus, the lower temperature and relative humidity condition will result in greater thermal hazard distances.

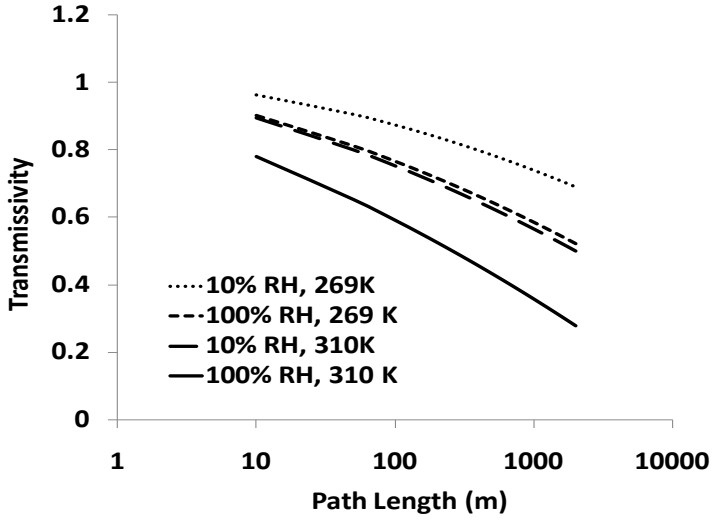

Figure 3-2: Effect of relative humidity and temperature variation on transmissivity.

Additional factors that affect thermal hazard distances include the parameters of flame height, burn rate, flame emissivity, and surface emissive power. Time-averaged flame height or length is usually defined as the distance at which the visible flame intermittency reaches a value of 0.5, while maximum height or length is defined at an intermittency level of 0.05. Intermittency is defined as the fraction of time the flame is at a certain height or length. The flame height, H, or in the case of tilted fires, flame length, L, is a function of the burn rate, where higher burn rates result in an increase in flame height or length. The flame height affects the view factor which determines how much radiative flux an object receives, so is directly related to thermal hazard. Thus, an increase in flame height will increase the view factor and will result in an increase in the heat flux to an object, thereby increasing the thermal hazard distances. Note that comparison of flame height data among different researchers is difficult due to differences in flame height definition, outdoor conditions, and instrumentation [10].

Flame height is also a function of pool shape as demonstrated from trench fire data [11, 12]. Trench fires are pool fires that are rectangular with the longest dimension a factor of four or more greater

than the shorter dimension. The flame height is on the order of the shortest dimension of the pool, thus a very narrow trench fire provides a much lower flame height to diameter ratio than a circular pool of equivalent area. The difference could be an order of magnitude depending on the area and trench dimensions.

The burn rate affects thermal hazard distances not only through the flame height, but also by altering the size of an unconstrained or spreading pool where higher burn rates result in smaller pools and lower burn rates in larger pools. While an increase in burn rate for uncontained pools will tend to reduce hazard distances by the reduction in pool diameter, the associated increase in flame height will tend to increase hazard distances. The competing effect that dominates will depend upon the diameter of the fire. If the pool is contained, an increase in burn rate will result in greater flame heights without any change in the pool size, thus thermal hazard distances will increase by a relative amount that is dependent on the fuel and pool size. For uncontained or spreading pools, the burn rate is also affected by the spill rate, substrate characteristics such as thermal properties, porosity, and topography, and fuel properties such as surface tension. A comprehensive quantification and understanding of how these parameters affect the burn rate and pool geometry is an area of active research, thus universal correlations are not available.

Pool burning is also affected by boil-over which can occur when water is present at the bottom of the pool. In this instance, a high-temperature region, also termed "hot zone", develops through the fuel depth and reaches the fuel-water interface. If the temperature of this region is sufficient to vaporize water, steam will expand through the fuel layer resulting in fuel ejection and a rapid increase in the intensity and size of the fire. This can lead to fire propagation to nearby structures and to heightened endangerment of emergency personnel. Typically, fuels that have components which span a range of boiling points will result in boil-over [13]. Convective currents which induce mixing are believed to be the cause of the propagation of the hot zone which can be described as follows [14]. At the burning fuel surface, a thin layer of fuel is initially heated by conduction and partially by radiative absorption from the heat transferred from the flame to the fuel surface. Within this layer, lower boiling point components vaporize before the higher boiling point components which creates an upward motion of lower density components and downward motion of higher density components, thereby creating a convective current. As this layer becomes mixed and the temperature uniform, the heat is progressively propagated by conduction to the adjacent layer of un-distilled fuel, which in turn leads to convective currents and hence mixing and temperature uniformity. Due to temperature uniformity, the fuel feed temperature does not affect the burn rate for fuels that display this behavior. This process continues until the hot zone reaches the water interface. A boil-over event, though short in duration, can be extremely dangerous to emergency responders due to enhanced fire size and intensity and potential for spread.

Parameters encompassing radiative properties include the emissivity and surface emissive power. If a fire is optically thick, the flame emissivity will be approximately equal to one. For most heavy hydrocarbons, fires greater than about 3 m in diameter will emit thermal radiation from the outer surface of the flame envelope originating at a layer near the surface and not within the flame's interior. This criterion defines the condition for a fire to be considered optically thick. Optically thin fires will have radiation emitted from the interior from product gases, mainly water and carbon dioxide. For optically thin fires, the flame is considered transparent. However, for optically thick fires, the local soot production becomes saturated to the point that local radiation emission is absorbed within the flame envelope except within a relatively thin layer at the plumes surface.

For optically thick fires, the surface emissive power (SEP), which is the energy emitted per unit time per unit area, is a function of the surface area of the flame and not the volume as for optically thin

fires which have lower SEP values due to the predominance of gas band radiation. For increasing diameters, the combustion process becomes increasingly incomplete due to radiative losses and limited oxygen supply with the result that increasing levels of soot and smoke are produced. Soot particles at temperatures above ~600°C are responsible for the luminosity of the fire. If they are not oxidized within the flame, they will escape the flame envelope and cool and become part of the smoke from the fire. Smoke is made up of a mixture of gases, condensable aerosols, and particulate matter from a fire. Carbon particulates, or soot, is included as a particulate matter of smoke and is the black clouds often seen around fires. A sufficient layer of black smoke will absorb a sizable portion of the radiation emitted from the flame, resulting in a much lower emission to the surroundings and hence reduced thermal hazard distances. Large hydrocarbon fires on the order of 10's of meters or greater will generate copious quantities of smoke. A relatively small portion of the flame will be persistently visible near the base of the fire, with the rest shrouded in black smoke. Thus, with increasing pool diameter the average SEP over the flame will first increase with increasing fire diameter due to reaching the optically thick limit and then decrease with further increases in fire diameter due to the increasing smoke layer coverage [15].

Wind can also affect both the dynamics of the fire plume and the level of smoke shielding. In wind conditions, the structure of the plume can change by the creation of fire whirls which can occur in pool fires such as burning of a crude oil spill on water [16]. The structure of fire whirls consists of an upward convective current generated by the fire and a swirling motion (vortex) generated via interaction of the ascending hot plume with ambient air. Fire whirls are affected by local wind shear as well as the local topography. In addition to the capability of altering flame structure, wind can result in local areas of smoke removal with or without the occurrence of fire whirls. Such effects have been observed in fire whirls produced by JP4 and JP8 fuel fires in the presence of wind [17]. As shown in Figure 3-3, experiments with an 18.9 m JP-8 pool fire in a 2-4 m/s wind have demonstrated that fire whirls will occur at the downwind edge of the fire plume, resulting in removal of smoke and allowing luminous zones to be exposed [17]. These tests indicate that the formation of these vortex structures occur at regular intervals and are roughly half a diameter in extent. They can occur in pairs or alternate from side to side. This effect will change the surface emissive power not only by the removal of smoke, but also due to the increased surface emissive power associated with fire whirls [18]. Due to the high combustion rates in these vortices very high spot SEP values occur.

Figure 3-3: Fire whirls forming on the downwind edge of an 18.9 m JP-8 pool fire in a 2-4 m/s wind [17].

For an object engulfed in a fire there is no smoke blockage effect and heat flux to the object can vary from 100 kW/m^2 to 400 kW/m^2 depending on the environment. Based on several experiments conducted at Sandia, typical heat flux values of around 150 kW/m^2 have been measured for JP-8 under quiescent conditions [19, 20]. However, in wind conditions heat fluxes of up to 400 kW/m^2 can be attained on the downwind surfaces of engulfed objects [7, 21, 22]. The heat flux is also affected by pool size. For increasing diameters, as the amount of smoke covering the flame envelope increases it will tend to increase interior flame temperatures due to the absorption of thermal radiation. Thus, an engulfed object will be subject to higher heat fluxes.

3.1.1. Comparison of thermal hazard distances

The thermal hazard created by a pool fire is the heat transferred to nearby objects and populations potentially causing thermal damage. The heat transferred is typically expressed in terms of a flux, that is heat per unit time per unit area since thermal damage is a function of heat flux and the duration of exposure. Thus, a thermal hazard assessment involves using a model to predict heat flux as a function of distance external to the fire and assessing the duration of the fire.

The comparison of thermal hazards distances among the crude oils tested is carried out using an integral model [23]. Integral models require the pool size and shape, burn rate, surface emissive power, flame emissivity, atmospheric quantities such as wind speed and direction, temperature, and humidity as parameter inputs. An integral model represents the surface of a circular pool fire with a simple, usually cylindrical, geometry as shown in Figure 3-4. The radiative heat flux as a function of distance is determined from the equation, $q'' = EF\varepsilon\tau$. The thermal radiation, E, is uniformly emitted from the model surface and is the average surface emissive power (SEP). For an assumed geometry, the geometric view factor, F, which is the fraction of radiant energy from the fire that is received by a target object's field of view, can be determined exactly. The flame emissivity, ε, ranges from values of 0 to 1 and approaches 1 for optically thick fires. The transmissivity, τ, ranging from values of 0 to 1 is the degree of atmospheric attenuation due principally to H_2O and CO_2. To capture the tilting of the flame due to wind, a tilted cylindrical flame shape is used. Flame length, tilt and drag necessary to determine flame shape and view factors are based upon empirical correlations.

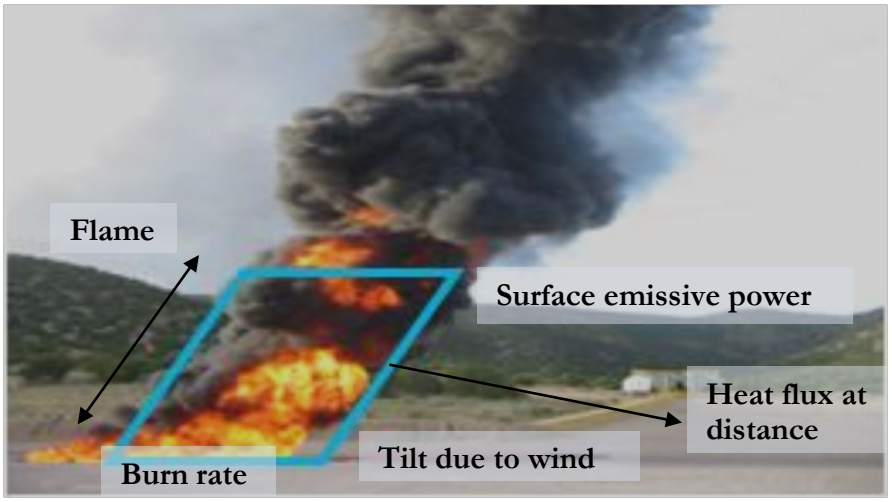

Figure 3-4: Tilted cylinder representation using solid flame model.

For the comparison, the pool fire is modeled as a cylinder for a quiescent condition and a tilted cylinder for a wind condition. A description of the view factor equations can be found in reference [23]. The experimental measurements of burn rate and surface emissive power are used. Based on the size of the pool and the fuel type, an emissivity value of one is assumed. For flame length and tilt angle, correlations [24] are used rather than measurement because the tests did not have the same atmospheric conditions. This correlation is considered conservative since it tends to overpredict the average flame height which is preferable to one that under predicts [25]. To have fair comparison, similar atmospheric conditions are used. For transmissivity, the formula developed by Wayne [9] assuming an atmospheric temperature of 20°C and humidity of 50% is used for all oils. The combustion parameters in Table 3-1 are used for the comparison and are based on the measurements.

Table 3-1: Combustion parameters.

Fuel	Density (kg/m^3)	Mass burning rate (kg/m^2s)	Net heat of combustion (MJ/kg)	Average SEP (kW/m^2)
Tight 1 (Bakken)	811.4	0.062	48.5	77.4
Tight 2 (Tx Shale)	837.3	0.038	44.7	77.2
SPR	860.2	0.041	43.2	78.2

Note that the net heat of combustion for alkane fuels are typically between 40 to 50 MJ/kg as shown in Table 3-2. The values for the crude oils tested in this study are also provided and are similar to other alkanes. The values for alcohols are lower and typically range between 30 to 40 MJ/kg.

Table 3-2: Net heat of combustion for various alkane fuels [26]

Fuel	Net Heat of combustion (MJ/kg)
Benzene	39.9
n-Decane	44.2
Ethane	47.2
n-Heptane	44.4
n-Hexane	44.7
Kerosene	43.1
Methane	50.0
n-Octane	44.8
n-Pentane	45.3
Propane	46.3
Gasoline (73 octane)	44.1
Jet-A	42.8
SPR*	43.2
Tight 1(Bakken)*	48.5
Tight 2 (Tx Shale)*	44.7

*property measured in the current work

The metric for the comparison of thermal hazard distance is the distance away from the center of the fire at which a heat flux level of 5 kW/m^2 is reached. This level is commonly used as a criterion to specify exclusion zones for emergency personnel [27]. For reference, this heat flux level causes 2nd degree burns to bare skin after about 30 seconds of exposure [28]. Effects on people from exposure

to different levels of radiant heat flux is provided in Table 3-3. Damage to structures and some materials after 30 minutes exposure to different heat flux levels is provided in Table 3-4.

Table 3-3: Effect on people from exposure to different levels of radiant heat flux [28].

Radiant heat flux (kW/m^2)	Pain or Injury
1.0	No harm – solar constant on a summer day.
2.1	Pain after 1 minute.
5	Pain after 10 s. 1st degree burn after 20 s. 2nd degree burn after 30 s exposure to bare skin.
10	2nd degree burns after 20 s.
30	3rd degree burns to bare skin and 50% lethality after 30 seconds exposure.

Table 3-4: Damage to structures and materials from radiant heat flux [29].

Radiant heat flux (kW/m^2)	Damage after 30 minutes
12.5 -15	Piloted ignition of wood
18 - 20	Cable insulation degrades
25 - 32	Unpiloted ignition of wood. Steel deformation.
35 - 37.5	Process equipment and structural damage
100	Steel structure collapse

Two pool diameters were evaluated, namely 5 m and 50 m, to compare results as a function of size. In addition to pool size, different wind speeds were also considered for contained and uncontained pools. The results for 5 m and 50 m pool fires subject to different wind speeds are shown in Table 3-5, Figure 3-5, and Figure 3-6 for non-spreading pools and Table 3-6, Figure 3-7, and Figure 3-8 for spreading pools. A non-spreading pool pertains to situations in which the fuel spilled is physically bounded such as in an impoundment. Wind speed is included because as previously noted it can affect flame length and tilt and thus will impact thermal hazard distances.

The variation in the distances were determined using the range of measured values for burn rate and surface emissive power for both the 5-m and 50-m pools. The justification for using the measured values for the 50-m pool fire predictions is provided in sections 3.1.2.1 and 3.1.2.2. The results for a non-spreading pool indicate that for a 5-m diameter pool and even for a pool an order of magnitude larger, the distances to 5 kW/m^2 are similar. The Tight 1 (Bakken) has slightly higher flame heights due to its higher burn rate, however, this does not result in significant differences in the thermal hazard distances, which are within 7% of each other.

For the uncontained or spreading pools the comparison assumes a spill rate of 0.1 m^3/s which corresponds to 1584 gal/min. A breached rail car carrying 30,000 gallons of oil would deplete within about 19 minutes at this spill rate. A spill rate providing depletion on the order of minutes was chosen since this is likely more reflective of an accident scenario, rather than a spill lasting on the order of hours or an instantaneous release. The pool diameter calculation is simplified by assuming a steady-state condition in which the mass flow into the pool is balanced by the mass flow out from the burning of the pool. The results indicate that the pool diameter for Tight 1 (Bakken) is smaller than the other oils due to its higher burn rate. Due to the smaller pool, the distances to 5 kW/m^2 are as much as 27%

lower compared to the other oils. In the presence of wind, this difference reduces to about 16% due to tilt and changes in flame length.

It should not be concluded from this comparison that the Tight 1 oil (Bakken) is less hazardous than the other oils. Given potential variation in accident scenarios, atmospheric conditions, and parameter input uncertainty, what should be concluded is that thermal hazard distances do not differ greatly. For contrast, consider Liquefied Natural Gas (LNG) which would have roughly twice the thermal hazard distance than the oils considered here for equivalent pool diameters and atmospheric conditions.

Table 3-5: Predicted thermal hazard distances to 5 kW/m^2 for non-spreading pools.

Non-spreading pool				
Fuel	**Wind speed (m/s)**	**Diameter (m)**	**Flame height* (m)**	**Distance to 5 kW/m^2 (m)****
Tight 1 (Bakken)	0	5	9.43 ±0.05	13 ±1
Tight 2 (Tx Shale)		5	8.31 ±0.24	13 ±1
SPR		5	8.36 ±0.08	13 ±1
Tight 1 (Bakken)		50	70.4 ±0.4	107 ±10
Tight 2 (Tx Shale)		50	62.0 ±1.8	103 ±8
SPR		50	62.4 ±0.6	104 ±10
Tight 1 (Bakken)	5	5	8.91 ±0.05	16 ±1
Tight 2 (Tx Shale)		5	7.81 ±0.23	15 ±1
SPR		5	7.85 ±0.08	15 ±1
Tight 1 (Bakken)		50	68.8 ±0.4	130 ±9
Tight 2 (Tx Shale)		50	60.1 ±1.8	123 ±8
SPR		50	60.6 ±0.6	124 ±9
Tight 1 (Bakken)	10	5	8.64 ±0.05	16 ±1
Tight 2 (Tx Shale)		5	7.55 ±0.23	14 ±1
SPR		5	7.61 ±0.08	15 ±1
Tight 1 (Bakken)		50	66.7 ±0.4	131 ±8
Tight 2 (Tx Shale)		50	58.3 ±1.8	122 ±8
SPR		50	58.8 ±0.6	123 ±8

*based on correlation[24].
**values have been rounded

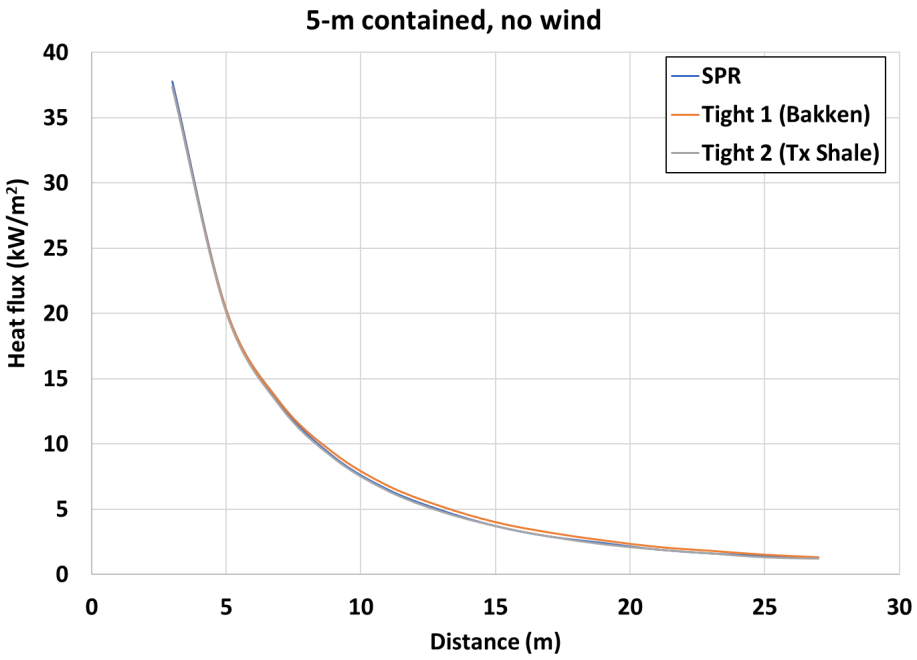

Figure 3-5: Predicted heat flux versus distance for 5-m diameter pool.

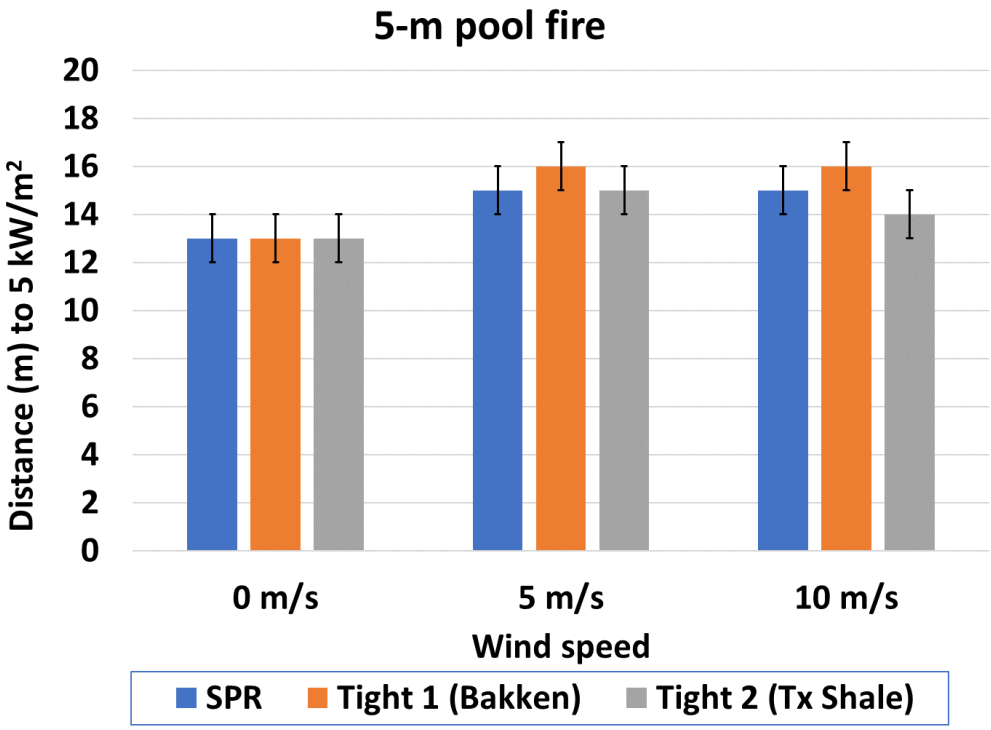

Figure 3-6: Comparison of predicted distances to 5 kW/m² for a 5-m diameter pool fire for various wind speeds.

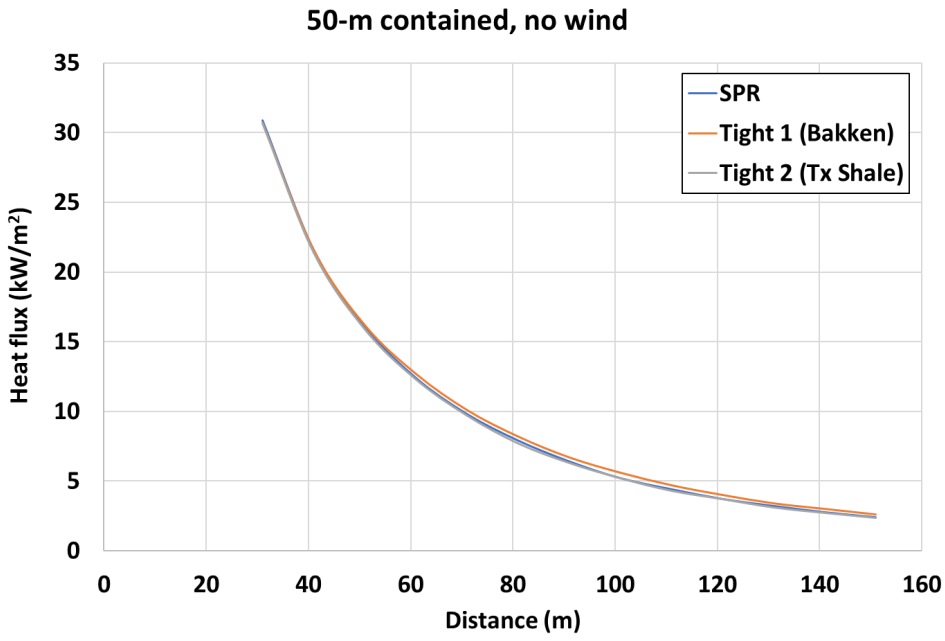

Figure 3-7: Predicted Heat flux versus distance for 50-m diameter pool.

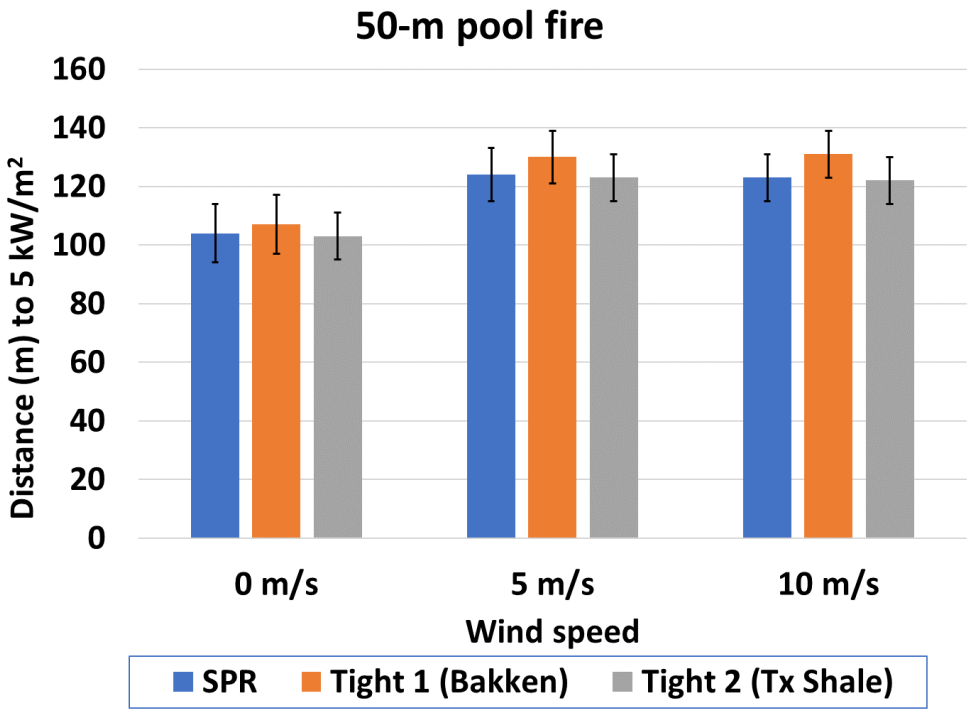

Figure 3-8: Comparison of predicted distances to 5 kW/m² for a 50-m diameter pool fire for various wind speeds.

Table 3-6: Predicted Thermal hazard distances to 5 kW/m^2 for spreading pools assuming a spill rate of 0.1 m^3/s.

Spreading pool				
fuel	**Wind speed (m/s)**	**Diameter (m)**	**Flame height (m)***	**Distance to 5 kW/m2 (m)****
Tight 1 (Bakken)	0	40.8 ±0.4	58.9 ±0.2	89 ±7
Tight 2 (Tx Shale)		53.2 ±3.0	65.5 ±1.3	109 ±3
SPR		53.2 ±1.0	65.9 ±0.5	110 ±9
Tight 1 (Bakken)	5	40.8 ±0.4	57.4 ±0.2	109 ±7
Tight 2 (Tx Shale)		53.2 ±3.0	63.5 ±1.2	130 ±2
SPR		53.2 ±1.0	64.0 ±0.4	131 ±7
Tight 1 (Bakken)	10	40.8 ±0.4	55.7 ±0.2	109 ±7
Tight 2 (Tx Shale)		53.2 ±3.0	61.6 ±0.4	129 ±2
SPR		53.2 ±1.0	62.1 ±0.4	130 ±7

*based on correlation[25].
**values have been rounded.

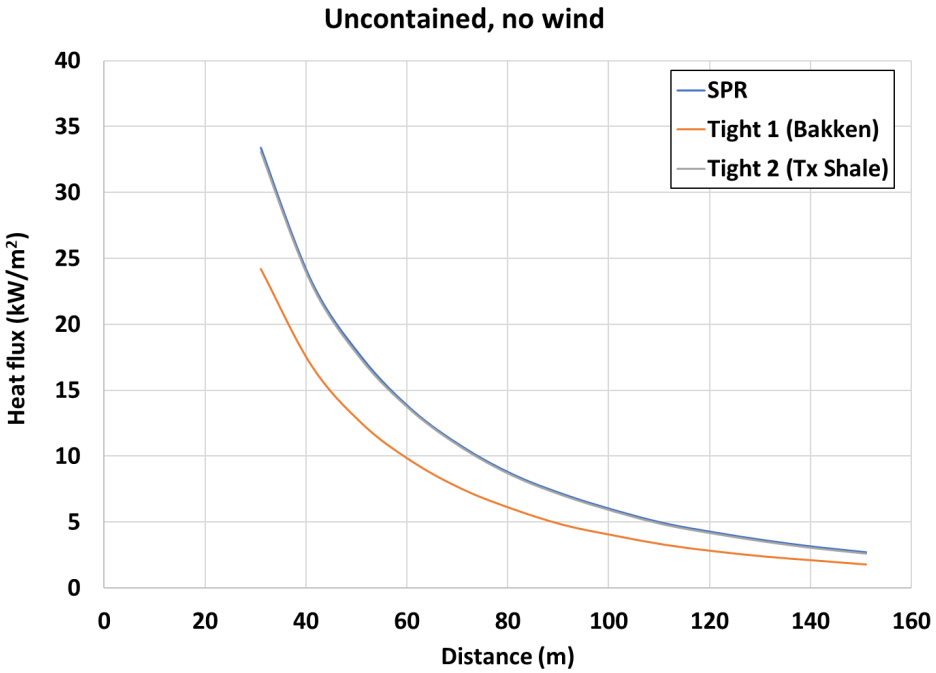

Figure 3-9: Predicted heat flux versus distance for uncontained pool, assuming a spill rate of 0.1 m^3/s.

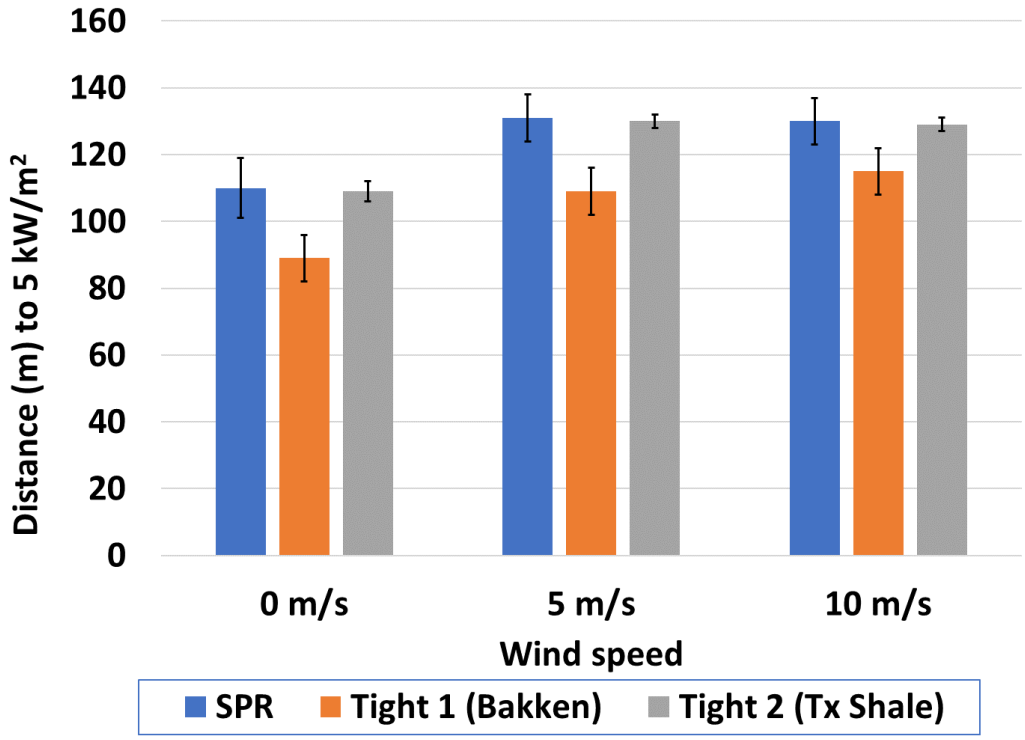

Figure 3-10: Comparison of distances to 5 kW/m² for spreading pool fire for various wind speeds based on model predictions, assuming a spill rate of 0.1 m³/s.

The above model predictions pertain to heat flux to an object external to the fire. With regards to engulfed objects the experimental results indicated the average heat flux to the calorimeter for the SPR crude oil is roughly 10% higher than the other oils (Table 2-1). However, it must be kept in mind that the wind conditions were not similar among the tests. Thus, engulfment of the calorimeter was not equivalent due to the tendency of the wind to periodically expose the calorimeter, thereby affecting the incident heat flux.

3.1.2. Comparison of parameters with other fuels

3.1.2.1. Burn rate

Figure 3-11 provides a comparison of burn rate among several types of fuel. The comparison indicates that none of the crude oils tested in this study display outlier behavior compared to other hydrocarbons with regards to burn rate. The cryogens, liquefied natural gas (LNG) and liquefied petroleum gas (LPG), are plotted to provide examples of outliers. Note that some of the variation among the fuels could be due to wind effects since these studies were conducted in outdoor conditions. Also, note that benzine (naphtha) is considered most similar to gasoline for the referenced study. The lower burn rate of benzine compared to gasoline most likely is due to difference in physical properties which were not reported.

As indicated in Figure 3-11, for several fuels the burn rate begins to asymptote at diameters exceeding somewhere between 5 to 10 meters. Based on these trends for the Arabian light crude oil, the burn

rate for the tested oils would increase at most by about 20% for large diameters (>20 m) and most likely would range between about 0.05 kg/m^{2}s to 0.07 kg/m^{2}s. As previously discussed however, the burn rate is also affected by the substrate which could affect these trends. Since large-scale data is not available comparing the burn rate for various fuels over various substrates, it is uncertain what the trend would be in the case of a particular accident scenario.

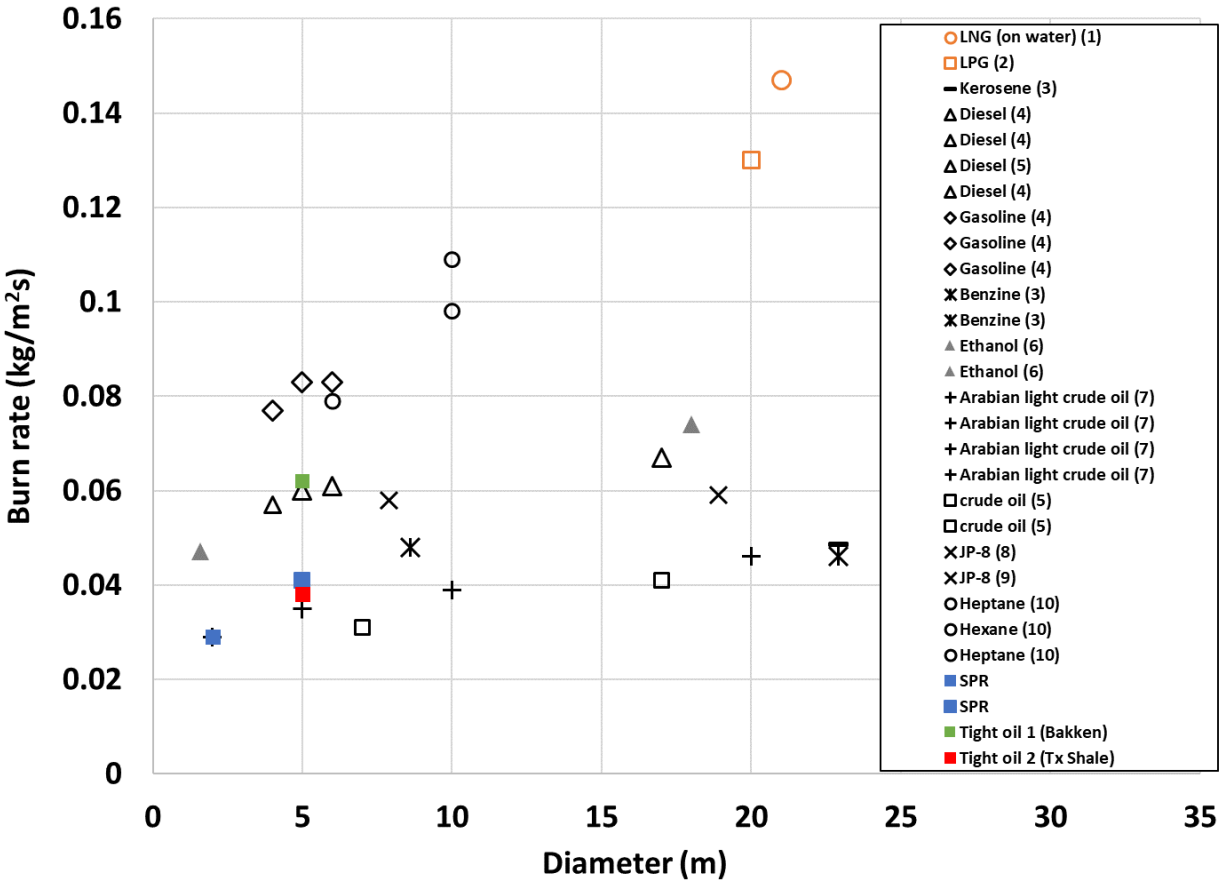

Figure 3-11: Comparison of burn rate with other fuels (1 – ref.[30], 2 – ref.[31], 3 – ref.[32], 4 – ref.[25], 5 – ref.[33], 6 – ref.[34], 7 – ref.[35], 8 – ref.[8], 9 –ref.[7], 10 – ref.[36]).

3.1.2.2. Surface emissive power

Figure 3-12 provides a comparison of average surface emissive power for several fuels indicating that the crude oils tested are similar to diesel fuel and gasoline. LNG is plotted to provide an example of an outlier. Due to increasing smoke production the average surface emissive power decreases with increasing pool diameter. This trend is shown in Figure 3-13 from data obtained from radiometer measurements for 30-m and 50-m diameter pools for kerosene [37].

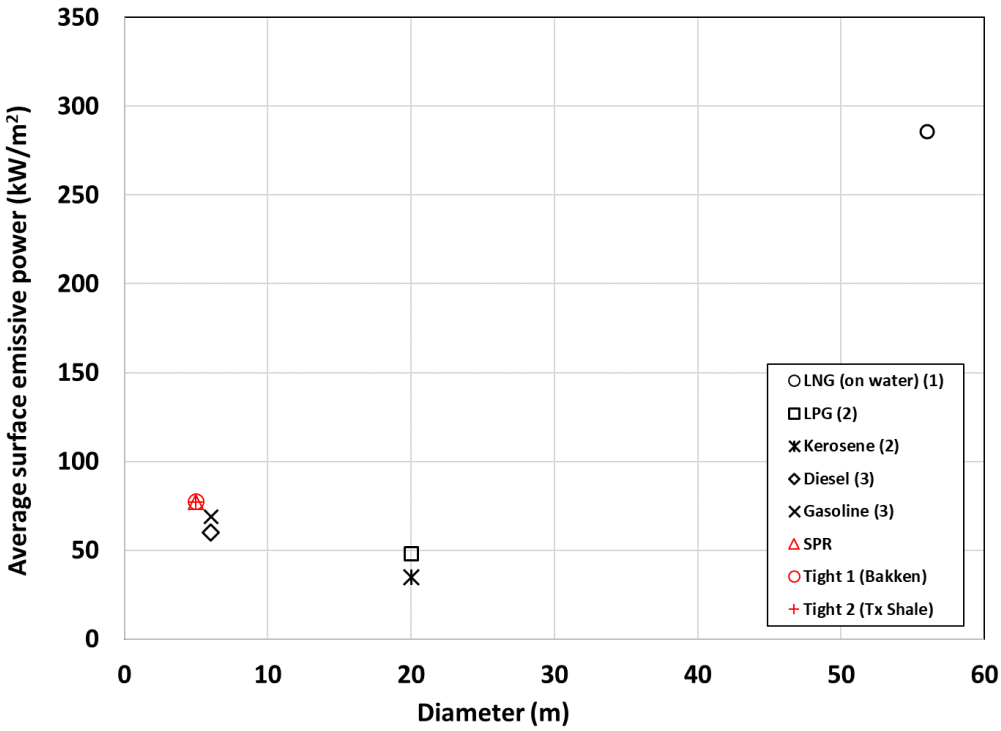

Figure 3-12: Comparison of average surface emissive power with other fuels (1- ref.[30], 2 – ref.[31], 3 – ref.[25]).

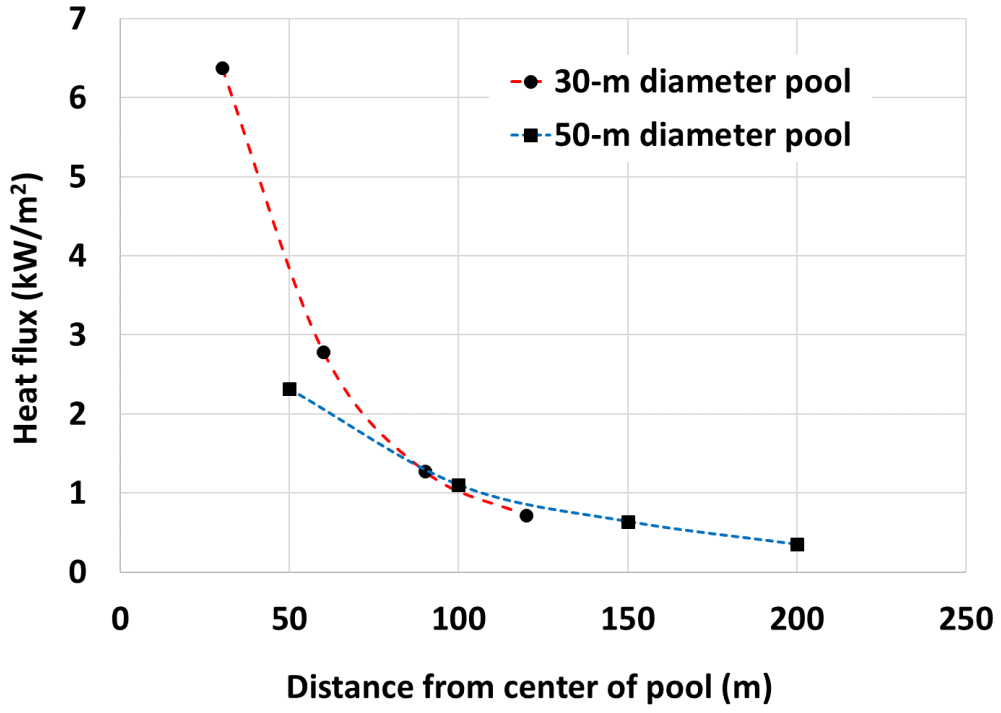

Figure 3-13: Heat flux from radiometer measurements for kerosene pool fires[37].

It would be expected that higher heat fluxes would result for the 50-m diameter pool compared to the 30-m diameter pool, but the data indicates that they are similar, and at 50-m from the center of the pool the larger pool even results in a lower heat flux value. This trend has also been documented in terms of radiative fraction from pool fires of increasing diameter as shown in Figure 3-14. The radiative fraction is defined as

$$\boldsymbol{\eta = q_{rad}/q_{total}}. \quad (1)$$

The denominator is the total energy potential of the fire and assumes complete combustion. It is determined by

$$\boldsymbol{q_{total} = \dot{m} H_c}. \quad (2)$$

where $\dot{m}$ is the burn rate (kg/s) and H_c is the heat of combustion (J/kg). The numerator, q_{rad}, is the total radiative power output and is typically determined by representing the fire as a point source and utilizing radiometer measurements. This representation becomes more accurate as radiometer measurements are taken further away from the fire due to the decreasing influence of view factor (detail in flame geometry) on the calculation. Thus, assuming isotropy, the radiative power output q_{rad} is determined by

$$\boldsymbol{q_{rad} = 4\pi r^2 q_o} \quad (3)$$

where r_o is the distance between the center of the pool and a radiometer which measures the heat flux, q_o. In the crude oil tests, most radiometers at the 20-m location failed thus cannot be used for comparison. However, measurements of the average surface emissive power can be utilized to estimate the radiative fraction by the following equation which assumes the shape of the flame is a cylinder.

$$\boldsymbol{\eta = \frac{SEP}{\dot{m}'' H_c}\left(1 + 4\frac{H}{D}\right)} \quad (4)$$

where SEP is average surface emissive power (kW/m^2), $\dot{m}''$ is mass flux (kg/m^{2}s), H is average flame height (m), and D is pool diameter (m). This is considered an estimate because of the dependence on the flame surface area. Very different values can be obtained depending on what shape is used to represent the flame. Table 3-7 provides the radiative fraction using equation (4) for the studied crude oils. The variance was determined by considering the propagation of uncertainty for measured SEP, mass flux, and flame height. As shown in Figure 3-14, the radiative fraction for the Tight 1 (Bakken) oil is closer to gasoline [36], while the Tight 2 (Tx Shale) and SPR oils are closer kerosene [36] and a crude oil whose type was not specified [36]. However, given the range of uncertainty provided in Table 3-7, the values could overlap.

Table 3-7: Radiative fraction for the crude oil 5-m pool fire tests

Oil	Radiative fraction
Tight 1(Bakken)	0.12 ±0.08
Tight 2 (Tx Shale)	0.25 ±0.15
SPR	0.23 ±0.12

Video coverage of railcar accidents involving crude oil confirms that a substantial amount of smoke is produced and heavily shrouds the fire. Thus, it is anticipated that the crude oils evaluated in the current work would follow the same trend as shown in Figure 3-13. Measurements of the surface

emissive power for smoke range from 20 kW/m^2 [28] to 40 kW/m^2 [25]. Thus, the surface emissive power would decrease to slightly above this range for accident scale fires. The reason that the surface emissive power would not be entirely equivalent to that of smoke is because large pool fires (>20 m) display a persistent luminous zone up to heights roughly 0.2 times the diameter [35] and the formation of intermittent luminous zones roughly about a diameter above the pool [38].

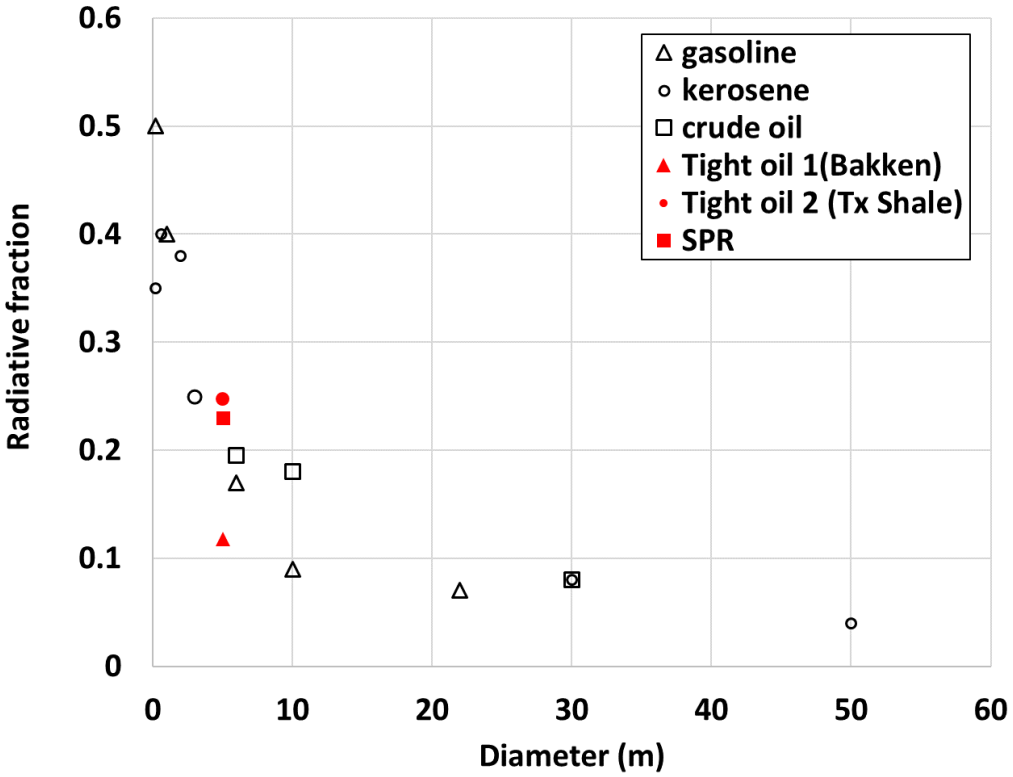

Figure 3-14: Radiative fraction for various pool diameters [36].

3.1.2.3. Flame length

There is very limited reported data on flame length for pool diameters of 5-m. The most complete reporting of flame length performed at a similar scale involve gasoline and diesel pool fire experiments testing pool diameters of 1.5, 3, 4, and 6 m [25] and is used here for comparison. Even though a 5-m diameter pool was not tested, a best-fit correlation was determined in [25] which allows for a comparison at a pool diameter of 5-m. The correlations provided in terms of an average and maximum length to diameter ratio are the following.

$$\left(\frac{L}{D}\right)_{ave} = 7.74(m^*)^{0.375}(u^*)^{-0.096} \quad (5)$$

$$\left(\frac{L}{D}\right)_{max} = 8.44(m^*)^{0.298}(u^*)^{-0.126} \quad (6)$$

where,

$$m^* = \frac{\dot{m}''}{\rho_a \sqrt{gD}} \tag{7}$$

$$u^* = \begin{cases} u_w/u_c & if\ u_w \geq u_c \\ 1 & if\ u_w < u_c \end{cases} \tag{8}$$

$$u_c = \sqrt[3]{\frac{g\dot{m}''D}{\rho_a}} \tag{9}$$

In the above equations, $\dot{m}''$ is mass flux (kg/m^{2}s), g is gravity (9.81 m^2/s), D is pool diameter (m), and ρ_a is atmospheric density (kg/m^3).

The criteria used in [25] to determine flame height is intermittency, which is defined as the fraction of time in which the flame length is at least higher than a length, L. The average flame length is defined as the length at which the intermittency reaches the value of 0.5. They used real-time cameras to determine the intermittency. Their approach is similar to the method used in the current work in which frames spaced by equal time increments are obtained from real-time cameras and statistics gathered that provide an average, minimum, and maximum height. Figure 3-15 and Figure 3-16 provide the comparison between the correlations and the crude oil data for average and maximum L/D, respectively. The comparison indicates agreement for average flame length within about 24% for Tight 1 (Bakken) oil, 16% for Tight 2 (Tx Shale) oil, and 3% for SPR. The comparison indicates agreement for maximum flame length within about 3% for Tight 1 (Bakken) oil, 11% for Tight 2 (Tx Shale) oil, and 5% for SPR. This is good agreement given the uncertainty introduced by testing in outdoor conditions with time-varying wind speeds and directions.

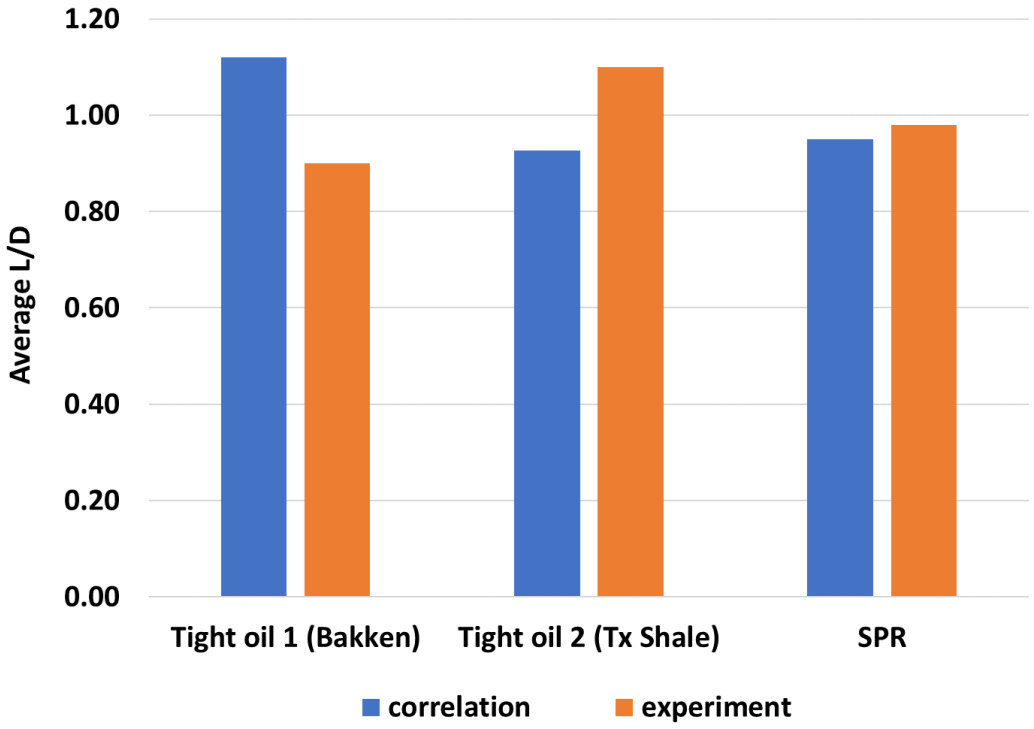

Figure 3-15: Comparison of average L/D (length/diameter) with correlation and crude oil data.

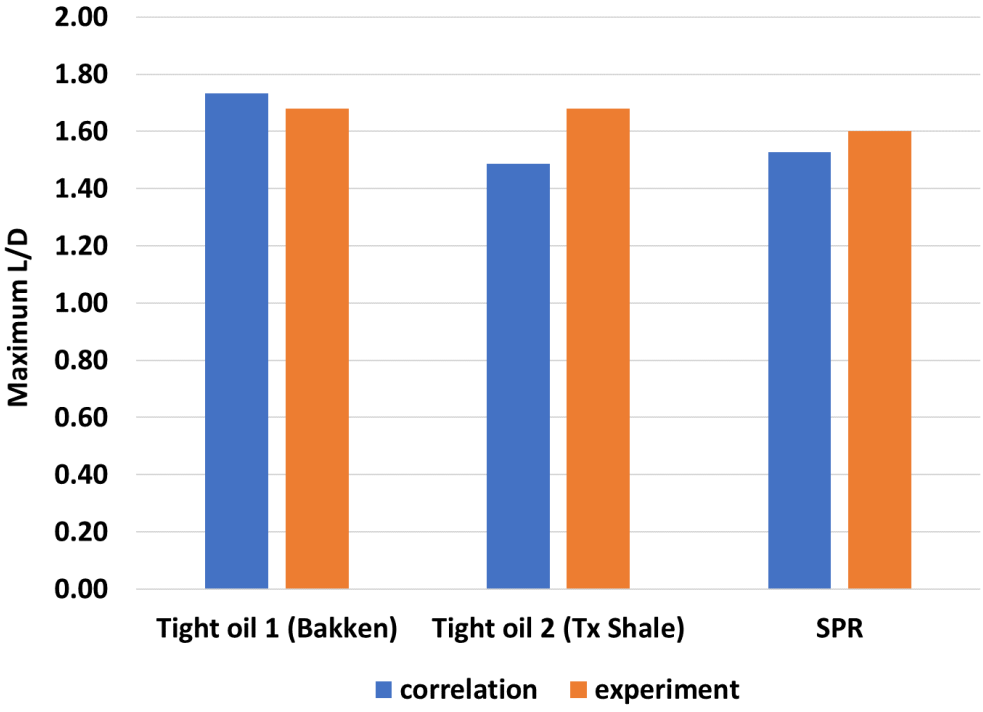

Figure 3-16: Comparison of maximum L/D with correlation and crude oil data.

3.2. Fireballs

The key parameters that influence fireball thermal hazard distances are diameter, rise height, duration, and surface emissive power. These quantities vary in time and as such the transient functions can be incorporated into simplified models for thermal hazard analyses. However, due to the lack of available time-varying data, the traditional approach is to use empirical correlations that identify maximum or averaged parameter values.

Empirical correlations have been developed by several researchers for these parameters [39]. Most are based on data from small-scale experiments, typically using fuel masses below 50 kg. The empirical correlations are of the form of a power law in which the fuel mass is raised to some exponent, b, and then the result multiplied by some factor, a. The factors 'a' and 'b' are determined by fitting a power-law curve to data. The values of these factors have not been consistent among various researchers because of differences in test configuration, scales, fuel-types, instrumentation, and parameter definitions.

There is consensus, however, that the exponent on fuel mass used to determine maximum diameter is approximately 1/3, thus this parameter has the least variation among researchers [39]. This agreement can be anticipated given that most hydrocarbon fuels require a similar volume of air for complete combustion. The growth of the fireball has also been shown to have a 1/3 power dependence where the growth is proportional to $t^{1/3}$, where t is time (s) [39].

The greatest variation among the equations exists for fireball duration, basically due to the use of different criteria for what defines duration and release configurations. Some definitions include: the time at which the fireball area exceeds half the maximum value [40], twice the time up until lift off [41], and twice the time until there is a half-release of energy [42]. The duration can also be affected by release configuration, for example if a test vessel ruptures in a way that allows fuel to be released close to the ground, the fireball will expand initially along the ground and then begin liftoff, whereas if a test configuration allows for only an upward vertical release, then the expansion phase along the ground is circumvented.

Large variation also exists for rise height due to differences in definition which include: the height at which the fireball breaks up, height at which maximum diameter occurs, and height at which the fireball area is steady state.

Correlations have not been developed for the surface emissive power mainly due to the lack of measurement of this parameter. It has been measured for a limited number of experiments and most have used indirect approaches by employing radiometer measurements in conjunction with video coverage. More direct measurements are infrared cameras which offer the additional advantage of tracking the fireball over time to provide more detailed information. The surface emissive power is not amenable to a power law form. The Center for Chemical Process Safety (CCPS) recommends a value of 350 kW/m^2 [43]. The CCPS is a non-regulatory organization within AIChE that addresses process safety of hazardous materials. They gather input from manufacturers, government agencies, consultants, academia and insurers to provide recommendations on process safety.

An important aspect to note regarding the use of correlations is variation in results even for repeat experiments. As demonstrated in references [42, 44] variation of about ±20% resulted for measurements of maximum diameter, radiated energy, and surface emissive power testing propane, butane, diesel, and kerosene fuel.

3.2.1. Comparison of thermal hazard distances

For events that have exposure to a high heat flux level over a short duration such as a fireball, a common measure for the effects from radiant heat exposure is thermal dose or also termed thermal dosage. It is determined by integrating the exposure heat flux over time. It has been found that the heat flux raised to a power provides a better fit to empirical data on injury [45]. Thus, a commonly used equation for thermal dose is the thermal dose unit (TDU), that is,

$$\text{thermal dose unit}(t) = \int_0^t q(t)^{4/3} dt \quad (10)$$

where q(t) is the time varying radiant flux (kW/m^2) and t is the duration of exposure (s). This is sometimes referred to as thermal load. Empirical models to determine thermal hazard distances for fireballs typically assume static conditions, that is, constant diameter, height, and SEP. Thus, the thermal dose evaluation is simply $q^{4/3}t$ since the heat flux is constant at a location. A constant heat flux level of 5 kW/m^2 over 30 seconds exposure, for example, corresponds to a TDU of 256 $(kW/m^2)^{4/3}s$.

Table 3-8 provides the mean and range of TDU values that result in different levels of injury [46]. A range is typically reported in the literature because various researchers have used different test methodologies, such as, type of test subject (animals versus human), clothed or bare skin, and different exposure sources. Thermal dose is utilized in probit equations for quantitative risk-analysis to estimate the probability of fatality. A 50% probability of fatality corresponds to TDU values ranging from about 1000 to 4000 $(kW/m^2)^{4/3}s$, with the existence of a range due to the reasons given above.

Table 3-8: Injury for different thermal dose levels

Injury	Thermal dose $(kW/m^2)^{4/3}s$	
	mean	range
pain	92	86-103
Threshold 1st degree burn	105	80-130
Threshold 2nd degree burn	290	240-350
Threshold 3rd degree burn	1000	870-2600

For comparison of fireball thermal hazard distances, a thermal dose level of 240 $(kW/m^2)^{4/3}s$ is used as the criteria, which is the lower value of the range provided in Table 3-8 for 2nd degree burns. An integral model is used for the comparison and assumes view factor equations pertaining to a sphere radiating to a randomly oriented differential area [47]. Three sets of model predictions are performed. The first is of the 400-gallon tests using experimental values of spatially-averaged SEP, effective diameter, and rise height at the time of maximum power. The second is of the 400-gallon tests that uses the same experimental SEP values as the first comparison, but uses a correlation by Roberts [39] to predict diameter and an assumption that the height is equivalent to the diameter. Comparison of Robert's correlation to other data is provided in section 3.2.2.2. This set of comparisons is performed because it is used for predicting larger releases and allows for evaluation of the performance of the correlation against the predictions using experimental parameters. The final set of model predictions using this approach is then performed for a release volume representative of that expected from a railcar.

The assumption that the height is equivalent to the diameter is based on observation from the fireball experiments where the height was determined to be approximately equivalent to the diameter at

maximum power for the Tight oils tested in this work, and equal to 1.3 times the diameter for the SPR oil. All model predictions use a fireball emissivity of one, a transmissivity value of 0.8, a 45 degree angle for target surface, and an assumption that the fireball is stationary. The uncertainty range is based on the experimental uncertainties of the IR measurements provided in section D.1.2.15.

Experimental parameter values are an average of the X6900 IR cameras measurements from the east and north views (Table 3-9). Values at peak power are used since the combination of diameter, height, and spatially-averaged SEP at that point are optimal in terms of determining larger hazard distances. The resultant values are greater than if later times were selected, such as, when the maximum diameter is attained, where SEP values are much lower and height much higher than at these early times (Figure 3-17 and Figure 3-**18**).

Table 3-9: Data for 400-gallon fireball experiments

Oil		Tight 1† (Bakken)	Tight 2 (Tx Shale)	SPR
Mass (kg)		1229	1269	1303
	View			
Time to maximum power (s)	East	1.53	1.24	-
	North	1.69	1.19	2.46
Maximum power (MW)	East	770	677	-
	North	757	696	665
Projected area at maximum power (m^2)	East	2453	2380	-
	North	2777	2265	2958
Average SEP at maximum power* (kW/m^2)	East	314	284	-
	North	273	306	225
Maximum average SEP*	East	367	326	-
	North	317	347	276
Time to maximum average SEP* (s)	East	0.58	0.50	-
	North	1.12	0.57	1.04
Maximum SEP** (kW/m^2)	East	894	729	-
	North	717	748	723
Time to maximum SEP** (s)	East	2.26	0.43	-
	North	1.07	0.59	1.63
Maximum projected area (m^2)	East	2712*†	3364	-
	North	2905*†	3202	3742
Time to maximum projected area (s)	East	2.59	6.68	-
	North	2.77	6.41	3.52

†Data obtained for 3.3 s before fireball went out of camera view
*Spatially averaged SEP
**Maximum SEP of local regions
*†Infrared data obtained up to 3.3 s. Video coverage indicates area did not exceed 2905 m^2

Figure 3-17 shows a comparison of time variations in fireball power over 0-4 seconds for the three crude oils. The power is determined by evaluating the product of the spatially-averaged SEP and projected area over time. The range of time in Figure 3-17 is chosen to provide direct comparison among the oils since the IR cameras for the Tight 1 (Bakken) oil did not capture the entire duration of the test. The curves indicate that the Tight 1 (Bakken) oil has the highest peak power, followed by

the Tight 2 (Tx Shale) oil, then the SPR. Figure 3-**18** shows a comparison of the time-variations in fireball power for Tight 2 (Tx Shale) and SPR oils over the entire test duration. Results indicate that lower values of power occur at later times suggesting that values of peak power were captured for all fuels.

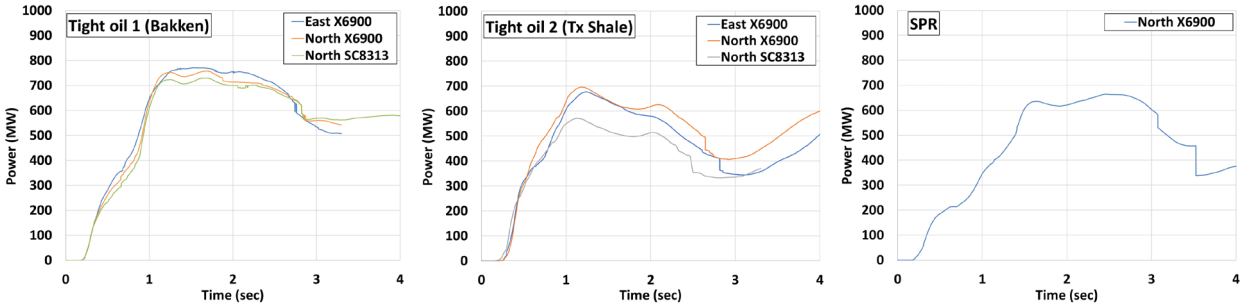

Figure 3-17: Power versus time for the crude oils (0 - 4 seconds).

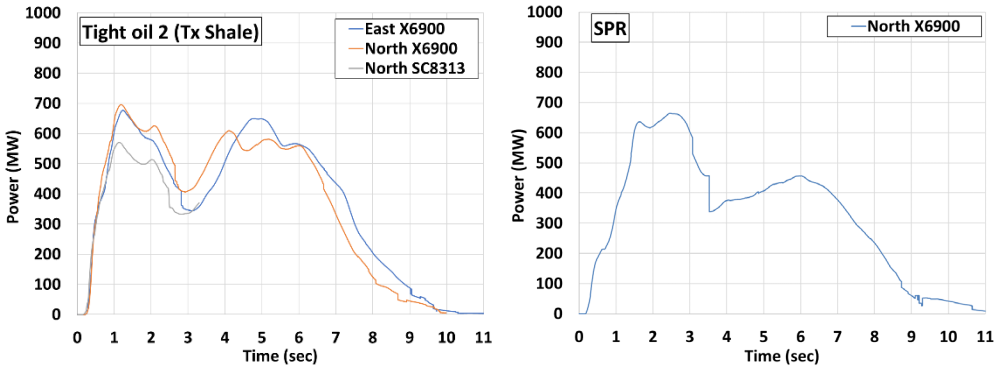

Figure 3-18: Power versus time for Tight 2 (Tx Shale) and SPR (0 - 11 seconds).

The total energy can be determined by integrating the power curves over time. The integral is approximated by summing the product of power and sampling time (0.001 s) for the time periods of 0 – 3.3 seconds for comparison among all oils, and 0 – 11 seconds to compare values between Tight 2 (Tx Shale) and SPR oils. The comparison for the shorter duration is provided because this is the duration over which the X6900 IR cameras captured data for the Tight 1 (Bakken) oil test, the common camera type among the tests. The longer duration comparison provides an indication of the approximate energy percentage emitted up until 3.3 seconds, which can be used to estimate the total energy for the Tight 1 (Bakken) (Table 3-10). Using a percentage of 40% based on results from the other two oils, the total energy is approximately 4556 MJ.

Table 3-10: Power and Energy from crude oil fireball experiments

Oil	Maximum Power(MW)	Energy (up to 3.3 sec) (MJ)	Total Energy (up to11 sec) (MJ)	Percentage of total energy up to 3.3 seconds
Tight 1 (Bakken)	764 ±107	1823 ±256	-	-
Tight 2 (Tx Shale)	686 ±96	1515 ±211	3916 ±470	39
SPR	665 ±80	1491 ±179	3531 ±424	42

The assumptions and parameters used for model predictions of thermal hazard zones, as well as the results for distances corresponding to a TDU of 240 $(kW/m^2)^{4/3}s$ are provided in Table 3-11 for 400-gallon and 30,000-gallon fireballs for all three crude oils. Since all of the crude oil tests had a duration of approximately 9 s, this duration corresponds to a heat flux of 11.7 kW/m^2 for a TDU of 240 $(kW/m^2)^{4/3}s$. Duration predictions for a 30,000-gallon release is approximately 30 seconds, which corresponds to a heat flux of about 4.6 kW/m^2 for a TDU of 240 $(kW/m^2)^{4/3}s$.

Table 3-11: Model assumptions, parameters, and thermal hazard distances for TDU of 240 $(kW/m^2)^{4/3}s$ for 400-gallons and 30,000 gallon crude oil fireballs

Model Assumptions	fuel	Mass (kg)	SEP (kW/m^2)	Diameter (m)	Height (m)	Distance (m)
400-gallon release						
Model uses measured parameters at maximum power	**Tight 1 (Bakken)**	1229	293	58	55	114
	Tight 2 (Tx Shale)	1269	295	54	52	106
	SPR	1303	225	61	81	88
Model uses correlation for diameter and height equivalent to diameter	**Tight 1 (Bakken)**	1229	293	62	62	120
	Tight 2 (Tx Shale)	1269	295	63	63	123
	SPR	1303	225	63	63	105
30,000-gallon release						
Model uses correlation for diameter and height equivalent to diameter	**Tight 1 (Bakken)**	92205	293	262	262	835
	Tight 2 (Tx Shale)	95148	295	265	265	855
	SPR	97750	225	267	267	745

Figure 3-19 shows model results for TDU versus distance for a 400-gallon fireball based on measured parameters at maximum power for the Tight 1(Bakken), Tight 2 (Tx Shale), and SPR oils. Figure 3-20 compares modeled distances to a TDU of 240 $(kW/m^2)^{4/3}s$ using measured parameters at maximum power (blue columns) and using the correlation to predict diameter with height equivalent to the diameter (orange columns) across the same three oils. The comparison indicates that when measurements are used, the Tight 1 (Bakken) results in the furthest distance, while the SPR the lowest. The range between these crude oils is a difference of about 30% and the difference between Tight 2 (Tx Shale) and SPR is about 20%. The range of uncertainties overlap, thus this difference is not significant. Also, note that other researchers have found that measurements can vary by 20% for repeat tests (see section 3.2.2).

The results shown in Figure 3-20 also indicates that the model predictions using the correlation are similar to those using measured test results. Both these sets of predictions are conservative due to the steady-state assumption. Using the time-varying experimental data with the model, distances to a TDU of 240 $(kW/m^2)^{4/3}s$ are 38.5 m and 38 m for the Tight 2 (Tx Shale) and SPR tests, respectively, which is underpredictive for the Tight 2 (Tx Shale) oil and overpredictive for the SPR oil as can be seen in Figure 3-21, showing the thermal dose from the radiometer measurements from the tests. Comparison of these values to model predictions which assumes steady-state conditions (Table 3-11), indicates that the steady state assumption is overpredictive by over a factor of 2 for these tests, which is appropriate for public protection where a safety factor of at least 2 is often used. The Tight 1 (Bakken) is not included for the time varying comparison because time-varying data was collected only up until 3.3 s from the X6900 IR cameras.

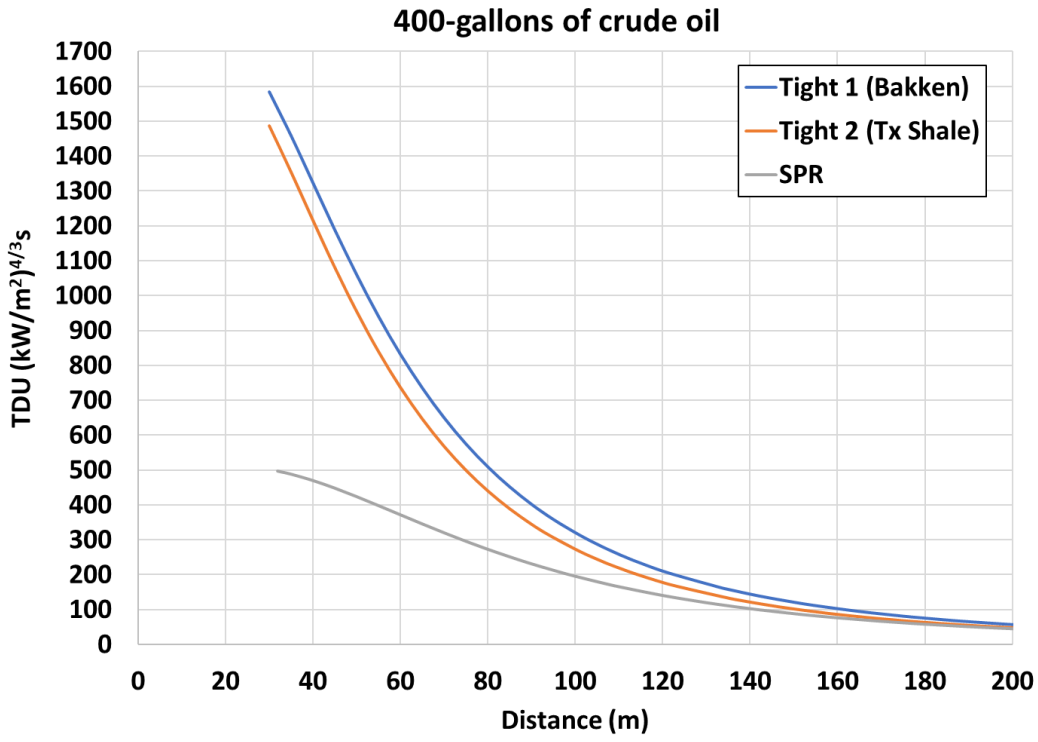

Figure 3-19: TDU versus distance from model predictions for a 400-gallon release.

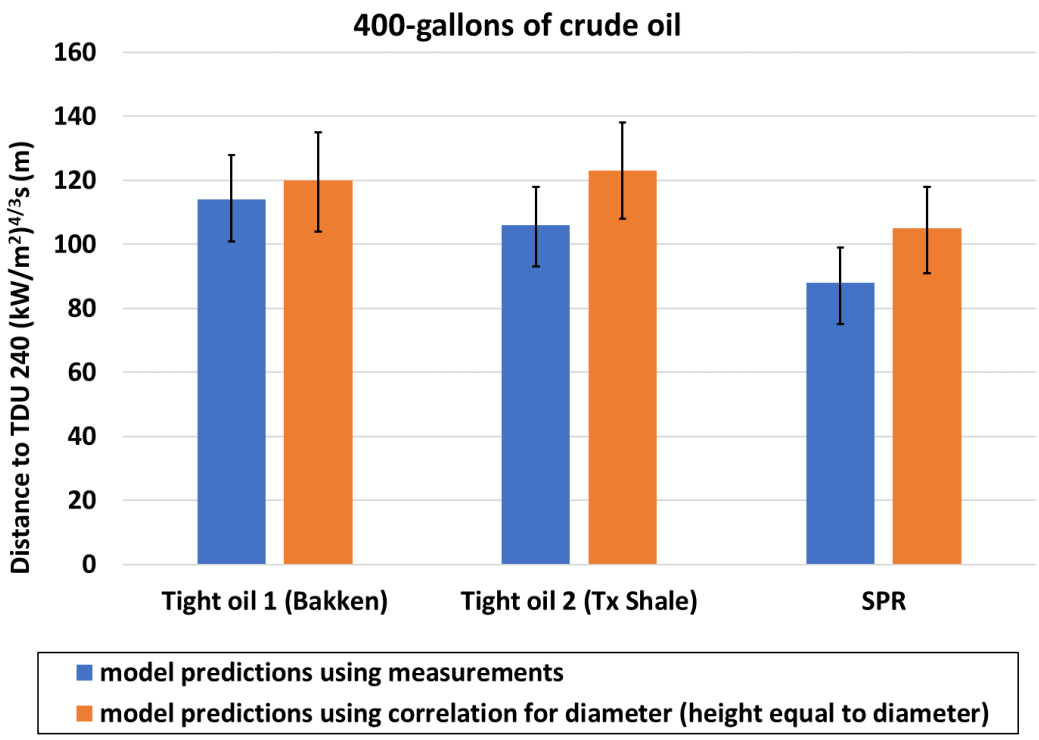

Figure 3-20: Comparison of predicted distances to TDU of 240 $(kW/m^2)^{4/3}s$ for a 400-gallon release fireball.

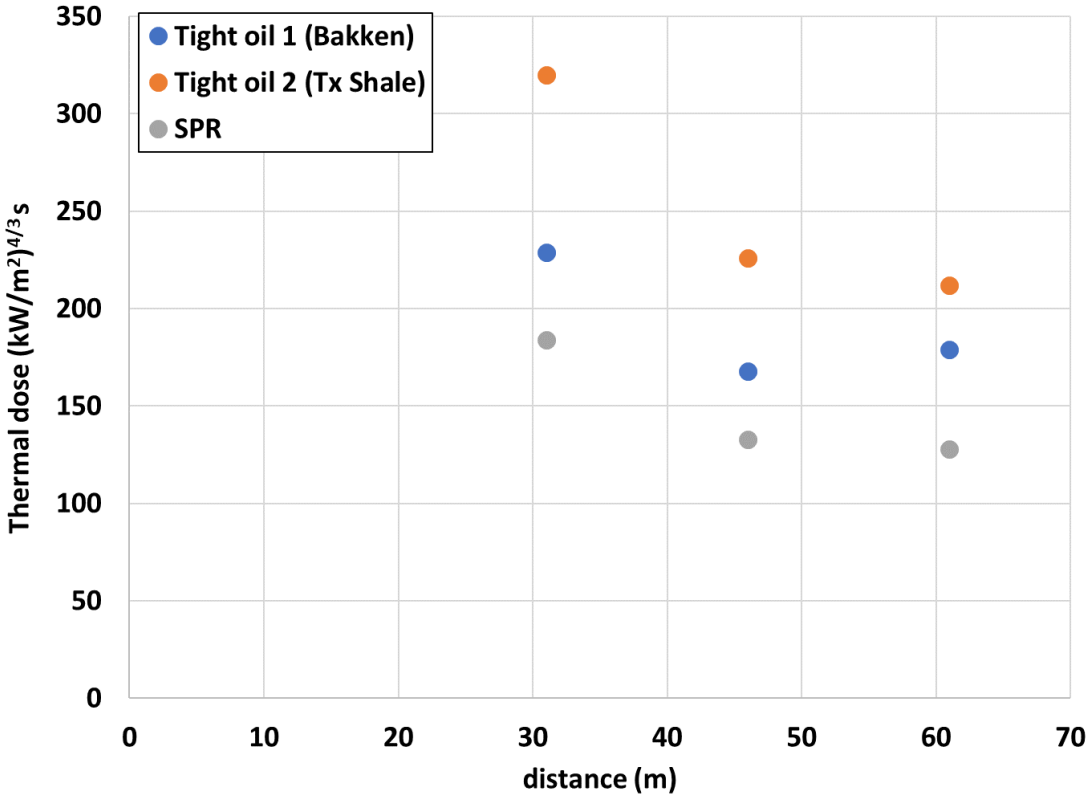

Figure 3-21: Thermal dose from radiometer measurements.

Figure 3-22 and Figure 3-23 provides the results for 30,000 gallon fireballs for all three oils using the model to predict the diameter and assuming the height equal to the diameter. The result indicate that the distances for the Tight oils are similar and have greater hazard distances than the SPR oil by about 12%. Since the range of uncertainties overlap, these results indicate that the Tight oils are not significantly different than the SPR oil with regards to thermal hazard distances.

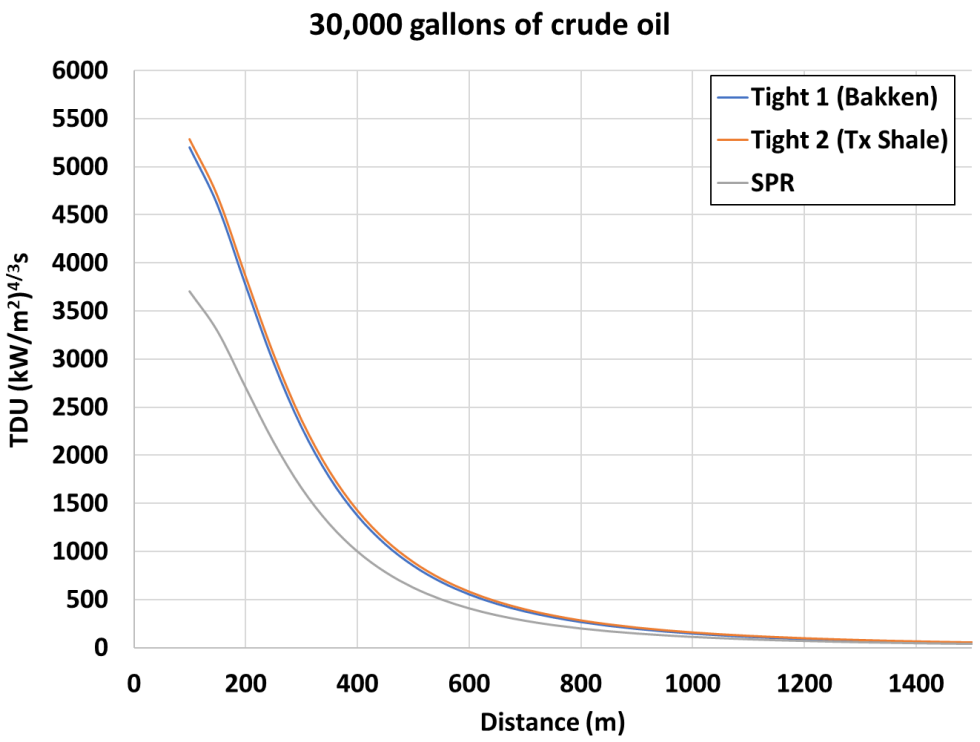

Figure 3-22: TDU versus distance from model predictions for a 30,000-gallon release.

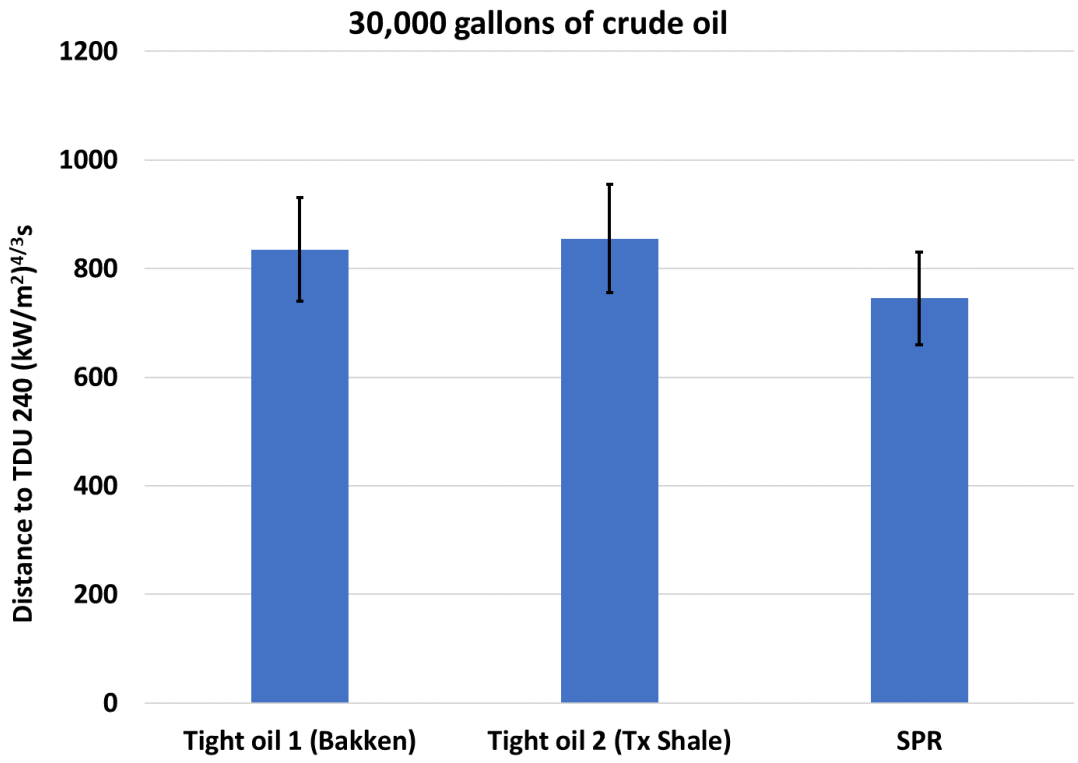

Figure 3-23: Comparison of predicted distances to TDU of 240 $(kW/m^2)^{4/3}s$ for a 30,000-gallon release fireball.

To predict duration, the correlation by Roberts [39] is used in which $t=0.83m^{0.316}$, where m is the fuel mass (kg). This time is defined as when visible radiation from the fireball ceases and does not include the initial period following the release where momentum forces dominate buoyancy forces. For the crude oil experiments this initial period is identified as the time to maximum power since up until this time momentum dominance was evident from the rapid ejection and resulting columnar-shape. As the buoyancy force increased a spherical shape subsequently formed after this time and then became the dominant force. Table 3-12 provides the results of duration from the 400-gallon experiments and from predictions using the correlation. The correlation predictions are within the uncertainty of the experimental values, thus providing confidence in the use of the correlation for extrapolation to larger release volumes.

Table 3-12: Comparison of fireball duration from 400-gallon experiments and correlation

Fuel	mass (kg)	Time to maximum power (s)	Time at which visible radiation ceases (s)	Duration from experiments (s)	Predicted duration using correlation [39] (s)
Tight 1 (Bakken)	1229	1.61	10 ±1	8.4 ±1	7.9
Tight 2 (Tx Shale)	1269	1.21	10 ±1	8.8 ±1	7.9
SPR	1303	2.46	11.5 ±1	9.0 ±1	8.0

Table 3-13 provides the results of predicted duration for a 30,000-gallon release for the three crude oils using the correlation. Review of video coverage of a fireball from a railcar accident involving Tight 1 (Bakken) agrees with the 30 second prediction. As mentioned previously, the heat flux at a distance will be time-varying and thus a model that assumes stationary behavior will overpredict exposure duration from a heat flux level, but it is the approach used here to provide conservative estimates for hazard prediction. The predicted distances also suggest that the evacuation zones up to 1600 m established by emergency personnel based on reports from historic accidents is appropriate.

Table 3-13: Predicted duration for a 30,000-gallon fireball

Fuel	mass (kg)	Predicted duration using correlation (s) [39]
Tight 1 (Bakken)	92205	30.8
Tight 2 (Tx Shale)	95148	31.1
SPR	97750	31.3

3.2.2. Comparison of parameters with other fuels

To compare the crude oil parameters gathered in this study to data obtained by other researchers, large-scale experiments that provide information for most, if not all parameters was identified and is provided in Table 3-14. The parameter definitions and instrumentation used to obtain the data for these studies is provided in Table 3-15.

Table 3-14: Large-scale fireball experiments

Study	Fuel	Test configuration	Mass (kg)	Release pressure (psig)
Johnson and Pritchard [44]	Butane Propane	• Cylindrical vessel horizontally oriented • Pressurized with electric immersion heaters • Vessel failure initiated linear shaped charge along vessel's top longitudinal centerline resulting in a propagated fracture leading to catastrophic failure	1000 - 2000	109 - 218
Roberts, et al. [48]	Propane	• Cylindrical vessel horizontally oriented • Pressurized and failed by a propane jet fire engulfing at least three quarters of vessel	279 - 1708	239 - 354
Betteridge and Phillips [49]	LNG	• Cylindrical vessel horizontally oriented • Vessel failure initiated linear shaped charge along vessel's top longitudinal centerline resulting in a propagated fracture leading to catastrophic failure	247-1306	88 - 198
Dorofeev, et al. [42]	Gasoline Kerosene Diesel fuel	• Cylindrical vessel of equal diameter and height • Vessel failure by placing TNT charge inside the vessel with the fuel	100 – 100,000	Unpressurized

Table 3-15: Parameter definitions and instrumentation for large-scale fireball experiments

Study	Diameter	Duration	Rise Height	SEP (kW/m^2)
Johnson and Pritchard [44]	• Equivalent diameter from measured areas • Video recordings	• Identified times to: ignition, maximum diameter, lift off, and extinction (visible radiation from fireball ceases) • Video recordings	• Breakup of fireball • Video recordings	• Averaged over the visible flame over time • Back-calculated using radiometers and video recordings
Roberts, et al. [48]	• Equivalent diameter from measured areas • Infrared cameras	• Extinction (visible radiation from fireball ceases) • Infrared cameras	• Height of maximum diameter • Infrared cameras	• Averaged over the visible flame over time • Local maximum SEP over time • Infrared cameras
Betteridge and Phillips [49]	• Equivalent diameter from measured areas • Video recordings	• Identified times to: ignition, maximum diameter, lift off, and extinction • Video recordings	• Breakup of fireball • Video recordings	• Averaged over the visible flame over time. • Back-calculated using radiometers and video recordings
Dorofeev, et al. [42]	• Equivalent diameter from measured areas • Real-time and Infrared cameras	• Double the duration of energy half-release • Thermal flux transducers and • r^{-2} function	• Not reported • Video recordings of fireball formation obtained	• Averaged over the visible flame over time • Infrared cameras

3.2.2.1. Surface emissive power

A comparison among the studies provided in Table 3-14 and of the experiments conducted in this work for spatially-averaged maximum SEP is provided in Figure 3-24. This comparison is approximate in that the criteria differ among the studies. For instance, Johnson and Pritchard [44] report a spatially-averaged SEP that is averaged over the duration in which the fireball size was nearly constant. Roberts et al. [48] report values of spatially-averaged SEP at maximum power and at maximum area. Betteridge and Phillips [49] report spatially-averaged SEP values 3 seconds after rupture. Dorofeev, et al. [42] report a range of spatially-averaged SEP values that appear to be based on the maximum energy released. The values for the crude oil tests are based on the time at which a spherical shape first forms which are approximately 1.7 s, 1.8 s, and 2.5 s for the Tight 1 (Bakken), Tight 2 (Tx Shale), and SPR, respectively. After these times the spatially-averaged SEP decreases, thus these values can be considered the spatially-averaged maximum SEP over the duration in which a spherical shape existed. Larger SEP values occur before these times, but do not result in the highest heat flux values at a distance based on the radiometer measurements. This is due to the smaller size of the columnar shape prior the formation of a spherical shape.

The comparison indicates that the fireballs observed from the present crude oils are within the range of values previously found for fireballs of propane and butane for similar fuel masses. There appears to be agreement with one LNG test, but it was noted in reference [49] that the much lower reading compared to the other LNG tests is still unresolved. Thus, the other two LNG tests performed are

most likely more representative of the potential magnitudes which are much higher than the other fuels.

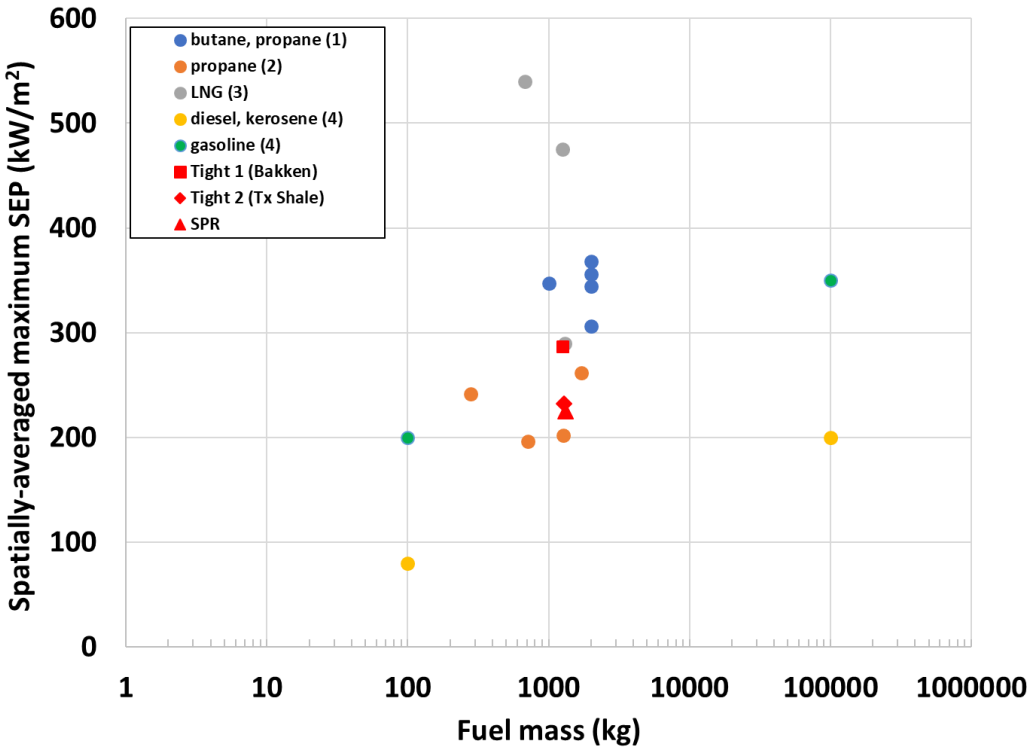

Figure 3-24: Comparison of spatially-averaged SEP versus fuel mass (1 – ref.[44], 2 – ref.[48], 3 – ref., 4 - ref.[42]).

3.2.2.2. Diameter

A comparison among the studies provided in Table 3-14 and of the experiments conducted in this work for maximum effective diameter versus fuel mass is provided in Figure 3-25. The diameter is termed 'effective' since it is calculated by using area measurements to determine an equivalent diameter assuming a perfect circle. The comparison indicates that maximum effective diameters for the crude oils are similar with the other fuels and do not display outlier behavior.

As discussed in section 3.2.1, the correlation by Roberts for maximum diameter, $D=5.5m^{1/3}$, where m is the fuel mass (kg), is used for extrapolation for releases representative from railcars. Figure 3-26 provides a comparison of Robert's correlation with experimental data and indicates good agreement with results from the present experiments.

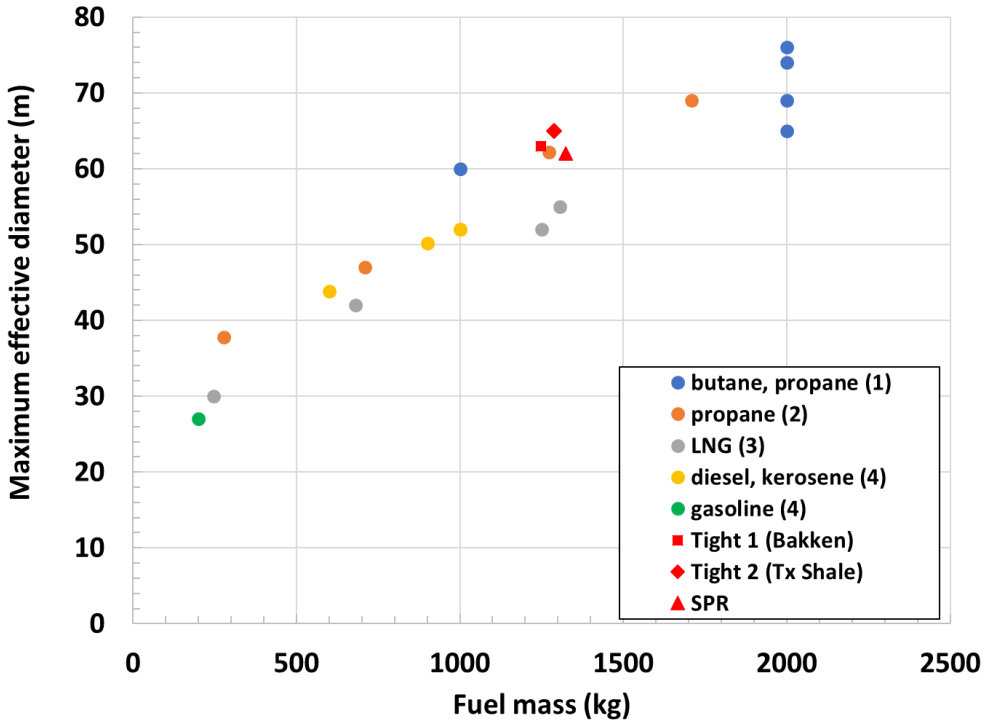

Figure 3-25: Comparison of maximum effective diameter versus fuel mass data (1 – ref.[44], 2 – ref.[48], 3 – ref.[49] , 4 - ref.[42]).

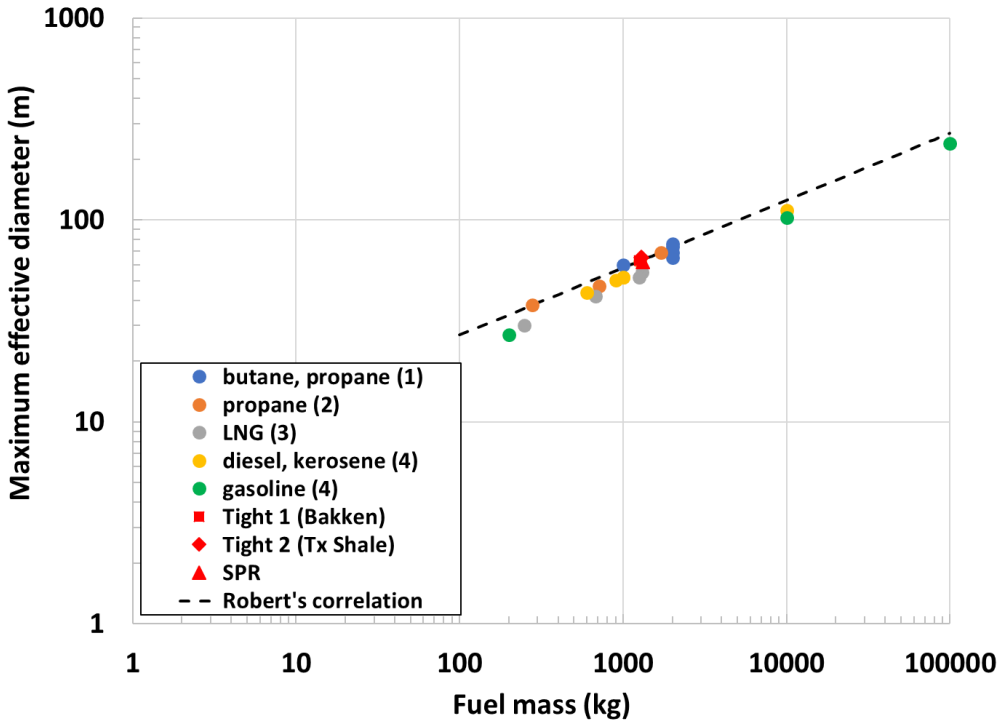

Figure 3-26: Comparison of Roberts' correlation with large-scale data (1 – ref.[44], 2 – ref.[48], 3 – ref.[49] , 4 - ref.[42]).

3.2.2.3. Maximum Rise Height

A comparison of maximum rise height versus fuel mass is provided in Figure 3-27. The studies from Table 3-14 used for comparison are those that provide information regarding the maximum rise height. The other studies did not report the maximum rise height, thus are not included. The maximum rise height is defined as the height at which the fireball starts to break up. Since the criteria defining breakup are not provided in these studies, this is an approximate comparison. The comparison indicates that the maximum rise heights of the crude oils tested are much higher than those of the other fuels. This can be attributable to the different test configuration. For the crude oil tests, the fuel was directed only in the upward vertical direction, whereas the other fuels had a release that allowed for the fuel to be released horizontally as well as vertically near the ground. This type of configuration results in the fireball first expanding along the ground and then lifting off to form a spherical shape. In the latter configuration, lower rise heights result since a portion of the energy is distributed in the horizontal and downward vertical direction. Observation of crude oil railcar accidents indicate that the oil is released in the upward vertical direction issuing from a thermal tear along the topside of the railcar. Thus, the configuration used in the current test series is more applicable to observed railcar accidents.

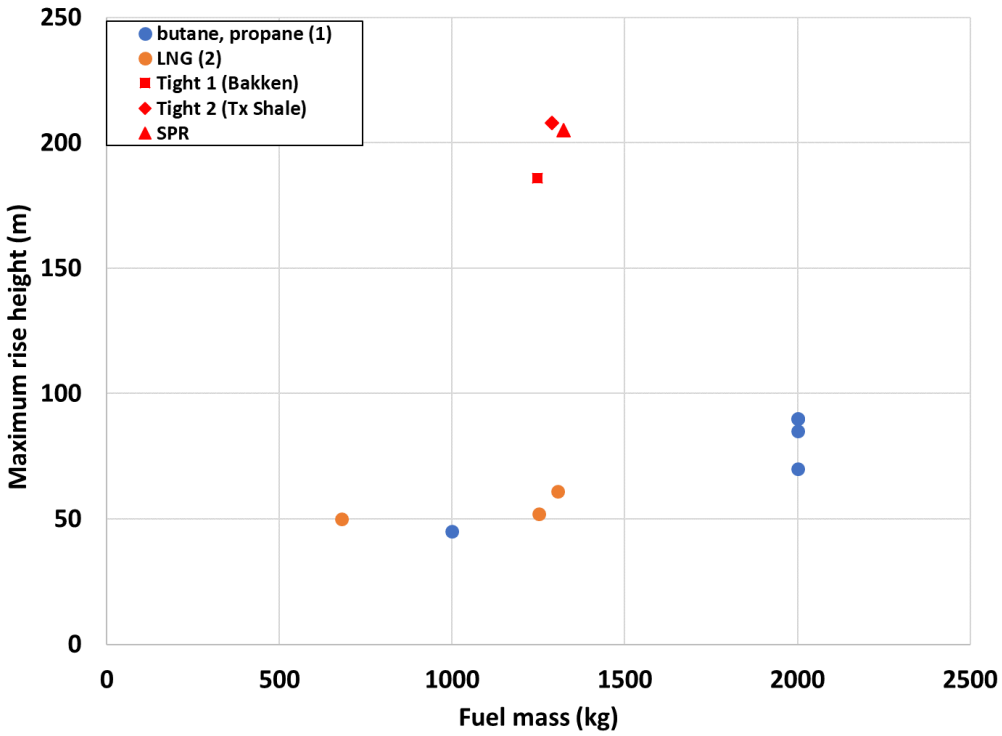

Figure 3-27: Comparison of maximum rise height versus fuel mass (1 – ref.[44], 2 – ref.[49]).

3.2.2.4. Duration

A comparison of duration until extinction versus fuel mass is provided in Figure 3-28. The studies from Table 3-14 used for comparison are those that provide information regarding the time to extinction. The definition for extinction used in these studies is the time at which visible thermal radiation ceases. The comparison indicates that the crude oil fireballs in these tests have longer durations until extinction than the other fuels. Note, however, that results can differ by up to 50%

among repeat tests as shown for tests conducted by Johnson and Pritchard [44]. Also note that for the crude oil tests the radiometers indicated heat flux impacts lasted for up to about 9 to 10 seconds. Thus, only minor regions of burning, that lasted an additional 1 to 2 seconds, were observed beyond that time. Given the inherent stochastic nature of fireball tests and the different test configurations, the results for the crude oils tests are not considered to be outliers compared to the other fuels.

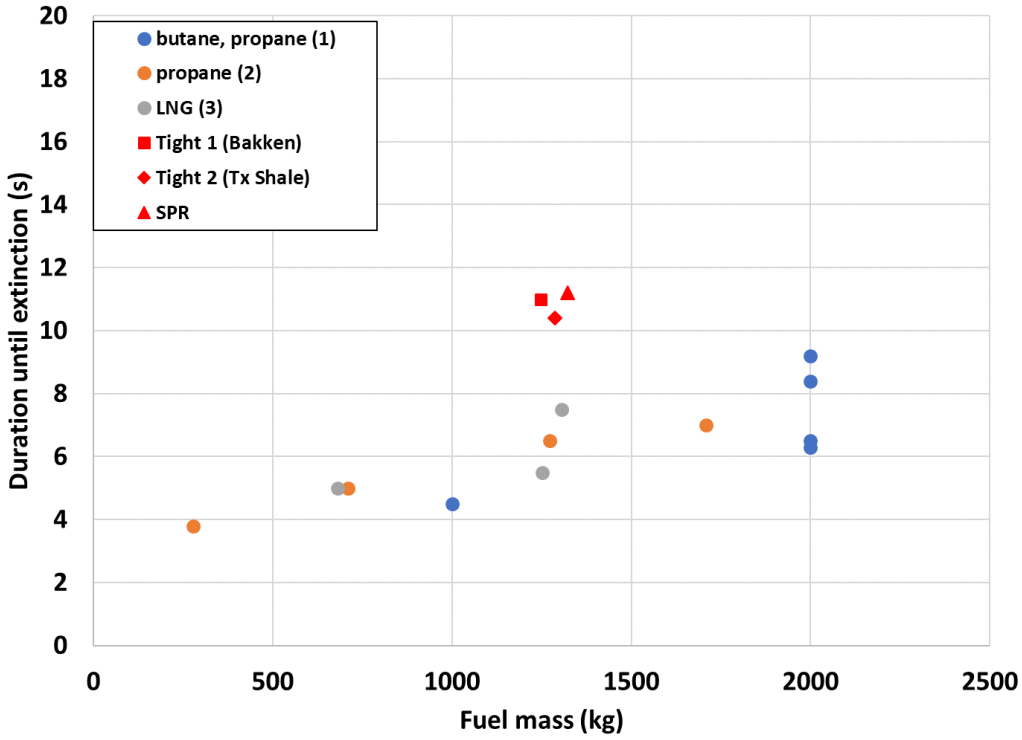

Figure 3-28: Comparison of duration until extinction versus fuel mass (1 – ref.[44], 2 – ref.[48], 3 – ref.[49])

3.2.2.5. Dosage

Of the studies provided for comparison in Table 3-14, only Johnson and Pritchard [44] and Roberts, et al. [48] report dosage versus distance. Dosage is determined by integrating heat flux measurements from radiometers over time using the equation

$$\text{dosage}(t) = \int_0^t q(t)dt. \quad (11)$$

This parameter is used to compare time-varying heat flux measurements from radiometers. The 1708 kg propane test by Roberts, et al. is provided here since it is the test with the nearest fuel mass to the crude oil tests.

Figure 3-29 shows the heat flux curves over time from the three wide-angle radiometers placed at 31 m, 46 m, and 61 m for the crude oil tests. Since the data collection frequency is 1 second intervals, curve-fits in conjunction with numerical integration are used to approximate the integral. The results are provided in Table 3-16 and Figure 3-30 which indicate that the Tight 2 (Tx Shale) has the highest dosage at the measurement locations and SPR the lowest. Note that for the Tight 2 (Tx Shale) test,

the wind speed (2 m/s (4.5 mph)) was the highest among the tests which caused the fireball to drift in the northeast direction toward the radiometers. Thus, it is anticipated that the measurements would be higher under this wind condition versus the lower wind conditions (< 1.3 m/s (3 mph)) for the other tests.

The effect of wind is demonstrated in Figure 3-31 which shows the dosage results from a 1708 kg release of propane from a test conducted by Roberts, et al. [48] in a windspeed of 2 m/s. The dosage based on the radiometer measurements differ by 50% or more for instruments placed at equal distances at different radial positions. The effect of fireball drift is evident by comparing Line A in the upwind direction with Lines D and E in the downwind direction at the distance of 100 m. As shown in Figure 3-31, the dosage for Line A is about 55 kJ/m^2 and for Lines D and E dosage values are 110 kJ/m^2, and 95 kJ/m^2, respectively. Thus, the dosage is about 50% higher downwind. Roberts, et al. also provide heat flux curves over time from the radiometer measurements at 100 m which show peak values of about 25 kW/m^2 and 28 kW/m^2 for Line D and E, respectively, versus about 14 kW/m^2 for Line A.

Note that dosage values for the propane tests at 50 m are about a factor of two higher than that for the crude oils tests at 46 m. This is anticipated since the average crosswind SEP for the propane test was about 312 kW/m^2 with a diameter of about 74 m versus values below 300 kW/m^2 and diameters around 60 m for the crude oil tests. Even though this comparison is not for quantities of fuel of equivalent mass, it does provide indication that dosage values for the crude oil tests are consistent with anticipated trends with regards to the effect of SEP and diameter. This does not conclude that the results for Tight 2 (Tx Shale) test should be reduced by half, but rather provides other evidence to make the point that it is likely the Tight 2 (Tx Shale) measurements would be closer to the results for the Tight 1 (Bakken) and SPR tests if conducted under calm conditions.

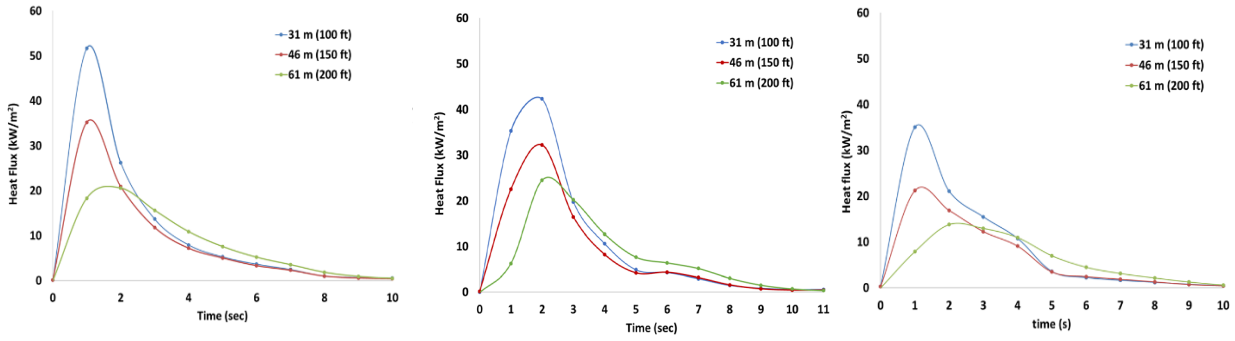

(a) (b) (c)

Figure 3-29: Radiometer data for (a) Tight 1 (Bakken), (b) Tight 2 (Tx Shale), and (c) SPR.

Table 3-16: Dosage from radiometer measurements for the crude oils (kJ/m^2)

Crude oil	31 m (100 ft)	46 m (150 ft)	61 m (200 ft)
Tight 1(Bakken)	84	68	76
Tight 2 (Tx Shale)	109	85	87
SPR	73	59	60

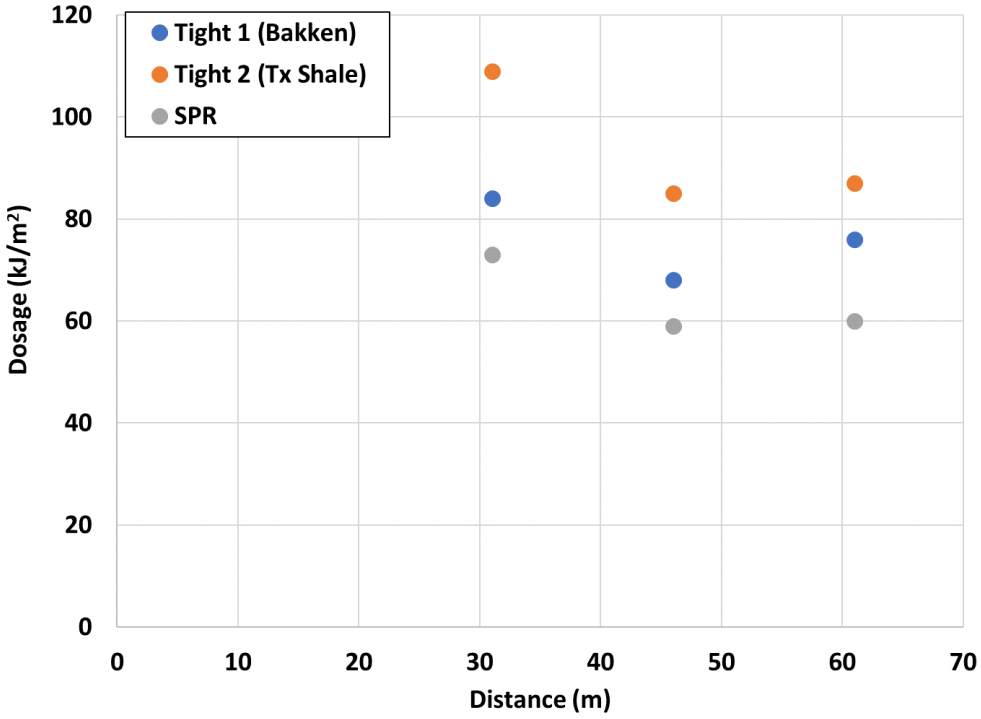

Figure 3-30: Dosage from radiometer measurements among the oils.

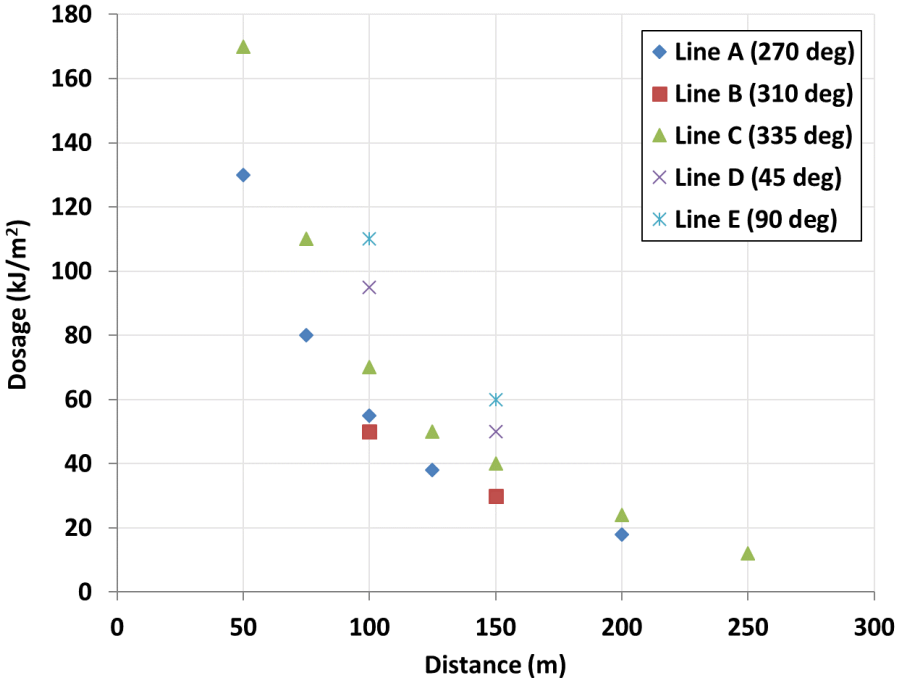

Figure 3-31: Dosage versus distance, propane (1708 kg release)[48].

3.3. Comparison to higher vapor pressure, lighter fuels

The oils directly tested in this experimental study exhibited vapor pressures in the range $VPCR_4$(100°F) ~ 2 – 11 psia. Additional $VPCR_4$ data obtained from public literature plotted in Figure F- 63 indicate that crude oils sampled from the supply chain can exceed this range to about 14 psia. While the oils directly tested here measured up to 11 psia, the conclusions are considered pertinent to oils and other hydrocarbons with potentially higher vapor pressure. Evidence to this effect is shown in Figure 3-12 and Figure 3-24 where the Sandia crude oil combustion data were co-plotted with literature data for comparison fuels, showing that the surface emissive power for the oils tested here is similar to propane, butane, gasoline, and kerosene.

Example vapor pressure ranges for these comparison fuels are summarized in Table 3-17. As encountered many times during this research, the authors were unable to find public data on VPCR for hydrocarbon liquids obtained by the D6377 method. For nearly pure substances like commercial grade propane and butane, the vapor pressure is straightforward and primarily a function of temperature. For multicomponent fluids like the crude oils, gasoline, and kerosene, vapor pressure shows a dependency on measurement method, vapor-liquid ratio, and open versus closed handling (see related discussion in [1]). This creates challenges for comparing vapor pressure data generated in the current work against vapor pressures available from public sources.

For commercial fuels and many crude oils, the only available measure in public databases is typically Reid Vapor Pressure (RVP). There are well-known issues associated with RVP methodology and subsequent comparison to D6377 VPCR due to the important differences in open versus closed handling during the sampling and testing procedures that grow more pronounced with higher volatility test fluids [50]. Above considerations notwithstanding, a loose comparison can be made between RVP and D6377 VPCR provided the temperature (T = 100°F) and V/L ratio are set to the same conditions for the vapor pressure measurement. A simple correlation for converting from $VPCR_4$ to a Reid Vapor Pressure equivalent (RVPE) is given in ASTM D6377-16 section X1 [50], and conversion factors range from ~0.8-0.9 for crude oils, and are heavily caveated in the standard. While access to ASTM D6377 VPCR data on all comparison fuels would be preferable, RVP is often the only choice and is preferred to having no vapor pressure information at all. Using the correlation described in ASTM D6377-16, the Sandia $VPCR_4$ values for Bakken and Texas Shale were converted to RVPE for rough comparison among fuels and listed in Table 3-17. The authors note that the relative bias in VPCR versus RVP and associated uncertainty of these measurements is relatively small when compared to the differences between end member vapor pressures (propane versus Bakken or Bakken versus Jet A). The primary message is that vapor pressures of the end member comparison fuels are very different from the crudes and cover a substantial range in vapor pressure property space.

Returning to the data in Table 3-17, propane and butane exhibit clearly higher vapor pressures than the crudes tested here, based on Gas Processors Association (GPA) specifications [51] for commercial grade liquefied propane and butane that list maximum vapor pressures at 223 psia and 85 psia at 100°F, respectively. Another comparison fuel, gasoline, is regulated in the U.S. to vapor pressure specifications [52] for RVP ranging 7-9 psia that compare fairly closely to the RVPE for the Sandia Bakken and TX Shale samples. Jet A, which has composition very similar to kerosene, was the lowest vapor pressure fuel tested in the Sandia series with $VPCR_4$(100°F) = 0.6 psia.

Not shown on the abovementioned Figure 3-12 and Figure 3-24, but potentially relevant to the overall topic of combustion hazards, are hydrocarbon liquids known as condensates that are produced in association with natural gas and characterized by high API gravity (>50° API). Condensates generally have larger concentrations of C3-C6 components than the light and medium crudes that were tested

here, though they are often handled and transported within the same infrastructure as crude oils. Sandia located property data on several representative condensates that will be discussed here as examples. Peace Condensate [53] is gathered from gas plant operations northwest of Edmonton, Alberta Canada, and exhibits steady properties with time as evidenced by its published 6-month, 1-year, and 5-year average property data. While $VPCR_4$(100°F) was not given for this stream, RVP by ASTM D323A [54] was given and will be taken as the closest available analog. Note that specifications on sampling methods for obtaining the material for RVP measurements were not given. Peace Condensate exhibited a 5-year average API gravity = 54 and RVP = 10 psi. As such, this particular condensate has a vapor pressure similar to the Tight 1 (Bakken) sample tested here.

Table 3-17 also lists weight% of light components for each of the comparison fuels as an alternative measure of fuel volatility. Similar to vapor pressure, this oil property showed no significant effects on combustion properties for the pool fire and fireball tests run in Task 3. This relationship extends to the same broader range of comparison fuels as vapor pressure. At the upper end, commercial grade propane and butane exhibit effectively 100 wt% <C6. Condensates comprise the next reasonable step in a continuum of hydrocarbon fuels, exhibiting significant mass% of light hydrocarbons, with a balance of middle hydrocarbons and few if any heavy hydrocarbons. Aggregate data from a dozen US and Canadian condensates from a 2015 study sponsored by Transport Canada [55] showed a wide range of light component compositions, from 5-64 wt% <C6, overlapping with an example gasoline at 19 wt% and Peace condensate at 13 wt% <C6. The three crude oils tested at Sandia showed from 6.2 down to 1.4 wt% <C6%, while Jet A was at the low end at 0.01 wt% <C6. The fact that the surface emissive power of all these products and crude oils were similar (see again Figure 3-12 and Figure 3-24) implies that hydrocarbon fuels containing a wide range of light ends content, to include condensates, would exhibit similar burn characteristics and associated thermal hazards for pool fires and fireballs. The hydrocarbon that is the exception is Liquefied Natural Gas (LNG) which has surface emissive power that is about a factor of four or more higher than other hydrocarbons.

Table 3-17. Comparison table of hydrocarbon fuel vapor pressures and wt% <C6

Fuel Name	Vapor Pressure @100˚F (psia)	< C6 Content (wt%)	Vapor Pressure Method	Source
Commercial Propane	<223	100%	ASTM D1267 [53]	GPA 2140-17 [50]
Commercial Butane	<85	100%	ASTM D1267	GPA 2140-17
Various US/Canadian Condensates	N/A	5-64%	N/A	Transport Canada 2015 Report [55] <C6 content by GOR flash + ASTM D8003 [56]
Peace Condensate [a]	10	13%	RVP	https://Crudemonitor.ca/

Fuel Name	Vapor Pressure @100˚F (psia)	< C6 Content (wt%)	Vapor Pressure Method	Source
Tight 1 (Bakken)	9.5-11.2	5.9-6.2%	$VPCR_4$ by ASTM D6377	Current report
	8.0-9.3		RVPE	Current report, calculated from $VPCR_4$ using conversion factor [50]
Gasoline	7-9	19%	RVP	https://www.epa.gov/gasoline-standards/gasoline-reid-vapor-pressure < C6 content provided with permission from SPL, Inc. using GPA 2186 [57]
Tight 2 (Tx Shale)	7.6-8.6	4.0-4.3%	$VPCR_4$ by ASTM D6377	Current report
	6.3-7.2		RVPE	Current report, calculated from $VPCR_4$ using conversion factor [50]
SPR [b]	1.9-7.0	1.4-3.7%	$VPCR_4$ by ASTM D6377	Current report
Jet A [b]	0.6	0.01%	$VPCR_4$ by ASTM D6377	Current report

[a] Data from Crudemonitor.ca may be subject to higher uncertainty due to lack of specificity on sampling and analysis methodology

[b] Reid Vapor Pressure equivalent not calculated since $VPCR_4$ data were outside the correlation range

This page intentionally blank

4. DISCUSSION

To facilitate understanding of the following discussion, the reader should first be reminded of what motivated this study, the context under which it was performed, and the study's objective. The study was motivated by the number of occurrences and severity of railcar accidents involving Tight 1 (Bakken) oils. In response to these accidents, questions arose, namely, why are these accidents happening? Further, what is different about tight oils versus conventional crude oils? It was suspected by the public and governing agencies that it might be due to the higher vapor pressure or increased flammability of the tight oils when compared to conventional oils. Thus, the initial phase of this project, Phase I, which involved a literature survey [1], identified research needs to address these questions.

One of the conclusions from the Phase I effort is that ignition potential cannot be identified by a single index, but rather involves several properties which include: flashpoint, flammability limits, auto-ignition temperature, minimum ignition energy, and burning velocity. When comparing two fuels, the one with a lower flashpoint, wider range of flammability limits, lower auto-ignition temperature, lower minimum ignition energy, and higher maximum burning velocity is considered more flammable. Additionally, vapor generation alone is not the only requirement to support combustion. Rather, the vapor must mix with an oxidizer, typically air, within a range of fuel-air concentration ratios. The minimum fuel-air concentration ratio that can support combustion is termed the lower flammability limit (LFL). In theory, the flash point is the temperature at which the vapor pressure of a liquid fuel can support the LFL; however, this measurement can provide significant scatter and is not necessarily correlated with the LFL since the tests for each parameter are performed under different test configurations [58, 59].

It should be kept in mind that ignition is fundamentally a function of chemical kinetics, heat, and mass transfer. As such, determination of any of the above properties associated with ignition will depend upon the measurement configuration. Thus, different methods of measurement can provide different results, which can also vary among laboratories using the same method [58, 59]. The identification of the above properties is useful as a relative comparison among fuels using equivalent measurement conditions; however, the question remains of how these parameters are useful for practical applications given the vast range of physical conditions that can result from a railcar accident.

An example of how physical conditions can affect ignition is demonstrated by some of the Jet-A pool fire experiments performed at Sandia. In low-temperature conditions it is often difficult to ignite Jet-A, despite direct application of a propane torch to the fuel surface. At the location where the propane torch is applied, the properties used to identify packing group, that is, flash point and the initial boiling point of Jet-A is most certainly reached. However, the localized ignition is not sufficient to sustain a flame that will propagate across the entire pool. On the other hand, when the torch is applied to a wick wetted with and placed in the Jet-A pool, the wick readily ignites. Similar to a candle, vapors are continually supplied to the ignited wick. An area of the pool surrounding the wick then subsequently ignites allowing for a flame to propagate across the rest of the pool. The wick can be ignited because it has a greater area-to-volume ratio than the configuration of the pool. This reduces the heat loss into its volume relative to the vapor generation rate on its surface.

Thus, these two configurations differ in the balance of mass and heat transfer. The heat transferred from the propane torch to the fuel's surface has heat losses into the depth of the pool which the torch cannot overcome. Thus, the size and strength of the ignition source will determine whether it is sufficient to result in ignition across the pool. In this instance, the torch is not powerful enough; conversely, the wick is of sufficient size to ignite the entire pool.

Thus, the potential for a fuel to ignite and sustain a flame is very configuration dependent and it is difficult to apply laboratory-controlled conditions to practical applications. Performing ignition research related to railcar accidents would be most meaningful if done for the configuration of interest, namely, an impact involving a loaded railcar. This experimental setup would require numerous tests to provide statistical significance, and such an endeavor would be cost prohibitive.

Furthermore, in an accident scenario, a derailment most likely will lead to damage to the railcars. The degree of damage will depend on train speed, number and type of cars, and whether collision occurred with another train [60]. Thus, there is potential for the railcar to rupture and release some of its contents in the form of a spray or atomized fuel while at the same time producing fragments and sparks. Fuel in atomized form is easier to ignite due to a greater surface area for a given mass, which allows imparted energy to more efficiently produce vapors [59]. The kinetic energy imparted in a high impact event has a high potential to produce sparks [61] and hot fragments which can serve as ignition sources for the atomized fuel [62]. A fuel with a low vapor pressure can ignite under such conditions. There is ample evidence to support this; for example, in airplane crashes involving jet fuel.

The intent of featuring the above discussion is to address why this study did not include experiments involving ignition potential. Based on the Phase I effort, the premise is that most train accidents provide enough kinetic energy to exceed the parameter thresholds indicating flammability; consequently, ignition is highly probable regardless of the crude oil type.

Additional support of the this premise comes from a recent doctoral statistical study analyzing data collected from the Pipeline and Hazardous Materials Safety Administration's database of rail incidents involving crude oil for the years spanning 2007-2016 [63]. The study found insufficient evidence to show that light sweet crude oil from the Bakken region significantly increased the probability of fire and explosion in case of release.

The focus of the current study thus turned to addressing common fire outcomes, namely, pool fires and fireballs. These outcomes were evaluated by measuring parameters that affect thermal hazard distances, and by addressing the question of whether vapor pressure affects these parameters.

The results of this research have found that all the oils have comparable thermal hazard distances. Furthermore, none of the oils studied indicate outlier behavior and are consistent with other alkane-based hydrocarbons. It is important to recognize that the thermal hazard distances provided should be interpreted as relative comparisons only, and not as absolute or reflective of an accident scenario. Historic accidents have demonstrated that hazards can exceed the distances calculated in this work due to the thermal damage arising from numerous railcars leading to significant amounts of oil contributing to a fire which can then propagate to surrounding fuels sources, such as wooden structures, vegetation, and other hydrocarbons. The emergency response guide book issued by PHMSA for first responders on the initial phase of a transportation incident recommends an evacuation radius of 800-m (1/2 mi.) for a crude oil rail car involved in a fire [64]. In practice, evacuation areas encompassing up to a ~1600 m (1 mi.) have been enforced by emergency personnel for historic accidents as reported in several National Transportation Safety Board (NTSB) reports [65, 66].

Another aspect to realize regarding the thermal hazard distances is that they pertain to static conditions and do not provide information on the rate of fire propagation. Their usefulness is to provide information on the initial evacuation area that should be enforced in the event of a fire. This is the reason why the accidents reported by NTSB have evacuation distances exceeding the recommendations by PHMSA.

With regards to fire propagation to other fuel sources, when comparing two oils, the one with a greater thermal hazard distance will have a farther impact in its potential to ignite surrounding fuel sources. This could affect the timing of an evacuation. For example, consider a house fire in which the fire begins in a corner. A fire with a low thermal impact would have a smaller ignition region of surrounding combustibles. Potentially one would have the ability to extinguish the fire before it became overwhelming. However, a fire of high thermal impact would have a larger ignition region of surrounding combustibles, thereby potentially necessitating imminent evacuation due to potential rapid growth of the initial fire.

In addition to fire propagation, there are other hazards such as smoke exposure which is one of the major causes of death from fires due to asphyxiation, carbon monoxide inhalation, and inhalation of toxic gases such as cyanide [67]. Additionally, as pointed out in the Phase I effort, there is a potential for fragments to be generated from a boiling liquid expanding vapor explosion (BLEVE). A BLEVE is commonly defined as "an explosion resulting from the failure of a vessel containing a liquid at a temperature significantly above its boiling point at normal atmospheric pressure" [43]. Such an outcome is possible when a non-breached railcar is exposed to a pool fire. The outcome from an overpressure release is typically a fireball and thrown projectiles and/or fragments. Although no evidence of thrown fragments have been found from accidents involving the tight crude oils resulting in fireballs, it does not preclude an occurrence. It is unknown under what heat exposure conditions the full-hazard potential from a BLEVE could occur for fuels with differing vapor pressure. Knowledge of when a railcar could potentially BLEVE is important for the protective actions taken by emergency responders.

To address the hazards posed by fires, it is preferable to prevent accidents from occurring rather than use mitigation. An example of prevention is the U.S. federally mandated requirement for railroads to implement Positive Train Control (PTC) which is a safety control system that automatically decreases train speeds when needed and takes control in situations where a train operator fails to take appropriate action. The requirements for the system is to demonstrate prevention of train-to-train collisions, overspeed derailments, incursion into an established work zone, and movement through a main line switch in an improper position. Other strategies that may play a role in risk management are the number of train cars and train miles [68], hazmat railcar position [69] enhanced railcar safety features [70], and the inspection, maintenance, and repair of track and train components.

Although several proven strategies are emerging in the U.S. to improve safety, there are difficulties regarding government regulation compliance, inspection, and enforcement that impact the ability to manage risks [71]. The solution to reducing the number and severity of railcar accidents involves several factors which requires a multi-strategy approach involving cooperation between rail operators and government agencies. Although prevention and implementation issues are beyond the current scope of this work, they are mentioned to emphasize the complexity of the problem which unfortunately cannot be addressed with a simple solution such as the alteration of a fuel's vapor pressure.

The 2015 version of the Sampling & Analysis Plan for the Crude Oil Characterization Research Study [2] framed the project in terms of six tasks, the first four of which were authorized by the federal agency sponsors. This report marks the completion of Task 3. The follow-on Task 4 was formulated as an opportunity to generate a comprehensive data set of properties on multiple crude types to provide a better understanding of which types are associated with higher versus lower thermal hazards for pool fires and fireballs. The relative independence of thermal hazards on crude properties like vapor pressure removes the need for additional data to find which crude types exhibit certain property ranges. The empirical data gathered by Sandia during the Task 3 work, coupled with publicly available

data cited in the report, provide sufficient data on which to draw the conclusions contained herein. As such, additional data collection in a Task 4 effort is not required to support Task 3.

5. CONCLUSION

The main conclusions from this study are the following:

General:

- The similarity of pool fire and fireball burn characteristics pertinent to thermal hazard outcomes of the three oils studied indicate that vapor pressure is not a statistically significant factor in affecting these outcomes. Thus, the results from this work do not support creating a distinction for crude oils based on vapor pressure with regards to these combustion events.
- Based on comparison to combustion data from public literature on common liquid fuels (primarily commercial grade propane and butane), the results of this study are considered to be pertinent to crude oils and most hydrocarbon liquids that exceed the vapor pressures of the crude oils tested here.

Pool Fires:

- The experimental results indicate that measured values of surface emissive power and flame height among the oils tested are within 1 % and 24% of each other, respectively, with standard deviation ranges overlapping. The burn rate for the Tight 1 (Bakken) oil is about a factor of 1.5 higher than that for other tested oils.
- The predicted thermal hazard distances are similar among the oils tested for contained pool fires and are within 14% of each other, with standard deviation ranges overlapping. Distances were evaluated using the measured parameters, an integral model, and the injury criterion of 2^{nd} degree burns after 30-second exposure to a radiant heat flux of 5 kW/m^2 for both a 5-m and a 50-m diameter contained pool fire. A 50-m pool diameter is representative of a 114-m^3 (30,000-gallon) release. Predicted thermal hazard distances are for comparison purposes only and not intended to be applied to railcar accidents.
- The predicted thermal hazard distances using the measured parameters and a 2^{nd} degree burn criterion for an uncontained or spreading pool resulting from a 114-m^3 (30,000-gallon) release indicate that the Tight 1 (Bakken) oil results in lower distances compared to the other oils by 16%-27%.
- Historic accidents have demonstrated that hazards can exceed the distances calculated in this work due to damage of numerous railcars leading to significant amounts of oil contributing to a fire which can then propagate to surrounding fuels sources, such as wooden structures, vegetation, and other hydrocarbons.
- The measurements of burn rate, flame height, surface emissive power, and heat flux to an engulfed object are consistent with other alkane-based liquid hydrocarbons for all oils tested.

Fireballs:

- The experimental results indicate that the average surface emissive at maximum power for the two tight oils are about 30% higher than the SPR oil.

- The maximum fireball diameters measured were similar among the three oils (~62-65 m).
- The Tight 1 (Bakken) oil had a 10% lower height to fireball extinction than the other oils.
- The times to fireball extinction were similar among the oils (~10-11 s).
- The predicted thermal hazard distance using the injury criterion of 2nd degree burns after 30-second exposure to a thermal dose level of 240 $(kW/m^2)^{4/3}s$ was evaluated for a 400-gallon release for all oils tested. The results indicate the distances for the tight oils are similar, but are about 20-30% higher than the distance predicted for the SPR oil.
- Predicted thermal hazard distances, for a 30,000-gallon release, among the crude oils differ by about 12% with the range of uncertainties overlapping. Thus, the predicted thermal hazard distances among the oils are comparable.
- The observed measurements of diameter, duration, and surface emissive power for the tested crude oils are consistent with experiments performed by other researchers testing similar volumes for propane, butane, gasoline, and diesel as fuels.
- The maximum average surface emissive power for all oils are below the Center for Chemical Process Safety (CCPS) recommendation to use a value of 350 kW/m^2 [43] for thermal hazard evaluation. It is anticipated that the oils will not exceed this value for larger releases. The CCPS is a non-regulatory organization within AIChE that addresses process safety of hazardous materials. They gather input from manufacturers, government agencies, consultants, academia and insurers to provide recommendations on process safety.

REFERENCES

[1] D. Lord, A. Luketa, C. Wocken, S. Schlasner, R. Allen, and D. Rudeen, "Literature Survey of Crude Properties Relevant to Handling and Fire Safety in Transport," Sandia National Laboratories, Albuquerque, NM, Unclassified Unlimited Release SAND2015-1823, 2015.

[2] SNL, "Crude Oil Characteristics Sampling, Analysis and Experiment (SAE) Plan," http://energy.gov/fe/articles/crude-oil-characteristics-research, 9-Jul 2015.

[3] D. L. Lord, R. G. Allen, and D. K. Rudeen, "DOE/DOT Crude Oil Characterization Research Study, Task 2 Test Report on Evaluating Crude Oil Sampling and Analysis Methods," Sandia National Laboratories, Albuquerque, NM, Unclassified Unlimited Release SAND2017-12482, November 2017.

[4] D. Lord, R. Allen, D. Rudeen, C. Wocken, and T. Aulich, "DOE/DOT Crude Oil Characterization Research Study, Task 2 Test Report on Evaluating Crude Oil Sampling and Analysis methods, Revision 1 - Winter Sampling," Sandia National Laboratories, Albuquerque, NM, Unclassified Unlimited Release SAND2018-5909, 2018.

[5] EIA, "Annual Energy Outlook 2018," U.S. Energy Information Administration #AEO2018, February 2018.

[6] ANSI/API, "Classifying and Loading of Crude Oil into Rail Tank Cars," Recommended Practice 3000, American Petroleum Institute, Washington, DC, 2014.

[7] J. M. Suo-Anttila and L. A. Gritzo, "Thermal Measurements from a Series of Tests with a Large Cylindrical Calorimeter on the Leeward Edge of a JP-8 Pool Fire in Cross-Flow," Sandia National Laboratories, Albuquerque, NM SAND2001-1986, 2001.

[8] T. K. Blanchat, D. Sundberg, and A. Brown, "Well-Characterized Open Pool Experiment Data and Analysis for Model Validation and Development," Sandia National Laboratories, Albuquerque, NM, Unclassified Unlimited Release SAND2006-7508, 2006.

[9] D. F. Wayne, "An Economical Formula for Calculating Atmospheric Infrared Transmissivities," *J. Loss Prev. Process Ind.,* pp. 85-92, 1991.

[10] C. S. Lam and E. J. Weckman, "Wind-blown pool fire, PartII: Comparison of measured flame," *Fire Safety Journal,* vol. 78, pp. 130-141, 2015.

[11] P. Croce, K. Mudan, and J. Moorhouse, "Thermal Radiation from LNG (Liquefied Natural Gas) Trench Fires. Volume 1. Main Report," Arthur D. Little, Inc., Cambridge, MA, PB85129096, 1984.

[12] P. Croce, K. Mudan, and J. Moorhouse, "Thermal Radiation from LNG Trench Fires. Volume 2. Data," Arthur D. Little, Cambridge, MA, PBS85159465, 1984.

[13] A. Buang, "Boilover in liquid hydrocarbon tank fires," *Doctoral thesis,* p. Loughborough University, 2014.

[14] K. Bulent, F. Fabi, M. Munoz, J. Arnaldos, and J. Casal, "Velocity of Convective Currents in Boilover," *Chemical Engineering Science,* vol. 61, pp. 2550-2556, 2006.

[15] H. Koseki and G. W. Mulholland, "The Effect of Diameter on the Burning of Crude Oil Pool Fires," *Fire Technology,* pp. 54-65, Feb. 1991.

[16] S. Soma and K. Saito, "Reconstruction of Fire Whirls Using Scale Models," *Combustion and Flame,* vol. 86, pp. 269-284, Aug 1991.

[17] S. R. Tieszen, V. F. Nicolette, L. A. Gritzo, J. A. Holen, D. Murray, and J. L. Moya, "Vortical Structures in Pool Fires: Observation, Speculation, and Simulation," Sandia National Laboratories, Albuquerque, NM, Unclassified Unlimited Release SAND96-2607, November 1996.

[18] A. Luketa, T. K. Blanchat, S. M. Adee, and C. McCoy, "Fire Whirl Investigation," Sandia National Laboratories, Albuquerque, NM, Unclassified Unlimited Release SAND2018-10354, September 2018.
[19] L. A. Gritzo, J. L. Moya, and D. Murray, "Fire Characterization and Object Thermal Response for a Series of Tests with a Large Flat Plate Adjacent to a Large JP4 Fuel Fire," Sandia National Laboratories, Albuquerque, NM, Unclassified Unlimited Release SAND97-0047, 1997.
[20] T. K. Blanchat and L. Manning, "Mock B52 Bomb Bay Fire Experiment Data and Analysis for Model Validation and Development," Sandia National Laboratories, Albuquerque, NM SAND2002-0145, January 2001.
[21] J. M. Suo-Anttila and L. A. Gritzo, "The Effects of Wind on Fire Environements Containing Large Engulfed Cylinders," *Comb. Sci. Tech.,* vol. 181, pp. 68-77, January 2009.
[22] J. M. Suo-Anttila and L. A. Gritzo, "Thermal Measurements for a JP-8 Pool Fire in Cross-Flow with a C-141 Fuselage Section Located on the Leeward Edge," Sandia National Laboratories, Albuquerque, NM, Unclassified Unlimited Release SAND2001-0313, 2001.
[23] K. S. Mudan, "Geometric View Factors for Thermal Radiation Hazard Assessment," *Fire Safety Journal,* pp. 89-96, 1987.
[24] J. Moorhouse, "Scaling criteria for pool fires derived from large scale experiments," *I. Chem. Sym.,* vol. 71, pp. 165-179, 1982.
[25] M. Munoz, J. Arnaldos, J. Casal, and E. Planas, "Analysis of the geometric and radiative characteristics of hydrocarbon pool fires," *Combustion and Flame,* vol. 139, pp. 273-277, 2004.
[26] *SFPE Handbook of Fire Protection Engineering*: National Fire Protection Asscoiation, 1995.
[27] NFPA, *Standard for the Production, Storage, and Handling of Liquefied Natural Gas (LNG)*: National Fire Protection Association, 2019.
[28] K. S. Mudan, "Thermal radiation hazards from hydrocarbon pool fires," *Prog. Energy Combust. Sci.,* vol. 10, pp. 59-80, 1984.
[29] J. LaChance, A. Tchouvelev, and A. Engebo, "Development of uniform harm criteria for use in quantitative risk analysis of the hydrogen infrastructure," *Int. J. Hydrogen Energy,* vol. 36, pp. 2381-2388, 2011.
[30] T. Blanchat, P. Helmick, R. Jensen, A. Luketa, R. Deola, J. Suo-Anttila*, et al.*, "The Pheonix Series Large Scale LNG Pool Fire Experiments," Sandia National Laboratories, Albuquerque, NM, Unclassified Unlimited Release SAND2010-8676, 2010.
[31] G. A. Mizner and J. A. Eyre, "Large-scale LNG and LPG Pool Fires," *I. Chem. E. Symposium Series,* vol. No. 71, pp. 147-163, 1982.
[32] V. I. Blinov and G. N. Khudiakov, "Diffusive Burning of Liquids," Translated for the US Army Engineer Research and Development Laboratories, AD 296762, 1961.
[33] D. D. Evans, G. W. Mulholland, H. R. Baum, W. D. Walton, and K. B. McGrattan, "In Situ Burning of Oil Spills," *Journal of Research of the National Institute of Standards and Technology,* vol. 106, pp. 231-278, 2001.
[34] J. Sjostrom, F. Amon, and G. Appel, "Thermal exposure from large scale ethanol fuel pool fires," *Fire Safety Journal,* vol. 78, pp. 229-237, 2015.
[35] H. Koseki and Y. Iwata, "Tomakomai Large Scale Crude Oil Fire Experiments," *Fire Technology,* vol. 36, pp. 24-38, 2000.
[36] H. Koseki, "Combustion Properties of Large Liquid Pool Fires," *Fire Technology,* pp. 241-255, August 1989.
[37] T. Yamaguchi and K. Wakasa, "Oil Pool Fire Experiment," *Fire Safety Science Proceedings of the first international symposium,* pp. 911-918, 1986.

[38] N. Takahashi, S. Masataro, R. Dobashi, and T. Hirano, "Behavior of luminous zones appearing on plumes of large-scale pool fires of kerosene," *Fire Safety Journal,* vol. 33, pp. 1-10, 1999.
[39] A. F. Roberts, "Thermal radiation from releases of LPG from pressurised storage," *Fire Safety Journal,* vol. 4, pp. 197-212, 1982.
[40] K. Hasegawa and K. Sato, "Study on the fireball following steam explosion of n-pentane," *Loss prevention and safety promotion in the process industries: proceedings,* vol. VI, p. 297, 1978.
[41] H. C. Hardee, D. O. Lee, and W. B. Benedick, "Thermal Hazard from LNG Fireballs," *Combustion science and technology,* vol. 17, pp. 189-197, 1978.
[42] S. B. Dorofeev, et al., "Fireballs from Deflagration and Detonation of Heterogeneous Fuel-rich Clouds," *Fire Safety Journal,* vol. 25, pp. 323-336, 1995.
[43] CCPS, *Guidelines for Vapor Cloud Explosion, Pressure Vessel Burst, BLEVE and Flash Fire Hazards* Wiley, 2011.
[44] D. M. Johnson and M. J. Pritchard, "Large scale experimental study of Boiling Liquid Expanding Vapour Explosions (BLEVEs)," *GASTECH (1990): International LNG/LPG Conference and Exhibition Conference Papers,* vol. 1, pp. session 3, paper 3.3, 1990.
[45] I. A. Papazoglou and O. N. Aneziris, "Uncertainty quantification in the health consequences of the boiling liquid expanding vapour explosion phenomenon," *Journal of Hazardous Materials,* vol. 67, pp. 217-235, Jun 30 1999.
[46] J. L. Woodward and P. R.M., *LNG Risk Based Safety Modeling and Consequence Analysis*. Hoboken, N.J.: John Wiley & Sons, Inc., 2010.
[47] J. M. Cabeza-Lainez, J. A. Pulido-Arcas, and M. V. Castilla, "New configuration factor between a circle, a sphere and a differential area at random postions," *J. of Quantitative Spectroscopy & Radiative Transfer,* vol. 129, pp. 272-276, 2013.
[48] T. Roberts, A. Gosse, and S. Hawksworth, "Thermal Radiation from Fireballs on Failure of Liquefied Petroleum Gas Storage Vessels," *Trans IChemE,* vol. 78, pp. 184-192, 2000.
[49] S. Betteridge and L. Phillips, "Large scale pressurised LNG BLEVE experiments," *Institution of Chemical Engineers Symposium,* pp. 353-364, 2015.
[50] ASTM, "Standard Test Method for Determination of Vapor Pressure of Crude Oil: VPCRx(Expansion Method)," ASTM D6377-16, ASTM International, West Conshohocken, PA 19428-2959, 2016.
[51] GPA, "Liquefied Petroleum Gas Specifications and Test Methods," GPA 2140-17, GPA Midstream Association, Tulsa, OK 74135, 2017.
[52] USEPA. (2019). *Gasoline Reid Vapor Pressure.* Available: https://www.epa.gov/gasoline-standards/gasoline-reid-vapor-pressure
[53] Crudemonitor. (2019). Available: https://crudemonitor.ca/
[54] ASTM, "Standard Test Method for Vapor Pressure of Petroleum Products (Reid Method)," ASTM D323-08 (Reapproved 2014), ASTM International, West Conshohocken, PA 19428-2959, 2014.
[55] A. Prefontaine, "Final Report: Crude Oil Sampling and Analysis (Version 2)," Alberta Innovates Technology Futures, 10-Aug 2015. Available: https://www.tc.gc.ca/eng/tdg/safety-menu-1242.html
[56] ASTM, "Standard Test Method for Determination of Light Hydrocarbons and Cut Point Intervals in Live Crudes and Condenates by Gas Chromatography," ASTM D8003-15, ASTM International, West Conshohocken, PA 19428-2959, 2015.
[57] GPA, "Method for the Extended Analysis of Hydrocarbon Liquid Mixtures Containing Nitrogen and Carbon Dioxide by Temperature Programmed Gas Chromatography," GPA Standard 2186-14, Gas Processors Association, Tulsa, OK 74145, 2014.

[58] P. F. Thorne, "Flash Points of Mixtures of Flammable and Non-flammable Liquids," *Fire and Materials,* vol. 1, pp. 134-139, 1976.
[59] DOT/FAA, "A Review of the Flammability Hazard of Jet A Fuel Vapor in Civil Transport Aircraft Fuel Tanks," DOT/FAA/AR-98/26, June 1998.
[60] D. Y. Jeong, "Probabilistic approach to conditional probability of release of hazardous materials from railroad tank cars during accidents," *Proceedings of IMECE2009, 2009 ASME International Mechanical Engineering Congress and Exposition, November 13-19, Lake Buena Vista, Florida, USA.*
[61] L. Holländer, T. Grunewald, and R. Graetz, "Influence of material properties of stainless steel on the ignition probability of flammable gas mixtures due to mechanical impacts," *Chemical Engineering Transactions,* vol. 48, pp. 307-312, 2016.
[62] M. A. Finney, T. B. Maynard, S. S. McAllister, and I. J. Grob, "A study of ignition by rifle bullets," U.S. Department of Agriculture, RMRS-RP-104, 2013.
[63] A. Iranitalab, "Statistical Investigation of Road and Railway Hazardous Materials Transportation Safety," *University of Nebraska, Dissertation,* 2018.
[64] PHMSA, *2016 Emergency Response Guidebook*: U.S. Department of Transportation and Transport Canada, 2016.
[65] NTSB, "Derailment and Hazardous Materials Release of Union Pacific Railroad Unit Ethanol Train, Graettinger, Iowa, March 10, 2017 " National Transportation Safety Board NTSB/RAR-18/02, 2018.
[66] API, "In-Situ Burning, The Fate of Burned Oil," Washington, DC API Publication 4735, 2004.
[67] A. H. Hall and R. Schnepp, "Cyanide: Fire Smoke's Other "Toxic Twin"," *Fire Engineering,* 2011.
[68] D. H. Schafer II and C. P. Barkan, "Relationship Between Train Length and Accident Causes and Rates," *Transportation Research Record: Journal of the Transportation Research Board, No. 2043, Transportation Research Board of the National Academies, Washington, D.C.,* pp. 73-82, 2008.
[69] M. Verma, "Railroad transportation of dangerous goods: A conditional exposure approach to minimize transport risk," *Transportation Research Part C,* vol. 19, pp. 790–802, 2011.
[70] C. Reschovsky, M. Flowers, and D. Smallen, "Fleet Composition of Rail Tank Cars Carrying Flammable Liquids: 2018 Report," *Bureau of Transportation Statistics, US Department of Transporation,* 2018.
[71] GAO, "Federal Transit Administration Can Strengthen Safety Oversight by Improving Guidance in States," March 2018.
[72] GPA, "Obtaining Liquid Hydrocarbons Samples for Analysis by Gas Chromatography," GPA 2174-14, Gas Processors Association, Tulsa, OK 74145, 2014.
[73] M. L. Janssens, "Measuring Rate of Heat Release by Oxygen Consumption," *Fire Technology,* pp. 234-248, 1991.
[74] H. Biteau, T. Steinhaus, C. Schemel, A. Simeoni, G. Marlair, N. Bal*, et al.*, "Calculation Methods for the Heat Release Rate of Materials of Unknown Composition," *Fire Safety Science, Proceedings of the Ninth International Symposium,* pp. 1165-1176, 2008.
[75] D. L. Lord, "Technical Proposal for Acquiring Crude Oil Samples to support US DOE/DOT Crude Oil Characterization Research Study," Sandia National Laboratories, Albuquerque, NM SAND2016-1636M, Feb-2016 2016.
[76] G. Berndsen, J. Maldonado, P. Mihalik, and D. Lord, "U.S. Strategic Petroleum Reserve Vapor Pressure Committee 2009 Annual Report," Sandia National Laboratories, Albuquerque, NM, Unclassified Unlimited SAND SAND2010-3016, 2007.

[77] D. L. Lord, R. Allen, and J. Hogge, "Fuels Characterization Methods & Results for National Research Council Canada 2m Pool Fire Test Series," Sandia National Laboratories, Albuquerque, NM In Press, 2019.
[78] J. G. Speight, *The Chemistry and Technology of Petroleum*, 2nd ed. New York: M. Dekker, 1991.
[79] GPA, "Tentative Method for the Analysis of Natural Gas Condensate Mixtures Containing Nitrogen and Carbon Dioxide by Gas Chromatography," GPA Standard 2103-03, Gas Processors Association, Tulsa, OK 74145, 2003.
[80] ASTM, "Standard Test Method for Boiling Range Distribution of Petroleum Fractions by Gas Chromatography," ASTM D2887-16a/IP 406, ASTM International, West Conshohocken, PA 19428-2959, 2016.
[81] ASTM, "Standard Test Methods for Flash Point by Small Scale Closed Cup Tester," ASTM D3828-16a, ASTM International, West Conshohocken, PA 19428-2959, 2016.
[82] S. S. Alqaheem and M. R. Riazi, "Flash Points of Hydrocarbons and Petroleum Products: Prediction and Evaluation of Methods," *Energy & Fuels,* vol. 31, pp. 3578-3584, 2017.
[83] M. J. Amani, M. R. Gray, and J. M. Shaw, "On correlating water solubility in ill-defined hydrocarbons," *Fuel,* vol. 134, pp. 644-658, 2014/10/15/ 2014.
[84] ASTM, "Standard Test Method for Distillation of Petroleum Products and Liquid Fuels at Atmospheric Pressure," ASTM D86-16a, ASTM International, West Conshohocken, PA 19428-2959, 2016.
[85] R. J. Hill, Y. C. Tang, and I. R. Kaplan, "Insights into oil cracking based on laboratory experiments," *Organic Geochemistry,* vol. 34, pp. 1651-1672, 2003.
[86] M. V. Kök and O. Karacan, "Pyrolysis Analysis and Kinetics of Crude Oils," *Journal of Thermal Analysis and Calorimetry,* vol. 52, pp. 781-788, June 01 1998.
[87] ASTM, "Standard Test Method for Heat of Combustion of Liquid Hydrocarbon Fuels by Bomb Calorimeter," ASTM D240-14, ASTM International, West Conshohocken, PA 19428-2959, 2014.
[88] PHMSA, "Operation Safe Delivery Update," U.S. Department of Transportation, Washington, D.C., July 2014.
[89] J. R. Auers, R. M. Couture, and D. L. Sutton, "The North Dakota Petroleum Council Study on Bakken Crude Properties," Turner, Mason & Company, Bismarck, ND 58501, Aug 4 2014.
[90] SPL, "Pressurized Hydrocarbons Liquids Sampling and Analysis Study, Data Assessment and Analysis Report," Southern Petroleum Laboratories, Inc., 8850 Interchange Drive, Houston, TX, February 2018.

This page left blank

APPENDIX A. TEST DESCRIPTION AND RESULTS

A.1. Two Meter Pool Fire Tests

Table A-1: Summary of results for 2-m pool fire tests.

Test	Oil	Fuel Supply Temperature (°C)	Burn rate (mm/min)	Flame Height (m)	Average Surface Emissive Power* (kW/m^2)	Average heat flux to calorimeter **(kW/m^2)	Heat release rate (MW)
1	SPR	6.9 ±0.35	2.12 ±0.01	5.0 ±2	47.4 ±17.7	74.3 ±2.6	4.3 ±0.1
2	SPR	59.5 ±4.5	1.95 ±0.02	2.9 ±1.6	43.0 ±23.3	103.2 ±5.9**	3.7 ±0.6

*averaged over time, narrow-angle radiometers

**averaged over all thermocouples and over time. Calorimeter was 0.5" lower in elevation within flame for the 'hot' fuel test.

A.1.1. SPR, cold

A.1.1.1. Description

On the day before the test, the 200-gallon tank positioned outside of the FLAME facility was first filled with water to purge all air out of the tank. The tank was then filled with approximately 150 gallons of SPR oil causing the displacement of water back into the water tote and leaving approximately 50 gallons of water in the tank. The tank was pre-conditioned with regards to temperature using a heat exchanger described in section C.8. Before pre-conditioning commenced to cool the tank, sampling was performed by an analytical laboratory under contract to Sandia to characterize the oil before each test. The sampling took approximately 4 hours. Cooling of the tank occurred on the following day, early morning.

On the day of the test, after the tank was pre-conditioned to almost 5°C, water was pumped into the bottom of the tank to push oil out of the top of the tank and into the fuel pan within the FLAME facility. Temperature readings from thermocouples within the fuel pan were monitored to determine when to stop filling the pan. Approximately 51.2 gallons of fuel was pumped into the pan with a height of approximately 2.45", leaving almost 2" of pan height above the fuel. The fuel was then readily ignited with two propane torches.

The fire became fully developed and showed regularity up until about 22 minutes after ignition. Regularity is indicated by steadiness in the burn rate, average flame height, radiometer measurements, and visual observation. During the time of steady burning, the differential pressure gauge within the pan signaled the fuel valve to open and close to maintain a constant fuel level. At 22 minutes, fuel began spilling over the edge of the pan and down into the basement, resulting in a fire in the basement. The test was immediately aborted by stopping the water pump and initiating the emergency drain down. The spillage quickly ceased and the fire in the pan died down approximately 1.5 minutes after test abort. No severe damage occurred from the basement fire; however, a tar-like crust of crude oil remained that required clean-up.

There are several indications that water entrainment is the cause for the fuel spillage over the pan. The first indication is the temperature readings from thermocouples within the 200-gallon tank. One thermocouple at approximately 9" from the top of the tank was immersed within the oil region, while

the bottom thermocouple at about 36" from the top of the tank was immersed within the water region. The water level was about 32" from the top of the tank. The internal height of the tank is approximately 50". Figure A-1 indicates that the top thermocouple was about 8.5°C and the bottom was about 5°C. It can be seen that by the end of the pan fill, the two thermocouple readings reach a temperature that is approximately their average, indicating the oil and water became mixed before ignition.

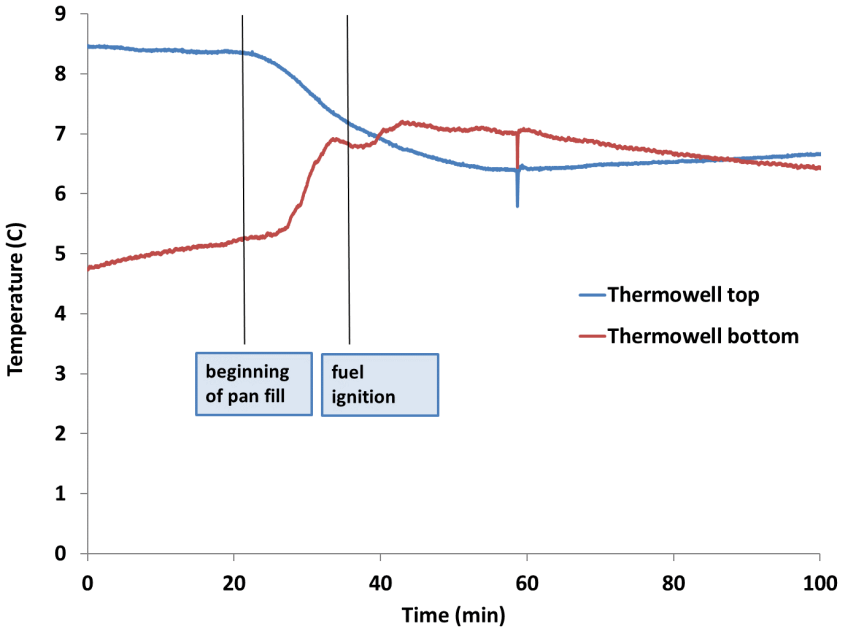

Figure A-1: Thermocouple temperatures within 200-gallon tank.

The second indication is shown in Figure A-2 which provides temperatures from thermocouples within the pool. The 29 thermocouples are placed at the side of the pool and are 2 mm apart vertically. Thus, the thermocouple rake provides temperature as a function of depth over time. The thermocouple at approximately the fuel level is shown as a dashed red line (TC 14).

Typically, what is observed is that temperatures indicated by thermocouples below the fuel level thermocouple are much lower than temperatures from thermocouples above since they are fully immersed in the fuel. The thermocouples above are in the vapor generation region just above the top of the fuel and will indicate much higher temperatures. Thus, there will be a clear demarcation of these regions as shown in Figure A-3 during a Jet-A pool test conducted just prior to the SPR pool fire test in FLAME using a 2-m diameter pan. The shift in temperatures at approximately 78 minutes is a manual adjustment of the tolerance of the differential pressure gauge within the pool. The rapid rise in all of the thermocouples at 110 minutes is due to termination of the test thereby causing full exposure to the fire as the fuel level decreases.

As shown in Figure A-2, the thermocouples below the fuel level continue to rise and not remain steady as for Jet-A. The lowest thermocouple, approximately 1.3" above the bottom of the pan or 1.2" from the fuel level, reached above 100°C at about 17 minutes after ignition and about 250°C just before spillage. This would indicate that a temperature of 100°C was reached at even greater depths, thereby causing any water within the pan to vigorously boil causing rapid expansion and ultimately spillage.

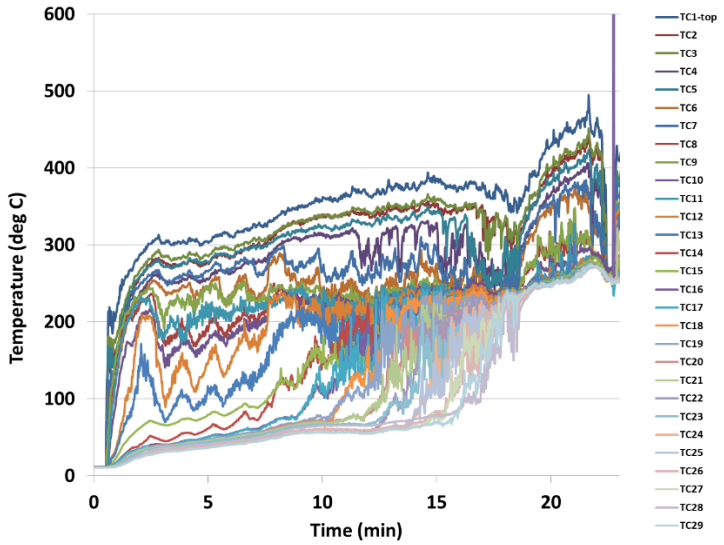

Figure A-2: SPR crude oil 'cold', 2-m pool fire test; thermocouple temperatures within fuel pan.

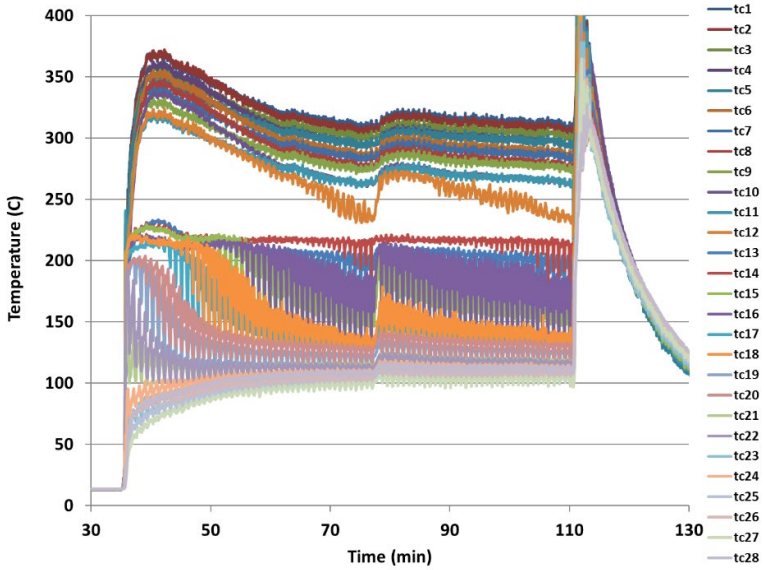

Figure A-3: Jet-A pool fire test; thermocouple temperatures within fuel pan.

The third indication is from post-test sampling from the fuel line leading to the pan. The sample developed a stratified layer with oil on the top and water on the bottom, providing compelling evidence for water entrainment. Pre-test sampling at the SPR loading site showed no water content. Thus, there was no inherent water present in the SPR oil.

Crude oil pool fires are known to have relatively high temperatures throughout the depth of the fuel which can result in violent boiling if water is present. One theory, is that a stratified distillation process is responsible in which higher level regions become denser than lower region levels leading to mixing by virtue of unstable stratification. Fuels that have principal components with a large range of boiling points (i.e. crude oil) have a significantly higher chance of displaying a higher, more constant

temperature fuel profile than fuels with a narrow range of boiling points (i.e. jet fuel). A direct comparison of component chemistry by carbon number for the crude oils and jet fuel used in burn testing at Sandia is discussed in F.3.3.3 and illustrated in Figure F- 39 The mixing effects observed in large boiling-range fluids occur because the higher boiling point components are able to transport heat to the rest of the fluid before they vaporize. To prevent water entrainment in future tests, above that contained inherently within a crude oil, the crude oil will be pumped into the pan using similar crude oil instead of water. Also, since a crude oil may inherently have some water content, a deeper fuel pan of approximately 12" was used to prevent spillage within the FLAME facility.

A.1.1.2. Radiometer and Directional Flame Thermometer measurements

For the 2-m pool fire test in the FLAME facility, six narrow-angle radiometers and five total heat flux gauges were used to measure the spot surface emissive power (SEP) and total heat flux; respectively, from the flame plume as a function of height. The total heat flux gauge measurements include convective and radiative heat transfer. The narrow-angle gauges measure radiative heat transfer, that is, the incident heat transferred to the gauge. The narrow-angle radiometer is a Medtherm model NVRW(ZnSe)-FTP-5.5-96-21261, 5.5° view angle, range of 300 kW/m^2 and the total heat flux gauge is a windowless Medtherm model 64-2-18 with a view angle of 180°, and range of 15 kW/m^2. They were mounted near the FLAME wall at a distance of 28.64 ft. (8.73 m) from the center of the fire. The spot diameter for the narrow-angle gauges (at 9 m) is about 0.8 m. The narrow-angles radiometers are at heights of 0.5, 1, 1.5, 2, 3, and 4 m, while the total heat flux gauges are at heights of 1, 1.5, 2, 3, and 4 m. The line of sight for each gauge was set to pass through the centerline of the fire at the height of the gauge. All heat flux gauges are water-cooled.

Figure A-4 shows heat flux from the six narrow-angle and five wide-angle radiometer measurements. Heat flux values time-averaged over the duration at which a steady-state occurred (10 – 17 minutes) are provided in Table A-2. The highest narrow-view heat flux reading occurs at a height of 2-m above the pool, then decreases at greater heights. All of the wide-angle radiometers readings are similar due their field of view which receives radiant heat from the flame and outside the flame, thus their readings will be lower than narrow-angle radiometers which focus on a spot region of the flame and are not impacted by the much cooler surroundings.

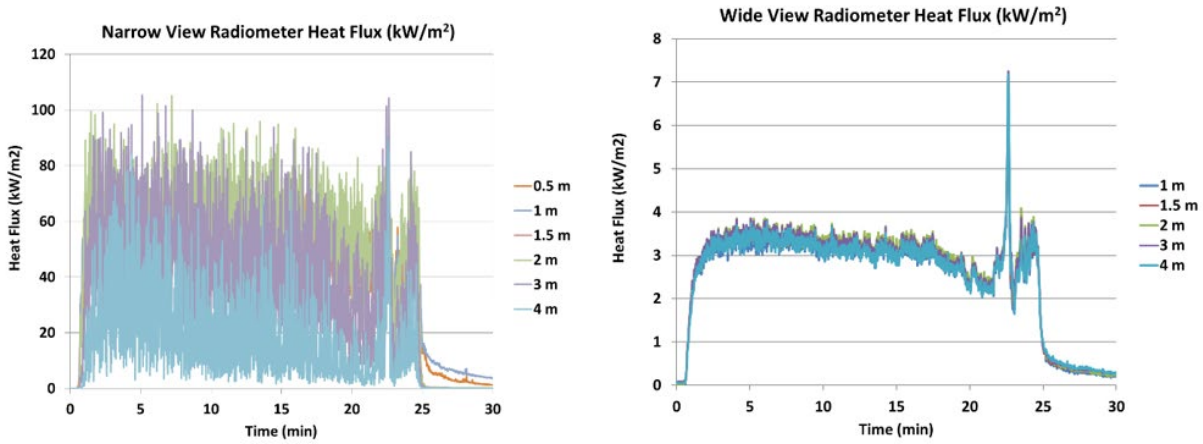

Figure A-4: Wide-view and narrow-view radiometer heat flux at different elevations.

Table A-2: Time-averaged heat flux values from radiometers.

height (m)	wide-angle heat flux* (kW/m^2)	narrow-angle heat flux* (kW/m^2)
0.5		52.5 ±5.0
1	3.1 ±0.1	54.6 ±4.1
1.5	3.1 ±0.1	54.8 ±9.9
2	3.2 ±0.1	63.1 ±11.6
3	3.3 ±0.1	43.7 ±17.2
4	3.1 ±0.1	17.5 ±12.5

*averaged over steady-state duration (10-17 minutes)

To measure heat flux as a function of distance from the center of the pan, directional flame thermometers (DFT) which measure the total heat flux, that is, it includes convective and radiative heat transfer, were placed external to the fire (Table A-3). The description of the DFT instrumentation is provided in section D.3. Time-averaged DFT thermocouple measurements are reduced to determine incident and absorbed heat flux as described in section D.3. The period of averaging is over the test duration of 10 – 17 minutes.

Table A-3: Average absorbed and incident heat flux as a function of distance for 2-m pool fires from DFT measurements.

Distance from center of pool (m)*	Average absorbed heat flux (kW/m^2)	Average incident heat flux (kW/m^2)
2	-2.4 ±0.8	30.8 ±0.7
3	-1.9 ±0.7	17.8 ±0.4
4	-1.6 ±0.5	12.1 ±0.4
5	-1.5 ±0.4	9.7 ±0.2

* DFTs at height of 1-m from the ground

A.1.1.3. Calorimeter

Figure A-5 and Figure A-6 show thermocouple measurements and derived total heat flux values at corresponding locations. The height of calorimeter is 1-m from its centerline to the surface of the pan. Descriptions of the calorimeter and thermocouple locations are provided in section D.4. Table A-4 provides heat flux values time-averaged over 10 – 17 minutes.

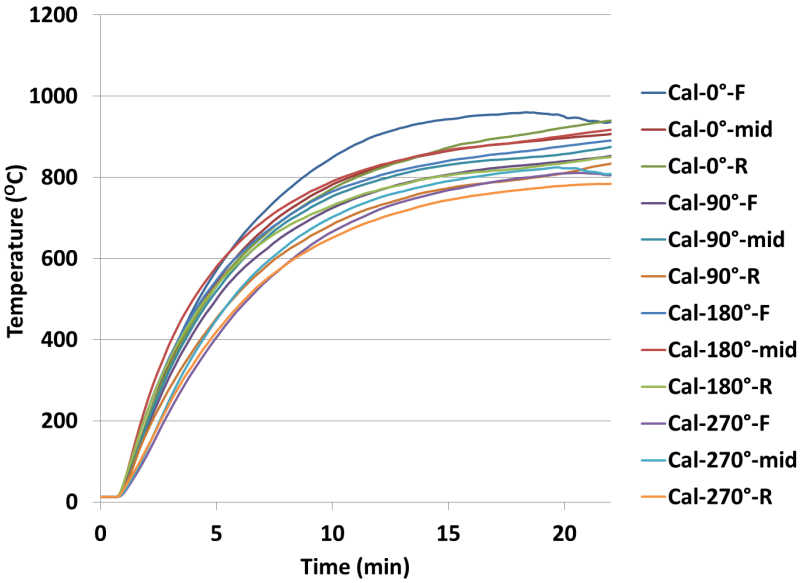

Figure A-5: Calorimeter thermocouple measurements.

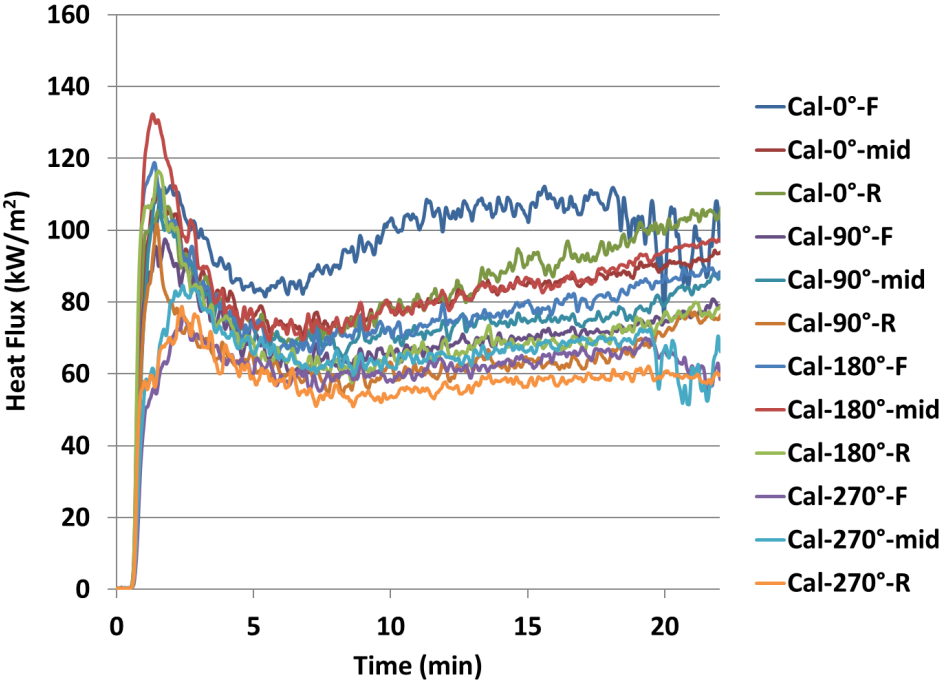

Figure A-6: Heat flux values derived from thermocouple measurements on calorimeter.

Table A-4: Time-averaged heat flux values over 10–17 minutes.

Thermocouple location	Heat flux (kW/m2)
Top	
0°-F	105.7 ± 2.6
0°-mid	82.7 ± 3.0
0°-R	86.1 ± 5.4
Average	91.5 ± 3.7
Side	
90°-F	69.0 ± 2.0
90°-mid	73.7 ± 2.1
90°-R	62.1 ± 1.8
Average	68.3 ± 2.0
Bottom	
180°-F	76.4 ± 2.9
180°-mid	82.6 ± 3.0
180°-R	67.5 ± 2.1
Average	75.5 ± 2.7
Side	
270°-F	62.6 ± 2.2
270°-mid	66.0 ± 2.0
270°-R	57.0 ± 1.6
Average	61.9 ± 1.9

A.1.1.4. Flame Height

The visible cameras are used to determine the length of the fire (Figure A-7 and Figure A-8). The method used to determine these flame height values is provided in section D.1.1.2. The average flame height is 5 m with a 2-sigma standard deviation of about ±2 m.

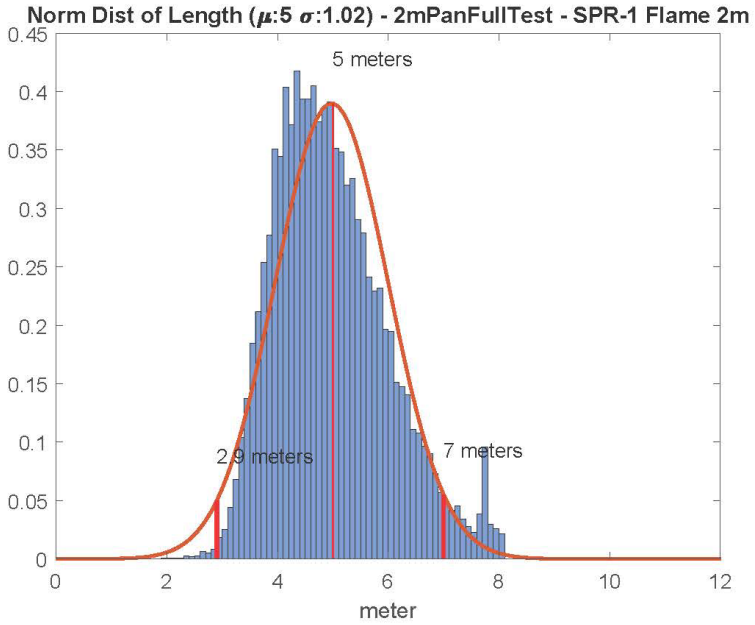

Figure A-7: Flame height distribution for SPR (cold) 2-m pool fire test.

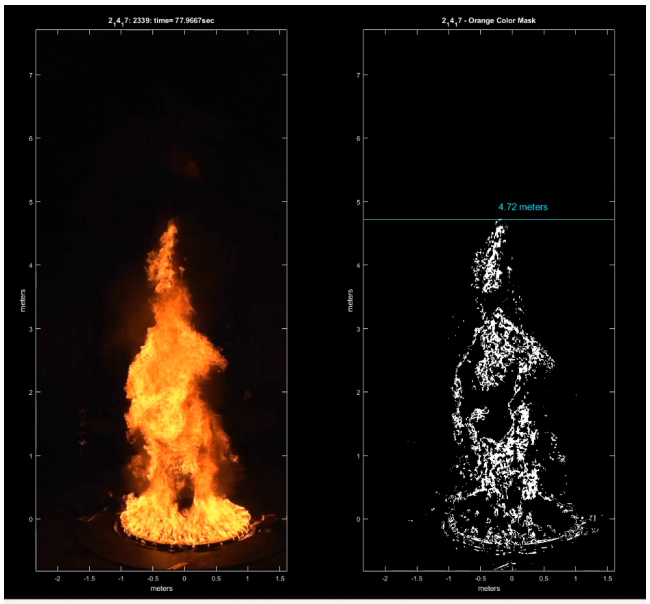

Figure A-8: Frame from SPR (cold) 2-m pool fire test. Post-processing software to determine flame length.

A.1.1.5. Burn rate

The water used to push the oil out of the conditioning tank was placed in a tote on a scale. The decrease in weight of the tote in units of pounds was converted to gallons to determine the gallons per minute as shown in Figure A-9. The slope during which the weight decreases, highlighted in red, is used to determine the burn rate. The slope indicates that 25.2 gallons was burned in in about 14.2 minutes which corresponds to an average burn rate of 2.12 mm/min. Note that the spike just before the beginning of the test is interference from radio communications which are made to notify personnel within the Thermal Test Complex that testing will commence.

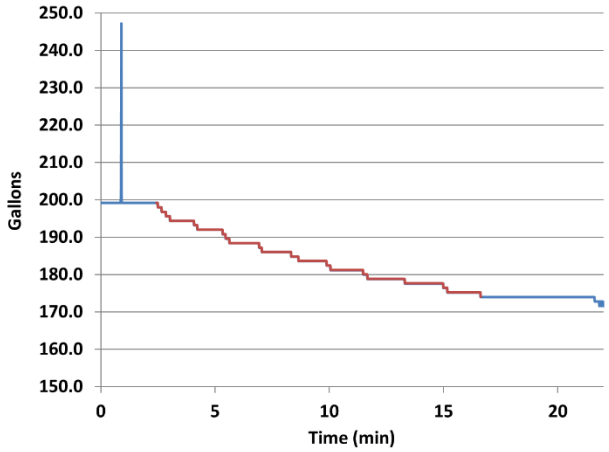

Figure A-9: Water scale measurement over time converted to gallons.

A.1.2. SPR, hot

A.1.2.1. Description

For this test, the SPR crude oil was heated over the course of approximately 3 hours to 60ºC. To prevent boil-over, modifications were made based on the recommendations discussed in the previous section pertaining to the 'cold' feed SPR pool fire. The pan lip was increased from 4" to 12" and the oil was driven into the pan using SPR oil. Since air contamination was not of concern for this non-pressurized oil, it was unnecessary to use water to purge the tank of air. Thus, there was no potential for water in the system and boil-over did not occur. The fuel level was kept at a constant level of approximately 3". Note that this level is 0.55" higher than the 'cold' SPR pool fire test. In addition to the differential pressure gauge which provides indication of the fuel level, a float with reference markings was placed within the pool to allow for constant visual monitoring to alert for rapid rise in the fuel level. The float is shown in Figure A-10.

The burn lasted for approximately 60 minutes. The constant fuel level condition was maintained for approximately the first 30 minutes, and the fuel was then allowed to burn down for the last 30 minutes.

Figure A-10: Float used to monitor fuel level.

Post-test there was significant residue left in the pan, on the calorimeter, and valves. Figure A-11 shows the pan and calorimeter where a porous residue formed. Figure A-12 shows both a view underneath the fuel pan and the fuel pump. The outlet for draining was filled with solid residue that required chiseling to be removed. The fuel valve was filled with a highly viscous residue that also required cleaning.

Figure A-11: Post-test residue left in the pan and on the calorimeter stand.

Figure A-12: View underneath pan showing pipe for draining fuel filled with solid residue (left) and fuel valve port filled with highly viscous residue (right).

A.1.2.2. Fuel rake temperatures

Figure A-13 shows a comparison of thermocouple temperatures within the fuel pan for the 'hot' and 'cold' SPR, 2-m pool fire tests. Note the top thermocouple failed for the 'hot' test. Significant temperature differences in the lower thermocouples occur for approximately the first 15 minutes of the fire due to the different fuel feed temperatures. However, by approximately 18 minutes the temperature range of both tests are similar, indicating that fuel feed temperature does not have a significant effect on in-depth fuel temperatures after the initial transient. The in-depth fuel temperature profile affects the availability of energy that contributes to vaporization of the fuel. For Jet-A (Figure A-3) the in-depth fuel temperature profile has a significant slope indicating that part of

the energy arriving from the flame onto the pool surface is being transferred in the form of conductive heat transfer into the pool. Thus, less energy is available to contribute towards vaporization or burn rate. For crude oils, since the temperature profile has a much lower gradient and is nearly isothermal, the conductive loss impacting the burn rate is much lower. Thus, the profiles for both the 'hot' and 'cold' tests evolved to be similar, it indicates that the fuel feed temperature does not have a significant effect on the burn rate.

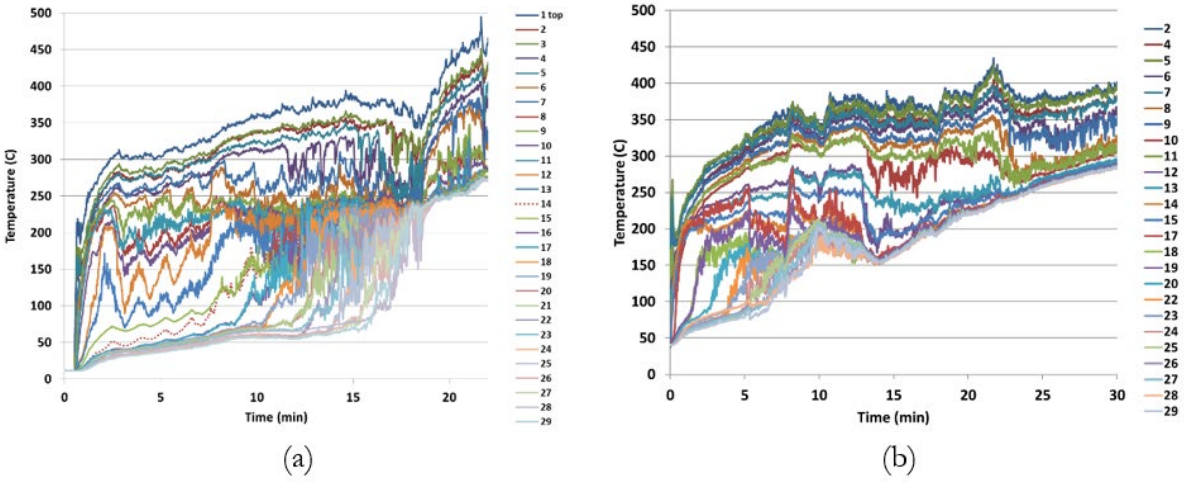

Figure A-13: SPR crude oil 2-m test: comparison of thermocouple temperatures within fuel pan, (a) 'cold' test and (b) 'hot' test.

A.1.2.3. Radiometer and Directional Flame Thermometer measurements

The radiometers used for this test were the same used for the 'cold' SPR test. Description of the radiometers and their location is provided in section A.1.1.2. Figure A-14 provides wide and narrow view radiometer heat flux values for the different height locations, while Table A-5 provides time average values over the period of 4 – 30 minutes. The wide view radiometers for both the 'cold' and 'hot' tests are in close agreement, while the vertical profile for the narrow view radiometers for the 'hot' and 'cold' tests differ. This is attributable to the difference in pan lip between the tests. Narrow view radiometers are focused on a location and slight shifts can result in different readings, while wide view radiometers due to their much wider viewing angle will provide more spatially averaged readings. Table A-6 provides average heat flux values over 4-30 minutes from the DFT instruments placed at different radial locations from the fire. Readings from the 'hot' and 'cold' tests are in close agreement.

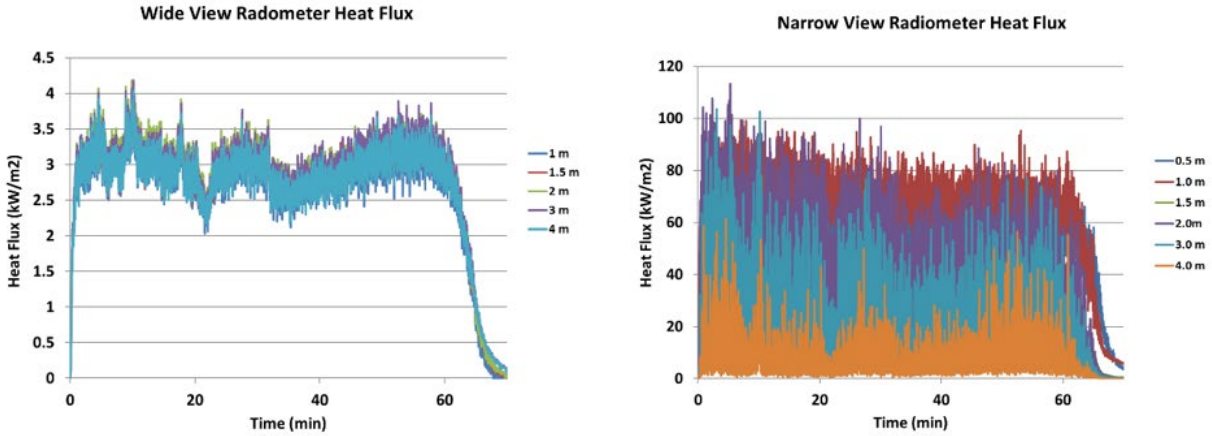

Figure A-14: Wide-view and narrow-view radiometer heat flux at different elevations.

Table A-5: Time-averaged heat flux values from radiometers.

height (m)	wide-view heat flux (kW/m^2)	narrow-view heat flux (kW/m^2)
0.5		54.7 ±7.2
1	2.9 ±0.3	73.1 ±7.4
1.5	3.0 ±0.3	43.0 ±17.1
2	3.1 ±0.3	47.0 ±19.9
3	3.1 ±0.3	22.6 ±17.1
4	3.0 ±0.3	7.3 ±7.4

*averaged over 4-30 minutes

Table A-6: Average absorbed and incident heat flux as a function of distance for 2-m pool fires from DFT measurements.

Distance from center of pool (m)*	Average absorbed heat flux (kW/m^2)	Average incident heat flux (kW/m^2)
2	-3.5 ±3.6	36.8 ±1.8
3	-2.5 ±2.4	21.0 ±1.0
4	-1.9 ±1.6	13.8 ±0.6
5	-1.6 ±1.2	10.5 ±0.5

* DFTs at height of 1-m from the ground

A.1.2.4. Calorimeter

Figure A-15 and Figure A-16 provide thermocouple and heat flux values over time, respectively. The height of calorimeter is 1-m from its centerline to the surface of the pan. Note that most of the thermocouples failed after about 30 minutes, except for three (0°, 90°, and 270° rear). Thus, these

readings may be reliable up until 30 minutes, but could be suspect since they are slightly higher than the thermocouples that didn't fail. Indication of this can be observed in Table A-7 which provides time-averaged values between 10 – 20 minutes. The three thermocouples that did not fail have an average heat flux value of 97.8 kW/m^2, whereas the others have an average of 105.9 kW/m^2.

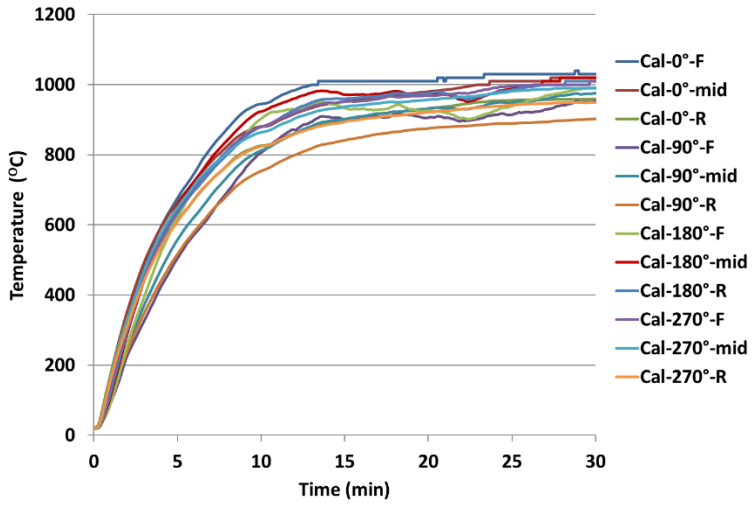

Figure A-15: Calorimeter thermocouple measurements.

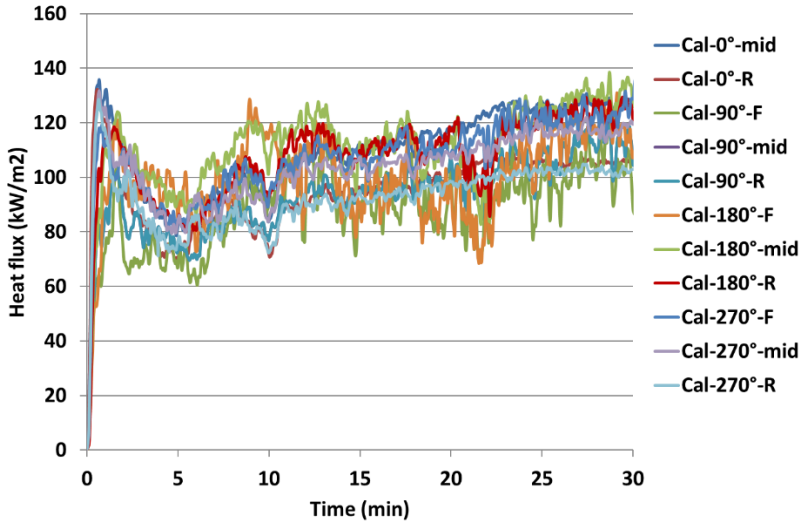

Figure A-16: Heat flux values derived from thermocouple measurements on calorimeter.

Table A-7: Averaged heat flux to calorimeter, 2-m, SPR ('hot') test.

Thermocouple location	Heat flux (kW/m2)
Top	
0°-F	125.8 ±4.8*
0°-mid	109.4 ±6.1*

Thermocouple location	Heat flux (kW/m2)
0°-R	93.9 ±6.0
Average	109.7 ±5.6
Side	
90°-F	93.2 ±9.0*
90°-mid	94.8 ±4.7*
90°-R	94.8 ±4.7
Average	94.3 ±6.1
Bottom	
180°-F	99.3 ±10.6*
180°-mid	113.5 ±6.6*
180°-R	111.1 ±5.1*
Average	108.0 ±7.4
Side	
270°-F	107.9 ±4.5*
270°-mid	103.3 ±4.4*
270°-R	91.3 ±4.8
Average	100.8 ±4.6

*Thermocouples failed after 30 minutes, thus readings are suspected of being unreliable

A.1.2.5. Flame height

The visible cameras are used to determine the length of the fire (Figure A-17 and Figure A-18). The method used to determine these flame height values is provided in section D.1.1.2. The average flame height is 2.9 m with a 2-sigma standard deviation of ±1.6 m. The average flame height is much lower for this test due to the increased lip height which affects the entrainment of air and the dynamics of the plume. In comparing to the 'cold' test, the 2-sigma standard deviations between the two tests do overlap. Thus, the maximum flame height for the 'cold' test overlaps with the minimum flame height for the 'hot' test.

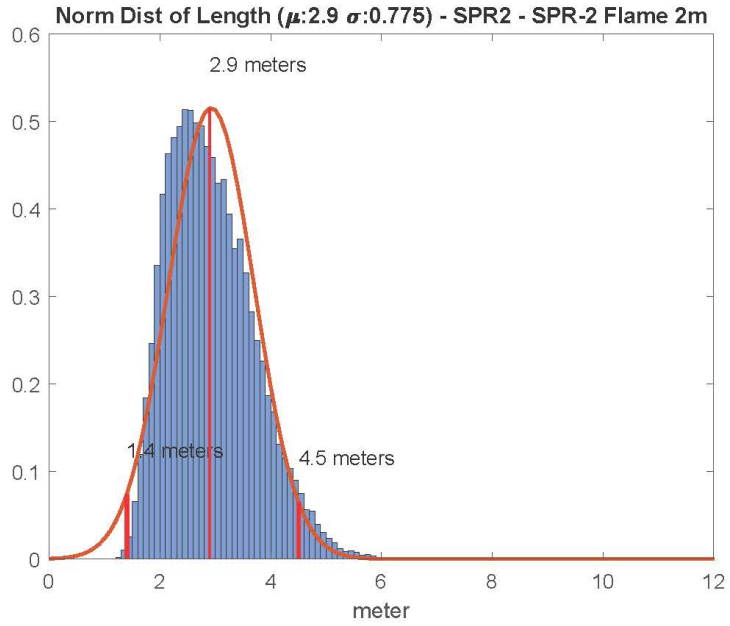

Figure A-17: Flame height distribution for SPR (hot) 2-m pool fire test.

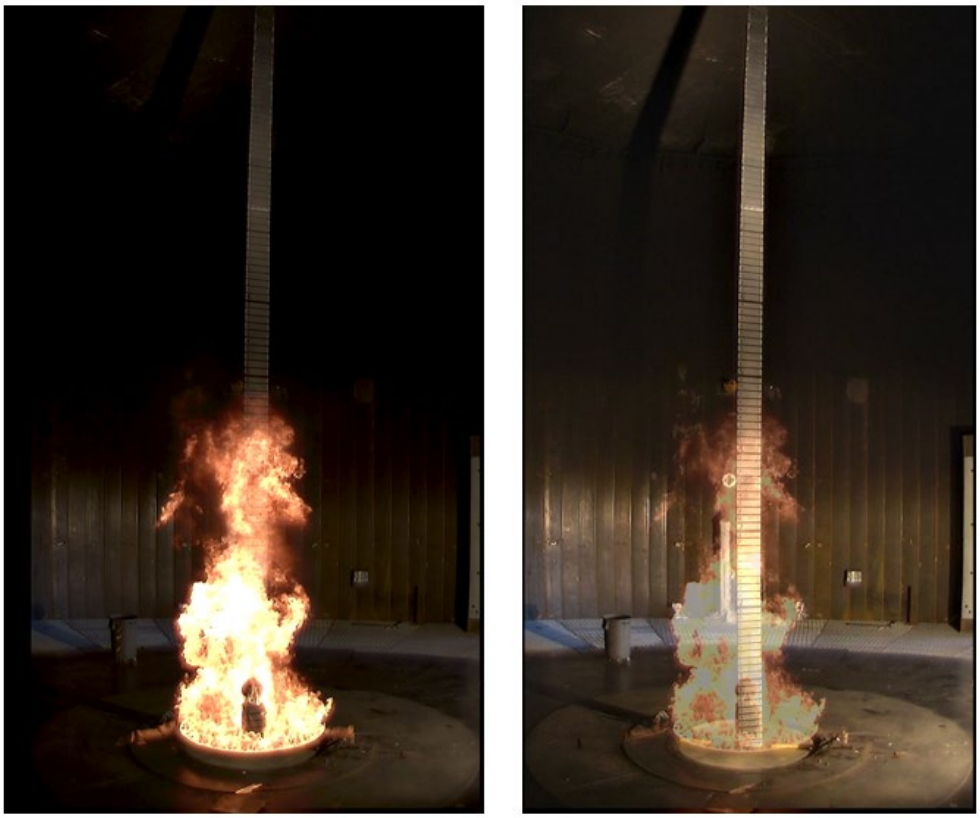

Figure A-18: Stadia board providing measure of flame height.

A.1.2.6. Burn rate

Due to the changes in the fuel feed method, namely not using water to push the oil out of the preconditioning tank; a scale was not utilized to determine the burn rate. Rather the meter on the fuel pump was used to determine the number of gallons per minute. The pump indicated that 48.5 gallons was burned in 30 minutes which corresponds to an average burn rate of 1.95 mm/min.

A.2. Five Meter Pool Fire Tests

A.2.1. SPR, hot

The test was conducted at the Lurance Canyon Burn Site using the 1000-gallon tank as the conditioning tank to pre-heat the fuel. The fuel feed temperature for this test was 54 ± 2.7°C. Due to the lack of circulation within the 1000-gallon tank, the desired temperature of 60°C was not attained overnight. It was decided to continue with testing due to the relatively low wind conditions that typically occur in the morning hours, approximately between 5:00 am and 8:00 am. If the test was aborted, preparations would have been repeated to test the following morning, thereby incurring additional costs, unwarranted since the fuel temperature was within 17% of target value.

The 5-m diameter pan was placed in the 30 ft by 60 ft containment pool and the calorimeter placed in the center of the pan (Figure A-19). The height of calorimeter is 1-m from its centerline to the

surface of the pan. The positions of the radiometers are provided in Figure A-20. The inner radial locations had collocated instruments comprised of wide and narrow-angle radiometers and DFTs at a height of 1-m above the ground (Figure A-21). The outer radial locations had wide-angle radiometers and real-time cameras.

Figure A-22 shows the residue left in the 5-m pan after the test. The fuel valve did not become plugged with hardened residue.

Figure A-19: Set-up of 5-m pool fire pan.

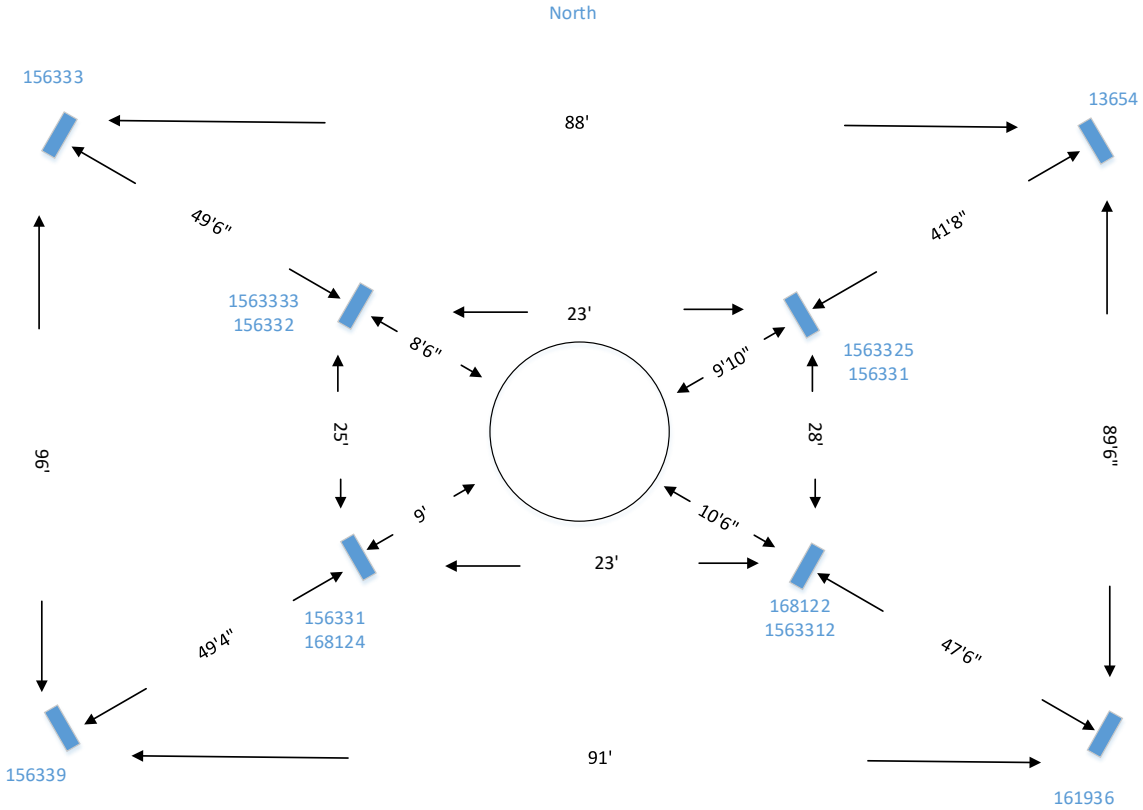

Figure A-20: Location of radiometers.

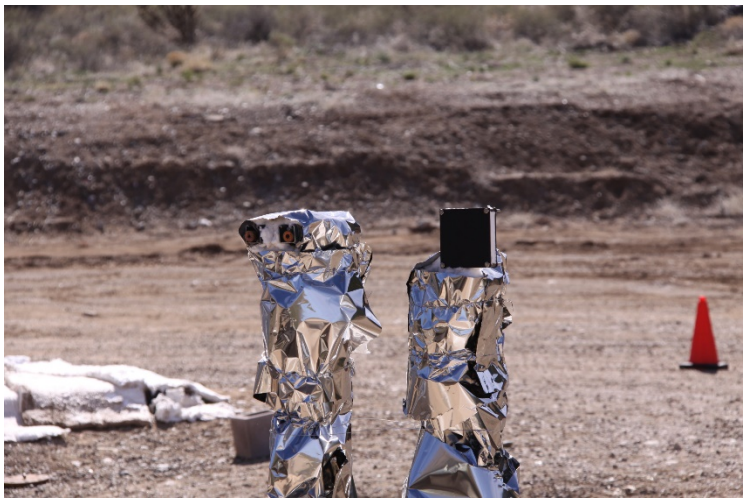

Figure A-21: Collocated radiometers and differential flame thermometers.

Figure A-22: Post-test residue left in 5-m pan after SPR 'hot' test.

A.2.1.1. Weather conditions

A challenge of performing outdoor tests is the variability in the wind conditions as evident from the wind data for this test. The wind speed varied between 1 – 5 mph and the wind direction was predominately coming from the East as shown in Figure A-23 and Figure A-24, respectively. Thus, the pool fire is shown in Figure A-25. As shown in Figure A-26 and Figure A-27, the temperature ranged from about 36°F to 45°F and the relative humidity from 30% to 40%, respectively.

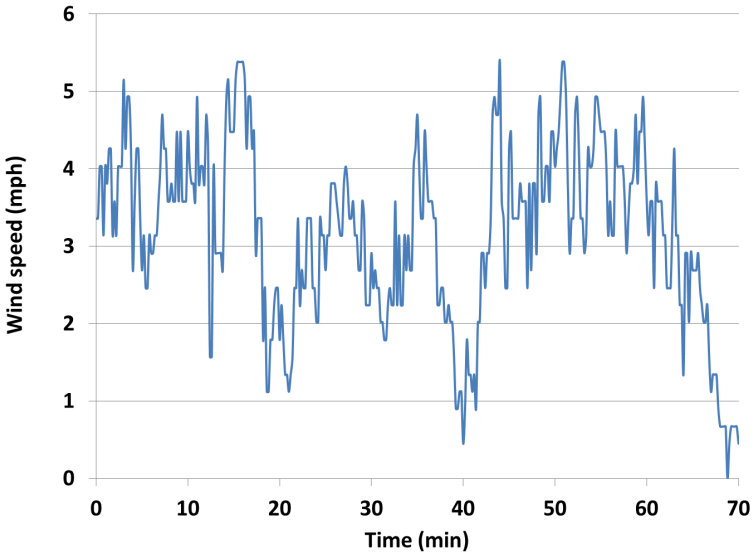

Figure A-23: Wind speed during the 'hot' 5-m SPR pool fire test.

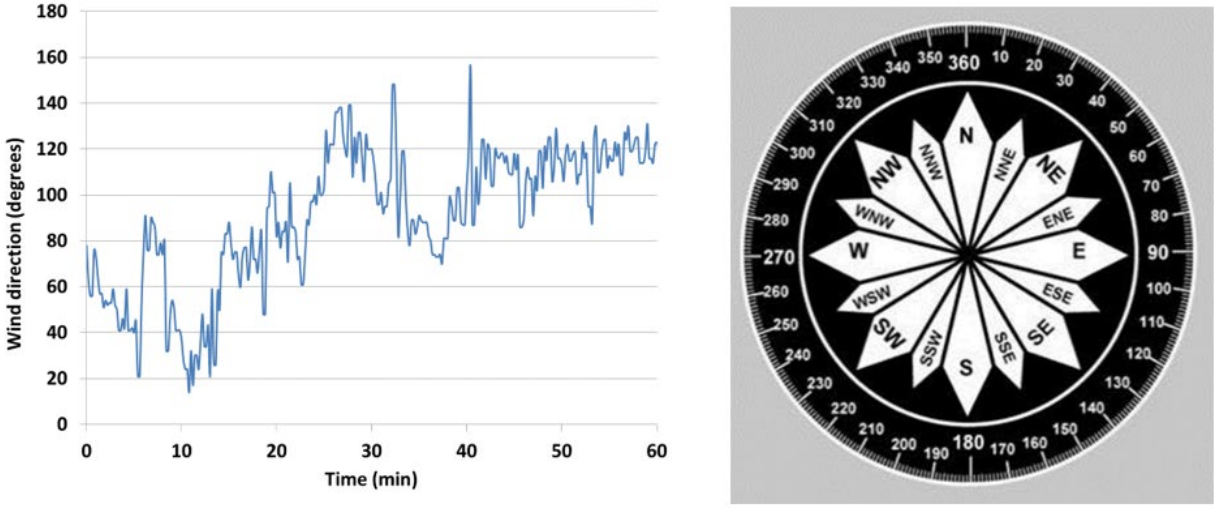

Figure A-24: Wind direction during the 'hot' 5-m SPR pool fire test.

Figure A-25: SPR 'hot' 5-m pool fire test.

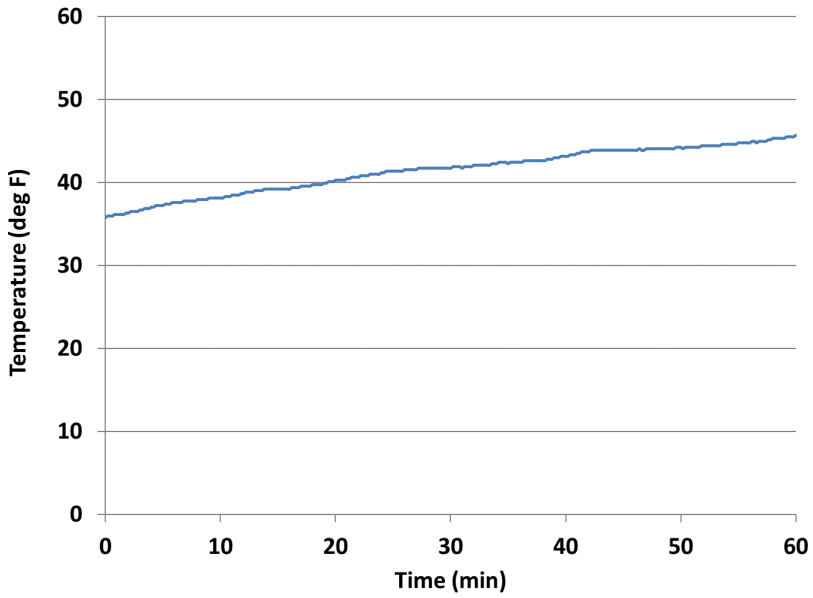

Figure A-26: Atmospheric temperature during the 'hot' 5-m SPR pool fire test.

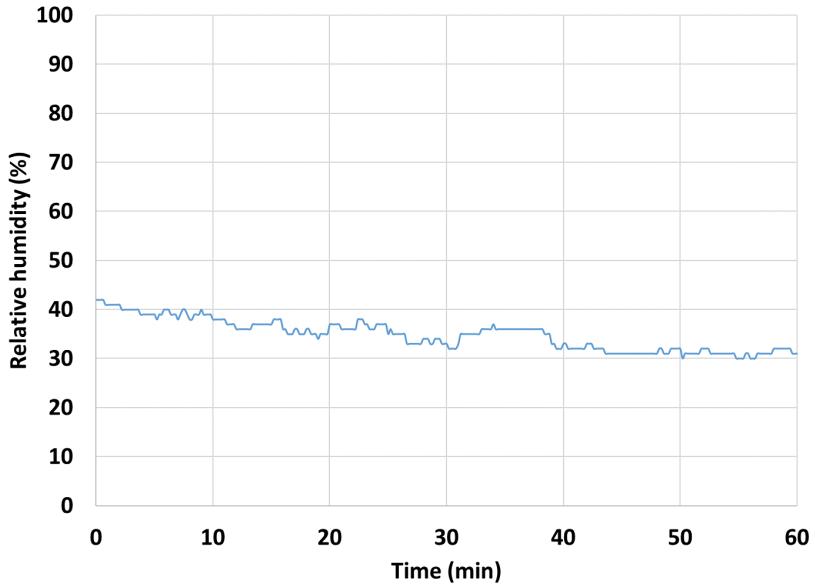

Figure A-27: Relative humidity during the 'hot' 5-m SPR pool fire test.

A.2.1.2. Fuel rake temperatures

Figure A-28 provides the thermocouple measurements within the fuel. The fuel level was maintained at a height of about 3 inches. The lowest thermocouple at 2 mm from the bottom of the pan increased to a temperature of about 250°C after approximately 10 minutes. This contrasts with the 2-m, hot, SPR test in which the lowest thermocouple took over 20 minutes to reach this temperature. The period in which the temperature decreases is most likely due to the shifting in the wind direction as seen in Figure A-24. In wind conditions the flame will be driven closer to the surface of the fuel and will tend to have greater heat transfer from the flame to the fuel surface on the downwind side. Thus, if the fuel rake is on the upwind side it will experience less heat transfer than if it is on the downwind side.

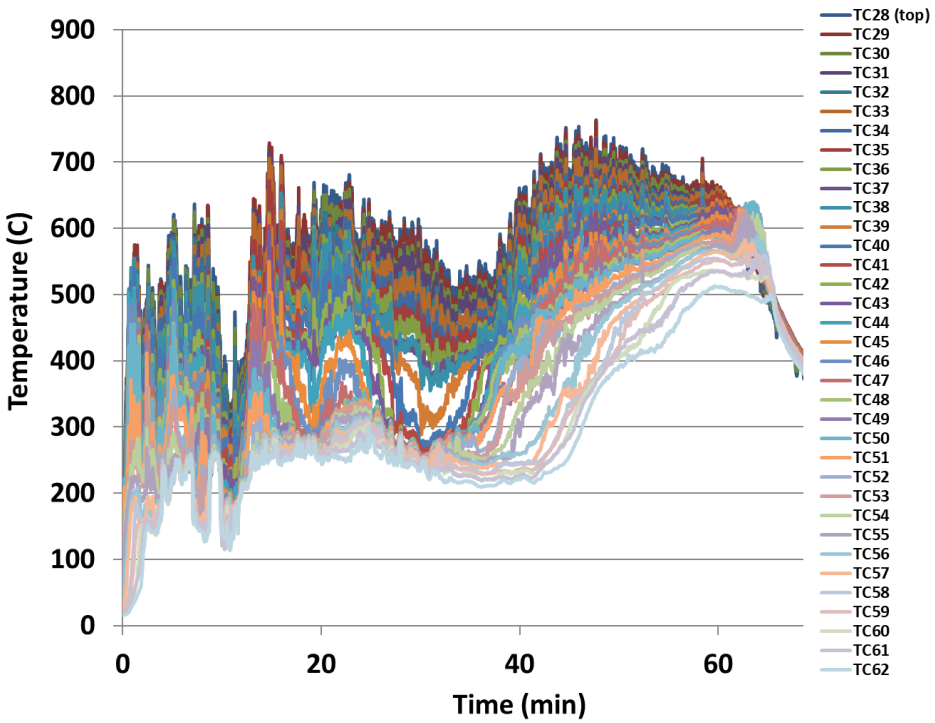

Figure A-28: Fuel rake temperature for the 'hot' SPR (hot) 5-m pool fire test.

A.2.1.3. Radiometers

Heat flux from wide-view and narrow-view radiometers are shown in Figure A-29. Heat flux values averaged over the steady-state constant fuel feed duration, that is 5-30 minutes, are provided in Table A-8. Three wide-view radiometers failed at the 20-m distance, thus only the radiometer at the SW location is provided. For this test the radiometers were used with the intent of determining the surface emissive power, however due to the variability in the location of flame it was determined that the radiometers would not provide adequate information to fully characterize the flame's average surface emissive power. Thus, for the other tests in the series it was decided to use IR cameras to determine the surface emissive power.

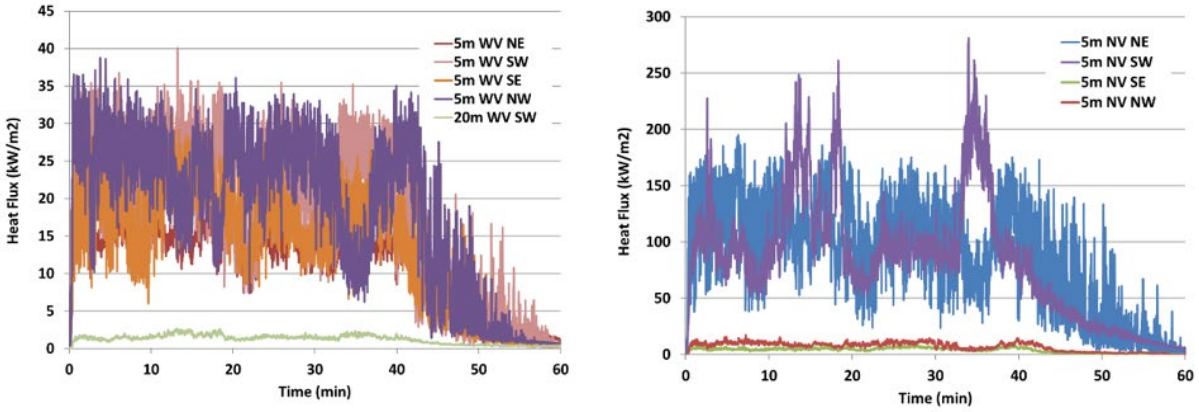

Figure A-29: Wide-view (left) and narrow-view (right) radiometer heat flux at various locations, SPR (hot).

Table A-8: Time-averaged heat flux values from radiometers.

location	wide-view heat flux (kW/m^2)	narrow-view heat flux (kW/m^2)
5 m, NE	14.3 ±2.3	115.1 ±31.5
5 m, NW	24.7 ±4.8	9.7 ±1.7
5 m, SE	19.0 ±4.9	5.2 ±1.0
5 m, SW	22.7 ±5.9	105.0 ±38.7
20 m, SW	1.6 ±0.4	

A.2.1.4. Calorimeter

Figure A-30 provides temperature measurements for the calorimeter. Figure A-31 shows the absorbed and total heat flux to the calorimeter. Due to the impact of wind conditions large variability in heat flux values occurred as indicated in these figures. Table A-9 provides heat flux values averaged over 5-30 minutes at each location and averaged among all measurement locations, indicating an average absorbed heat flux of -10.0 ± 34.4 kW/m^2 and average total heat flux of 89.6 ± 34.4 kW/m^2.

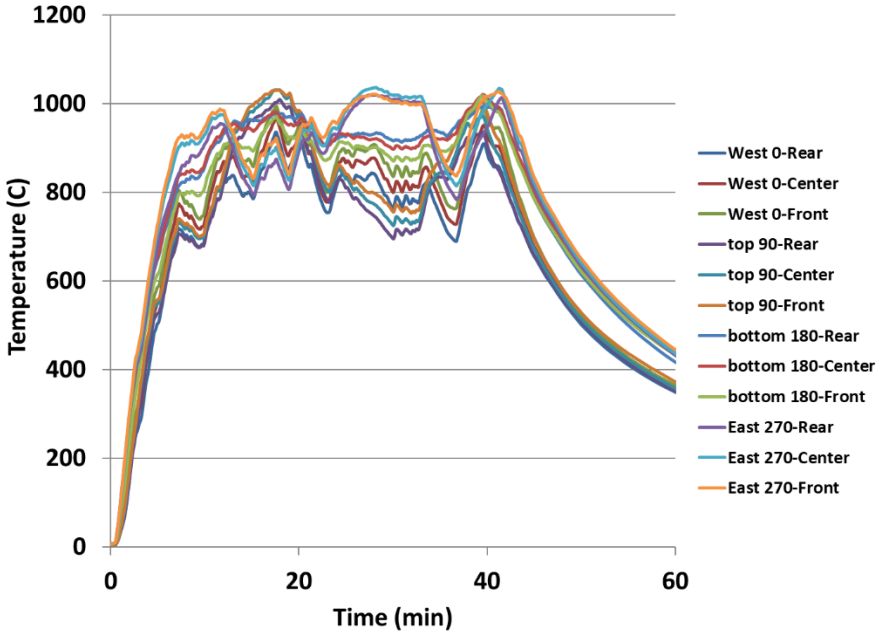

Figure A-30: Calorimeter thermocouple temperatures for SPR (hot) test.

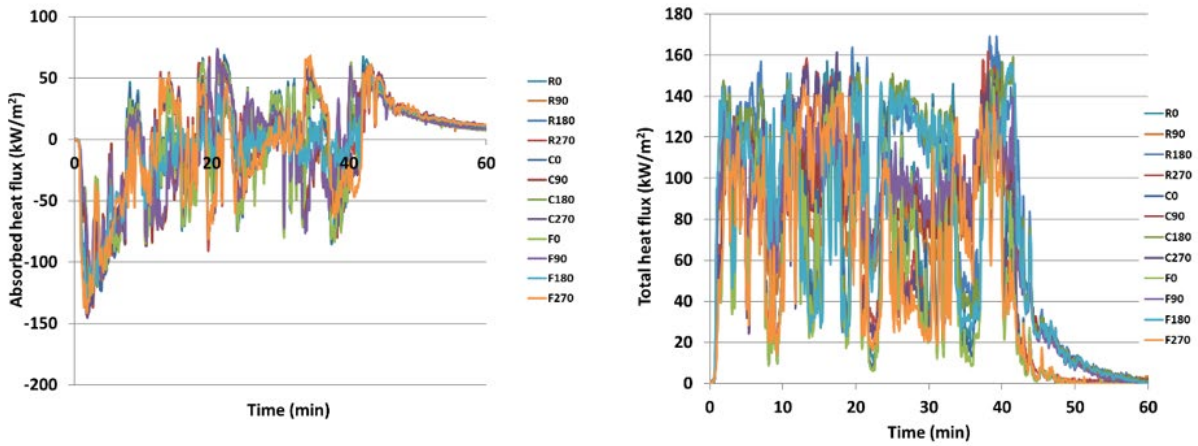

Figure A-31: Absorbed and total heat flux to calorimeter for 5-m SPR (hot) test.

Table A-9: Average total and absorbed heat flux for calorimeter for 5-m SPR (hot) test.

	Average Heat Flux (kW/m^2)*			
position	**absorbed**	**sd**	**total**	**sd**
center 0-deg	-9.9	43.0	78.6	40.7
center 90-deg	-7.3	37.2	98.6	18.4
center 180-deg	-9.9	24.0	105.3	36.3
center 270-deg	-12.4	35.2	81.2	43.7
left 0-deg	-10.0	42.6	85.9	40.7
left 90-deg	-8.0	35.6	89.8	22.2
left 180-deg	-10.1	26.2	107.4	34.8
left 270-deg	-11.6	35.7	84.4	42.0
right 0-deg	-9.9	41.5	70.1	39.1
right 90-deg	-7.0	36.2	100.0	17.3
right 180-deg	-10.6	22.3	98.9	35.4
right 270-deg	-13.0	33.6	75.2	42.0
average	-10.0	34.4	89.6	34.4

*averaged over 5-30 minutes

A.2.1.5. Directional flame thermometers

Figure A-32 provides the absorbed and incident heat flux from DFT measurements over time and Table A-10 provides heat flux values averaged over 20-40 minutes. The NW DFT measured the highest flux due to the tilt of flame by the prevalent wind. Note that the SW DFT failed.

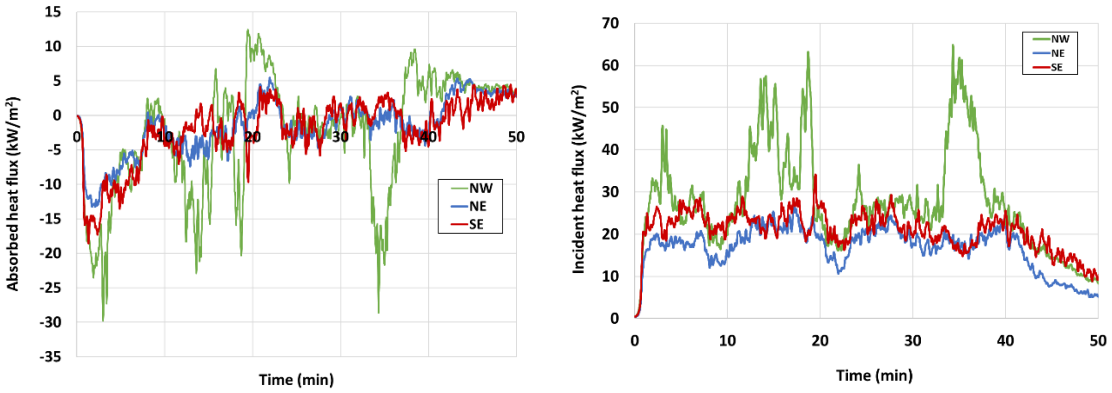

Figure A-32. Absorbed and incident heat flux from DFT measurement for 5-m SPR (hot) test.

Table A-10. Average heat flux values from DFT measurements for 5-m SPR (hot) test.

location	absorbed heat flux (kW/m^2)	incident heat flux (kW/m^2)
NW	-1.0 ±7.4	30.0 ±10.8
NE	-0.6 ±2.2	18.4 ±30.0
SE	-0.4 ±2.3	21.2 ±3.1
SW*	-	-

*DFT failed

A.2.1.6. Flame height

The visible cameras are used to determine the length of the fire (Figure A-34 and Figure A-33). The method used to determine these flame height values is provided in section D.1.1.2. The average flame height is 6.0 m with a 2-sigma standard deviation of ±3.6 m.

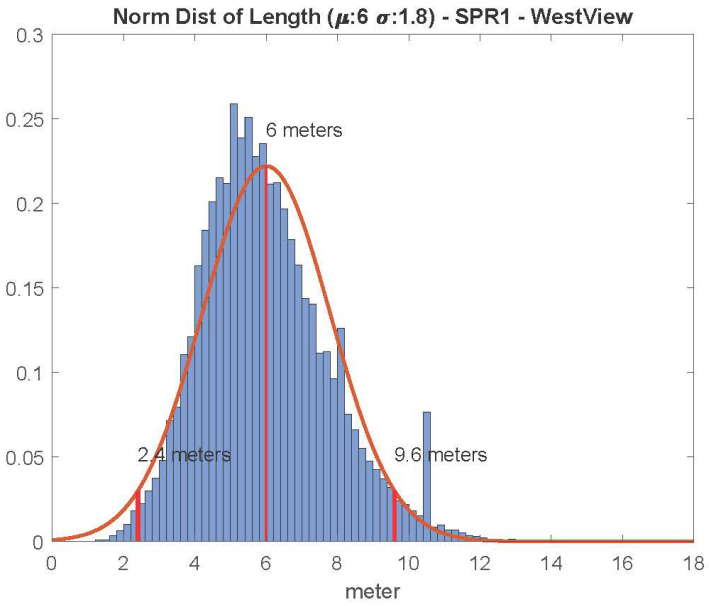

Figure A-33: Flame height distribution for SPR (hot) 5-m pool fire test.

Figure A-34. Frame from SPR (hot) 5-m pool fire test. Post-processing software to determine flame length.

A.2.1.7. Burn rate

The average burn rate was determined by viewing video coverage of the fuel meter which reported the number of gallons of fuel consumed per minute. The average burn rate was 2.99 mm/min. Approximately 650 gallons was burned.

A.2.2. SPR, atmospheric

For this test the fuel was not preconditioned to a specific temperature, rather it was tested at the atmospheric temperature which was 27°C. At approximately 22 minutes after ignition, boil over occurred causing the test to be aborted by turning off the fuel pump. The ignited fuel spilled into the 30 ft x 60 ft outer pool which had water puddles due to the heavy rains that occurred just prior to the test. Intense popping sounds were heard just prior and during boil over.

In preparation for the test, the pan was filled with water to test the liquid level control and was subsequently drained. Since the pan had a thin crust layer that remained from the previous test, it is plausible that this layer could have not been completely void of water due to the liquid fill test and was responsible for the boil over. Thus, any residual layer was completely removed for future tests. Despite the boil over event, all pertinent data was successfully obtained.

A.2.2.1. Weather conditions

The wind speed varied between 4 – 10 mph and the wind direction was predominately coming from the Southwest as shown in Figure A-35 and Figure A-36, respectively. Thus, the flame was predominantly tilted towards the Northeast. As indicated in Figure A-37 and Figure A-38, the atmospheric temperature and relative humidity were about 68°F and 53%, respectively.

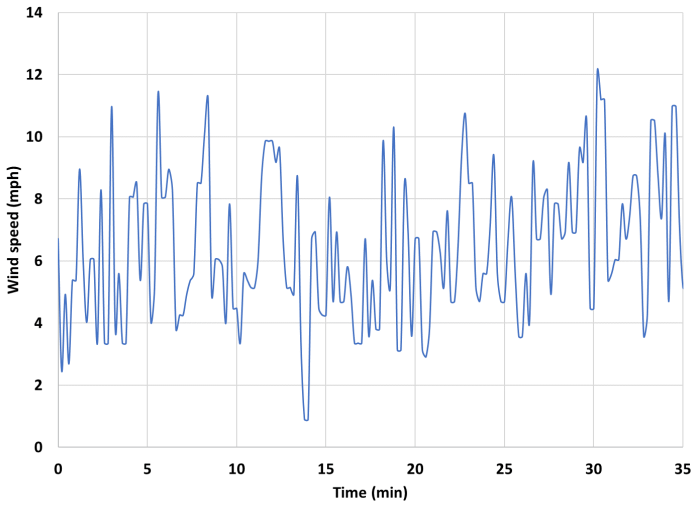

Figure A-35: Wind speed during the 5-m SPR (atmospheric) pool fire test.

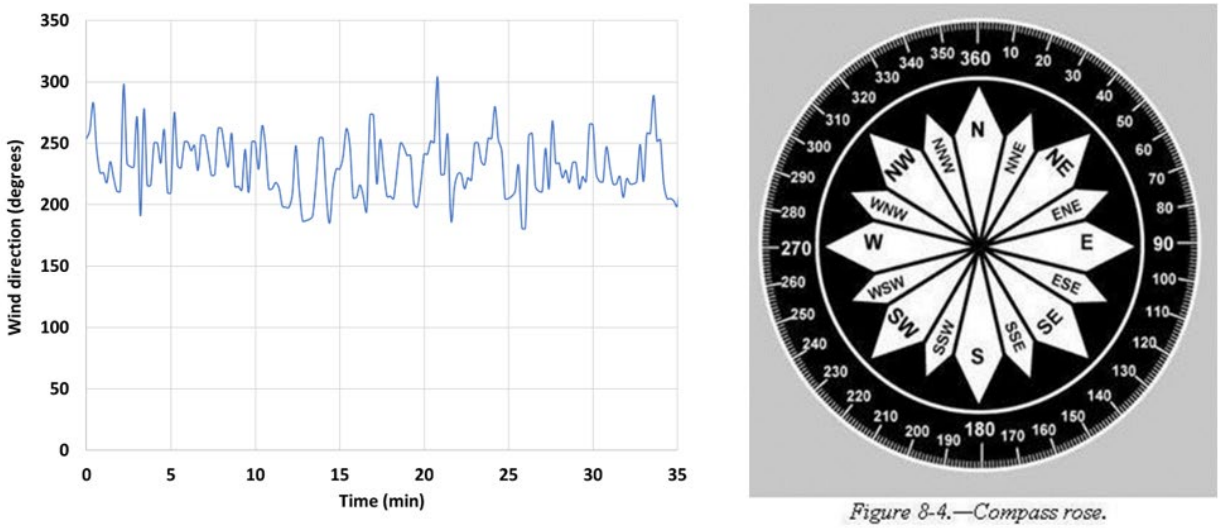

Figure A-36: Wind direction during the 5-m SPR (atmospheric) pool fire test.

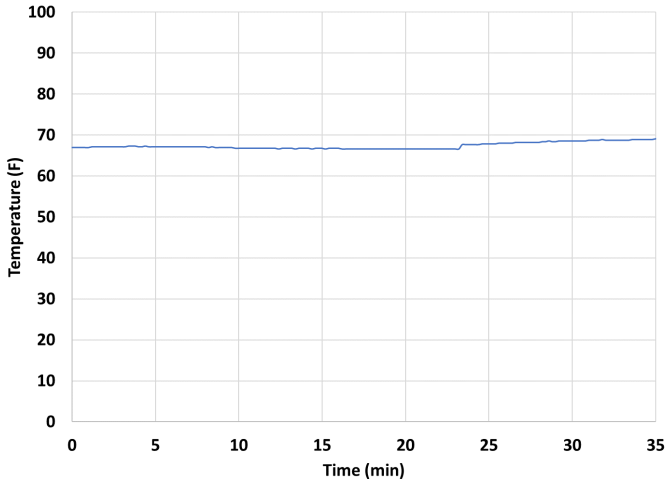

Figure A-37: Surrounding temperature during the 5-m SPR (atmospheric) pool fire test.

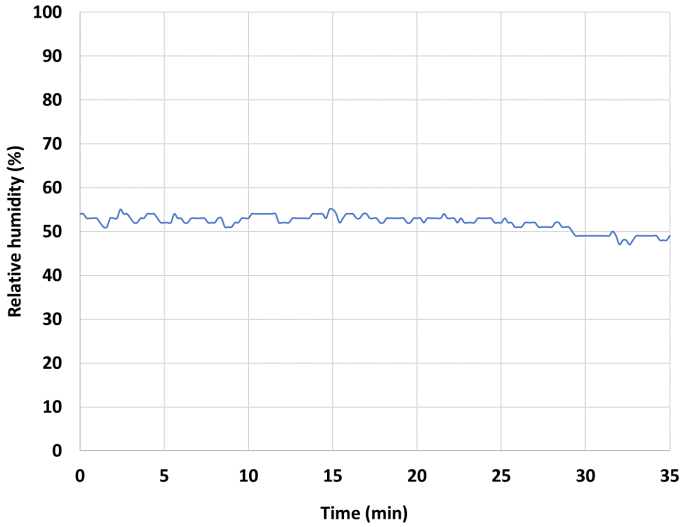

Figure A-38: Relative humidity during the 5-m SPR (atmospheric) pool fire test.

A.2.2.2. Fuel rake temperatures

Figure A-39 provides the thermocouple measurements within the fuel. The thermocouple at 2 mm from the bottom of the pan increased to a temperature of about 100°C after approximately 20 minutes. Note that some bottom thermocouples were within the residual crust layer which was not greater than 13 mm (0.5"). The fuel level was maintained at a height of about 11 cm (4.5 inches).

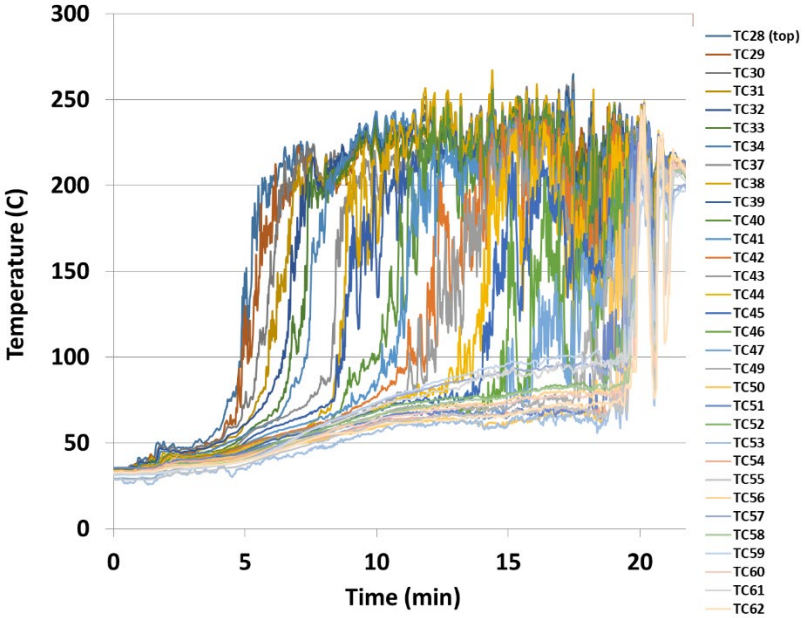

Figure A-39: Fuel rake temperature for SPR (atmospheric) 5-m pool fire test.

A.2.2.3. Radiometers

Heat flux from wide-view and narrow-view radiometers are shown in Figure A-40. Heat flux values averaged over 2-15 minutes are provided in Table A-11. Three wide-view radiometers failed at the 20-

m distance, thus only the radiometer at the SE location is provided. As noted previously, the IR camera was used to determine the surface emissive power rather than the radiometers.

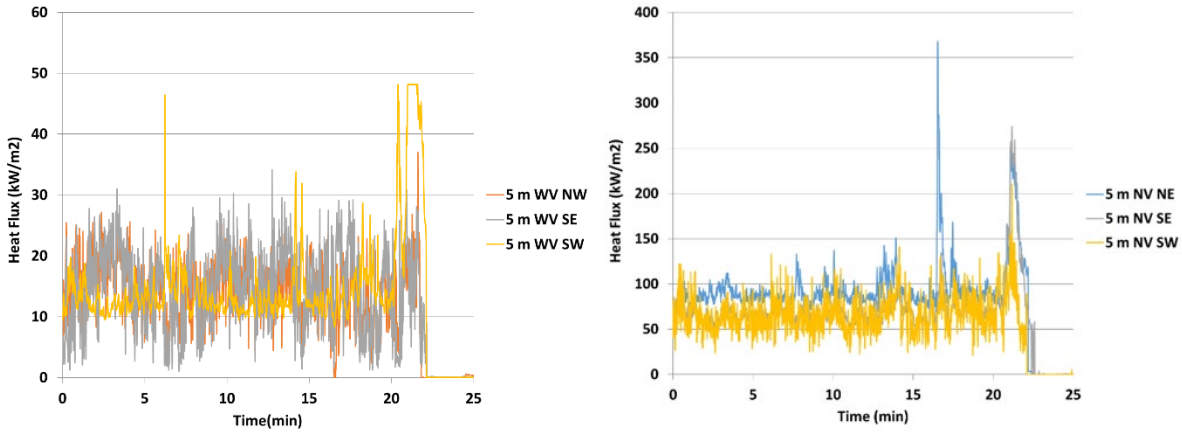

Figure A-40: Wide-view (left) and narrow-view (right) radiometer heat flux at various locations, SPR (atm).

Table A-11: Time-averaged heat flux values from radiometer measurements for 5-m SPR (atm) test.

location	wide-view heat flux (kW/m^2)	narrow-view heat flux (kW/m^2)
5 m, NE	NA*	89.7 ±12.0
5 m, NW	14.6 ±4.6	NA*
5 m, SE	15.1 ±6.2	67.6 ±8.3
5 m, SW	13.1 ±3.3	63.5 ±18.1
20 m**	-	-

*radiometer failed
**all wide-angle radiometers at 20 m locations failed

A.2.2.4. Calorimeter

Figure A-41 provides temperature measurements for the calorimeter. Figure A-42 shows the absorbed and total heat flux to the calorimeter. Table A-12 provides heat flux values averaged over 5-20 minutes at each location and averaged among all measurement locations, indicating an average absorbed heat flux of -24.2 ± 29.6 kW/m^2 and average total heat flux of 90.0 ± 33.8 kW/m^2.

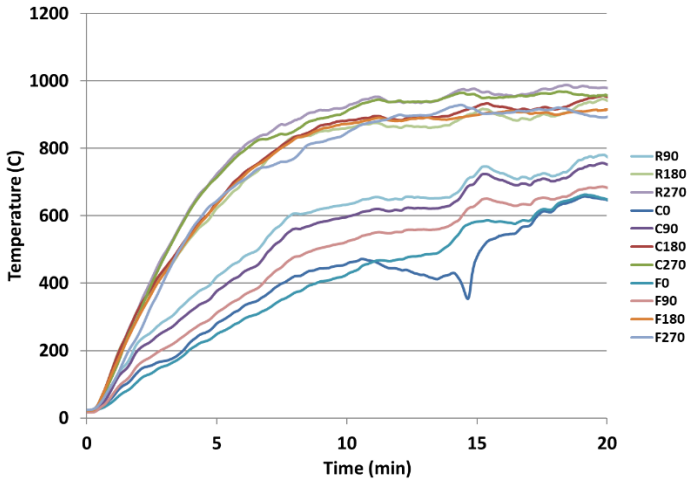

Figure A-41: Calorimeter thermocouple temperatures for SPR (atm) test.

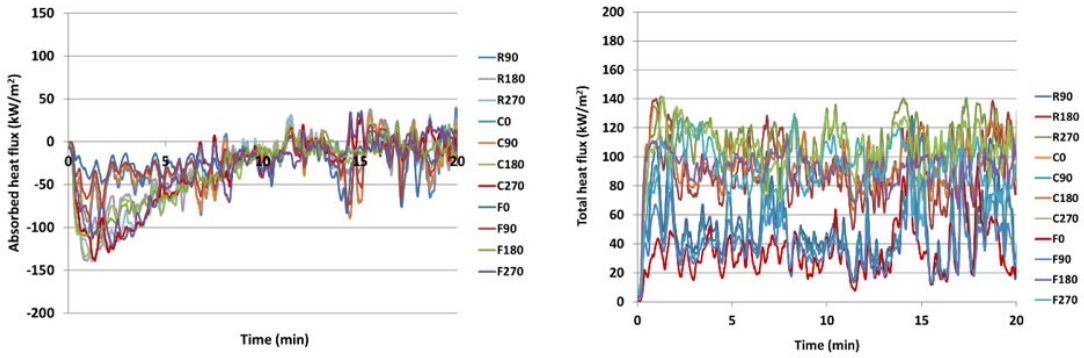

Figure A-42: Absorbed and total heat flux to calorimeter for 5-m SPR (atm) test.

Table A-12: Average total and absorbed heat flux for calorimeter for 5-m SPR (atm) test.

	Average Heat Flux (kW/m^2)*			
position	**absorbed**	**s.d.**	**total**	**s.d.**
center 0-deg	-19.7	45.8	78.6	40.7
center 90-deg	-22.0	23.9	98.6	18.4
center 180-deg	-26.7	28.3	105.3	36.3
center 270-deg	-27.7	35.6	81.2	43.7
rear 0-deg**	-	-	-	-
rear 90-deg	-22.3	26.0	89.8	22.2
rear 180-deg	-26.2	29.8	107.4	34.8
rear 270-deg	-27.9	35.5	84.4	42.0
front 0-deg	-20.7	17.9	70.1	39.1
front 90-deg	-20.6	18.9	100.0	17.3
front 180-deg	-26.0	29.1	98.9	35.4
front 270-deg	-26.9	34.9	75.2	42.0
average	**-24.2**	**29.6**	**90.0**	**33.8**

*averaged over 2-20 minutes, **thermocouple failed

A.2.2.5. Directional flame thermometer

Figure A-43 provides the absorbed and incident heat flux from DFT measurements over time and Table A-13 provides heat flux values averaged over 2-20 minutes. The NE DFT measured the highest flux due to the tilt of flame by the prevalent wind. Note that the SW DFT failed.

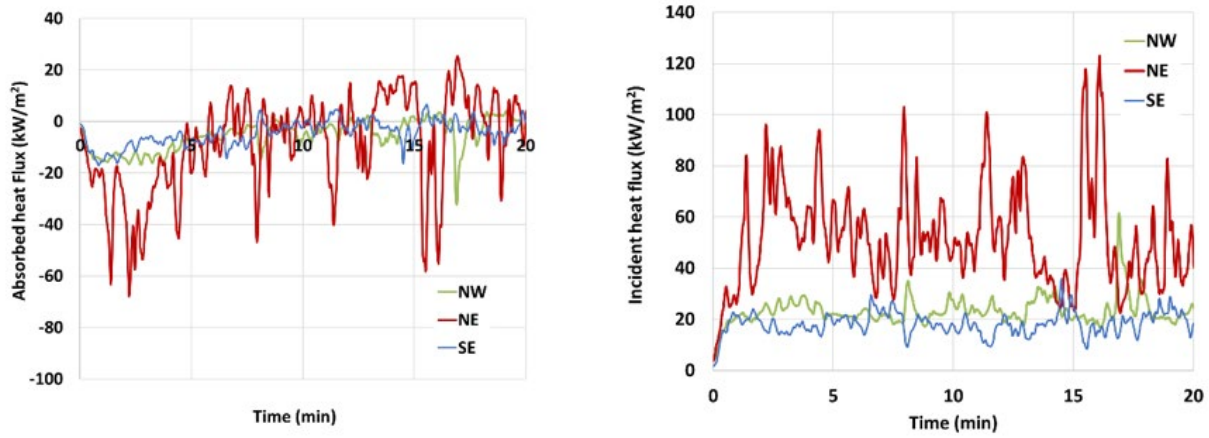

Figure A-43: Absorbed and incident heat flux from DFT measurement for 5-m SPR (atm) test.

Table A-13: Average heat flux values from DFT measurements for 5-m SPR (atm) test.

location	absorbed heat flux (kW/m^2)	incident heat flux (kW/m^2)
NW	-4.6 ±5.6	23.9 ±5.3
NE	-7.0 ±18.5	54.1 ±19.0
SE	-3.7 ±4.0	18.3 ±4.1
SW*	-	-

*DFT failed

A.2.2.6. Flame height

Flame height values over the entire duration of steady burning were determined from real-time cameras at different locations (Table A-14). The method used to determine these flame height values is provided in section D.1.1.2.

Table A-14: Flame height statistics for 5-m diameter SPR (atm.) pool fire

	2-Sigma	Length	2-Sigma
	Min	**Mean**	**Max**
NW View	1.6	4.8	8.1
NE View	1.6	4.2	6.7
SW View	0.7	4.6	8.5
SE View	3.1	5.9	8.7
average	1.8	4.9	8.0

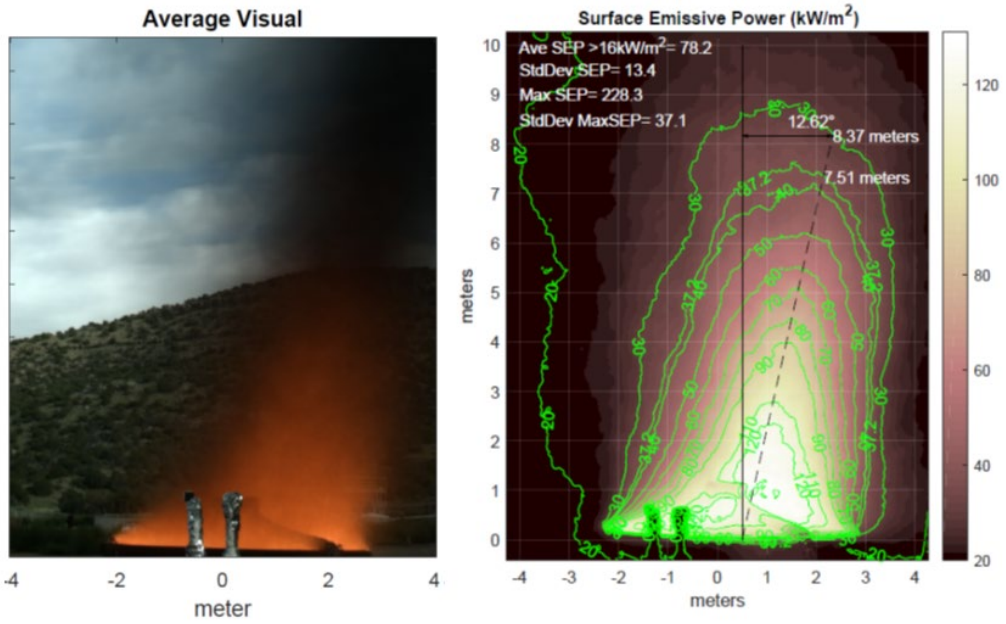

Figure A-44: Averaged flame image and corresponding average SEP values for 5-m SPR (atmospheric) test.

A.2.2.7. Burn rate

The pan was filled initially with about 587 gallons of oil corresponding to a height of 4.5" within the pan. Through video observation of the fuel meter, the burn rate was determined during an 11-minute duration approximately 10 minutes after the beginning of the test. During the 11 minutes of steady burning, the reading from the differential pressure gauge was constant up to the time of the boil over. The fuel meter indicated 484 - 487 barrels/day which corresponds to an average burn rate of 2.7 ± 0.1 mm/min.

A.2.2.8. Surface emissive power

The surface emissive power and flame temperature was determined from IR camera measurements. Since the fire was affected by the wind, periods in which the flame was the most vertically oriented and thus in the viewing range of the camera were extracted. These images were then averaged and are shown Figure A-45 for flame temperature and surface emissive power. From these images an average value for flame temperature and surface emissive power were determined by assessing values above 750 K and 16 kW/m^2, respectively. The average temperature is 870.6 ± 121 K and the average maximum temperature is 1222.3 ± 59 K. The average surface emissive power is 78.2 ± 13.4 kW/m^2 and the average maximum SEP is 228.3± 37.1 kW/m^2.

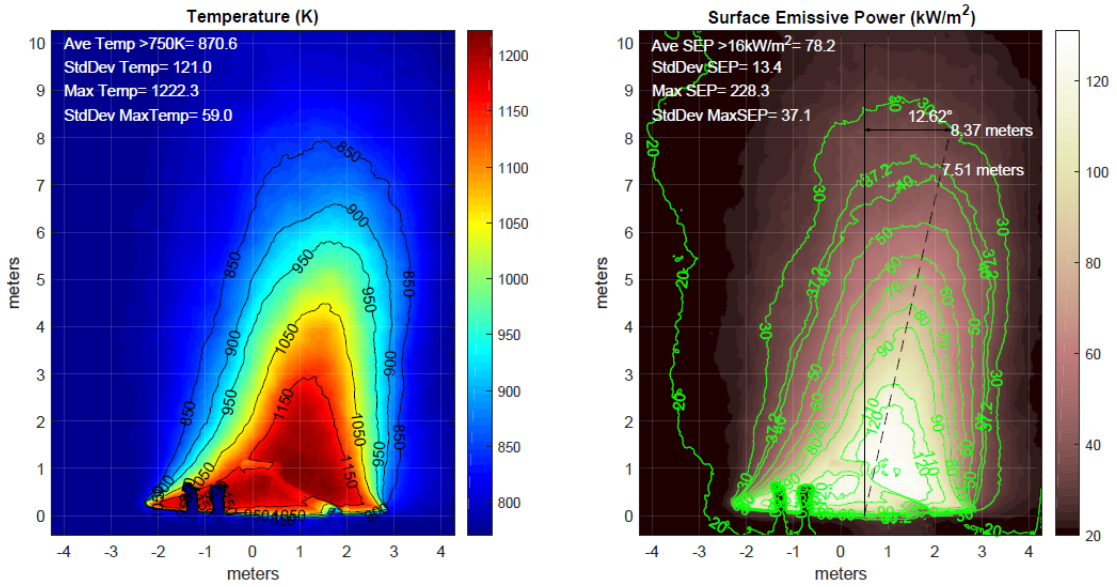

Figure A-45: SPR (atm) crude oil: X6900 IR camera, 3-5 um cold filter, 25 mm lens at 62 m, emissivity of 1 and transmissivity of 0.89.

A.2.3. Tight 1 (Bakken)

Due to the boil over event, the fuel pan was moved outside of the 9.15 m x 18.3 m (30 ft x 60 ft) pool and placed inside a larger pan with a diameter of 7.9 m (25.9 ft) to prevent necessitating extensive cleanup in the larger pool in the event of another boil over. Additionally, tanks were installed below the fuel pan to allow the fuel to be quickly drained in the event of a boil over. Sight glasses were also installed to monitor the liquid level via video coverage in the control room. A differential pressure (dP) gauge is typically used to control the liquid fuel height but, based on the past crude oil pool fire experiments, the gauge starts to fail due to temperature effects from the in-depth heating of the oil. The new configuration is shown in Figure A-46.

For this test, Bakken crude oil from North Dakota was tested. The oil was not preconditioned and was tested at its atmospheric temperature of 14°C. Water was used to push the oil out of the specialized tanker which fed directly into the fuel pan. Prior to the test, the oil in the specialized tanker was circulated and pressurized to ensure that any vapor was dissolved back into the liquid and to have a homogenous mixture. The oil was assessed for adequate mixing by monitoring tanker pressure while circulating. After tanker pressure stabilized, indicating full absorption of gases, a minimum of 3 oil volumes were circulated to insure homogeneity of the oil. After the mixing process was complete, oil samples were taken for analysis.

The test was successfully carried out without a boil over event. In contrast to the SPR crude oil, the Bakken crude oil did not leave appreciable residue as shown in Figure A-47. Thus, the cleanup effort was minor. Note that the fire had two distinct time spans of steady-state burning. This is due to the differential pressure gauge malfunctioning and thus required relying on the sight glass and flow meter to control the liquid level. Since the visibility of the sight glass became obscured the control of the fuel level resulted in the fire burning down after about 15 minutes. The fuel supply was increased, and another time span of steady burning occurred between about 24-30 minutes.

Figure A-46: Fuel pan placed in a 7.9 m pan with drain down tanks.

Figure A-47: Pan post-test indicating minor residue for Bakken crude oil.

A.2.3.1. Weather conditions

The wind speed varied between 6 – 12 mph and the wind direction was predominately coming from the Southwest as shown in Figure A-48 and Figure A-49, respectively. Thus, the flame was predominantly tilted towards the Northeast. As indicated in Figure A-50 and Figure A-52, the atmospheric temperature and relative humidity were about 58°F and 20%, respectively.

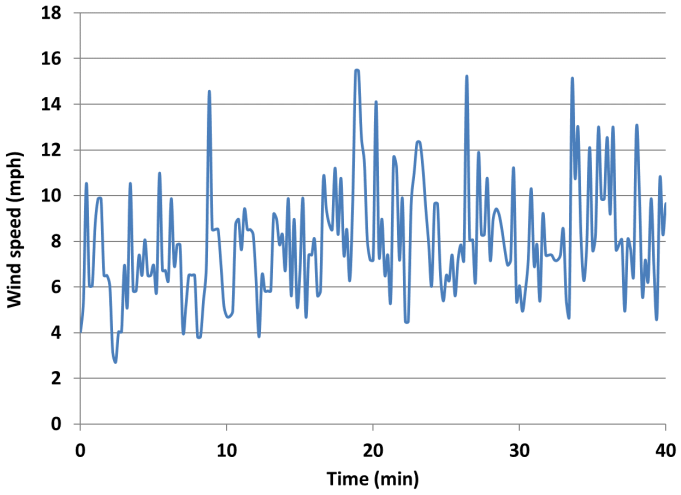

Figure A-48: Wind speed during the 5-m Bakken pool fire test.

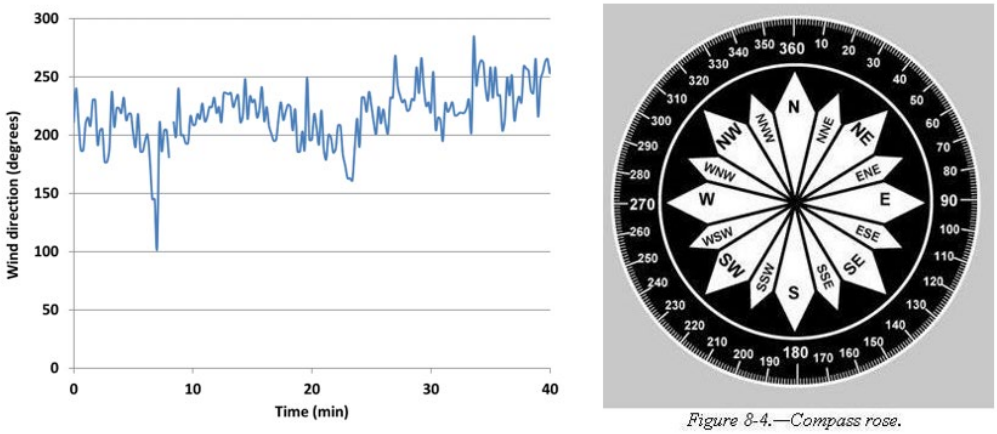

Figure 8-4.—Compass rose.

Figure A-49: Wind direction during the 5-m Bakken pool fire test.

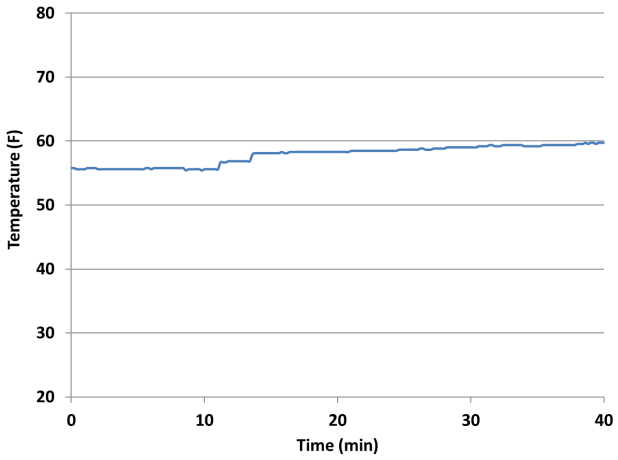

Figure A-50: Surrounding temperature during the 5-m Bakken pool fire test.

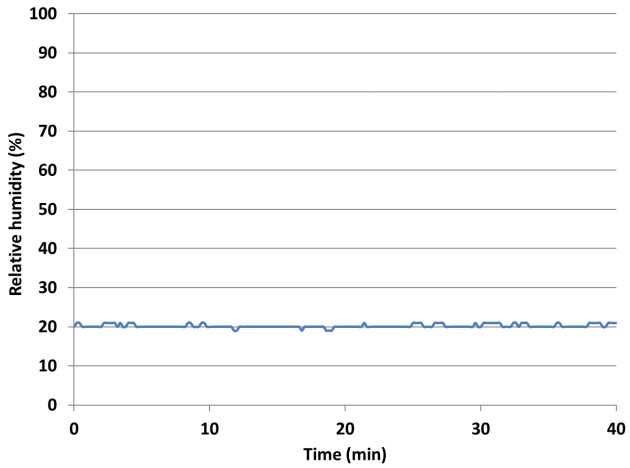

Figure A-51: Relative humidity during the 5-m Bakken pool fire test.

A.2.3.2. Fuel rake temperatures

Figure A-53 provides the thermocouple measurements within the fuel. All thermocouples increased to a temperature of about 100°C after approximately 5 minutes and continued to steadily rise throughout the test. The thermocouple closest to the bottom of the fuel pan was placed at a height of 6 mm and the subsequent thermocouples vertically spaced 2 mm apart.

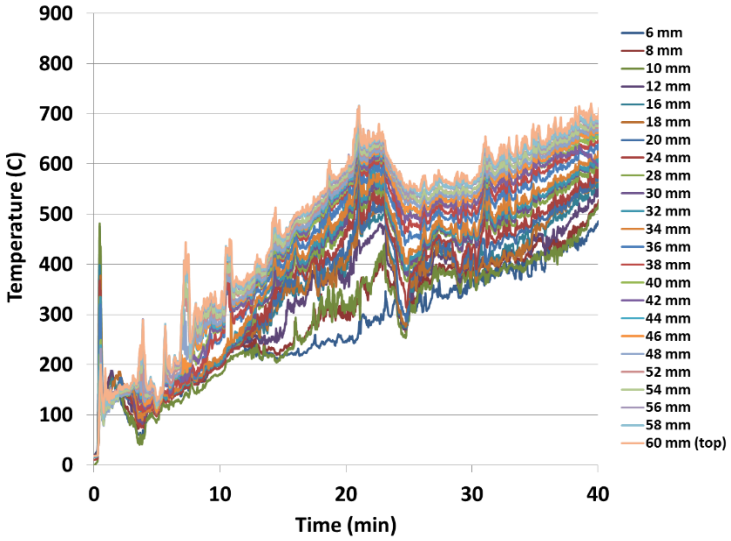

Figure A-52: Fuel rake temperature for 5-m Bakken pool fire test.

A.2.3.3. Radiometers

Heat flux from wide-view and narrow-view radiometers are shown in Figure A-54 and Figure A-55 for the 5-m and 20-m locations, respectively. Heat flux values averaged over 5-15 minutes and 24-30

minutes are provided in Table A-15. As noted previously, the IR camera was used to determine the surface emissive power rather than the radiometers.

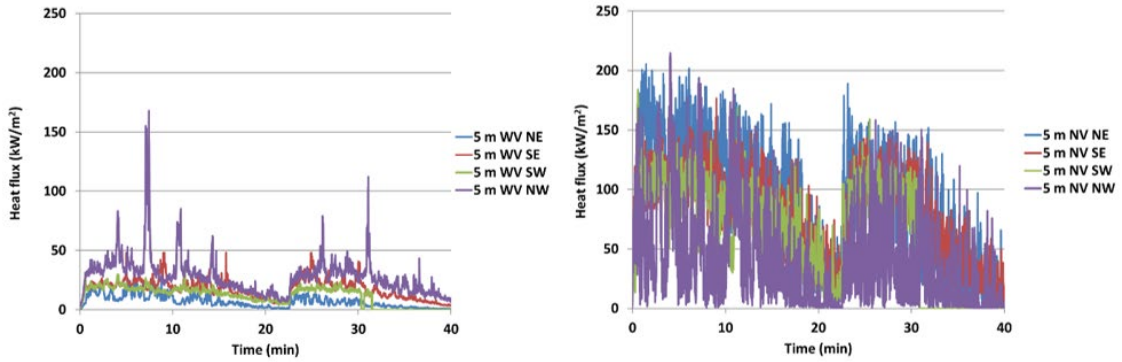

Figure A-53: Wide-view (left) and narrow-view (right) radiometer heat flux values at 5-m locations, Bakken.

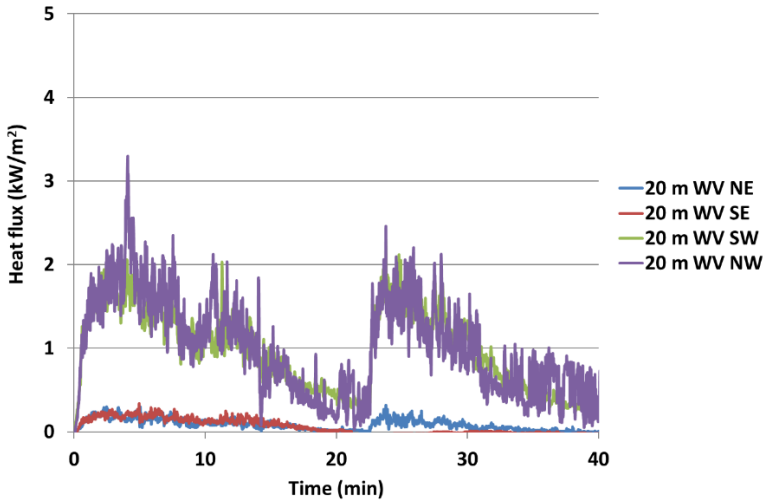

Figure A-54: Wide-view radiometer heat flux values at 20-m locations, Bakken.

Table A-15: Time-averaged heat flux values from radiometer measurements for 5-m Bakken test.

location	wide-angle heat flux (kW/m^2)	narrow-angle heat flux (kW/m^2)
5 m, NE	10.1 ±5.0	110.4 ±36.0
5 m, NW	36.0 ±17.5	50.4 ±42.0
5 m, SE	23.2 ±6.4	101.0 ±20.2
5 m, SW	17.2 ±2.5	87.9 ±23.7
20 m, NE	0.1 ±0.04	-
20 m, NW	1.3 ±0.4	-
20 m, SE	0.1 ±0.1	-
20 m, NW	1.3 ±0.3	-

A.2.3.4. Calorimeter

Figure A-56 provides temperature measurements for the calorimeter. Figure A-57 shows the absorbed and incident heat flux to the calorimeter. Table A-16 provides heat flux values averaged over the time spans of 2-15 minutes and 24-30 minutes at each location and averaged among all measurement locations, indicating an average absorbed heat flux of -21.3 ± 26.4 kW/m^2 and average incident heat flux of 70.5 ± 25.8 kW/m^2.

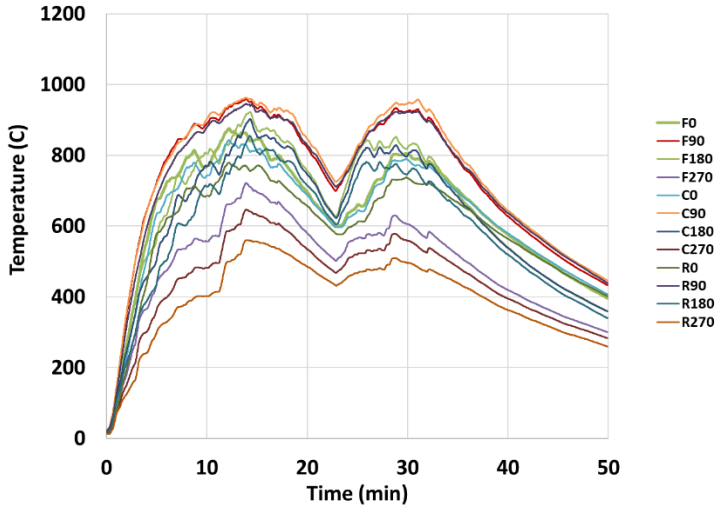

Figure A-55: Calorimeter thermocouple temperatures for Bakken test.

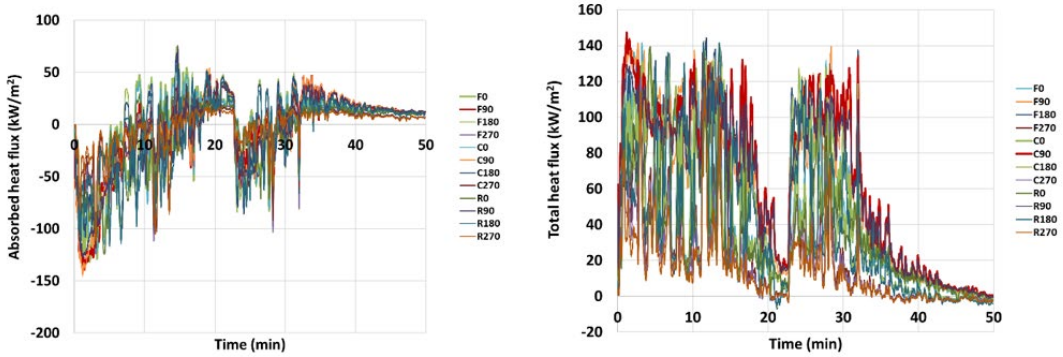

Figure A-56: Absorbed and total heat flux to calorimeter for 5-m Bakken test.

Table A-16: Average total and absorbed heat flux for calorimeter for 5-m Bakken test.

	Average Heat Flux (kW/m^2)*			
position	**absorbed**	**sd**	**total**	**sd**
center 0-deg	-28.9	37.3	72.7	28.6
center 90-deg	-30.9	30.5	104.7	13.9
center 180-deg	-27.6	39.9	74.8	34.4
center 270-deg	-19.7	27.3	36.0	25.4
left 0-deg	-27.2	34.3	62.3	27.1
left 90-deg	-30.9	29.7	98.9	12.4
left 180-deg	-26.1	37.5	64.3	33.3
left 270-deg	-17.1	23.3	28.4	22.0
right 0-deg	-29.6	39.1	78.4	29.7
right 90-deg	-30.0	34.0	101.8	18.4
right 180-deg	-27.4	42.5	80.6	35.5
right 270-deg	-21.3	31.5	43.7	28.7
average	**-26.4**	**33.9**	**70.5**	**25.8**

*averaged over 2-15 min and 24-30 min.

A.2.3.5. Directional flame thermometers

Figure A-58 provides the absorbed and incident heat flux from DFT measurements over time and Table A-17 provides heat flux values averaged over 2-15 minutes and 24-30 minutes. Similar to the second SPR pool fire test, the NE DFT measured the highest flux due to the tilt of flame by the prevalent wind.

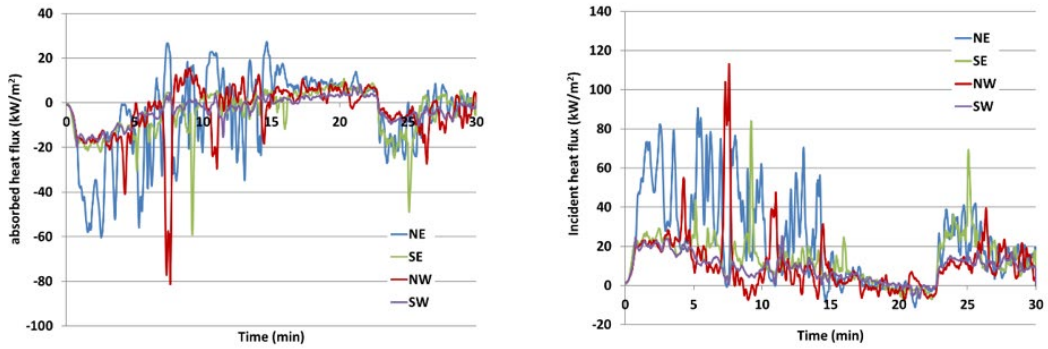

Figure A-57: Absorbed and total heat flux from DFT measurement for 5-m Bakken test.

Table A-17: Average heat flux values from DFT measurements for 5-m Bakken test.

location	absorbed heat flux (kW/m^2)	incident heat flux (kW/m^2)
NW	-6.1 ± 13.7	15.2 ± 16.1

location	absorbed heat flux (kW/m^2)	incident heat flux (kW/m^2)
NE	-7.0 ±17.9	30.3 ±21.3
SE	-6.1 ±9.6	17.1 ±10.5
SW	-4.7 ±4.9	11.4 ±4.9

A.2.3.6. Flame height

Flame height values over the entire duration of steady burning were determined from real-time cameras at different locations (Table A-18). The method used to determine these flame height values is provided in section D.1.1.2.

Table A-18: Flame height statistics for 5-m diameter Tight 1 (Bakken) pool fire

	2-Sigma Length		2-Sigma
	Min	Mean	Max
NW View	0.7	4.7	8.7
NE View	0.8	4.1	7.3
SW View	0	4.3	8.9
SE View	0.9	4.8	8.8
average	0.6	4.5	8.4

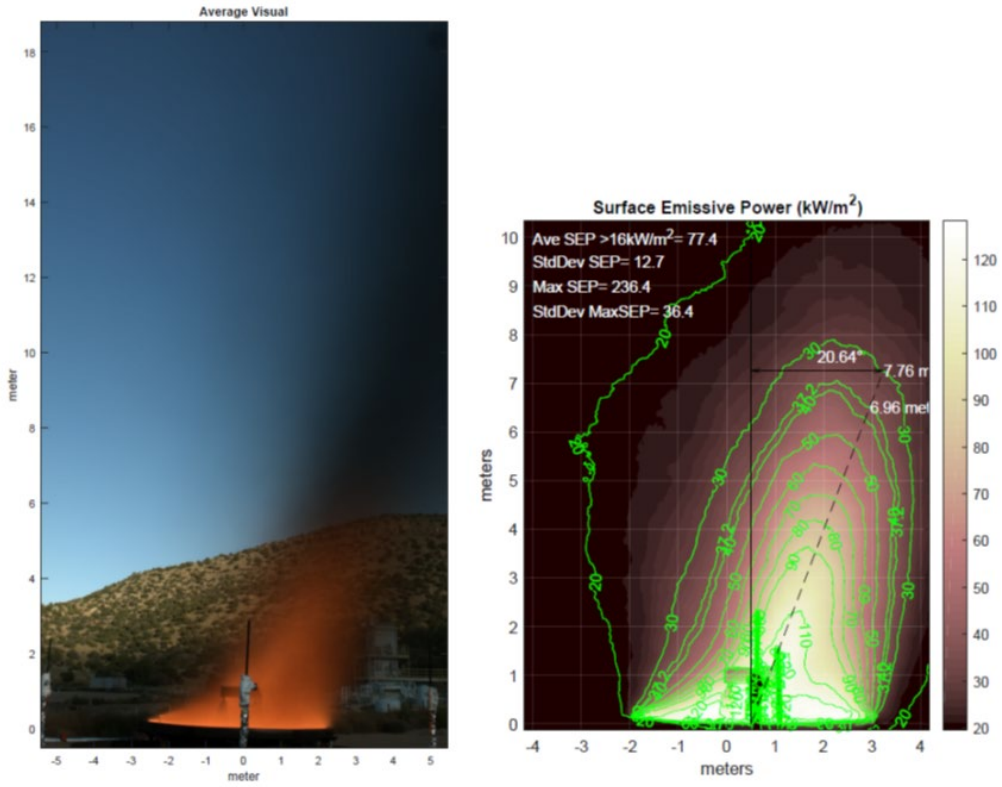

Figure A-58: Averaged flame image (left) and corresponding average SEP values (right) for 5-m Bakken.

A.2.3.7. Burn rate

Approximately 416 gallons of fuel was supplied to the pan over about 30 minutes. The fuel was steadily fed for approximately the first 11 minutes of the test, but then the targeted fuel level was not maintained, and the fire began to burn down at approximately 15 minutes. At about 24 minutes the fuel level was brought back up and for about 5 to 6.5 minutes the fuel level was visible in the sight glass and appeared steady. Also, during this time, the thermocouple rake indicated that the level was filled to about 1.34" or 34 mm. Note that a height of 34 mm corresponds to 176 gallons of fuel in the pan. From observation of the video taken of the flow meter on the tanker, the burn rate was determined during this period by assessing the barrels per second. The average burn rate based on the flow meter is 4.6 ± 0.1 mm/min.

A.2.3.8. Surface emissive power and flame height

The surface emissive power and flame temperature were determined from IR camera measurements. Since the fire was affected by the wind, periods in which the flame was the most vertically oriented and thus in the viewing range of the camera were extracted. These images were then averaged and are shown in Figure A-59 for flame temperature and surface emissive power. From these images an average value for flame temperature and surface emissive power were determined by assessing values above 750 K and 16 kW/m^2, respectively. The average temperature is 851.5 ± 116 K and the average

maximum temperature is 1221.8 ± 54.9 K. The average surface emissive power is 77.4 ± 12.7 kW/m^2 and the average maximum SEP is 236.4 ± 38.4 kW/m^2.

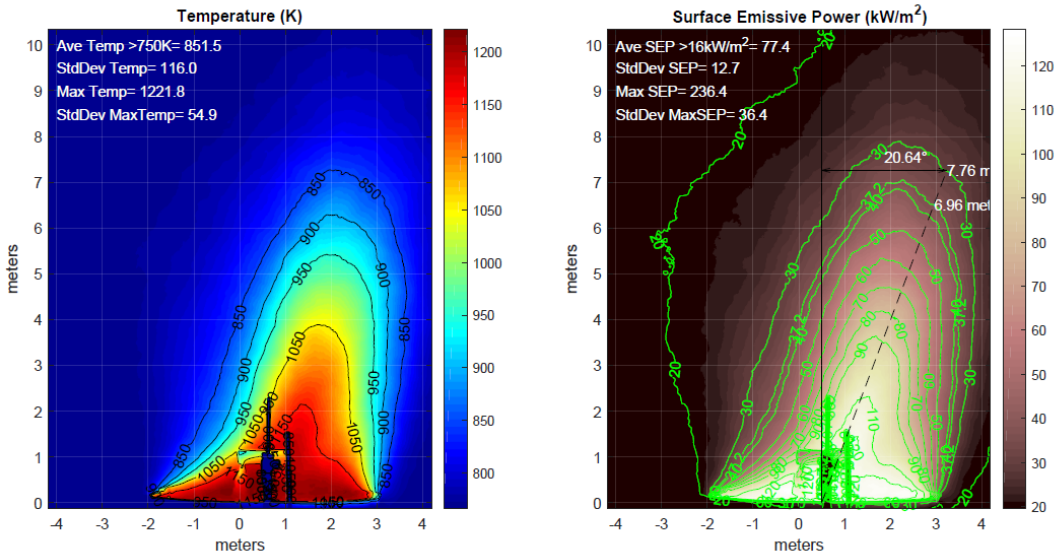

Figure A-59: Bakken crude oil: X6900 IR camera, 3-5 um cold filter, 25 mm lens at 62 m, emissivity of 1 and transmissivity of 0.91.

A.2.4. Tight 2 (Tx Shale)

This test for Tight 2 oil was conducted using the same configuration as for the Tight 1 oil, that is, the fuel pan was inside a larger pan with a diameter of 7.9 m (25.9 ft) and tanks were present below the fuel pan to allow the fuel to be quickly drained in the event of a boil over. Sight glasses were also used to monitor the liquid level via video coverage in the control room.

The oil was not preconditioned and was tested at its atmospheric temperature of about 20°C. Water was used to push the oil out of the specialized tanker which fed directly into the fuel pan. Prior to the test, the oil was circulated and pressurized to ensure that any vapor was dissolved back into the liquid and to have a homogenous mixture, as done for Tight 1 oil. After the mixing process was complete, additional oil samples were taken for analysis.

Boil-over occurred approximately 25 minutes after the beginning of the test. Prior to the test the lines were flushed with water to remove air, as was done for. Residual water left in the Tight 1 test line could have been introduced into the pan to cause the boil-over.

A.2.4.1. Weather conditions

For this test, weather data was not successfully obtained from local instrumentation. Thus, data was obtained from SNL meteorology stations. The stations provide data every 15 minutes which implies that two readings will span the length of the test. Based on this data, the wind speed was about 7 mph, wind direction 280°, relative humidity 36%, and temperature 7.5°C.

A.2.4.2. Fuel rake temperatures

Figure A-61 provides the thermocouple measurements within the fuel. All thermocouples increased above a temperature of about 150°C after the start of the test and continued to steadily decrease up until 10 minutes into the test. All thermocouples then measured similar temperatures as they rose to

a value of about 200°C just before boil-over. This behavior indicates that the fuel level height was above the thermocouple rake which is at a height of 2.4" (60 mm). Based on an estimation of the burn rate, the fuel level would not have exceeded 4", below the 6" depth of the pan. Further discussion on evaluating the burn rate is provided in section A.2.4.7.

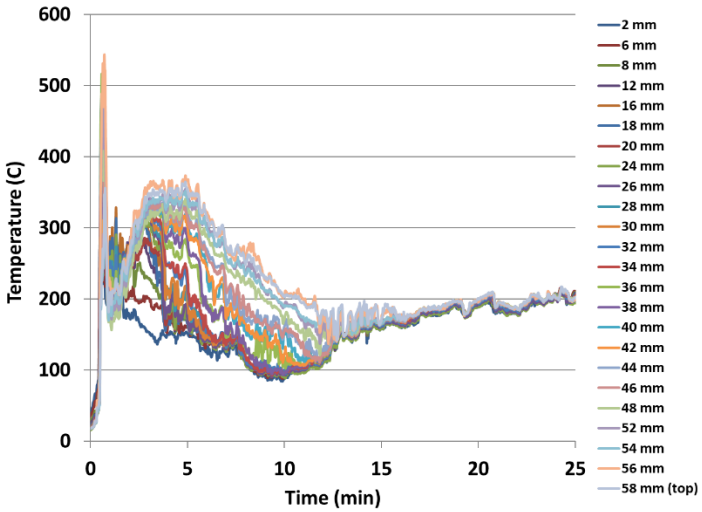

Figure A-60: Fuel rake temperature for Tight 2 (Tx Shale) 5-m pool fire test.

A.2.4.3. Radiometers

Heat flux from wide-view radiometers are shown in Figure A-62 for the 5-m and 20-m locations. Narrow-view radiometers were not available in time for the test. Since IR camera measurements were being taken to determine the surface emissive power, the decision was made to proceed with the test. The wide-angle radiometer heat flux values averaged over 5-20 minutes are provided in Table A-19.

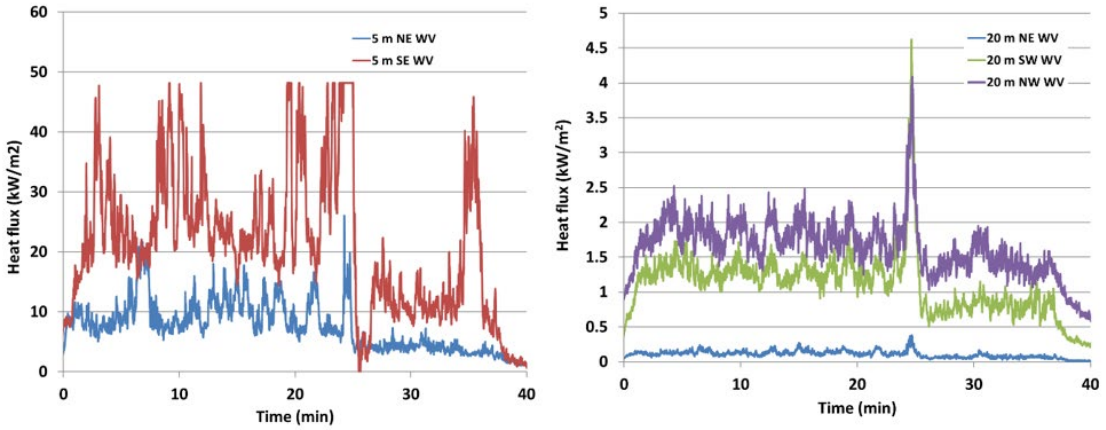

Figure A-61: Wide-view radiometer heat flux values at 5-m (left) and 20-m (right) locations, Tight 2 (Tx Shale).

Table A-19: Time-averaged heat flux values from radiometer measurements for 5-m Tight 2 (Tx Shale).

location	wide-view heat flux (kW/m^2)
5 m, NE	10.7 ±3.4
5 m, NW	NA*
5 m, SE	25.5 ±7.7
5 m, SW	NA*
20 m, NE	0.1 ±0.03
20 m, NW	1.8 ±0.2
20 m, SE	NA*
20 m, NW	1.3 ±0.1

*failed

A.2.4.4. Calorimeter

Figure A-63 shows the absorbed and incident heat flux to the calorimeter. Table A-21 provides heat flux values averaged over the time spans of 2-24 minutes at each location and averaged among all measurement locations, indicating an average absorbed heat flux of -23.7 ± 32.7 kW/m^2 and average total heat flux of 78.3 ± 18.0 kW/m^2.

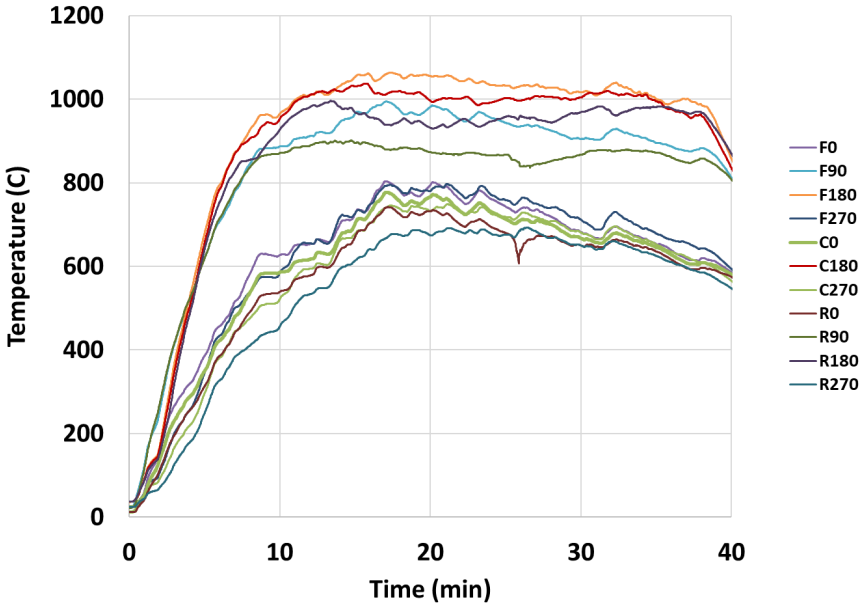

Figure A-62: Calorimeter thermocouple temperatures for Tight 2 (Tx Shale) test.

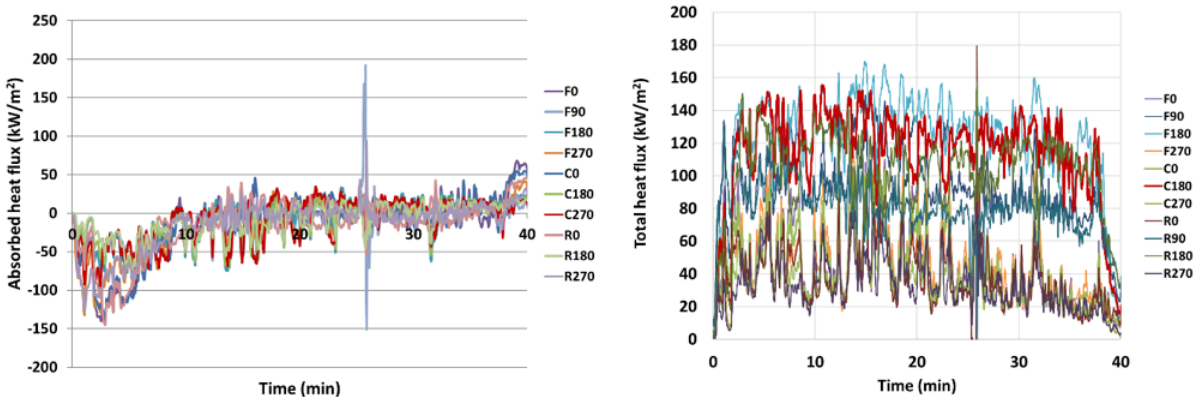

Figure A-63: Absorbed and total heat flux to calorimeter for 5-m Tight 2 (Tx Shale) test.

Table A-20: Average total and absorbed heat flux for calorimeter for 5-m Tight 2 (Tx Shale) test

	Average Heat Flux (kW/m^2)*			
position	**absorbed**	**sd**	**total**	**sd**
center 0-deg	-28.6	42.6	50.9	20.5
center 90-deg**	-	-	-	-
center 180-deg	-20.6	24.2	125.2	15.7
center 270-deg	-20.0	29.2	48.6	18.9
rear 0-deg	-27.2	41.7	45.9	17.5
rear 90-deg	0.02	0.03	87.4	12.8
rear 180-deg	-19.4	19.5	109.4	18.0
rear 270-deg	-20.8	31.8	41.0	14.7
front 0-deg	-30.1	42.8	55.5	23.5
front 90-deg	-19.0	23.3	105.2	17.3
front 180-deg	-21.8	28.5	135.4	16.2
front 270-deg	-24.5	33.9	56.5	22.4
average	**-21.71**	**28.9**	**78.3**	**18.0**

*averaged over 5-24 minutes
**thermocouple failed

A.2.4.5. Directional flame thermometer

Figure A-64 provides the absorbed and incident heat flux from DFT measurements over time and Table A-21 provides heat flux values averaged over 2-24 minutes. The NE and SE DFT instruments are similar in value and approximately a factor of two higher than the NW and SW DFTs, also similar in value. This is due to the wind tilting the flame towards the east. Note that the heat flux greatly increased during the time of boil over.

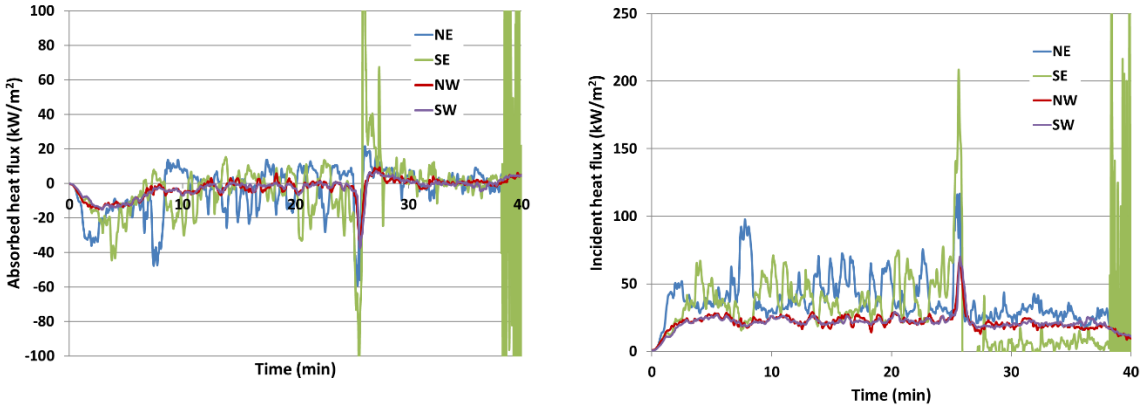

Figure A-64: Absorbed and incident heat flux DFT measurements for 5-m Tight 2 (Tx Shale) test.

Table A-21: Average heat flux values from DFT measurements for 5-m Tight 2 (Tx Shale) test.

location	absorbed heat flux (kW/m^2)	incident heat flux (kW/m^2)
NW	-4.2 ±4.6	23.2 ±2.8
NE	-6.3 ±13.2	44.1 ±14.6
SE	-6.7 ±12.1	38.0 ±12.9
SW	-4.4 ±4.4	22.6 ±2.1

A.2.4.6. Flame height

Based on measurements from the visible cameras, the minimum, mean, and maximum flame heights were determined (Table A-22). The method used to determine these flame height values is provided in section D.1.1.2.

Table A-22: Flame height statistics for 5-m diameter Tight 2 (Tx Shale) pool fire

	2-Sigma	Length	2-Sigma
	Min	**Mean**	**Max**
NW View	2.1	5.6	9
NE View	3.4	5.6	7.7
SW View	2.5	5.9	9.3
SE View	2.3	4.9	7.6
average	2.6	5.5	8.4

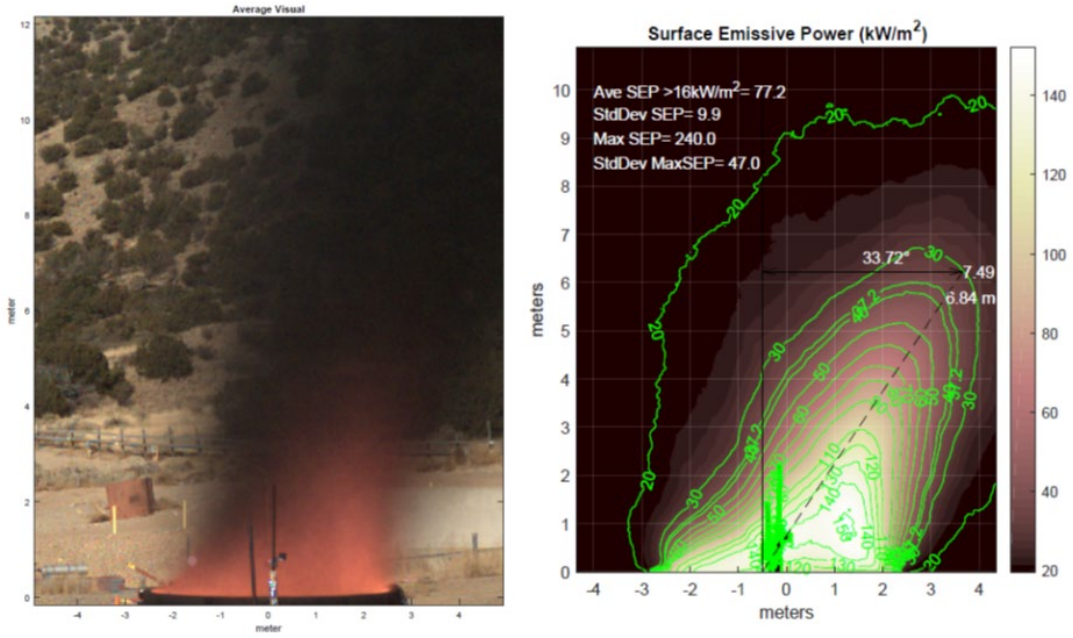

Figure A-65: Averaged flame image (left) and corresponding average SEP values (right) for 5-m Tight 2 (Tx Shale) test.

A.2.4.7. Burn rate

The method to determine the burn rate is primarily the differential pressure (dP) gauge at the bottom of the pan. To protect the gauge from potential thermal damage a fluid, typically water, is used to cover the sensor. Since water's boiling point is below the typical temperatures reached in-depth for the crude oil within the pan it is not a viable fluid. Thus, for this test, motor oil was used for protection. The gauge ended up failing, the cause of which is uncertain. It is suspected that the motor oil degraded due to reaching temperatures of around 200°C. Thus, changes in fluid properties could have occurred, thereby resulting in unreliable gauge performance. Both SPR tests used Jet-A for thermal protection of the dP gauge and this was effective in maintaining the integrity of the gauge for at least 30 minutes. Jet-A will be used for the final test in this test series. The rational for switching to motor oil was that it could potentially provide more robust performance, but this proved not to be the case.

The other method to determine the liquid level in the pan is the sight glass, but the glass became completely obscured during the test. A modification from the previous test was made that would enhance visualization of the sight glass by blowing nitrogen onto the glass to push smoke away. The flow rate of the nitrogen could have been potentially too high causing enhanced smoke production locally by its quenching effect and possibly enhancing obscuration by smoke entrainment into the jet towards the sight glass. Thus, the liquid level could not be determined.

An average burn rate can be estimated, however, based upon knowledge of the total burn time and the amount of fuel introduced into the pan. The total time over which the fire burned steadily was approximately 40 minutes. Approximately a total of 706 gallons of fuel was introduced into the pan, after accounting for oil remaining in the lines. However, the fuel remaining in the pan during the time in which the fire was burning down is unknown. Also, the fuel that was spilled during the boil over is unknown.

To provide an estimate of the burn rate, different percentages to account for these 'losses' can be assumed. Table A-23 provides the results from assuming up to a 30% loss in fuel that did not contribute to steady burning. The results indicate that if a 20% loss is assumed, the potential variation in the burn rate is ±12.5%. Since the burn time of the spilled oil was relatively short (~2 minutes) and the burn down time was about 5 minutes, which is about 15% of the total burn time, the burn rate will be estimated by assuming a 20% loss. Thus, the estimated burn rate is 2.7 ± 0.3 mm/min.

Table A-23: Burn rate assumed various percentages of loss

Fuel loss (percent of total fuel introduced)	Fuel loss (gallons)	Fuel consumed during steady burning (gallons)	Burn rate (gallons/min)	Burn rate (mm/min)
10%	71	635	15.9	3.06
20%	141	565	14.1	2.72
30%	212	494	12.4	2.38

A.2.4.8. Surface emissive power and flame height

The surface emissive power and flame temperature were determined from IR camera measurements. Since the fire was affected by the wind, periods in which the flame was the most vertically oriented and thus in the viewing range of the camera were extracted. These images were then averaged and are shown in Figure A-66 for flame temperature and surface emissive power. From these images an average value for flame temperature and surface emissive power were determined by assessing values above 750 K and 16 kW/m^2, respectively. The average temperature is 853.4 ± 134.1 K and the average maximum temperature is 1266.4 ± 119.5 K. The average surface emissive power is 77.2 ± 9.9 kW/m^2 and the average maximum SEP is 240.0 ± 47.0 kW/m^2.

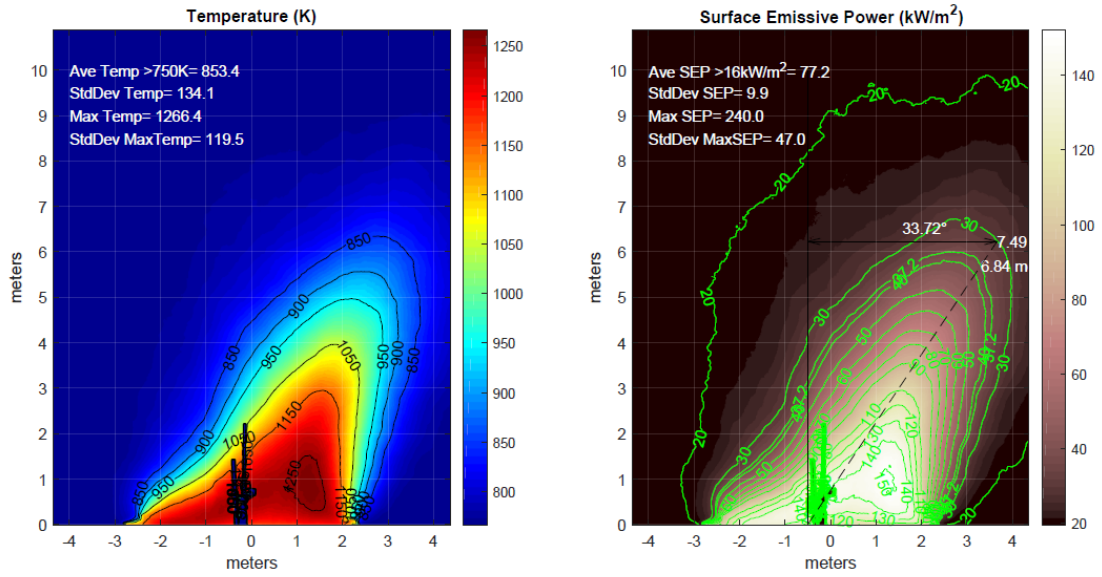

Figure A-66: Tight 2 (Tx Shale): X6900 IR camera, 3-5 um cold filter, 25 mm lens at 62 m, emissivity of 1 and transmissivity of 0.91.

A.3. Fireball Tests

A.3.1. 100-gallon tank

A.3.1.1. Steam test

The objective of this test was to assess system components such as performance of the ram, rupture disc, tank, associated valves and piping, ballistic blanket, tank monitoring and control, heaters, and break wires. This test is the first of two tests to assess performance before testing with crude oils. The next test continued this effort by using a 'surrogate' fuel (mixture of Jet A and gasoline) to assess system performance involving combustion.

The day before the test, the tank was filled with 18 gallons of water and heated over the course of about 5.5 hours to achieve the desired temperature range. The rupture disc that was used was rated to 480 ± 20 psi, which for water corresponds to a temperature of about 235°C. To prevent disc failure before activation of the ram, the pressure for activation was chosen to be 400 psi, well below the tolerance of the disc. Once we achieved this pressure, the ram was activated, but failed to puncture the disc. On inspection of the close-up video, the ram was deflecting such that there was not sufficient distance between it and the rupture disc, thus it simply pushed against the disc. The support frame was not strong enough to provide resistance to the ram action.

It was then decided to go to a higher pressure of 470 psig to increase the ability of the ram to puncture the disc. Once a pressure of 462 psig was reached, the disc failed due to reaching tolerance pressure and not from the ram, resulting in the ejection of the water in the form of a white vapor cloud that rose to over 100 ft. Fragments of the rupture disc were thrown upward, and the ram support frame was broken off and thrown 10s of feet. The ballistic blanket and insulation were shredded. Thus, the ballistic blanket was ineffective and was not used in future tests since it could present a fire danger if it becomes fuel soaked. The ram was also altered with additional support to prevent deflection.

A.3.1.2. Surrogate test

The objective of this test was to assess additional system components beyond those tested with steam by using a 'surrogate' fuel (50/50 mix of Jet A and gasoline). The additional systems of interest include the process of driving the fuel into the tank with water, purging tank of water, preventing air from contacting fuel, GWR performance, heating fuel within a 12-hour window, performance of modified ram, ability to ignite the fuel, and obtaining heat flux data by the photometric team.

Prior to performing the test, the 100-gallon tank was first filled with water to purge all the air inside the tank and lines. Water was then used to push 40 gallons of fuel out of the fuel drum and into the tank. The remaining 60 gallons of water was then driven out of the tank by heating the tank to 100°C. Once completely purged of water, as confirmed with the sight glass and sampling at a needle valve below the tank, an 800 ft hazard zone was put in place. Heating commenced at approximately 8:00 pm anticipating a 12-hour heating window for an 8:00 am test start time the next morning.

On the day of the test, the fuel was at a temperature of 330°C and pressure of 394 psig, respectively, inside the tank. This temperature and pressure was reached in about 12 hours. Three propane torches, each on their own support pole, were then activated and confirmed to be operating. The ram was then activated and after puncturing the disc, it remained in place and was not immediately retracted. The ram design was to puncture the disc, and then retract immediately from the disc failure. Thus, the rupture disc did not fail immediately and allowed vapors to start escaping at a low flow rate. These vapors ultimately ignited within about a minute and a small torch fire approximately 1-ft in length on

top of the tank was sustained for under a minute. It was then realized that it was manually necessary to retract the ram since it was providing structural support, preventing the disc from fully rupturing. Once retracted, failure occurred, and a high velocity jet of vapor was released which did not ignite. The vapors were visible, indicating that the fuel was comprised of droplets and gas, but no rain-out occurred indicating that the droplets were not large. Fencing material used to replace the ballistic blanket was thrown upward and appeared to reduce the momentum of the fragments since they were found in roughly half the proximity to the tank as compared to using the ballistic blanket. Insulation placed on top of tank was shredded due to the passage through the fencing material. After the vapors were ejected, flames approximately 2 feet in length periodically appeared from the tank for under a minute.

The outcome of this test indicated that the propane torches are not a reliable/effective source of ignition. Thus, the use of explosives as the means of ignition was explored due to this outcome.

The Sandia shock-physics code, CTH, was used to design the C-4 charge. Several exploratory cases were performed to determine the appropriate size, placement, shape, timing of detonation relative to the rupture of the disc, and potential to damage the tank. The effectiveness of the C-4 was determined by assessing the persistence of hot explosive products to provide ignition and the ability to create effective mixing of the released fuel and surrounding air.

The simulation results indicated that the design for the 100-gallon tank requires a 0.25-lb, spherical, C-4 charge placed 1-m above the disc and initiated within 1-ms, whereas the 1000-gallon tank requires a 1-lb, spherical, C-4 charge place 1-m above the disc and initiated within 1-ms. The explosives team also recommended, as added assurance, to surround the C-4 charge with a layer of zirconium particles to serve as an additional source of ignition once they are heated and thrown by the explosive charge.

A.3.1.3. Jet-A test

The objective of this test was to assess whether the 0.25-lb of C-4 explosive with a zirconium shell could ignite 40 gallons of Jet-A fuel, released from the 100-gallon tank at a pressure of about 265 psig and temperature of about 370°C, to create a fireball. Three propane torches with spark ignitors were also placed around the tank as a secondary source of ignition.

Preparation for the test took place the day before in which the tank was first filled with water to evacuate all the air. Fuel was then fed in through the top of the tank to displace an equal amount of water from the tank. The remaining 60 gallons of water had to be evacuated by heating the tank to about 100°C, thereby increasing the pressure through vapor generation and liquid expansion. It was expected to take about 2-3 hours, but instead started to exceed 4 hours. This is due to the Jet-A not containing appreciable light end hydrocarbons. It was then decided to inject argon at about 50 psi into the top of the tank to drive the water out which took about 5 minutes. The total amount of fuel in the tank was about 38 gallons. The Arming and Fire (AF) team then proceeded to install the C-4 charge. Heating to about 370°C occurred overnight between 10:30 pm to about 5:00 am the next morning. The tank pressure was not to exceed 275 psig.

The next day at test execution, the C-4 was armed and the ram was actuated, creating a hole in the top of the tank allowing vapor to escape. The ram control sequence was designed to retract the ram, but due to human error the incorrect de-activation sequence was entered from the DAQ. After 20 seconds the error was identified, and the ram retracted, thus allowing the rupture disc to fully open and trigger the C-4 break wire. The C-4 charge then detonated and proceeded to ignite the fuel, resulting in a fireball (Figure A-67).

Figure A-68 is data captured from the IR camera. The surface emissive power was determined by using an emissivity of 0.98 and transmissivity of 0.8. Figure A-69 shows the surface emissive power over time obtained from the IR camera. Figure A-70 provides the diameter and height from the ground to the center of the fireball over time. Table A-24 provides the average maximum and mean surface emissive power over time. The mean is averaged over the surface of the fireball. The results indicate that the surface emissive power is not uniform across the surface of the fireball, rather there are regions with very high fluxes occurring. Note that the mean surface emissive power is the pertinent parameter for hazard analysis. Table A-25 provides additional parameters for the Jet-A fireball test.

The results for the 100-gallon tank Jet-A test indicated that the band heaters, ram, and C-4 charge were operationally successful, however, performance with regards to the 1000-gallon tank was unproven.

Figure A-67: 100-gallon tank, Jet-A fireball.

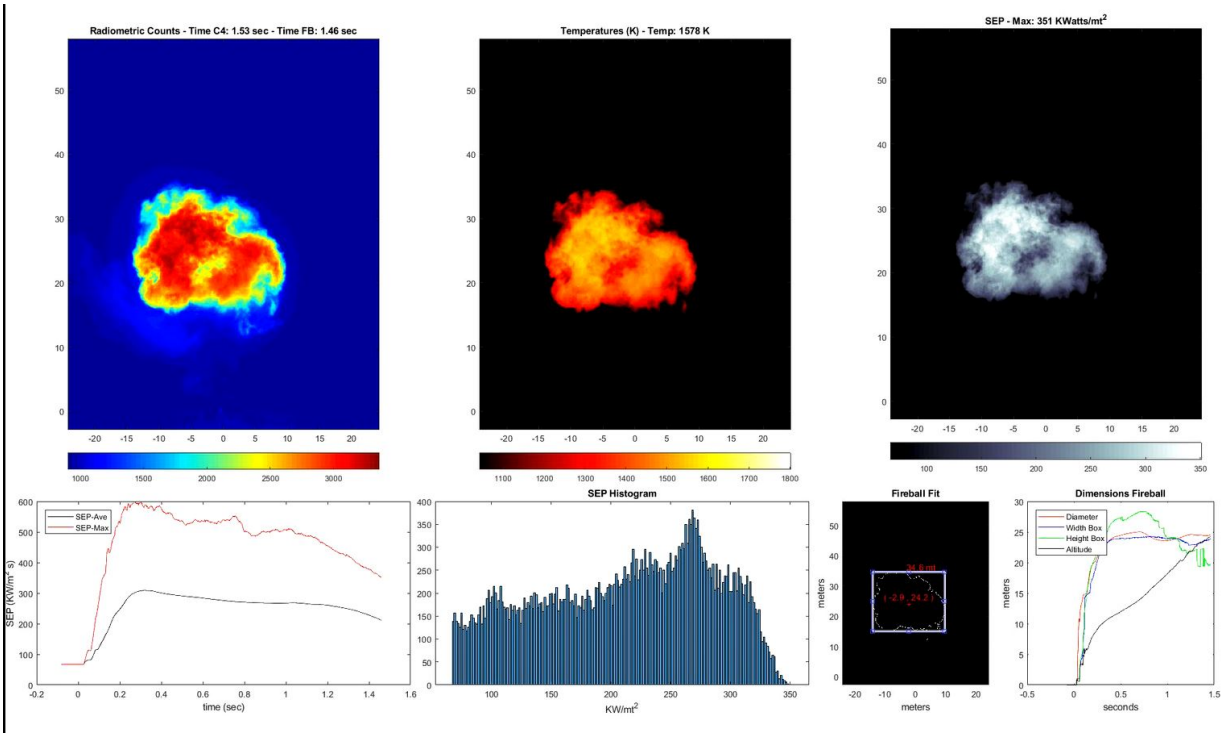

Figure A-68: IR camera data capture, 38-gallon Jet-A fireball test.

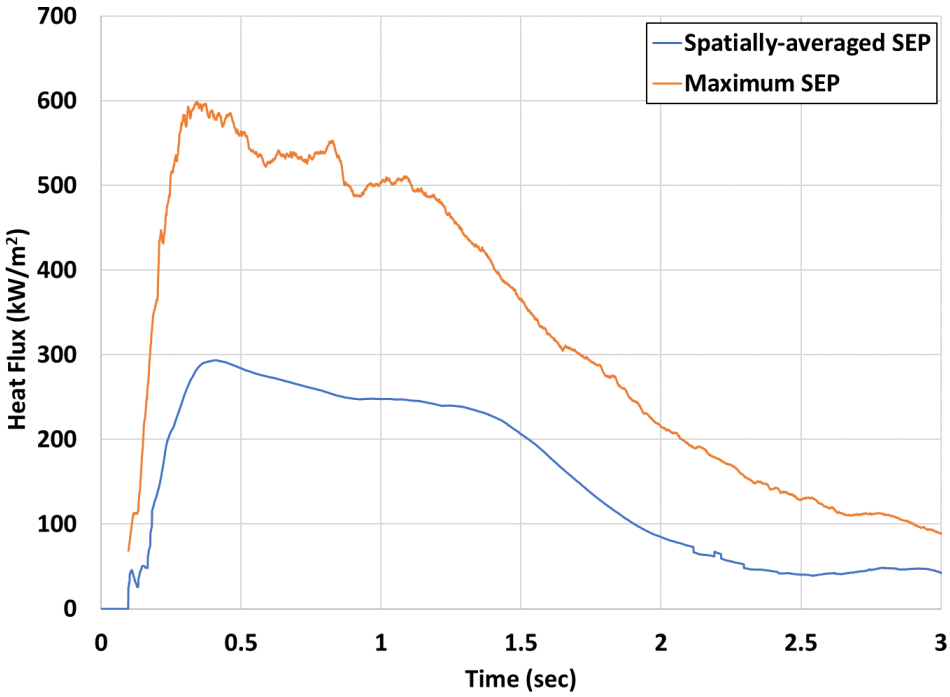

Figure A-69: Surface emissive power of 38-gallon Jet-A fireball.

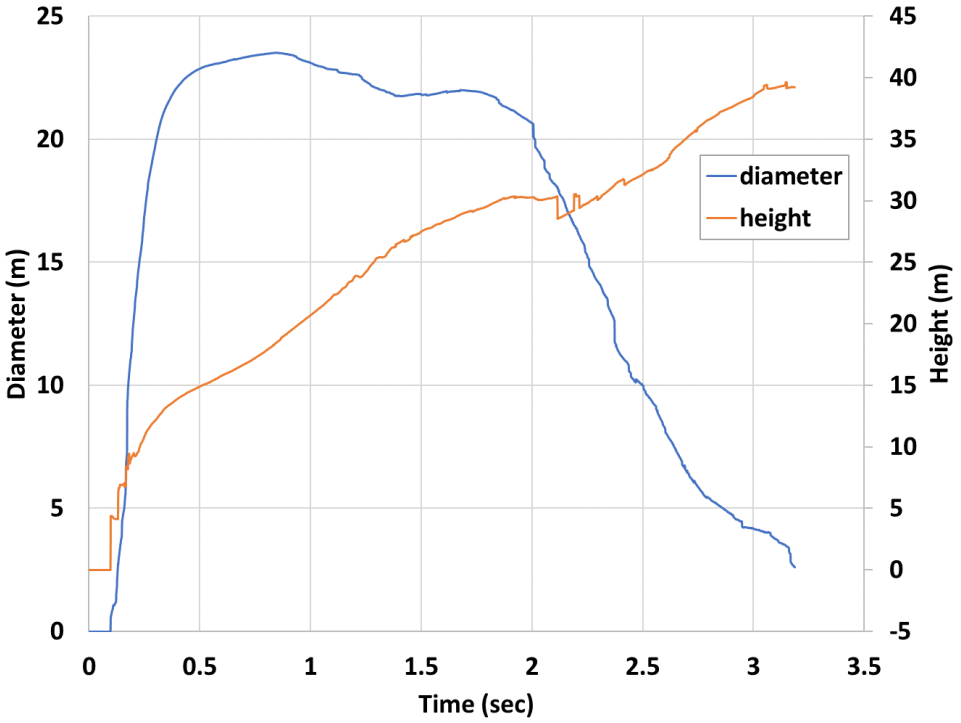

Figure A-70: Diameter and rise height of 38-gallon Jet-A fireball.

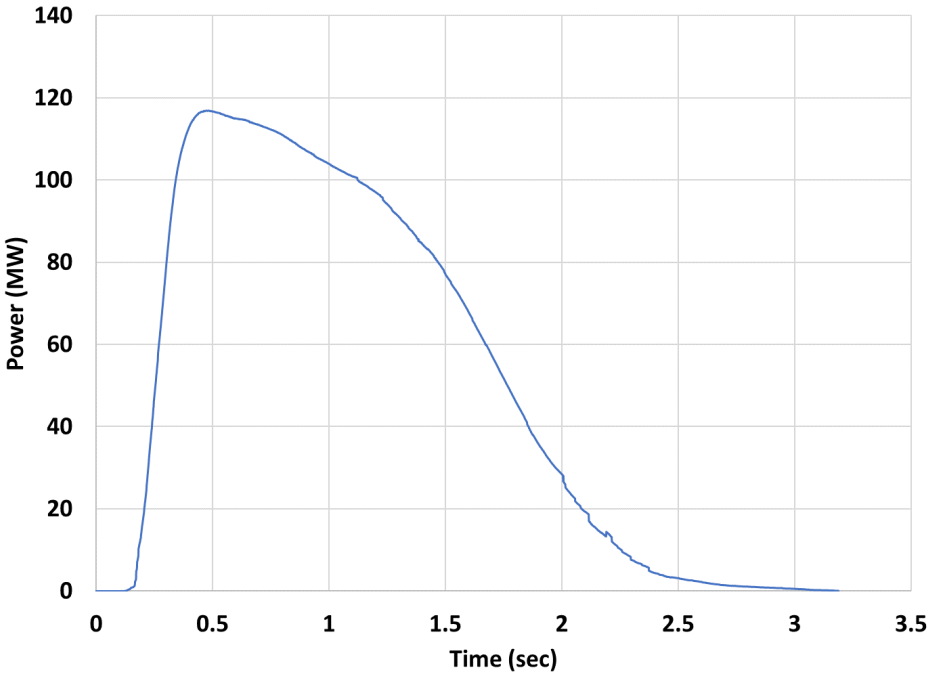

Figure A- 71: Power over time for 38-gallon Jet-A fireball.

Table A-24: Data for 38-gallon Jet-A fireball

Mass (kg)	116
Time to maximum power (s)	0.48
Maximum power (MW)	117
Projected area at maximum power (m^2)	408
Average SEP at maximum power (kW/m^2)	287
Maximum average SEP (kW/m^2)	294
Time to maximum average SEP (s)	0.42
Maximum SEP (kW/m^2)	599
Time to maximum SEP (s)	0.34
Maximum projected area (m^2)	435
Time to maximum projected area (s)	0.84

Table A-25: Parameters for 100-gallon Jet-A fireball

Mass (kg)	Diameter* (m)	Height*† (m)	Duration** (s)	Maximum Average Surface Emissive Power*** (kW/m^2)	Maximum Power (MW)	Energy (MJ)
116	23 ±1	15 ±1	3.2 ±0.2	287 ±17	117±14	162 ±19

*Effective diameter based on projected area measurements at time of maximum power

*† Distance from ground to fireball center at time of maximum power

**Time until visible thermal radiation ceases

***Spatially averaged and at time of maximum power

A.3.2. 1000-gallon tank

A.3.2.1. Preparatory activities

Initial Attempts

There were two initial attempts to conduct a Jet-A fireball test using the 1000-gallon tank. The first test resulted in the inability to heat the oil to the target temperature and pressure due to the heaters failing from shorting (dark regions shown in Figure A-72). It was thought initially that water from rain had seeped underneath the heaters, but after inspection this was not the case. The defective heaters were replaced as directed by program leads and another test attempted. The same failure occurred with the cause of the heater failure uncertain. It was then decided that radiant heaters would be a more reliable method to heat the tank. The description of the band heaters and radiant heaters is provided in Appendix C, section C.7.

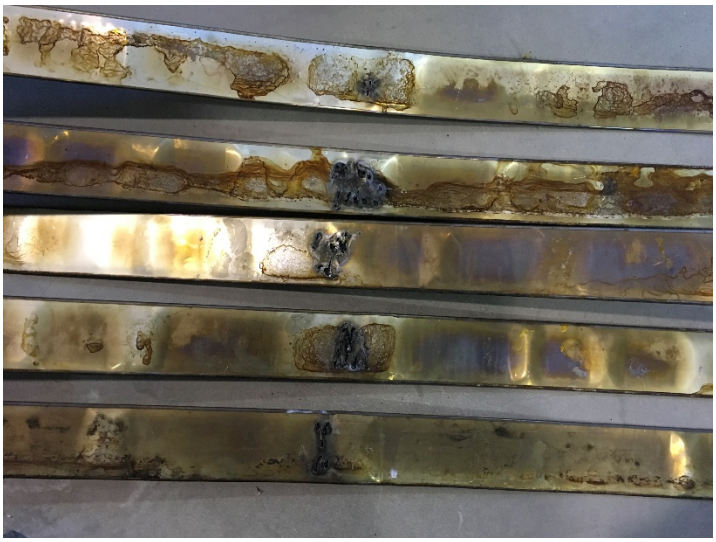

Figure A-72: Band heaters that failed after first test attempt.

The radiant heaters were installed and then used for the next attempt at a Jet-A fireball test. They were enclosed in a protective structure to prevent water ingress and to reduce heat loss when heating (Figure A-73). The radiant heaters proved to be robust in heating the tank to 350°C, however the ram was not effective in rupturing the 48" disc. Thus, the test was unsuccessful. The ram punctured through the middle of the disc resulting in a 1" hole that allowed high-speed vapor to escape (Figure A-74). To prevent a vapor dispersion event, the 1-lb C-4 charge was detonated with a manual override. The vapor was ignited, and a jet fire resulted (Figure A-75). Due to this outcome it was decided to not use the ram for future tests, but use linear-shaped charges as the method to rupture the disc.

Figure A-73: Radiant heaters in protective enclosure surrounding 1000-gallon tank.

Figure A-74: Hole created in disc from ram.

Figure A-75: Jet fire after vapor ignited with C-4 charge.

Figure A-76 and Figure A-77 provide measurements of SEP and height from two IR cameras, respectively. The results indicate steady-state spatially-average SEP values of about 100 to 125 kW/m^2 and local maximum values of 275 to 300 kW/m^2. The height of the flame was about 12 m at steady-state.

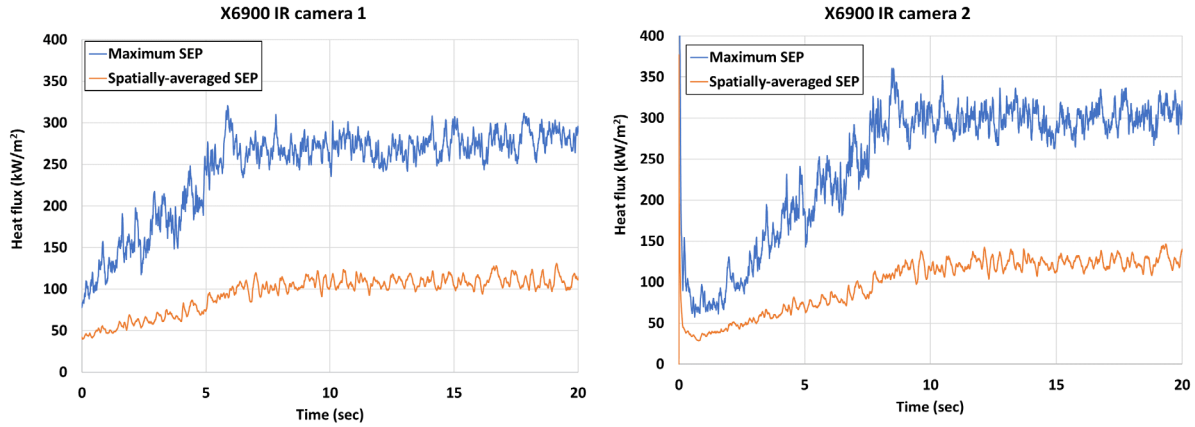

Figure A-76: SEP from IR measurements for Jet-A flare.

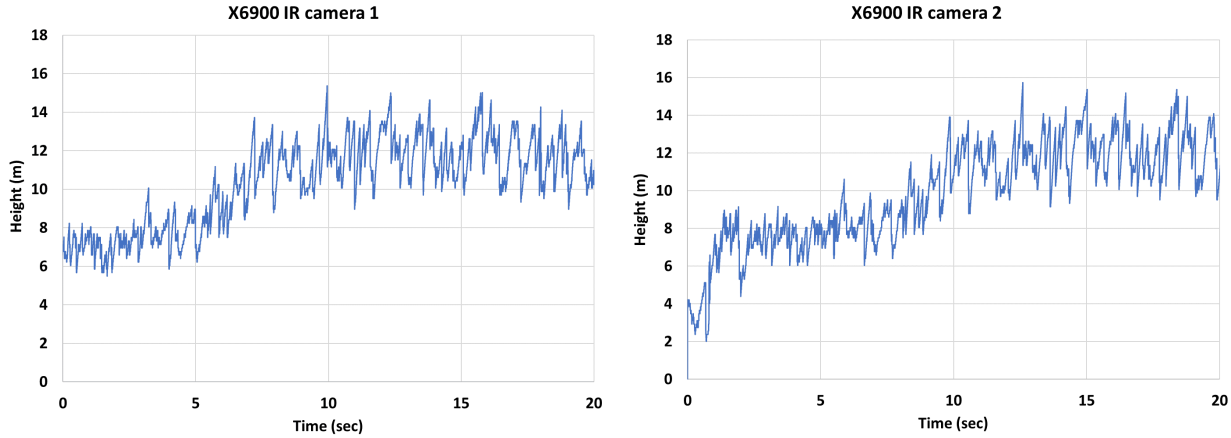

Figure A-77: Height from IR measurements for Jet-A flare.

Design and Testing of Linear-Shaped Charges

The design of the linear shaped charges was undertaken by the explosives team. The challenge was to determine the appropriate charge size that would provide clean cuts while not damaging the tank. The other aspect that proved to be challenging is the requirement of a stand-off distance from the disc due to the thermal environment. The further away that the charges are from the target material the greater the degradation of performance.

The testing involved a graded approach, beginning with simple to more complex configurations. Thus, initially several exploratory tests using steel plates, equivalent to the thickness of the disc (0.075”), and witness plates to determine damage were performed. Then the next set of experiments involved testing the charge surrounded by a box structure to assess lateral damage (Figure A-78). Various grain sizes were tested, first without insulation and then the next set of experiments had insulation.

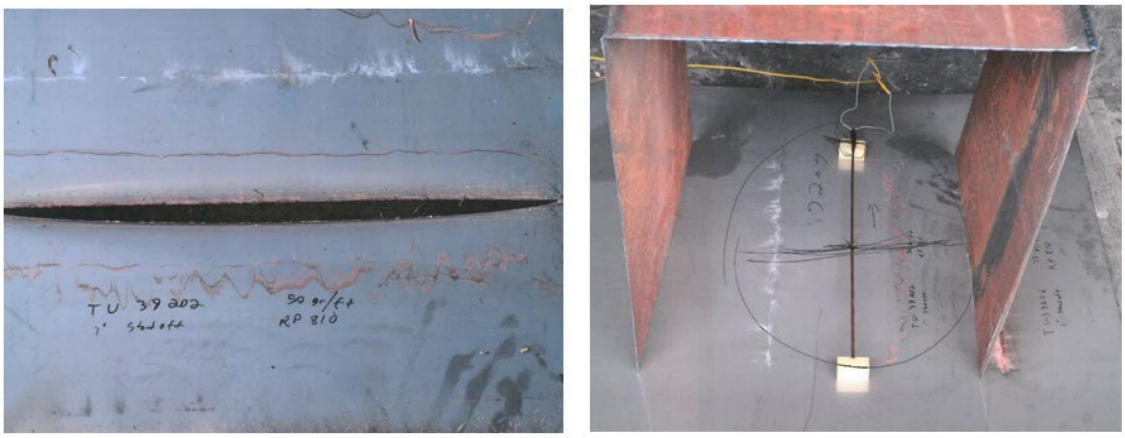

Figure A-78: Exploratory tests to determine appropriate linear-shaped charge; plate test (left) and box-structure test (right).

Due to the critical thermal threshold of the linear-shaped charge, the disc was required to be covered with insulation. The exploratory tests indicated that the insulation degraded the performance of the charges, thus it was decided to have a small gap in the insulation above the disc's score lines. This would require some form of protection from the radiant heat transfer that would occur at the gaps and would impact the charges. Thus, foil tape was placed over the gaps to significantly reduce the heat transfer. The insulation that would provide the required thermal protection was determined through numerical simulation. The results from the simulation of temperature as a function of distance from the surface of the disc is shown in Figure A-79. It was found that the foil tape with 1" of insulation was successful in providing temperatures below 100°C, the required conservative temperature to protect the charges. The temperatures should be in the range of 75°C to 100°C just above the foil tape for a disc temperature of 350°C. In addition to performing simulations to design the thermal protection, experiments were performed for validation. The experiments utilized the damaged disc from the last 1000-gallon tank test.

The disc was covered with the 1" thick insulation, allowing for ¼" gaps at the score lines. Foil tape was placed over the gaps and the disc heated to 350°C. Numerous thermocouples were placed above the foil tape to assess temperature. The experimental results indicate that thermocouple temperatures over time are below 100°C (Figure A-80). Note that for the crude oil, the disc will be at a temperature of 300°C which results in temperatures between 50°C to 75°C above the foil tape, well below the already conservative threshold temperature required to protect the charges. Thus, numerical and experimental results in indicate that the specified insulation with foil tape will provide the required thermal protection.

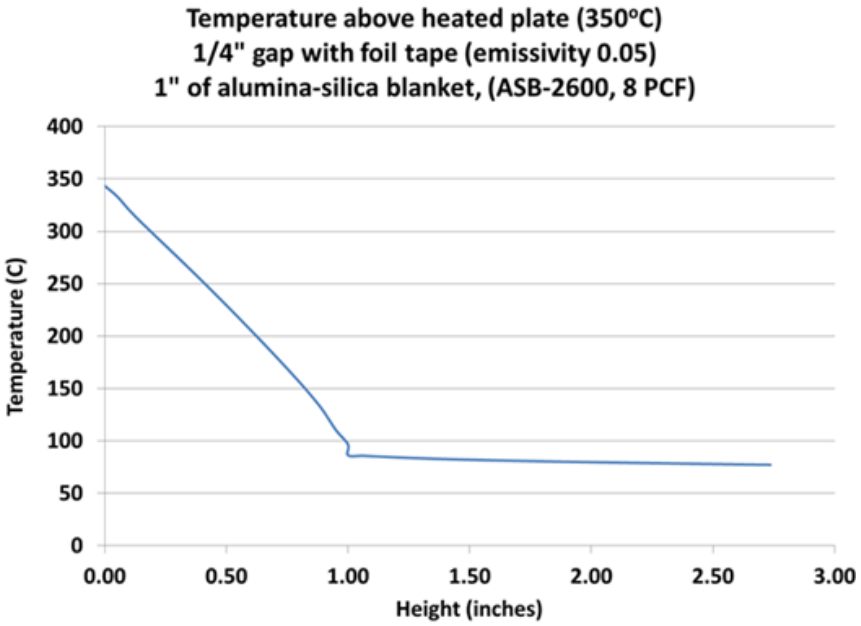

Figure A-79: Simulations of insulation with foil tape.

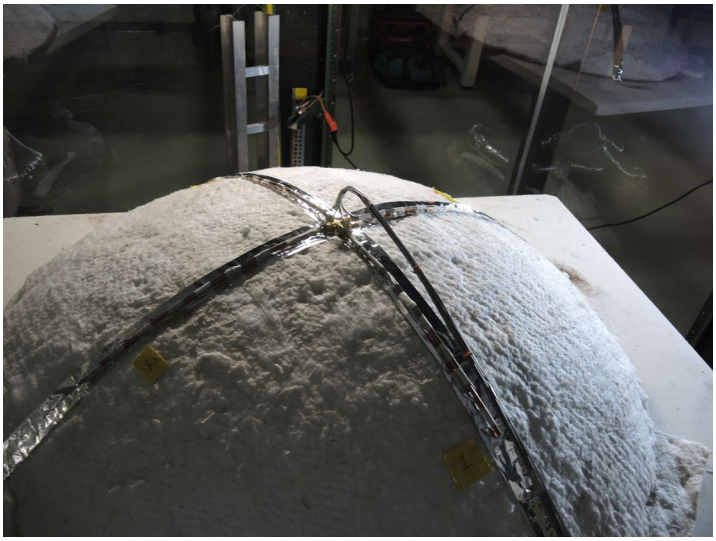

Figure A-80: Experimental set-up of disc with insulation and foil tape.

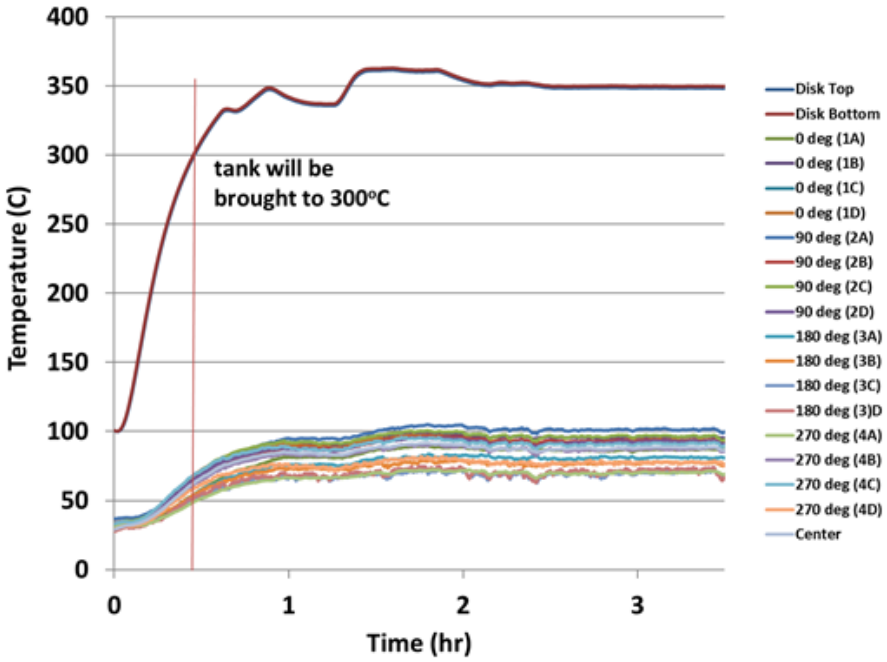

Figure A-81: Experimental results of disc with insulation.

The next phase of testing involved testing the timing of the linear-shaped charges in conjunction with the 1-lb C-4 charge (Figure A-82). This included using the damaged disc and a dual firing set to control the detonation of the charges. High-speed video was obtained to confirm that the disc is ruptured before the C-4 is detonated. Figure A-83 shows that the disc was cleanly cut at the score line and Figure A-84 shows the shock-wave from the shaped charges and the C-4 fireball. Inspection of the high-speed video indicated that the desired timing was achieved.

Figure A-82: Experimental set-up of disc, linear-shaped charges, and 1 pound of C-4.

Figure A-83: Disc with clean cuts at score lines.

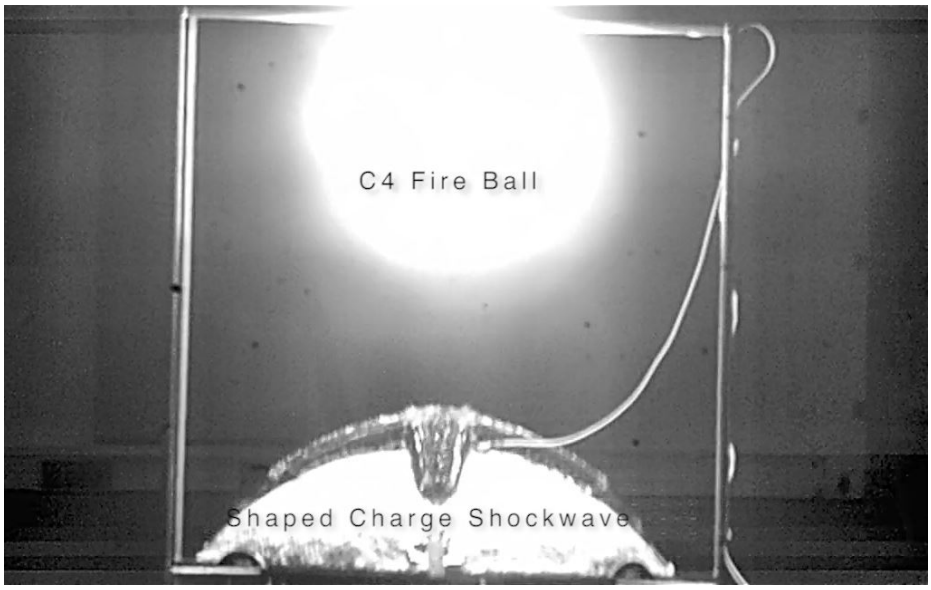

Figure A-84: Linear-shaped charge shock wave and C-4 fireball.

Moving the Test Site

Lurance Canyon Burn Site, where the 100-gallon tank fireball and 5m pool fire test series were run, posed special challenges for cleanup if a crude oil fireball failed to ignite and a crude oil aerosol was released to the environment. Several other test sites at Sandia were explored, and a lower-risk option was identified. In summer 2018, the test infrastructure was moved to the alternative site. The description of the site is provided in section B.3. Thus, the test site was moved from the burn site to another site named herein as "Pad B".

Instrumentation at alternative site (Pad B)

Figure A-85 provides the instrumentation and their distances from the test tank.

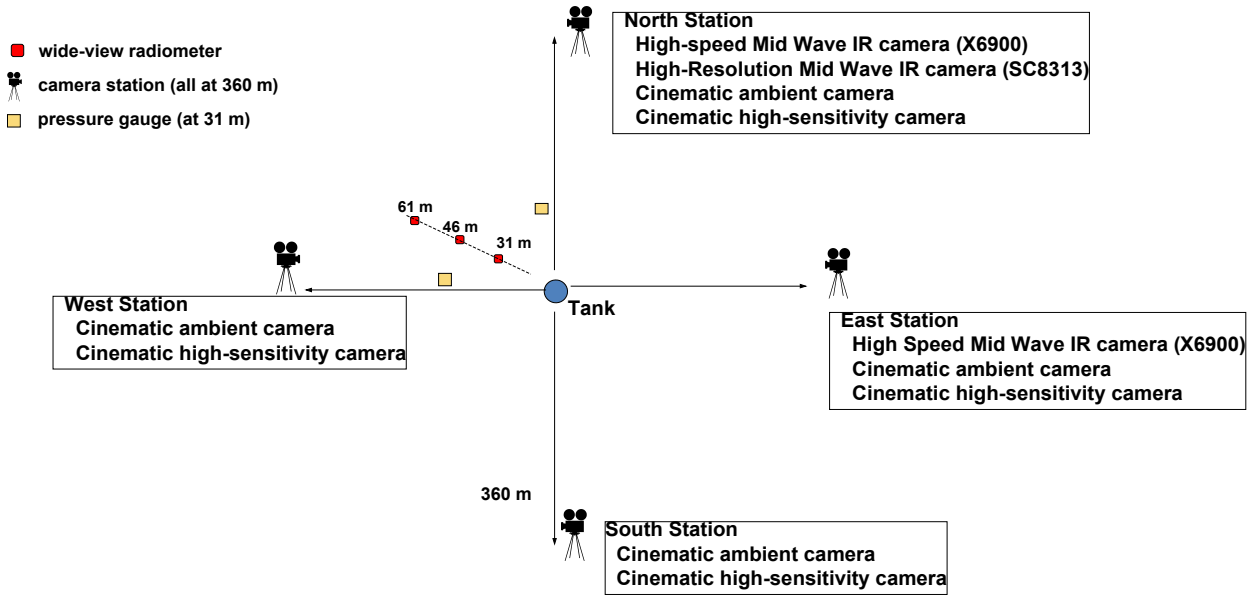

Figure A-85: Instrumentation layout at Pad B.

Initial test attempt using Tight 1

An initial attempt to perform a fireball test using Tight 1 resulted in the linear shaped charges failing to detonate and the C-4 charge detonating. The tank failed to open and thus no oil was spilled. The oil in the tank was judged to be still satisfactory for testing and thus was pumped back into the tanker. The linear shape charges were successfully recovered and were not damaged. Some large fragments of the detonator were also recovered. It was determined through experimental testing that the detonator did not operate at full power due to thermal degradation. The testing involved examining fragment patterns of full strength detonators to the detonator fragments recovered post-test, as well as testing different charge stand-off distances to the detonator and comparing the resulting damage to the linear shaped charges to the recovered charges.

The thermal degradation was due to an uncommunicated operational change when the explosives were being placed. The designed thermal configuration was altered by cutting the foil tape above the gaps. The charge assembly was then installed above the exposed gaps, thereby subjecting them to a heat flux of about 4 kW/m^2 at a stand-off distance of 1". The design required that the foil tape directly cover the gaps to serve as a radiant barrier. After the charge assembly was installed it was then entirely covered with foil tape. This further enhanced the heat received to the copper-lined charges. Since copper is highly conductive, heat was readily transmitted to the detonator. This would explain the source of the thermal degradation.

To verify the adequacy of the thermal environment, an additional test was performed in the field using the disc left in place on the 1000-gallon tank after the attempted test. The configuration of the insulation and foil tape were the same as used for the indoor test and for the attempted test, that is, the disc was covered with the 1" thick insulation, allowing for ¼" gaps at the score lines, and foil tape place over the gaps. In addition to placing the insulation and foil tape, a mock assembly of the detonator and linear shape charges was installed. The tank was heated to a maximum temperature similar to that on the attempted test (Figure A-86 and Figure A- 87). Numerous thermocouples were placed between the insulation and the assembly to measure temperatures for several hours (Figure A-

88). The results indicate that the thermocouple temperatures range from 30°C to 70°C depending on the wind speed (Figure A-88 and Figure A-89). As indicated in Figure A-89, as the wind speed increases the temperatures decrease due to convective cooling. As an added measure for the next test, an air curtain was installed around the charge assembly to further enhance convective cooling in addition to any wind present. Figure A-90 provides a comparison of wind speeds between the field thermal test and attempted test. The results from the thermal field test provided further validation that the thermal configuration was adequate to protect the linear-shaped charges.

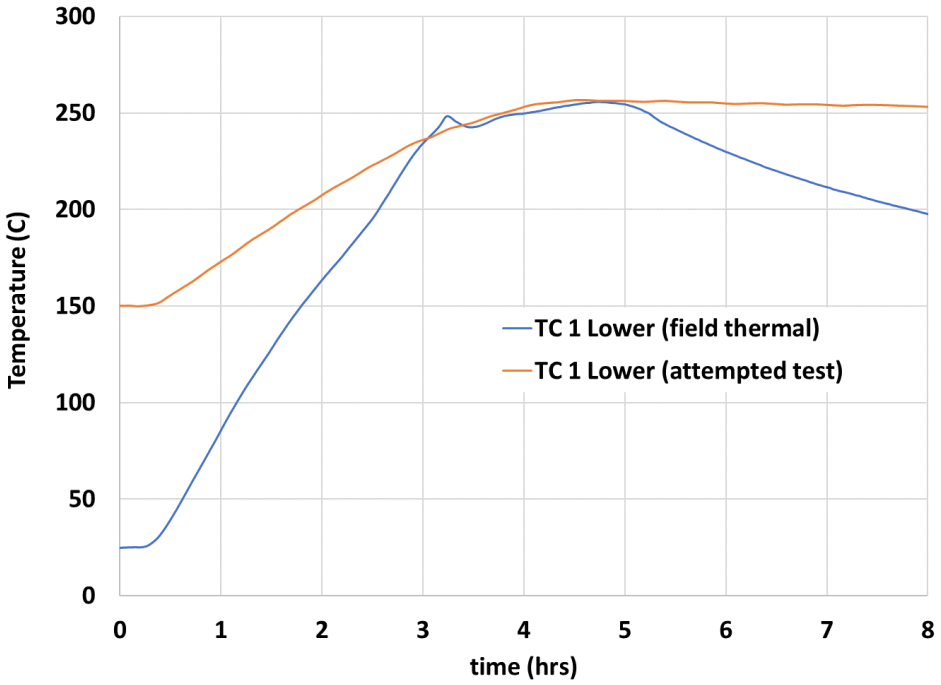

Figure A-86: Internal tank temperature for outdoor thermal field test and attempted test.

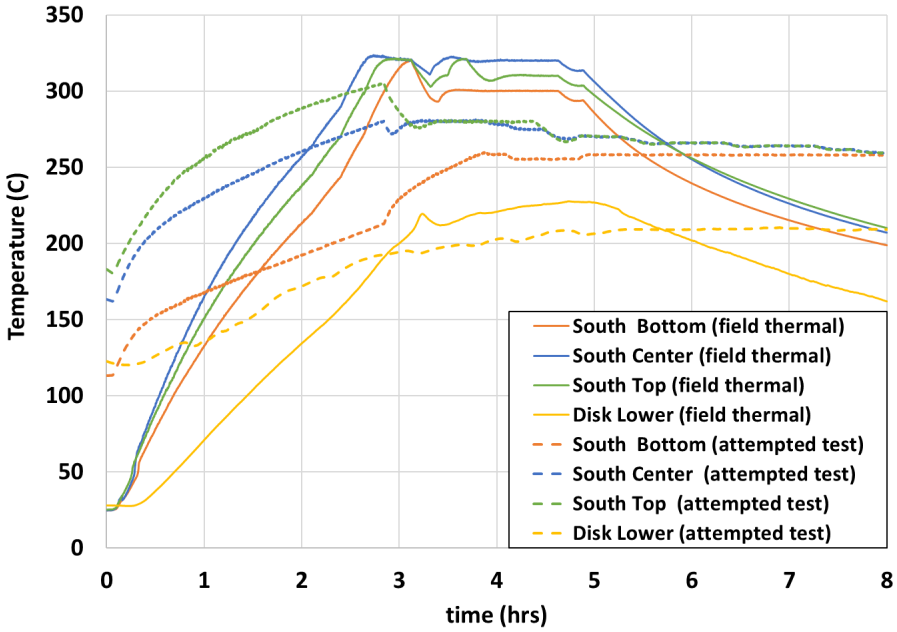

Figure A- 87: Thermocouple temperatures on heaters and disc for thermal field test and attempted test.

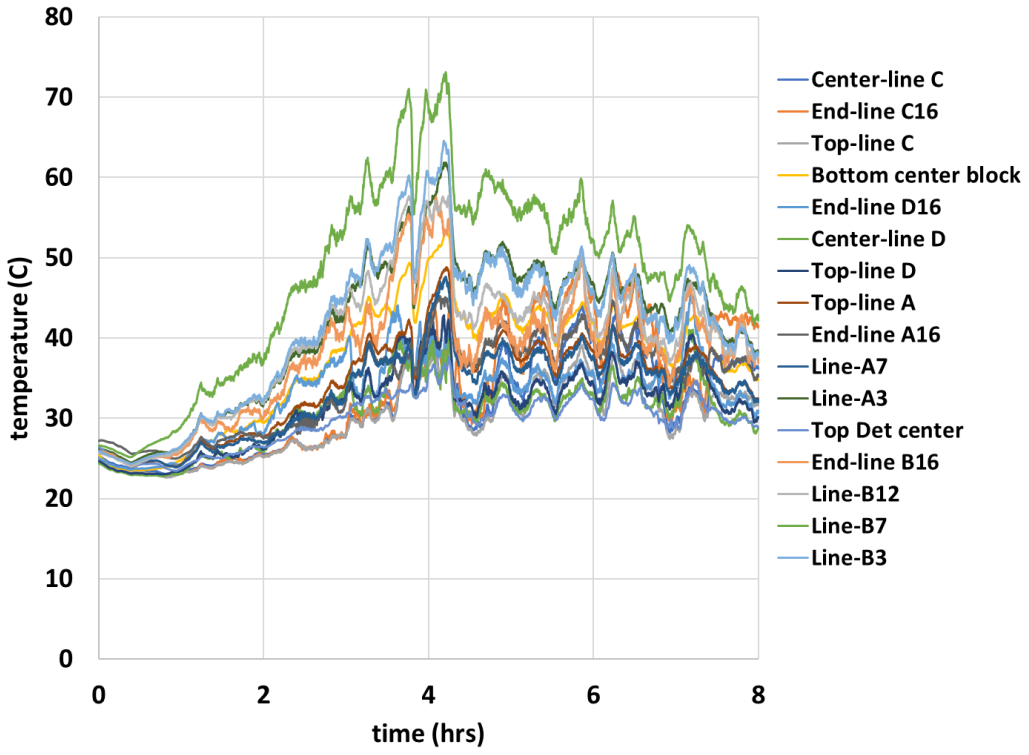

Figure A-88: Thermocouple temperature underneath charge assembly from field test.

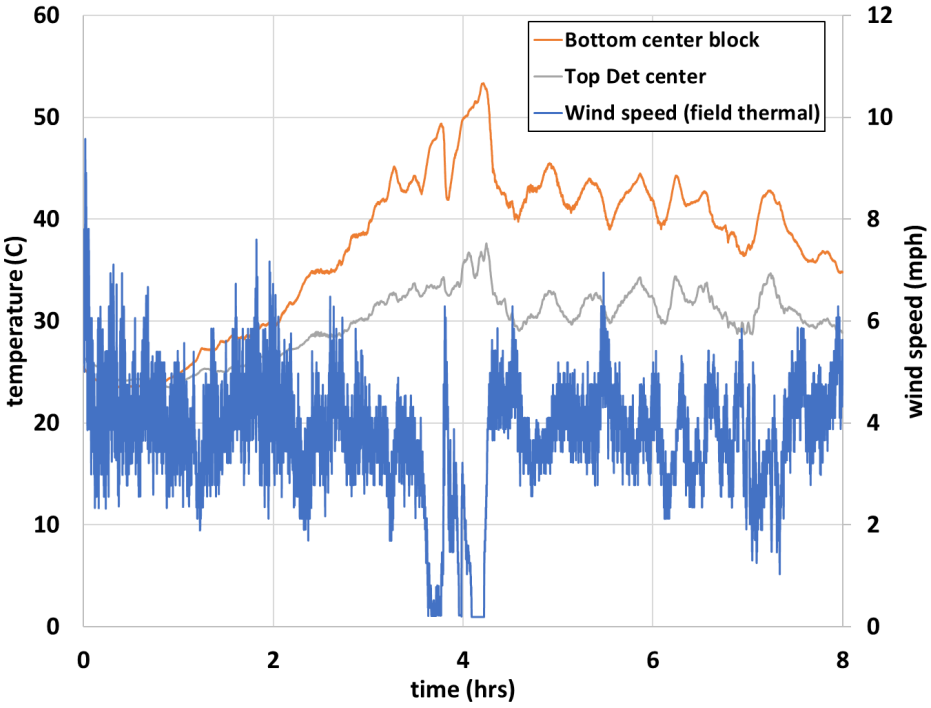

Figure A-89: Thermocouples temperatures under and on top of detonator influenced by wind speed.

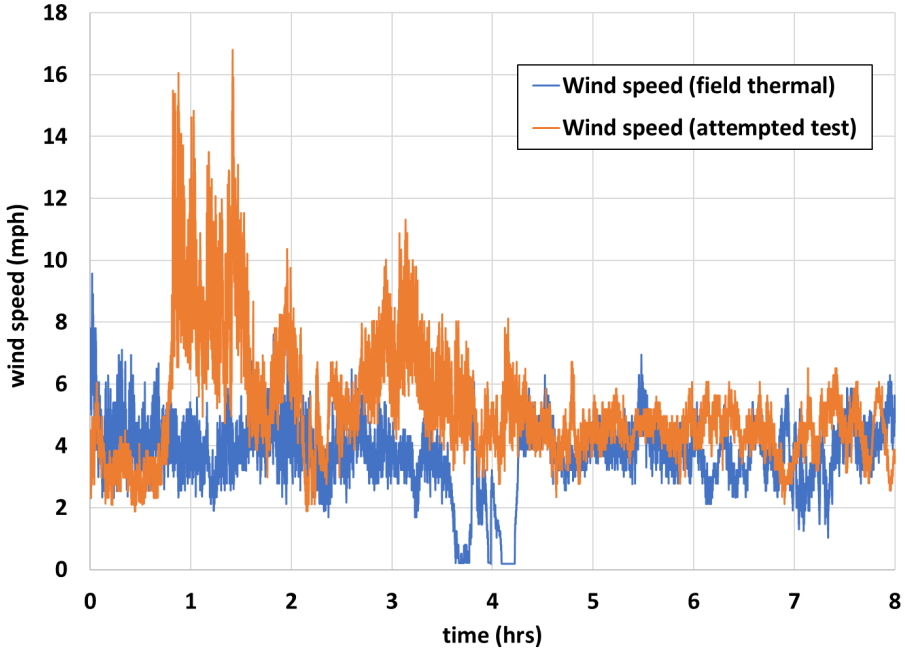

Figure A-90: Wind speeds during field thermal test and attempted test.

A.3.2.2. Tight 1 (Bakken)

Another attempt using the Tight 1 (Bakken) oil was made about one month later resulting in a successful test. The test was conducted just prior to sunrise, under clear skies and calm winds (< 1.3 m/s (3 mph)). The tank was heated overnight to reach a temperature and pressure of about 275°C and 250 psig, respectively, at test time (Figure A-91). Note that the pressure was limited by the allowable temperature of 300°C, which if exceeded could result in compositional changes to the oil.

The thermocouples in the lower and upper part of the tank measure temperatures in the liquid and vapor regions, respectively. Although the tank was pre-tested to a pressure of 280 psig, it was decided to proceed with the test at a lower pressure since the thermocouple temperatures surrounding the detonator were at 80°C. The intent was to keep the temperature well below the limit temperature of 100°C.

The high-speed cameras clearly captured the C-4 detonation, followed by apparently no activity, then the emergence of multiple pockets of fuel vapor igniting from the C-4 products. The duration of apparent no activity is the time required for mixing. The oil vapors must mix with air to provide mixtures within the flammability range before ignition can occur. Once regions of the cloud are adequately mixed they will ignite if in contact with regions of hot C-4 combustion products.

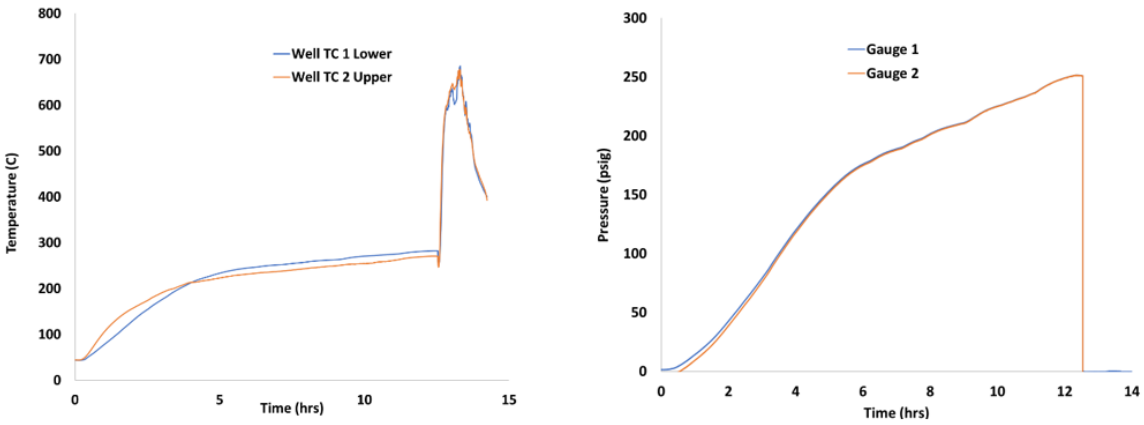

Figure A-91: Tank temperature and pressure for 1000-gallon Tight 1 (Bakken) test.

All IR, high-speed, and real-time cameras were successful in acquiring data. Images from a real-time and IR camera are shown in Figure A-92 and Figure A-93, respectively. Three IR cameras collected data to determine the surface emissive power, diameter, rise height, and duration. The vertical viewing range of the IR cameras were not sufficient to capture the entire duration of the fireball. Thus, the SEP data measurements are provided up until 4 seconds. However, since the highest spatially-averaged surface emissive power occurs in the first half of the fireball's duration, the data collecting allows for pertinent comparison among the oils. The SC8313 IR (north) camera captured up to 130 m, while the X6900 (north) captured up to 120 m, and the X6900 (east) captured up to 110 m.

Figure A-92: Tight 1 (Bakken) fireball.

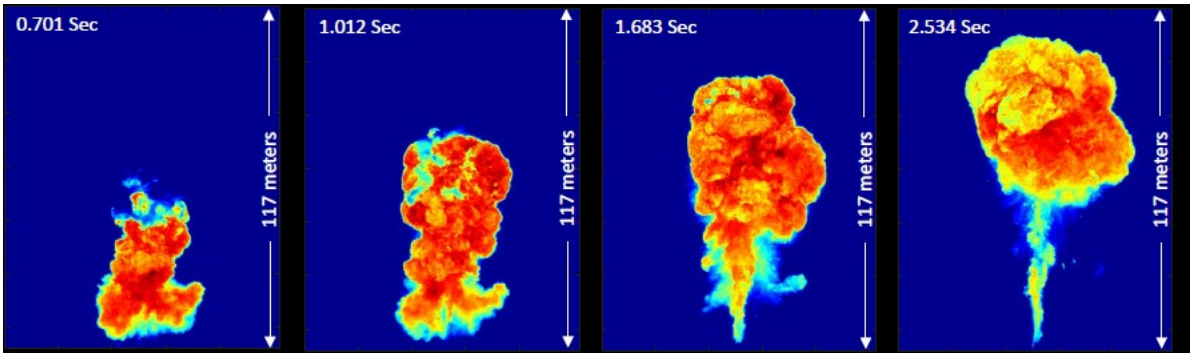

Figure A-93: Infrared images, Tight 1 (Bakken).

Figure A-94: Real-time camera providing rise height and diameter beyond 5 seconds.

When the fuel was ignited it emerged as a columnar shape up until about 1.4 s then subsequently began to form a stem. The width of the columnar shape with a stem was about 45 m. The column then transformed into a spherical shape with a stem at approximately 1.7 seconds as marked in Figure A-95 and Figure A-96 which show the spatially-averaged SEP and local maximum SEP values over time, respectively. The stem then burned out to leave only a spherical shape at approximately 2.6 seconds. At the time of spherical formation (1.7 s), the spatially-averaged SEP is 287 kW/m^2 and the maximum SEP of localized regions attained 744 kW/m^2 averaged among the X6900 IR cameras. These cameras are used for averaging since they provided more time-resolved measurements than the SC8313, intended to be a back-up camera. The results indicate that the east side of the fireball has higher values than the north. Also, note that the measurements from the SC8313 IR camera are lower than the X6900 IR camera at the same location. This is because of the lower collection of data from the SC8313 which has a sampling rate of 125 frames per second versus 1000 frames per second for the X6900.

The effective diameter as a function of time is provided in Figure A-97 and the rise height from the ground to the center of the fireball over time is provided in Figure A-98. The rise height is an area-weighted centroid and includes the burning regions of the stem. The diameter is considered an effective diameter since it is determined by using area measurements and assuming a perfect sphere. The area measurements include contributions from any burning morphology, thus cylindrical and spherical shapes are included. The sudden decline at approximately 2.7 seconds reflects as significant decline of burning regions of the stem. Thus, the IR cameras after this point are measuring data principally from the spherical shaped region and thus more reflective of the diameter of the fireball. At 9 seconds the fireball reached a height a little under 200 m to burnout and a maximum diameter of about 60 m based on real-time video coverage (Figure A-94). The radiometers also confirm that the fireball lasted approximately 9 seconds.

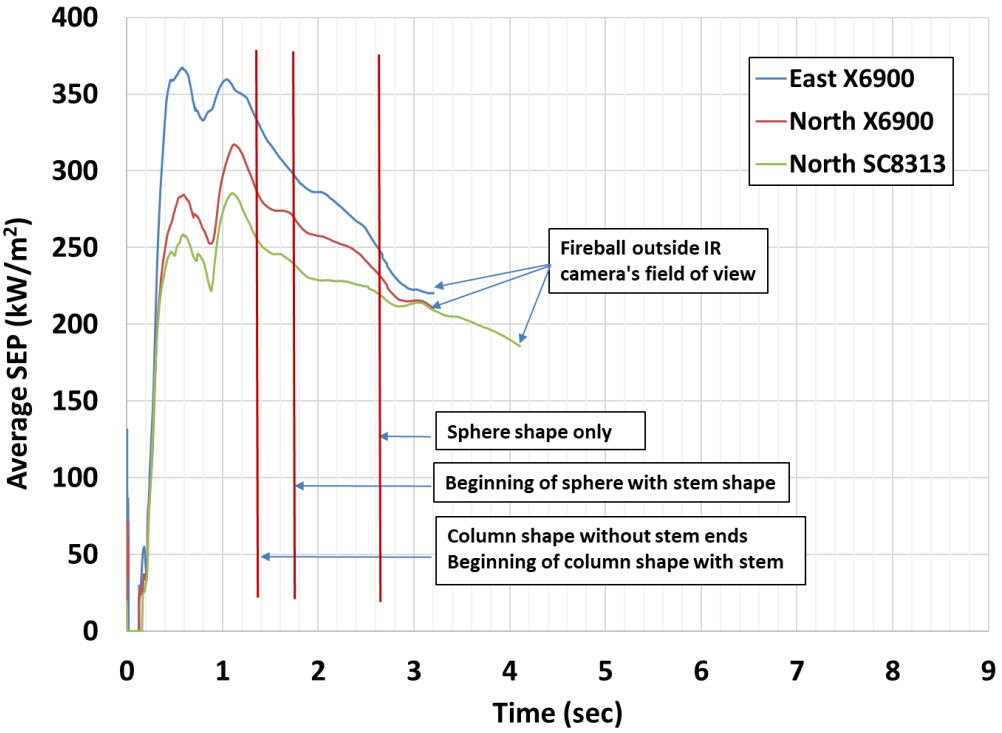

Figure A-95: Spatially-averaged SEP, Tight 1 (Bakken).

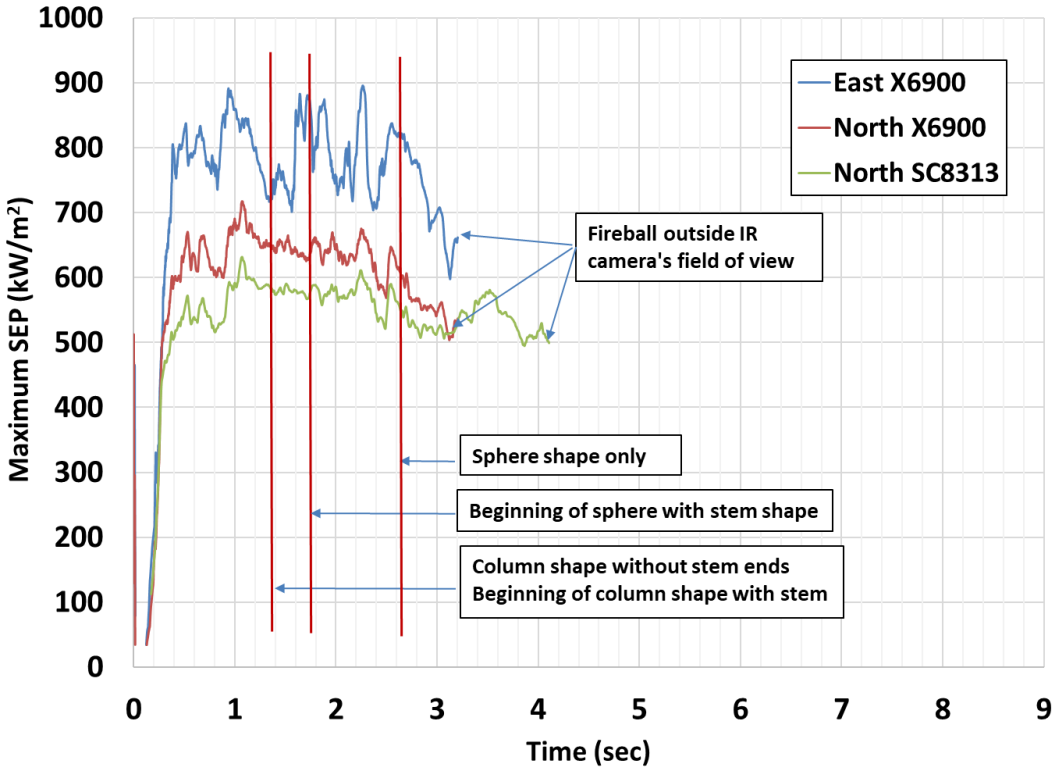

Figure A-96: Maximum SEP from local regions, Tight 1 (Bakken).

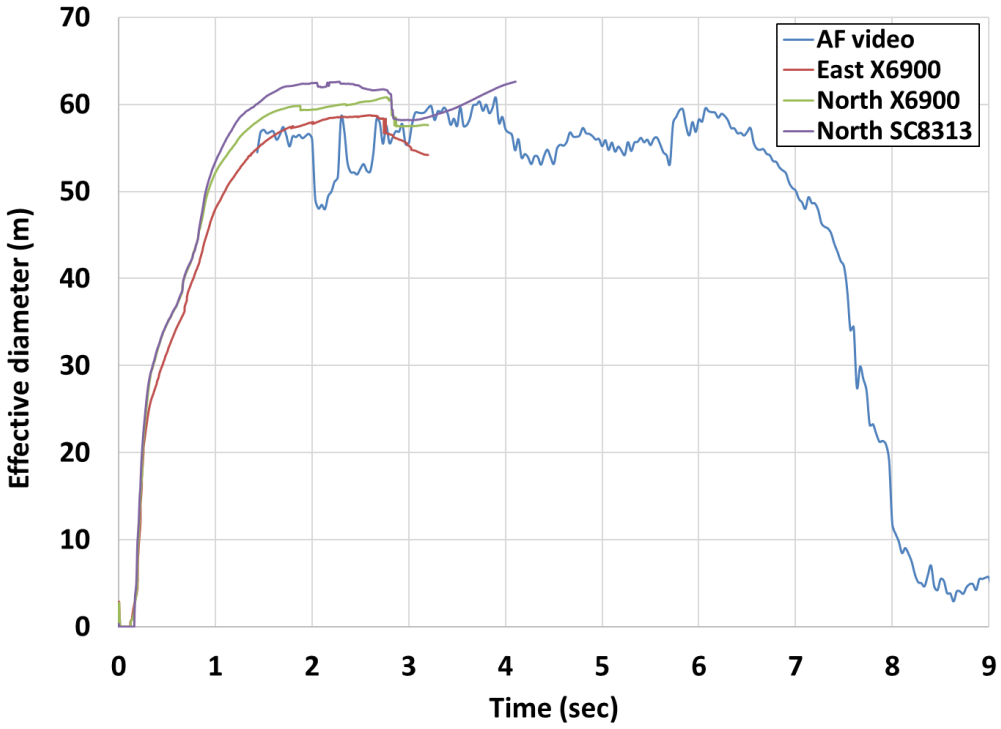

Figure A-97: Effective diameter as a function of time, Tight 1 (Bakken).

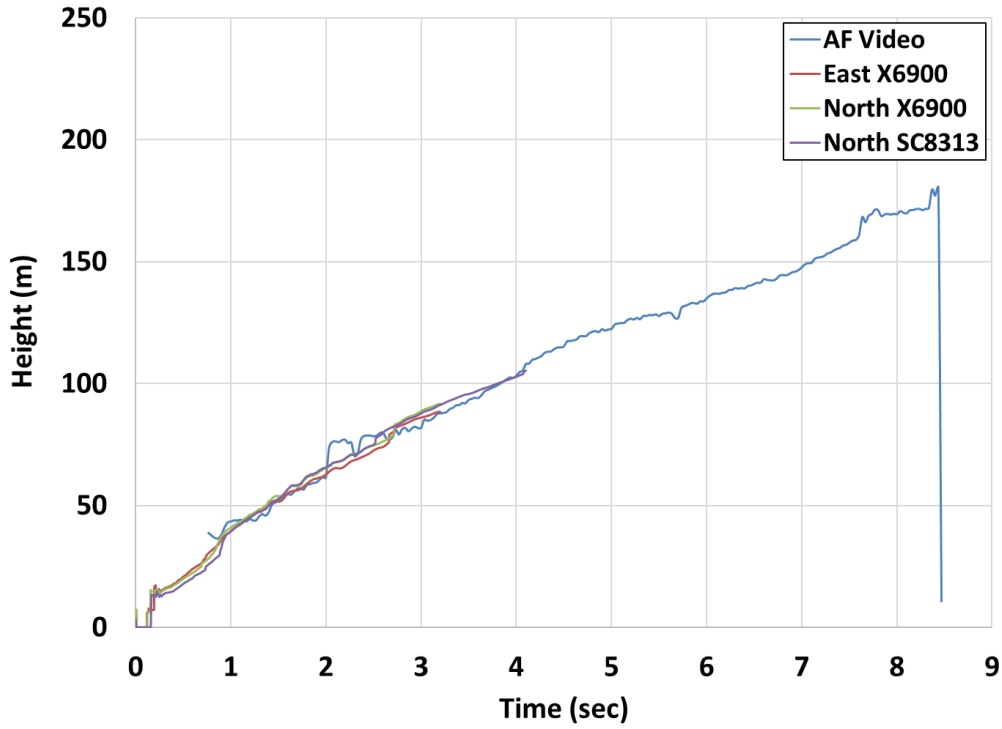

Figure A-98: Height from center of fireball to ground, Tight 1 (Bakken).

Figure A-99 provides heat flux measurements from wide-view radiometers placed at 31 m (100 ft), 46 m (150 ft), and 61 m (200 ft) from the center of the tank in the NE direction. All radiometers were aimed at a location 31 m (100 ft) above the tank. The results from the IR camera measurements should provide approximately the same values as measured by the radiometers if the IR data for diameter, height, and average surface emissive power are used as input for an integral model. This comparison was performed using an integral model which assumes that the fireball is a perfect sphere, thus the duration over which the IR data indicated that the fireball was most similar to a sphere was used for the comparison, namely 2 to 4 seconds. The transition to an approximate sphere took place slightly before 2 seconds. A nearly spherical shape with as stem can be seen in the still images at 1.683 seconds in Figure A-93. Since the radiometers collect data in 1 second increments the comparison had to begin at the 2 second mark. Note that the heat flux from the furthest radiometer peaked when only a spherical shape formed, while the other two radiometers peaked during the time in which the columnar shape is formation a stem.

The view factor equations used for the integral model pertain to a sphere radiating to a randomly oriented differential area[47]. The view factor equations account for the angle of the radiometers and the changing height of the fireball. The data for diameter, height, and SEP, based on an average among the X6900 IR cameras at 2, 3, and 4 seconds, are used in the model (Table A-26). The emissivity was assumed to be 1 and transmissivity values used at the radiometer locations are 0.90, 0.88, and 0.87 at 31 m (100 ft), 46 m (150 ft), and 61 m (200 ft), respectively. Figure A-100 provides the comparison between the radiometer measurements and model calculations using the IR measurements at the select times. The comparison indicates good agreement at 3 and 4 seconds at all locations. The calculated values are higher than measured values at 2 seconds because the shape of the fireball was further from an idealized sphere. Given the idealized assumptions of the model, exact agreement is not expected, but only approximate. If the comparison provided significantly different results this would be an indication that either measurement error or an error in data reduction occurred.

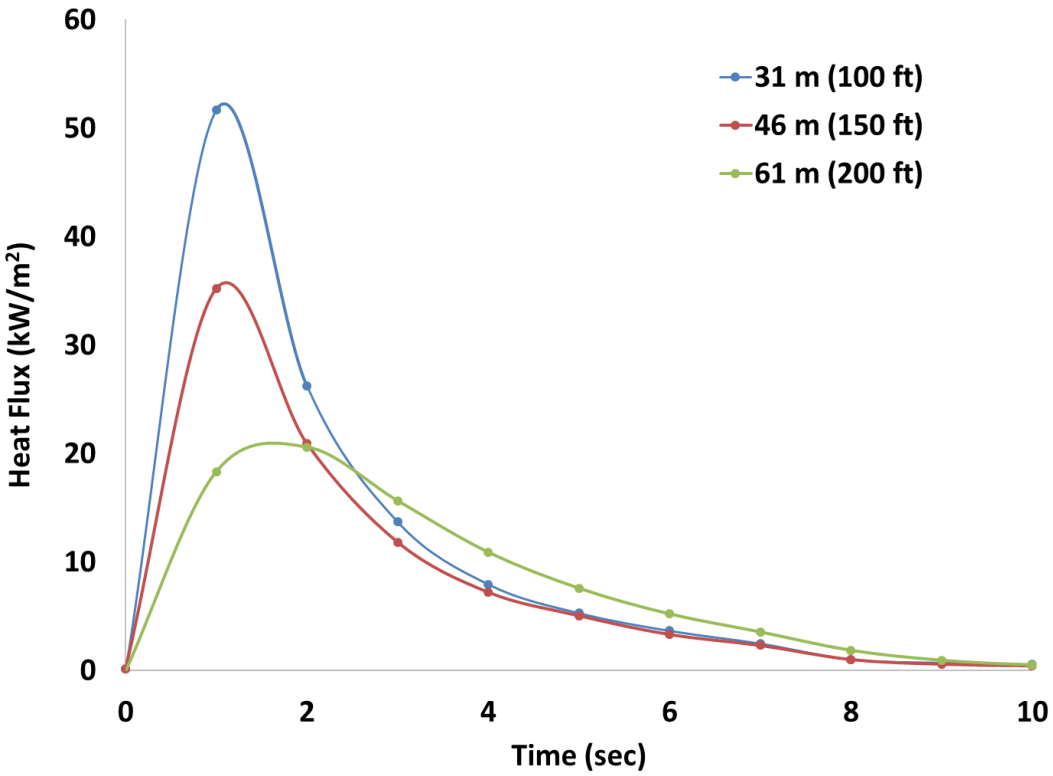

Figure A-99: Heat flux over time from wide-view radiometers, Tight 1 (Bakken).

Table A-26: Data averaged among X6900 IR cameras at select times, Tight 1 (Bakken)

Time (s)	diameter (m)	height (m)	Ave SEP (kW/m²)
2	58	63	278
3	56	86	229
4	55	99	187

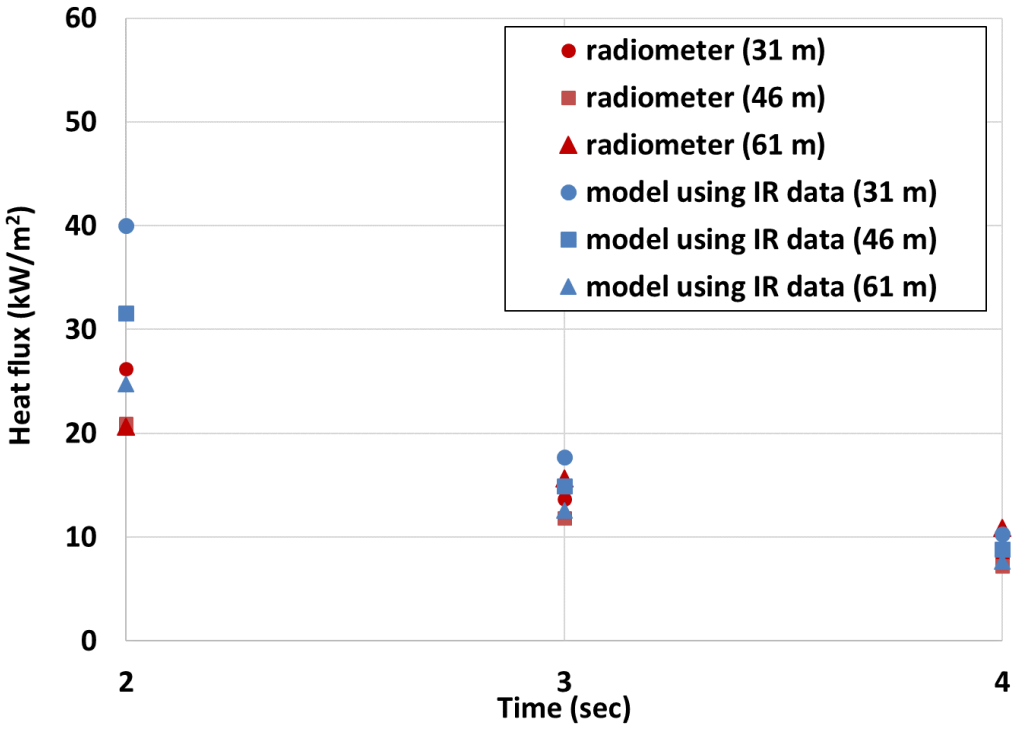

Figure A-100: Heat flux comparison from radiometers and model using IR data, Tight 1 (Bakken).

To measure pressure external to the tank, two Bikini gauges were placed 9.2 m (30 ft) from the center of the tank in the north and east directions and at a height of 1 m measured from ground to plate bottom. Figure A-101 indicates that the smallest hole size ruptured is 77 cm (2.75") (yellow arrow) which corresponds to 2.8 psi (Table A-27).

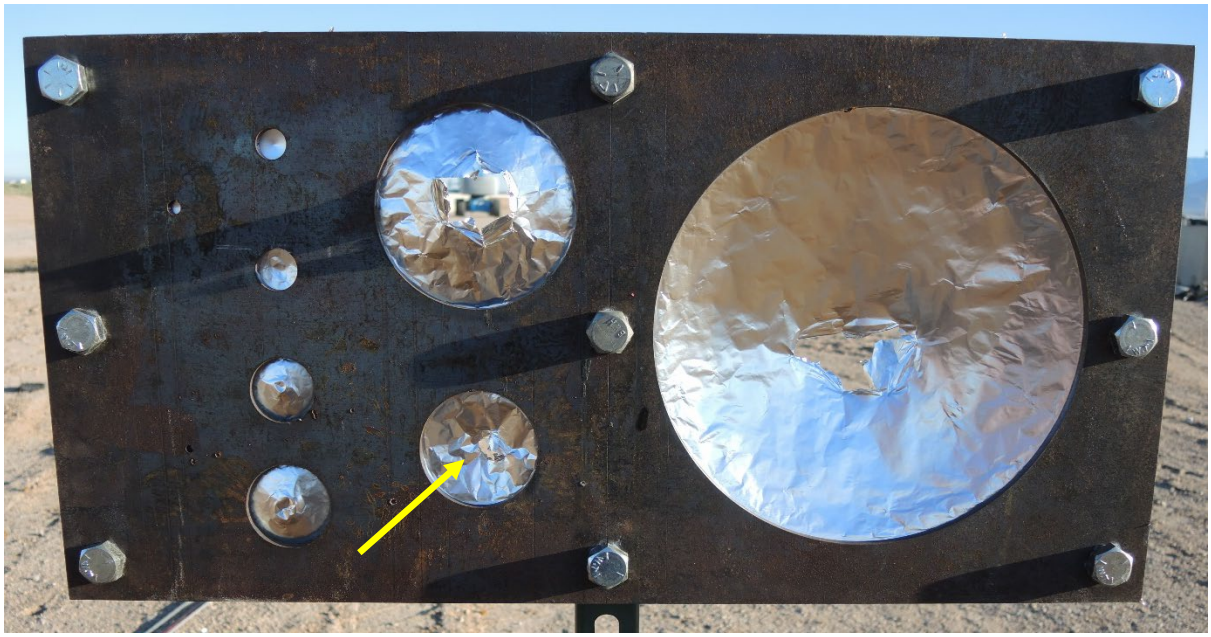

Figure A-101: Bikini gauge post-test: arrow indicating smallest hole size of 2.75" ruptured, Tight 1 (Bakken).

Table A-27: Rupture pressures for Bikini gauge placed 30 ft from tank.

Hole diameter (in)	Pressure to rupture (psi)
10	1.0
4.5	1.9
2.75	2.8
2	3.7
1.5	4.6
0.938	6.9
0.672	9.1
0.297	18.0
0.172	28.0

A.3.2.3. SPR

The test using 400-gallons of SPR was conducted just prior to sunrise under calm winds (< 1.3 m/s (3 mph)) and partial cloud cover. The tank was heated overnight to reach a temperature and pressure of about 293°C and 168 psig, respectively, at test time (Figure A-102). Note that the pressure was limited by the allowable temperature of 300°C, which if exceeded could result in compositional changes to the oil.

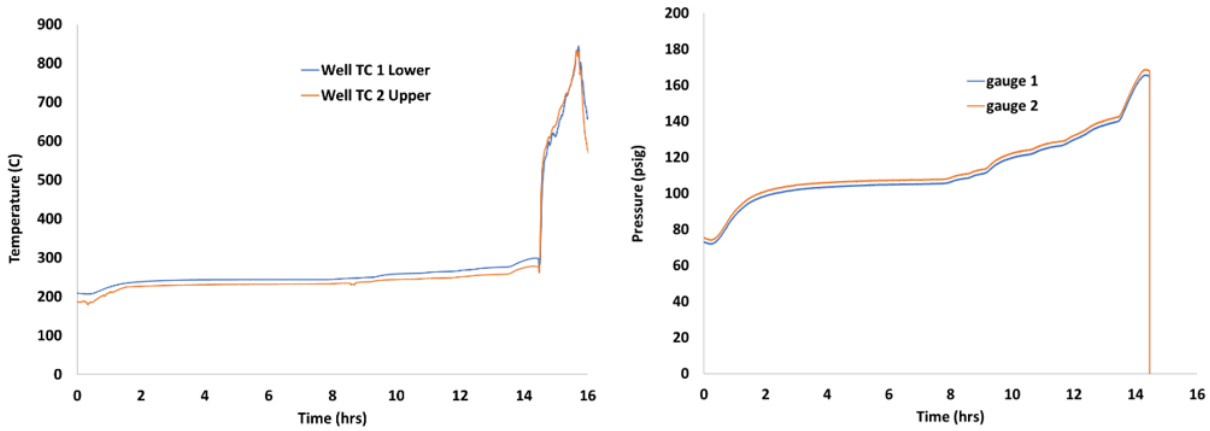

Figure A-102: Tank temperature and pressure for 1000-gallon SPR test.

One of the IR cameras failed to start filming and another failed to be adequately focused. However, the third camera, X6900 (north), was successful in obtaining the required data for SEP, diameter, rise height, and duration. The intent of having three IR cameras was to prepare for the potential failure of some cameras as demonstrated with this test. Based on the results from the Tight 1 (Bakken) test, all cameras were adjusted to capture the full evolution of the fireball. Figure A- 103 shows an image of the SPR fireball from one of the real time cameras.

When the fuel was ignited it emerged as a columnar shape up until about 1 s then subsequently began to form a stem (Figure A- 104). The width of the columnar shape with a stem was about 50 m. At the time of spherical formation (2.7 s), that is, a spherical shape with stem, the spatially-averaged SEP is 209 kW/m^2 and the maximum SEP of localized regions is 518 kW/m^2. Note that the SEP plateaus around 4 seconds but then increases slightly and subsequently decreases again as the fireball burns out. The inflection in the plot of SEP with time is due to the intermittent exposure of luminous regions emerging from the smoke layer that formed around the exterior of the fireball. Much more smoke was produced in the SPR fireballs than the Tight 1 oil. It took the SPR fireball approximately 1 second longer than the Tight 1 oil until a sphere shape formed. After the formation of a spherical shape with a stem, the sphere detached from the stem. The stem, which was larger than that for the Tight 1 (Bakken), continued to burn separately from the detached sphere up until about 5.7 seconds after initiation.

Figure A- 103: SPR fireball test

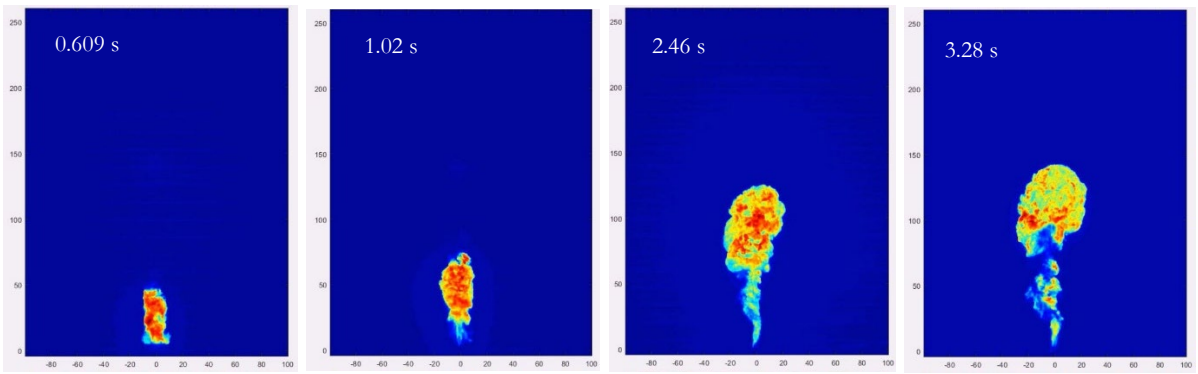

Figure A- 104: Infrared images, SPR.

The spatially-averaged surface emissive power as a function of time from the IR camera is provided in Figure A-105. The maximum SEP of local regions of the fireball from the IR camera is provided in Figure A-106. The diameter as a function of time is provided in Figure A-107 and the rise height from the ground to the center of the fireball over time is provided in Figure A-108. The IR measurements indicate that the fireball duration was approximately 9 seconds. The maximum effective diameter after at formation of a spherical shape was approximately 60 m and the maximum rise height was approximately 200 m.

Figure A-107 and Figure A-108 provide the effective diameter and height from the center of the fireball to the ground over time, respectively. The sudden decline in diameter at approximately 3.5 seconds reflects a decline of burning regions of the stem and a developing smoke layer. Thus, the area of the stem does not contribute to the area used to determine the effective diameter. The IR cameras after this point are measuring data principally from the spherical shaped region and is more reflective of the diameter of the fireball. The rise height is an area-weighted centroid and includes the burning regions of the stem. Once the fireball detaches from the stem the area of the stem is no longer included in the determination of the rise height. The sudden increase of the height at about 3 seconds is the detachment of the fireball from the stem.

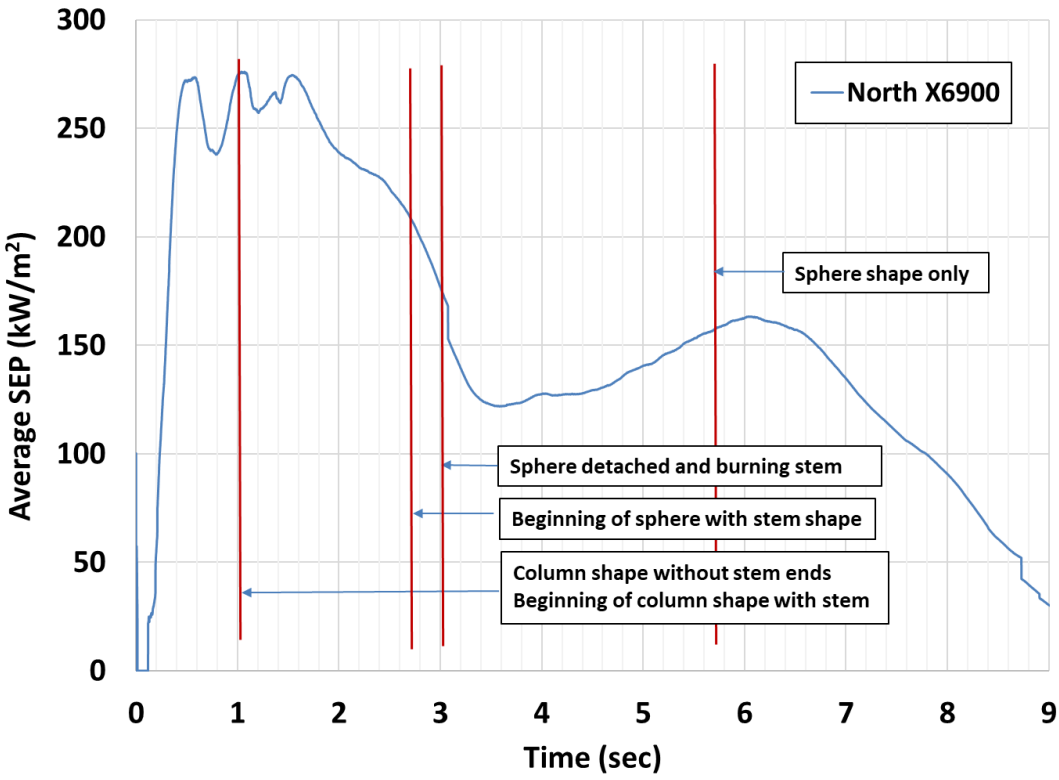

Figure A-105: Spatially-averaged SEP, SPR.

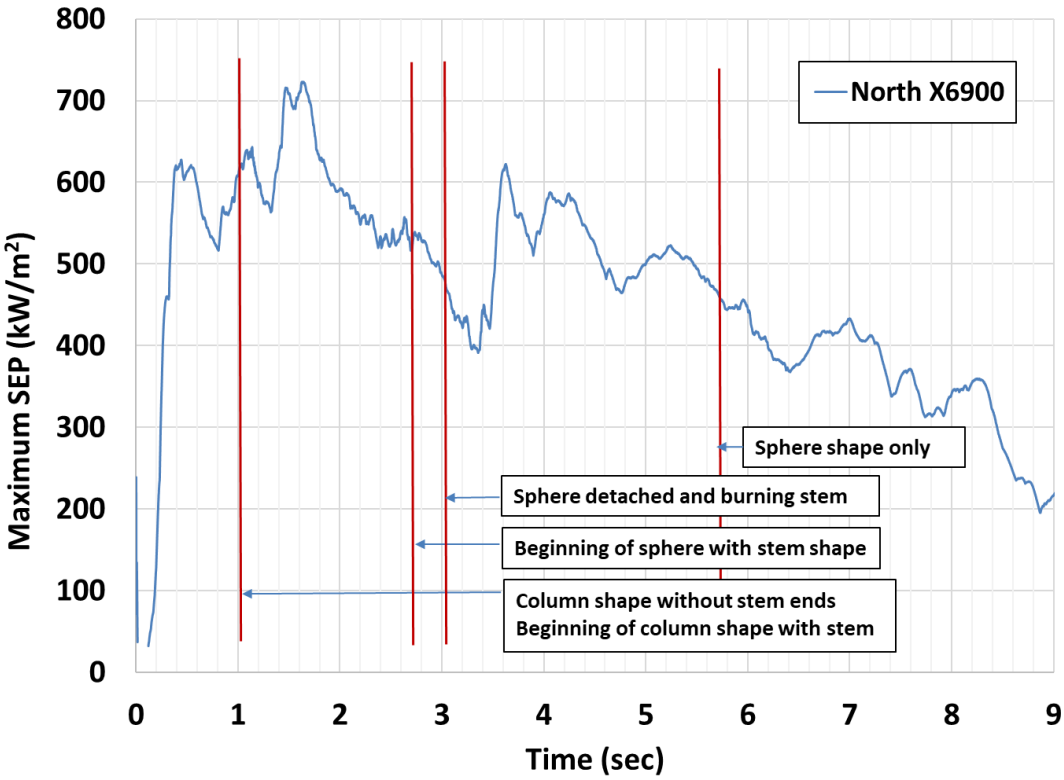

Figure A-106: Maximum SEP of local regions, SPR.

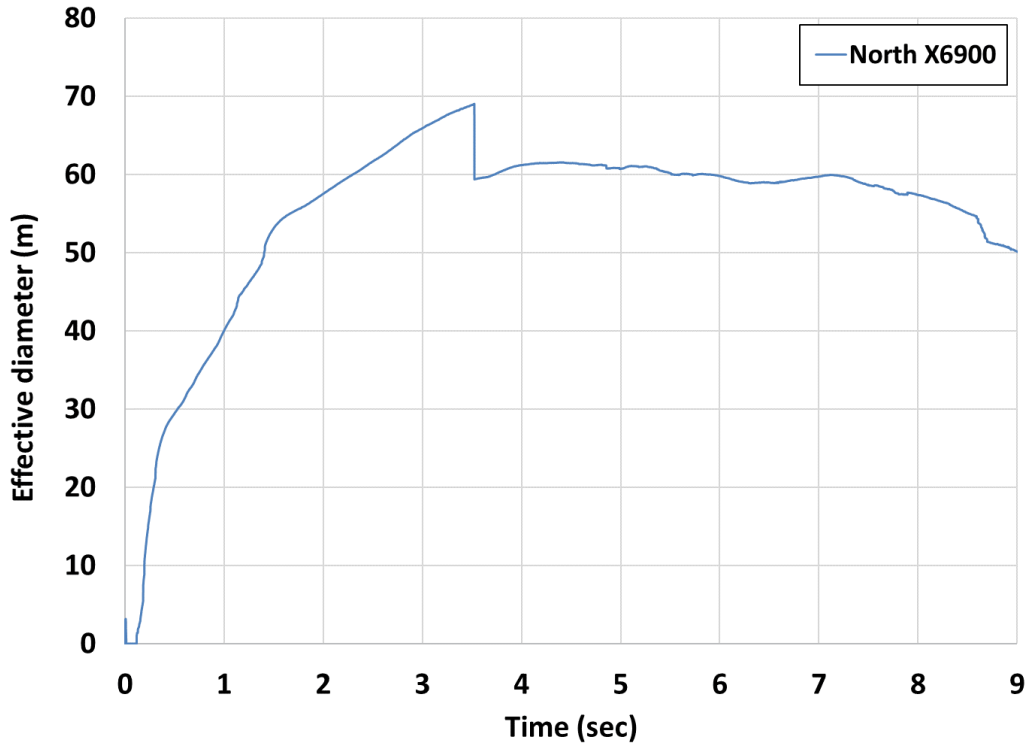

Figure A-107: Diameter as a function of time, SPR.

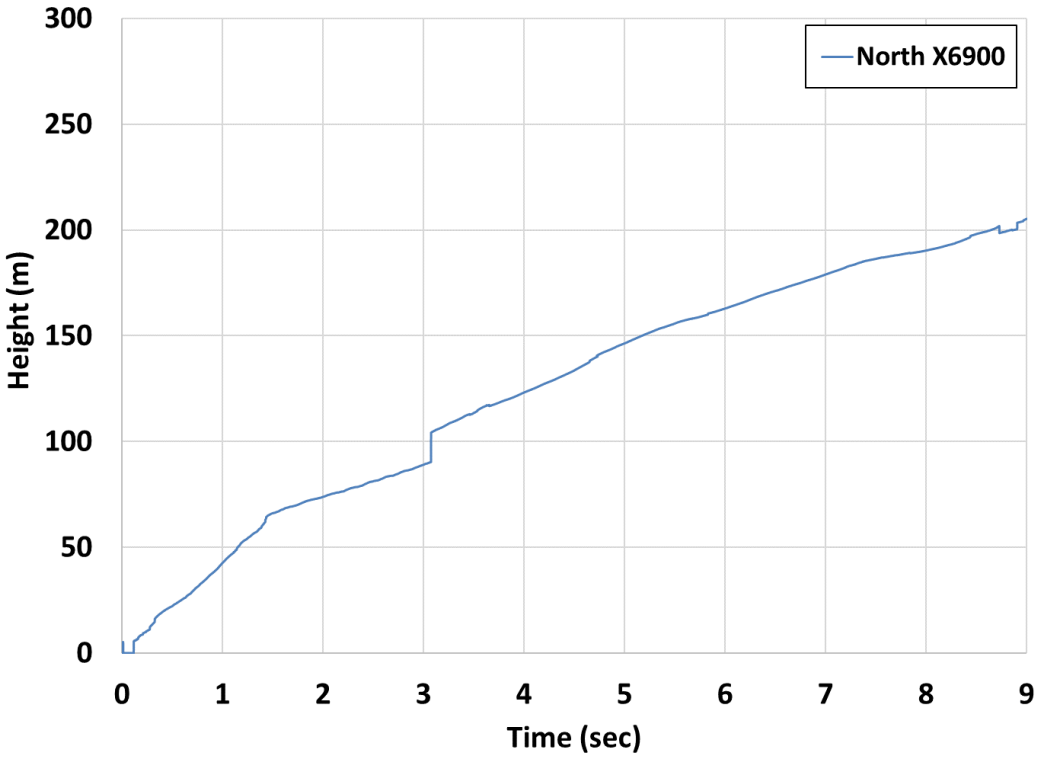

Figure A-108: Height from center of fireball to ground, SPR.

Figure A-109 provides heat flux measurements from the wide-view radiometers placed at 31 m (100 ft), 46 m (150 ft), and 61 m (200 ft) from the center of the tank in the NE direction. All radiometers were aimed at a location 31 m (100 ft) above the tank. The same method for Tight 1 (Bakken) is used to compare the results from the IR camera measurements to radiometer measurements using the IR data for diameter, height, and average surface emissive power in an integral model for the SPR oil. Figure A-100 provides the comparison between the radiometer measurements and model calculation using the IR measurements. As shown in Figure A-110 the comparison improves when only a spherical shape exists, that is beyond 5.7 seconds. This is expected since the model idealizes the fireball as a perfect sphere. The higher values from the radiometer measurements at 4 and 5 seconds reflect that heat was being received from both the burning stem and sphere. Since the model is not capturing the burning stem it will result in lower values. The relatively good agreement at 3 seconds could be due to the IR camera accounting for the area of the burning stem which will provided a larger effective diameter (66 m) to be used in the model. After 3.5 seconds the area no longer included contributions from the stem and hence the effective diameter is reduced.

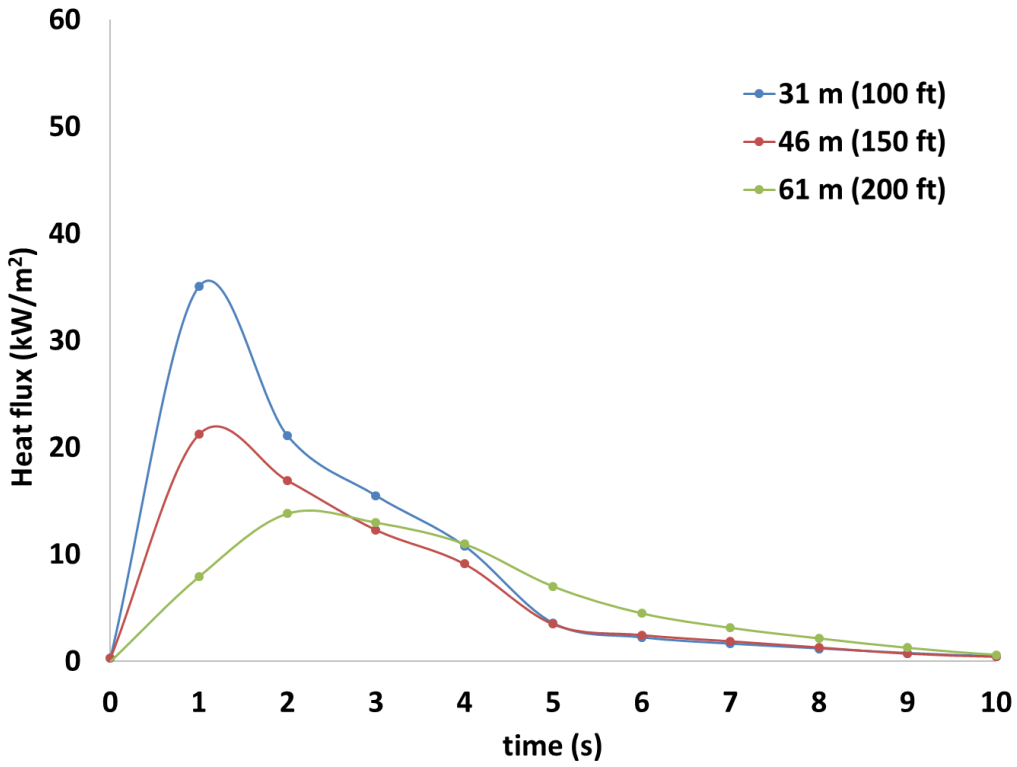

Figure A-109: Heat flux over time from wide-view radiometers (SPR).

Table A-28: Data from IR camera at select times, SPR

Time (s)	diameter (m)	height (m)	Ave SEP (kW/m²)
3	66	89	177
4	61	123	128
5	61	146	141

6	60	163	163
7	60	179	135
8	57	190	91
9	50	205	30

Figure A-110: Heat flux comparison from radiometers and model using IR data, SPR.

Similar to the Tight 1 (Bakken) test, two Bikini gauges were placed 9.2 m (30 ft) from the center of the tank in the north and east directions and at a height of 1 m measured from ground to plate bottom. The pressure at that distance was similar to the Tight 1 (Bakken) test as shown in Figure A-111 which indicates that the smallest hole size ruptured is 77 cm (2.75") (yellow arrow) which corresponds to 2.8 psi (Table A-27).

Figure A-111: Bikini gauge post-test: arrow indicating smallest hole size of 2.75" ruptured, Tight 2 (Tx Shale).

A.3.2.4. Tight 2 (Tx Shale)

For this test, 400-gallons of Tight 2 (Tx Shale) oil was used to create a fireball. The test was conducted just prior to sunrise under low wind speeds (2 m/s (4.5 mph)) and clear skies. The tank was heated overnight to reach a temperature and pressure of about 300°C and 250 psig, respectively, at test time (Figure A-112). Note that the pressure was limited by the allowable temperature of 300°C, which if exceeded could result in compositional changes to the oil.

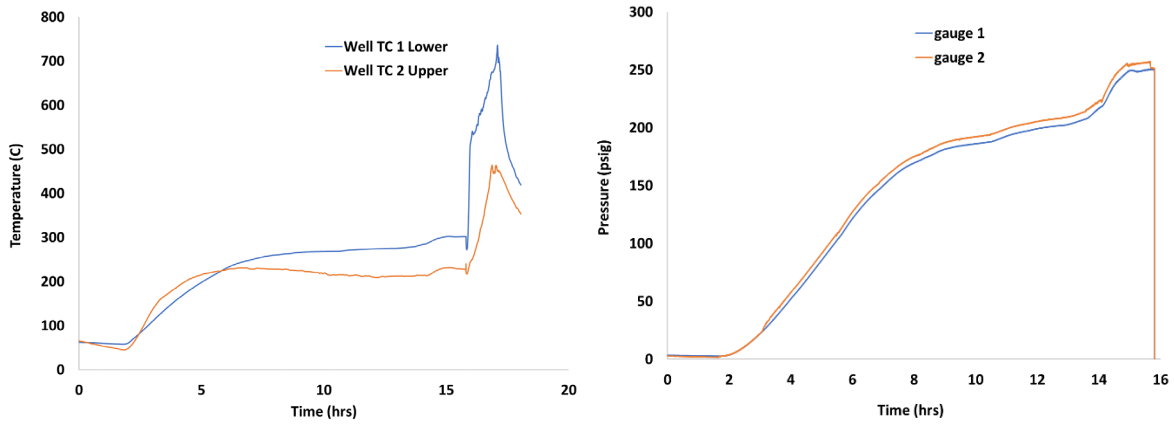

Figure A-112: Tank temperature and pressure for 1000-gallon Tight 2 test.

All IR cameras acquired measurements with the X6900 IR cameras capturing the full field of view over the duration of the test. The SC8313 IR camera was kept at the same field of view as for the Tight 1 (Bakken) test to allow similar comparison between the tests. Thus, the camera acquired full field view data up until about 3.3 seconds. Figure A-113 shows an image of the Tight 2 (Tx Shale) fireball from one of the real time cameras.

Similar to the other oils, when the fuel ignited it emerged as a columnar shape up until about 1.2 s then subsequently began to form a stem (Figure A-114). The width of the columnar shape was about 40 m. The column then transformed into a spherical shape with a stem at approximately 1.8 seconds as marked in Figure A-115 and Figure A-116 which show the spatially-averaged SEP and local maximum SEP values over time, respectively. The stem then burned out to leave only a spherical shape at approximately 2.6 seconds. At the time of spherical formation (1.8 s), the spatially-averaged SEP is 232 kW/m^2 and the maximum SEP of localized regions attained 604 kW/m^2 averaged among the X6900 IR cameras. The results indicate that the north side of the fireball has higher values than the east. Also, note that the measurements from the SC8313 IR camera are lower than the X6900 IR camera at the same location. This is because of the lower collection of data from the SC8313 which has a sampling rate of 30 frames per second versus 1000 frames per second for the X6900.

Figure A-113: Tight 2 (Tx Shale) fireball test.

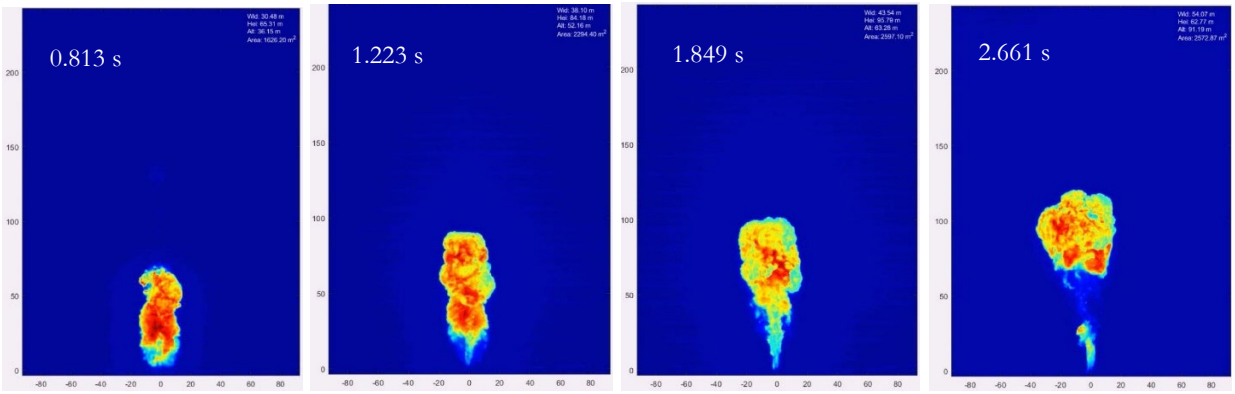

Figure A-114: Infrared images, Tight 2 (Tx Shale).

The effective diameter as a function of time is provided in Figure A-117 and the rise height from the ground to the center of the fireball over time is provided in Figure A-118. The rise height is an area-weighted centroid and includes the burning regions of the stem. The diameter is considered an effective diameter since it is determined by using area measurements and assuming a perfect sphere. The area measurements include contributions from any burning morphology, thus cylindrical and spherical shapes are included. The sudden decline at approximately 2.5 seconds reflects as significant decline of burning regions of the stem. Thus, the IR cameras after this point are measuring data principally from the spherical shaped region and thus more reflective of the diameter of the fireball. The sudden increase of the height at about 2.7 seconds is the detachment of the fireball from the stem. The IR measurements indicate that the fireball duration was approximately 9 seconds and the average effective diameter and rise height were approximately 60 m and 200 m, respectively.

The Tight 2 (Tx Shale) oil displayed similar smoke coverage to the Tight 1 (Bakken) oil and took approximately the same time for a sphere shape to develop. After the sphere detached from the stem it continued to burn until about 4 seconds. The size of the burning stem was similar to the stem that developed in the Tight 1 (Bakken) test.

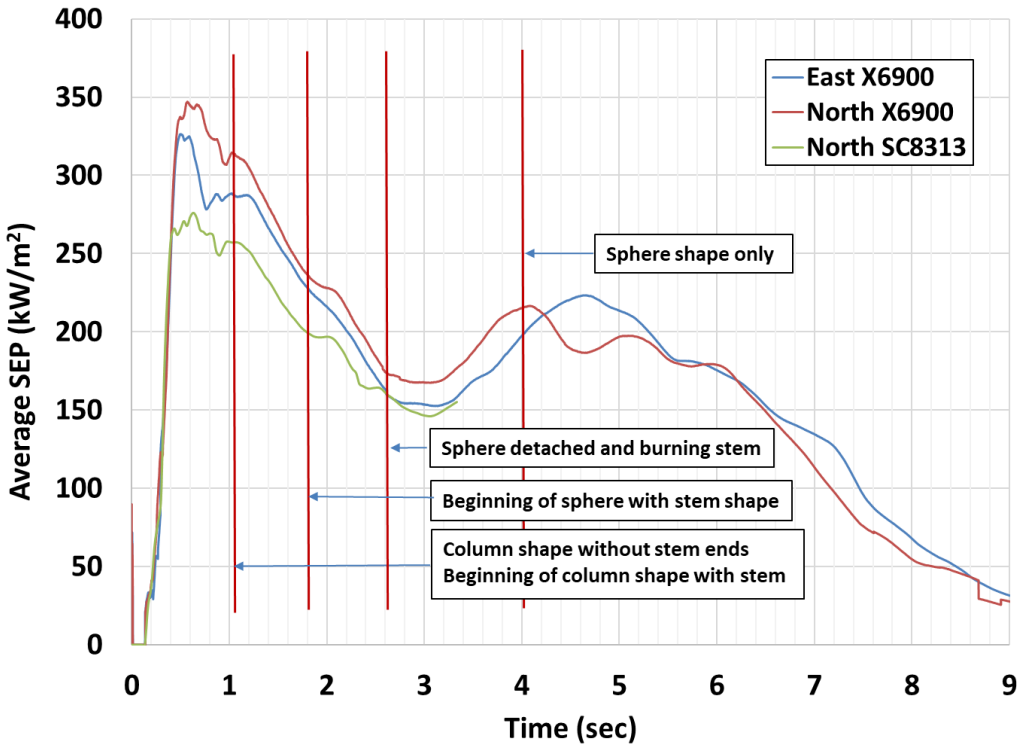

Figure A-115: Spatially-averaged SEP, Tight 2 (Tx Shale).

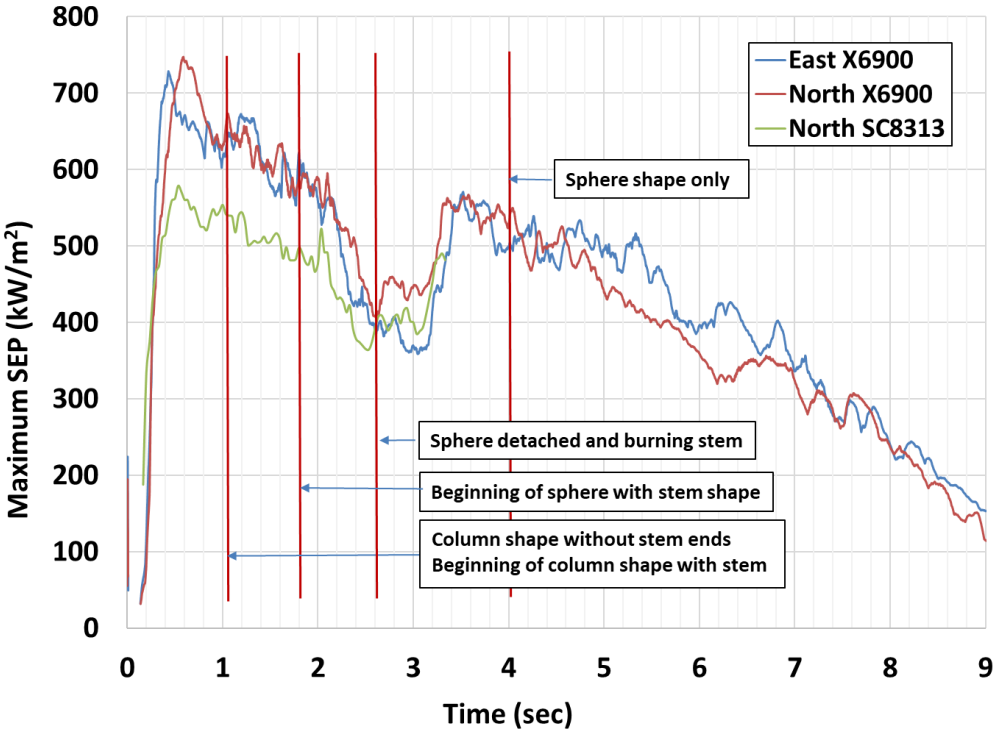

Figure A-116: Maximum SEP of local regions, Tight 2 (Tx Shale).

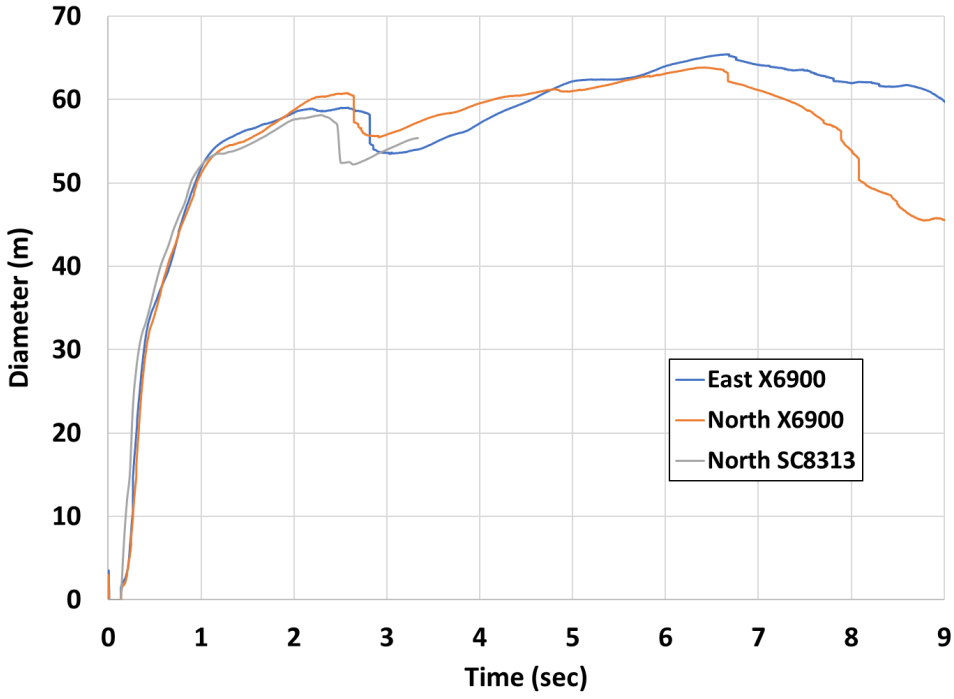

Figure A-117: Effective diameter as a function of time, Tight 2 (Tx Shale).

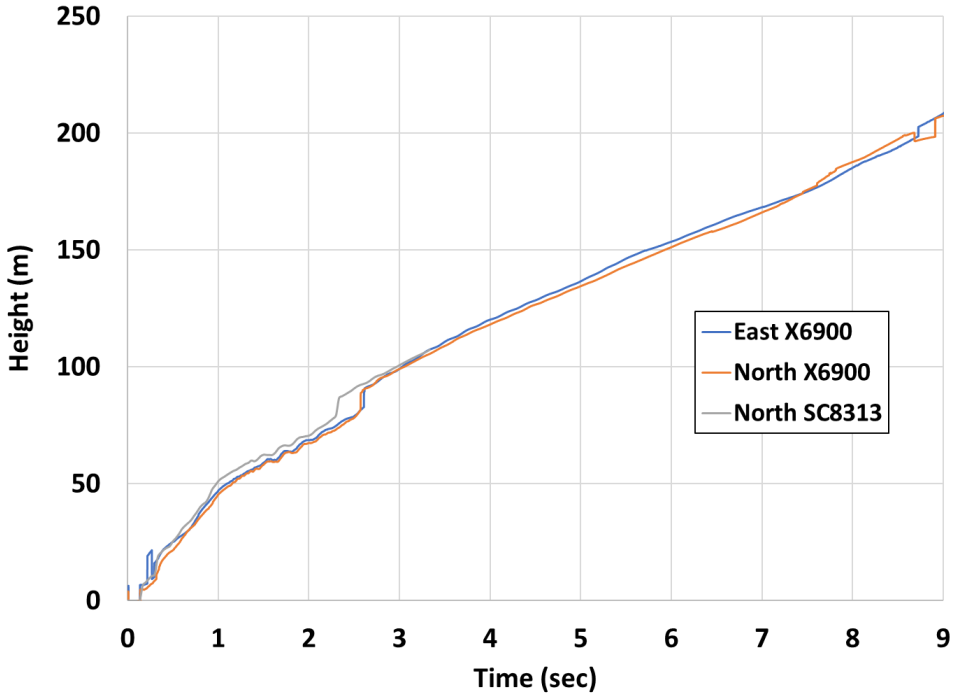

Figure A-118: Height from center of fireball to ground, Tight 2 (Tx Shale).

Figure A-119 provides heat flux measurements from the wide-view radiometers placed at 31 m (100 ft), 46 m (150 ft), and 61 m (200 ft) from the center of the tank in the NE direction. All radiometers were aimed at a location 31 m (100 ft) above the tank. The same method as used for the other oils is used to compare the results from the IR camera measurements to radiometer measurements using the IR data for diameter, height, and average surface emissive power in an integral model for the SPR oil. Figure A- 120 provides the comparison between the radiometer measurements and model calculation using the IR measurements. As shown in Figure A- 120, the comparison improves when only a spherical shape exists, that is beyond 3 seconds.

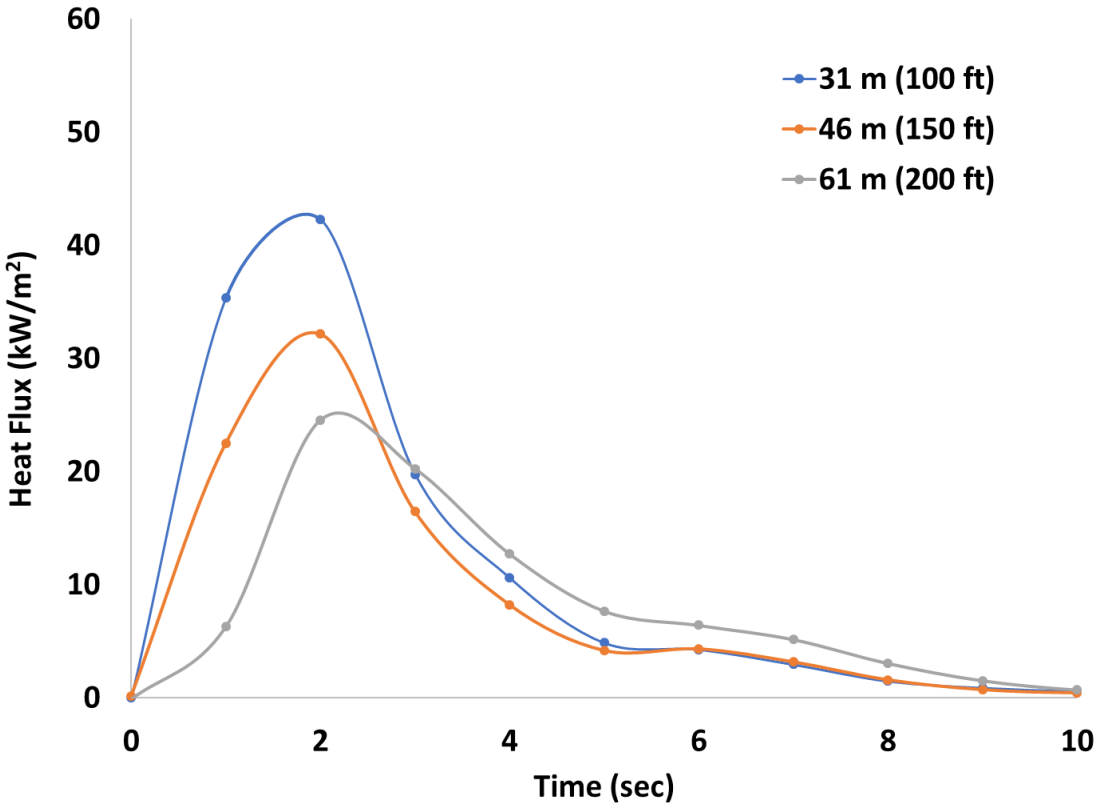

Figure A-119: Heat flux over time from wide-view radiometers, Tight 2 (Tx Shale).

Table A-29: Data averaged among X6900 IR cameras at select times, Tight 2 (Tx Shale)

Time (s)	diameter (m)	height (m)	Ave SEP (kW/m²)
2	59	68	222
3	55	99	161
4	58	119	206
5	62	136	205
6	64	152	177
7	63	167	124
8	58	186	61
9	53	208	30

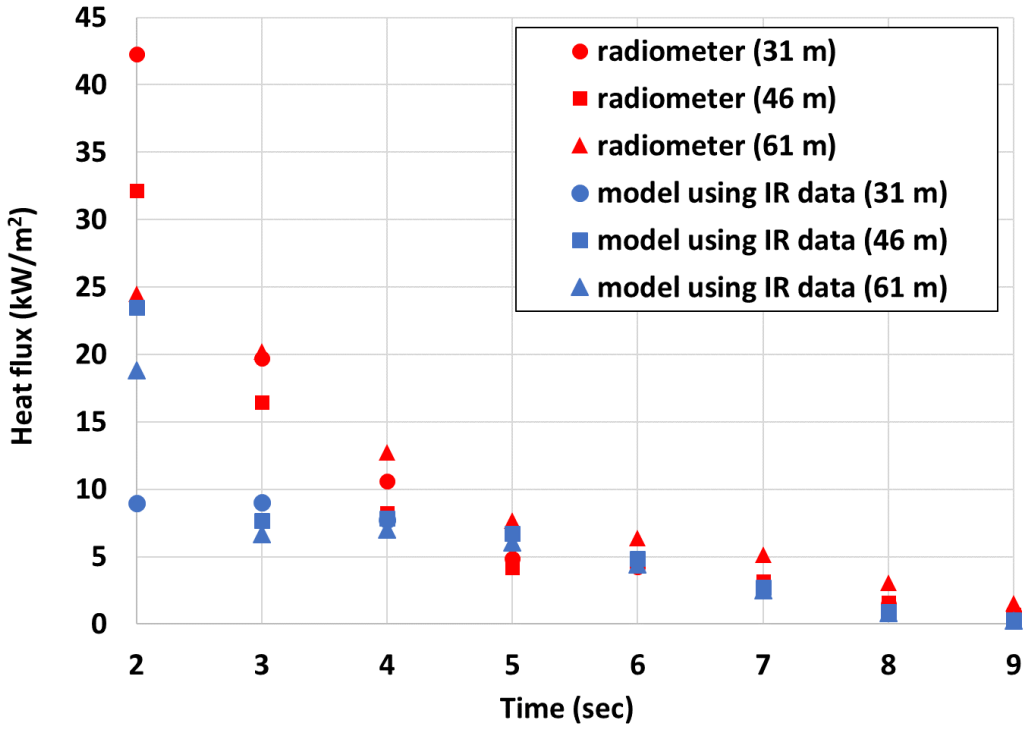

Figure A- 120: Heat flux comparison from radiometers and model using IR data, Tight 2 (Tx Shale).

The two Bikini gauges were placed 9.2 m (30 ft) from the center of the tank in the north and east directions and at a height of 1 m measured from ground to plate bottom indicates similar pressures to the other two oils. As shown in Figure A-121, the smallest hole size ruptured is 7 cm (2.75") (yellow arrow) which corresponds to a pressure of 2.8 psi (Table A-27).

Figure A-121: Bikini gauge post-test: arrow indicating smallest hole size of 2.75” ruptured, Tight 2 (Tx Shale).

APPENDIX B. TEST FACILITIES

B.1. FLAME facility

The 2-m pool fire tests were conducted in the Fire Laboratory for Accreditation of Models and Experiments (FLAME) test cell in the Thermal Test Complex at Sandia, Figure B-1. This facility is designed to provide well-controlled boundary conditions for code validation and test repeatability. This is in contrast to outdoor conditions where the presence of wind, variable over time and in direction, can prevent repeatability.

The main test chamber of FLAME is cylindrical in shape, 60 ft. (18.3 m) inner diameter with a height around the perimeter of 40 ft. (12.2 m). The ceiling slopes upwards (~18º) from the perimeter walls to a height of 48 ft. (14.6 m) over the center of the facility. A round hole at the top of the facility 16 ft. (4.9 m) diameter transitions to a 10 ft. by 12 ft. (3.0 m by 3.7 m) chimney duct. A large electrostatic precipitator downstream of FLAME collects soot prior to combustion products being sent to the exhaust stack. The outer walls are made of steel channel sections welded together and are filled with water for cooling during tests.

The ground level of FLAME can be divided into three concentric sections. At the center of the facility is a fuel pan or gas burner. The facility can operate a gas burner (He, H_2, CH_4, etc.) or a liquid fuel pool (JP-8, methanol, etc.) from 1 m to 3 m in diameter. There is a steel spill plate surrounding the fuel pan, which extends to a diameter of 12.7 m. The floor of the outer section is made of a steel grating, through which air is supplied to the test chamber during fire experiments. The floor is flush with the top of the pan edge.

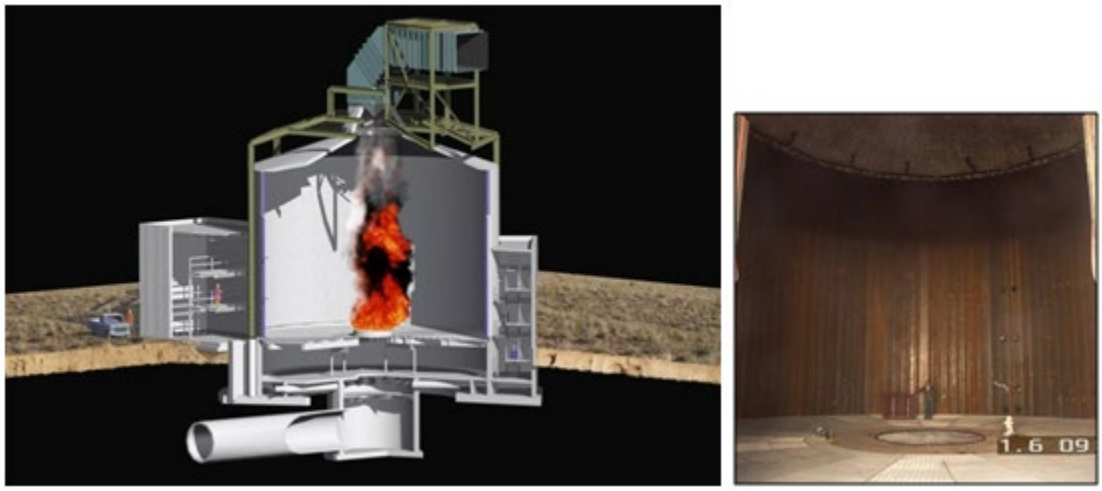

Figure B-1: A cutaway view and interior of the FLAME facility. The view shows a liquid pool fire at the ground level, pipes supplying air flow through the basement, exhaust ductwork, and instrumentation rooms outside the FRH chamber.

Combustion air is supplied from the forced draft (FD) fan in a central utility building (not shown) through a large underground pipe (12 ft. diameter) to a plenum that feeds 18 radial pipes (3 ft. diameter) to a 4 ft. by 4 ft. annular ring in the FLAME basement. Air exits the grated top of the annular ring and enters the ground level steel grating. An induced draft (ID) fan just before the exhaust stack automatically adjusts speed to maintain the differential pressure (to ambient) within the facility to near zero. Flowrate through the test cell is measured with instrumentation (calibrated pitot tubes) located

inside the forced draft fan (providing air input into the test chamber), and additional instrumentation located at the exhaust stack.

B.2. Lurance Canyon Burn Site Facility

The 5 m pool fire tests and the small fireball tests were performed near the East boundary of the Lurance Canyon Burn Site (LCBS) facility (Figure B-2). The test site is property withdrawn from the Forest Service and is controlled and monitored by both Sandia and Kirtland air force base (KAFB). Any potential hazards do not extend onto public lands.

Significant locations at the LCBS below are:

- A: Test operations trailer
- B: 5050-gallon crude oil trailer
- C: 1000-gal water tank
- D: DAQ Bunker
- E: small fireball test tank
- F: 5-m diameter pool fire test pan

Figure B-2: The Lurance Canyon Burn Site.

B.3. 1000-gallon Tank Fireball Test Site, Pad B

This site is in Tech area III and is typically used for explosive testing. In contrast to the Lurance Canyon Burn site, it is not surrounded by hills and is on a flat, thus allowing for easier fire-fighting efforts in the event of a grass fire. A fire breaking out at the Burn site has a much higher potential for a forest fire, whereas Pad B would most likely result in only a grass fire. There are also surrounding roads that serve as firebreaks. Figure B-3 shows the overlay of identified hazard exclusion zones at

Pad B test site. The largest hazard exclusion zone is from noise exposure due to the shock waves generated from the fuel release and from the explosives.

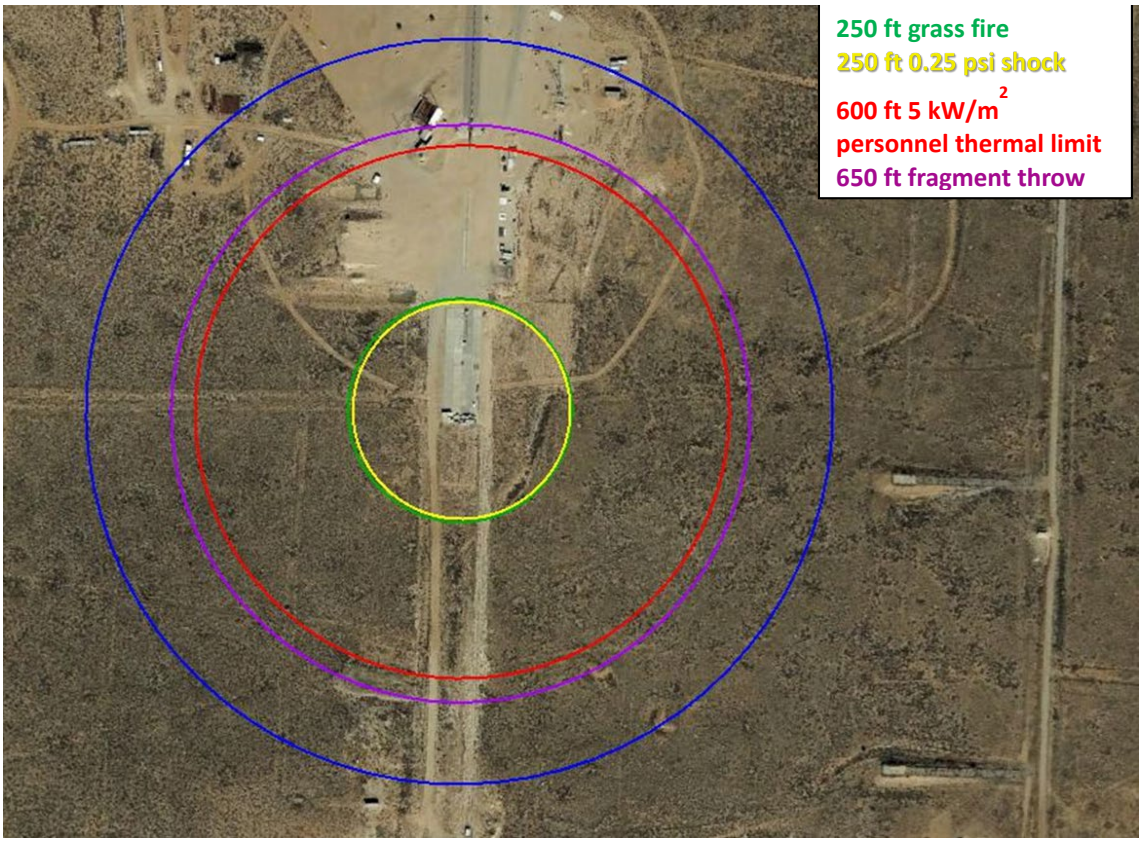

Figure B-3: Pad B test site.

APPENDIX C. TEST INFRASTRUCTURE

C.1. Tanker/Trailer for Oil Transport

Two different tanker designs were employed in this work. Custom, pressurized tanks were used to handle the tight oils obtained from North Dakota and Texas, and unpressurized tanks were used to handle the stabilized Strategic Petroleum Reserve (SPR) oil.

C.1.1. Pressurized Tanker Design

Due to the unique requirements of maintaining the composition of the oil from acquisition site to test site, a pair of special 4,800-gallon transport tankers was designed and built for this test series. A photo of one tanker is shown in Figure C-1. The tankers utilize a water-displacement principle based on industry standard GPA 2174, "Method for obtaining liquid hydrocarbons for analysis by gas chromatography" [72], upscaled from liter-scale to tanker scale. The tanker is designed to be first completely filled with water and then loaded with oil to the desired level while displacing water, so that the oil is not exposed to air in the loading process.

NOZZLE SCHEDULE	
NOZZLE	DESCRIPTION
M-1	MANWAY
V-1	3" WATER INLET/OUTLET
V-2	2" OIL INLET/OUTLET
V-3	2" OIL RECIRCULATION/MIXING INLET (USE WHEN TANK IS NOT FULL)
V-4	1" VAPOR VENT
V-5	2" OIL RECIRCULATION/MIXING INLET (USE WHEN TANK IS FULL OF OIL)
V-6	3" DRAIN
V-7	PRESSURE RELIEF VALVE
B-1	NOZZLE FOR BLADDER

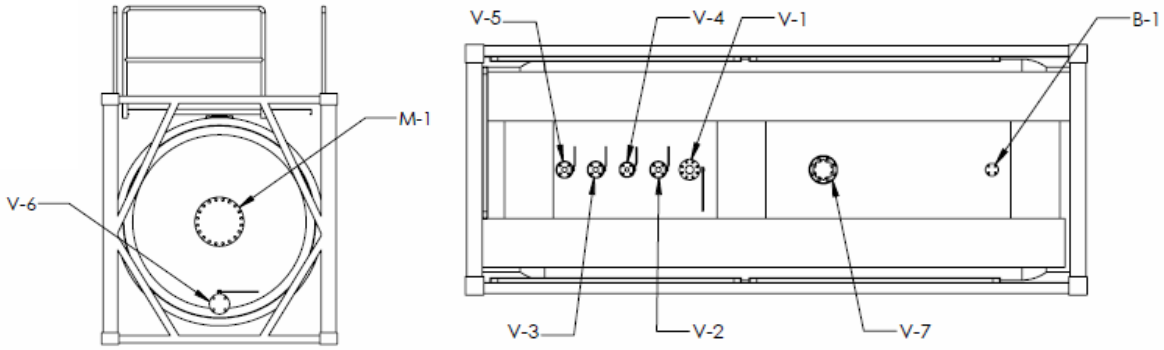

Figure C-1. Photo of Sandia custom Tanker #1 along with nozzle schedule, back external view, and top external view schematics.

Tank design requirements included:

- Maximum allowable working pressure (MAWP) of at least 250 pounds per square inch gauge pressure (psig).
- Meets DOT Specification 51 for steel portable tanks
- Capable of maintaining vacuum down to 20 inches mercury (-9.8 pounds per square inch gauge pressure, psig).
- Tanker built to ASME Section VIII, division 1 Boiler and pressure vessel code
- The pressure relief valves, hand valves and instrumentation constructed to eliminate leakage under vacuum conditions.
- Pressure relief valve supplied by Contractor. Pressure relief valves capacity shall be determined by the larger capacity required by ASME or DOT
- Float level indicator for oil-water level (oil SG = 0.658, water SG = 1.0) inside tank.
- Tank is mounted on a trailer (tank chassis) approved for road transport, meeting all applicable US DOT regulations.

C.1.2. Pressurized Tanker Operations

C.1.2.1. Loading Operations

The pressurized tanker was transported to the operator facilities empty. Once at the operator's facility the tanker was positioned and levelled to the best extent possible. The tanker was then filled from a water tank/pump truck, with locally acquired fresh water, to remove all air from tanker and sample line to process connection. Once tanker and sample line are purged of air, the water tank truck is connected to the pressurized tanker water outlet back pressure regulator which holds backpressure on the water stream being displaced from the tanker by the crude oil sample. The backpressure regulator is set to hold the pressurized tanker pressure a minimum of 20 psi greater than the sampled crude oil BPP, at sampling temperature. Once the 2000-3000 gallons of crude oil is loaded on the pressurized tanker, the water outlet is isolated, and the tanker pressurized from the sample source to the lesser of sample line pressure or 75 psig. Once tanker is pressurized the backpressure regulator is removed, and the tanker water outlet line is connected to a vacuum truck. Water is then removed from the pressurized tanker until the total pressurized tanker weight (with tractor/trailer) is below regulatory limits. For both Bakken and Texas Shale the transport was accomplished under positive pressure conditions.

C.1.2.2. Re-Pressurization and Mixing Operations

Prior to utilizing the oil for burn tests and oil quality sampling, the oil in the tanker is in a 2-phase condition for safe storage and transport and must be brought back to a single liquid hydrocarbon phase and thoroughly mixed, prior to sampling and testing. To accomplish this reconstitution of the liquid oil sample, the tanker is filled with water raising the tanker pressure and forcing the reabsorption of the vapor back into the crude oil.

The tanker was designed with an oil mixing nozzle installed on mixing valve V-5. The nozzle consists of a pipe extension 6" below the top of the tanker with a 90^{o} elbow directing flow towards the head

of the tanker. This is designed to provide enough momentum to generate full circulation of total oil inventory above a quiescent water layer.

C.1.2.3. Transfer Operations

Once the re-pressurization/mixing operation is complete the oil in the tanker is as near as possible to the "as sampled" composition, and ready for pre-burn test sampling for crude oil characterization and delivery to the burn test equipment, pool fire and fireball. For both the pool fire and fireball tests the same water displacement method is utilized to deliver the oil under pressure from the tanker to the test devices. A water pump with variable frequency drive (VFD) is used to maintain the desired pressure on the tanker as the oil is being delivered from the tanker.

C.1.3. Unpressurized Tanker Operations

Several considerations, including technical and schedule logistics, led to a decision to acquire, transport, and store the stabilized SPR oil in unpressurized tankage. The transport tanker was rented from an oilfield service company, and a local fuel tank was used at Sandia for local storage. Two connections for mixing the oil in each tank were installed to minimize possible effects of density stratification on sub-sampling and delivery of homogeneous material to the combustion test apparatus. Additional detail on the unpressurized tanker operations relevant to mixing and subsampling is also given in Appendix F.

C.1.3.1. Loading

The loading of the SPR crude oil was performed as a standard loading process for standard crude oil transport tanker with no special handling or loading procedures.

C.1.3.2. Mixing

Prior to each testing/sampling event the unpressurized tanker contents were mixed by pumping the oil from the front-most bottom off- loading connection and returning oil to the back most connection on trailer for a minimum of 3 tank turnovers. The oil return line was extended below the liquid free surface to minimize the potential for static buildup in a hydrocarbon vapor, oxygenated environment.

C.1.3.3. Transfer

Transfer of SPR oil to the testing equipment was performed by simply pumping the oil from the tanker with the crude oil pumps while the tanker was open to atmosphere.

C.2. Small Scale (100 gallon) Fireball Test Tank

At the Lurance Canyon Burn Site (LCBS), a 100-gallon test tank was used for the small-scale fireball tests to aid in the experimental design of the larger fireball tests involving a 1000-gallon tank. The tank is designed to heat 40 gallons of oil to 350ºC with a resultant maximum pressure of ~500 psia. The tank is designed to have a minimum safety factor of 1.5 to yield at 350ºC and 600 psig. The minimum anticipated safety factor is 2.1 in the tank body. While the tank is designed in accordance with ASME pressure vessel guidelines, it does not meet ASME MAWP requirements due to the intentional use of rupture disks to release the contents. Note that there are no manned operations within an exclusion area when the vessel temperature exceeds 100ºC or 200 psi when preparing for the fireball test.

Figure C-2 shows a drawing of the 100-gallon test tank. The tank is fabricated using carbon steel with minimum yield strength of 70ksi (i.e. ASME SA-106 Gr. C, or ASME SA-105). The tank OD is 24 inches and the ID is 23 inches. The overall height from platform to the top is about 76 inches (6.3 ft). The thickness of the cylindrical wall and 2:1 ellipsoidal lower head is 0.5 inches. Its weight is ~2000 lbs., without the head closure.

Two-inch penetrations are provided for oil inlet (tank top) and water inlet (tank bottom). Additional penetrations in the flange are used for air venting and pressure measurements. Finally, two thermowells provide access for liquid and vapor temperature measurements.

Figure C-2 shows the small-scale fireball test tank attached to a metal skid, attached for ease of transportation. Also attached is a chamber used for a Guided Wave Radar (GWR) probe to measure the tank liquid surface level and oil/water interface. Note that the tank wall and the GWR chamber must be heated simultaneously at the same rate to obtain accurate level indications.

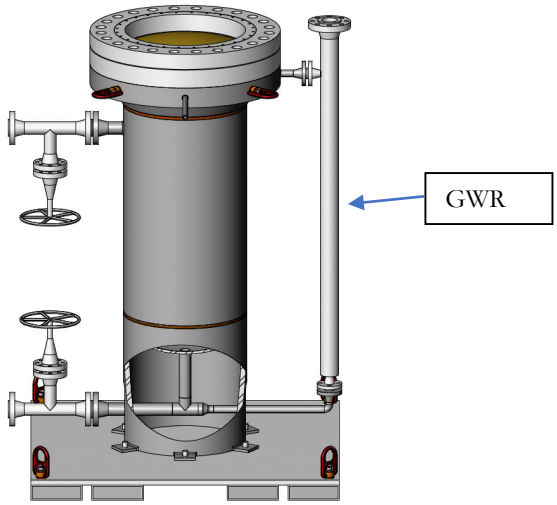

Figure C-2: Fireball Test Tank with GWR chamber attached to skid.

C.3. Large Scale (1000 -gallon) Pool Fire and Fireball Test Tank

A 1000-gallon test tank is used for the large-scale fireball tests. The tank is designed to heat 400 gallons of oil to ~350ºC with a resultant maximum pressure of ~500 psia. Radiant heaters on the outside of the tank were used to heat the tank. The sample size of 400 gallons liquid fuel (at ambient conditions) in the 1000-gallon tank was selected to allow sufficient space for liquid thermal expansion when the fuel was heated from 20°C to ~350°C.

The tank is fabricated using carbon steel with minimum yield strength of 70ksi (i.e. ASME SA-106 Gr. C, or ASME SA-105). The tank's top opening has an OD of 48 inches and an ID of 45 inches. The wider portion of the tank has a diameter 72 inches. The overall height from platform to the top is ~109 inches (9.15 ft). The thickness of the cylindrical wall and 2:1ellipsodial lower head is 1.5 inches and has a total weight of ~25,000 lbs., without the head closure (~6,700 lbs.).

Two-inch penetrations are provided for oil inlet (tank top) and water inlet (tank bottom). Additional penetrations in the flange are used for air venting and pressure measurements. Finally, two thermowells provide access for liquid and vapor temperature measurements.

Figure C-3 shows the test tank attached to a metal skid. Similar to the 100-gallon tank, a chamber was attached for the Guided Wave Radar (GWR) probe to measure the tank liquid surface level and oil/water interface.

For the fireball test conditions, the tank is designed to have a safety factor of 1.5 to yield at 350ºC and 600 psig. Similar to the 100- gallon tank, the 1000-gallon tank is designed in accordance with ASME pressure vessel guidelines but does not meet ASME MAWP requirements due to the intentional use of the rupture disks to release the contents.

For the first SPR pool fire test, the tank was fitted with a blank flange shown in Figure C-4. In this instance, the tank is certified to ASME MAWP requirements and has appropriate pressure relief systems installed. Note that oil was discharged from the tank through a penetration in the blank flange.

Figure C-3: 1000-gallon tank.

Figure C-4: Blank flange for 5-m diameter pool fire tests.

C.4. Small Scale (200-gallon) Pool Fire Test Tank

At the Thermal Test Complex FLAME facility, a 200-gallon test tank was used for the small scale indoor pool fire tests (Figure C-5). The tank is designed to heat 150 gallons of oil to ~60ºC with a maximum pressure of ~25-50 psia. The tank is nearly identical to the small-scale fireball test tank but scaled to accommodate the increased volume and lower pressure requirements. Since the upper head

closure is a blank flange, the tank is certified to ASME MAWP requirements and has appropriate pressure relief systems installed.

The tank is fabricated using carbon steel with minimum yield strength of 70ksi ((i.e. ASME SA-106 Gr. C, or ASME SA-105). The tank's top opening has an OD of 36 inches and an ID of 35.38 inches. The overall height from platform to the top is ~65 inches (5.4 ft). The thickness of the cylindrical wall and 2:1ellipsodial lower head is 0.31 inches and has a total weight of ~3,500 lbs., without the head closure (~1,700 lbs.).

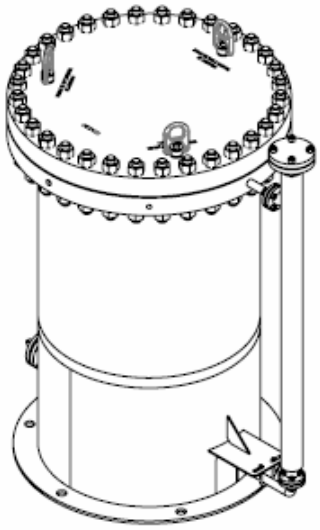

Figure C-5: 200-gallon tank for 2-m diameter pool fire tests.

C.5. Test Tank Top Closure for Fireball Testing

A rupture disc assembly was used for 100-gallon and 1000-gallon test tanks for the fireball tests. The rupture disk assembly consists of a rupture disk holder (a base and a top flange) and a cross-scored disc. The 100-gallon and 1000-gallon tank required 24" and 48" diameter rupture discs, respectively, which were manufactured by Fike.

C.6. Liquid Level

A Rosemount 3302 Guided Wave Radar (GWR) probe is inserted into a Rosemount 9901 chamber (external mounting is necessary as no penetrations are allowed through the rupture disc) to measure simultaneously the surface level and the oil/water interface. A remote transmitter with a 3 m long armored cable is used to protect the device during testing.

The GWR operates by sending low power, nano-second microwave pulses, guided down a probe submerged in the process media. When a microwave pulse reaches a media with a different dielectric constant, part of the energy is reflected back to the transmitter. The transmitter uses the residual wave of the first reflection for measuring the interface level. Part of the wave, which was not reflected at the upper product surface, continues until it is reflected at the lower product surface. The speed of this wave depends fully on the dielectric constant of the upper product. The time difference between the transmitted and the reflected pulse is converted into a distance, and the total level or interface level

is then calculated. The reflection intensity depends on the dielectric constant of the product. The strength of the reflection increases with higher values of the dielectric constant. Note that water has a dielectric constant of ~80 and the oil is expected to be in the range of 3.

C.7. Heaters for fireball tests

For the fireball tests, heaters were placed on the external surface of the tank to heat the oil to the desired temperature and pressure. For the 100-gallon tank, 480-volt band heaters purchased from Wattco were used. The heaters were distributed at four levels, providing a total power output of 14.8 kW (Figure C-6). The 1000-gallon tank used six, 400-volt, 15 kW band heaters providing a total power output of 90 kW (Figure C-7).

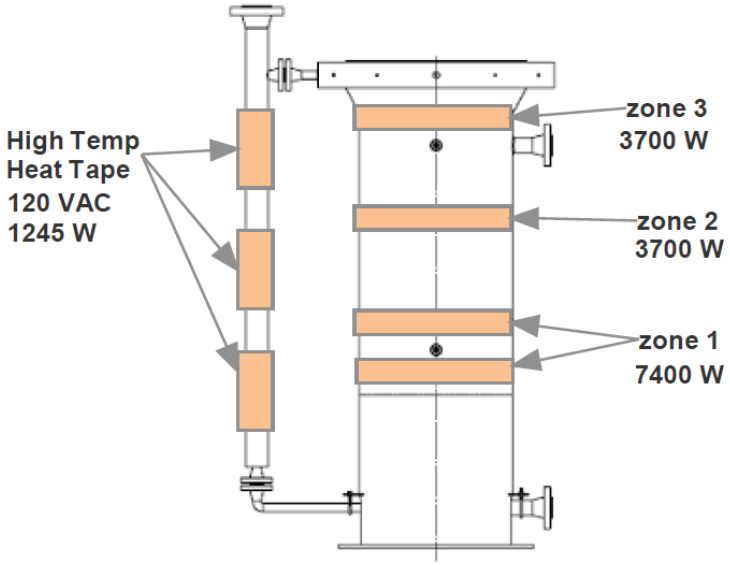

Figure C-6: Heater layout for 100-gallon tank.

Figure C-7: Band heaters on 1000-gallon tank.

The band heaters for the 1000-gallon tank resulted in repeated failure, thus 12 radiant heaters were used instead. Each heater is a quarter arc and thus four are needed to encompass the tank at each of three levels (Figure C-8). The heaters, purchased from Zircar, are high-temperature fibrous ceramic radiant heaters and are 480-volt, 8 kW each, providing a total power output of 96 kW.

Figure C-8: Radiant heaters at three levels surrounding 1000-gallon tank.

C.8. Test Tank Cooling and Heating

The following tables provide the assumptions and parameters used to estimate the oil heating and cooling power requirements for all tests tanks. For cooling, the initial temperature is assumed to be 40°C and the final test temperature is assumed to be 0°C, yielding a delta T of 40°C. For heating, the initial temperature is assumed to be 0°C and the final test temperature is assumed to be 60°C for the pool fire tests and 350°C for the fireball tests, yielding a delta T of 40°C and 350°C, respectively. Duration to heat or cool the oil is assumed to be 12 hours for tests involving the 100-gallon and 1000-gallon tanks and 4 hours for tests involving the 200-gallon tank. All test tanks were insulated where a 20% loss is assumed. Power requirements are based on the summation of the power needed to heat/cool both the insulated steel tank and the oil and assuming a 20% loss factor.

$$Q = \sum \dot{m}\, c_p \Delta T$$

Where

$\dot{m}$ = mass flow rate (kg/s)

Q = power (kW)

C_p = heat capacity (J/kgK)

ΔT = temperature change (K)

To meet the power requirements, a 10-ton heater/chiller unit manufactured by OptiTemp was used with a 35 kW power supply (1 kW = 3410 BTU/hr).

Table C-1: Power requirements for large tank heating and cooling.

Large Tank - LCBS	Pool Fire	Pool Fire	Fireball	Fireball
Power to heat or cool oil & tank	**Heat**	**Cool**	**Heat**	**Cool**
Delta T (C)	60	40	350	NA
Duration to heat (hrs)	12	12	12	
OIL				
Volume (gal)	800	800	400	
heat capacity Btu/Lbm-F	0.7	0.7	0.7	
Specific Heat (KJ/kgK)	2.9	2.9	2.9	
Mass (kg)	2415	2415	1208	
Energy (KJ)	424684	283122	1238661	
Power (kW)	10	7	29	
Steel				
Mass (lbs)	12000	12000	12000	
Mass (kg)	5455	5455	5455	
Specific Heat (KJ/kgK)	0.5	0.5	0.5	
Energy (KJ)	163636	109091	954545	
Power (kW)	4	3	22	
Total Power (kW) (with 20% loss)	16	11	61	
Total Power (BTU/hr)	55727	37151	207745	
Available Voltage	208	208	208	
Required Current (Amps)	79	52	293	

Table C-2: Power requirements for small tanks heating and cooling.

Small Tank - LCBS	Fireball	Fireball
Power to heat oil & tank	**Heat**	**Cool**
Delta T (C)	350	NA
Duration to heat (hrs)	12	
OIL		
Volume (gal)	40	
heat capacity Btu/Lbm-F	0.7	
Specific Heat (KJ/kgK)	2.9	
Mass (kg)	121	
Energy (KJ)	123866	
Power (kW)	3	
Steel		
Mass (lbs)	2000	
Mass (kg)	909	
Specific Heat (KJ/kgK)	0.434	
Energy (KJ)	138091	
Power (kW)	3	
Total Power (kW) (with 20% loss)	7	
Total Power (BTU/hr)	24813	
Available Voltage	208	
Required Current (Amps)	35	

Small Tank - TTC	Pool Fire	Pool Fire
Power to heat or cool oil & tank	**Heat**	**Cool**
Delta T (C)	60	40
Duration to heat (hrs)	4	4
OIL		
Volume (gal)	150	150
heat capacity Btu/Lbm-F	0.7	0.7
Specific Heat (KJ/kgK)	2.9	2.9
Mass (kg)	453	453
Energy (KJ)	79628	53085
Power (kW)	6	4
Steel		
Mass (lbs)	1000	1000
Mass (kg)	455	455
Specific Heat (KJ/kgK)	0.434	0.434
Energy (KJ)	11836	7891
Power (kW)	1	1
Total Power (kW) (with 20% loss)	8	5
Total Power (BTU/hr)	25991	17327
Available Voltage	208	208
Required Current (Amps)	37	24

C.9. Large Pool Fire Test Pan

A 5-m diameter pan was used for the pool fire tests at the LCBS. The pan is constructed with 0.5" carbon mild steel and has a flanged 2-inch diameter outlet at the pan center for the crude oil constant feed. The pan is flat, i.e., has 0-inch slope from the edge to the center and has an 8-inch lip. The tests were performed with constant level at ~3 inches of fuel (measured at the pan edge). A 6- inch diameter deflector plate is mounted approximately 1 inch above the pan surface, centered over the fuel inlet to force a radial spread of the incoming fuel. A ½ inch penetration at the pan bottom near the pan edge allowed connecting dP transducers to facilitate the constant level control. The 5-m pan was placed inside the 30 ft x 60 ft concrete lined, 3-ft deep, open pool at LCBS, flush with the ground surrounding the open pool for the SPR crude oil tests. A boil-over event happened for the second SPR crude oil test resulting in an extensive clean-up effort of the 30 ft x 60 ft containment pool. Thus, a decision was made to move the 5-m pan into a 7.9 m diameter circular pan outside and adjacent to the 30 ft x 60 ft pool.

C.10. Water Tank for Oil Movement

Water is used to evacuate air from the test tank prior to oil filling, move the oil liquid from the tanker to the test tank. The water is used as a piston; the higher density water (SG = 1) enters the tanker bottom and the lower density oil (SG <0.8) is pushed out the tanker top. The required water capacity needs to be slightly greater than the test tank; therefore a 1200-gallon water tank is used in the LCBS

test series. Total weight, with water is ~10,200 lbs. For the 2-m pool fire tests conducted at the TTC FLAME facility, a 300-gallon plastic tote was used, and load cells were utilized to determine the burn rate.

The water pump has the capacity of 30 gpm and 100-150 psi discharge pressure allowing for approximately 50 psi greater than the maximum oil vapor pressure (VP). Filling flow rates for the test tank are in the range of 5-10 gpm. However, for the large pool fire tests, required flowrates are in the range of 15-30 gpm. The water pump is equipped with a variable frequency drive (VFD) which is used to maintain the desired pressure on the tanker as the oil is being delivered.

APPENDIX D. MEASUREMENTS AND INSTRUMENTATION

Table D-1 presents a summary list of the instrumentation for the fireball and pool fire crude oil tests.

Table D-1: Crude oil instrument list summary.

Measurement	Instrument	Range	Resolution
Air Blast Pressure	Endevco model 8510B piezoresistive pressure transducers	0-1 psig	200 mV/psi sensitivity 55,000 Hz resonance frequency
Air Blast Pressure	Bikini gage		
Heat Flux	DFTs with Type-K TC 40 mil	-200 to 1250°C (~300 kW/m^2)	Greater of 1.7°C or 0.5% of reading
Heat Flux	Medtherm Schmidt-Boelter Total (windowless) heat flux gauge (Medtherm model 64-2-18), 180º view angle, water cooled	15 kW/m^2	±3% of responsivity 63.2% time constant is 35 ms
Heat Flux	Medtherm Schmidt-Boelter Radiometer, 5.5º view angle, with zinc selenide window, water cooled	300 kW/m^2	±3% of responsivity 63.2% time constant is 35 ms
Near Fire Surface Heat Flux	Calorimeters with Type-K TC 40 mil	-200 to 1250°C (~300 kW/m^2)	Greater of 1.7°C or 0.5% of reading
Fuel Pan Liquid Level	Type-K TC 40 mil	-200 to 1250°C	Greater of 1.7°C or 0.5% of reading
Heat Release Rate	IRGAS FTIR/O_2 gas analyzer	CO (0-2000 ppm), CO2 (0-8.5%), NO2 (0-200 ppm), NO (0-500 ppm), SO2 (0-200 ppm)	5 – 10 ppb
Fuel Pan Liquid Level	Rosemount Model 3051 differential pressure gauge		
Video (numerous)	CCD camera		30-500 fps
Surface Emissive Power	FLIR X6900sc IR Camera	80 – 350ºC 500 – 1200ºC 800 – 3000ºC Can also accept user calibration temperature ranges	3 - 1000 fps ±1% of reading
Data Acquisition System Low Speed	DAQ PXI-1052	na	±2-3% of reading
Data Acquisition System High Speed	PXI-1031/PXI-6132	na	±2-3% of reading

D.1. Pool Fire and Fireball Heat Flux and Surface Emissive Power Instrumentation

D.1.1. Pool Fires

To determine the surface emissive power and flame height of the pool fire tests, two Mid-Wave Infrared (MWIR) cameras were used. One was a FLIR X6900sc IR Camera, used as a spectral imaging radiometer (Figure D-1). The other IR camera, a FLIR SC8313 IR camera, was placed at the same location as the X6900 camera to serve as a back-up. A scientific grade visible camera Phantom V1212c was synchronized to one of the IR cameras. This camera has 1280x800 pixels with a Bayer filter pattern for color detection. The camera is intended for high speed imaging (12,000 fps at full frame) but it was used in this test with the main MWIR camera at 3 fps. These type of cameras, as the MWIR X6900sc, allow for synchronization with an external clock. This synchronization allows matching the frames from MWIR camera to the visible camera. The matched images can then be compared to relate flame and smoke in the visible camera to hot and cold areas in the IR camera. The FLIR X6900sc collects infrared radiation between 3 and 5 μm, uses a 100-mm lens, and has 640 by 512 pixels, with the 640 aligned along the vertical axis.

Figure D-1: X6900sc MWIR camera picture (source FLIR.com)

Infrared work at long distances is usually performed at two atmospheric windows, 3-5 μm or MWIR, and 7-14 μm or LWIR (Figure D-2). The bands where atmospheric transmission is low, the light is usually absorbed by water and/or CO_2. Soot in crude oil pool fires is semitransparent at the LWIR range which makes the measurement of temperature, and correspondingly SEP, complicated by not being able to assume that the soot acts as a blackbody. At the MWIR range the soot is not transparent and we can use the blackbody/graybody assumption when interpreting the collected data.

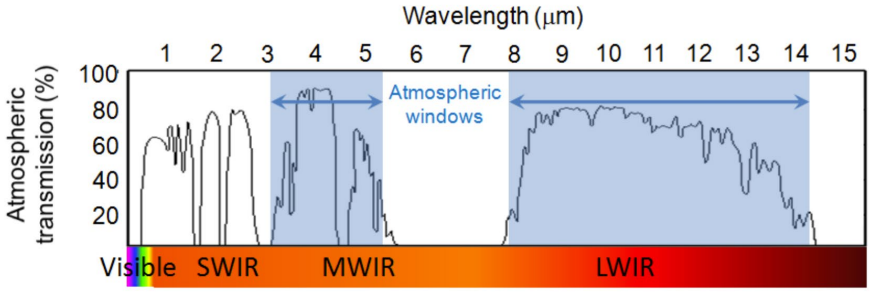

Figure D-2: Atmospheric windows for infrared imaging (source http://www.irradianceglass.com/2016/08/09/irg-educational-series-infrared-the-light-we-cannot-see/)

The camera has an InSb FPA with a spectral response of 1.5 μm to 5.0 μm. A bandpass (3-5 μm) filter and a ND-2 filter was placed between the FPA inside a sterling cooled Dewer and the lens. The 3-5 μm bandpass reduces the sensitivity to the adjacent water bands; we still need to correct losses attributed to CO_2 and other atmospheric gasses inside the 3-5 μm band by direct measurements or calculating with help from an atmospheric absorption software (in this case Hitran). The ND-2 filter provides an attenuation factor of 100. The camera exposure during the tests was set at 36.7 μs. The two filters, and the exposure are intended to guarantee that the camera works in its linear region for temperature ranges between 500ºC and 1200ºC (773.15K and 1473.15K). The linear response region of the camera is between 3000 and 13000 photon counts at each pixel. The main MWIR camera came with factory calibrations but, the second IR camera did not have factory calibrations and "User Calibrations" where created for this instrument with similar temperature ranges as the ones used in the main camera. The cameras were run at 3 fps with the purpose of gathering data through the whole 30 to 40 minutes duration of the tests.

The main camera placement was determined by the 100 mm and factory calibrated lens; the need to be as far as possible to image a full vertical flame; and the need for geographical conditions that maintain line of sight on the fire and are accessible. By following these conditions, the camera was placed 62 meters southeast of the pool fire (Figure D-3). These conditions were maintained through all three tests.

The second camera was added as a backup on the second test. It only has a 50-mm lens specifically designed for its cold 3-5 μm filter, not compatible with the main camera. Because the camera lens has a focal length of 50-mm the camera was placed ~31 meters from the fire to match the main camera field of view (Figure D-3). The because the ND-2 filter was procured after purchase of the camera, calibrations ("User Calibrations") were performed in house with blackbodies that can go up to 3000ºC (3273.15 K) and large area blackbodies for the NUC that will go up to 400ºC and 600ºC (673.15K and 873.15K). On the third test, the visible camera was placed adjacent to the main IR camera. The two cameras were synchronized to a common external clock with the purpose of comparing flame and smoke conditions to thermal and SEP data.

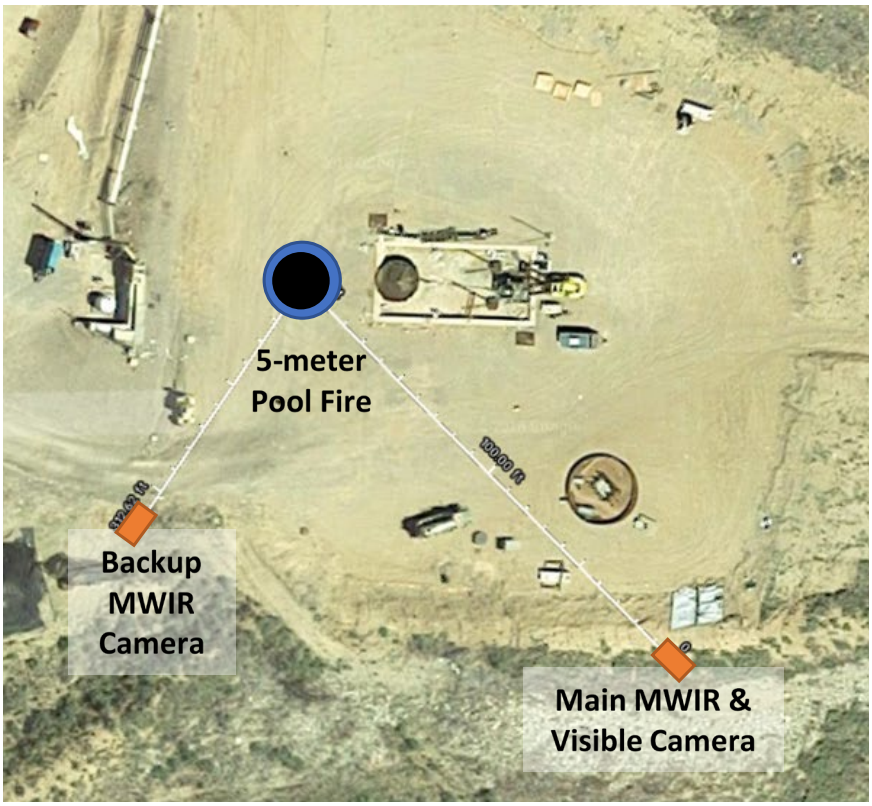

Figure D-3: Camera placements for the 5-m pool fire tests.

D.1.1.1. Data Processing

The X6900 MWIR camera is calibrated to receive photon counts with a 95% efficiency. The camera is considered linear between 487.7°C to 1308.8°C (760.85K to 1581.95K). If pixels have temperatures in each frame that are out of the temperature range, then the data is considered uncalibrated and the pixels is assigned a NaN value. The NaN pixel values will not be considered or have any effect in future calculations.

The data from the main camera can be saved in two formats when using the factory calibration:

1. Three files:
    a. .sfmov which contains the actual measured counts for each frame, and
    b. . inc contains the camera condition during the test.
    c. . pod contains the metada related for each frame

    The name of the files cannot be changed as they contain pointers for the original file names.
2. One file with.ats extension. This file format encapsulates all the files related to the measurement in one file. This format is not usable when trying to change calibration but has the advantage of containing all the data in one location.

The temperature data on each frame is then converted to surface emissive power by the following equation:

$$SEP = \sigma T^4$$

Where SEP is the surface emissive power, σ is $\frac{2\pi^5\kappa^4}{15c^2h^3}$, T is the temperature in Kelvins, κ is the Boltzmann's constant, h is Planck's constant and c is the speed of light. Figure D-4 shows images taken from the camera where the top-left panel is the photon count, top-center panel the temperature (K), and top-right panel the SEP in kW/m^2 at 1059.3 seconds after ignition. The graphical output below the panels (from left to right) show the maximum and mean SEP through time; the instantaneous histogram of the SEP; instantaneous bounded dimensions of the fire; and the dimension through time.

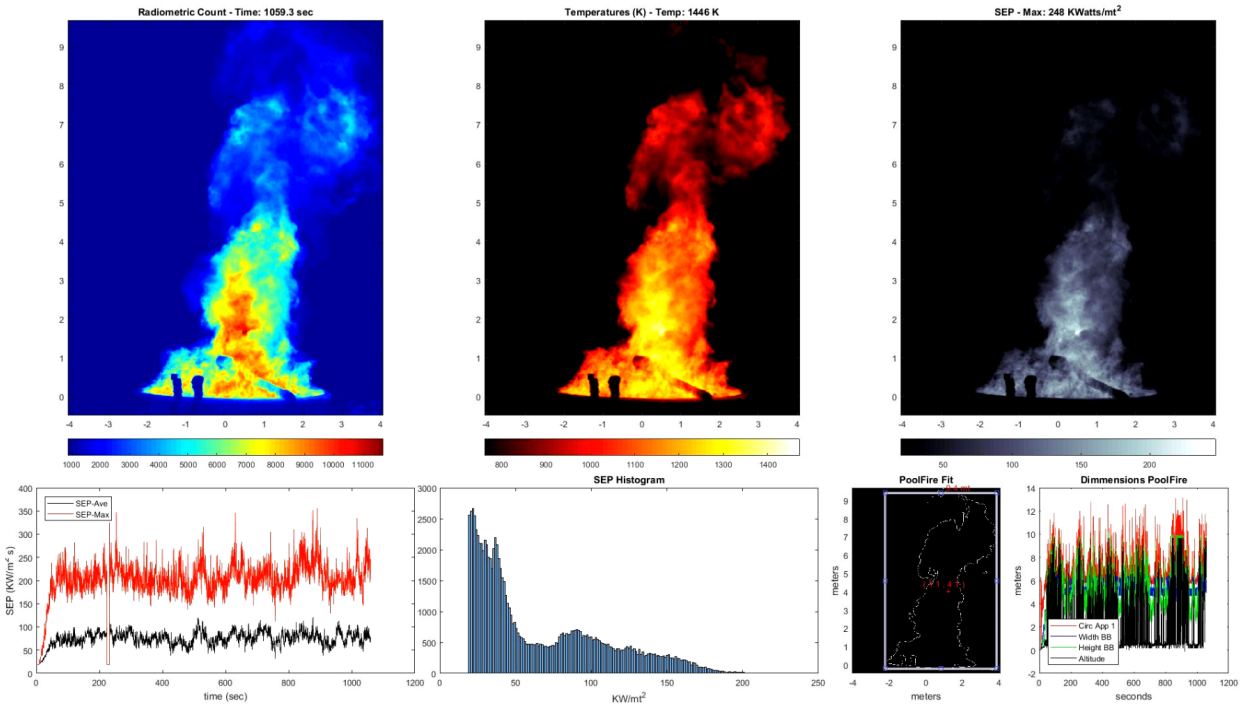

Figure D-4. Data frames with (top row) images from MWIR camera (from left to right) photon counts, temperature, and SEP. From left to right – bottom row: History curves for maximum and average SEP, histogram for the instantaneous SEP, dimensions box, and fire dimension history.

To calculate the representative flame temperature and flame SEP distribution the data was reviewed over the test duration and frames were selected in which flame was nearest to vertical and within the view of the IR cameras. Those frames were averaged for temperature and SEP (Figure D-5). Similarly, the maximum values for temperature were determined for each frame and averaged. The SEP graph reports the maximum extent of the flame identified using a threshold SEP value of 30 kW/m^2. This extent is along the line of the inclination of the flame indicated by the dashed line. Despite the selection of the most vertical flames, there is always a residual angle to the flame direction. Because the camera was located south east for the pool fire, the wind was northeast bound.

Because the tests were performed at ~1950 meters over the sea level and at different seasons with corresponding various levels of humidity, the calculations of air path transmission were estimated using HiTran for a 62-meter path, with the assumption of "SubArtic Lat 60° N summer" for the SPR test; "Mid Lat 45° N winter" for the Tight 1 (Bakken) and Tight 2 (Tx Shale) tests. "SubArtic Lat 60° N summer and winter" and "Mid Lat 45° N winter" are some of six environmental options provided for partial pressure estimations in HiTran. While Albuquerque is located at 35-degree latitude north,

its desert area location tends to behave more like the "SubArtic Lat 60° N" or "Mid Lat 45° N winter" depending on the season when the test is performed. For the 3-5μm transmission band, water and CO_2 are the main gases that will affect absorption. CO_2 is ubiquitous no matter the season and location and its effect on absorption are well defined after a couple of meters. Water absorption effects get pronounced after 5 meters, and the calculations with HiTran predict transmissivity values of 0.89 to 0.91.

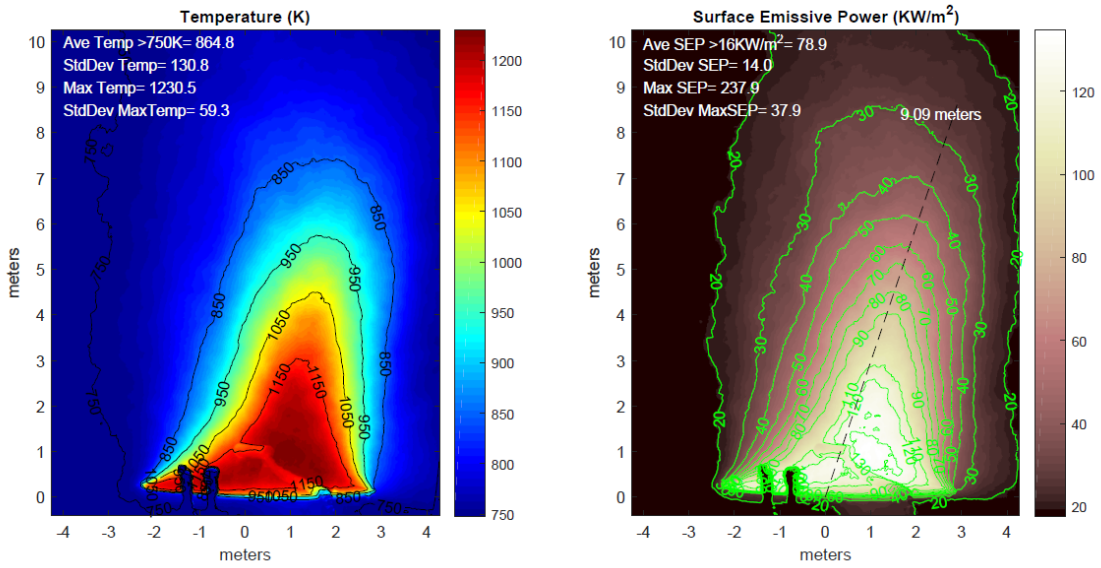

Figure D-5. Average temperature and SEP from frames with minimum wind from SPR test.

The data from videos taken during the first two tests were not synchronized to the IR data, however, for the Tight 2 (Tx Shale) test the main MWIR camera and a scientific visible camera were placed together and synchronized with an external clock, making sure that the cameras were not only collecting frames at the same rate but at the same phase. Figure D-6 shows the synchronized data from MWIR and scientific visual camera. The data correlates well between the visible and the infrared data, indicating that the cameras were synchronized. The shape of the bright red-orange flame coincides with the shape of elevated temperatures and SEP values, while regions of black smoke coincides with lower temperatures and SEP values. SEP data lower than 19 kW/m^2 (or 761 K) is uncalibrated data and not reported.

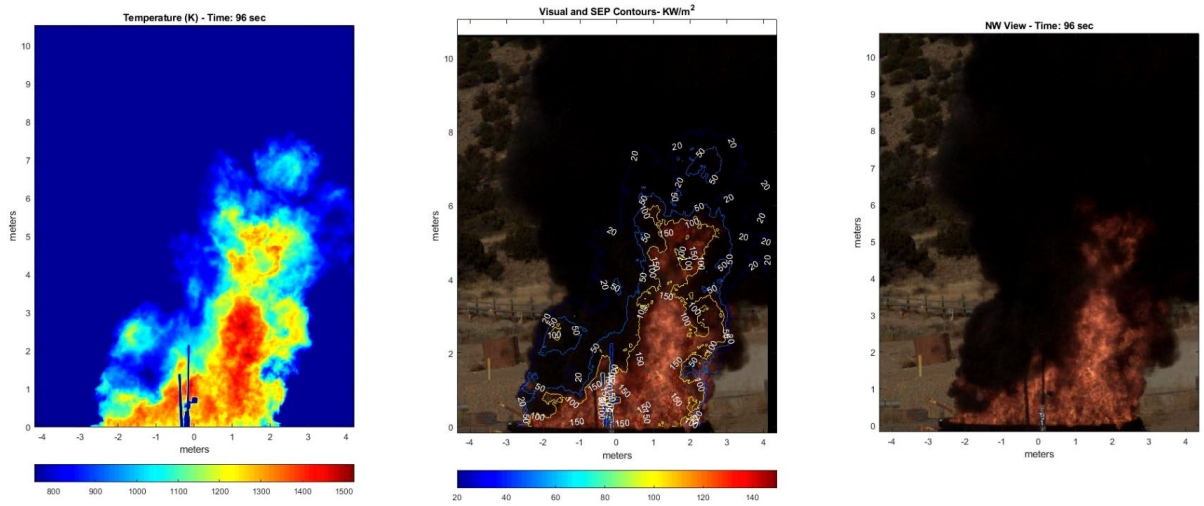

Figure D-6. Synchronization of IR data with visible data during the Tight 2 (XTO) test. Panel on the left shows temperature distribution from MWIR camera; panel in the center shows superimposed SEP contours on top of visible data; panel on the right shows visible data from visible scientific camera.

In addition to the IR cameras, a combination of Medtherm Schmidt-Boelter narrow-view and wide-view radiometers were used to measure spot surface emissive power and total heat flux external to the 5-m pool fires, respectively. The wide-angle radiometers have a field of view larger than the fire ensuring that they collect the entire signal from the event emitted in their direction. The narrow field of view radiometers have a view within a region of fire and are focused on a spot region.

D.1.1.2. Flame Height

The visible cameras are used to determine the length of the fire, instead of the IR camera, because they have a larger field of view. For this measurement we used four "Blackmagic Design Micro Cinema" cameras located at the North-West, South-West, North-East and South-East of the pool fire. Each camera had a 14 mm Olympus lens and was located 22 meters away. The cameras took three images every second during the duration of each test. This provided at a minimum of 3600 frames per view at each test.

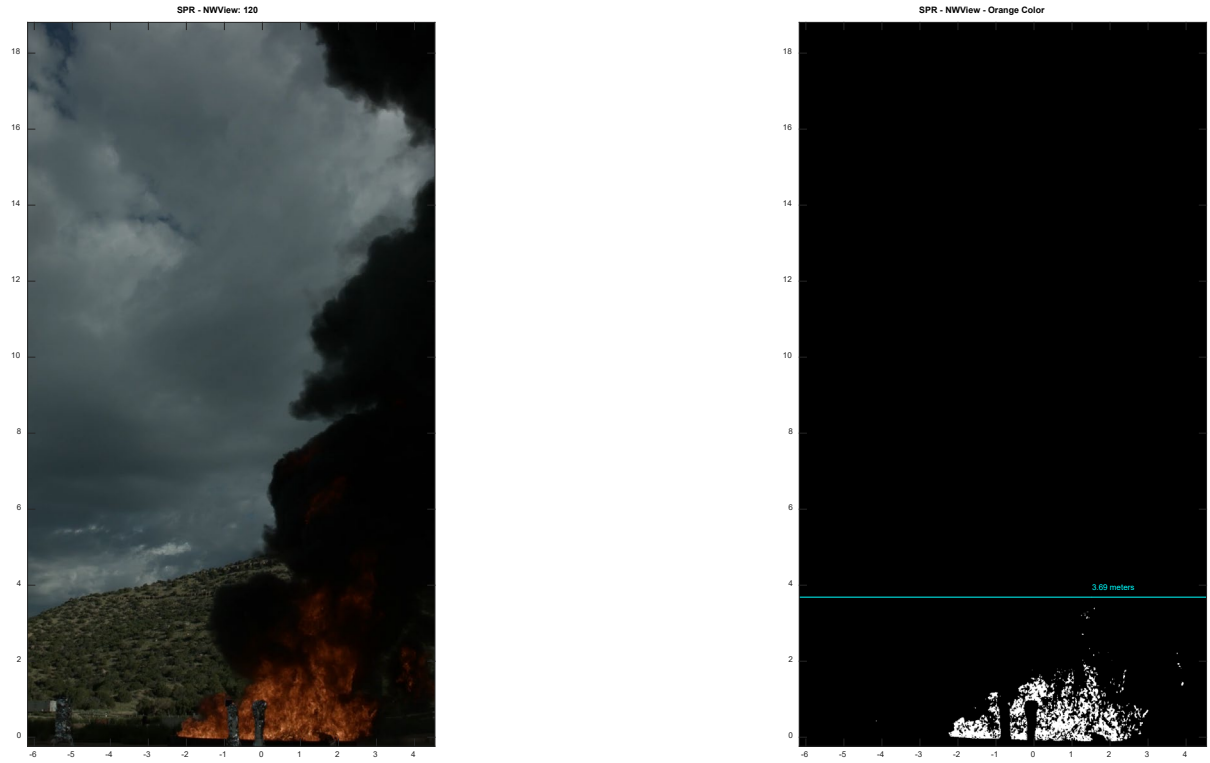

Figure D-7: Algorithm tracking the orange color. Left image is an original frame taken from the video camera. The right image is a black and white representation that tracks the location of the flame.

The obtained videos were processed in an algorithm that looks for the orange color of the flame at each pixel (Figure D-7). When orange was detected, the pixels was set to one. Pixels are set to 0 if they have colors different than orange or their intensity is below a threshold. With this masking it is possible to determine the length of the fire for each frame and with this data we can generate a histogram of the overall length of the fire, see Figure D-8. From this data a histogram is fit to a normal distribution curve where the 2-sigma values are the maximum and minimum lengths of the fire, and the location of the peak of the curve is the mean length. It is important to notice that in some of the views the minimum and maximum height can be affected by the amount of smoke coverage in each direction. Note that frames were not synchronized between the four cameras, thus the provided statistical data is uncorrelated for the different views. The distributions are provided in Figure D-9, Figure D-10, and Figure D-11 for the SPR, Tight 1, and Tight 2, respectively.

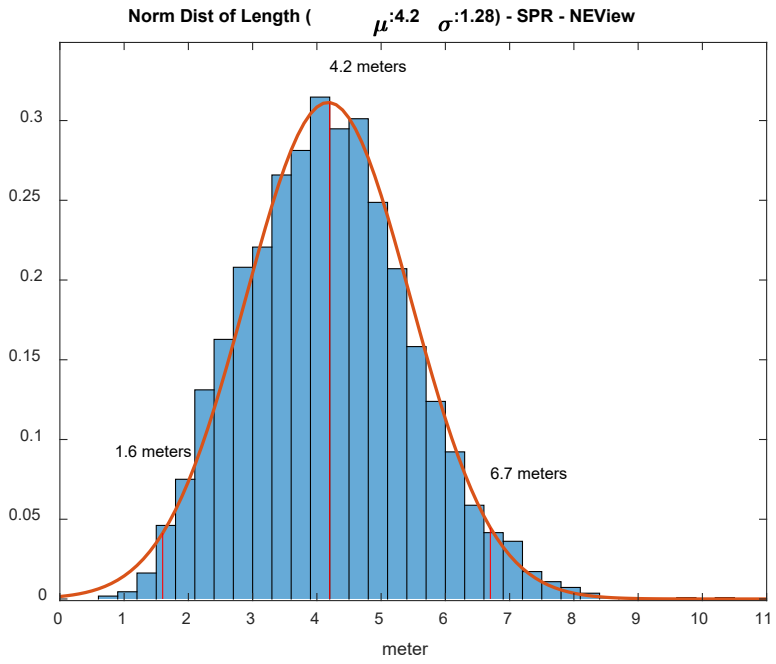

Figure D-8: Northeast view of the normalized histogram for the length measurement of the flame. The normalized distribution has a mean length of 4.2 meters, a maximum of 6.7 meters and a minimum of 1.6 meters (2-sigma).

The mean, minimum, and maximum (2-sigma) flame height values at each camera position are provided in Table D-2 for the SPR pool fire test. Note that the flame did not tilt exactly parallel to one of the cameras viewing direction due to the varying wind direction, thus the mean flame height determined from the cameras on opposite sides of the fire are not equal.

Table D-2: Length of the flame for the SPR 5-meter pool fire.

	2-Sigma	Length	2-Sigma
	Min	Mean	Max
NW View	1.6	4.8	8.1
NE View	1.6	4.2	6.7
SW View	0.7	4.6	8.5
SE View	3.1	5.9	8.7
average	1.8	4.9	8.0

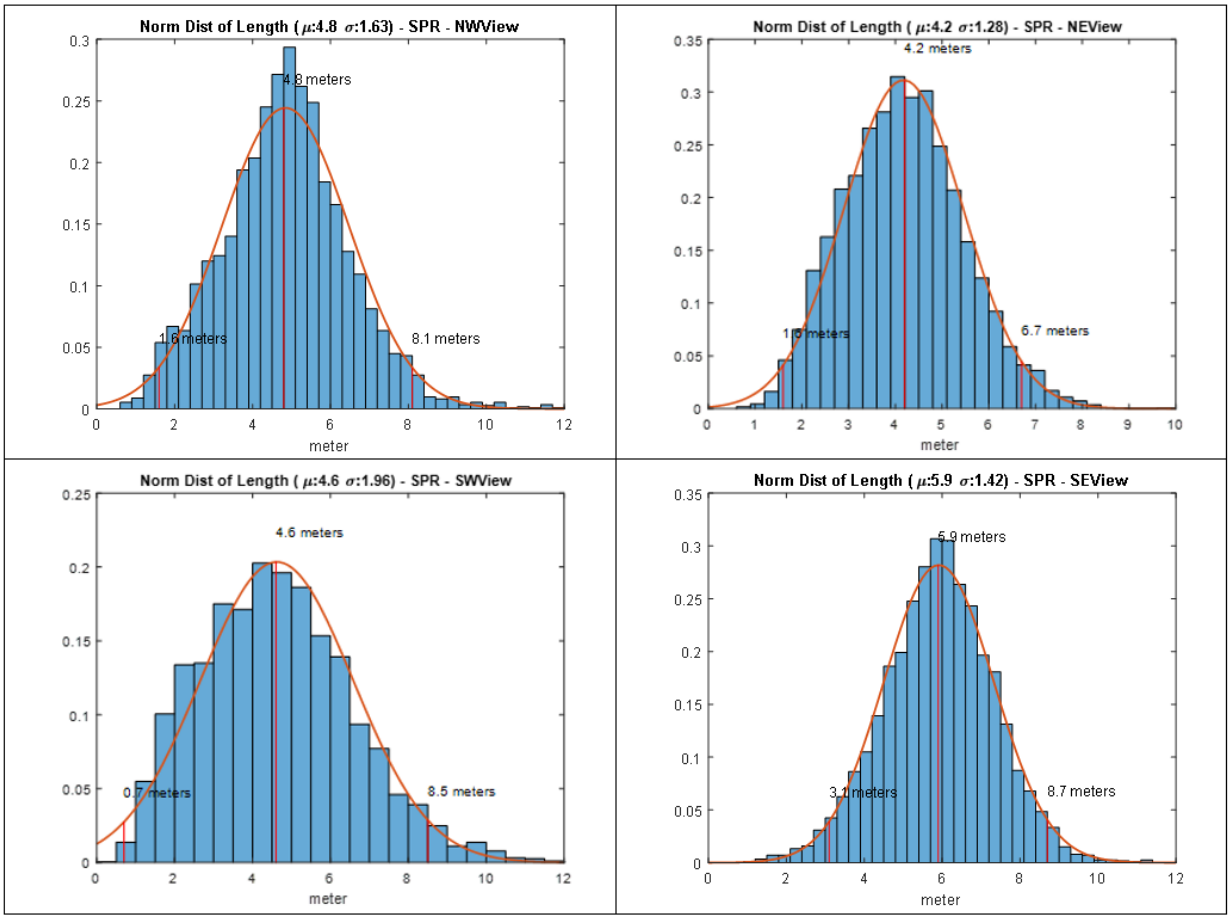

Figure D-9: Normal distribution of the flame length for the SPR 5-meter pool fire.

The mean, minimum, and maximum (2-sigma) flame height values at each camera position are provided in Table D-2 for the Tight 1 (Bakken) pool fire test. Note that the flame did not tilt exactly parallel to one of the cameras viewing direction due to the varying wind direction, thus the mean flame height determined from the cameras on opposite sides of the fire are not equal. The minimum values reflect the occurrence of smoke coverage and not the extinction of the fire. The shape of the distribution differs from the other crude oil tests due to the higher wind speed, causing the flame to be outside the viewing angle of the camera.

Table D-3: Length of the flame for the Bakken 5-meter pool fire.

	2-Sigma Min	Length Mean	2-Sigma Max
NW View	0.7	4.7	8.7
NE View	0.8	4.1	7.3
SW View	0	4.3	8.9
SE View	0.9	4.8	8.8
average	0.6	4.5	8.4

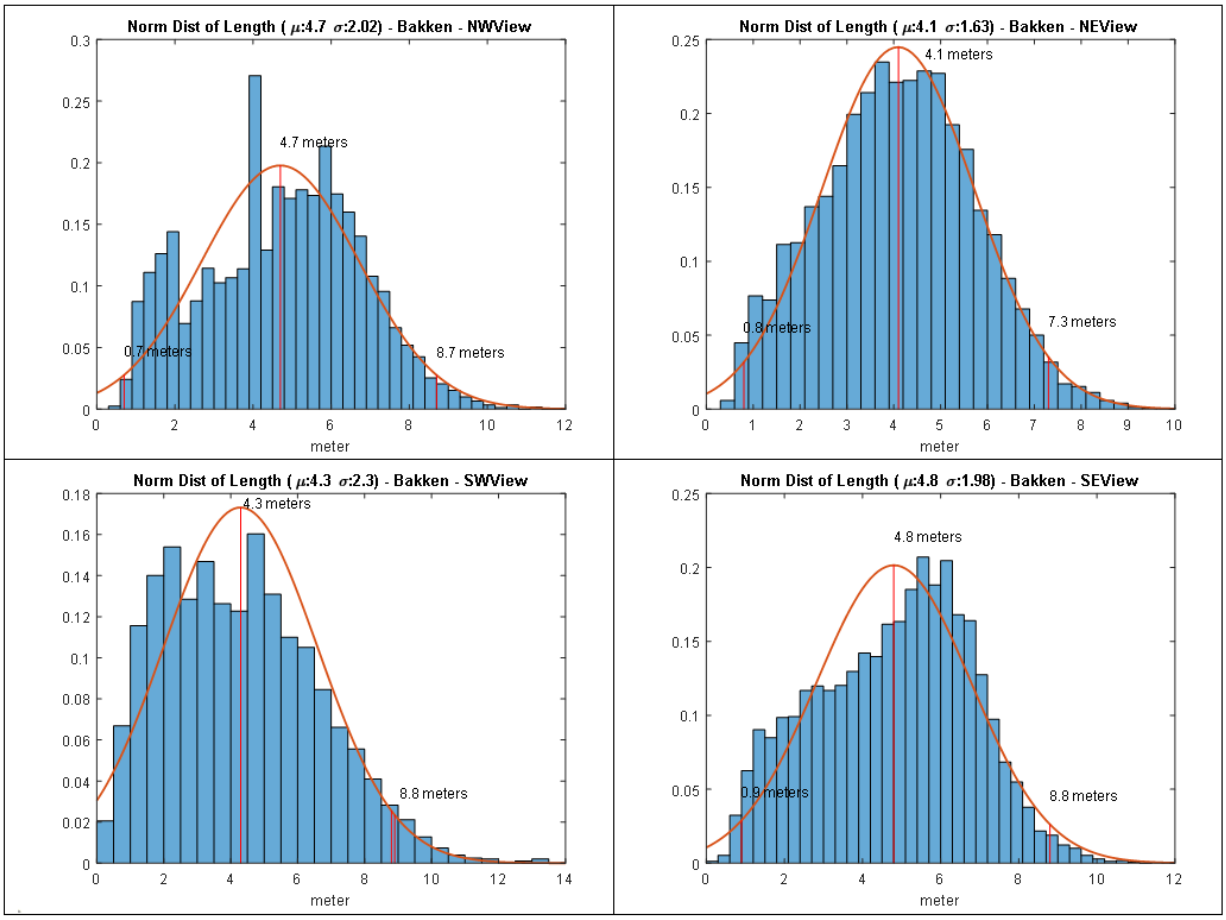

Figure D-10: Normal distribution of the flame length for the Tight 1 (Bakken), 5-meter pool fire.

The mean, minimum, and maximum (2-sigma) flame height values at each camera position are provided in Table D-4 for the Tight 2 (Tx Shale) pool fire test. Note that the flame did not tilt exactly parallel to one of the cameras viewing direction due to the varying wind direction, thus the mean flame height determined from the cameras on opposite sides of the fire are not equal.

Table D-4: Length of the flame for the Tight 2 (Tx Shale), 5-meter pool fire.

	2-Sigma Length		
	Min	Mean	Max
NW View	2.1	5.6	9
NE View	3.4	5.6	7.7
SW View	2.5	5.9	9.3
SE View	2.3	4.9	7.6
average	2.6	5.5	8.4

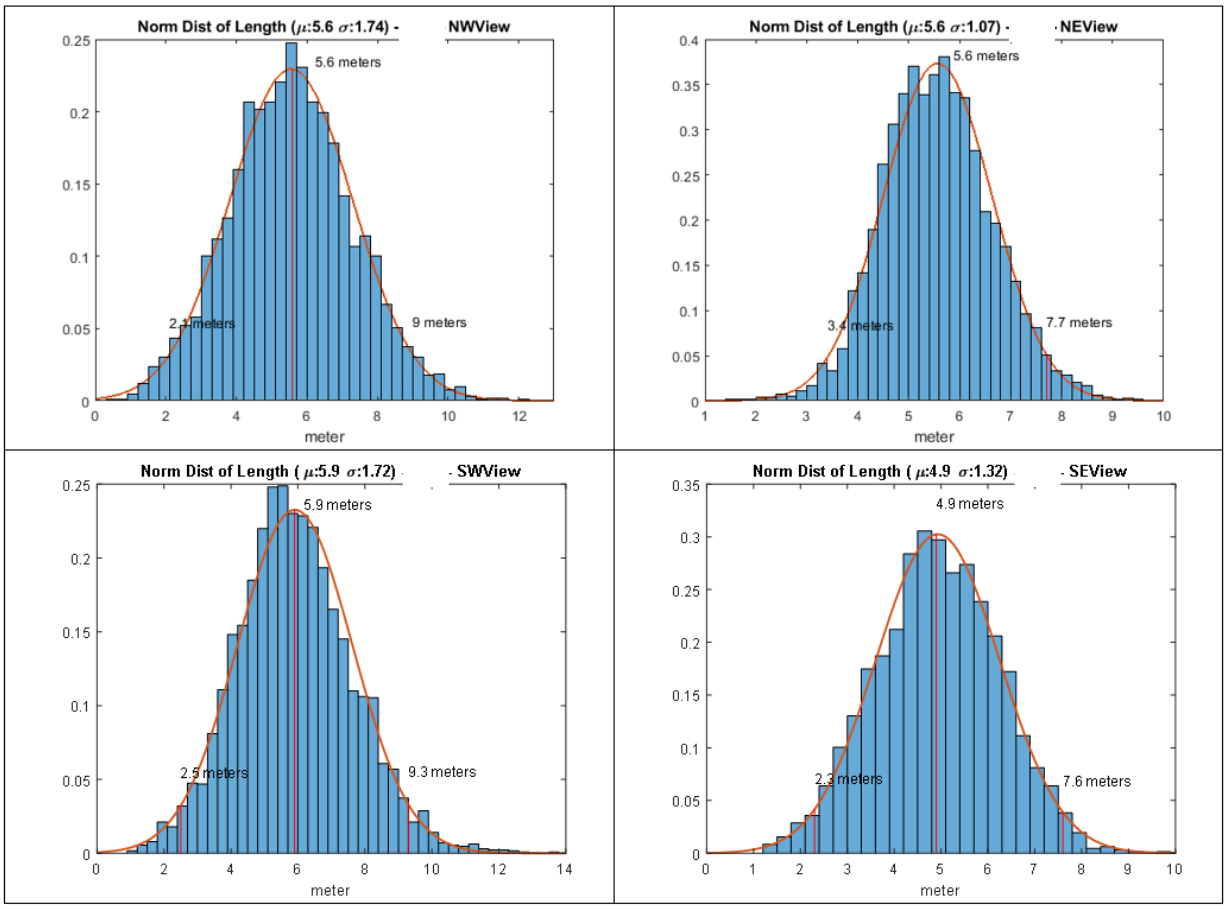

Figure D-11: Normal distribution of the flame length for the Tight 2 (Tx Shale), 5-meter pool fire.

D.1.1.3. Sensitivity Analysis

A sensitivity analysis was performed varying the atmospheric transmission from 0.97 to 0.89 and different emissivity values from 1 to 0.97 to assess the effect on temperature and SEP data. The results are provided for all the crude oils in Table D-5 through Table D-10. The results indicate the change in average SEP values vary almost linearly with changes in transmissivity and linearly with changes in emissivity for all the oils. For a percent change for either the emissivity or transmissivity, the percent difference in the maximum SEP is about a factor of 1.5 for all the oils. For example, a 12% increase in transmissivity results in a 19% difference in the maximum SEP. For conservative estimates, the lower bound of the potential range in transmissivity values and the upper range of the emissivity was applied to the data.

Table D-5. Transmissivity sensitivity analysis, SPR (atm.) 5-m pool fire test

Transmissivity (emissivity held constant) (%diff)	Maximum SEP (kW/m^2) (%diff)	Average SEP (kW/m^2) (%diff)	Maximum Temperature (K) (%diff)	Average Temperature (%diff)
0.12	-0.19	-0.13	-0.04	-0.02

Table D-6. Emissivity sensitivity analysis, SPR (atm.) 5-m pool fire test

Emissivity (transmissivity held constant) (%diff)	Maximum SEP (kW/m^2) (%diff)	Average SEP (kW/m^2) (%diff)	Maximum Temperature (K) (%diff)	Average Temperature (%diff)
0.05	-0.07	-0.05	-0.02	0.01

Table D-7. Transmissivity sensitivity analysis, Tight 1 (Bakken) 5-m pool fire test

Transmissivity (emissivity held constant) (%diff)	Maximum SEP (kW/m^2) (%diff)	Average SEP (kW/m^2) (%diff)	Maximum Temperature (K) (%diff)	Average Temperature (%diff)
0.12	-0.19	-0.13	-0.04	-0.01

Table D-8. Emissivity sensitivity analysis, Tight 1 (Bakken) 5-m pool fire test

Emissivity (transmissivity held constant) (%diff)	Maximum SEP (kW/m^2) (%diff)	Average SEP (kW/m^2) (%diff)	Maximum Temperature (K) (%diff)	Average Temperature (%diff)
0.05	-0.07	-0.05	-0.02	0.02

Table D-9: Transmissivity sensitivity analysis of Tight 2 (Tx Shale) 5-m pool fire test

Transmissivity (emissivity held constant) (%diff)	Maximum SEP (kW/m^2) (%diff)	Average SEP (kW/m^2) (%diff)	Maximum Temperature (K) (%diff)	Average Temperature (%diff)
0.12	-0.28	-0.14	-0.09	-0.02

Table D-10. Emissivity sensitivity analysis of Tight 2 (Tx Shale) 5-m pool fire test

Emissivity (transmissivity held constant) (%diff)	Maximum SEP (kW/m^2) (%diff)	Average SEP (kW/m^2) (%diff)	Maximum Temperature (K) (%diff)	Average Temperature (%diff)
0.05	-0.07	-0.05	-0.02	0.01

D.1.1.4. IR measurement u ncertainty

	Temperature (K)				Average uncertainty Temperature (%)	Average uncertainty SEP (%)
Source	600	800	1000	1200	1.12	4.6
Factory calibration	612	805	1007	1214		
Percent difference	2	0.63	0.70	1.17		

D.1.2. Fireballs

Two MWIR cameras were used to gather temperature and surface emissive power and dimensions from the fireball. Scientific grade visible cameras were synchronized to the MWIR cameras to provide non-IR imagery of the distribution of flame and smoke.

A MWIR camera capable of 125 fps was used as a back-up for the faster (1000 fps) MWIR cameras. Multiple cinematic real-time cameras were used to get ambient light images and multiple Digital Single-Lens Reflex (DSLR) cameras were positioned and used to collect high-resolution images from the event. All the cameras were positioned at two trailers north and south, at about 359 meters from ground zero (Figure D-12). Four cinematic cameras were adjusted for high sensitivity and positioned, north, south, east and west of ground zero to collect images in case of an un-ignited release (Figure D-13). The images from these cameras were intended to provide the location of ground contamination regions to facilitate cleaning efforts.

For the SPR and Tight 2 (Tx Shale) tests, one GoPro camera was placed near ground zero (~25 meters). For the Tight 2 (Tx Shale) test, three GoPro cameras were placed north, south east and south west of ground zero (Figure D-14).

For the Tight 2 (Tx Shale) test, a high-speed color camera was placed 2 km from ground zero on top of the Electrostatic Precipitator (ESP) at the Thermal Test Complex (TTC) (NE station in Figure D-12). Figure D-15 and Figure D-16 show the photometrics imaging equipment deployed at the two trailers.

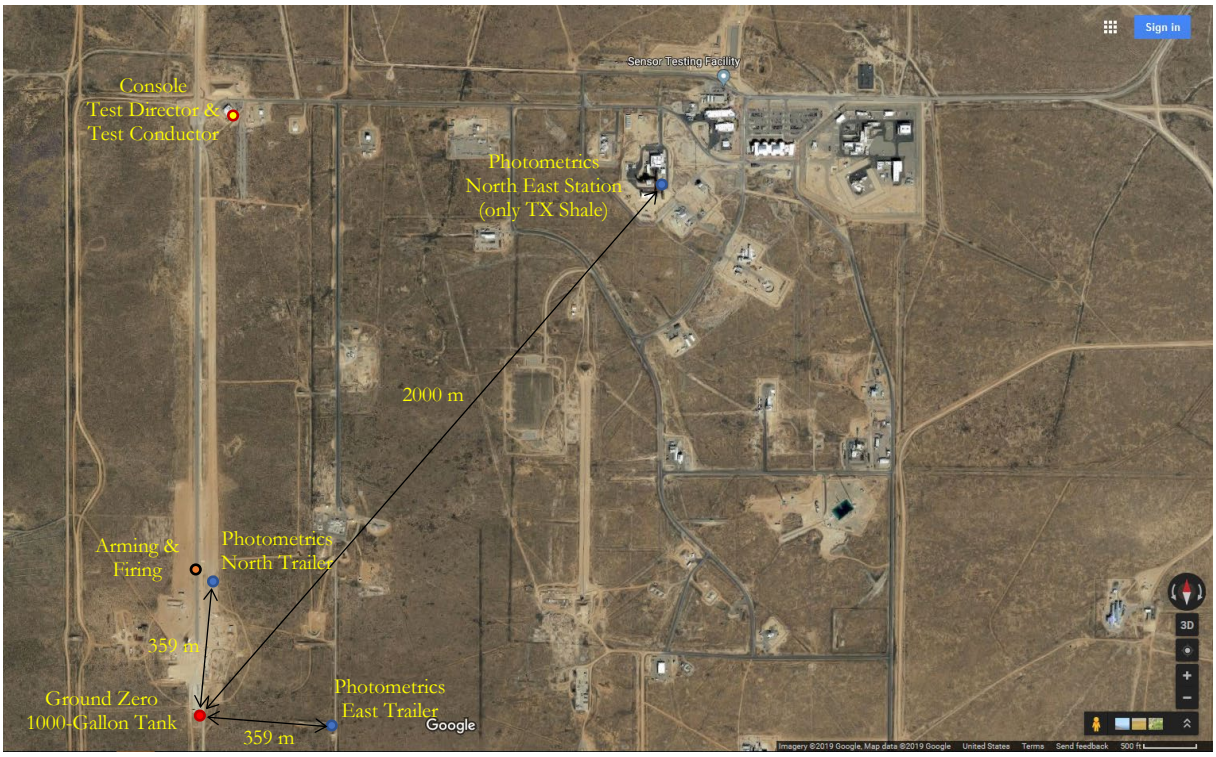

Figure D-12. Cameras placement with respect to the 1000-gallon tank (source maps.google.com).

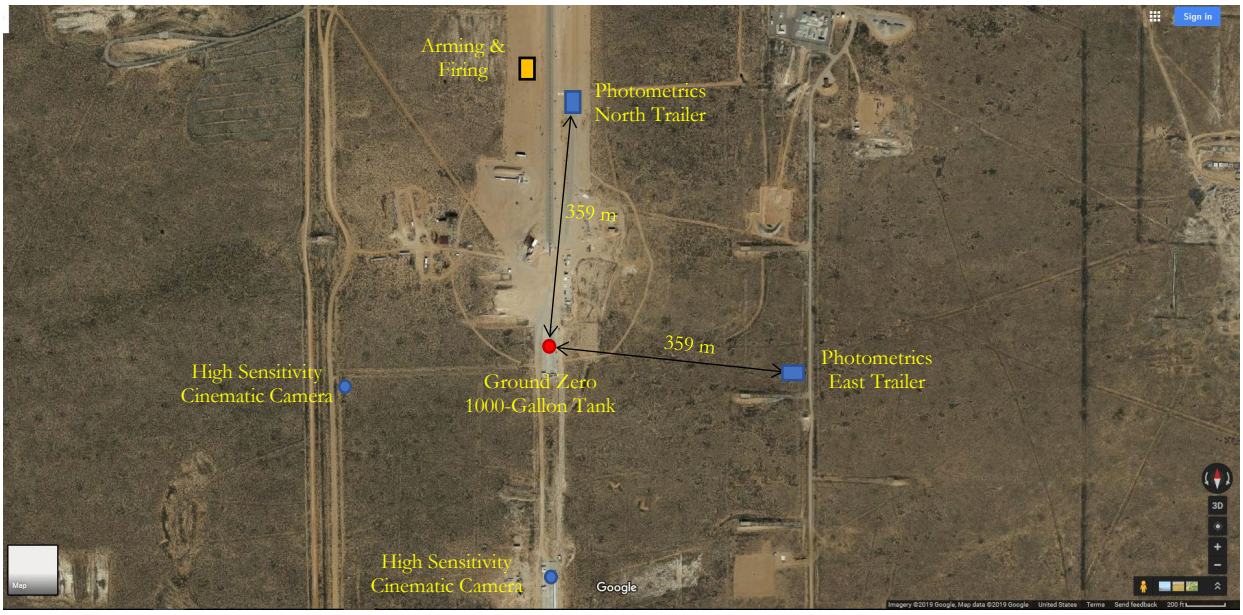

Figure D-13. Cameras placement near ground zero. The trailers at the north and east of ground zero have the IR cameras, scientific grade visible cameras and the cinematic cameras. The south and west sites only have a cinematic camera set to high sensitivity (source maps.google.com).

Figure D-14. GoPro placement at ground zero. Tight 1 (Bakken) test (orange marker). SPR test (green marker). For the Tight 2 (Tx Shale) test, (blue markers) (source maps.google.com).

(a) (b)

Figure D-15. Camera layout at the east trailer. Panel (a) from left to right: cinematic camera set to high sensitivity, cinematic camera set at ambient light, scientific grade visible camera synchronized to high speed IR camera (right). Panel (b) from left to right, three high speed cameras (~100K fps) and two DSLRs for slow frame rate but high-resolution images.

Figure D-16. Camera layout at the north trailer. From left to right: scientific grade visible camera synchronized to high speed IR camera (2nd from left), back up slow IR camera, cinematic camera set at ambient light, and cinematic camera set to high sensitivity. Outside the trailer two DLSRs were used to collect slow frame rate but high-resolution images.

D.1.2.1. Primary Mid -Wave IR Camera

Two FLIR X6900sc (Figure D-17) were used to collect infrared radiation between wavelengths 3 and 5 μm. The cameras have 640 by 512 pixels, with the 640 aligned along the vertical axis. For the data collection, the cameras were placed north and east at ~359 meters from the 1000-gallon tank. The cameras used 50-mm lenses for the Tight 1(Bakken) test and 25-mm lenses for the SPR and Tight 2 (Tx Shale) tests. The lens was switched after the Tight 1 (Bakken) test since it was realized that the 50-mm lens did not provide a sufficient field of view.

Figure D-17. X6900sc MWIR camera picture (source FLIR.com)

Infrared measurements at long distances are usually performed at two atmospheric wavelength windows, 3-5 μm (MWIR) and 7-14 μm (long-wave infrared, LWIR) (Figure D-18). For the bands where atmospheric transmission is low, the light is usually absorbed by water and/or CO_2. To select a working band, we need to keep in mind that the soot in crude oil pool fires is semitransparent at the LWIR range. This makes the measurement of temperature, and correspondingly SEP, complicated by not being able to assume a blackbody emission behavior at the LWIR band. At the MWIR range the soot is not transparent and we can use the blackbody/graybody assumption when interpreting the collected data.

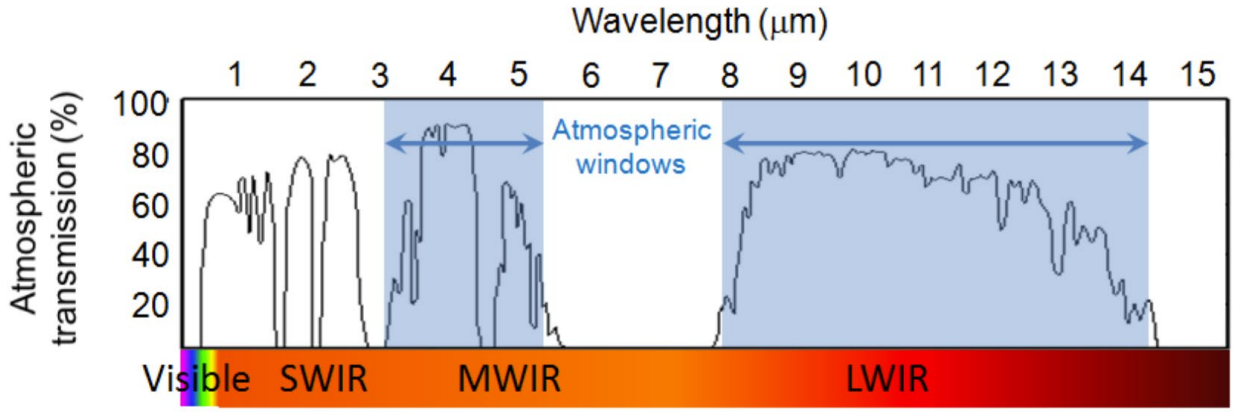

Figure D-18. Atmospheric windows for infrared imaging (source http://www.irradianceglass.com/2016/08/09/irg-educational-series-infrared-the-light-we-cannot-see/)

The cameras had InSb Focal Plane Arrays (FPA) with a spectral response of 1.5 μm to 5.0 μm. A bandpass (3-5 μm) filter and a ND-2 filter were placed between the FPA inside a stirling cooled Dewer and the lens for the north camera, and the bandpass filter was inside the cooled Dewer for the east camera. The 3-5 μm bandpass reduces the sensitivity to the adjacent water bands; we still need to correct for losses attributed to CO_2 and other atmospheric gases inside the 3-5 μm band by direct measurement or using an atmospheric absorption software (in this case Hitran) estimation of the

effect. The ND-2 filter provides an attenuation factor of 100. The camera exposure during the tests was set between 16 and 19 μs. The two filters, and the exposure are intended to guarantee that the cameras work in their linear region for temperature ranges between 600ºC and 1800ºC (873.15K and 2073.15K). The linear response region of the camera is between 2000 and 13000 photon counts at each pixel. Both MWIR cameras were calibrated ("User Calibrations") at Sandia for the 50 and 25 mm lenses. The cameras were run at 1000 fps with 6 seconds of pre-trigger data and 20 seconds of post-trigger, knowing that a fireball event will last approximately 10 to 13 seconds. Trigger was provided by the "Arming & Firing" team controlling the explosives that ruptured the burst disks in the 1000-gallon tank and ignited the oil.

D.1.2.2. Backup Mid -Wave IR Camera

One FLIR Sc8313 camera was used as a backup camera to collect infrared radiation between 3 and 5 μm (Figure D-19). The camera has 1340 by 784 pixels, with the 1340 aligned along the vertical axis. For the data collection, the camera was placed north at ~359 meters from the 1000-gallon tank. The camera used 50-mm lenses for the Tight 1(Bakken) and Tight 2 (Tx Shale) tests. The camera did not capture data during the SPR test due to failure of the high-speed recorder. This camera has a similar spectral response as the X6900sc with a 3-5 μm band pass filter inside the Stirling cooled Dewar. The camera was using an ND-3 attenuation filter (attenuation of 1000 and a factory calibration for temperatures between 800C and 3000C. The camera provided data at a rate of 124.25 fps for the Bakken test. Given the failure during the SPR test, the camera was used in the Tight 2 (Tx Shale) test with a reduced recording speed of 30 fps to prevent the failure from occurring again.

Figure D-19. Sc8313 MWIR camera picture (source FLIR.com)

D.1.2.3. Scientific Grade Visible Cameras Synchronized with IR cameras

The Phantom VEO640 cameras (Figure D-20) were synchronized to the X6900sc MWIR cameras. These cameras have 2560x1600 pixels with a Bayer filter pattern for color detection. The cameras were intended to be set up to run at 1000 fps and their clock signal used to synchronize the X6900sc. This synchronization allows us to match the frames from MWIR camera to the visible camera. The matched images can be used to compare flame and smoke in the visible cameras to hot and cold areas in the IR cameras.

Figure D-20. Phantom VEO640S camera picture (source http://www.phantomhighspeed.com)

D.1.2.4. Scientific Grade Visible Cameras at SEP

A VEO4K 990 camera was used to collect imagery from the NE location, 2 km from ground zero. The color (Bayer filter pattern) camera was set to run at its maximum resolution 4096x2304 pixels at a speed of 200 fps. The speed was dictated by the integration time of 4 ms. The camera has the same body as the VEO640 (Figure D-20).

D.1.2.5. Scientific Grade High Speed Visible Camera – Timing

A Phantom 2011 is a full spectrum (no color filters – monochrome images) camera that was set to look at the timing of the events: Ignition of the C4, shockwave from the shape charges, and ignition of the fuel. The camera field of view was reduced to 384x384 pixels to run at 100,000 fps. The camera at full resolution (1280x820 pixels) will run at 20,000 fps. This camera was located at the east trailer (Figure D-21).

Figure D-21. Phantom V2011 camera picture (source http://www.phantomhighspeed.com)

D.1.2.6. Scientific Grade High Speed Visible Cameras – Tight View in the Tank and Crude Oil Jet

Two Phantom v2511s, full spectrum (no color filters – monochrome images), cameras were aimed just above the 1000-gallon tank to capture the oil jet ejecting from the tank before ignition. The cameras field of view were reduced to 208x1280 pixels with an exposure of 10 µs for one and 384x288 with an exposure of 4 µs for the second one; both running at 95,000 fps. The cameras at full resolution (1280x820 pixels) will run at 25,000 fps. The cameras were located at the east trailer and the body of the cameras looks like the V2011 (Figure D-21).

D.1.2.7. Cinematic Came ras – Blackmagics

Blackmagic micro-cinema cameras were located at the east and north trailers and their sensitivity was set at a fixed gain for ambient light. They recorded images at 60 fps and recorded sound. Four cameras were placed at four cardinal points surrounding ground zero and were setup at their highest sensitivity to record the propagation of the vaporized crude oil in case it did not ignite. This type of camera has a 1920 x1080 pixel resolution (Figure D- 22).

Figure D- 22. Blackmagic micro cinema picture (source https://www.blackmagicdesign.com)

D.1.2.8. Cinematic Cameras – GoPros at Ground Zero

GoPro cameras were located at ground zero for each test, one for the Bakken, one for the SPR, and three for the Texas Shale. The increase from one to three cameras at the final test was based on the increase in confidence that the cameras would survive near the test site. These cameras were set to have automatic gain control, run at 29.97fps, resolution of 1920x1080 pixels, and record sound (Figure D-23).

Figure D-23. GoPro camera picture (source www.rei.com)

D.1.2.9. Digital Single -Lens Reflex Camera for High Resolution Imagery

One Canon 6d (5472x3648 pixels) was stationed at the east trailer for the Tight 1 (Bakken) test. High-quality images from this test indicated that deploying three more cameras (one extra Canon 6d and two Nikon D5) would allow collection of high-resolution images of the SPR and Tight 2 (Tx Shale) tests (Figure D-24). Sequential images of the tests are shown in section D.1.2.24.

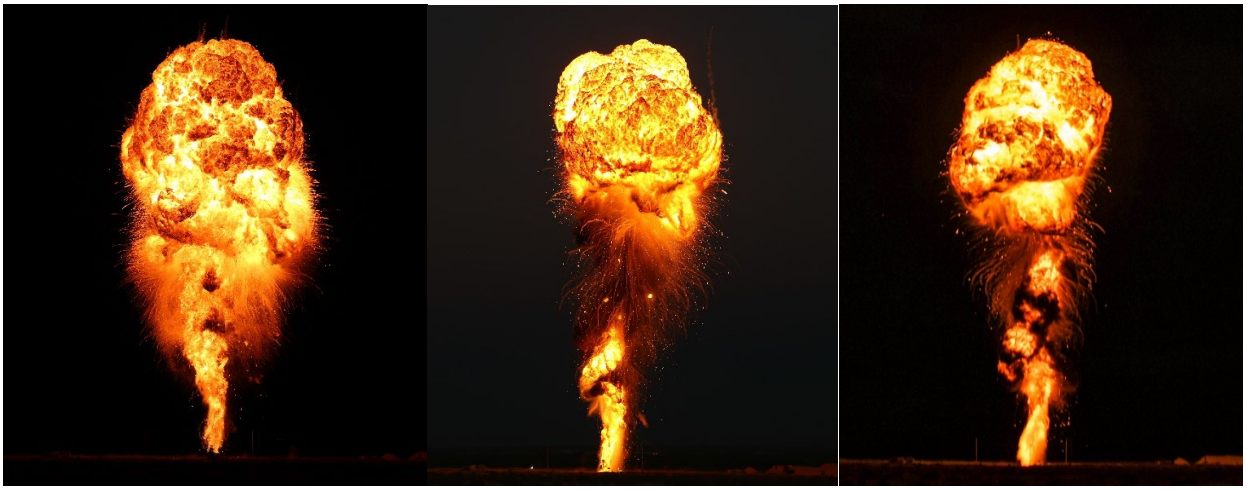

(a) (b) (c)

Figure D-24. Pictures from a Canon 6d for the a) Tight 1 (Bakken) test, b) Tight 2 (Tx Shale) test, and c) a Nikon D5 for the SPR test.

D.1.2.10. Air Transmission Losses Measurement

(a) (b)

Figure D-25. Large area blackbody. Panel a) day before the Bakken test by the 1000-gallon tank, and panel b) same day of the SPR test.

The measurement of temperature and consequently the SEP calculation; requires knowing the air transmission fraction at the waveband (3-5μm) where the IR cameras work. Air transmission measurements were performed the day before and same time of the test, or an hour after the test on the same day. The air transmission measurement is collected using a MWIR camera with a 100 mm lens. This lens (or longer focal length ones if available) guarantees that there are at least 10 pixels across in the image of the large area blackbody at ~359 meters away from the camera (Figure D-25). A second measurement was performed near the black body and the ratio of the photon counts between the long-distance and the near distance measurements is the air transmission fraction. The black body is a metal frame with a copper sheet 91.5x91.5 mm^2, painted black on both sides for high emissivity. Behind the metal sheet there is a board with sixteen 200-Watt (each) heating light bulbs, configured in two independent banks of lights that heat the copper sheet.

Table D-11 shows the measured air transmission. Notice that the table has a second column with corrected measurements and the SPR Tx set at 0.7931 instead of the original 0.77424. The ambient temperature and relative humidity was monitored during each test. Data of ambient temperature and relative humidity show the actual water pressure to be low for both SPR and Texas Shale (higher air transmission fraction), while the data in Table D-11 for SPR indicates a lower measured transmission fraction (higher actual water pressure). Review of the video taken from the black body at ~359 meter seems to indicate that there was higher turbulence in the image than previously seen. This tends to reduce the ability to focus the camera and it will report a lower signal and therefore result in a lower air transmissivity fraction. Thus, the actual water pressure of 0.0057 atmospheres provided in Table D- 12 was used to estimate the air transmission fraction, providing a value of 0.7931. This difference between the estimated value from the atmospheric conditions and the measured values provides an error of 2.4% for the SEP values.

An additional calculation with HiTran using the atmospheric conditions for the Tight 2 (Tx Shale) test resulted in an air transmission fraction of 0.82. This calculation is coarser because the program has a reduced number of available models for water pressure but seems to indicate an upper limit for the

air transmission fraction, with an error in SEP of 2.9%. Looking at different deltas between the different tests an estimate that the air transmissivity error is between 3% to 5%, using the conservative delta of 5% for air transmissivity fraction.

Table D-11. Air transmissivity for the three tests and correction

Test	Black Body Measurement Transmissivity	Black Body Measurement Transmissivity Corrected
Bakken	0.76551	0.76551
SPR	0.77424	0.7931
Texas Shale	0.79657	0.79657

Table D- 12. Environmental conditions at the time of the fireball tests.

Test	Temperature (°C)	Saturated Water Pressure (Atmospheres)	Reported Relative Humidity	Actual Water Pressure (Atmospheres)
Bakken	18.33	0.0209	0.65	0.0136
SPR	5.56	0.0090	0.64	0.0057
Texas Shale	6.06	0.0093	0.511	0.0047

D.1.2.11. Spatial Calibration

For each test, the X6900sc, Sc8313 and VEO640 were spatially calibrated by placing two lights at both sides of the 1000-gallon tank, aligned east-west for the north trailer and north-south for the east trailer. Pixel size was determined by dividing the distance between the lights by the number of pixels between the lights. The lights were selected for their large thermal signature that allowed them to be seen by the IR cameras, and by the visible cameras (Figure D-26).

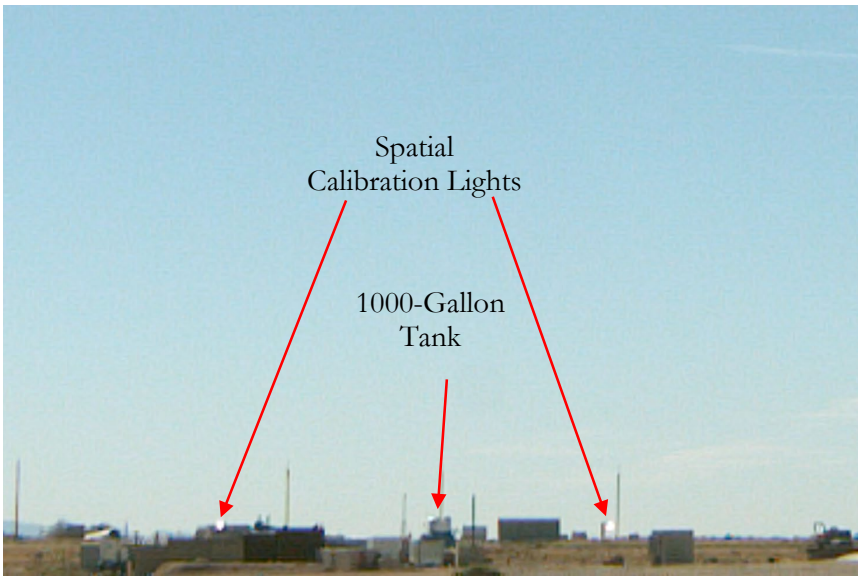

Figure D-26. Calibration lights used to determine pixel size.

D.1.2.12. Measurement uncertainty of IR cameras

The measurement uncertainty provided by FLIR for the InSb MWIR cameras is +/-2% at 37°C. This number is limited to lower temperature ranges. To address the error at higher temperature, a higher temperature range calibration was performed. During the two X6900sc calibrations (600°C to 1800°C), the temperature measured by the camera looking at a black body varies with the temperature of the black body as shown in Figure D- 27 a). There is a variance of +2.78% for the warm filter camera and +3.57% /-1% for the cold filter camera. The corresponding SEP indicates a variance of +11.6% for the warm filter camera and +15%/-3% for cold filter camera. The Sc8313 has a factory calibration with a range of 850°C to 2000°C. The camera shows an error in the order of ±2% for temperature (Figure D- 27 (a)), and ±8.24% for SEP (Figure D- 27 b)).

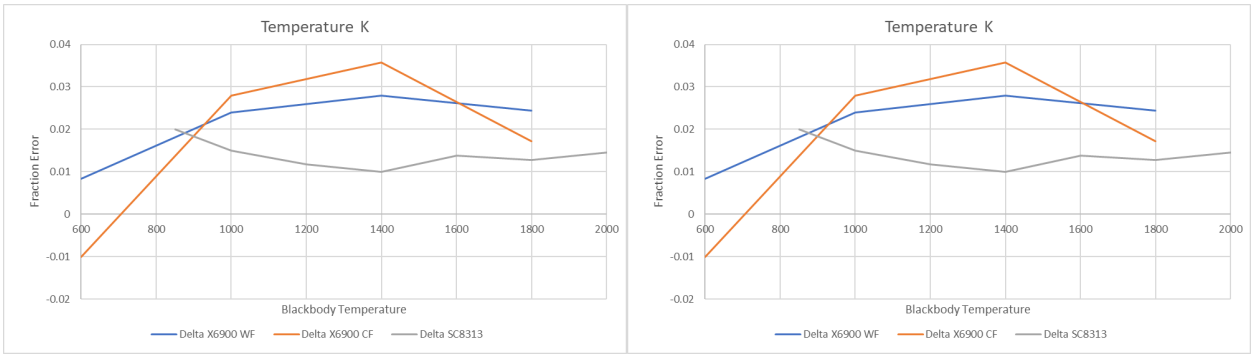

(a) (b)

Figure D- 27. Panel a) shows temperature fraction of error reported by the two X6900sc and the Sc8313. Panel b) shows the corresponding fraction of error for SEP. The X6900sc cameras were calibrated at Sandia from 600°C to 1800°C and the Sc8313 was factory calibrated from 850°C to 2000°C.

D.1.2.13. Measurement uncertainty of X6900sc (warm filter)

One of the X6900sc doesn't have a cold filter inside the Dewar that keeps the FPA cryocooled at 77K. Thus, the filter is at ambient temperature. Assuming a temperature of 300K (26.85°C), for example, means that the filter will contribute 0.459kW/m^2 to derived values of SEP. For the lowest SEP value of 20kW/m^2, a value assigned to smoke, the error is 2.3%, for maximum temperatures on the order of 1800K, the SEP is about 595.3kW/m^2 with an error of 0.08%. For the averages seen in all fireballs of 200kW/m^2, the error is in the order of 0.23%, and at 8 or 9 seconds the average is in the order of 100kW/m^2, with errors in the order of 0.46%.

D.1.2.14. Measurement uncertainty associated with fireball emissivity

The test data was reduced assuming the fireballs were optically thick, that is having an emissivity value of 1. This is a reasonable assumption due to the scale and heavily soot-producing fuels used and it would be difficult to justify using a value much below 1. A value of 0.95 is used to perform a sensitivity analysis to determine the uncertainty associated with the emissivity assumption. The sensitivity analysis indicates by lowering the emissivity to 0.95, the SEP increases by 5.3% (Figure D- 28).

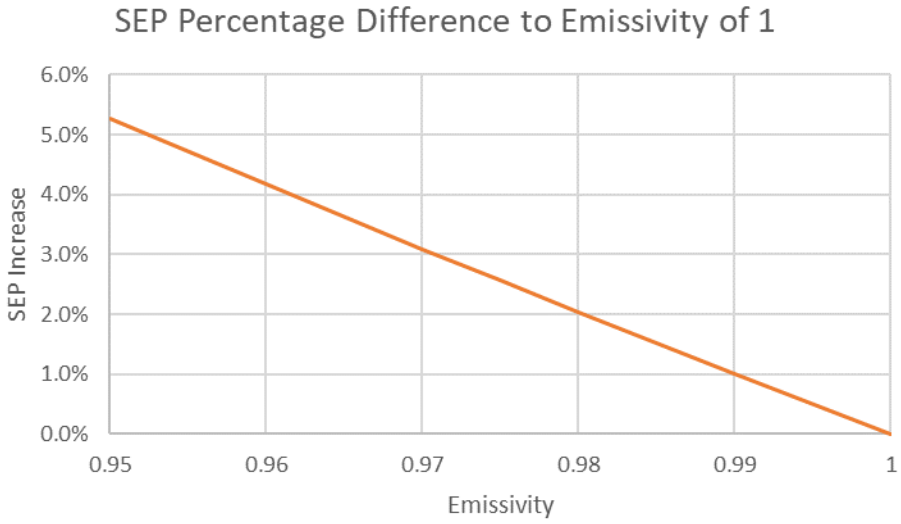

Figure D- 28. SEP percentage increase with reduction of emissivity.

D.1.2.15. Overall measurement uncertainty

The overall measurement uncertainty for all IR cameras is estimated using the uncertainty for the FPA, transmissivity, and the warm filter (Table D-13).

Table D-13: Overall uncertainty for IR cameras

Camera	FPA uncertainty	Transmissivity uncertainty	Warm filter uncertainty	Overall uncertainty
X6900sc (warm filter)	0.116	0.05	0.0046	±6.32%
X6900sc (cold filter)	0.180	0.05	0.0	±9.34%
Sc8313 (warm filter)	0.082	0.05	0.0046	±2.40%

If an emissivity of 0.95 is assumed the errors increase slightly to ±6.79%, ±9.67%, and ±2.71% for the X6900sc (warm filter), X6900sc (cold filter), and the sc8313 (warm filter), respectively. Since this is a minor difference and since a value of 0.95 is more difficult to justify than a value of 1, the values provided in Table D-13 will be considered the overall uncertainty.

D.1.2.16. 100mm, to 50mm, to 25mm lens transitions

The first fireball test was performed at the Lurance Canyon Burn Site facility using a 100-gallon tank and 38 gallons of Jet A. Data was collected with an X6900sc camera, located ~359m from ground zero, with a 100 mm lens. The fireball rose to ~35 meters before temperatures dropped below the calibration point of the 100 mm lens. The field of view in this configuration was 65 meters by 50 meters. From this data, there was the expectation of performing a test with Jet-A using the 1000-gallon tank, after perfecting methods to open the rupture disk and igniting the fuel. This test would allow us to dial the lens options for the IR cameras (50mm or 25 mm). The best estimates indicated that 50 mm lens would double the field of view, and the 25 mm lens will quadruple the view. But, as the field of view increases, there is a corresponding reduction in pixel resolution. For the Tight 1 (Bakken) test we decided to use the 50 mm lens, which provided sufficient data from both X6900sc cameras and the Sc8313 camera to determine the peak signal and the formation of the fireball itself. Unfortunately, we were not able to see the decaying process of the fireball. However, a video taken by the A&F team was used to complement dimensional data of the Tight 1 (Bakken) test. This data was calibrated using the height of one of the three torches at ground zero. After this test it was decided the use of 25 mm lenses for the X6900sc cameras to achieve a greater field of view, even if there was a loss in pixel resolution. The Sc8313 was maintained with the 50 mm lens to keep continuity in field size between tests.

D.1.2.17. Data Processing – Temperature and SEP

The main MWIR camera is calibrated to receive photon counts with a 95% efficiency. The camera is considered linear between 300ºC to 1800ºC (573.15K to 2073.15K) for the 50 mm lens used in the Tight 1 (Bakken) test, and 540ºC to 1800ºC (813.15K to 2073.15K) for the 25 mm lens used in the SPR and Tight 2 (Tx Shale) tests. If pixels have temperatures in each frame that are out of the temperature range, then the data is considered uncalibrated and the pixels are assigned a NaN value. The NaN pixel values will not be considered or have any effect in future calculations.

The data from the main camera is saved in one format for cameras calibrated at Sandia. The file formats are the following:

1. .sfmov which contains the actual measured counts for each frame, and
2. . inc contains the camera condition during the test.
3. . pod contains the metadata related for each frame

Also, Nonlinear Uniformity Correction (NUC) and temperature calibration files from calibrations performed at Sandia have the following file formats:

4. . cal contains the calibration temperature calibration
5. . inc contains the camera condition during the calibration
6. .sbp contains a map of the bad pixels during the NUC

7. .scg contains a map of the pixel gain distribution during the NUC
8. .sco contains a map of the pixel offset distribution during the NUC

The name of the files cannot be changed as they contain pointers for the original file's names.

The temperature data on each frame is converted to surface emissive power by the following equation:

$$SEP = \varepsilon \frac{\sigma T^4}{\tau}$$

Where SEP is the surface emissive power, σ is $\frac{2\pi^5 \kappa^4}{15c^2h^3}$, T is the temperature in Kelvins, κ is the Boltzmann's constant, h is Planck's constant and c is the speed of light, and τ is the air transmissivity fraction, and ε is the emissivity which is assumed to be 1. An example of the data generated for each test is shown in Figure D-29 for the SPR test which provides the photon counts from the camera (top-left panel), temperature in Kelvin (top-center panel), and SEP in kW/m^2 (top-right panel) at 3.282 seconds after release. The panels at the bottom (from left to right) show the max and mean SEP through time; the instantaneous histogram of the SEP; instantaneous bounded dimensions of the fire; and the rise height through time. Section D.1.2.23 provide post-processed IR images for all the tests.

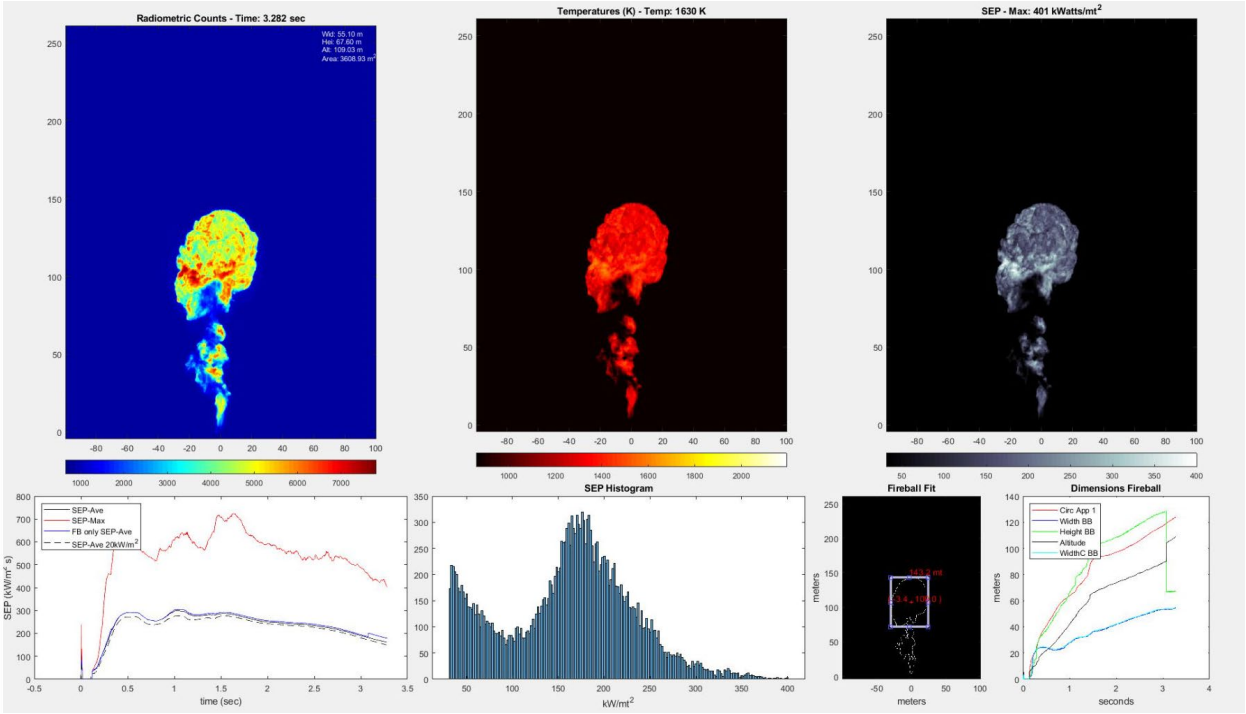

Figure D-29. Data frame with (top row) images from MWIR camera (from left to right) counts, temperature, and SEP. From left to right – bottom row: History curves for maximum and average SEP, histogram for the instantaneous SEP, Box fit for flame, and fire dimension history. Sample frame of the data from the SPR test and north side station.

Two tabulated data sets are generated and saved as excel files. One file contains the average SEP, max SEP, the average and maximum SEP when the fireball has a shape of a sphere; and average and maximum SEP that includes the smoke.

Smoke is assumed to have a SEP value of 20 kW/m^2, which would be expected from a perfect emitter (emissivity of 1) at about 770 K with no air transmission losses. This works perfectly with a 50 mm focal length lens where the linear calibration range covers 770 K, but for the 25 mm focal length lenses the lower end of the calibrated range is about 24 kW/m^2. For this, the pixels locations that cover the 20 kW/m^2 and the lower level of the calibrated range, are estimated by comparing it to the data collected with the 50 mm lens.

The second file contains physical dimensions of the fireball, that is, diameter from a fit that assumes a sphere, the width and height of a box fit, and its altitude, the width of the box when including smoke, the area of the fireball, and the area of the fireball when including the smoke.

D.1.2.18. Data Processing – IR and Visible Synchronization

The two X6900 MWIR cameras were synchronized to their adjacent VEO640s using the VEO's clock and had closely matched field of views. The synchronized images in Figure D-30 are of temperature (a), SEP (b), and visible color camera (c).

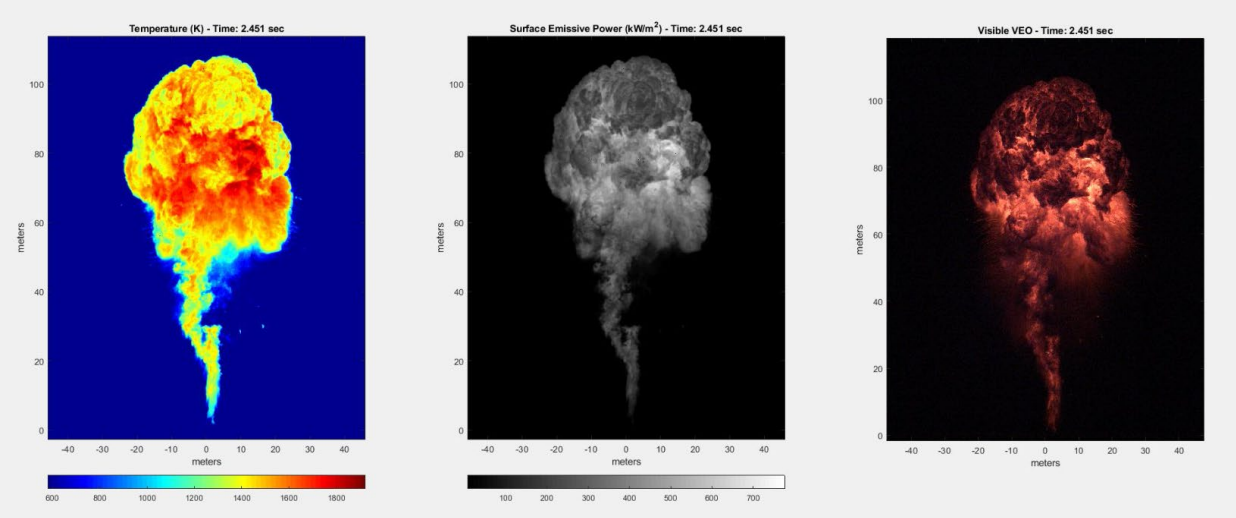

(a) (b) (c)

Figure D-30. Synchronized data from the X6900sc camera (temperature (a) and SEP(b)) and VEO640 (visible color camera(c)).

D.1.2.19. Data Processing – Estimating Speed of Gasified Crude Oil

With the high-speed cameras, the objective is to estimate the speed of escaping gasified crude oil from the 1000-gallon tank before ignition (Figure D-31). The image shows the escaping crude oil, a section of the image shows some of the oil already ignited, and at the bottom of the image we can see the tank mouth. The image also shows the location of where the speed of the crude oil is assessed. Figure D-32 shows a closeup section of where the velocity of the gas is tracked. The image shows vectors (blue arrows) generated by optical flow algorithms which provide an estimate of gas velocity. These cameras were used for the SPR (one camera) and Tight 2 (Tx Shale) tests. The SPR test used one high-speed camera and the velocity distribution results indicate an average velocity of 61.9 m/s (Figure D-

33). Three high-speed cameras were used for the Tight 2 (Tx Shale) test and the velocity distribution results indicate an average speed of 51.5 m/s, averaged among the cameras (Figure D-34).

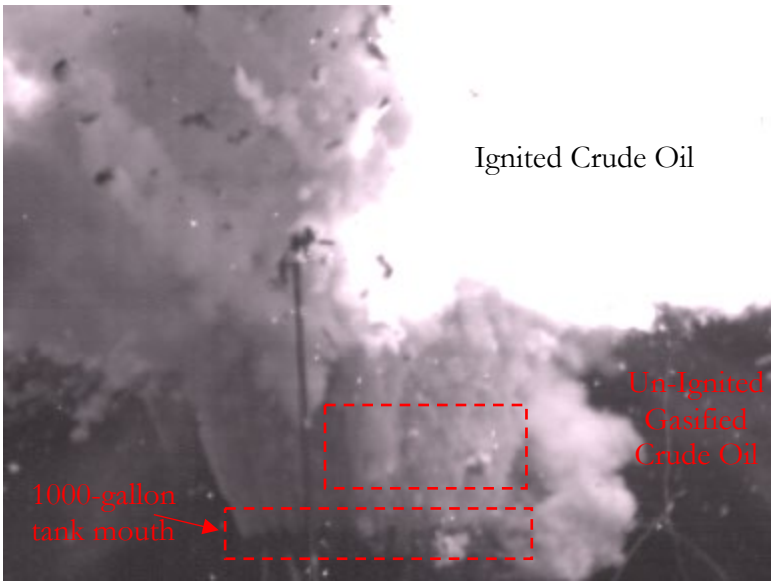

Figure D-31. Image from high speed camera 0.227 seconds after linear shaped charge ignition.

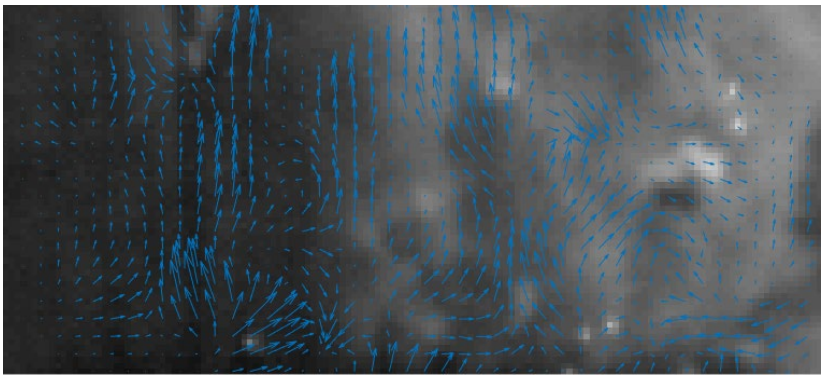

Figure D-32. Shows subsection of image (Figure D-31) where the speed of the crude oil is estimated. Blue arrows indicate gas speeds estimated by optical flow.

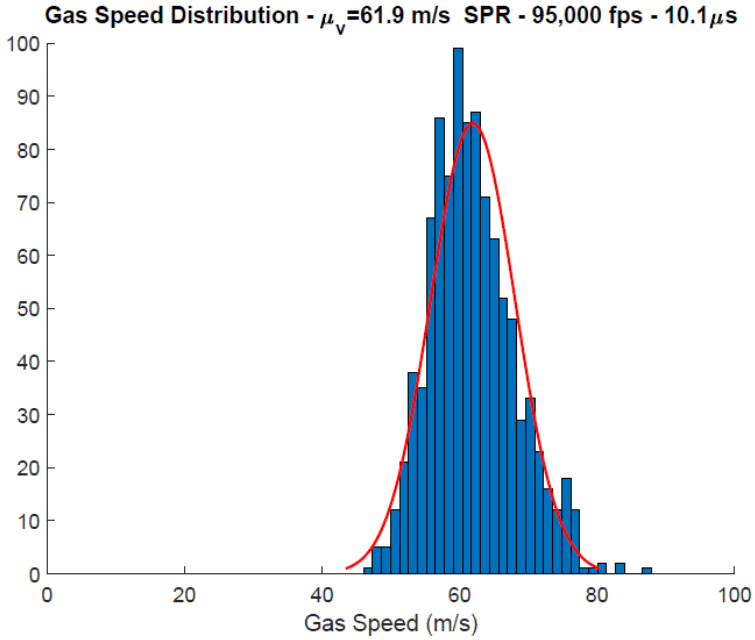

Figure D-33. Gas velocity distribution above tank right after release, SPR fireball test.

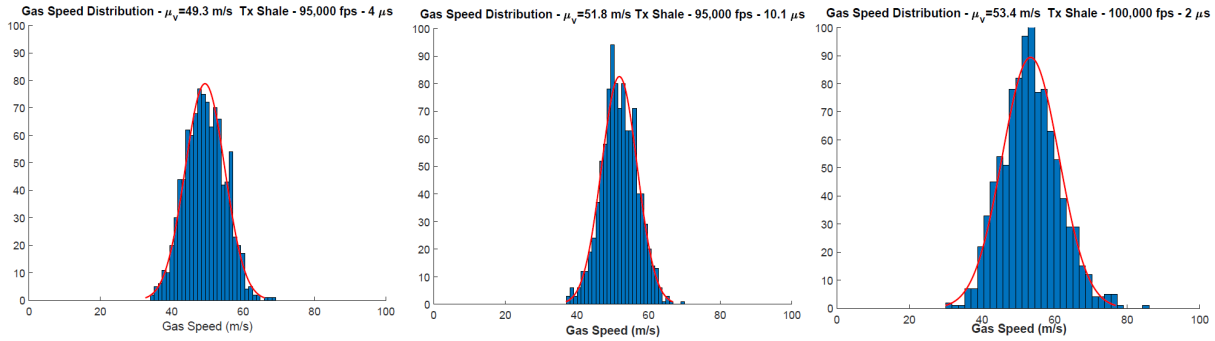

(b) (b) (c)

Figure D-34. Gas velocity distribution above tank right after release, Tight 2 (Tx Shale) fireball test. (a) Phantom V2511 cameras (b) Phantom v2511 camera, and (c) Phantom v2511 camera.

D.1.2.20. 100-Gallon Tank - Jet A Fireball Test

Data was collected for the 100-gallon tank with 38-gallons of Jet A conducted at the Lurance Canyon Burn Site facility (Figure D-35). For this test only the X6900sc with warm filters was used. IR data from this test was used to develop the analysis techniques used for subsequent tests. Post-processed data from the X6900sc IR camera is shown in Figure D-36.Video and tabular data are of the format specified in section D.1.2.17.

Figure D-35. Photometric trailer location at Lurance Canyon Burn Site facility.

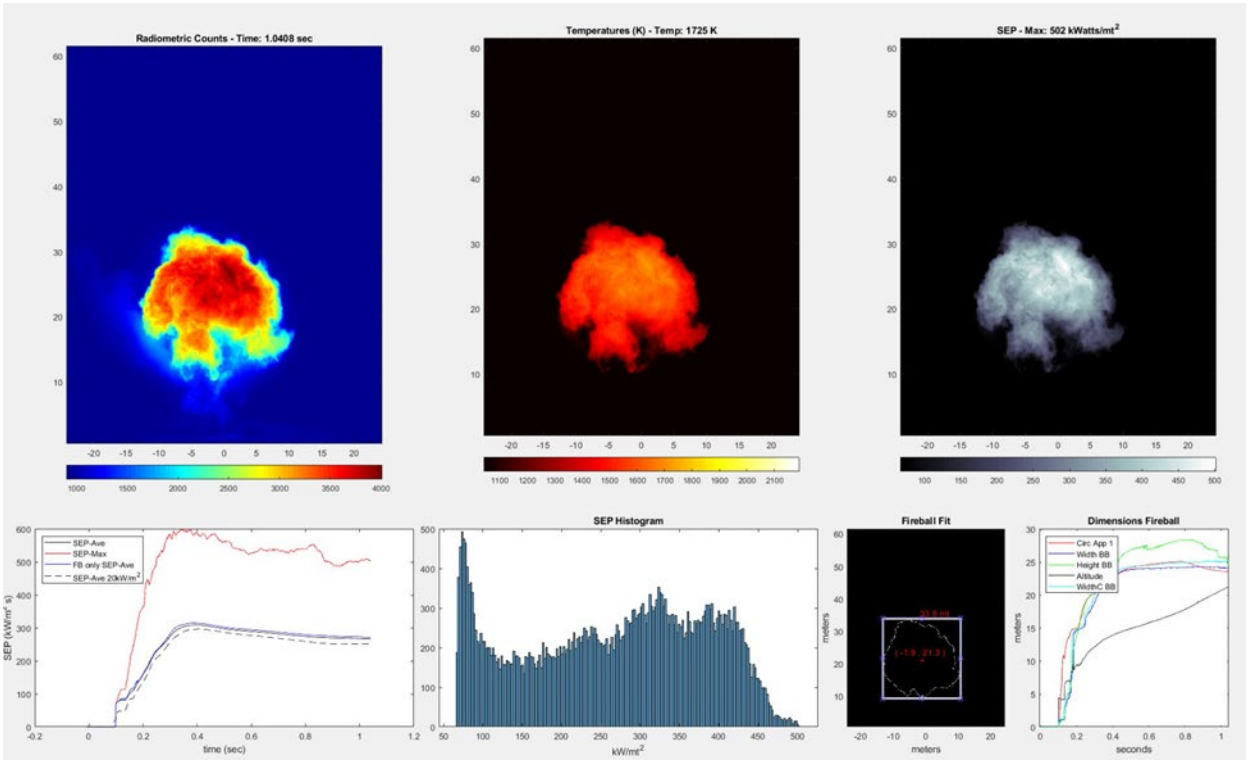

Figure D-36. Post-processed IR images from X6900sc (warm filter), 100-gallon Jet-A test.

D.1.2.21. 1000-Gallon Tank - Jet A Fireball Test - Flare

This test performed at the Lurance Canyon Burn Site Facility used 400-gallons of Jet-A. Instead of resulting in a fireball, the event resulted in a narrow flare about 10 to 15-meter long (see section A.3.2.1). For this test the two X6900sc IR cameras were used. Figure D-37 and Figure D-38 show post-processed data for the warm and cold filter IR cameras, respectively. Video and tabular data are of the format specified in section D.1.2.17.

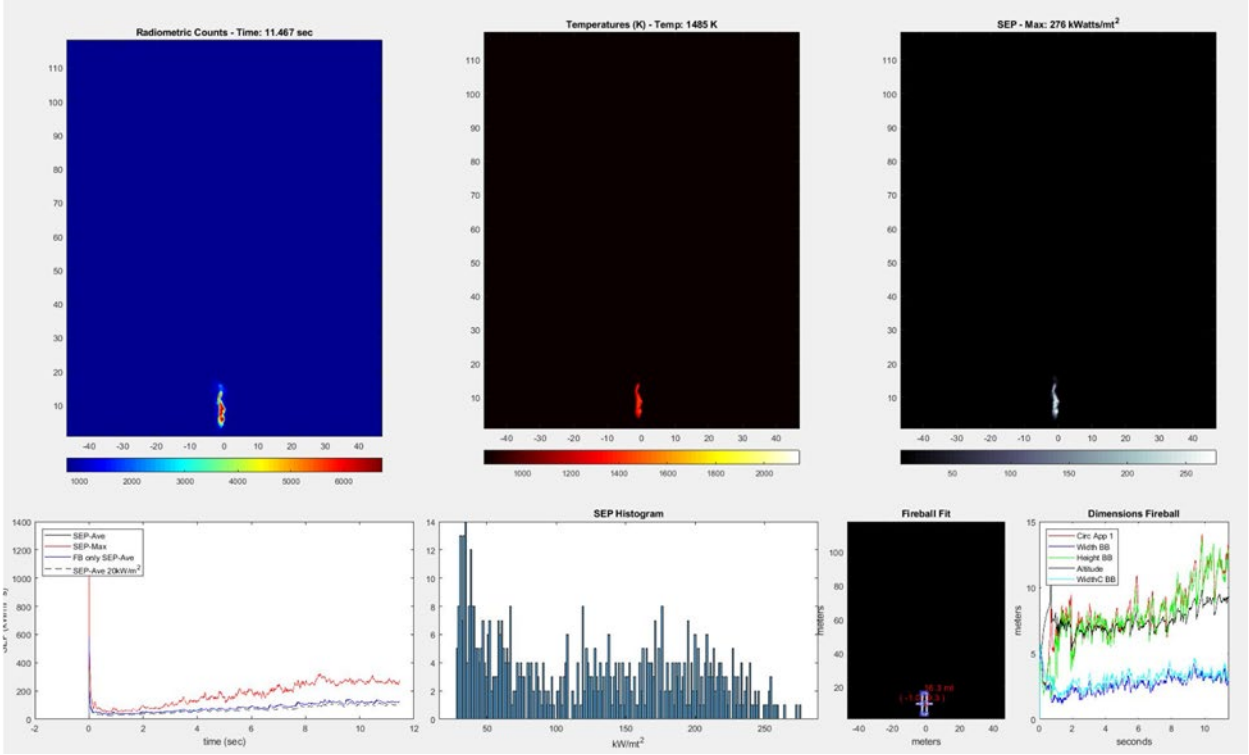

Figure D-37. Post-processed IR images from X6900sc (warm filter), 1000-gallon Jet-A test.

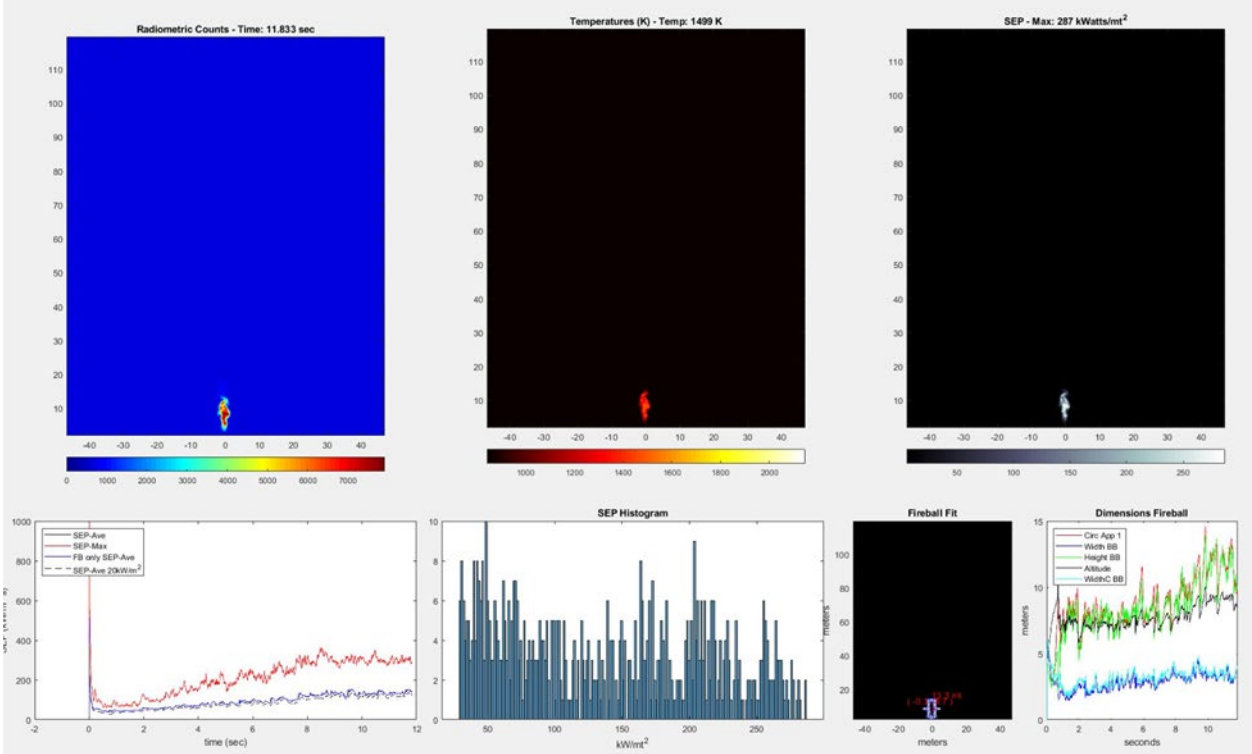

Figure D-38. Post-processed IR images from X6900sc (cold filter), 1000-gallon Jet-A test.

D.1.2.22. Explosiv e Synchronization Test

This test was performed at the Pad B to check the timing of the linear shaped charge that opens the rupture disk and the C4 charge used for ignition. To capture the timing, a Phantom v2511 camera running at 110,000 fps was used. Figure D-39 (a) shows the location of the camera and Figure D-39 (b) shows the rupture disk and explosive assembly. The sequence in Figure D-40 shows the ignition and shock wave of the linear shaped charge and the ignition of the C4 from the high-speed camera.

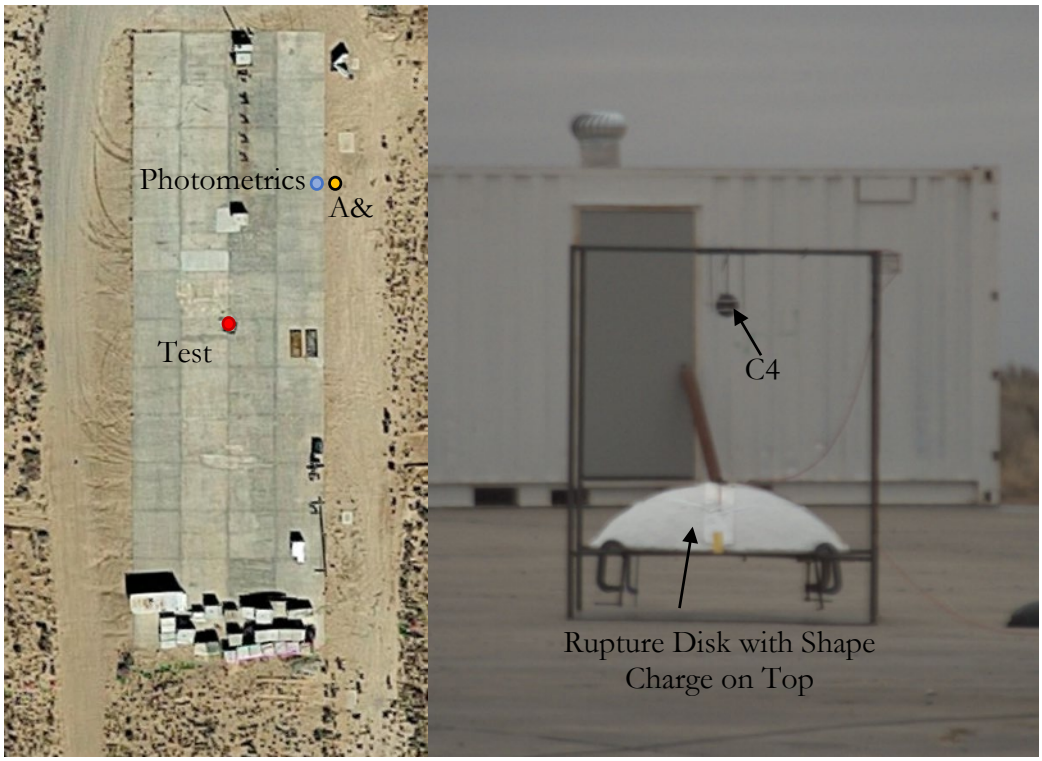

Figure D-39. Panel a) View on top of the synchronization check test at the south of the 10K feet sled track. Panel b) image of rupture disk with linear shaped charge and C4.

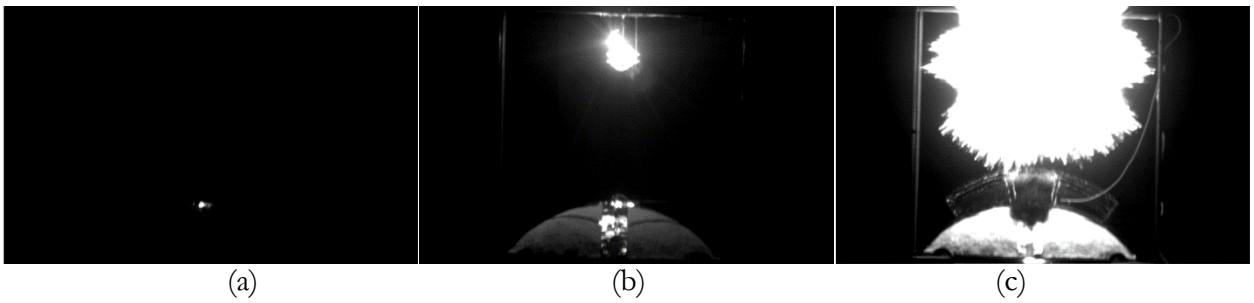

Figure D-40. Panel a) shows the flash from the detonator. Panel b) shows the ignition of the C4 9.7 μs later. Panel c) shows the shock wave from the linear shaped charge intersecting with the ignited zirconium encapsulating the C4 charge 226.75 μs later.

D.1.2.23. Post-processed IR images for 1000 -gallon fireball tests

Figure D-41 through Figure D-53 show post-processed images from the IR cameras for each of the tests.

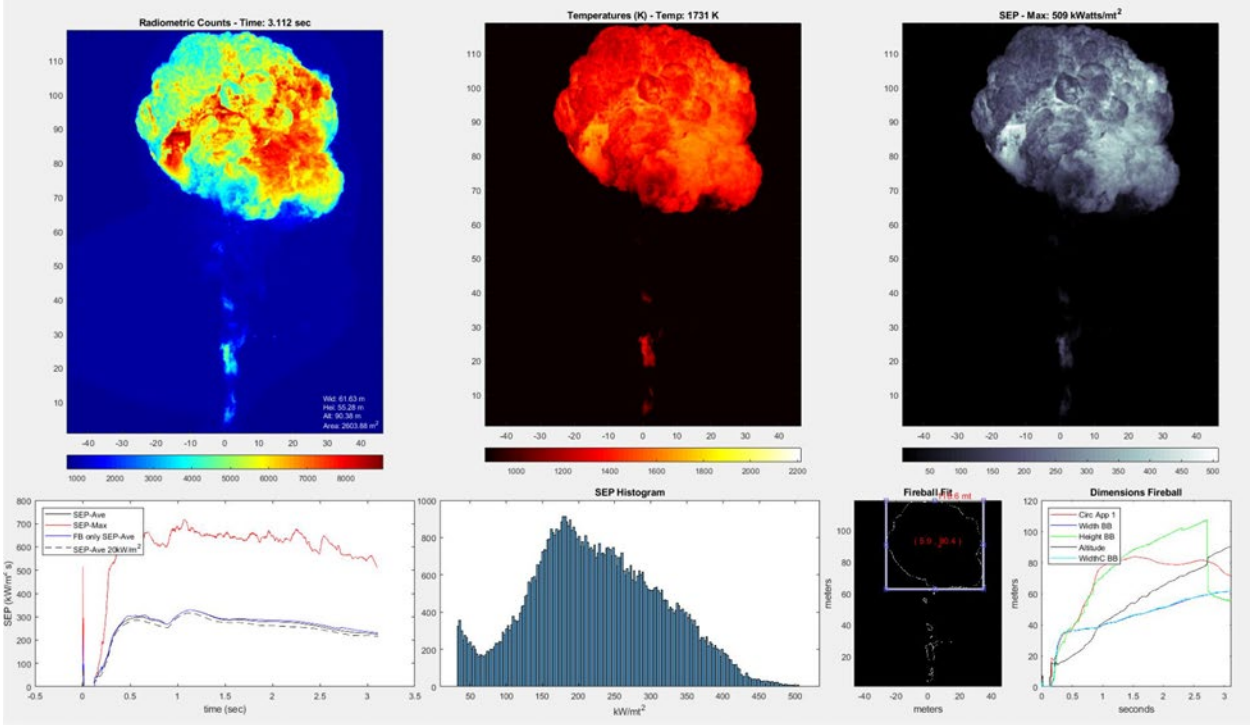

Figure D-41: Post-processed IR images from XT6900sc (cold filter, north trailer), Tight 1 (Bakken) test.

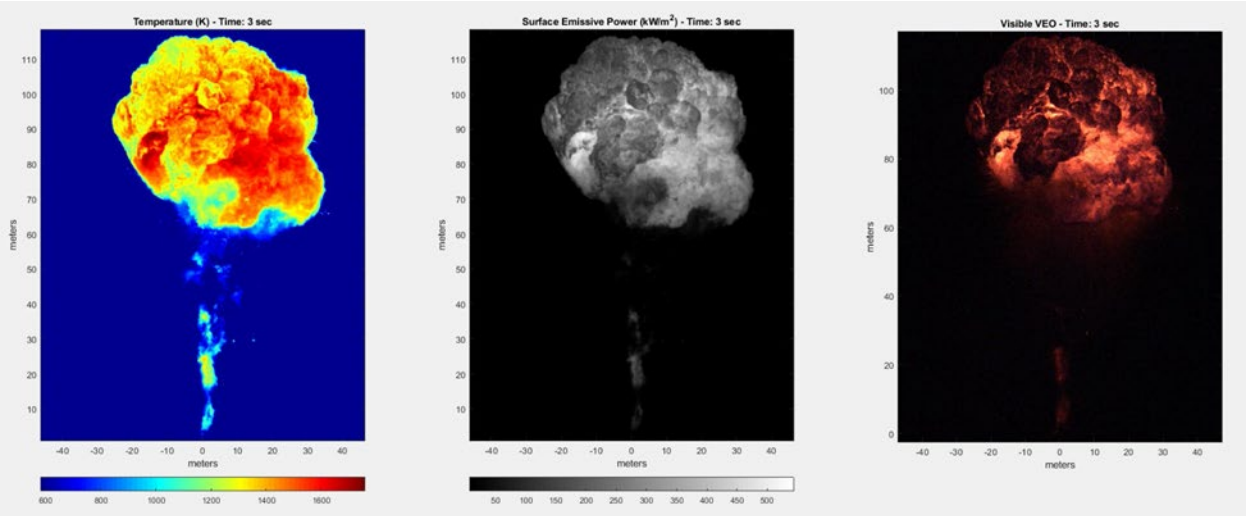

Figure D-42: Post-processed IR images from XT6900sc (warm filter) with VEO640 (north trailer), Tight 1 (Bakken) test.

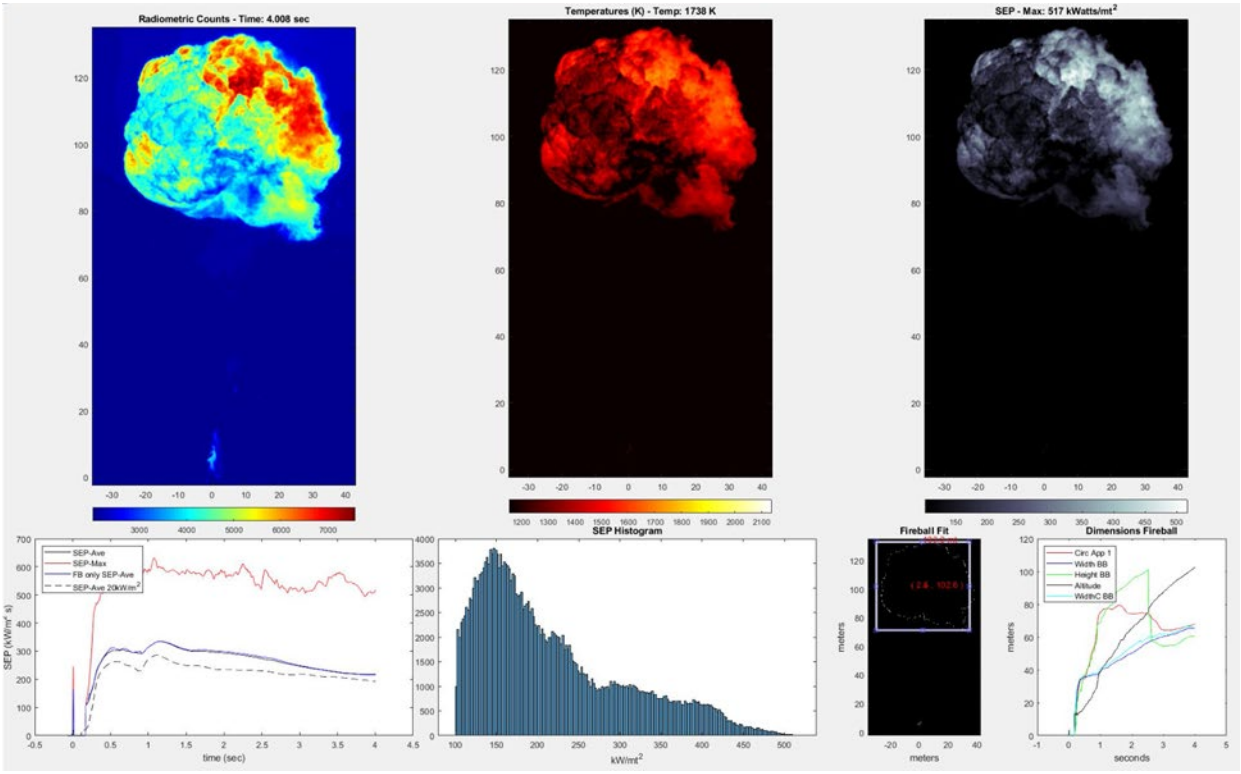

Figure D-43: Post-processed IR images from SC8313 (warm filter, north trailer), Tight 1 (Bakken) test.

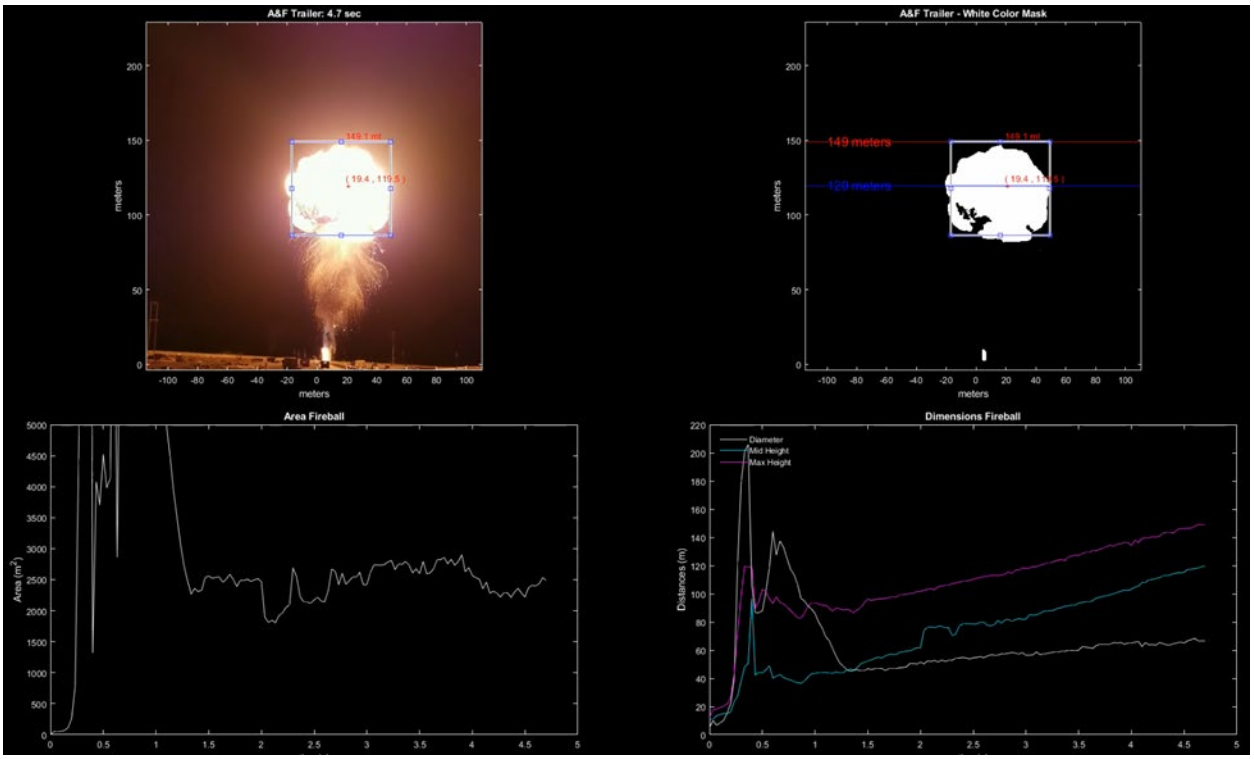

Figure D-44. Arming and Firing (A&F) post-processed video (north), Tight 1 (Bakken) test.

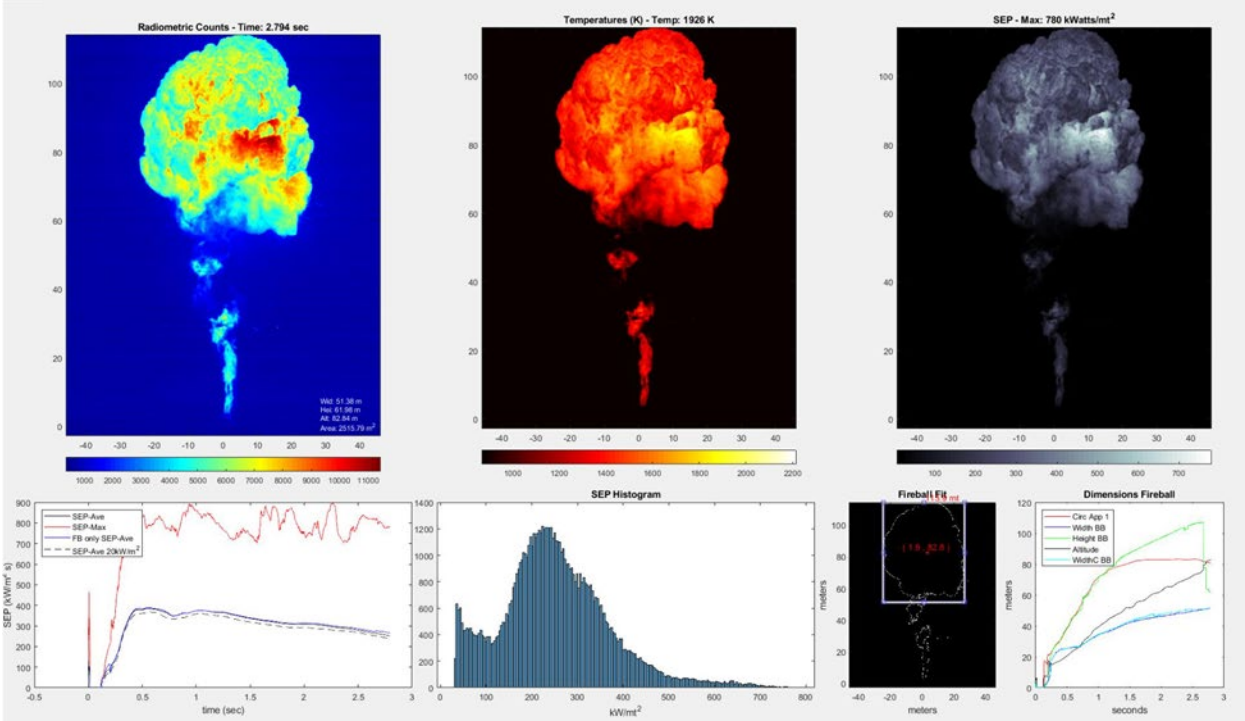

Figure D-45: Post-processed IR images from XT6900sc (cold filter, east trailer), Tight 1 (Bakken) test.

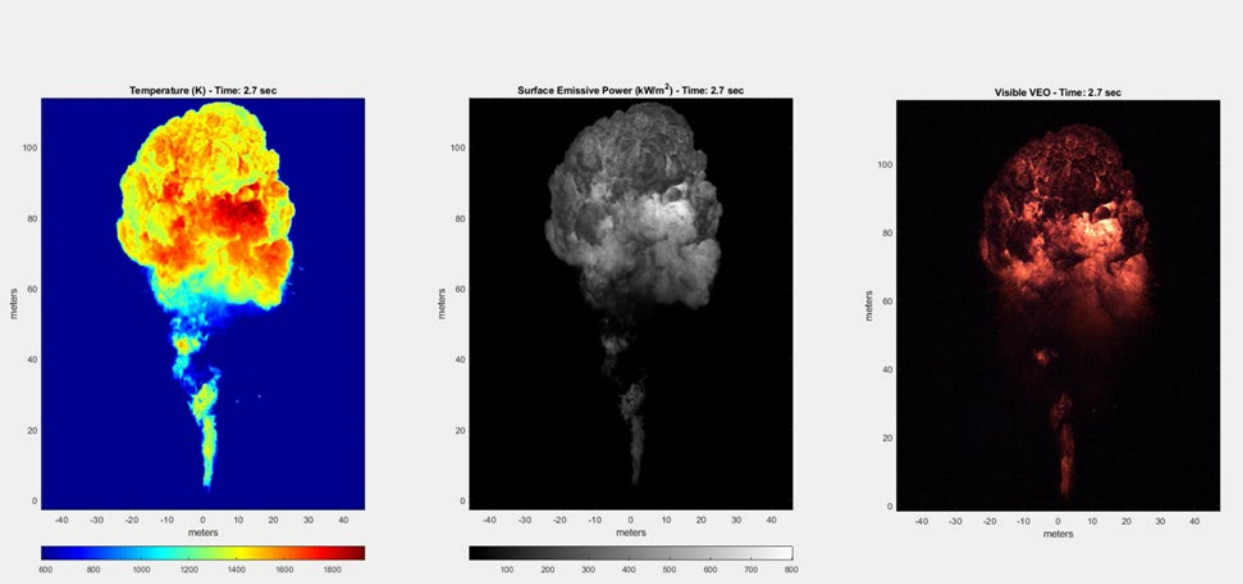

Figure D-46. Post-processed IR images from XT6900sc (cold filter) with VEO640 (east trailer), Tight 1 (Bakken) test.

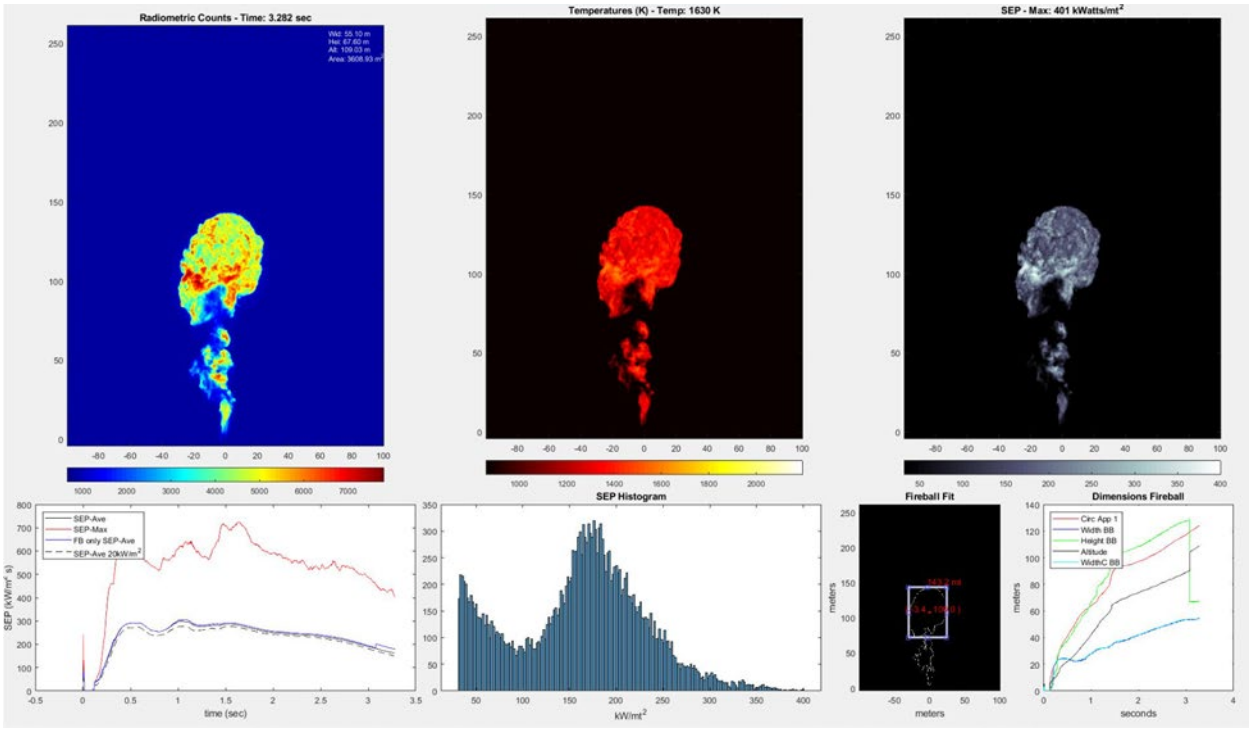

Figure D-47. Post-processed IR images from XT6900sc (cold filter, north trailer), SPR test.

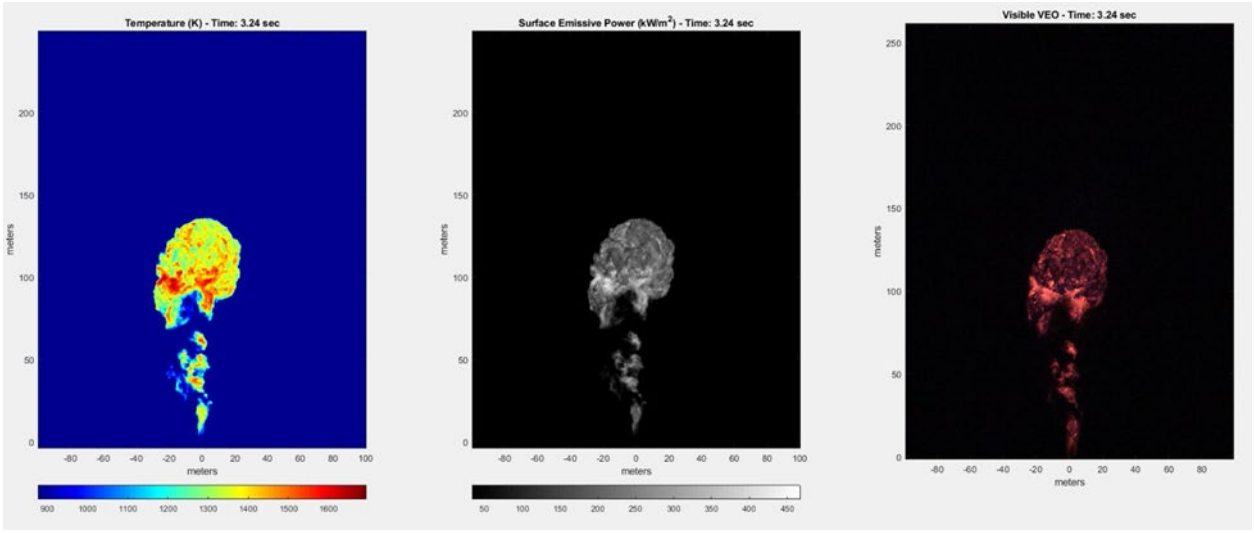

Figure D-48. Post-processed IR images from XT6900sc (warm filter) with VEO640 (north trailer), SPR test.

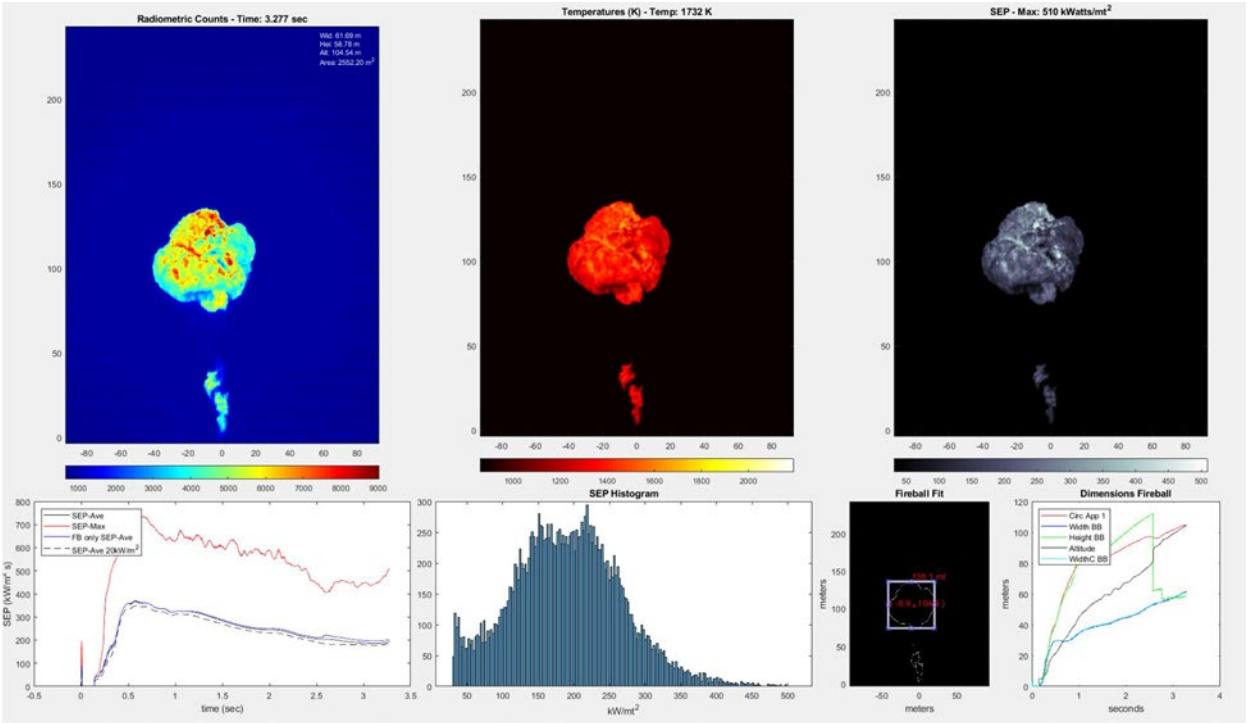

Figure D-49. Post-processed IR images from XT6900sc (cold filter, north trailer), Tight 2 (Tx Shale) test.

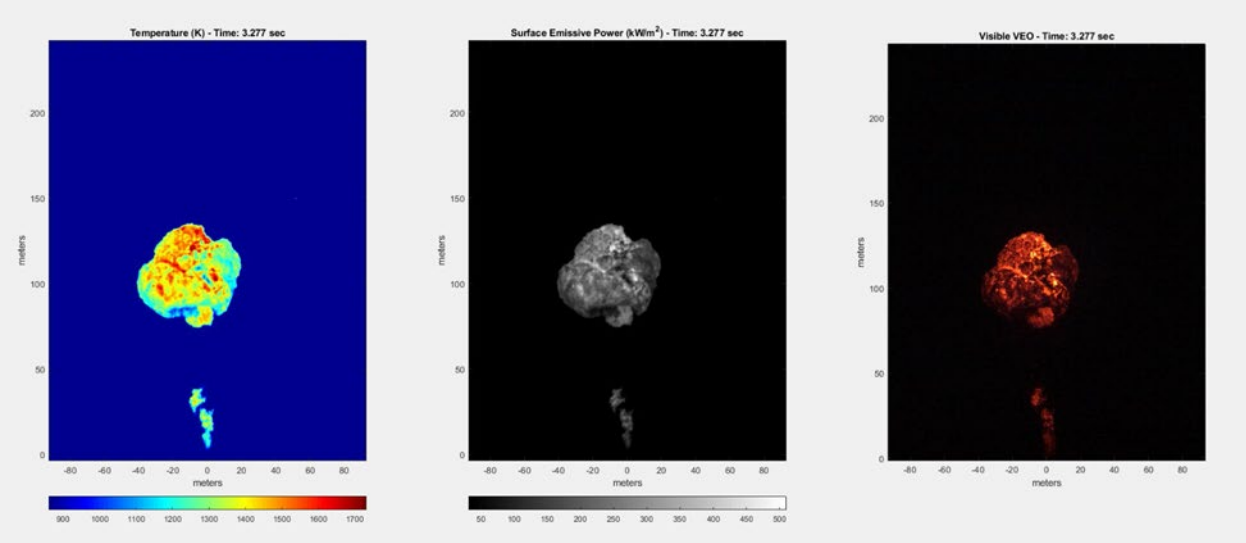

Figure D-50. Post-processed IR images from XT6900sc (warm filter) with VEO640 (north trailer), Tight 2 (Tx Shale) test

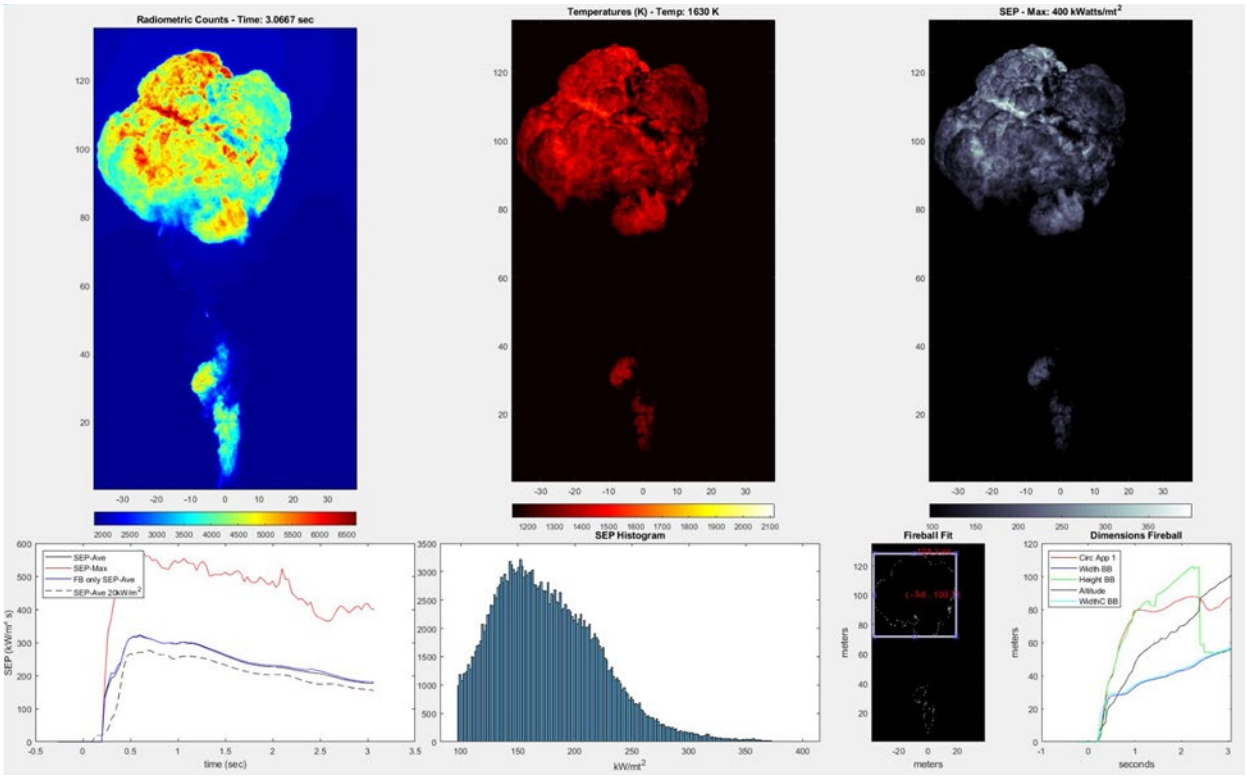

Figure D-51. Post-processed IR images from SC8313 (warm filter, north trailer), Tight 2 (Tx Shale) test.

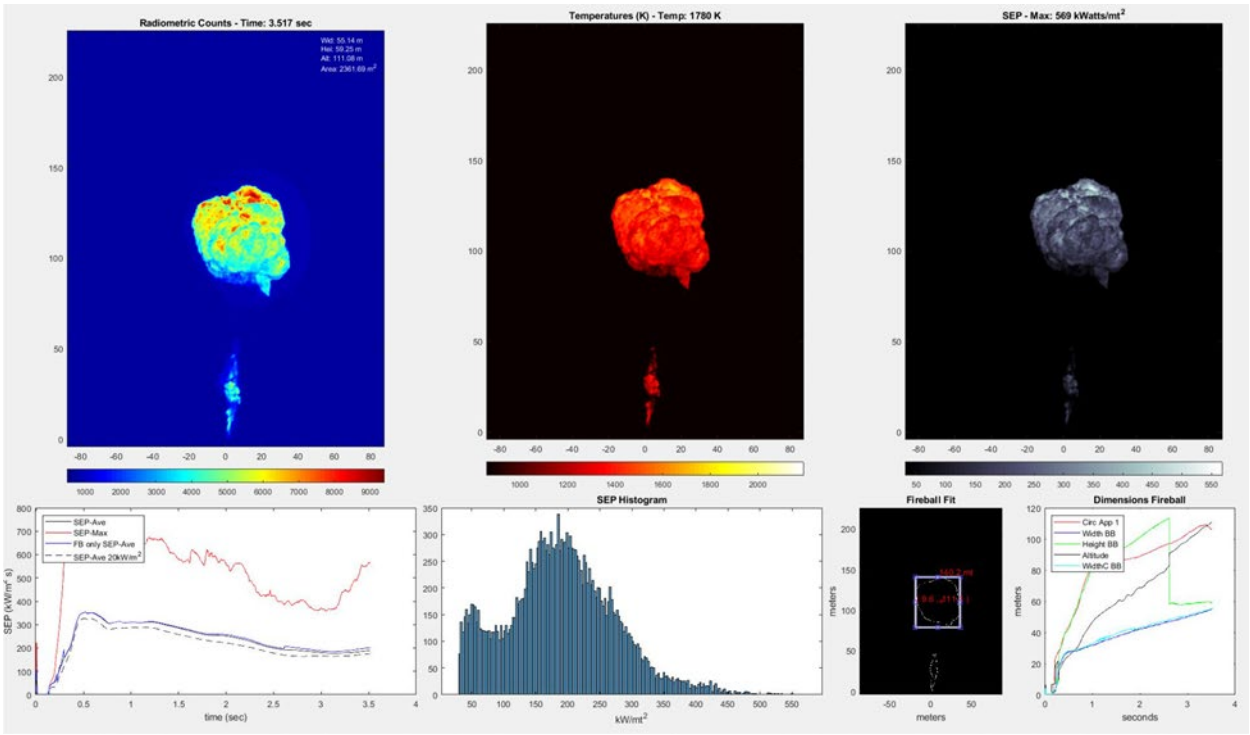

Figure D-52. Post-processed IR images from XT6900sc (cold filter, east trailer), Tight 2 (Tx Shale) test.

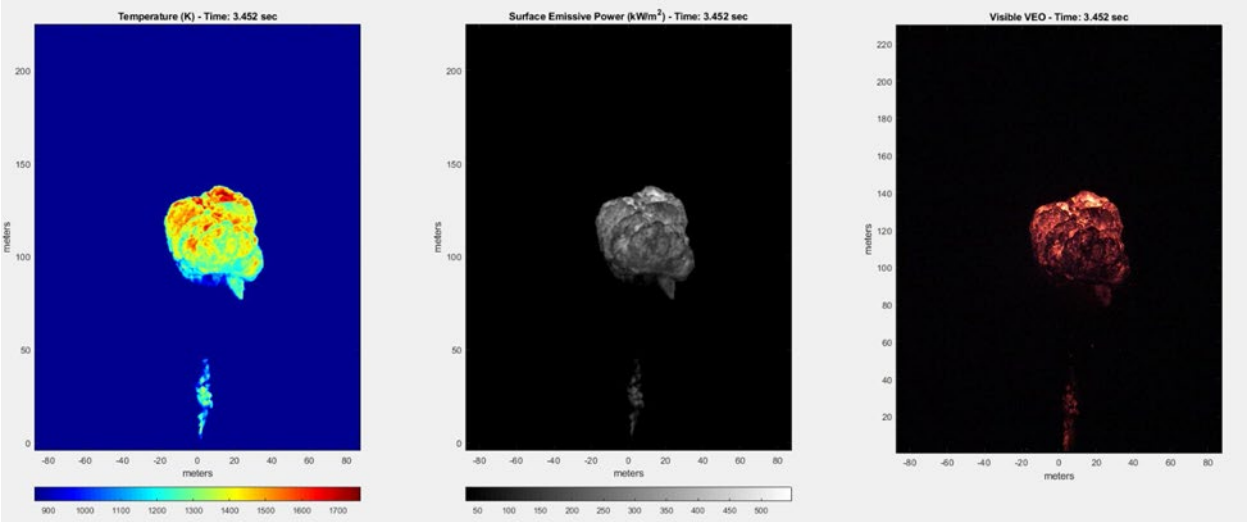

Figure D-53. Post-processed IR images from XT6900sc (cold filter) with VEO640 (east trailer), Tight 2 (Tx Shale) test.

D.1.2.24. Test progression images

Figure D-54 though Figure D-56 show sequential images taken from digital single-lens reflex (DSLR) cameras for each of the tests.

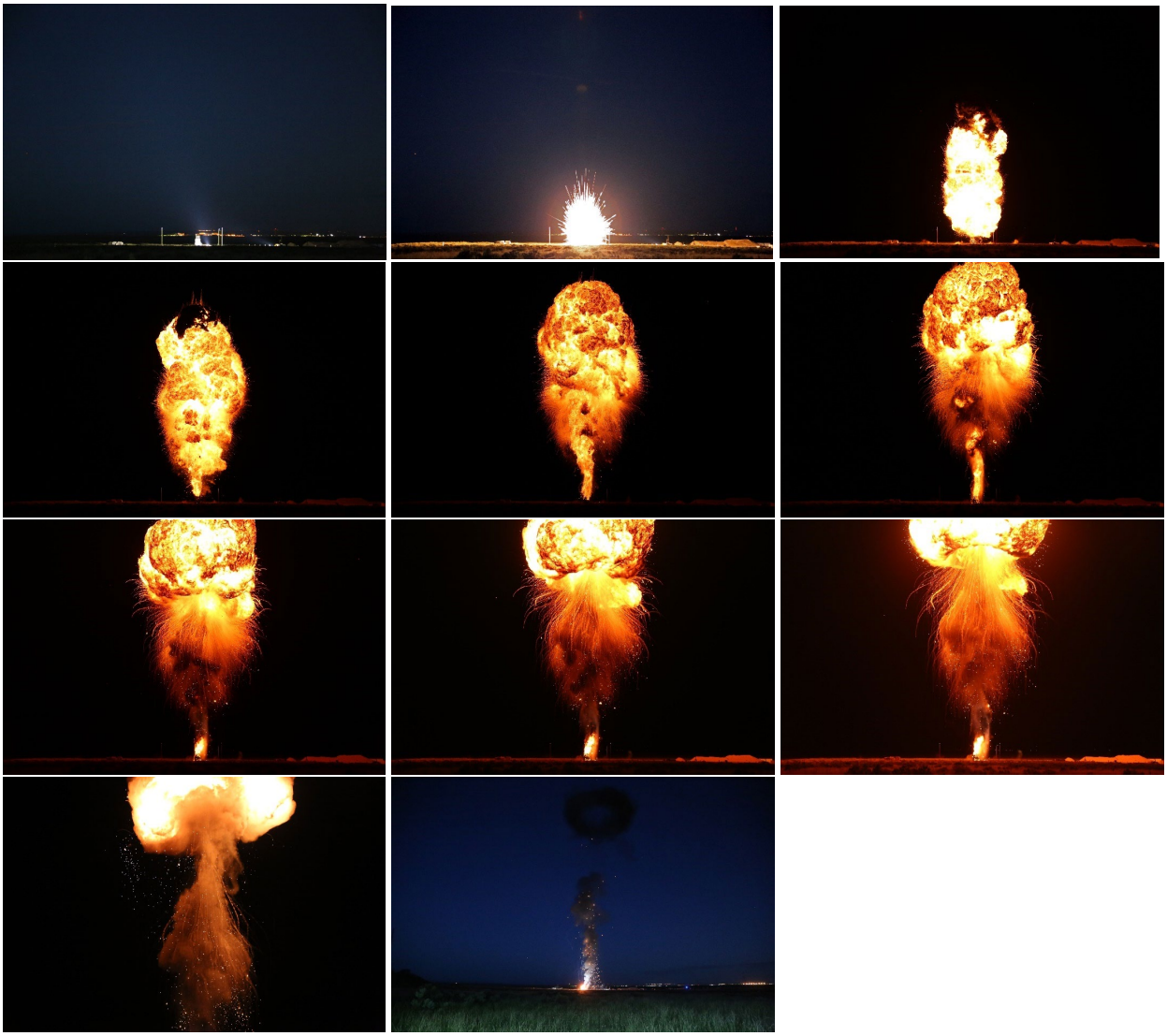

Figure D-54. Sequential images of Tight 1 (Bakken) test (east trailer).

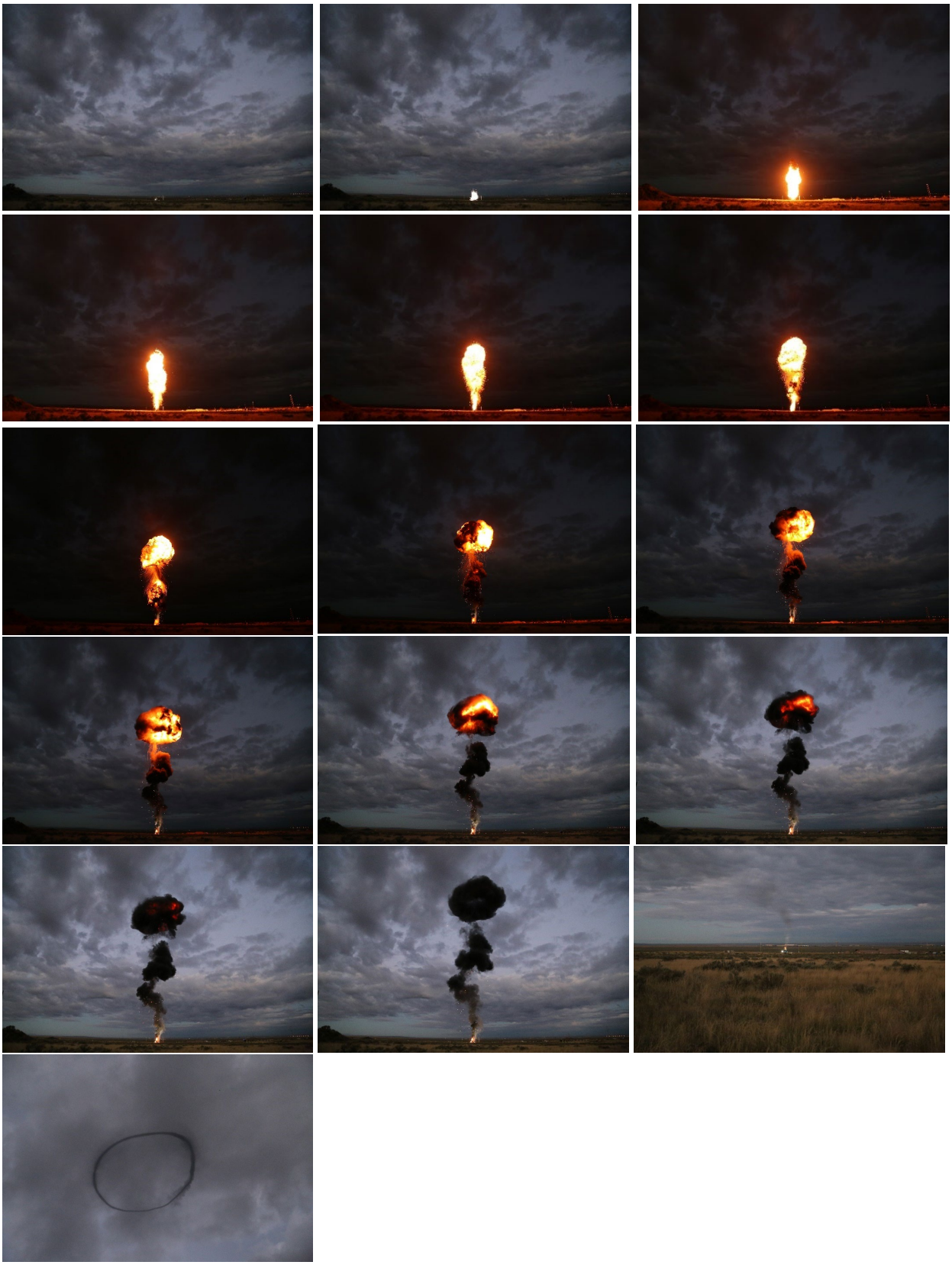

Figure D- 55: Sequential images of SPR test (east trailer).

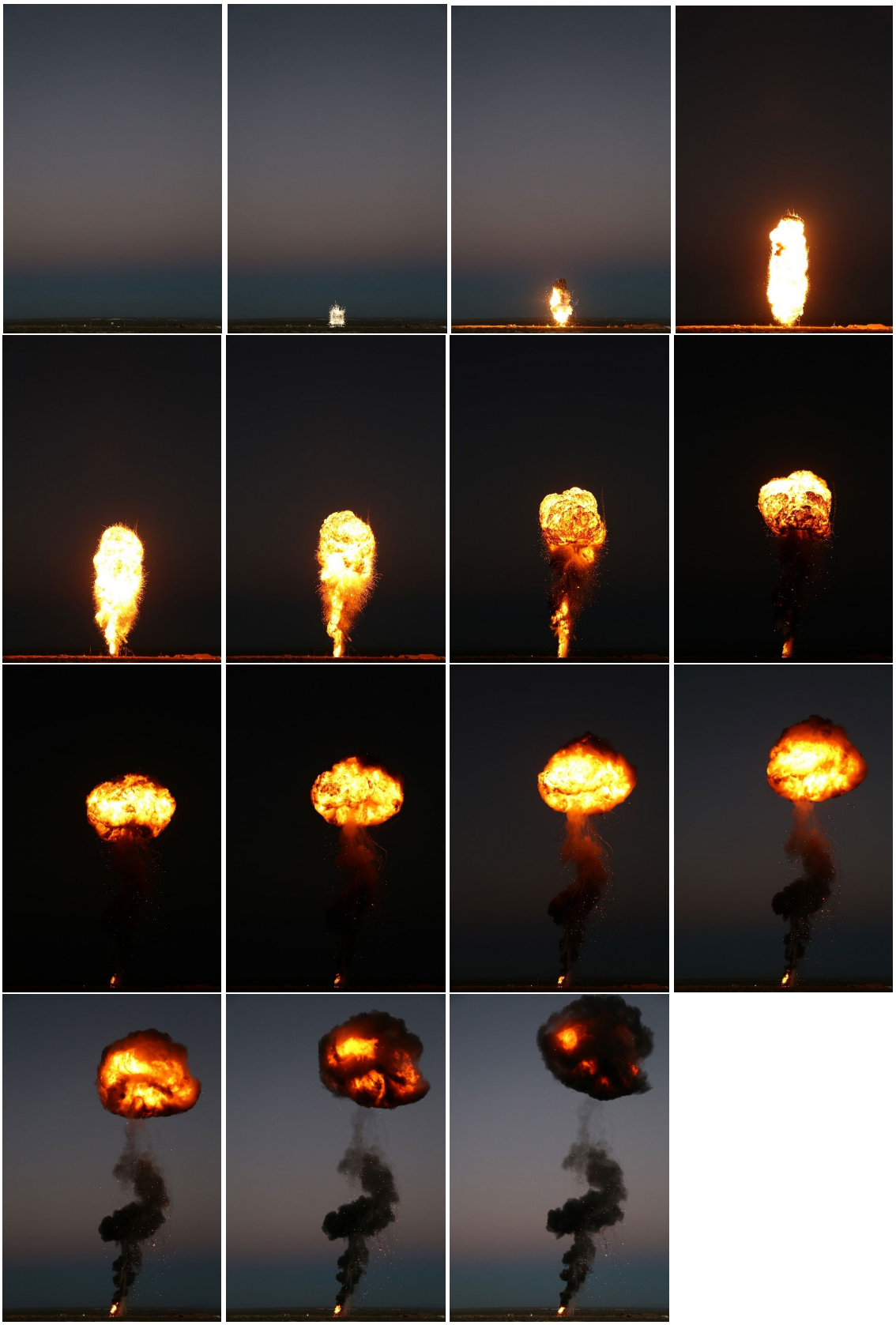

Figure D-56. Sequential images of Tight 2 (Tx Shale) test (east trailer).

D.1.2.25. GoPro camera images

Figure D-57 through Figure D- 59 show sequential images from GoPro cameras for each of the tests.

Figure D-57: Images from GoPro camera at ~30-m from tank, Tight 1 (Bakken) test.

Figure D-58: Images from GoPro camera at ~7.6-m from tank, SPR test.

Figure D- 59. Images from GoPro cameras at ~7.6-m from tank, Tight 2 (Tx Shale) test. Left to right: southwest camera, north camera and southeast camera.

D.1.2.26. Far-field sequential images of Tight 2 (Tx Shale) test

Figure D-60 shows sequential images of the Tight 2 (Tx Shale) test taken from the northeast camera 2 km away.

Figure D-60. Sequential images from far-field camera located 2 km away, Tight 2 (Tx Shale) test.

D.2. Atmosphere Attenuation

The calculations of air path transmission were estimated using HiTran, with the assumption of "SubArtic Lat 60N," during winter time. "SubArtic Lat 60N" is one of six environmental options provided for partial pressure estimations in HiTran. While Albuquerque is located at 35-degree latitude north, its desert area location tends to behave more like the "SubArtic Lat 60N" for the level of humidity. Note that for the 3-5μm transmission band, water and CO_2 are the main gases that will affect absorption. CO_2 is ubiquitous regardless of the season and location and its effect on absorption are well defined after a couple of meters. The effect of water absorption is pronounced after 5 meters, and the calculations with HiTran predicts 0.94 but given the dryness during the tests in December of 2017 and January of 2018, it was selected 0.95. Due to the uncertainty in values for emissivity and transmissivity, a sensitivity analysis was performed using various values.

D.3. Directional Flame Ther mometers (DFT)

Directional flame thermometers were used for both the 2-m and 5-m pool fire tests. A DFT consists of two Inconel plates (5-inch x 5 inch, 1/16 to 1/8 inch thick) sandwiching a lightly compressed, ceramic fiber blanket (Cerablanket, 8 lb/ft^3, 1 inch nominal thickness compressed to ¾ inch). Ungrounded junction, metal sheathed thermocouples are attached to the center of the *unexposed faces* of the metal plates by forming thin Nichrome foil tightly over the tip of the thermocouple and spot welding it around the thermocouple.

The 1-inch thick Cerablanket compressed to ¾-inch using SS standoffs in the all thread between the Inconel plates yields an effective insulation density of 170.7 kg/m^3 (nominal x1.333).

A typical DFT assembly usually has two MIMS type-K thermocouples attached to the inside center of each plate; thin SS shim stock straps were welded over the tip of each TC.

To obtain a uniform emissivity, the plates are normally cleaned with acetone, and then baked at 1000^0C for one hour. The post-bake emissivity of the DFT top plate outer surface will be measured with a SOC-410C Handheld FTIR Reflectometer.

Another means of providing uniform and known emissivity is to paint the DFTs with Pyromark® paint. Typical average and standard deviation of the emissivity of painted devices is 0.80 ± 0.02.

The temperature response of the plate, along with the assumption of 1-dimensional conduction and an insulated back surface allows one to use two methods to estimate the net flux to the surface from the TC measurements. Data reduction can be performed using either the Excel macro developed for the Sandia Heat Flux Gage (SNL-HFG) (Blanchat et al. 2005) or by use of an inverse heat conduction code called "Inverse Heat Conduction Program 1-Dimensional (IHCP1D) (Version 7.0) (Beck 1999). Other inverse heat-conduction programs are available, e.g., Sandia One Dimensional Direct and Inverse Thermal program (SODDIT) (Blackwell et al. 1980), but IHCP1D was chosen because it is commercially available, has a graphical user interface (GUI), and can be used on an IBM-compatible personal computer.

Input parameters of an inverse heat conduction program are wall thickness, thermal conductivity, and volumetric heat capacity; insulation thickness, thermal conductivity, and volumetric heat capacity, boundary conditions, temperature sampling period; and numerical inputs. One-dimensional heat transfer was assumed in all cases.

The following energy balances were assumed for the DFT and calorimeter heat flux calculations.

Calorimeter:

$$q_{total} = q_{absorbed} + \epsilon\sigma T_{surface}^4$$

DFT:

$$q_{incident} = \frac{q_{absorbed}}{\alpha} + \sigma T_{surface}^4 + \frac{h}{\alpha}\left(T_{surface} - T_\infty\right)$$

Figure D-61 provides the dimensions, materials, and measured emissivity values used for the calculations.

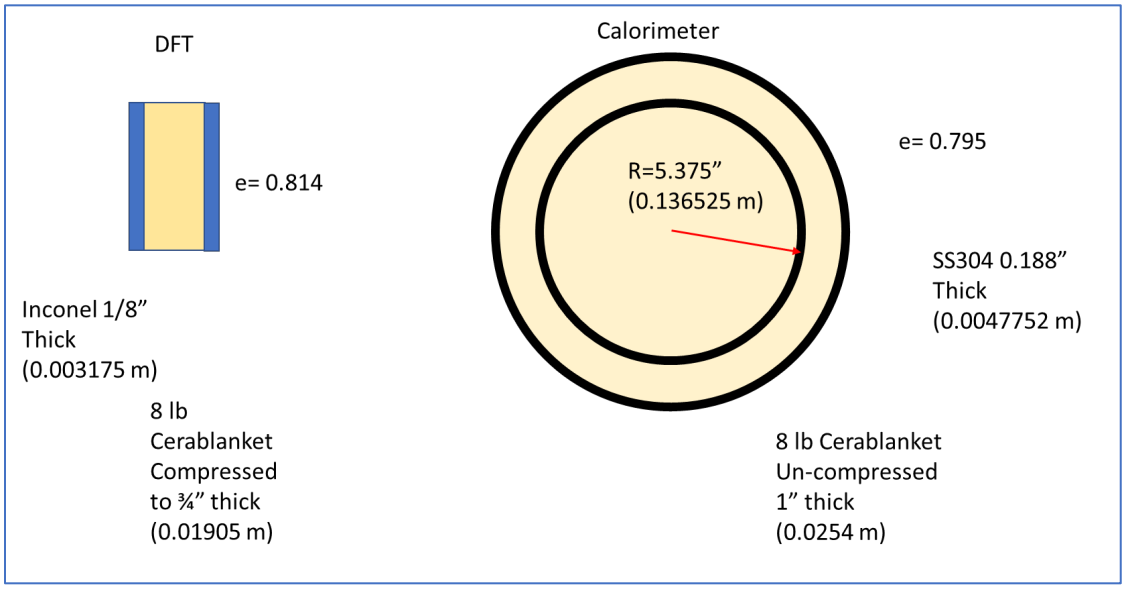

Figure D-61: DFT and Calorimeter specifications for heat flux calculations.

The thermal properties used for the calculations are the following.

Equations for density, thermal conductivity, and specific heat for SS304:

- $\rho = -0.4678\,T + 7877$ (kg/m^3) where T is in °C.
- $k = 14.898 + 0.015703\,T - 1.56 * 10^{-6}\,T^2$ (W/m-K) where T is in °C.
- $C_p = -5592 + 2731\,ln(T) - 417.9\,ln(T)^2 + 22.07\,ln(T)^3$ (J/kg-K) where T is in K.

Equations for density, thermal conductivity, and specific heat for Inconel 600:

- $\rho = -0.000035549 * T^2 - 0.36036496 * T + 8348.313$ (kg/m^3) where T is in °C.
- $k = 12.93 + 0.01664 * T$ (W/m-K) where T is in °C.
- $C_p = \begin{cases} 427 + 0.328\,T - 3.6x10^{-4}\,T^2 + 1.62x10^{-7}\,T^3, & T < 600^oC \\ 486 + 0.328\,T - 3.6x10^{-4}\,T^2 + 1.62x10^{-7}\,T^3, & T \geq 600^oC \end{cases}$ (J/kg-K) where T is in °C.

Equations for density, thermal conductivity, and specific heat for Cerablanket insulation:

- The density we are concerned with is 8 lb./ft^3 (128 kg/m3). The density does change when compressed, which occurs in DFTs. So, the compression from 1" blanket to ¾" when assembling DFTs increases the density by 1/3 to (1.33*8=) 10.67 lb./ft3 or 170.67 kg/m3
- $\ln(k) = -3.37 + 2.82x10^{-3} * T - 7.77x10^{-7} * T^2$ (W/m-K) where T is in °C. (compressed)
  $\ln(k) = -3.54 + 3.13x10^{-3} * T - 7.77x10^{-7} * T^2$ (W/m-K) where T is in °C. (uncompressed)
- $Cp = -0.00011 * T^2 + 0.39276 * T + 788.099$ (J/kg-K) where T is in °C

V. F. Figueroa (2005) determined how uncertainties in temperature measurements, material geometries, material properties, or code-input parameters can affect the estimation of heat flux when using an inverse heat conduction code. Results of the analysis showed that the most important parameters were temperature uncertainty (Nakos 2004), the surface metal thickness and volumetric heat capacity. The use of a constant thermal properties rather than temperature dependent values also made a significant difference in the resultant heat flux; therefore, temperature-dependent values should be used. The analysis determined a 15-19% uncertainty to 95% confidence when using inverse heat conduction methods, neglecting multidimensional effects.

D.4. Calorimeters

A calorimeter was place in the center of both the 2-m and 5-m pool fires to measure incident heat flux to objects engulfed in the fire. The calorimeters are constructed using a stainless-steel tube. The calorimeter dimensions are given in Table D-14.

Table D-14: Calorimeter dimensions

Length (inches)	OD (inches)	Thickness (inches)
39.25	10.75	0.375

Twelve (12) Type-K thermocouples (mineral-insulated, metal-sheathed (MIMS), 40 mil) are attached to the inside surface of each SS tube and the tube filled with rolled high-temperature ceramic fiber blanket insulation (CeraBlanket, 8 PCF).

The thermocouples were arranged in 3 rows in quarter increments along the length of the calorimeter as shown in Figure D-62. Four TCs, represented by the blue dots, were placed in each row at 90° intervals.

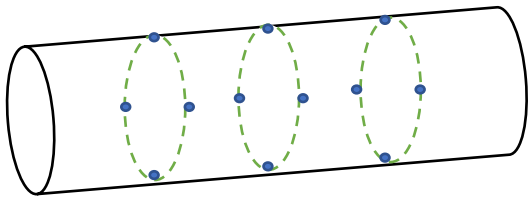

Figure D-62: Placement of TCs on inside surface of calorimeter.

The inverse heat conduction code called "Inverse Heat Conduction Program 1-Dimensional (IHCP1D) (Version 7.0) (Beck 1999) was used to reduce the temperature data to total heat flux. The calorimeters are painted with Pyromark paint. The calorimeter was place in the center of the pool and its bottom surface was at a distance 1-m above the bottom of the pan.

D.5. Fireball Shock Pressure

The Bikini gauge shown in Figure D-63 (8.5 x 11 inches) is a simple passive pressure gauge for air blast measurements. The use and theory of operation is described by Cooper (1984). A sheet of 1 mil (0.001 inch) aluminum foil is placed between the two steel plates, a shear (any amount) of the foil implies the pressure exceeded the rupture pressure shown in Table D-15, based on calibrations performed by Avery and Ball (1995).

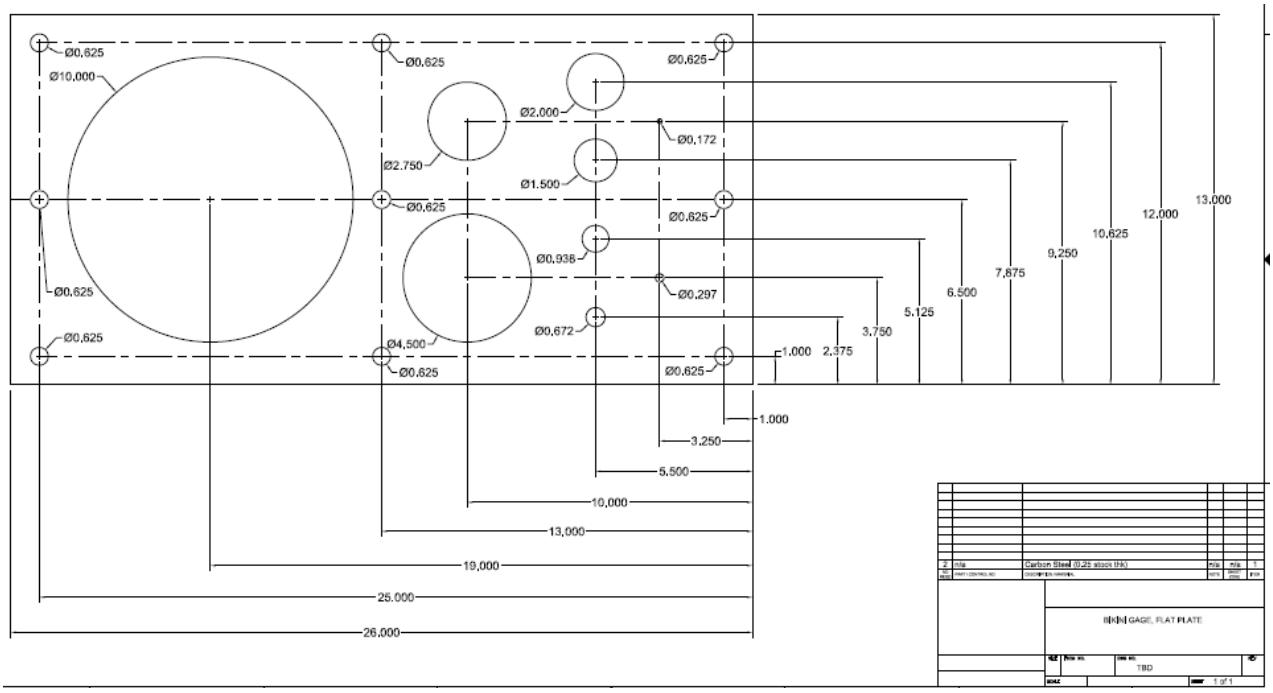

Figure D-63: Bikini air blast gauge.

Table D-15: Rupture pressure vs. Bikini gauge hole size.

Hole diameter (in)	Pressure to rupture (psi)
10	1.0
4.5	1.9
2.75	2.8
2	3.7
1.5	4.6
0.938	6.9
0.672	9.1
0.297	18.0
0.172	28.0

D.6. Pool Fire Fuel Liquid Level Control and Regression Rate

The pool fire tests were performed with a liquid level control system designed to maintain a constant level of liquid fuel in the pan (with ±1 mm of the desired height).

The test tank is connected to the fuel pan via a 1-inch and 2-inch penetration in the upper head and a 1-inch and 2-inch cycling control valve for the 2-m and 5-m pools, respectively. The original plan for the test series was to drive oil into the pool pans with water. Water entrainment occurred during the first 2-m pool fire test using SPR oil, leading to a boil over event. Thus, it was decided to use oil to push oil into the pan.

The fuel height in the pan is measured using a Rosemount Model 3051 differential pressure gauge. When the differential pressure measurement falls below the lower set point the controller opens the 2-inch fuel control valve forcing oil into the 5 m pan. When the differential pressure reading reaches the upper set point the controller closes the control valve. The mass loss rate from the pool is based on the fuel flow rate from the tanker. The fuel regression (mass loss) rate is then determined based on the crude oil density and the fuel pan area.

The liquid level and the temperature distribution across the depth of the liquid fuel in the fuel pan was monitored using a thermocouple rake. Thermocouples (type-K, mineral-insulated, metal-sheathed (Inconel), 0.040-inch diameter) were mounted on a steel rake. The thermocouple spacing is 2 mm to allow fine control of the fuel level.

D.7. Meteorolog y

The tests required meteorological support to assist with minimizing potential unanticipated environmental effects and identifying optimal burn conditions. Operational support includes the collection, analysis, and forecasting of meteorological data, ambient weather conditions, and weather criteria prior, during, and after the fire. The Environmental Programs and Assurance Department provides data acquisition and collection of near field meteorological information and weather forecasts to support the tests. The activities included Prognostic Meteorological Forecasts (various forecasts windows).

Meteorological data (wind direction and velocity, temperature, relative humidity and barometric pressure) were recorded with near-field instruments approximately 800 ft from the test site.

D.8. Temperature

The thermocouples used were mineral-insulated metal-sheathed (MINS) Type-K. Temperature range for Type-K thermocouples is -200 to 1250°C. Sheath diameters varied depending on the required use, for example, 0.04 inches for fuel rakes, 0.0625 inches for tank walls, and 0.25 inches for tank thermowells. The ANSI standard uncertainty for Type K thermocouple wire is 2.2ºC or 0.75% of reading (in ºC), whichever is greater. A quality control process is in place to inspect TCs upon receipt, check for damage, perform resistance checks, and verify TC functionality in both cold and hot conditions. Thermowell checks of the thermocouples at 100°C yielded an average and standard deviation of 98.8±2.0°C; at 0°C the checks yielded an average and standard deviation of 0.7±0.8°C. All thermocouples were fabricated from the same spool of wire; a few thermocouples that were fabricated from the spool were calibrated for QA purposes.

D.9. Gas Sampling and Heat Release Rate Instrumentation

For the indoor 2-m pool fires tests, oxygen consumption calorimetry was used to determine fuel heat release rate (HRR). An IRGAS FTIR/O2 GAS ANALYZER was used for the HHR measurements. The repeatability of both the IRGAS system and Oxymat 61 should be under 1%.

IRGAS FTIR Gas Analyzer System for the concentration measurements of O_2, CO, CO_2, NO, NO_2, & SO_2, consists of the following components:

9. ABB Bomem's MB3000 FTIR Spectrometer, ZnSe Optics,
10. DTGS detector, Preset At 2-Cm-1 resolution, pre-aligned Michelson-Type Interferometer
11. Scout-EN (15-Cm) gas cell, 316l SS cell body, Ni-plated coating, Kalrez O-rings, ZnSe Windows Heated
12. Integrated Plc + Pwr Supply for control of temperature and pressure sensor
13. Temperature & Pressure Sensors For Gas Cell
14. Hitran/PNNL calculated gas calibrations: CO (0-2000ppm), CO_2 (0-8,5%), NO_2 (0-200ppm), NO (0-500ppm), SO_2 (0-200ppm)
15. SPGAS specialty gas analysis software for weighted average multiband, multicomponent application
16. Siemens Oxymat 61 Paramagnetic Alternating Pressure (oxygen analyzer with calibration for 0-22% output), integrated with IRGAS output data and display.

The procedure to reduce the data following that from reference [73] was utilized since O_2, CO_2, CO and H_2O were measured.

The equations are as follows.

$$M_e = 18 + 4\left(1 - X^e_{H_2O}\right)\left(X^e_{O_2} + 4X^e_{CO_2} + 2.5\right) \tag{D.1}$$

$$\frac{\dot{m}_a}{M_a} = \frac{\left(1-X^e_{H_2O}\right)\left(1-X^e_{O_2}-X^e_{CO_2}-X^e_{CO}\right)}{\left(1-X^o_{H_2O}\right)\left(1-X^o_{O_2}-X^o_{CO_2}\right)} \frac{\dot{m}_e}{M_e} \tag{D.2}$$

$$\varphi = \frac{X^o_{O_2}\left(1-X^e_{CO_2}-X^e_{CO}\right)-X^e_{O_2}\left(1-X^o_{CO_2}\right)}{\left(1-X^e_{O_2}-X^e_{CO_2}-X^e_{CO}\right)X^o_{O_2}} X^e_{O_2} \frac{M_{O_2}}{M_e}\dot{m}_e \tag{D.3}$$

$$\dot{q} = \left[E\varphi - (E_{CO} - E)\frac{(1-\varphi)}{2}\frac{X^e_{CO}}{X^e_{O_2}}\right] M_{O_2} \frac{\dot{m}_a}{M_a}\left(1 - X^o_{H_2O}\right)X^o_{O_2} \qquad (MW) \tag{D.4}$$

where,

E – energy released by complete combustion per unit mass of oxygen consumed. Average value for hydrocarbons is 13.1 MJ/kg but if fuel composition is known then a more precise value can be used. However, the stoichiometric reactions for the crude oils are unknown, thus this average value

was used along with a standard deviation of 1.86 as a best estimate. The standard deviation value was taken from reference[74].

E_{co} – Net heat release per unit mass of O_2 consumed for combustion of CO to CO_2 (≈ 17.6 MJ/kg of O_2).
X – mole fraction
a – incoming air
e – exhaust gases
$\dot{m}$ – mass flow rate (kg/s)
o – value before combustion

To determine the theoretical heat release rate based on the burn rate and the measured heat of combustion the value of heat of combustion for the SPR oil was taken as 43,242 kJ/kg.

D.10. Data Acquisition System (DAQ) and Data Quality

The tests use National Instruments hardware and LabView software. The DAQ system for the tests at the Burn Site was a remote DAQ PXI-1052. The system is made up of the following hardware:

1. PXI-1031 Chassis – the chassis has 4 PXI slots
2. PXI-8102 Embedded Controller- embedded computer running LabVIEW
3. PXI-6251 DAQ Card
4. SCXI 1001 Chassis-12 SCXI slots
5. SCXI 1102 32 channel Thermocouple Mux- 3 ea.
6. SCXI 1104 32 channel 40 Volt Mux - voltage measurements
7. SCXI 1121 4 channel Isolated Input Card - Endevco pressure gauges
8. SCXI 1125 8 channel Isolated Input Card - Medtherm HF gauges
9. SCXI 1124 6 channel D/A Analog output Card - control signal for heaters
10. SCXI 1160 Digital Output Card – valve control

This system acquires low speed data at 1 Hz.

The fire ball test uses an additional PXI-1031/PXI-6132 system for high speed data acquisition at 10,000 Hz.

PXI-1031/PXI-6132 High Speed system is made up of the following hardware:

1. PXI-1031 Chassis – the chassis has 4 PXI slots
2. PXI-8820 Embedded Controller- embedded computer running LabVIEW
3. PXI-9132 4 channel High Speed DAQ Card – 2 ea. High speed pressure and heat flux measurements.

Power is provided to the DAQ system through an APC 1400 UPS. The earth ground runs through the APC UPS to the DAQ chassis.

The data acquisition system (DAQ) was calibrated via a TC calibrator (secondary standard). Calibrations were performed at 50°C increments from -100°C to +100°C for all thermocouple channels used during the experiments.

Historical calibration results for the DAQ indicates a $<0.5^0$C difference for all temperatures. Typical results for "normal" environments (e.g., maximum of 300-400 K) showed the total uncertainty to be

about ±1% of the reading in Kelvin which includes error contributions by the DAQ, instruments, and mounting to 95% confidence as documented in SAND2004-1023 (Nakos 2004).

In high temperature or high heat flux ("abnormal") thermal environments, total uncertainties range up to ±2-3% of the reading (maximum of 1300 K). The higher uncertainties in abnormal thermal environments are caused by increased errors because of imperfect thermocouple attachment to the test item.

Determination of the actual desired temperature (wall temperatures of an object or fluid temperatures) is subject to additional bias errors due to mounting. These bias uncertainties are very hard to accurately quantify, are application dependent, and are often the largest errors in the measurement system. For the present tests the bias error is assumed to be small compared to the thermocouple uncertainty.

This page intentionally blank

APPENDIX E. TEST PROCEDURES

E.1. Pool Fire Test Procedure

The tank filling and test operations required special procedures to maintain a pressure of 10-20 psi above the oil vapor pressure and prevent air contact. The overall procedure for the pool fire tests, using either the 200-gallon tank at the FLAME facility or the 1000-gallon tank at LCBS, involved first purging all air lines and tanks using water. Once purged of air, the tank is then filled with water. The oil is then introduced through a penetration near the top of the tank to drive the all water out of the tank. Oil is then introduced at a penetration near the bottom of the tank to drive the oil out the top of the tank and through a hose connecting the tank and pool pan. The fuel is immediately ignited once it starts filling the fuel pan. The schematic of the process and equipment involved in filling is provided in Figure E-1.

Note that the pressure in the tank and lines are monitored and maintained at 10-20 psi above the oil vapor pressure during the fill and test process. The water pump is equipped with a variable frequency drive (VFD) which is used to maintain the desired pressure on the tanker and feed lines to prevent a phase change. A throttle valve is used to set the flowrate.

A constant liquid fill method is used for both the 2-m and 5-m pool fires with a liquid height of about 2 to 3 inches and 3 to 4 inches, respectively. The pan level control uses a modulating valve to control oil flowrate to pan. A modulating valve was chosen for two reasons: to ensure that the flow to the pan did not exceed the water pump's capacity such as to lower the pressure below the oil vapor pressure, and to reduce flow surges in feed to pan. The liquid height in the pan was measured using a differential pressure gauge and the height controlled by opening and closing a valve to maintain a user defined differential pressure.

For tests that involved heating or cooling the oil, the oil was heated and cooled via the internal coils in the tanks which were connected to an external heat exchanger. For heating, the temperature was set to slightly above the desired maximum oil temperature to minimize the possibility of coking. For the tests involving oil at 5°C, the lines were pre-cooled using liquid nitrogen. For the tests involving oil at 60°C, the lines were pre-heated by the use of heat tape. The tank cooling and heating process, typically took several hours. The tanks were insulated to reduce heat gain/losses.

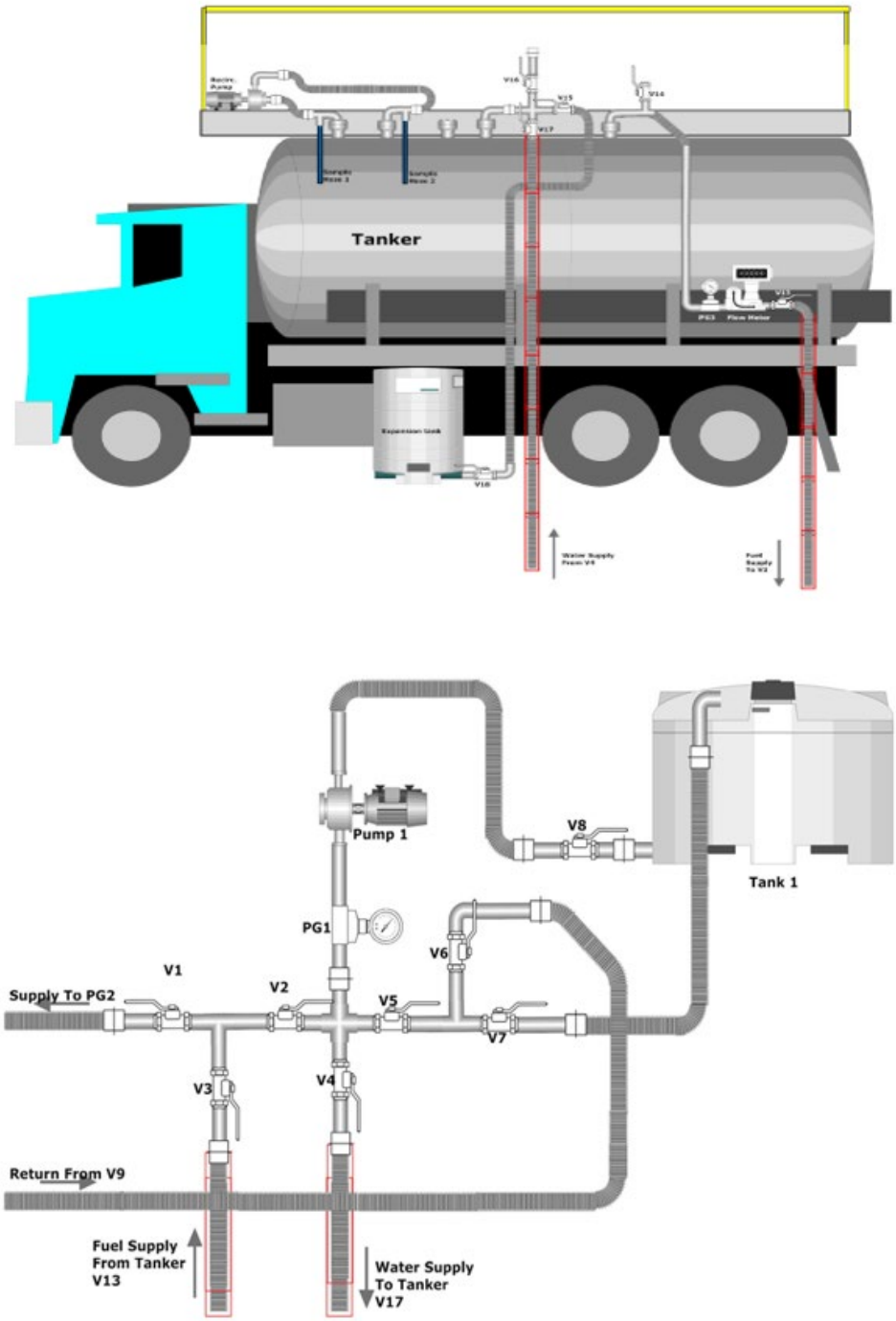

Figure E-1: Piping Schematic for Crude Oil Testing.

E.2. Fireball Test Procedure

The fireball test requirement is based on heating either 40 gallons or 400 gallons of crude oil in the test tanks to ~300ºC (bulk temperature) and ~280 psi and then releasing the superheated liquid and vapor mixture quickly (<1 s) to the atmosphere. The 100-gallon tank was used for proof of concept purposes.

In preparation prior to testing, the tank and lines are first purged of air by completely filling the tank with water. Then oil is introduced into the tank at the top penetration, filling the 100-gallon and 1000-gallon tanks with 40-gallons and 400-gallons of oil, respectively. The tank is then heated with Zircar ceramic radiant heaters to approximately 80-90ºC causing the expansion of oil vapors to drive all water out the bottom of the tank. The reason for purging water from the vessel at this point is to minimize the water vapor from contaminating the oil liquid/vapor layers. A total of 12 heaters, each covering a quadrant circumferentially and distributed among three levels, were specially fabricated for the 1000-gallon tank. The height, inner, and outer radius of each heater is 12", 74", and 80", respectively. The total power output from all 12 heaters is 96 kW.

Once water is evacuated the tank is heated so that the tank pressure reaches target pressure. Oil bulk temperatures are limited to about 300ºC due to changes in chemical properties that occur for temperature above this limit for the tested oils. Once the tank reaches target pressure the disc is ruptured with linear shaped charges placed above the four-score line and the fuel is ignited using an C-4 explosive surrounded by a zirconium shell to increase the after-burn duration. A 0.25 lb. and 1 lb. explosive charge is placed approximately 1-m above the rupture disc for the 100-gallon and 1000-gallon tank, respectively.

This page intentionally blank

APPENDIX F. CRUDE OIL SAMPLING

F.1. Introduction

This section, Appendix F, describes the methods and results associated with capture and analysis of crude oil samples for physical and chemical properties. Large-scale samples (100's to 1000's of gallons) were acquired for combustion testing and transported in tankers and stored at Sandia to supply the combustion test series. Sub-samples, defined here as small, typically liter-scale samples, drawn from much larger volumes of oil in tanks or process equipment, were collected from the tankers for property measurements at key opportunities during sample custody, including during sample loading into the tanker, and in close association with pool fire and fireball testing.

Large sample storage took two forms: (i) unpressurized, where pressure was controlled by local ambient conditions and the vapor space above the liquid contents could exchange with air at small pressure differential, and (ii) pressurized, where tanker contents were isolated from local ambient pressure to prevent gain or losses of volatiles and/or exposure to air. Analysis and discussion of the performance of these storage systems and the resulting oil quality is provided in this chapter as well.

F.2. Methodology

F.2.1. Large Sample Acquisition

Crude oil samples of sufficient volume to support the combustion tests were acquired from selected sampling points around the U.S., including:

(i) A truck off-loading terminal upstream of a rail loading facility that handles Bakken production in North Dakota
(ii) A production facility sales point that handles unconventional shale oil in Texas
(iii) A stabilized crude from the U.S. Strategic Petroleum Reserve West Hackberry storage site

Samples were selected to provide a measurable range of vapor pressure and light ends properties that may be observed among conventional and tight crudes within the domestic supply chain. The samples were not selected to represent any specific feature of a given producing region, such as an average or aggregate sample. Rather, they were spot samples from access points that lay within the supply chain that are of interest to the overall issue of transportation safety.

Crude oil samples of several thousand gallons were needed to complete the burn test series planned in this study. An important objective of this work was to preserve the properties of oil samples from the point of acquisition in the supply chain to the point of analysis at the testing facility. The intent was to feed each burn test at Sandia with oil that has properties (particularly light ends composition and vapor pressure) representative of when the oil was loaded into a railcar or pipeline. To achieve this, each large sample was collected and maintained in closed containment to prevent losses of light ends. Sandia designed and built a custom tanker to collect the oil from the field, transport it to the test facility in Albuquerque, NM, and feed it into the experimental systems under closed, pressurized conditions. Additional details on the tanker design and operation and associated sample feed systems into the experimental apparatus are given in Appendix C.

The following criteria were used to guide large sample selection and acquisition:

- Include oils that represent material within the North American supply chain, with at least one sample from rail transport.

- Include oils that span a measurable and distinct range of vapor pressure and light ends content. This is necessary to test the extent to which these physical/chemical properties affect pool fire and fireball combustion properties.
- Acquire oil from operators and facilities that are willing to grant site access to the Sandia team and custom tanker and ultimately permit the release of oil properties data in unclassified, unlimited release technical reports. See Lord [75] for the public solicitation for oil samples.

F.2.1.1. Tight Oils (Bakken and TX Shale Oil)

Two tanker-scale (2,000-3,000 gal) "tight oil" samples were collected for this work. One was from a terminal upstream of a rail loading facility that handled Bakken production in North Dakota. Another was from a production facility sales point in Texas that handled production from shale formations. Agreements between Sandia National Laboratories and the terminal operators prevent disclosure of the specific locations and operator names with these sampling events.

F.2.1.2. SPR Stabilized Oil

Oil from the U.S. Strategic Petroleum Reserve was also utilized in this study. SPR oil was desirable as a test oil because it was available in a "stabilized" state from a degasification plant at the USSPR, and would likely exhibit lower light component composition and VPCR than most other oils in the supply chain due to this additional treatment. The degasification program at USSPR is part of a mitigation strategy to assure that, in the event of a crude oil drawdown from the facility, there is assurance for worker safety and minimal impact on the environment from crude oil vapor emissions [76]. Oil at the USSPR is maintained in underground salt caverns for periods of time spanning months to decades, and this storage environment has the potential to increase the volatility of the oil relative to when it was received due to natural geothermal heating and methane intrusion from the salt dome. Degasification at SPR was achieved by flashing the crude in a processing plant to separate volatile gases where the excess gas was incinerated on-site and processed oil was re-injected into the cavern. The gas stream was processed to reabsorb some of the propane and H_2S and then the remaining gas, primarily nitrogen, methane, and ethane, was vented to a flare stack. Therefore, this crude exhibited a lower vapor pressure and light end content than the other large samples in this study, and could be treated as a low-volatility end member of the test matrix. The SPR oil was also readily available through agreements negotiated between the US Department of Energy's Petroleum Reserves Program office (oil donor) and the US Department of Energy's Oil & Gas Program office (project sponsor).About 3,000 gallons of SPR stabilized medium sour crude oil was collected from the West Hackberry SPR storage site and transported to Sandia in an unpressurized crude oil transport (see Figure F- 1). The unpressurized transport was utilized for several reasons:

- It was available four months ahead of the pressurized tanker, allowing combustion testing to commence when the other test infrastructure was available.
- Its use specifically for the stabilized SPR crude oil was deemed allowable because the starting vapor pressure of the oil was well below atmospheric pressure, which would minimize vapor losses in loading, transport, and storage.
- The condition of the stabilized SPR crude is an arbitrary low vapor pressure end-member to the sample matrix. Whether it is burned at the same conditions as when it was loaded from the SPR system is immaterial. What matters is whether it is still the low vapor pressure end-

member of the sample set when it is introduced into the burn tests and that the properties are known at the time of the burn test.

Figure F- 1: Unpressurized crude oil tanker utilized to load and transport SPR oil from West Hackberry, LA, to the testing site in Albuquerque, NM.

F.2.1.2.1. Additional Comments on the SPR Oil

SPR maintains an inventory of crude oil that exhibits a range of volatility, and the entirety of the SPR oil stockpile is not necessarily stabilized to the same extent as the particular sample used here. For context, Figure F- 2 summarizes a collection of Equation of State (EOS)-calculated individual storage cavern $VPCR_4$(100°F) values for the SPR sweet and SPR sour crudes as of early 2015 ranging from 6.5-11.5 psia. The measured $VPCR_4$ for the Task 3 SPR loading on 1/17/2017 was 6.5 psia, which is at the low end of the range shown. The Task 3 Loading sample VPCR4 was lower than the rest of the SPR samples shown in Figure F- 2 because it was taken from a stabilization plant return line going back into an SPR cavern. This test oil had just been "degassed" and had not yet been mixed with the remainder of the cavern contents. All of the other points on the figure represent data derived from spot sampling inside the cavern before the cavern contents were degassed. Given that these caverns were filled with oil acquired from the U.S. supply chain from approximately 1990-2010, these also give some perspective on API gravity and VPCR4 of medium sweet and sour conventional crudes that were on the market at the time and retained for storage at SPR.

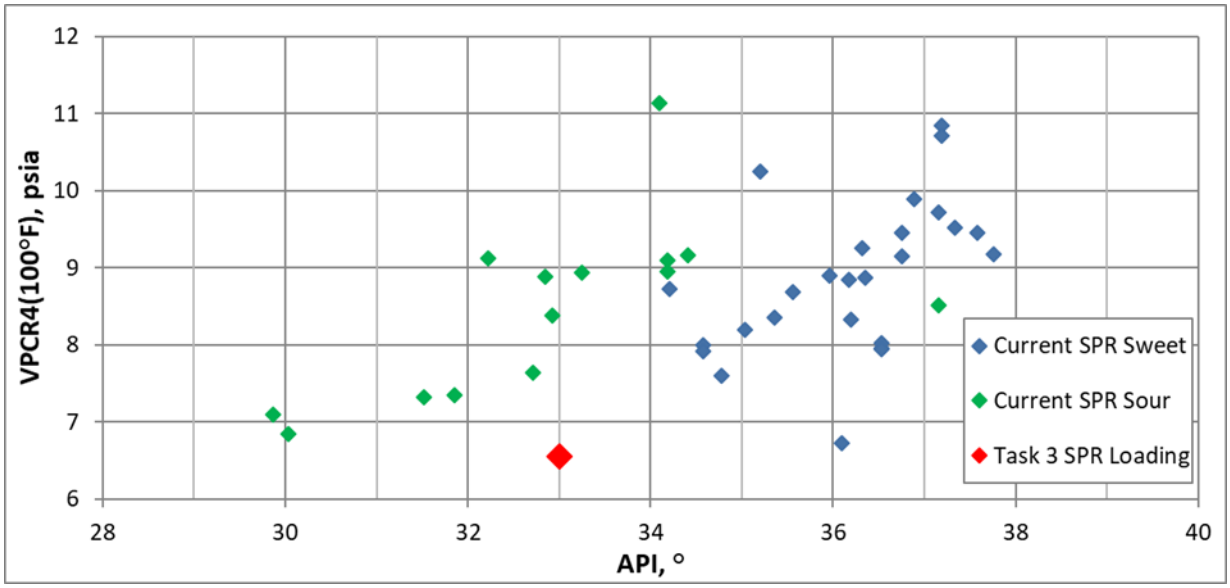

Figure F- 2: Calculated $VPCR_4(100°F)$ versus API gravity for several SPR oil samples gathered in the last 12 years.

F.2.1.3. Loading Conditions for Large Samples

Three large oil samples, SPR, Bakken, and Texas Shale Oil, were acquired for this phase of the research project. Date, quantity, and loading conditions for each is given in Table F- 1.

Table F- 1: Summary of loading conditions for tanker samples

Oil Type	Loading Date	Quantity (gal)	Line Pressure (psig)	Line Temperature (°F)	Ambient Temperature (°F)[1]
SPR	1/24/2017	3,000	145	110	62
Bakken	8/17/2017	2,100	156	76	72
TX Shale	11/28/2017	3,000	40	77	60

[1] Mean ambient temperature from local airport data on sampling date.

F.2.2. Subsample Acquisition

Subsamples are defined here as liter-scale volumes of oil that were acquired to characterize bulk oil properties in a tanker or process at a given time. Subsamples were acquired by professional crude oil sampling technicians under contract with Sandia using industry standard methods and equipment. Subsamples were taken during tanker loading (loading site subsampling), and again in close association with burn tests (burn site subsampling). A summary of the subsampling events is given in Table F- 2. The "Event Numbers" from Table 1-2 for the pool fires and Table 1-4 for the fireballs are listed, along with "Abbreviations" that place each event within the sequence of all the loading and burn-site subsamples.

Table F- 2: Summary of the loading and burn-site subsamples, including location and date.

Oil Name	Event Number	Abbreviation	Sampling Location	Sampling Date	Description
Jet Fuel A	--	JET	NM	8/9/2017	
SPR	--	SPR0	LA	1/24/2017	Loading
SPR	Pool 1	SPR1	NM	2/13/2017	2m Pool Fire
SPR	Pool 2	SPR2	NM	3/20/2017	2m Pool Fire
SPR	Pool 3	SPR3	NM	4/5/2017	5m Pool Fire
SPR	Pool 4	SPR4	NM	8/14/2017	5m Pool Fire
SPR	--	SPR5	NM	7/17/2018	July 2018
SPR	Fireball 6	SPR6	NM	10/2/2018	Fireball
Bakken	--	BKN0	ND	8/17/2017	Loading
Bakken	Pool 5	BKN1	NM	10/2/2017	5m Pool Fire
Bakken	--	BKN2*	NM	1/18/2018	2m Pool Fire
Bakken	--	BKN3*	NM	1/31/2018	2m Pool Fire
Bakken	--	BKN4	NM	7/18/2018	July 2018
Bakken	Fireball 4	BKN5	NM	10/3/2018	Fireball
Texas Shale	--	TXSh0	TX	11/28/2017	Loading
Texas Shale	Pool 6	TXSh1	NM	1/19/2018	5m Pool Fire
Texas Shale	--	TXSh2	NM	7/19/2018	July 2018
Texas Shale	Fireball 5	TXSh3	NM	10/2/2018	Fireball

* See note below re: BKN2 and BKN3 sampling events

Note on BKN2, BKN3: The BKN2 and BKN3 sampling events listed in Table F- 2 are not detailed in the methods below as they were collected under a different project. They are included here because the property results are presented later in this chapter and provide additional information on the long-term storage characteristics of the Bakken crude. More information on the BKN2 and BKN3 sampling methods may be found in [77].

F.2.2.1. Jet Fuel Subsampling

A jet fuel reference sample was collected once on 8/9/2017 from the Sandia Thermal Test Complex Jet A storage tank to enable laboratory analysis for selected properties. Six gallons were acquired using ASTM D4057, section 6.3, open sampling into metal cans. Ambient temperature at the time of sampling was 82°F according to local airport data. Cans were labeled and packaged for shipment and transported to off-site analytical laboratories.

F.2.2.2. SPR Crude Subsampling

The SPR crude oil was sampled seven times throughout the project, as indicated above in Table F- 2. The first subsample was drawn upon loading the tanker in West Hackberry, LA, and the remaining six were drawn from unpressurized storage tanks at the burn site at Sandia National Laboratories in Albuquerque, NM. Burn site subsampling was coordinated so that samples were acquired just prior to burn tests. Process details were adapted to meet the needs of each subsampling event, and a brief narrative of each subsampling event is given below.

F.2.2.2.1. SPR Loading Site Subsampling (SPR0)

Loading site subsampling at the West Hackberry SPR site in Louisiana was coordinated to serve as a baseline for oil properties at the time of loading on 1/24/2017. A sampling manifold was attached to fill line that connected the operator process piping to the transport tanker, and samples were collected from this line during the tanker fill process. Operator notes indicate that line pressure was 145 psig at the sampling valve, and oil temperature was 110°F.

Samples were acquired using three methods:

- ASTM D3700, Floating Piston Cylinder (compositional samples) (8 × 0.4L)
- GPA-2174, Water Displacement (retain samples) (6 × 0.4 L)
- ASTM D4057, Glass bottle (Boston Round) (6 × 0.7 L)

Sample cylinders were then labeled and packaged for shipment and transported to off-site analytical laboratories for analysis.

F.2.2.2.2. SPR 2m Pool Fire (SPR1)

Crude oil property samples for the cold (~7°C) 2m pool fire series were obtained by sampling from the 200-gallon pre-conditioning tank on 2/13/2017, the day prior to the pool fire tests. A hard pipe sampling tap extending from the side of the tank (see drawing in Figure F- 3) offered access to the single-phase liquid oil. A flexible sampling hose with a manual sampling valve was attached to the sampling tap to give the sampling technician safe access to the oil sample while remaining at ground level.

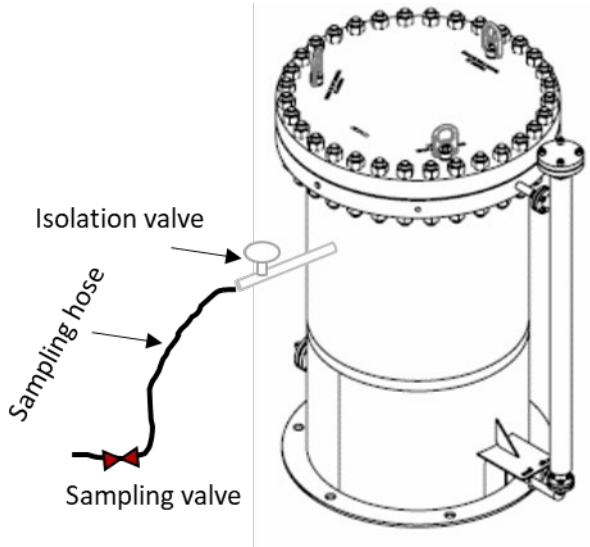

Figure F- 3: Drawing of 200-gallon oil pre-conditioning tank outfitted with sampling hose.

Samples were acquired using four methods:

- ASTM D3700, Floating Piston Cylinder (compositional samples) (2 × 0.4L)
- ASTM D8009, Manual piston cylinder (primary pressurized samples) (6 × 0.4 L)
- GPA-2174, Water Displacement (retain samples) (6 × 0.4 L)
- ASTM D4057, Glass bottle (Boston Round) (6 × 0.7 L)

Average oil pressure at the sampling valve was recorded at 22 psig, and average oil temperature was 68 °F. Samples were then prepared for shipment and sent offsite to commercial laboratories for analysis.

F.2.2.2.3. SPR 2m Pool Fire (SPR2)

Crude oil property samples for the warm (~60°C) 2m pool fire series were obtained by sampling from the 200-gallon pre-conditioning tank on 3/20/2017, two days prior to the pool fire tests on 3/22/2017. A hard pipe sampling tap extending from the side of the tank (see drawing in Figure F-3) offered access to the single-phase liquid oil. A flexible sampling hose with a manual sampling valve was attached to the sampling tap to give the sampling technician safe access to the oil sample while remaining at ground level.

Samples were acquired using three methods:

- ASTM D8009, Manual piston cylinder (primary pressurized samples) (6 × 0.4 L)
- GPA-2174, Water Displacement (retain samples) (6 × 0.4 L)
- ASTM D4057, Glass bottle (Boston Round) (6 × 0.7 L)

Average oil pressure at the sampling valve was recorded at 22 psig, and oil temperature was 68-70°F. Samples were then prepared for shipment and sent offsite to commercial laboratories for analysis.

F.2.2.2.4. SPR 5m Pool Fire (SPR3)

Crude oil properties for the hot (54°C) 5m pool fire were obtained by collecting subsamples from the 1,000-gallon pre-conditioning tank on 4/5/2017, the day prior to the pool fire test on 4/6/2017. A photo of the insulated pre-conditioning tank is shown in Figure F- 4. The pre-conditioning tank utilizes the same tank shell as the fireball tank but is fitted with a different top flange and internals depending on test requirements. Since the SPR oil was stored in an unpressurized tanker for months prior to this pool fire experiment, air exposure was permitted during handling associated with the pool fire test. The pre-conditioning tank was filled from the bottom up (displacing nitrogen) with SPR oil from the unpressurized tanker using a transfer pump through the hose shown at the bottom of Figure F- 4. Once the tank had sufficient volume of oil for the pool fire test (~600 gallons), the headspace was pressurized with nitrogen to maintain about 20 psig crude oil pressure at the sampling valve shown at the bottom of Figure F- 4. A zoom of the configuration for the sampling hose for ASTM D4057 unpressurized samples shown in Figure F- 5. A flexible hose with threaded connections coming off the same sampling valve was used for pressurized sampling (no photo available). Once sample acquisition was completed, nitrogen pressure over the oil was bled to 0 psig.

Figure F- 4: Photo of insulated 1,000-gallon pre-conditioning tank.

Figure F- 5: Photo of crude oil line from of 1,000-gallon pre-conditioning tank configured with sampling valve and dip tube for D4057 bottle sampling.

SPR subsamples were acquired on 4/5/2017 using four methods:

- ASTM D3700, Floating Piston Cylinder (compositional samples) (2 × 0.4L)
- ASTM D8009, Manual piston cylinder (primary pressurized samples) (6 × 0.4 L)
- GPA-2174, Water Displacement (retain samples) (6 × 0.4 L)
- ASTM D4057, Glass bottle (Boston Round) (6 × 0.7 L)

Average oil pressure at the sampling valve was recorded at 23 psig, and average oil temperature was 68 °F. Samples were then prepared for shipment and sent offsite to commercial laboratories for analysis.

F.2.2.2.5. SPR 5m Pool Fire (SPR4)

Crude oil properties for the ambient feed SPR 5m pool fire were obtained by collecting subsamples from the unpressurized transport tanker on 8/14/2017, one day before the pool fire test on 8/15/2017. The tanker contents were recirculated prior to subsampling by attaching a transfer pump to an oil delivery line off the bottom of the tanker and returning the flow through a flexible hose into the manhole at the top of the tanker. The hose was submerged into the oil at least 6" deep and a minimum of two tank volumes were circulated over a 2-hour period.

Sampling line pressure from the tanker was limited to ~2 psig head pressure as it was effectively an open system. The ASTM D8009-compliant cylinders brought to the sampling site required greater pressure differential than was available, even with manual assist, to move the pistons effectively. As such, the D3700 and D8009 methods were unable to collect samples in this event. Oil temperature was reported at 72°F.

SPR subsamples were acquired on 8/14/2017 using two methods:

- GPA-2174, Water Displacement (primary closed samples)
- ASTM D4057, Glass bottle (Boston Round)

Samples were then prepared for shipment and sent offsite to commercial laboratories for analysis.

F.2.2.2.6. SPR July 2018 (SPR5)

The SPR oil was held in an unpressured transport tanker from January 2017- January 2018 (recall Figure F- 1), and then transferred to a ~900 gallon portable tank (see Figure F- 6) and stored at the Lurance Canyon Burn Site (LCBS). A sub-sample of opportunity was taken in July 2018 while personnel and equipment were available ahead of a series of planned fireball testing. To homogenize the oil and provide sufficient line pressure for subsampling prior to the fireball, a recirculation loop was added according to the drawing in Figure F- 7. The system recirculated three tank volumes of oil prior to subsampling. A backpressure valve between the pump discharge and the return line provided adequate pressure (10-25 psig) to facilitate sample capture. Recirculation was continuous during the 4-5 hour sampling event. Operator notes indicated oil temperature at 70°F during sample capture.

Figure F- 6: Unpressurized storage tank (~900 gal capacity) used to hold SPR oil from January – October 2018.

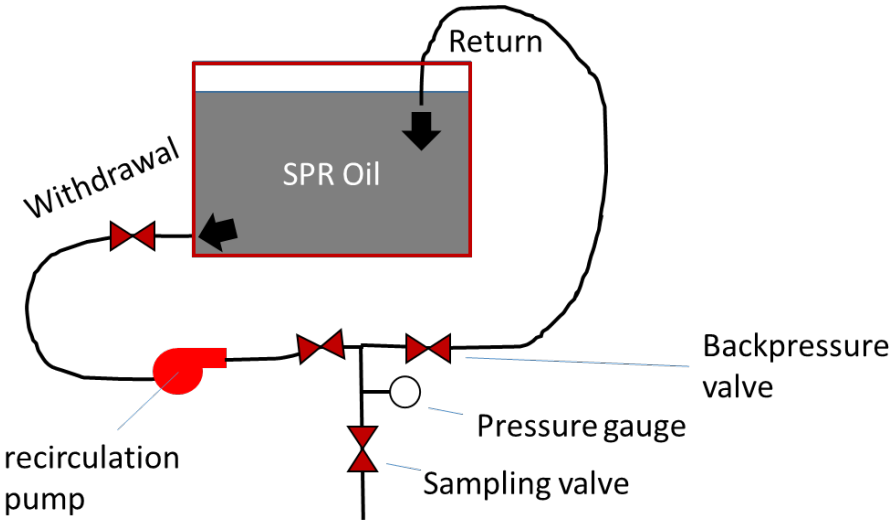

Figure F- 7: Conceptual drawing of recirculation system for SPR oil tank setup for pre-fireball sampling.

SPR subsamples were acquired on 7/17/2018 using four methods:

- ASTM D3700, Floating Piston Cylinder (compositional samples) (2 × 0.4L) (see Figure F- 8)
- ASTM D8009-B, Manual piston cylinder (primary pressurized samples) (6 × 0.4L)
- GPA-2174, Water Displacement (retain samples) (6 × 0.4 L)
- ASTM D4057, Glass bottle (Boston Round) (6 × 0.7 L) (see Figure F- 9)

Samples were then prepared for shipment and sent offsite to commercial laboratories for analysis.

Figure F- 8: Floating piston cylinder during fill process with SPR oil.

Figure F- 9: ASTM D4057 glass bottle during fill process with SPR sample.

F.2.2.2.7. SPR Fireball (SPR 6)

Crude oil properties for the SPR fireball were obtained by collecting subsamples from the tank on 10/2/2018, one week before the fireball test on 10/11/2018. In order to homogenize the oil and provide sufficient line pressure for subsampling prior to the fireball, a recirculation loop was added according to the drawing in Figure F- 7. The system recirculated three tank volumes of oil prior to subsampling. A backpressure valve between the pump discharge and the return line provided adequate pressure (5-20 psig) to facilitate sample capture. Recirculation was continuous during the 4-5 hour sampling event. Sampling technician notes indicated oil temperature at 68°F during sampling operations.

SPR subsamples were acquired on 10/2/2018 using four methods:

- ASTM D3700, Floating Piston Cylinder (compositional samples) (2 × 0.4L)
- ASTM D8009-B, Manual piston cylinder (primary pressurized samples) (5 × 0.4L)
- GPA-2174, Water Displacement (retain samples) (6 × 0.4 L)
- ASTM D4057, Glass bottle (Boston Round) (6 × 0.7 L)

Samples were then prepared for shipment and sent offsite to commercial laboratories for analysis.

F.2.2.3. Bakken Crude Subsampling

The Bakken crude oil was subsampled six times throughout the project, as indicated above in Table F- 2. The first subsample was drawn upon loading the tanker in North Dakota, and the remaining five were drawn from pressurized storage tanks at the burn site at Sandia National Laboratories in Albuquerque, NM. Burn site subsampling was coordinated so that samples were acquired within a few days of burn tests. Process details were adapted to meet the needs of each subsampling event, and a brief narrative of each subsampling event is given below.

F.2.2.3.1. Bakken Loading Subsample (BKN0)

Loading site subsampling in North Dakota was coordinated to serve as a baseline for oil properties at the time of loading on 8/17/2017. A sampling manifold was attached to fill line that connected the operator process piping to the pressurized Sandia transport tanker, and samples were collected from this line during the tanker fill process.

Bakken subsamples were acquired on 8/17/2017 using four methods:

- ASTM D3700, Floating Piston Cylinder (compositional samples) (2 × 0.4L)
- ASTM D8009, Manual piston cylinder (primary pressurized samples) (6 × 0.4L)
- GPA-2174, Water Displacement (retain samples) (6 × 0.4 L)
- ASTM D4057, Glass bottle (Boston Round) (6 × 0.7 L)

Line pressure at the sampling manifold was recorded at 157 psig, and oil temperature was reported at 75°F. Sample cylinders were then labeled and packaged for shipment and transported to off-site analytical laboratories for analysis.

F.2.2.3.2. Bakken 5m Pool Fire (BKN1)

Crude oil properties for the Bakken 5m pool fire were obtained by collecting subsamples from the Sandia pressurized Tanker #1 on 10/2/2017, one week prior to the pool fire test on 10/9/2017. Since the oil in the pressurized tanker was stored for long term (weeks to months) in a two-phase (vapor + liquid) condition, it was necessary to re-pressurize to a single-phase liquid prior to sampling. Addition

of small metered volumes of water into the tanker while monitoring pressure was used to confirm that the sample was condensed to single phase at 60 psia and exhibited the compressibility of a liquid-filled tank.

Once compressed to a single phase, oil in the tanker was circulated for several hours by a dedicated pump and recirculation loop for at least three tanker volumes to homogenize the contents prior to subsampling (see drawing in Figure F- 10). Subsamples were then pulled from a manifold system attached to the recirculation loop. The pump was left running to maintain pressure and flow in the loop during sampling. A photo of the tanker parked at the burn site after sampling was completed is shown in Figure F- 11.

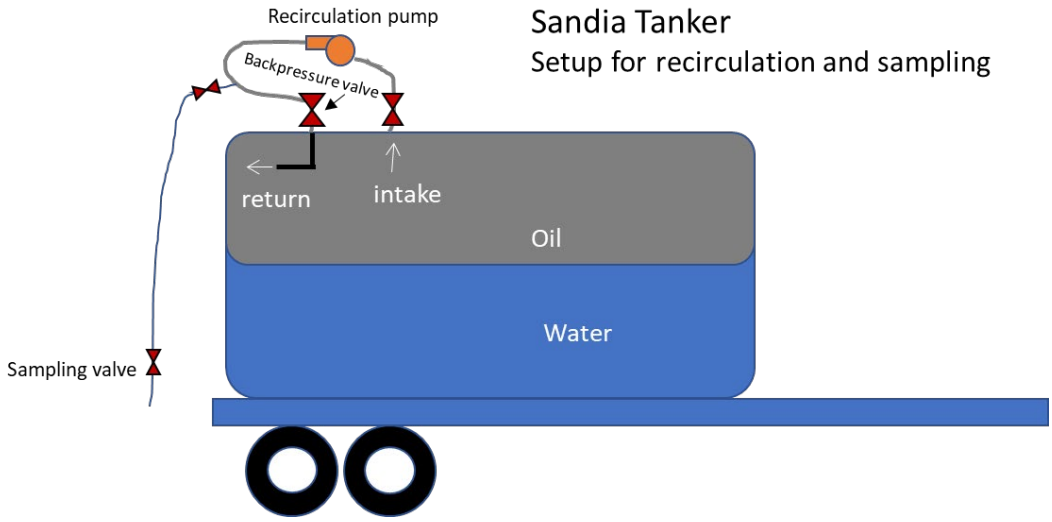

Figure F- 10: Conceptual drawing of tanker recirculation loop and sampling valve.

Figure F- 11: Photo of Sandia Tanker #1 containing Bakken oil in October 2017 after subsampling for the 5m pool fire was completed.

Bakken subsamples were acquired on 10/2/2017 using four methods:

- ASTM D3700, Floating Piston Cylinder (compositional samples) (2 × 0.4L)
- ASTM D8009, Manual piston cylinder (primary pressurized samples)
- GPA-2174, Water Displacement (retain samples)
- ASTM D4057, Glass bottle (Boston Round)

Average line pressure at the sampling valve was 45 psig, and tanker temperature during sampling was reported at 70°F. Samples were then prepared for shipment and sent offsite to commercial laboratories for analysis.

F.2.2.3.3. Bakken Pre-Fireball (BKN4)

Pre-fireball properties for the Bakken sample were obtained by collecting subsamples from the Sandia pressurized Tanker #1 on 7/18/2018, 7 weeks before the fireball test on 9/5/2018. The re-pressurization to single liquid phase, recirculation period, and sampling manifold configuration were the same as described above in section F.2.2.3.2 (BKN1 – 5m Pool Fire Sampling). Sampling pressure was recorded at 55-70 psig. Tanker fluid temperature during sampling was reported at 72-75°F.

Bakken subsamples were acquired on 7/18/2018 using four methods:

- ASTM D3700, Floating Piston Cylinder (compositional samples) (2 × 0.4L)
- ASTM D8009, Manual piston cylinder (primary pressurized samples) (6 × 0.4L)
- GPA-2174, Water Displacement (retain samples) (6 × 0.4 L)
- ASTM D4057, Glass bottle (Boston Round) (6 × 0.7 L) (see Figure F- 12)

When sub-sampling was completed, cylinders were prepared for shipment and sent offsite to commercial laboratories for analysis.

Figure F- 12: ASTM D4057 glass bottle during fill process with Bakken sample.

F.2.2.3.4. Bakken Handling History in Unsuccessful 8/9/2018 Fireball Test

An attempt to run a fireball test on 8/9/2018 was unsuccessful in opening the fireball tank. During the test attempt, the 400-gallon Bakken oil sample in the 1000-gallon fireball test tank was subjected to a heating and cooling cycle. Temperature monitoring data from the 8/9/2018 test, reproduced here in Figure F- 13, indicated that the maximum measured internal tank temperature from thermal wells (TC1, TC2) immersed in fluid was 260°C, and the maximum external temperature on the tank wall next to the radiant heaters was 325°C. The primary concern in temperature monitoring was to prevent thermal degradation of petroleum hydrocarbon molecules, known as "cracking," which occurs at temperatures over 350°C [78]. The monitoring data indicated that the oil was not exposed to any temperatures that would cause cracking. Internal tank pressure monitoring during the same heating and cooling cycle indicated that the starting and ending pressures agreed within 3 psi, providing further assurance that there was no thermal degradation of the original oil to lighter materials that would measurably raise the vapor pressure of the liquid after the cooldown cycle was complete. It is also important to note that the fireball tank loading and unloading processes were conducted with water drive, which prevents direct exposure of the oil to the atmosphere. The above observations present no evidence, direct or suggestive, that the sample quality had been altered by the unsuccessful test.

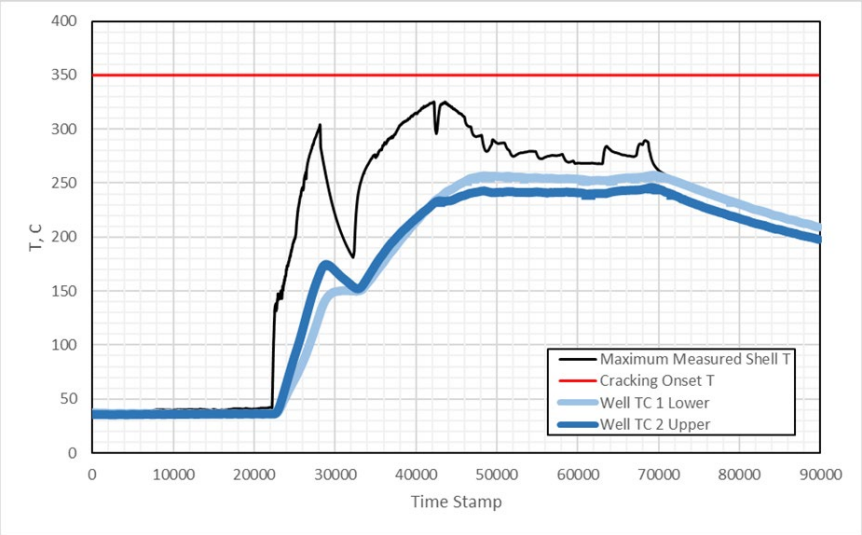

Figure F- 13: Temperature monitoring data for the fireball test tank during the heating and cooling period associated with the unsuccessful Bakken fireball test on 8/9/2018.

The test team determined that preserving the 400 gallons of oil in the test tank was important to reducing the risk of running out of oil before the test series was complete and developed a loading plan to move the oil back into the tanker under pressure. Moreover, plans were developed to subsample the Bakken tanker once more in association with the next fireball test to obtain direct data on the oil properties in the tanker and understand whether any changes had occurred since the July 2018 subsampling.

Thus, the Bakken fuel was loaded back into the Sandia pressurized tanker at Test Pad B and mixed with about 500 gallons of oil still in the tanker and depressurized to 2-phase for safe storage. To supply the next fireball test on 9/5/2018, the whole 900 gallons was again pressurized to single phase and mixed, of which 400 gallons was drawn to fill the fireball tank. The 500 gallons remaining in the tanker was depressurized to 2-phase and the tanker was relocated to the LCBS for four weeks until the next sampling opportunity in October 2018. Analysis results from the subsampling in July and October are addressed in section F.4.1.2.

F.2.2.3.5. Bakken Post-Fireball (BKN5)

Properties for the final 500 gallons of oil in the tanker were obtained by collecting subsamples from the Sandia pressurized Tanker #1 on 10/3/2018, 4 weeks after the fireball test on 9/5/2018. The re-pressurization to single liquid phase, recirculation period, and sampling manifold configuration were the same as described above for the 5m Bakken pool fire.

Bakken subsamples were acquired on 10/03/2018 using four methods:

- ASTM D3700, Floating Piston Cylinder (compositional samples) (2 × 0.4L)
- ASTM D8009-B, Manual piston cylinder (primary pressurized samples) (5 × 0.4L)
- GPA-2174, Water Displacement (retain samples) (6 × 0.4 L)
- ASTM D4057, Glass bottle (Boston Round) (6 × 0.7 L)

The sampling technician reported line pressure at the sampling valve at 20 psig and oil temperature at 66°F. When sub-sampling was completed, cylinders were prepared for shipment and sent offsite to commercial laboratories for analysis.

F.2.2.4. Texas Shale Oil Subsampling

The Texas shale oil was subsampled four times for property analysis: once upon loading in Texas and three times associated with burn test operations at Sandia in Albuquerque, NM.

F.2.2.4.1. Texas Shale Loading (TXSh0)

Loading site subsampling in Texas was coordinated to serve as a baseline for oil properties at the time of loading on 11/28/2017. A sampling manifold was attached to fill line that connected the operator process piping to the pressurized Sandia transport tanker, and samples were collected from this line during the tanker fill process.

TX Shale oil subsamples were acquired on 11/28/2017 using four methods:

- ASTM D3700, Floating Piston Cylinder (compositional samples) (2 × 0.4L)
- ASTM D8009-B, Manual piston cylinder (primary pressurized samples) (6 × 0.4L)
- GPA-2174, Water Displacement (retain samples) (6 × 0.4 L)
- ASTM D4057, Glass bottle (Boston Round) (10 × 0.7 L)

Line pressure at the sampling manifold was recorded at 40 psig, and oil temperature was reported at 77°F. Sample cylinders were then labeled and packaged for shipment and transported to off-site analytical laboratories for analysis

F.2.2.4.2. Texas Shale 5m Pool Fire (TXSh1)

A first attempt to compress the TX Shale oil sample to a single phase at ~70 psia in the tanker in December 2017 in preparation for sampling and pool fire testing resulted in a loss of several gallons of liquid oil through the pressure safety valve (PSV) located at the top of the tank. A troubleshooting effort indicated that the PSV malfunctioned and opened at ~30 psig, whereas the factory setting according to contract documentation was supposed to be 225 psig. While the PSV setting was lower than desired, it was greater than the bubblepoint pressure of the oil at ambient temperature, and the single-phase condition was achieved, albeit requiring careful pressure control not to exceed ~20 psig, in preparation for sampling and pool fire testing. Analysis of the crude's properties with regards to the PSV is further discussed in section F.4.1.2.

Crude oil properties for the TX Shale oil 5m pool fire were obtained by collecting subsamples from the Sandia pressurized Tanker #2 on 1/19/2018, four days after the pool fire test on 1/15/2017. Oil in the tanker was circulated for several hours by a dedicated pump and recirculation loop for at least three tanker volumes to homogenize the contents prior to subsampling (see drawing in Figure F- 10). Subsamples were then pulled from a manifold system attached to the recirculation loop. The pump was left running to maintain pressure and flow in the loop during sampling.

TX Shale oil subsamples were acquired on 1/19/2018 using four methods:

- ASTM D-3700, Floating Piston Cylinder (compositional samples) (2 × 0.4L)
- ASTM D8009-B, Manual piston cylinder (primary pressurized samples) (6 × 0.4L)
- GPA-2174, Water Displacement (retain samples) (6 × 0.4 L)
- ASTM D4057, Glass bottle (Boston Round) (6 × 0.7 L)

Line pressure on the pump discharge line at the sampling valve was recorded at 45 psig. Oil temperature was reported at 43°F. Samples were then prepared for shipment and sent offsite to commercial laboratories for analysis.

F.2.2.4.3. TX Shale July 2018 (TXSh2)

Interim properties for the TX Shale oil were obtained by collecting subsamples from the Sandia pressurized Tanker #2 on 7/19/2018. Oil in the tanker was circulated for several hours by a dedicated pump and recirculation loop for at least three tanker volumes to homogenize the contents prior to subsampling (see drawing in Figure F- 10). Subsamples were then pulled from a manifold system attached to the recirculation loop. The pump was left running to maintain pressure and flow in the loop during sampling.

Texas Shale subsamples were acquired on 7/19/2018 using four methods:

- ASTM D3700, Floating Piston Cylinder (compositional samples) (2 × 0.4L)
- ASTM D8009, Manual piston cylinder (primary pressurized samples) (6 × 0.4L)
- GPA-2174, Water Displacement (retain samples) (6 × 0.4 L)
- ASTM D4057, Glass bottle (Boston Round) (6 × 0.7 L)

Figure F- 14: ASTM D4057 glass bottle during fill process with TX Shale sample (July 2018).

Line pressure at the sampling valve was reported at 50 psig. Tanker temperature was 75-77°F. Samples were then prepared for shipment and sent offsite to commercial laboratories for analysis.

F.2.2.4.4. TX Shale October 2018 (TXSh3)

Crude oil properties associated with the TX Shale oil fireball test were obtained from the Sandia pressurized Tanker #2 on 10/02/2018 and 10/03/2018 in parallel with other oil testing on-site, and 5 weeks before the fireball test on 10/11/2018. Oil in the tanker was circulated for several hours by a dedicated pump and recirculation loop for at least three tanker volumes to homogenize the contents prior to subsampling (see drawing in Figure F- 10). Subsamples were then pulled from a manifold system attached to the recirculation loop. The pump was left running to maintain pressure and flow in the loop during sampling.

Texas Shale subsamples were acquired on 10/02/2018 and 10/03/2018 using four methods:

- ASTM D3700, Floating Piston Cylinder (compositional samples) (2 × 0.4L)
- GPA-2174, Water Displacement (retain samples) (6 × 0.4 L)
- ASTM D4057, Glass bottle (Boston Round) (6 × 0.7 L)
- ASTM D8009-B, Manual piston cylinder (primary pressurized samples) (6 × 0.4L)

Line pressure at the sampling valve was reported at 40 psig and line temperature was reported at 66°F. Tanker temperature was 72°F. Samples were then prepared for shipment and sent offsite to commercial laboratories for analysis.

F.2.2.4.5. Analysis Methods

The analytical methods employed to obtain crude oil properties are described here. All property analyses were run by offsite analytical laboratories and represent common industrial properties and standards used to characterize crude oils for sale, purchase, and transportation.

F.2.2.5. Loading Site Subsample Characterization

As described below, loading site subsamples underwent an extensive series of analyses and characterizations, with the objective of establishing a comprehensive database of chemical and physical properties for each of the crude oils subjected to Task 3 combustion testing. While the combustion test relevance of some of the chemical/physical property data points collected (such as vapor pressure, flash point, light ends analysis, and gross heat of combustion) is straightforward, many other data points with less obvious relevance were collected including basic nitrogen content, acid number, bromine number, asphaltene content, and others. The rationale for acquiring a wide-ranging data set for each loading sample was that 1) the combustion test outcomes were unknown, 2) different oils may result in specific outcome differences, and 3) it may be possible to associate or correlate different outcomes with one or more specific chemical and/or physical property differences. Analysis methods are organized below into pressurized and unpressurized test methods.

F.2.2.5.1. Pressurized Loading Site Subsample Analyses

Table F- 3 lists the analyses conducted at elevated pressure using subsample extracted at pressure from pressurized sample containers. Brief descriptions of each analytical procedure are provided below.

Table F- 3: Pressurized Loading Site Subsample Analyses

Method	Test	Unit
ASTM D6377 (M)	Vapor Pressure, VPCRx(T)	Psia or kPa
GPA 2103-M	Compositional Analysis (N_2–C30+)	mole%

F.2.2.5.1.1 ASTM D6377 VPCRx(T) Expansion Series

A series of pressure-expansion points was taken on oil from the loading subsample using ASTM D6377 methodology [50].[50]. The selected temperature and expansion points are given in A vapor pressure "curve" was developed by running a series of pressure-expansion points on oil from the loading subsample using ASTM D6377 methodology [50]. The selected temperature and expansion points are given in Table F- 4.

Table F- 4: Temperature and expansion settings for ASTM D6377 VPCRx(T) measurements run on loading site subsamples.

Temperature		Expansion Ratio (x)			
(°F)	(°C)	V/L	V/L	V/L	V/L
100	37.8	0.05	0.2	0.5	4.0

Samples must be allowed to reach an effective equilibrium for each expansion point, with 6377 instrument equilibration requirements given in Table F- 5. The equilibrium requirements and sample conditioning have been modified for this project, which changes these measurements from "D6377" to "D6377-M" results, as stated in the note below Table F- 5. Sandia recommended running this analysis in duplicate on separate cylinders to further understand variability among the samples.

Table F- 5: Instrument settings for "Equilibrium Time" and "Equilibrium dP/dt" required to confirm that the analysis run for each V/L has reached equilibrium conditions.

V/L	Minimum Equilibration Time (sec)	Equilibration dP/dt (kPa/min)
0.05	1200	0.2
0.20	900	0.2
0.50	600	0.15
4.0	300	0.1

Note: The "M" modifier on the ASTM D6377 test method above relates specifically to the equilibrium criteria above in Table F- 5 and the temperature conditioning of the test fluid. Sandia National Laboratories requires that the test fluid be pre-conditioned to the test temperature PRIOR TO PRESSURIZED INJECTION into the sample chamber in the 6377 device, and that the sample injection tubing and pressure regulators (if required) are also maintained at the test temperature. This is done in order to prevent liquid thermal expansion effects from further pressurizing the cell before the expansion sequence starts, leading to erroneously high-pressure values for low V/L.

F.2.2.5.1.2 Pressurized Compositional Analysis: GPA 2103-M with physical shrink and ASTM D2887 C7+ analysis

Samples were analyzed by a pressurized compositional methodology combining gas chromatography with physical property analysis and numerical recombination to yield a whole oil description with components to include N2, CO2, carbon number, and major isomers from C1-C29 with a lumped C30+. These data were used for direct comparison among oils for fixed gases and light ends

content as well as formed the input for equation of state modeling that was used to predict physical properties for each oil that could be compared with measured values.

The GPA 2103-M [79] process entails several analytical steps as follows: The GPA 2103-M [79] process entails several analytical steps as follows:

- Pressurized gas chromatographic (GC) analysis of N2, CO2, C1-C5 components using GPA 2177-13
- Physical liquid volume measurement of C6+ fraction by combination of physical shrink experiment on whole oil at controlled temperature and lab atmospheric pressure followed by an ASTM D2001 distillation to T = 107°F. Subsequent modified ASTM D86 distillation to provide C6-C10 fraction at T = 385°F and C11+ residual.
- Physical property measurements of stabilized C6+, C6-C10, and C11+ fractions for average MW by freezing point depression and RD by ASTM D5002-13
- Unpressurized GC analyses of the C6-C10 (by flame ionization detector) by GPA 2186-M and C6+ fractions (by flame ionization detector) by ASTM D2887-M [80]
- Numerical data merge using GC and physical properties data to a single whole oil carbon number (N2 – C30+) report with computed total MW and RD

Prior associated research identified the GPA 2103-M as one of several commercially available methods suitable for use in this research study. A critical factor for method performance was the ability to quantify fixed gas (N_2, CO_2) and light ends (C1-C5) composition (mole % and mass %) in relation to the whole oil, as these components drive the vapor pressure for crude oils near ambient temperature. The selection of GPA 2103-M over others with similar technical performance was driven by additional factors specific to Sandia's research needs at the time, including price and availability.

F.2.2.5.2. Unpressurized Loading-Site Subsample Analyses

Table F- 6 lists the analyses conducted at atmospheric pressure using subsample extracted from one or more of the unpressurized containers as needed. Test method and brief notes are given for each. The samples taken upon loading underwent more tests than pre-burn samples in order to better identify the oil. These extra tests were not done for properties that were expected to change appreciably throughout the duration of storage, or for properties that were not directly influential to this project. Several of these extra properties were requested by sponsors and are commonly used in industry to determine the type, nature, and origin of the oil.

Table F- 6: Unpressurized loading site subsample analyses

Property	Method	Unit	Instrument/Test	Notes
Average Molecular Weight		g/mol	Freezing point depression	Method not standardized for crude oil, but is an essential equation of state model input
Density, Relative Density, or API Gravity	ASTM D5002	g/mL or °API	Digital density analyzer	The mass of crude oil needed to fill a volume – commonly used to characterize crude oil
Kinematic Viscosity @100°F	ASTM D445	mm^2/s	Stabinger viscometer	Can help determine the power necessary to pump the crude oil
Flash Point	ASTM D56	°F	Tag closed cup tester	Lowest temperature an explosion hazard exists
Pour Point	ASTM D97	°C or °F	Pour test	Lowest temperature where crude oil flows
Gross Heat of Combustion	ASTM D240	BTU/lb	Bomb calorimeter	Heat released when crude oil is ignited
Acid Number	ASTM D664 (Procedure A)	mg KOH/g	Potentiometric titration	Amount of base required to titrate the crude oil
Basic Nitrogen	UOP 269	wt% or ppm	Titration	A measure of gas trapped in oil
Nitrogen	ASTM D4629	mg/kg	Oxidative combustion and chemiluminescence detection	A measure of gas trapped in oil
Average Bromine Number	ASTM D1159	Unitless	Electrometric titration	A measure of olefinic unsaturation
Iron	ASTM D5708 (Method B)	mg/kg	ICP atomic emission spectrometry	Can help determine value of crude oil
Nickel	ASTM D5708 (Method B)	mg/kg	ICP atomic emission spectrometry	Can help determine value of crude oil
Sodium	ASTM D5708 (Method B)	mg/kg	ICP atomic emission spectrometry	Can help determine value of crude oil
Vanadium	ASTM D5708 (Method B)	mg/kg	ICP atomic emission spectrometry	A mineral that can form corrosive compounds upon crude oil combustion
Salt Content (electrometric Cl)	ASTM D3230	lb/1000 bbl	Electrometric method	Determines whether crude oil desalting is necessary
Water and Sediment Content	ASTM D4007	vol%	Centrifuge method	Necessary to determine volumes of actual oil
Asphaltene Content	ASTM D6560	wt%	Chemical extraction	May indicate propensity of crude oil to create black smoke upon combustion
Ash Content	ASTM D482	wt%	Combustion residue	Solid residue remaining after combustion
Wax Content	UOP 46	wt%	Precipitation extraction	Increases viscosity and pour point
Water Content	ASTM D4928	vol%	Coulometric Karl Fischer titration	Applicable for water contents from 0.02 wt% to 5 wt%
Water Content	ASTM D4377	vol%	Potentionmetric Karl Fischer titration	Applicable for water contents from 0.02 wt% to 2 wt%

Property	Method	Unit	Instrument/Test	Notes
Carbon Content	ASTM D5291	wt%	Combustion gas analysis	Used to estimate processing and refining requirements
Hydrogen Content	ASTM D5291	wt%	Combustion gas analysis	Used to estimate processing and refining requirements
Nitrogen Content	ASTM D5291	wt%	Combustion gas analysis	Used to estimate processing and refining requirements
Organic Chloride	ASTM D4929 (Procedure B)	µg/g	Distillation, combustion, and microcoulometry	Not present in crude oils, but come from cleaning operations
Total Fluorine	ASTM D7359	mg/kg	Oxidative pyrohydrolytic combustion, followed by ion chromatography detection	Determines fluorine in aromatic hydrocarbons, which can be harmful to catalysts and lead to corrosion
Total Chlorine	ASTM D7359	mg/kg	Oxidative pyrohydrolytic combustion, followed by ion chromatography detection	Determines chlorine in aromatic hydrocarbons, which can be harmful to catalysts and lead to corrosion
Hydrogen Sulfide Content	UOP 163	Ppm	Potentionmetric titration	A measure of the toxic, explosive H_2S gas
Carbon Residue	ASTM D4530	wt%	Micro method – evaporation and pyrolysis residue	Tendency of crude oil to form a carbon residue with degradation
Sulfur Content	ASTM D4294	wt%	Energy dispersive X-ray fluorescence spectrometry	Determines whether crude oil is labeled “sweet” or “sour”
Saturate Content	ASTM D2007	wt%	Clay-gel absorption chromatography	Helps predict oil interaction with rubber
Aromatic Content	ASTM D2007	wt%	Clay-gel absorption chromatography	Helps predict oil interaction with rubber
Polar Content	ASTM D2007	wt%	Clay-gel absorption chromatography	Helps predict oil interaction with rubber
Asphaltene Content	ASTM D2007	wt%	Clay-gel absorption chromatography	May indicate propensity of crude oil to create black smoke upon combustion
UOP Characterization Factor (K)	UOP 375	Unitless	From relative density and distillation data	A general indicator of crude oil origin and nature
Estimated Molecular Weight	UOP 375	g/mol	From relative density and distillation data	Used to check freezing point depression molecular weight

F.2.2.6. Burn Site Subsample Characterization

Crude oil sub-samples were collected from the Sandia burn site to provide direct property data for the oil used in the burn test apparatus. Some optimization in sampling timeline and location was required to satisfy logistical and safety constraints associated with complex tests and personnel exclusion zones, so sub-samples were typically acquired within a few days of each combustion test from a pressurized oil pre-conditioning system. These burn site sub-samples also proved useful for monitoring crude oil quality during storage in the pressurized 4,800-gallon tank and—ideally—ensuring that storage had not resulted in any significant changes in crude oil vapor pressure, flash point, gross heat of combustion, or water content. Analysis methods are organized below into pressurized and unpressurized test methods.

F.2.2.6.1. Pressurized Burn-Site Subsample Analysis

Table F- 7 lists the analyses conducted at elevated pressure using subsample extracted at pressure from pressurized sample containers. Brief descriptions of each analytical procedure are provided below.

Table F- 7: Pressurized Loading Site Subsample Analyses

Method	Test	Unit
ASTM D6377 (M)	Vapor Pressure, VPCRx(T)	Psia or kPa
GPA 2103-M	Compositional Analysis (N_2–C30+)	mole%

F.2.2.6.1.1 ASTM D6377 VPCRx(T) Expansion Series

The series of pressure–expansion points shown in Table F- 8 was measured for each subsample, and each measurement was replicated, for a total of 12 discrete vapor pressure measurements. Samples were allowed to reach an effective equilibrium for each expansion ratio, via use of the vapor pressure testing instrument settings given in Table F- 9.

Table F- 8: V/L ratios used for burn-site subsample vapor pressure measurement

Temperature		Expansion Ratio (x)					
(°F)	(°C)	V/L	V/L	V/L	V/L	V/L	V/L
100	37.8	0.05	0.1	0.2	0.5	1.5	4.0

Sandia recommended running this analysis in duplicate on separate cylinders to further understand variability among the samples.

Table F- 9: Instrument settings used for burn-site subsample vapor pressure measurement

V/L	Minimum Equilibration Time (sec)	Equilibration dP/dt (kPa/min)
0.05	1200	0.2
0.10	1000	0.2
0.20	900	0.2
0.50	600	0.15
1.5	500	0.1
4.0	300	0.1

Note: The "M" modifier on the ASTM D6377 test method above relates specifically to the equilibrium criteria above in Table F- 9 and the temperature conditioning of the test fluid. Sandia National Laboratories requires that the test fluid be pre-conditioned to the test temperature PRIOR TO PRESSURIZED INJECTION into the sample chamber in the D6377 device, and that the sample injection tubing and pressure regulators (if required) are also maintained at the test temperature. This is done in order to prevent liquid thermal expansion effects from further pressurizing the cell before the expansion sequence starts, leading to erroneously high-pressure values for low V/L ratios.

F.2.2.6.1.2 Pressurized Compositional Analysis: GPA 2103-M with physical shrink and ASTM D2887 C7+ analysis

Samples were analyzed for composition by GPA 2103-M, described in section F.2.2.5.1.2.

F.2.2.6.2. Unpressurized Burn-Site Subsample Analyses

Table F- 10 lists the analyses conducted at atmospheric pressure for each unpressurized burn-site subsample. These analyses were selected because they are expected to have a close association with measured combustion properties. Water content was obtained to monitor whether emulsified water had entered the oil sample with the potential to affect burn properties or test performance.

Table F- 10: Unpressurized burn-site subsample analyses

Method	Test	Unit
ASTM D56 and D5828	Flash Point	°F
ASTM D240	Gross Heat of Combustion	BTU/lb
ASTM D4377	Water Content	Vol%

These methods were selected because they represent the industry standard for these property measurements.

F.2.2.7. Jet Fuel Subsample Characterization

Since Jet A was used as a surrogate for combustion testing, it was important to know the properties of the fuel.

F.2.2.7.1. Pressurized Jet A Subsample Analyses

Table F- 11 lists the analyses conducted at elevated pressure using subsample extracted at pressure from pressurized sample containers. Brief descriptions of each analytical procedure are provided below.

Table F- 11: Pressurized Loading Site Subsample Analyses

Method	Test	Unit
ASTM D6377 (M)	Vapor Pressure, VPCRx(T)	psia or kPa
GPA 2186 (M)	Compositional Analysis (C1–C30+)	mole%

F.2.2.7.1.1 ASTM D6377 VPCRx(T) Expansion Series

A series of vapor pressure-expansion points was taken on the jet fuel subsample. The selected temperature and expansion points are given in Table F- 12. Equilibrium requirements were the same as for the crude oils, with specifications given in section F.2.2.6.1.1.

Table F- 12: Temperature and expansion settings for ASTM D6377 VPCRx(T) measurements run on loading site subsamples.

Temperature		Expansion Ratio (x)			
(°F)	(°C)	V/L	V/L	V/L	V/L
100	37.8	0.05	0.2	0.5	4.0

F.2.2.7.1.2 Pressurized Compositional Analysis (GPA 2186-M)

The jet fuel composition was determined by Detailed Hydrocarbon Analysis (DHA), which employs gas chromatography to provide physical separation of individual components of a complex hydrocarbon mixture from nC1-nC30+. The GC results were then post-processed by commercial software and calibrated to a standard DHA blend to generate a carbon number report based on weight %, volume %, and mole% down to 10 ppm. The analysis is based on GPA 2186, "Method for the Extended Analysis of Hydrocarbon Liquid Mixtures Containing Nitrogen and Carbon Dioxide by Temperature Programmed Gas Chromatography ."

F.2.2.7.1.3 Unpressurized Jet A Subsample Analyses

Table F- 13 lists the analyses conducted at atmospheric pressure for the unpressurized subsample. These analyses were selected because they are expected to have a close association with measured combustion properties. Water content was obtained to monitor whether emulsified water had entered the oil sample with the potential to affect burn properties or test performance.

Table F- 13: Unpressurized Jet A subsample analyses

Method	Test	Unit
ASTM D56	Flash Point	°F
ASTM D240	Gross Heat of Combustion	BTU/lb
ASTM D6304	Water Content	mg/kg

These methods were selected because they represent the industry standard for these property measurements.

F.2.2.8. Equation of State (EOS) Modeling

Crude oil properties, to include vapor pressures (at selected V/L, temperature) and heats of combustion, were simulated via commercially available process simulation software commonly used in the oil & gas industry. Inputs to the process simulator were obtained from the pressurized compositional analyses described in Section F.2.2.5.1.2. This process simulation used a cubic equation of state (EOS) model for vapor-liquid equilibrium calculations. The process simulations provide value in several ways:

1. Producing modeled VPCRx from compositional data helps identify which compositional factors in a crude oil affect its vapor pressure, and in what ways.

2. Having access to a validated simulation model can enable predictions of oil properties where direct measurements are not feasible due to expense, difficulty, or safety concerns.
3. Favorable comparisons of measured versus modeled property data provides confirmation that the measurements and model are self-consistent. Conversely, disparities may flag QA/QC issues that need to be addressed and corrected that may improve the overall accuracy of the findings.

More information on the process simulation and EOS modeling procedures used here can be found in a previous study [4].

F.2.2.9. Post-Burn Solids Sampling

The crude pool fires have the potential to leave burn residue that may contain unburned oil, solid or semi-solid sheets, and/or a dense, viscous residue that is a mix of liquid and solid. The type and volume of residue correlates with the type of oil that is burned with no residue expected for very light to light oils, and increasingly measurable amounts of residue expected for medium and heavy oils. The "light, tight" oils will likely not leave much residue. More dense oils, such as the medium sour conventional SPR oil, have the potential to leave notably more residue—potentially enough to allow for analysis and also require pan clean-up and solids disposal. Where possible, solids were collected from the pool fire pan and weighed and compared with the mass of feed oil. Results are presented in section F.4.3.

F.3. Experimental Results

The experimental results of this study are given below, organized by measured property. Table F-14 through Table F- 17 summarize the physical properties of the jet fuel and crude oil subsamples.

Table F- 14: Selected physical properties for the Task 3 SPR oil subsamples

	Fuel		SPR	SPR1: 2m, Cold	SPR2: 2m, Hot	SPR3: 5m, Hot	SPR4: 5m, Cold	SPR5	SPR6: Fireball
	Sample Name		SPR0: Loading	SPR Burn Site 1	SPR Burn Site 2	SPR Burn Site 3	SPR Burn Site 4	SPR Burn Site 5	SPR Burn Site 6
Sampling Date			1/24/2017	2/13/2017	3/20/2017	4/5/2017	8/14/2017	7/17/2018	10/2/2018
Property Name	***Analysis Method***	***Units***							
VPCR0.2(100°F)	**ASTM D6377-M**	**psia**	13.4	12.9	11.0	11.4	9.0	6.5	6.7
VPCR0.2(100°F)	**Simulation**	**psia**	11.1	11.7	11.4	8.1	10.8		6.8
VPCR4(100°F)	**ASTM D6377-M**	**psia**	6.6	5.7	4.9	4.6	3.6	1.9	1.9
VPCR4(100°F)	**Simulation**	**psia**	7.3	6.4	5.7	5.0	3.5		2.2
API Gravity @ 60°F	**ASTM D5002**	**°API**	33.0	32.88	32.6	32.5	31.6	31.1	31.0
Relative Density @ 60/60°F	**ASTM D5002**	**(-)**	0.8602	0.8608	0.8623	0.8629	0.8678	0.8741	0.8709
Heat of Combustion	**ASTM D240**	**BTU/lb**	18591	18465	19734	18354	18626	18644	18562
Lower Heating Value	**Simulation**	**BTU/lb**	18987	18983	18987	18978	18965		18962
Higher Heating Value	**Simulation**	**BTU/lb**	20410	20405	20409	20398	20382		20377
< C6 wt%		**Wt %**	3.70	3.70	3.18	3.09	2.07		1.40
Flashpoint	**ASTM D56A**	**°F**	< 50	< 50	< 50	N/A	<50	< 50	< 50
Flashpoint	**ASTM D3828**	**°C**							
Water Content	**ASTM D4928**	**Vol %**	0			0.06	0.02		
Water Content	**ASTM D4928**	**Wt %**				0.069		0.031	0.027
Sulfur Content	**ASTM D4294**	**Wt %**	1.47						
Water + Sediment	ASTM D4007	vol%	0.03	0.75	0.075	N/A			0.024
Water Content	**ASTM D6304**	**ppm**							

Table F- 15: Selected physical properties for the Task 3 Bakken oil subsamples

	Fuel		BKN	BKN1: 5m	BKN2	BKN3	BKN4: Fireball	BKN5: Fireball
	Sample Name		BKN0: Loading	Bakken Burn Site 1	Bakken Burn Site 2	Bakken Burn Site 3	Bakken Burn Site 4	Bakken Burn Site 5
Sampling Date			8/17/2017	10/2/2017	1/18/2018	1/31/2018	7/18/2018	10/3/2018
Property Name	***Analysis Method***	***Units***						
VPCR0.2(100°F)	**ASTM D6377-M**	**psia**	17.5	19.3	20.0	21.8	19.3	18.0
VPCR0.2(100°F)	**Simulation**	**psia**	20.2	18.2	17.7	20.5	24.4	18.9
VPCR4(100°F)	**ASTM D6377-M**	**psia**	10.2	10.2	11.0	11.1	9.9	9.6
VPCR4(100°F)	**Simulation**	**psia**	11.2	10.5	10.5	10.8	11.6	11.0
API Gravity @ 60°F	**ASTM D5002**	**°API**	42.9	42.9	43.1	43.0	43.0	42.5
Relative Density @ 60/60°F	**ASTM D5002**	**(-)**	0.8107	0.8113	0.8104	0.8107	0.8	0.8133
Heat of Combustion	**ASTM D240**	**BTU/lb**	20834	21212	19785	19764	18958.0	21138
Lower Heating Value	**Simulation**	**BTU/lb**	19058	19070	19089	19094	19056.7	19063
Higher Heating Value	**Simulation**	**BTU/lb**	20497	20510	20540	20546	20496.7	20502
< C6 wt%		**Wt %**	6.17	5.99	5.91	6.22	5.9	6.21
Flashpoint	**ASTM D56A**	**°F**	<50	< 50			< 50	< 50
Flashpoint	**ASTM D3828**	**°C**			<-30.0	<-30.0		
Water Content	**ASTM D4928**	**Vol %**	0.01	0.01				
Water Content	**ASTM D4928**	**Wt %**		0.013			0.0	0.01
Sulfur Content	**ASTM D4294**	**Wt %**	0.0844					
Water + Sediment	ASTM D4007	vol%			0.025	0.145		0.005
Water Content	**ASTM D6304**	**ppm**			100	1600		

Table F- 16: Selected physical properties for the Task 3 Texas Shale oil subsamples

	Fuel		TXSh	TXSh1: 5m	TXSh2	TXSh3: Fireball
	Sample Name		TXSh0: Loading	TX Shale Burn Site 1	TX Shale Burn Site 2	TX Shale Burn Site 3
Sampling Date			11/28/2017	1/15/2018	7/19/2018	10/2/2018
Property Name	***Analysis Method***	***Units***				
VPCR0.2(100°F)	**ASTM D6377-M**	**psia**	16.6	15.7	15.7	15.8
VPCR0.2(100°F)	**Simulation**	**psia**	16.2	15.0		15.7
VPCR4(100°F)	**ASTM D6377-M**	**psia**	8.2	8.5	7.9	7.8
VPCR4(100°F)	**Simulation**	**psia**	9.2	8.6		9.1
API Gravity @ 60°F	**ASTM D5002**	**°API**	37.5	37.3	37.26	36.785
Relative Density @ 60/60°F	**ASTM D5002**	**(-)**	0.8375	0.8353	0.8385	0.8408
Heat of Combustion	**ASTM D240**	**BTU/lb**	19206	18469	18778	18598
Lower Heating Value	**Simulation**	**BTU/lb**	18992	18991		19005
Higher Heating Value	**Simulation**	**BTU/lb**	20412	20411		20427
< C6 wt%		**Wt %**	4.21	4.03		4.20
Flashpoint	**ASTM D56A**	**°F**	< 104	<50	< 50	< 50
Flashpoint	**ASTM D3828**	**°C**				
Water Content	**ASTM D4928**	**Vol %**	0.03	0.03		
Water Content	**ASTM D4928**	**Wt %**			0.025	0.023
Sulfur Content	**ASTM D4294**	**Wt %**	0.693			
Water + Sediment	ASTM D4007	vol%	0			0.019
Water Content	**ASTM D6304**	**ppm**				

Table F- 17: Selected physical properties for the Task 3 Jet A subsample

	Fuel		JET
	Sample Name		Jet A TTC
Sampling Date			8/9/2017
Property Name	***Analysis Method***	***Units***	
VPCR0.2(100°F)	**ASTM D6377-M**	**psia**	9.3
VPCR0.2(100°F)	**Simulation**	**psia**	
VPCR4(100°F)	**ASTM D6377-M**	**psia**	0.6
VPCR4(100°F)	**Simulation**	**psia**	
API Gravity @ 60°F	**ASTM D5002**	**°API**	43.12
Relative Density @ 60/60°F	**ASTM D5002**	**(-)**	0.8103
Heat of Combustion	**ASTM D240**	**BTU/lb**	19624
Lower Heating Value	**Simulation**	**BTU/lb**	19135
Higher Heating Value	**Simulation**	**BTU/lb**	20582
< C6 wt%		**Wt %**	0.01
Flashpoint	**ASTM D56A**	**°F**	139
Flashpoint	**ASTM D3828**	**°C**	
Water Content	**ASTM D4928**	**Vol %**	
Water Content	**ASTM D4928**	**Wt %**	
Sulfur Content	**ASTM D4294**	**Wt %**	
Water + Sediment	ASTM D4007	vol%	
Water Content	**ASTM D6304**	**ppm**	44

F.3.1. Crude Oil Visual Properties

Table F- 15 shows the three crude oils side-by-side during open bottle sampling from the week of July 16, 2018 at the Lurance Canyon Burn site at Sandia. Visual inspection alone can be used to segregate these crudes. The color of the oils varied from nearly black (SPR), to mocha-brown (TX shale), to olive green (Bakken). Generally speaking, crude oil color is driven by the heavy

component contents, so the darker the color, the heavier the oil. Visual inspection would therefore suggest that the SPR oil was the heaviest, followed by the TX shale oil, and then the Bakken oil. Also, when these oils were injected into Boston Round jars (as shown in the figure), the SPR oil formed almost no bubbles, the TX Shale oil showed some bubbles, and the Bakken oil formed a thick bubble layer. This information can be used to rank the volatilities of each oil: the SPR oil was essentially non-volatile, the TX shale oil was slightly more volatile, and the Bakken oil was the most volatile of the three at sampling conditions. Since volatility correlates with vapor pressure, the SPR oil appears to have the lowest vapor pressure, followed by the TX shale oil, and then the Bakken oil. In all cases, the bubbles quickly dissipated when the jars were closed, and the contents were mixed before any unpressurized property testing at the analytical laboratory. Contrast these observations to Jet A in Figure F- 16, an engineered fluid containing mostly C9-C15 molecules. In the absence of heavy components, the jet fuel was water white. Because there weren't any light molecules in the fuel, no boiling was apparent at the atmospheric conditions present during sampling. These qualitative conclusions were verified by quantitative property measurements.

Figure F- 15: Photos of the crude oil samples taken by open bottle sampling method the week of July 16, 2018 (oil temperature 75-80°F, ambient pressure ~11 psia @ ~7,000 ft elevation).

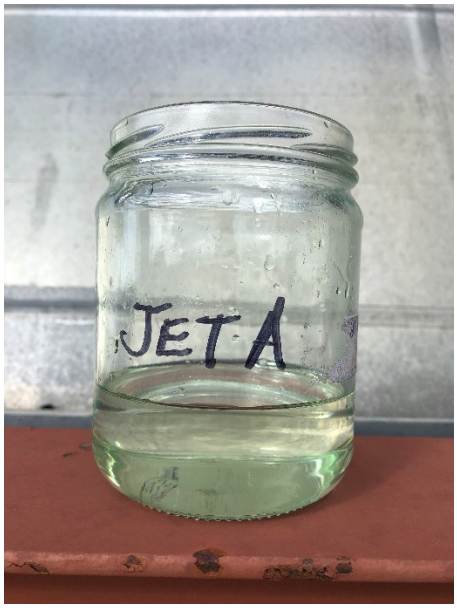

Figure F- 16: Photo of Jet A taken by open bottle sampling method the week of February 20, 2019.

F.3.2. Crude Oil Unpressurized Properties

Unpressurized samples of the oils were tested for several important properties, including molecular weight, density, heat of combustion, flash point, and water content.

F.3.2.1. Unpressurized Properties for Loading Subsamples

When the crude oils were first loaded into tankers, samples were withdrawn, and a variety of tests were performed, as shown in Table F- 18. The samples taken upon loading underwent more tests than the burn-site samples to better identify the oil. These extra tests were not done for properties that were expected to change appreciably throughout the duration of storage, or for properties that were not directly influential to this project. Several of these extra properties were requested by sponsors and are commonly used in industry to determine the type, nature, and origin of the oil.

The API Gravity measurements for these three subsamples taken at loading ranged from 33.0 (SPR), to 37.5 (TXSh) to 42.9 (Bakken). For additional context, a plot of U.S. crude oil production collected by the U.S. Energy Information Administration for the two-year period October 2016 – October 2018, segregated by API gravity range, is given in Figure F- 17. About 1/3 of lower 48 production had API gravity below the SPR sample, a little less than ½ was between the SPR and Bakken samples, and slightly less than ¼ had API gravity above the Bakken sample. This comparison indicates that the API gravities of the oils tested here provide some representation of current U.S production and span a significant range from the lower, middle, and upper thirds of the production volume-weighted API gravity spectrum.

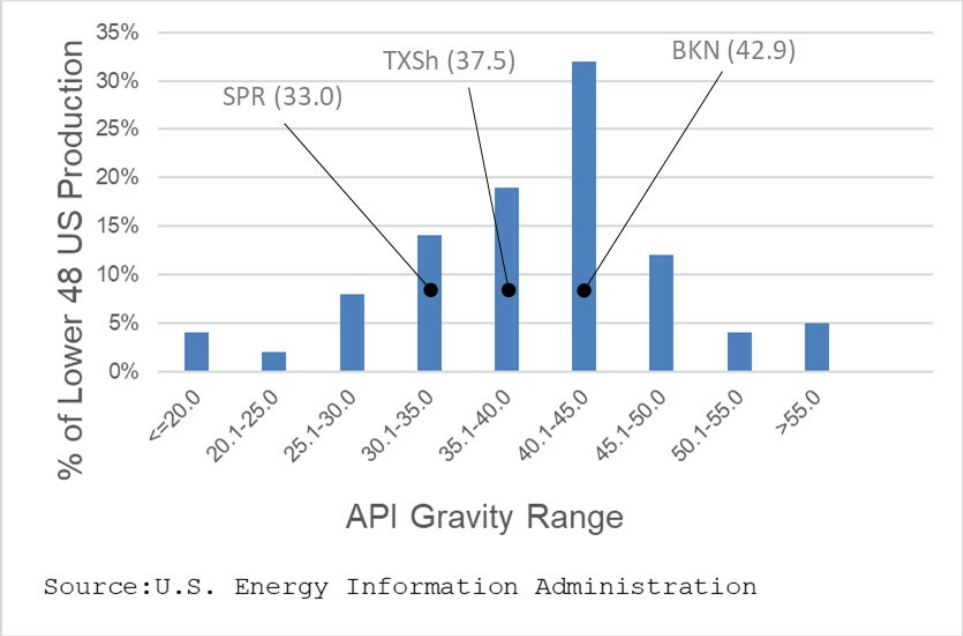

Figure F- 17: Percentage of lower 48 U.S. production (Oct 2016-Oct 2018) by API gravity.

The measured heats of combustion ranged from 18,591 BTU/lb (SPR) to 20,834 BTU/lb (Bakken) and appear to show a similar trend as API Gravity. However, when the compositions of these samples were used to predict heats of combustion using an EOS model, the heats of combustion were very similar across oils (ranging from 20,410 BTU/lb to 20,497 BTU/lb).

Table F- 18: Unpressurized properties for the loading subsamples

Property	Method	Units	SPR0	BKN0	TXSh0
Sample Material			SPR	Bakken	TX Shale
Sampling Date			1/24/2017	8/17/2017	11/28/2017
Molecular Weight	GPA 2103M	g/mol	211.19	158.55	179.81
API Gravity	ASTM D5002	°API	33.0	42.9	37.5
Relative Density @ 60/60°F	ASTM D5002	g/mL	0.8602	0.8107	0.8375
Kinematic Viscosity (T)	ASTM D445	mm^2/s	6.496(100°F)	1.996(40°C)	7.195(40°C)
Flash Point	ASTM D56	°F	< 50	< 50	< 104
Pour Point	ASTM D97	°F	< -27.4	< -27.4	-0.4
Gross Heat of Combustion	ASTM D240	BTU/lb	18,591	20,834	19,206
-- Simulated	EOS Model	BTU/lb	20,410	20,497	20,412
Acid Number	ASTM D664A	mg KOH/g	0.25	< 0.10	0.10
Basic Nitrogen	UOP 269	ppm	336	130	291
Nitrogen	ASTM D4629	mg/kg	1300		
Average Bromine Number	ASTM D1159	--	3.6	1.1	2.9
Iron	ASTM D5708	mg/kg	3.9	1.3	6
Nickel	ASTM D5708	mg/kg	7.9	< 0.1	2.7
Sodium	ASTM D5708	mg/kg	25.2	7.3	2
Vanadium	ASTM D5708	mg/kg	30.4	< 0.1	2.1
Salt Content (em Cl)	ASTM D3230	lb/1000bbl	4.9	3.8	7
Water+Sediment Content	ASTM D4007	vol%	0	< 0.05	0
Asphaltene Content	ASTM D6560	wt%	2.48	< 0.50	0.38
Ash Content	ASTM D482	wt%	0.019	0.003	0.001
Wax Content	UOP 46	wt%	4.1	< 5.0	< 5.0
Water Content	ASTM D4928	vol%	0.00	0.01	0.03
Water Content	ASTM D4377	vol%	0.00		
Carbon Content	ASTM D5291	wt%	84	75	78
Hydrogen Content	ASTM D5291	wt%	12.2	10.0	12.0
Nitrogen Content	ASTM D5291	wt%	< 0.75	0.10	< 0.75
Organic Chloride	ASTM D4929B	µg/g	< 1.0	< 1.0	< 1.0
Total Fluorine	ASTM D7359	mg/kg	< 1.00	< 1.00	< 1.00
Total Chlorine	ASTM D7359	mg/kg	[a]	1.20	2.4
Hydrogen Sulfide Content	UOP 163	ppm	8	< 1	12
Carbon Residue	ASTM D4530	wt%	4.35	0.53	1.59
Sulfur Content	ASTM D4294	wt%	1.47	0.0844	0.693
Saturate Content	ASTM D2007	wt%	32.3		
Aromatic Content	ASTM D2007	wt%	32.6		
Polar Content	ASTM D2007	wt%	30.1		
Asphaltene Content	ASTM D2007	wt%	5.07		
UOP Char. Factor (K)	UOP 375	--	11.91	12.11	
Estimated Molecular Weight	UOP 375	g/mol	310		
Molecular Weight	Ad Hoc	g/mol			187.25

[a] included in the total fluorine value

F.3.2.2. Unpressurized Properties for Pool Fire Subsamples

A smaller set of unpressurized properties were measured for the burn-site, pre-pool fire subsamples. These include API gravity/relative density, heat of combustion, flash point, and water content. Note that several water content test methods were used. Water and sediment were measured together for the 2m pool fires, while water was measured alone for the 5m pool fires and fireballs. Table F- 19 gives the measured unpressurized properties for the samples taken before the 2m pool fires. There was little difference between the densities, heats of combustions, and flash points of these two samples.

Table F- 19: Unpressurized properties for 2m pool fires

Property	Method	Units	SPR1	SPR2
Fuel			SPR	SPR
Burn Type			Cold 2m Pool	Hot 2m Pool
Sampling Date			2/13/2017	3/20/2017
Molecular Weight	GPA 2103M	g/mol	206.33	219.33
API Gravity @ 60°F	ASTM D5002	°API	32.88	32.6
Relative Density @ 60/60°F	ASTM D5002	(-)	0.8608	0.8623
Heat of Combustion	ASTM D240	BTU/lb	18,465	19,734
-- Simulated		BTU/lb	20,405	20,409
Flash Point	ASTM D56A	°F	< 50	< 50
Water + Sediment	ASTM D4007	vol%	0.75	0.075

Table F- 20 gives the measured unpressurized properties for the samples taken before the 5m pool fires. These samples show a range of densities as would be expected from the different crude oils, but many of the other properties are similar, including heat of combustion (verified by simulation) and flash point (measured at the limit of the test method ASTM 56A). The water contents were very low and do not indicate entrained free-phase water.

Table F- 20: Unpressurized properties for the 5m pool fires

Property	Method	Units	SPR3	SPR4	BKN1	TXSh1
Fuel			SPR	SPR	BKN	TXSh
Burn Type			Hot 5m Pool	Cold 5m Pool	5m Pool	5m Pool
Sampling Date			4/5/2017	8/14/2017	10/2/2017	1/15/2018
Molecular Weight	GPA 2103M	g/mol	210.73	219.66	153.83	181.15
API Gravity @ 60°F	ASTM D5002	°API	32.6	31.6	42.9	37.3
Relative Density @ 60/60°F	ASTM D5002	(-)	0.8629	0.8678	0.8113	0.8353
Heat of Combustion	ASTM D240	BTU/lb	18,354	18,626	21,212	18,469
-- Simulated		BTU/lb	20,398	20,382	20,476	20,411
Flash Point	ASTM D56A	°F		< 50	< 50	< 50
Water Content	ASTM D4928	vol%	0.06	0.02	0.01	0.03

F.3.2.3. Unpressurized Properties for Fireball Subsamples

Table F- 21 gives the measured unpressurized properties for the samples taken before the fireballs. In spite of the weathering of the SPR sample indicated by loss of light ends and very low VPCR (see ahead in sections F.3.3 and 0), the flash point is still < 50°F. The water contents were very low and do not indicate entrained free-phase water. Additionally, viscosity measurements were done on these subsamples, showing that the SPR oil was more viscous than the others. The Jet A fuel is included since it was used for the 100-gallon proof-of-concept fireball test, though the range of properties tested was more limited.

Table F- 21: Unpressurized properties for fireballs

Property	Method	Units	JetA	SPR6	BKN5	TXSh3
Fuel			JetA	SPR	Bakken	TX Shale
Burn Type				Fireball	Fireball	Fireball
Sampling Date			8/9/2017	10/2/2018	10/3/2018	10/3/2018
Molecular Weight	GPA 2103M	g/mol	162	228.29	159.77	178.76
API Gravity @ 60°F	ASTM D5002	°API	43.12	31.0	42.5	36.8
Relative Density @ 60/60°F	ASTM D5002	(-)	0.81	0.8709	0.8133	0.8408
Heat of Combustion	ASTM D240	BTU/lb	19,624	18,562	21,138	18,598
-- Simulated		BTU/lb	20,582	20,377	20,502	20,427
Flash Point	ASTM D56A	°F	139	< 50	< 50	< 50
Water Content	ASTM D4928	vol%	--	0.02	0.005	0.02
Kinematic Viscosity @ 60°F	ASTM D7042	mm^2/s		16.719	2.9291	5.4253

F.3.2.4. Comments on Flash Point

Flash point as measured by ASTM D56A returned the same value, < 50°F, for every crude oil subsample tested in this research project. This does not imply that the flash points, defined by ASTM as "the lowest temperature of the test specimen, adjusted to account for variations in atmospheric pressure from 101.3kPa, at which application of an ignition source causes the vapors of the test specimen to ignite under specified conditions of the test ," were identical for the Task 3 oils. Rather, this indicates that the test method as applied does not have the resolution to distinguish among these samples, all of which exhibit flash point < 50°F. ASTM D56A is one representative method among numerous ASTM and ISO standards listed in American Petroleum Institute Recommended Practice 3000 [6] that may be utilized for assignment of packing group for transportation of hazardous materials. Note that two of the Bakken sub-samples (BKN2, BKN3) were tested for flash point by ASTM D3828 [81], and both returned values at the lower detection limit of that method, <−30°C. In reviewing the RP3000 listing of flash point test methods applicable to packing group assignments, the low-end temperature for the flash point methods given there is −30°C. Finding the flash point of the oils used here at any better resolution than <−30°C would require use of methods capable of very low temperatures and are not within the current scope of this study. The only fuel utilized in Task 3 that exhibited a flash point distinct from the rest was Jet A collected from a storage tank at Sandia, which returned a flash point of 139°F.

With the compositions and vapor pressures of the subsamples in hand, a couple flash point prediction methods were employed to provide further context to the flash point measurements. Although there

have been no reliable methods for predicting the flash points of whole crude oils, there have been several generated for petroleum fractions and middle distillates, which are used here with caution. Figure F- 18 through Figure F- 20 show flash point predictions versus number of days since the loading events for the subsamples of oil using the Reid Vapor Pressure , the temperature at which 10 vol% of the oil vaporizes , and the normal boiling point [82], respectively. Measured $VPCR_4$ values for the SPR, BKN, and TXSh oils were used to approximate the Reid Vapor Pressure. Measured compositions were plugged into a commercially-available process simulation model to approximate the temperatures at which 10 vol% vaporizes. The process simulator was also used to calculate the temperatures at which 50 vol% of the material vaporizes, which was used to approximate the normal boiling points of the samples. In all three plots below, the lower limits of the analytical laboratories' ASTM D56A and ASTM D3828 capabilities are shown to provide context to the predictions.

Though the prediction methods have inherently high uncertainty and were not necessarily made for crude oils, the trends in the predictions were illuminating. First, all predictions were below the analytical laboratory's ASTM D56A flash point measurement method limit of 50 °F, which is consistent with experimental results. Also, the BKN2 and BKN3 predictions (about 150 days after loading) were all below the analytical laboratory's ASTM D3828 flash point measurement method limit at -30 °C, which is also consistent with the experimental results. Second, the BKN subsamples were predicted to have the lowest flash points, followed by the TXSh, and then the SPR, for all three prediction methods. This trend matches the understanding of volatility within the oils – higher light end contents would lead to lower flash points. Third, the three SPR flash point predictions increase with time, which correlates well with the weathering seen in the SPR sample (see section F.4.1.1 for further discussion). Meanwhile, the BKN and TXSh predicted flash points held steady through time, which would indicate little change in volatility. In all three prediction methods, the last couple of SPR flash points were above the ASTM D3828 detection limits, suggesting that separation in flash point results for the fireball subsamples could be possible with lower-temperature tests.

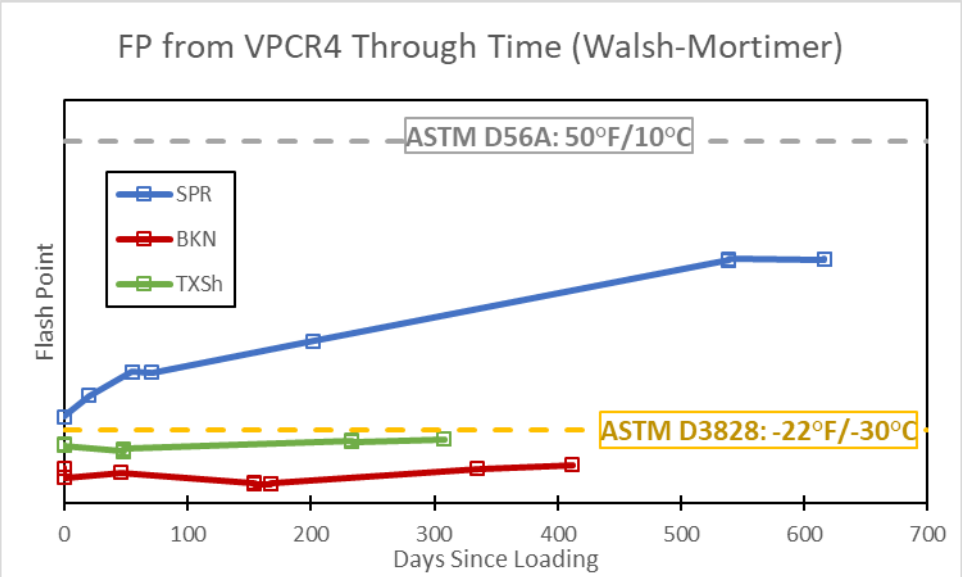

Figure F- 18: Flash points predicted using $VPCR_4$ for the subsamples through time, with measurement limits noted.

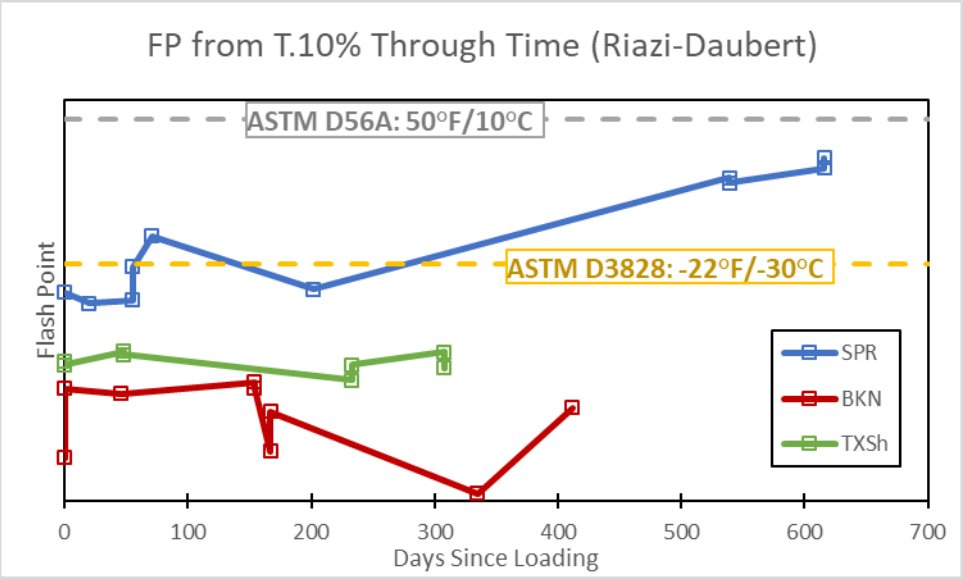

Figure F- 19: Flash points predicted using simulated temperatures at which 10vol% vaporizes for the subsamples through time, with flash point measurement limits noted (dashed lines)

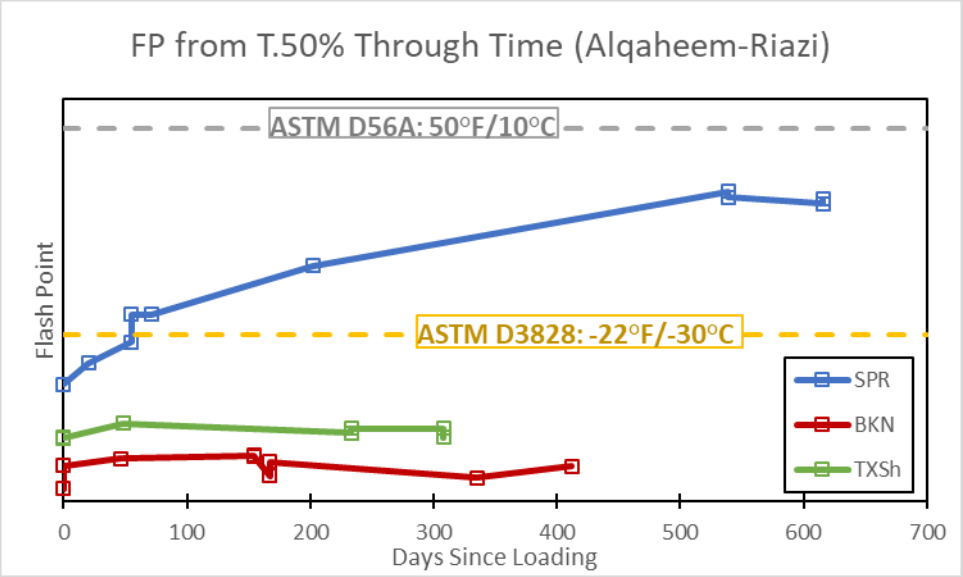

Figure F- 20: Flash points predicted using normal boiling point approximations for the subsamples through time, with flash point measurement limits noted (dashed lines)

F.3.2.5. Comments on Water Content

The measured water contents displayed previously deserve further context with regards to the solubility of water in oil. Water solubility in hydrocarbon mixtures can span a couple orders of magnitude, even at room temperature. To compare the measured water contents to the water content at which a free phase of water would form within the oils, the water solubilities for each of the subsamples were predicted using density and elemental hydrogen content [83]. The predicted water solubilities for subsamples of all three oils and the jet fuel were between 0.1 and 0.125 mass%.

Figure F- 21 shows the measured water contents (closed circles) with the predicted water solubilities (open squares) through time for the three crude oils. The mass% values marked with X's were

combined water and sediment volume% measurements using ASTM D4007 [84], which were converted to mass% using relative density. The second SPR subsample taken 20 days after loading and the fourth Bakken sample taken about 170 days after the loading showed water contents that would indicate water entrainment or emulsification. However, subsequent measurements showed water contents below the predicted water solubilities, indicating water movement out of the oil. These observations suggest that free-phase water is not regularly entrained in the crude oil subsamples (14 of 16 samples measured at or below predicted saturation), though the possibility exists. The specifics of the mixing and handling just prior to subsampling are probably the main contributors to water entrainment in the cases where it occurs. The SPR sample taken at 20 days since loading that measured 0.87 mass% water + sediment was associated with the first 2m pool fire (SPR cold) that boiled over during testing. It is possible that the subsample was indicating water entrainment issues as a function of early handling before the test started. Drawing a direct association between combustion test outcome and water content measured before the test is difficult because there are typically several process steps that occur after oil subsampling but before combustion testing that could lead to water entrainment in the oil or appearance in the test vessel that should not appear in pre-test oil quality assessments.

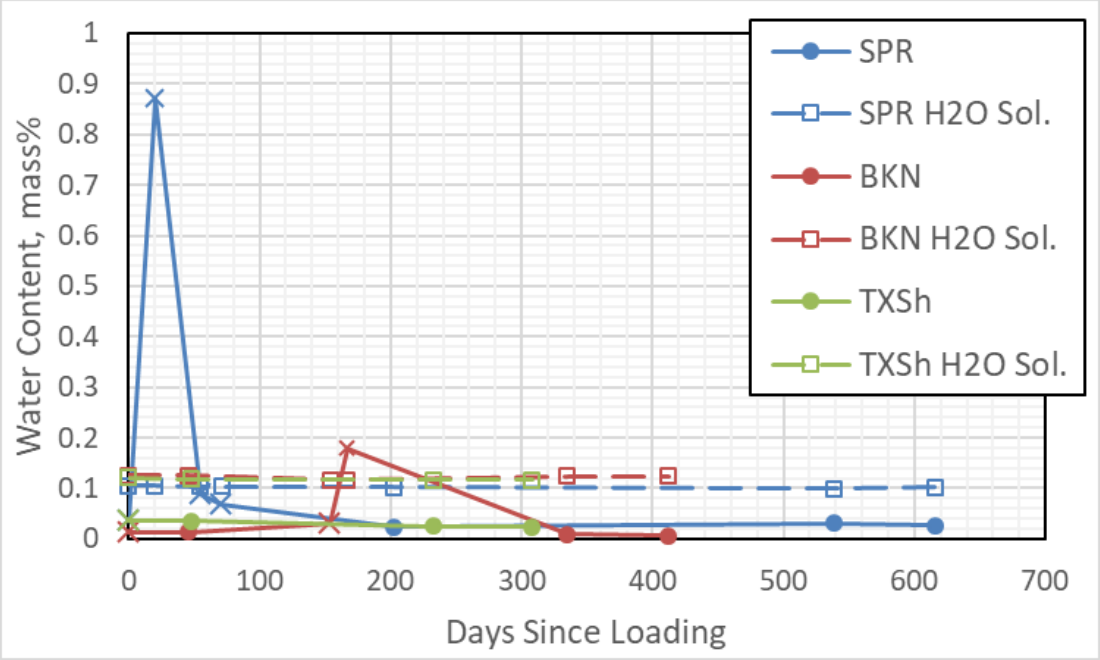

Figure F- 21: Measured water contents and water solubilities in subsamples through time

F.3.3. Crude Oil Compositions

Compositions for the crude oils in association with the various burn events are given in the following sections. It is important to note that the pool fire and fireball subsamples were all drawn from the tankers before or after the burn events. Logistical and safety considerations precluded taking subsamples directly from the fuel feed lines during the fire testing. Compositions are reported here in mole% relative to the "whole" oil. Mole% was chosen because it is the fundamental unit associated with vapor-liquid equilibrium and equation of state modeling, which are central to interpretation of these results. Mole% in whole oil may be converted to mass% or volume% with appropriate component and mixture parameters. The individual components of the "whole oil" analytical results

were grouped by carbon number for simplicity in plotting (full reports of the separate components are given at the end of this chapter).

F.3.3.1. Compositions for Loading Subsamples

The measured compositions for the samples taken at loading are given below. Figure F- 22 gives the fixed gases, while Figure F- 23 shows the light hydrocarbon content of the oils. Replicates for the Bakken and Texas Shale oils are given with outlined, checkered bars.

The fixed gas contents in Figure F- 22 vary from oil-to-oil: the Bakken oil shows larger N_2 content than the others, while the SPR oil shows lower C1 content, but relatively high CO_2 content. The fixed gas contents also vary from sample-to-sample: the N_2 content for the Bakken oil varies from 0.12 mol% (solid red bar) to 0.06 mol% (checkered red bar). The C1 content for the Bakken oil replicates also vary in similar manner. This sample-to-sample variation in fixed gas content might stem from the operation and performance of the sample cylinders, which use N_2 to create backpressure and maintain a single liquid phase on the sample side of the piston. The Bakken oil shows larger light ends compositions from C2-nC5, while the SPR oil has much lower C2 content than the other oils. The relatively low C1 and C2 observed in the SPR oil is partly a result of the stabilization process (degasification) that the oil was subjected to just prior to loading and shipment to Sandia. Average total light ends content (components smaller than C6) are given in Figure F- 24, showing that the three oils cover a range from 3.7 wt% (SPR oil) to 6.2 wt% (Bakken oil).

The whole oil compositions for the samples taken at loading are shown in Figure F- 25, with mass compositions given in Figure F- 26. The data generally show that among the three oils tested here, the Bakken had the most light ends, with TX Shale in the middle, and SPR showing the least light ends. The inverse is apparent for heavy ends: SPR > TXSh > Bakken.

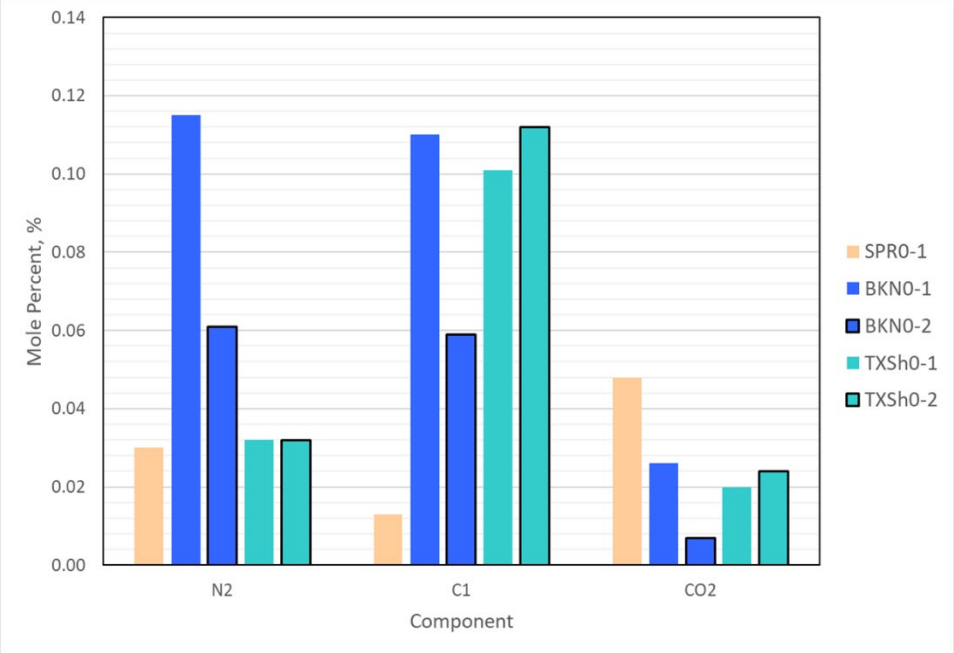

Figure F- 22: Fixed gas and methane compositions in the SPR, BKN, and TXSh oil samples taken at loading

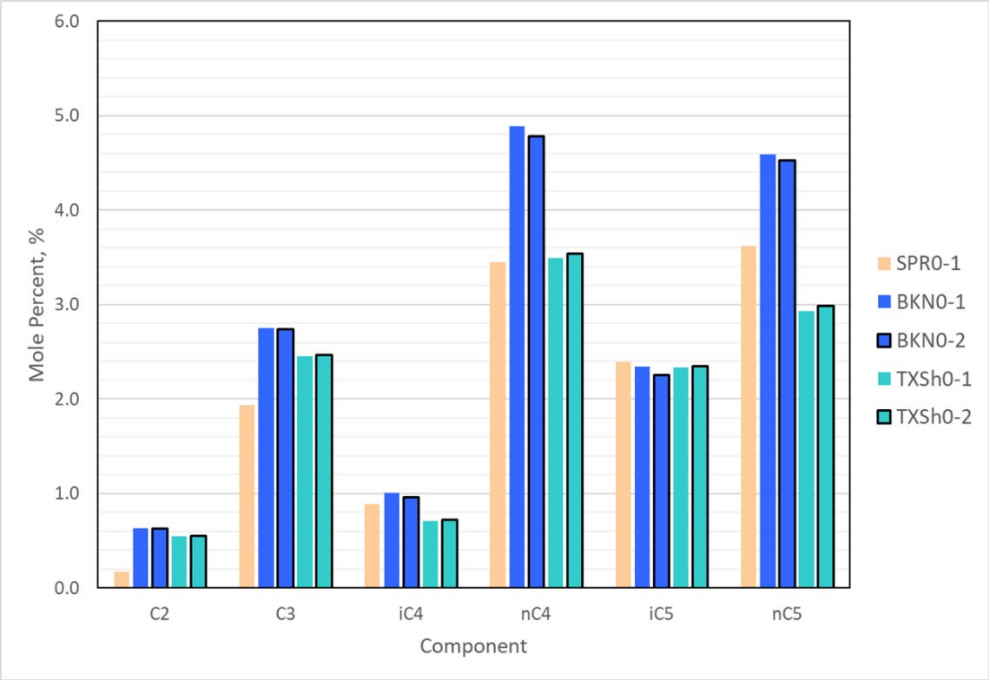

Figure F- 23: Light ends compositions (C2-nC5) in the SPR, BKN, and TXSh oil samples taken at loading

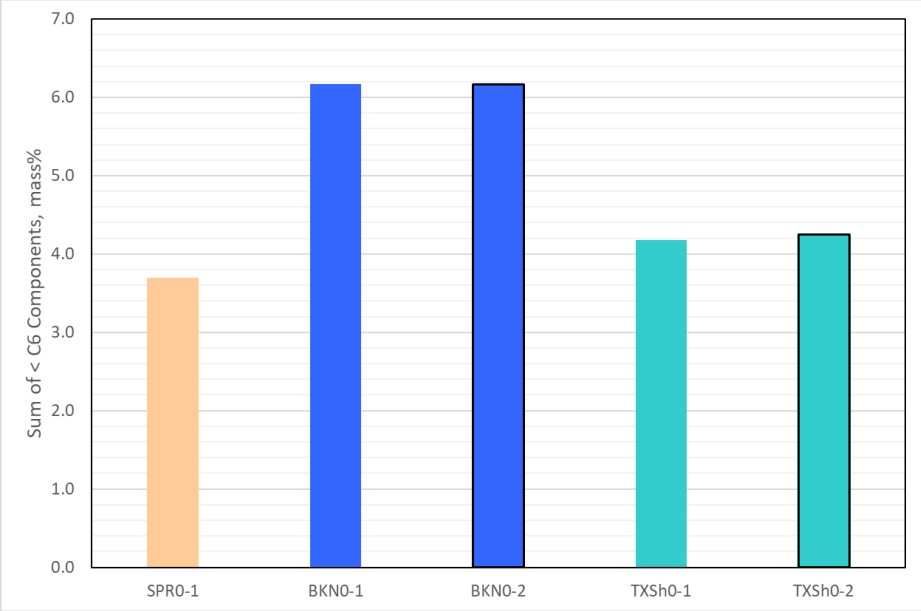

Figure F- 24: Total weight % of components smaller than C6 for the oil samples taken at loading

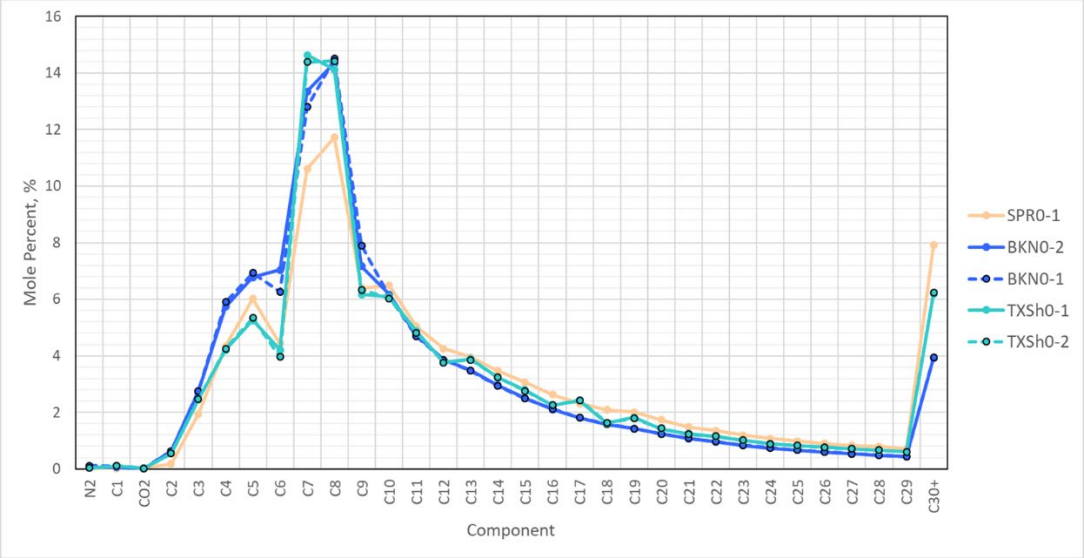

Figure F- 25: Whole oil composition line plot for the SPR, BKN, and TXSh oil samples taken at loading

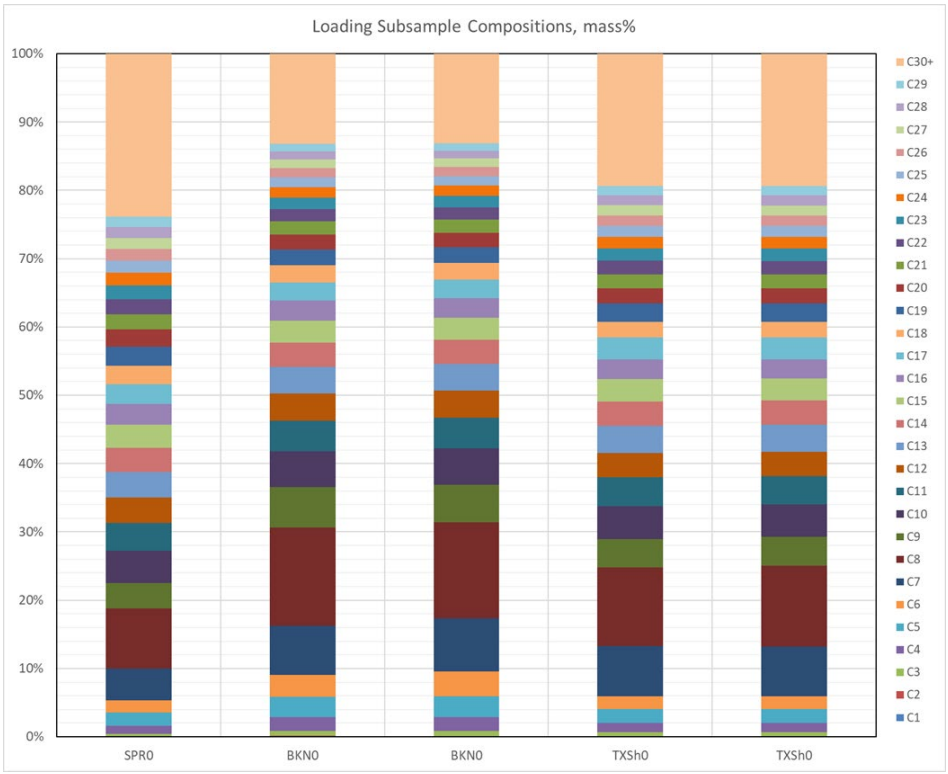

Figure F- 26: Whole oil mass composition stacked bar charts for the SPR, BKN, and TXSh oil samples taken at loading

F.3.3.2. Compositions for Pool Fire Subsamples

The measured compositions for the samples taken before the 2m pool fires are given below. Figure F- 27 gives the fixed gases, while Figure F- 28 shows the light hydrocarbon content of the oils. The fixed gas contents for these samples are similar, while the light hydrocarbons decreased from the 2m Cold to the 2m Hot SPR pool fires. In all, the light ends smaller than C6 fell slightly from 3.7 wt% for SPR1, to 3.2 wt% for SPR2. Figure F- 29: shows the whole oil composition for the 2m pool fires. The heavy ends content > C5 did not noticeably change from SPR1 to SPR2. Figure F- 29 and Figure F- 30 show the whole oil compositions of the two subsamples, which were similar.

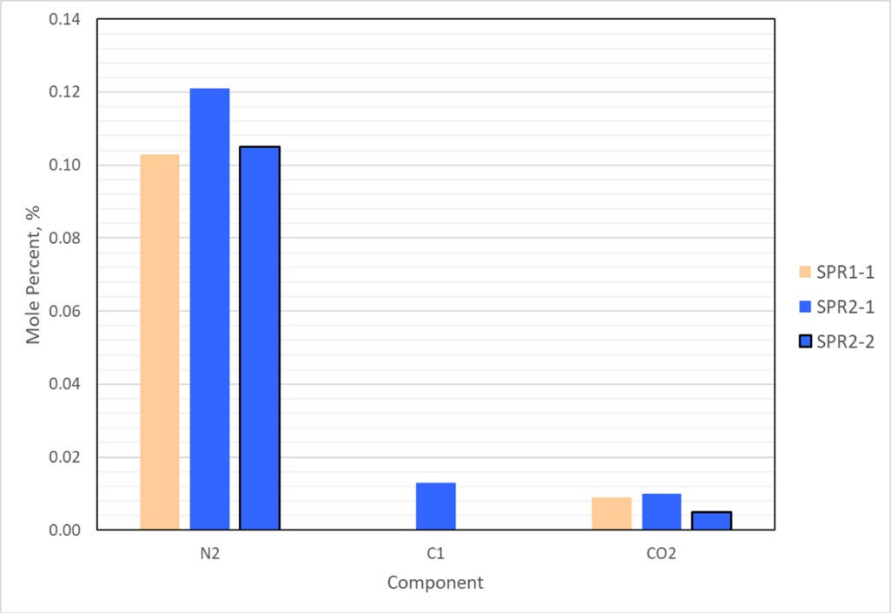

Figure F- 27: Fixed gas and methane compositions in the SPR oil samples taken for the 2m pool fires

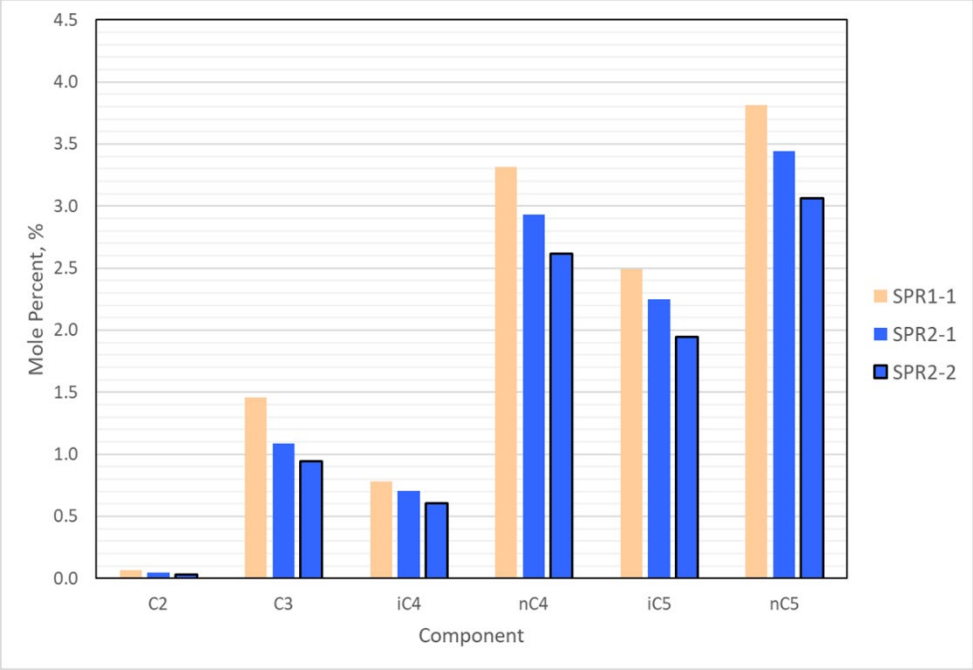

Figure F- 28: Light ends compositions (C2-nC5) in the SPR oil samples taken for the 2m pool fires

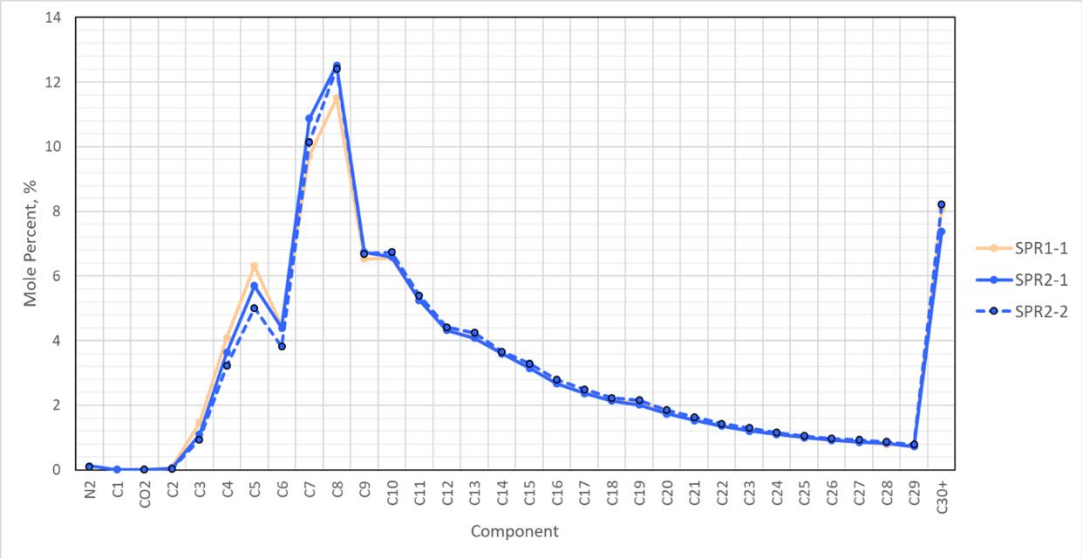

Figure F- 29: Whole oil composition line chart for the SPR oil samples taken for the 2m pool fires

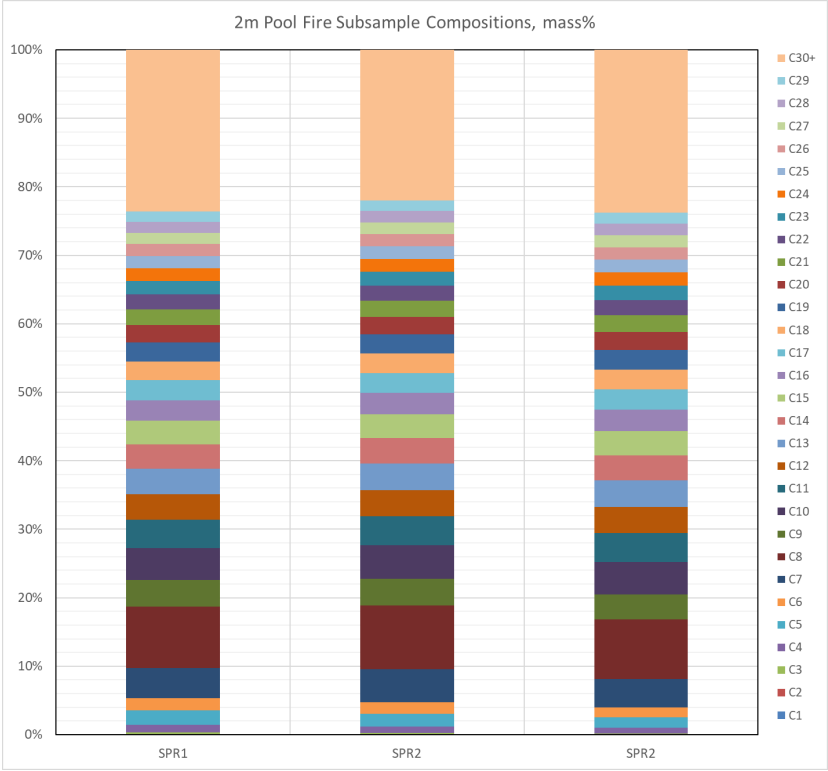

Figure F- 30: Whole oil mass composition stacked bar charts for the SPR oil samples taken for the 2m pool fires

The compositions of the oil samples taken before the 5m pool fires are shown below. Figure F- 31 shows the fixed gas compositions, and Figure F- 32 shows the light ends compositions. An analysis was performed on a replicate sample for the Texas shale 5m pool fire sample, so it is shown with outlined bars in both figures. Figure F- 33 gives the combined composition of components smaller than C6 for each of the samples. Of note, the Bakken oil sample clearly showed the largest light ends composition, followed by the Texas Shale, and then the SPR oil samples. Figure F- 34 gives the whole oil compositions, with the differences in light ends (< C6) apparent, while Figure F- 35 gives the whole oil mass composition as a stacked bar chart.

The 5m Hot and Cold pool fire samples of SPR oil were drawn from the same tanker in April and August, respectively, of the same year, but the composition appears to have changed. In particular, the light ends decreased from the first (SPR 3-1) to the second (SPR 4-1) sample. This is consistent with weathering, as is discussed in section F.4.1.1. There was also spike in N2 content at the SPR Cold sample. This may have been due to seasonal variability, sampling methodology, or sample-to-sample variation, though these factors could not be sufficiently separated to warrant a firm conclusion.

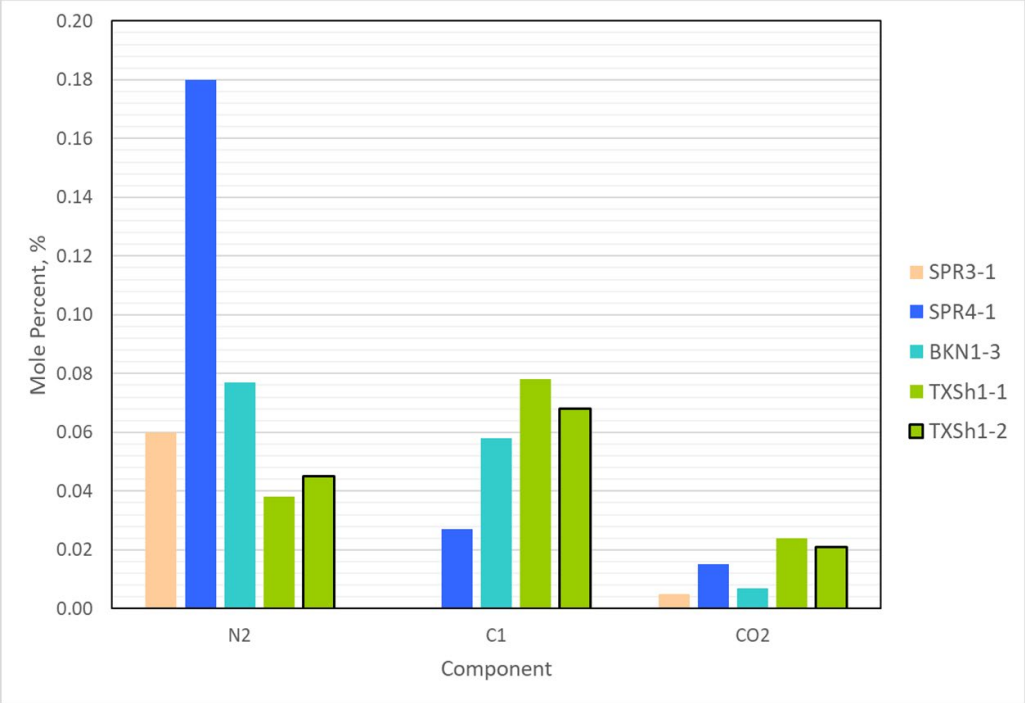

Figure F- 31: Fixed gas and methane compositions for the samples taken before the 5m pool fires

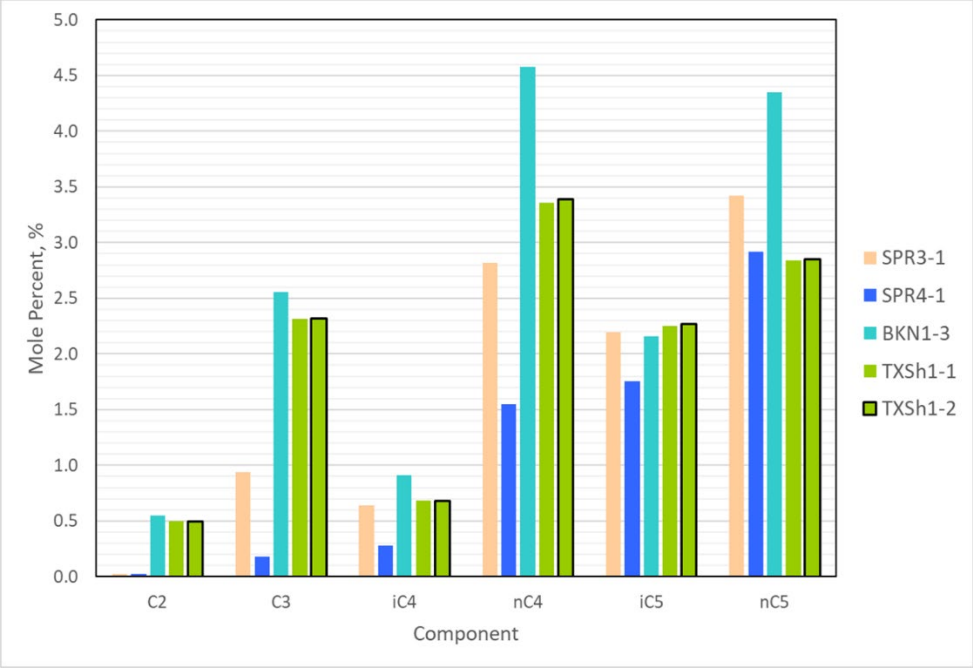

Figure F- 32: Light ends compositions (C2-nC5) for the samples taken before the 5m pool fires

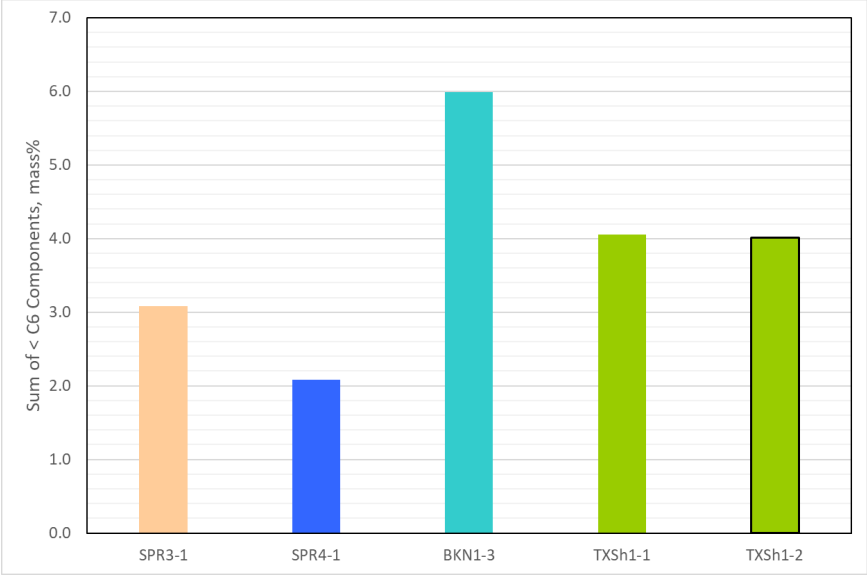

Figure F- 33: Total weight % of components smaller than C6 for the oil samples taken before the 5m pool fires

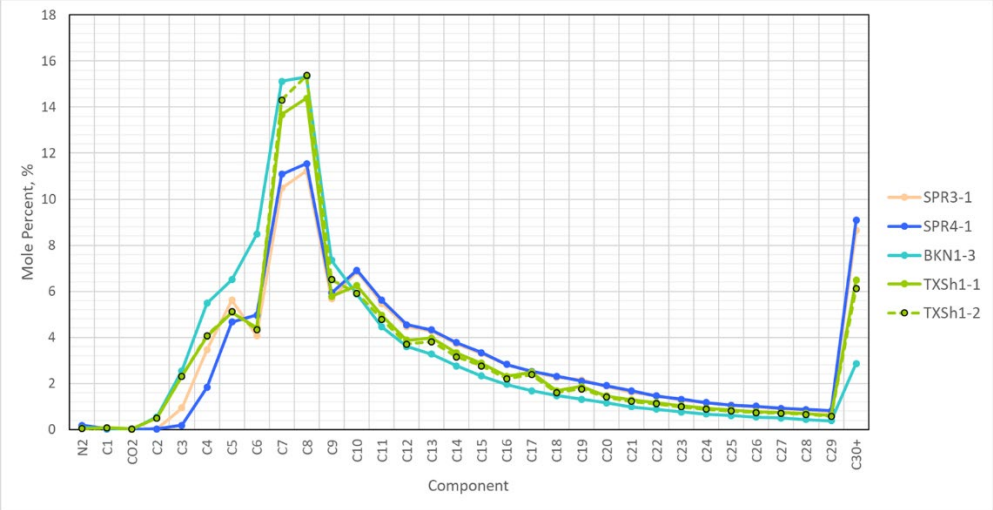

Figure F- 34: Whole oil composition line chart for the samples taken before the 5m pool fires

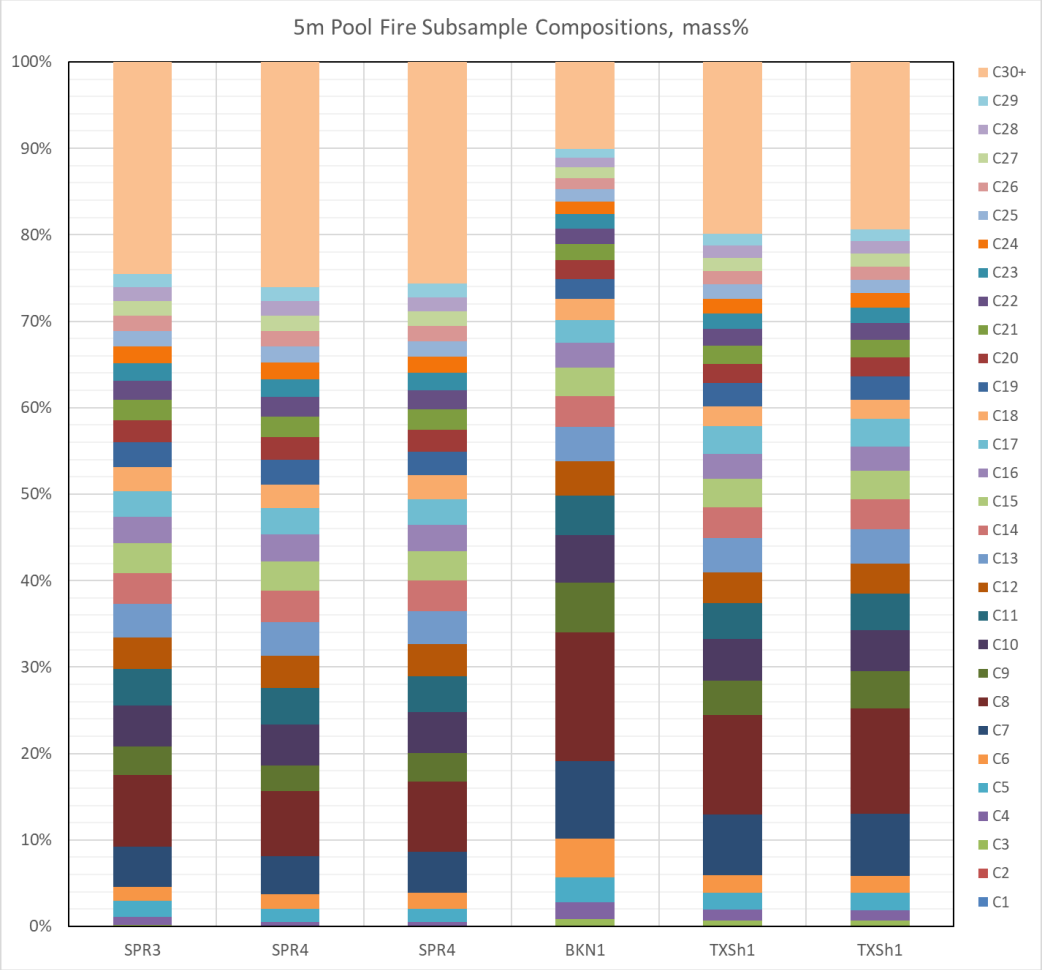

Figure F- 35: Whole oil mass composition stacked bar chart for the samples taken before the 5m pool fires

F.3.3.3. Compositions for Fireball Subsamples

The compositions of the oil samples taken before the fireball tests are shown below. Figure F- 36: shows the fixed gas compositions with replicates shown as bars with black outlines. There was little sample-to-sample variability in fixed gas content relative to previous samples. The N_2 contents for the SPR and BKN subsamples were both consistently high. Figure F- 37 shows the light ends compositions, which show clear separation of all the samples. Figure F- 38 gives the combined composition of components smaller than C6 for each of the oils. In all of these figures, the jet fuel showed no evidence of light ends, which reflects how the liquid was engineered through the refining process to yield a finished product with carbon numbers constrained to a specific band from C7-C16 that enable it to meet fuel performance specifications. Figure F- 39 shows the whole oil compositions for the four fireball fuels, while Figure F- 40 gives the whole oil mass composition as a stacked bar chart. The jet fuel – a cut of C7-C16 hydrocarbons – clearly differed from the crude oils – distributions of C1-C30+ hydrocarbons. The differences in light ends were also apparent in looking at the whole oil compositions, where Bakken had the most light ends, TX Shale was intermediate, SPR next, and finally jet fuel had the fewest light ends.

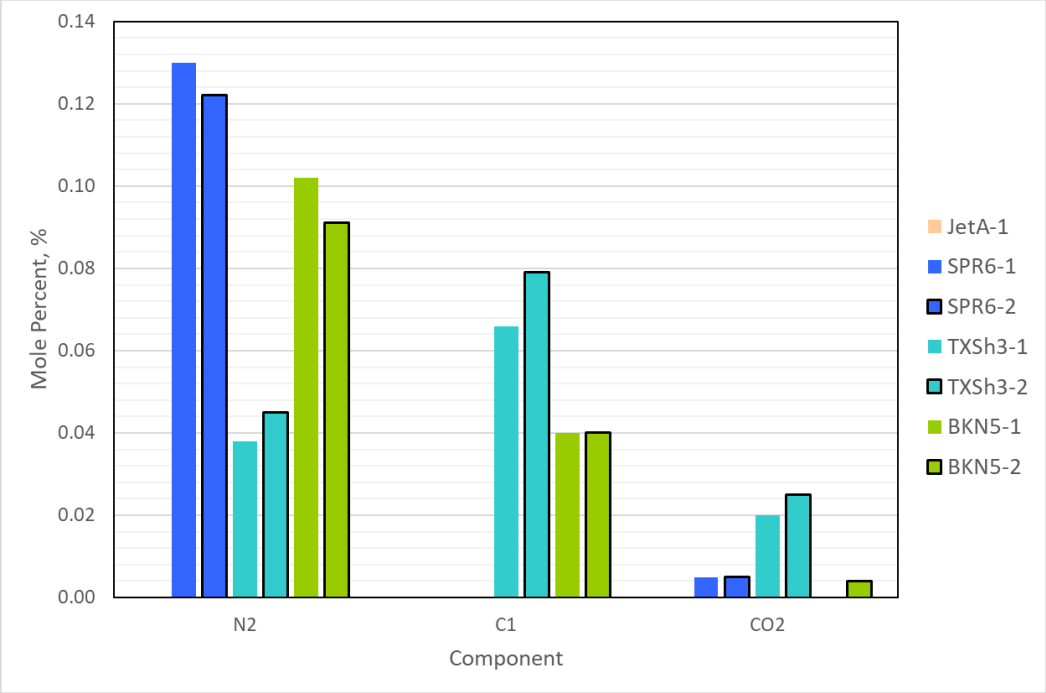

Figure F- 36: Fixed gas and methane compositions for the samples taken before the fireball tests.

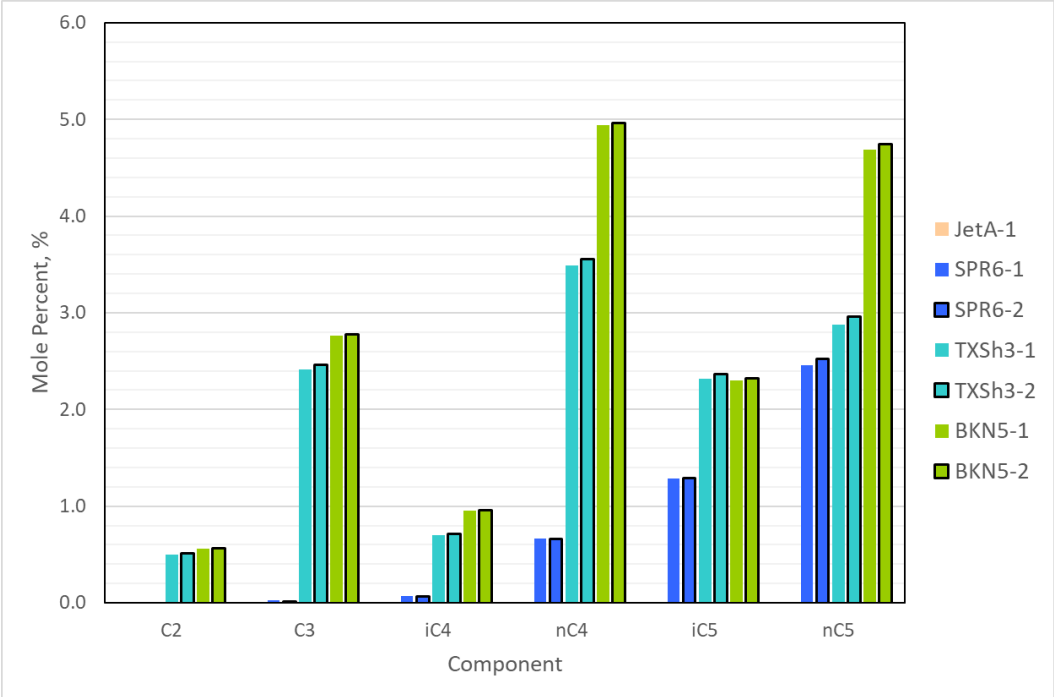

Figure F- 37: Light ends compositions (C2-nC5) for the samples taken before the fireball tests

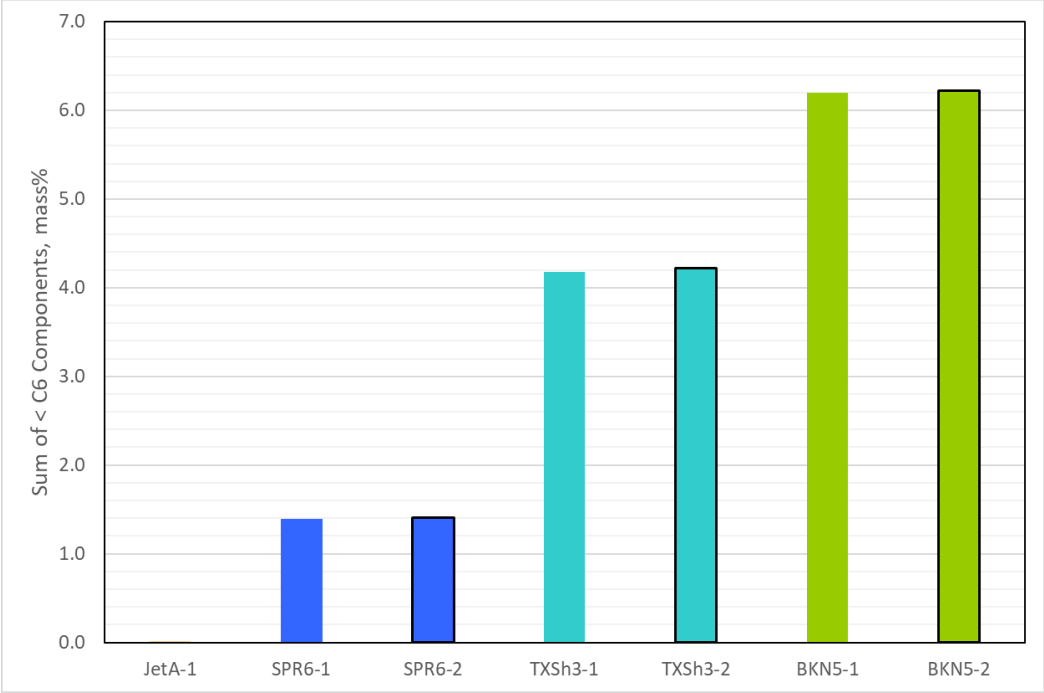

Figure F- 38: Total weight % of components smaller than C6 for the oil samples taken before the fireball tests

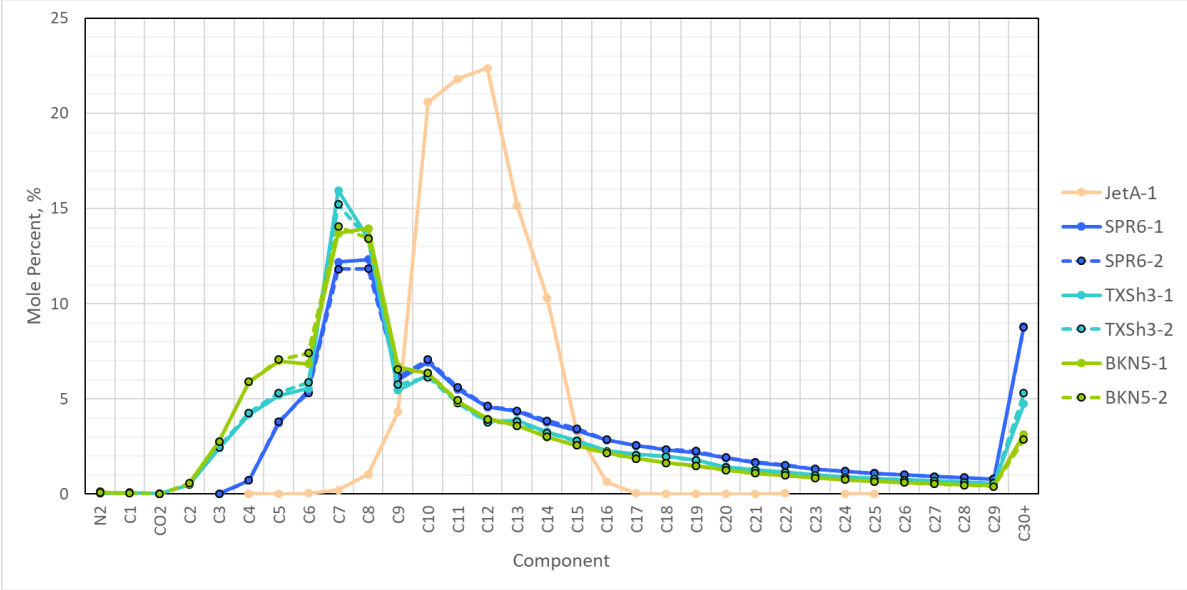

Figure F- 39: Whole oil composition for the samples taken before the fireball tests

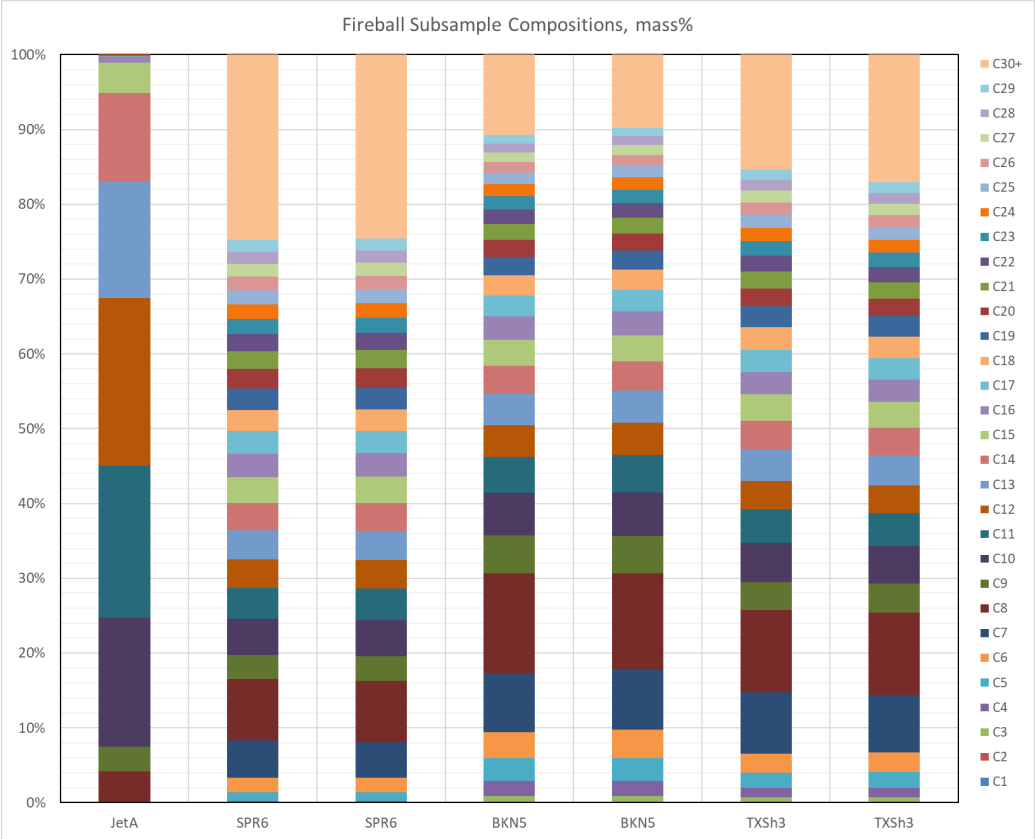

Figure F- 40: Whole oil composition stacked bar chart for the samples taken before the fireball tests

F.3.3.4. Comments on Initial Boiling Point

Initial boiling point (IBP) was also of interest in this study. defines two distinct methods for estimating initial boiling point – by distillation (ASTM D86) and by gas chromatography (ASTM D7169). In ASTM D86 distillation (ASTM 2016d), IBP is the corrected temperature at the instant the first drop of condensate falls from the condenser tube. ASTM D7169-16 (ASTM 2016a) is a standard test method for boiling point distribution by high temperature gas chromatography. It defines IBP as the temperature corresponding to an accumulated 0.5% of the total area of the eluted sample. For this study, a calculated IBP was determined from merged (discrete) whole oil carbon number reports provided by the analytical lab using pressurized method GPA 2103-M. Mass% for hydrocarbons C1 –Cn was summed until the cumulative mass exceeded 0.5%. IBP was the boiling temperature for the corresponding hydrocarbon. Table F- 22 gives the calculated initial boiling points using pressurized compositional data for the oils in this study, ordered by sampling event. The BKN and TXSh crudes saw little change in the low carbon number groups, so their IBP's held constant through all the sampling events at -44 °F. The SPR crude IBP started at 31 °F and increased to 97 °F as more of the light ends left the mixture through time.

Table F- 22: Initial boiling points for the oils, separated by sampling event

Oil	Event	IBP, °F	IBP, °C
SPR	SPR0	31	0
SPR	SPR1	31	0
SPR	SPR2	31	0
SPR	SPR3	31	0
SPR	SPR4	31	0
SPR	SPR5	97	36
SPR	SPR6	97	36
BKN	BKN0	-44	-42
BKN	BKN1	-44	-42
BKN	BKN2	-44	-42
BKN	BKN3	-44	-42
BKN	BKN4	-44	-42
BKN	BKN5	-44	-42
TXSh	TXSh0	-44	-42
TXSh	TXSh1	-44	-42
TXSh	TXSh2	-44	-42
TXSh	TXSh3	-44	-42

F.3.4. Crude Oil Vapor Pressures

The crude oil vapor pressures, $VPCR_x(T)$, were measured across several expansion ratios for each sampling event, as described in the previous sections. The measurements were compared to the Equation of State (EOS) modeled results for each of the events.

F.3.4.1. Vapor Pressure for Loading Subsamples

Figure F- 41 shows the $VPCR_x(100°F)$ measurements (ASTM D6377-M, solid bars) and EOS modeled results (-EOS, striped bars) for the loading samples. Error bars on the measurements represent twice the standard deviation (2σ) among the replicates. Error bars on the EOS results represent twice the standard deviation (2σ) among the compositional replicates, when available. The $VPCR_4(100°F)$ values followed an expected trend, with the Bakken sample at 10.2 psia, the Texas Shale sample at 8.2 psia, and the SPR sample at 6.6 psia. This trend is verified by the EOS results for $VPCR_4(100°F)$. At $V/L = 0.2$, there is significant overlap in the error bars for the VPCR measurements, though the trend holds true. VPCR measurements for $V/L < 0.2$ show deviation from expected results, but the EOS results keep the expected trend in VPCR (Bakken > Texas Shale > SPR).

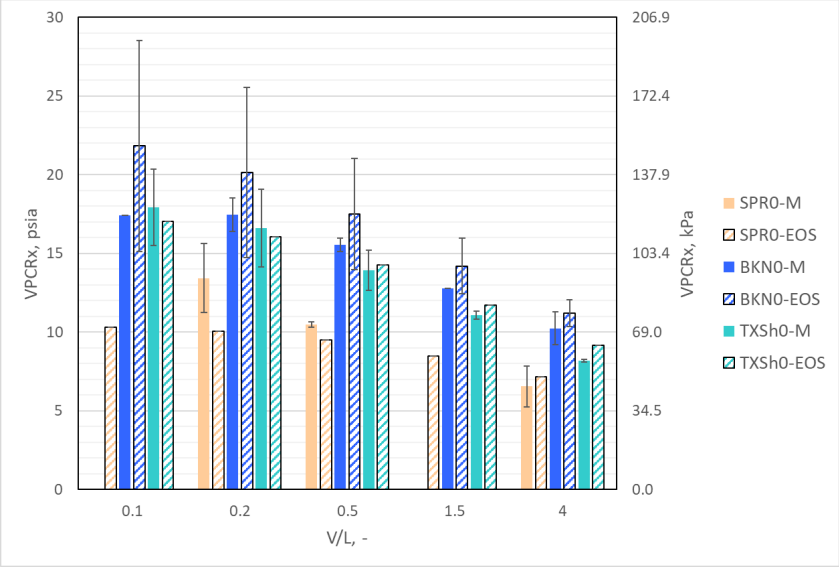

Figure F- 41: $VPCR_x(100°F)$ vs V/L for the loading samples. Solid bars indicate experimental measurements, striped bars are from Equation of State (EOS) calculations.

The replicate compositional results from Figure F- 22 and Figure F- 23 for the loading subsamples were used to create the replicate EOS $VPCR_x$ results in Figure F- 42 below. The first Bakken replicate showed about double the N_2, C1, and CO_2 contents than the second replicate, which led to about 5 psia (~25%) difference in $VPCR_{0.05}(100°F)$ when the EOS was used. This difference diminished with increasing V/L ($VPCR_4(100°F)$ values differed by 0.6 psia, or about 5%). In contrast, the two Texas Shale compositional replicates showed similar fixed gas contents, and only differed by ~2% in $VPCR_{0.05}(100°F)$, and 0.7% in $VPCR_4(100°F)$.

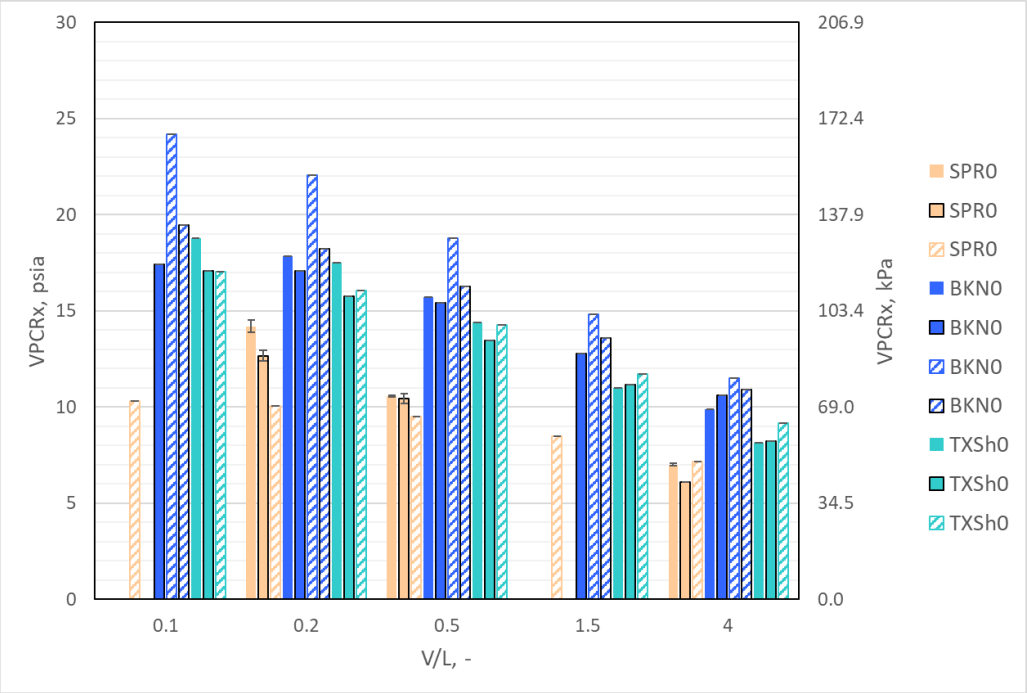

Figure F- 42: VPCR$_x$(100°F) vs V/L for the loading samples, showing all replicates. Solid bars indicate experimental measurements, striped bars are from Equation of State (EOS) calculations.

F.3.4.2. Vapor Pressures for Pool Fire Subsamples

Figure F- 43 shows the VPCR$_x$ measurements (ASTM D6377-M, solid bars) and EOS modeled results (-EOS, striped bars) for the SPR hot and cold 2m pool fire samples. The measurements show a drop in VPCR from the first 2m pool fire, SPR1 (tan), to the second, SPR2 (blue) for all V/L, though the uncertainties overlap. The EOS results are within 1.5 psi of the measured results for V/L > 0.2 and show a drop from SPR1 (striped tan) to SPR2 (striped blue).

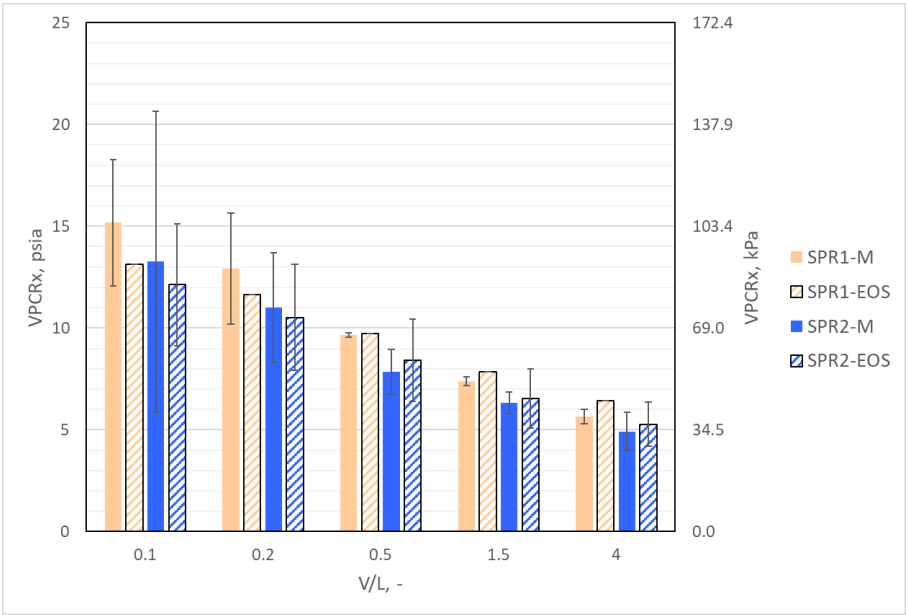

Figure F- 43: VPCR$_x$(100°F) vs V/L for the 2m pool fire samples. Solid bars indicate experimental measurements, striped bars are from Equation of State calculations.

Figure F- 44 shows the $VPCR_x$ measurements (ASTM D6377-M, solid bars) and EOS modeled results (-EOS, striped bars) for four 5m pool fires. Replicate measurements of $VPCR_x$ were performed on separate cylinders of the SPR3, SPR4, BKN1, and TXSh1 oil, so the average of the measurements is shown with 2σ error bands in the chart. Compositions were performed on separate cylinders of TXSh1 oil as well, so the average $VPCR_x$ EOS results are given in the chart. As expected, the degassed SPR oil showed the smallest $VPCR_x$, with the first 5m pool fire sample exhibiting larger $VPCR_4$ than the second due to decrease in the light ends content from weathering. The BKN oil gave the largest $VPCR_x$, with the TXSh oil slightly smaller. This trend is especially pronounced at large V/L where $VPCR_x$ measurement uncertainty is smaller.

In general, the EOS modeled results line up with the $VPCR_x$ measurements. This is especially true at large V/L. There was larger scatter in the measurements at V/L < 0.5, the same region where the EOS calculations are particularly sensitive to light ends composition. These trends in uncertainty were consistent with results from previous studies .

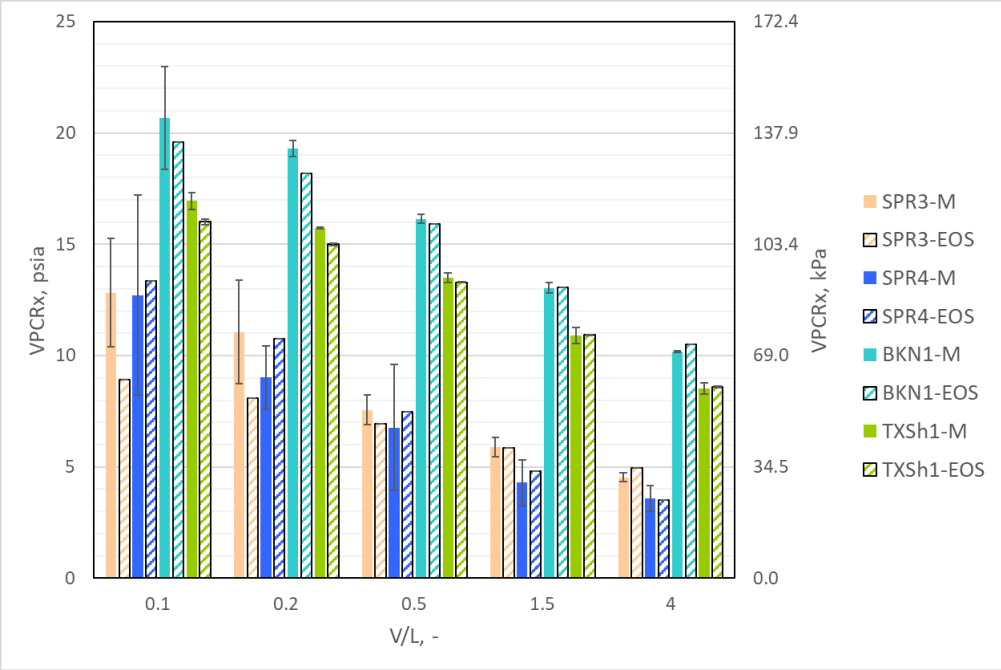

Figure F- 44: VPCRx(100°F) vs V/L for the 5m pool fire samples. Solid bars indicate experimental measurements, striped bars are from Equation of State calculations.

F.3.4.3. Vapor Pressures for Fireball Subsamples

Figure F- 45 shows the $VPCR_x$(100°F) measurements (ASTM D6377-M, solid bars) and EOS modeled results (-EOS, striped bars) for the samples taken before the fireball tests. Of note, the JetA $VPCR_x$ values were higher than SPR6 at low V/L, but lower than SPR6 at high V/L. Any of the fuels stored at ambient pressure-temperature conditions are expected to show nitrogen saturation and convergence to a common bubblepoint pressure at low V/L that is driven by storage conditions. The SPR6 and TXSh3 EOS results were consistent with the $VPCR_x$ measurements, indicating consistency between the $VPCR_x$ and compositional analyses. The BKN5 EOS values were all about 1-2 psia higher than the $VPCR_x$ measurements, which may be a result of uncertainty in the compositions of the middle C6-C9 fraction. Bakken VPCR is highest, followed by TX Shale. SPR and Jet A show significantly lower VPCR at every V/L due to their comparatively low light ends contents.

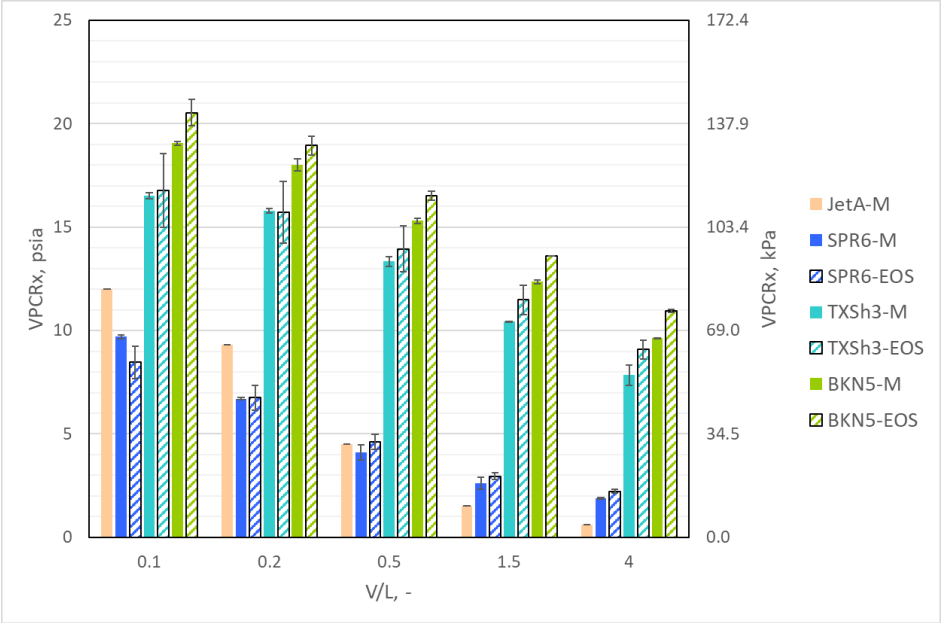

Figure F- 45: $VPCR_x$(100°F) vs V/L for the fireball samples. Solid bars indicate experimental measurements, striped bars are from Equation of State calculations.

F.3.5. High Temperature PVT

F.3.5.1. Process Design Calculations with EOS

The fireball tests were designed with four hundred gallons of crude oil added to the 1000-gallon fireball test tank at ambient conditions, resulting in a starting V/L = 1.5. The oils were then to be heated to temperatures high enough to support the formation of a fireball, but necessarily below the onset of thermal cracking to retain the original composition within the crude before the ignition event. This starting V/L = 1.5 was selected based on initial EOS design calculations that indicated liquid thermal expansion for the crudes could cause the liquid volume to double over the intended temperature range of 20-350°C. A starting V/L = 1.5 allowed for this magnitude of expansion with some remaining vapor space to prevent liquid-locking the test vessel, which could fail the rupture disc prematurely. During the heating process, the current-state vapor-liquid (V/L) ratios within the tank would change, though the mass and total volumes of the oils (i.e., specific volume) would remain constant. Crude oil properties were used to ensure that the fireball test design would meet sufficient conditions for the formation of a fireball.

Using the conditions described above, the pressure-volume-temperature (PVT) curves were simulated for each oil using an Equation of State (EOS) model with the most recent compositional data available at the time. The Bakken composition from July 2018 (BKN4), the SPR oil composition from August 2017 (SPR4), and the Texas Shale composition from January 2018 (TXSh1) were used to simulate the oils' responses to the fireball tank environment. This includes both the pressure (Figure F- 46) and the vapor mass fraction (Figure F- 47). These pressures were used to understand the state of the tank leading up to ignition, and the vapor mass fractions were used to verify that the thermodynamic state would produce a vapor cloud sufficient to support a fireball when the tank was ruptured during the ignition event. Target tank temperatures at the time of rupture were in the range 275-300°C. As shown in Figure F- 47, the EOS model predicted that all three oils, when ejected from the tank at these temperatures, would meet the minimum vapor mass fraction requirement for fireball creation [40], while keeping the compositions intact at temperatures below the onset of hydrocarbon cracking

[85, 86]. Section F.3.5.2 shows actual test data, confirming that these conditions were met for each of the fireball tests.

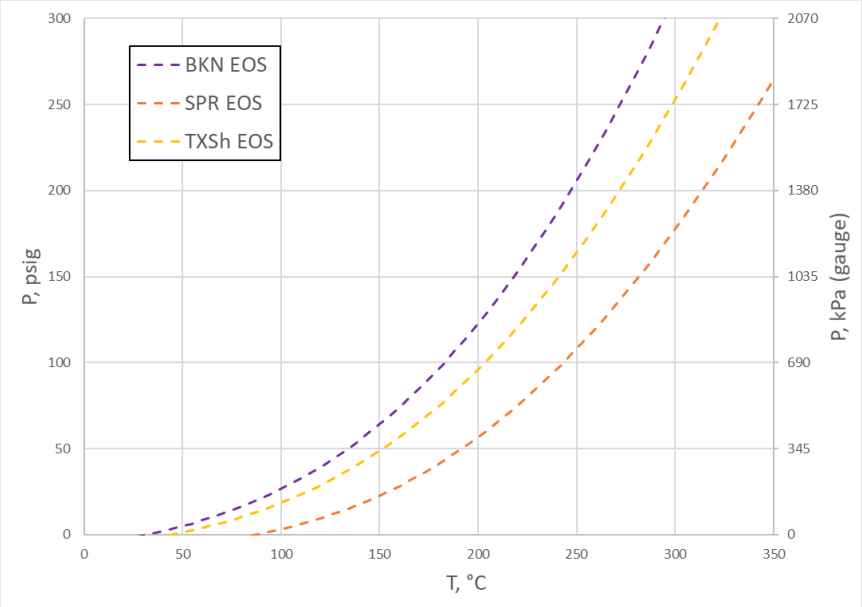

Figure F- 46: EOS model results for Pressure vs Temperature inside a closed tank for BKN, SPR, and TXSh oils with starting V/L = 1.5. This scenario simulates the heat-up cycle in the fireball tank prior to rupture and ignition.

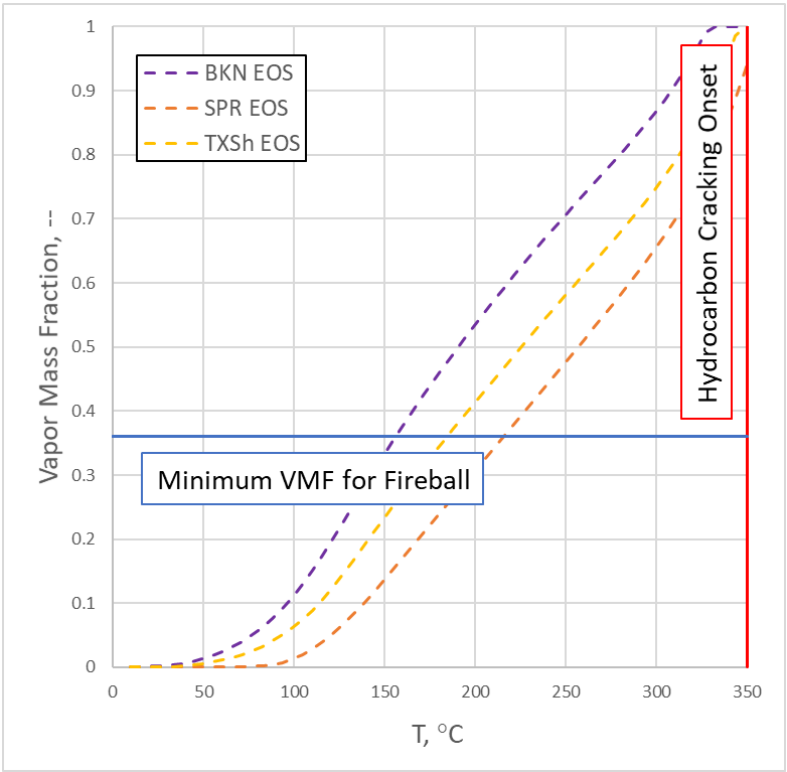

Figure F- 47: EOS model results for crude oil vapor mass fraction vs temperature for the three oils used in this study. indicated that a minimum 36% vapor mass fraction of fuel (blue horizontal line) is required to support complete combustion of a vapor cloud by fireball. Actual test temperatures were 280-300°C, well above what is needed to provide the minimum VMF for each oil.

F.3.5.2. PVT Monitoring of Fireball Fuel Heating Process

Pressures and temperatures were measured throughout the course of the fireball tank active heating and passive cooling cycles for each of the oils, and the simulated values above provided a useful comparison to measured data. As part of the fireball tank setup, one K-type thermocouple protruded approximately 6 inches into the bottom of the 72-inch diameter tank, measuring the temperature of the liquid. The placement of the thermocouple prohibited it from explicitly measuring the average bulk temperatures. Since the contents were heated from the outside, this means that the thermocouple measured a temperature that was higher than would be expected for the average bulk temperature. Two pressure transducers rated to 500 psig were plumbed from the same line at the top of the tank to measure the pressure of the tank in replicate. Even though these instruments wouldn't necessarily provide the actual thermodynamic equilibrium values, they were still compared to the EOS model predictions to ensure oil quality and tank integrity through the course of the experiments.

The resulting measurements from the fireball tanks are given as solid lines in Figure F- 48: with the EOS predictions from Figure F- 46 as dashed lines. The pressures shown in the figure are the averages of the two pressure transducers from the test tank. The semi-transparent lines in the figure represent the combined uncertainty of the pressure transducers (twice the standard deviation) and the thermocouple (the greater of 2.2 °C and 0.75%). Context and discussion surrounding the curves are given by oil in the following sections.

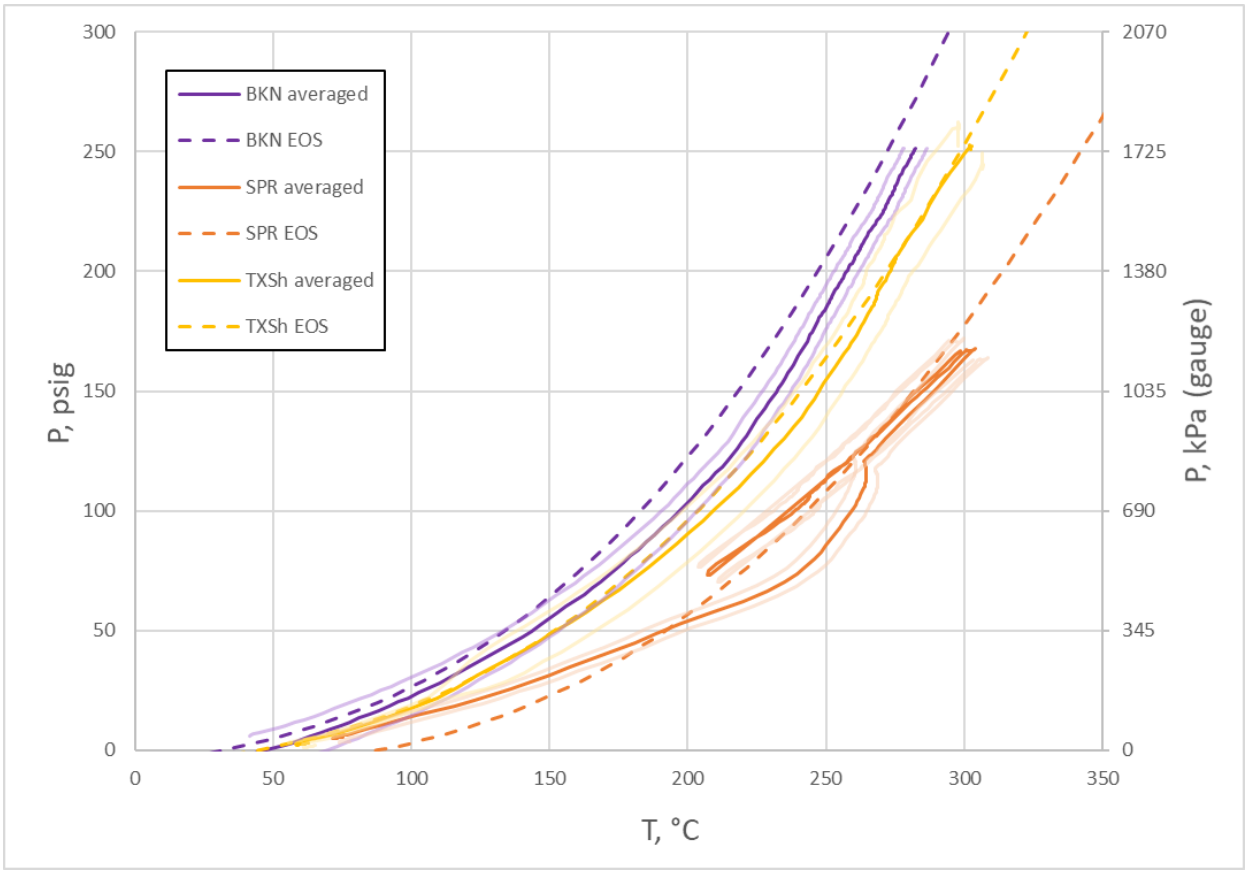

Figure F- 48: Pressure vs Temperature data for the three oils during fireball testing, including measurement data (solid lines), measurement uncertainty (semi-transparent lines), and simulated curves (dashed lines)

F.3.5.2.1. Bakken PVT Data

Four hundred gallons of Bakken oil were withdrawn from the tanker and injected into the fireball test tank. Thus, a set of PVT data contained temperature and pressure data from ambient temperature to around 250 °C (the initial conditions for the fireball). The measured curve was slightly shifted to the right relative to the simulated curve, which was expected since the measured temperature exceeded the average bulk temperature (see section F.3.5.2). In general, the model prediction performed well compared to the actual measurements.

F.3.5.2.2. SPR PVT Data

A single four-hundred-gallon sample of SPR oil was added to the test tank. A full heat ramp from ambient temperature to 300 °C was experienced in preparation for the fireball. However, the test was delayed one day, during which time the oil in the tank passively cooled. That next day, the SPR oil was heated once again. These events produced a full heating curve, followed by partial cooling, then re-heating to fireball conditions, which were all captured by the tank temperature and pressure data. At low temperatures, the SPR oil measured pressure (orange in Figure F- 48:) was above the prediction because the SPR oil was loaded using N_2 to reduce the possibility of vacuum conditions. Above 200 °C, the temperature for the SPR oil was higher than the actual representative thermodynamic state of the oil, resulting in measured pressures smaller than the predicted pressure. At around an oil temperature of 270 °C, the upper and middle heaters were switched off, and the effective heating rate dropped for the oil. At this point, the oil crept closer to the thermodynamic equilibrium state, resulting in a slowly increasing pressure at a single temperature. This was evident from the data – at 270 °C, the measured pressure increased to the EOS predicted pressure. From there, the oil was heated, cooled, and heated again slowly to 300 °C. These measured pressure traces compared much better to the EOS pressure, suggesting that they were more representative of the thermodynamic state than the initial heating ramp.

F.3.5.2.3. TX Shale PVT Data

Around four hundred gallons of Texas Shale oil was loaded into the test tank. The oil was heated to the fireball test condition before ignition without incident. Therefore, one heating curve and no cooling curves were captured by the instruments. The Texas Shale oil measured pressure (yellow in Figure F- 48:) was slightly shifted to the right relative to the simulated curve, which was expected since the measured temperature exceeded the average bulk temperature (see section F.3.5.2). In general, the data matched the EOS model well through the whole temperature range.

F.3.5.2.4. PVT Data Summary

Since the pressure/temperature measurements from industrial-grade instrumentation on the tank compared well to model predictions using compositional measurements, the oils sampled for property analysis can be taken to represent the oils loaded into the fireball tank. This means that the other oil properties measured previously (VPCRx, compositions, etc.) also represent the oils in the tank. Therefore, the modeled vapor mass fractions in Figure F- 47 can be used to approximate the conditions within the tank, including at the ignition temperatures. Tank conditions at ignition including measurements (temperature and pressure) and modeled results (vapor mass fraction) are given in Table F- 23.

Table F- 23: Fireball tank conditions at the point of ignition.

Oil	Tank T at Ignition (°C)	Tank P at Ignition (psig)	Vapor Mass Fraction (Modeled)
Bakken	275	250	0.79
SPR	293	168	0.63
Texas Shale	300	250	0.75

F.4. Additional Observations

The main purpose of the oil sampling & analysis program was to determine oil properties for the material used in the combustion tests, with the primary results presented above. The dataset created by this effort offered some additional value that allowed Sandia to observe oil responses to variations in storage and handling that occurred during the ~2-year project duration that were not necessarily part of the original project design. These variations included significant weathering of the SPR oil in unpressurized storage, pressure safety valve malfunction during fuel transfer operations, and heating-cooling cycles associated with troubleshooting during fireball testing. Additional observations related to these monitoring activities are summarized below.

F.4.1. Pressurized vs Unpressurized Storage

As mentioned in Section F.2.1, the SPR oil was stored in an unpressurized tanker, while the tight oil samples (Bakken, Texas Shale) were kept in Sandia-customized pressurized tankers. This allowed the SPR oil to change more than the other oils due to interactions with the atmosphere. Figure F- 49 shows the combined weight % of all components smaller than C6 in the SPR oil (blue), Bakken oil (red), and Texas Shale oil (green) as a function of time. From January 2017 to October 2018, the SPR oil showed a steady decrease from 3.7 wt% to 1.4 wt%. On the other hand, the Bakken < C6 content fluctuated between 5.9 wt% and 6.2 wt% from August 2017 to October 2018 without showing any consistent trend. TXSh oil remained between 4-0 and 4.1% < C6 over its 300-day storage period. The behavior of the SPR oil is characteristic of an oil sample that is experiencing "weathering" – the unpressurized tank acted as a long-term separator with the light components gradually leaving the system through time.

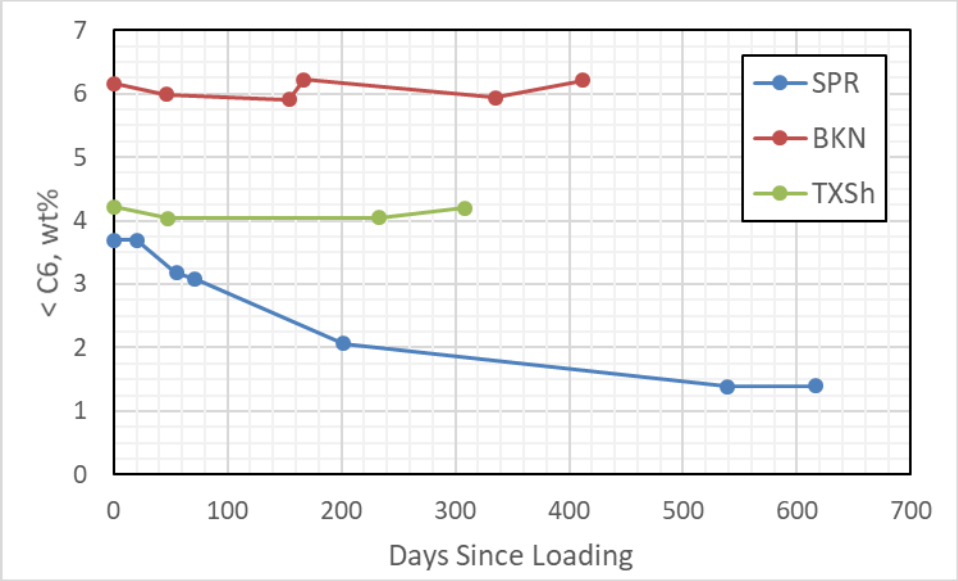

Figure F- 49: Measured weight % of components smaller than C6 of SPR, Bakken, and TX shale oils through time

Figure F- 50 shows the evolution of measured (solid lines, closed circles) and calculated (dashed lines, open squares) $VPCR_4(100°F)$ for the three oils over time since loading. The uncertainties in the measured values are given as the larger of 2σ and 0.62 psia – the reproducibility factor listed in the ASTM D6377 standard at V/L = 4 and 100 °F. In general, the BKN (red) and TXSh (green) $VPCR_4$ values held fairly constant within the uncertainties under pressurized storage. The EOS values for these oils were also relatively constant. The BKN $VPCR_4(100°F)$ measurements between 100-200 days since loading were done by a different analytical laboratory, which would explain the slight uptick for those two points that were still within the uncertainties of the other measurements. The SPR (blue) $VPCR_4(100°F)$ measurements and EOS calculations fell dramatically through time before levelling off around 520 days since loading. The weathering of the light components evident in Figure F- 49: caused a drop in $VPCR_4(100°F)$ until 2/3 of the < C6 content was lost and the $VPCR_4(100°F)$ measurements levelled off.

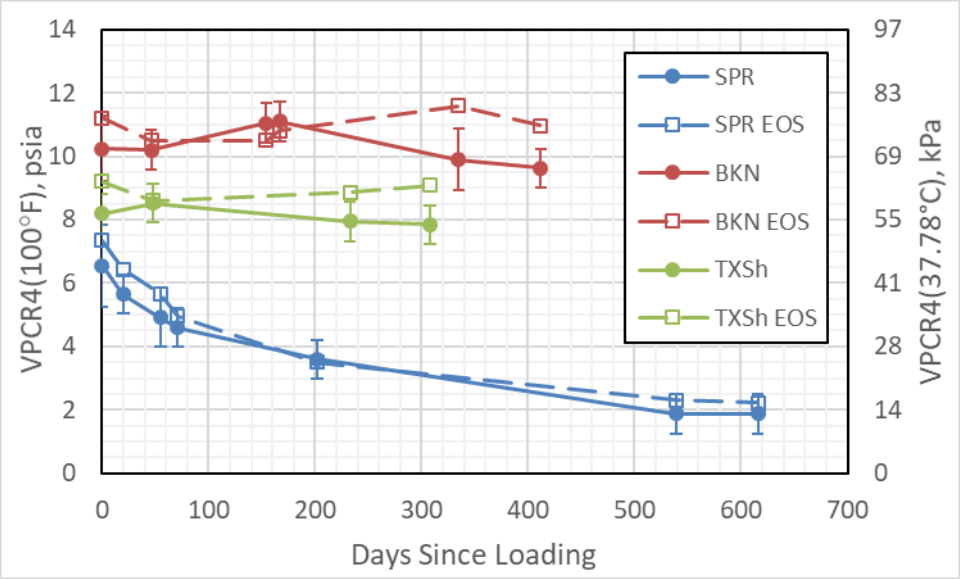

Figure F- 50: Measured and simulated (EOS) $VPCR_4$(100°F) of SPR, Bakken, and TX shale oils through time

Figure F- 51: shows the measured heats of combustion through time for the three oils, measured by ASTM D240 [87]. Though only one measurement was taken for each point, the test method lists the reproducibility as 170 BTU/lb, or 400 kJ/kg, which is smaller than the symbol size in the figure. Even so, there was little separation among the three oils, though the BKN heats of combustion were consistently larger and showed the widest variability through time. The SPR and TXSh oils were very similar through time. The weathering of the SPR oil did not seem to affect the heat of combustion of the material.

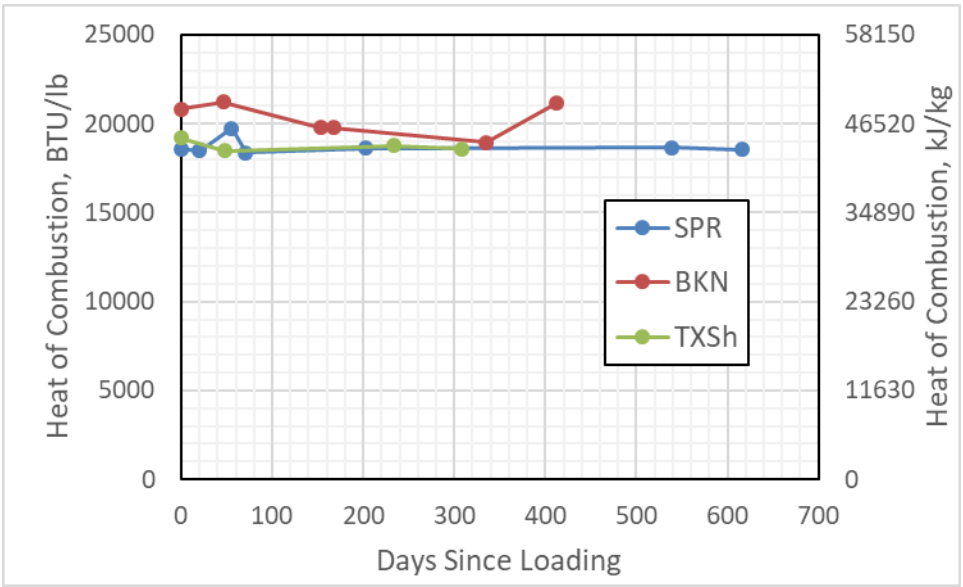

Figure F- 51: Measured heat of combustion for SPR, Bakken, and TX shale oils through time

The oils in these tanks underwent a couple of interesting events that deserve further analysis using the measured oil properties.

F.4.1.1. SPR Oil Weathering

Upon receipt at Sandia, the SPR crude was contained in unpressurized tank storage at ambient outdoor temperature for about 620 days from loading in January 2017 to final sub-sample capture in October 2018. Elevation at the storage location was nominally 7,000 ft above sea level with barometric pressure near 11 psia. The tank configuration was closed from the standpoint that a tank shell prevented rainwater, sunlight, wind, and airborne particulates from making direct contact with the oil. Pressure management was passive, and any daily changes in internal versus external tank pressure were self-moderated by vapor exchange through a PSV on the transport tanker or through a pressure relief port on top of the stationary tank. Air saturation of the oil coupled with loss of volatiles was expected with this configuration. While monitoring and documentation of long-term storage was not part of the original experimental design, the sub-sampling and analysis schedule supporting the pool fire and fireball test series summarized in Table F- 2 yielded a dataset that provides some insight into the weathering process, as well as provides a metric for what magnitude of change in oil properties can be expected as a result of storage and handling protocols.

F.4.1.1.1. Weathering Effects on Whole Oil

Evolution of the SPR whole oil composition during its storage lifetime at Sandia is shown in Figure F- 52. Each curve on the plot represents a different subsampling and analysis event. The numbering on subsamples is sequential, such that in temporal order, SPR0 was the first subsample, SPR1 was the second, through SPR6. The general direction of change with storage time was ever-lowering mole% on the lighter components, most visibly C3 through C5 at the current scale, with a slight rise in some of the heavier groups C10 and up. Since mole% must add up to 100% in the analytical procedure, it is important to understand that the rise in C10 and heavier components mole% does not imply that there was net mass transfer of these components from the environment into the oil; rather, the heavier components comprise a greater proportion of the remaining material once the lighter components have evaporated and been expelled through the pressure relief port.

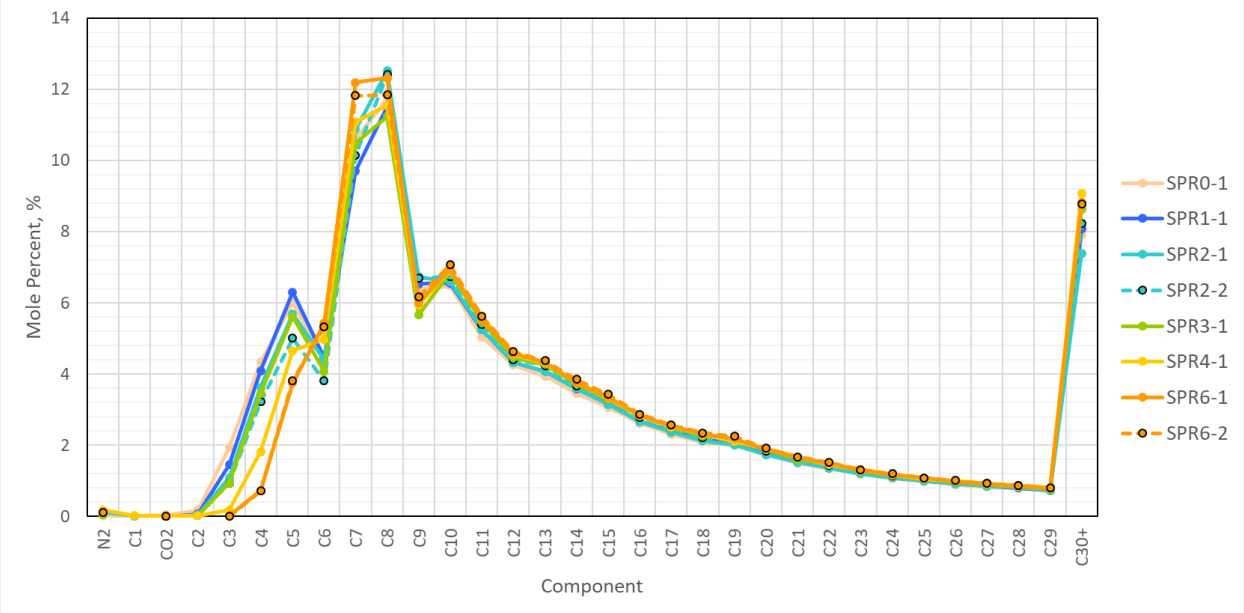

Figure F- 52: Overlay of whole oil compositions of subsamples of SPR oil during unpressurized tank storage at Sandia. Numbering implies sequence, so SPR0 was the first sample, SPR1 was the second, through SPR6 which was the last sample obtained over the storage period.

F.4.1.1.2. Weathering Effects on N2-C5

A closer look at the changes in concentrations of the volatiles in the SPR crude is afforded by limiting the components to those from N_2 – C5 and adjusting the concentration scales so that relative changes are evident for each component. Referring to Figure F- 53, N_2 mole % increases right after loading and remains elevated relative to its starting position. This would be expected for oil that was just stabilized (degassed) at the SPR facility in January 2017 and then exposed to air for the duration of the storage period. C1 appears to fluctuate between low values and no-detect, indicating that the methane concentration was near the detection limit from the start and was difficult to measure. CO_2 was highest at loading at 0.05 mole % and then remained at a steady 0.01 mole% for the duration of storage. Moving up the molecular weight scale to light hydrocarbons C2-C5 in Figure F- 54, all of these monitored light ends showed a visible decrease in mole % with storage time. These components were expected to volatilize because their pure component vapor pressures are high relative to ambient storage conditions. The solvent qualities of the liquid crude oil provide some chemical potential to hold the light ends in solution, preventing them from evaporating completely to no-detect, but their tendency to evaporate clearly diminished their concentration in the oil phase with storage time.

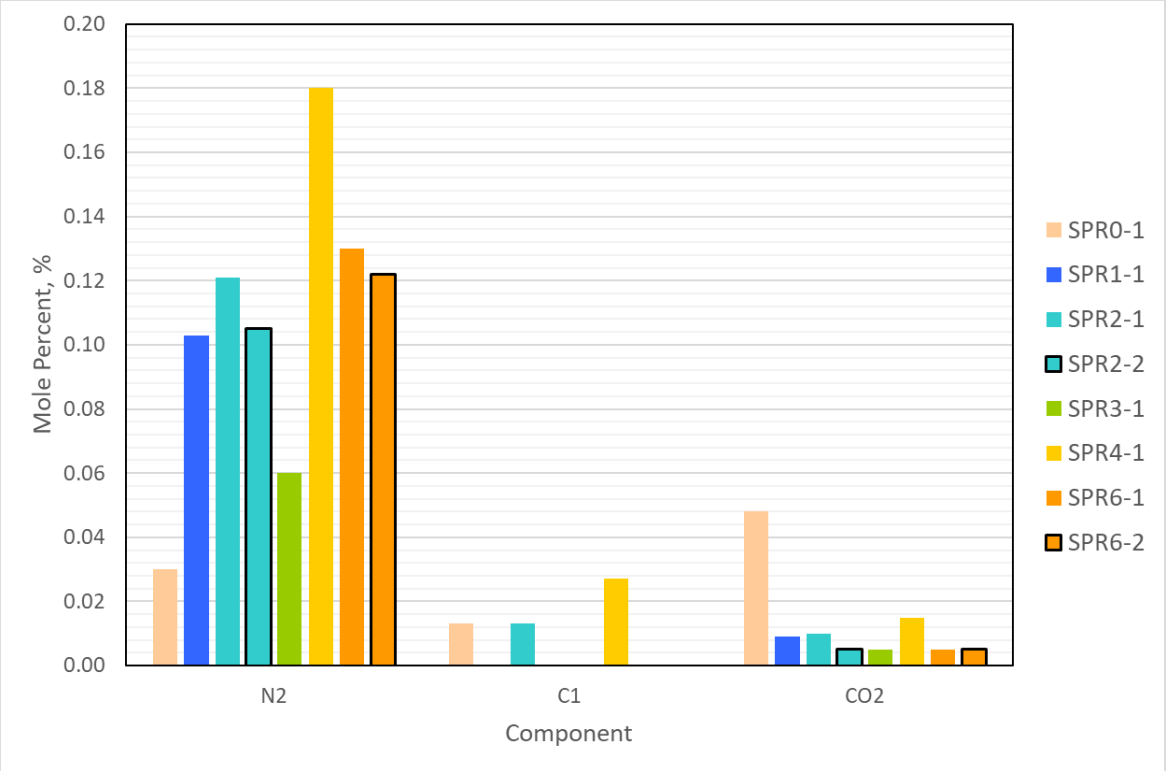

Figure F- 53: Mole % of fixed gases and methane in SPR subsamples during unpressurized tank storage at Sandia.

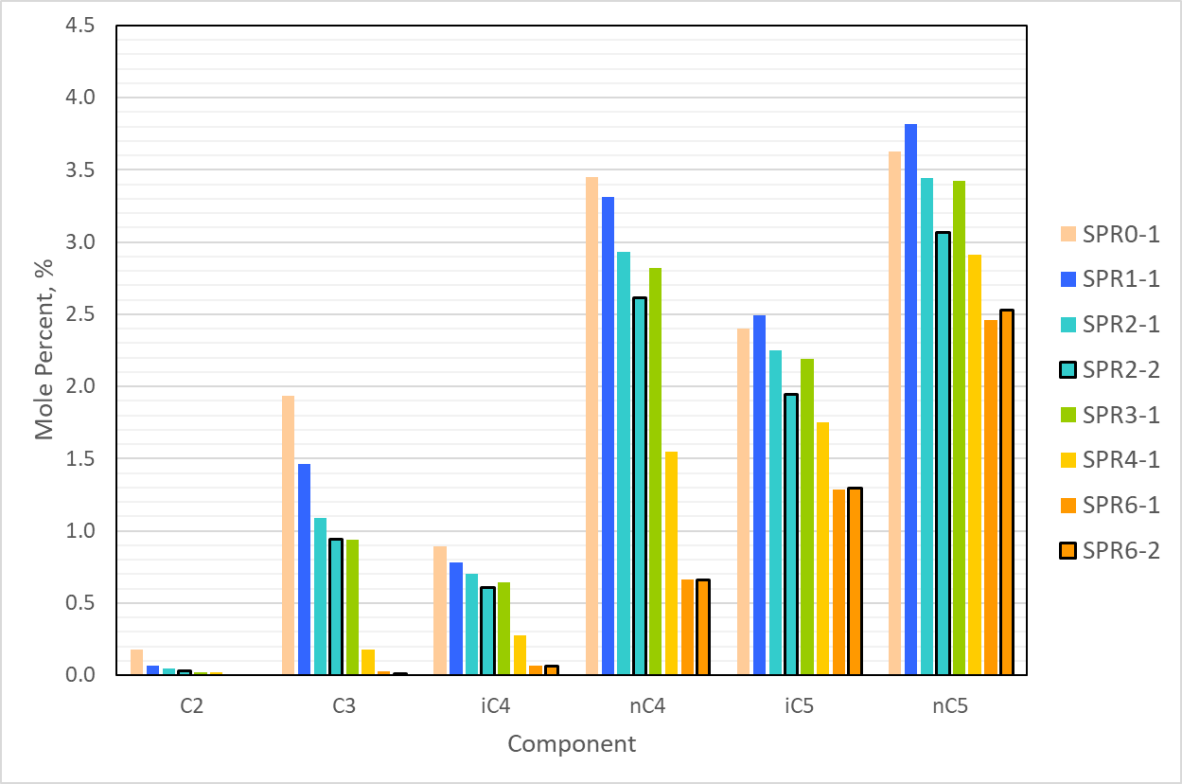

Figure F- 54: Mole % of light ends (C2-C5) in SPR subsamples during unpressurized tank storage at Sandia.

F.4.1.1.3. Weathering Effects on Measured and Modeled VPCR

The repeatable, measurable loss of volatiles from the SPR crude with time in unpressurized storage provides an instructive case study in understanding the relationship between mole% of volatiles and crude oil properties. Properties and composition can be brought together through EOS modeling, where a whole oil composition is introduced into a numerical simulator, and oil properties, with focus on vapor pressure, may be computed and compared to measured values for the same source material. This type of analysis provides insight in several areas: (i) degree of self-consistency between compositional and property measurements, (ii) effectiveness of the EOS model to simulate properties from composition, and (iii) how properties of individual components are expressed in complex mixtures such as crude oils.

A combined view of how SPR oil measured and modeled VPCRx(100°F) changed with light end losses during extended storage is shown in Figure F- 55. Each cluster of bars represents VPCR at given V/L indicated on the horizontal axis. ASTM D3677-measured VPCR values are shown as solid bars, and EOS-modeled VPCR values are shown as diagonally-striped bars. Bars are sorted within a given V/L with time from left to right. As such, for a given V/L, the loading subsample (SPR0) is shown on the left, and subsequent samples in time (SPR1, SPR2, …, SPR6) are shown moving to the right. Bars are then paired by sub-sampling event, with an ASTM D6377-measured value next to an EOS-modeled value.

There are a number of observations worth noting in this figure. First, the reduction in VPCR due to weathering loss of light hydrocarbons is noticeable at all V/L levels, and the magnitude of reduction far exceeds the uncertainty of the test methods. Second, measured versus model pairings for VPCR at a given V/L generally compare well, indicating that the analytical methods for vapor pressure and

composition were self-consistent, and were tied together well by the equation of state model employed in this work. This successful multi-point comparison provides confidence that the equation of state model is performing well for the current application and can accurately represent VPCR changes in the oil that can be attributed to compositional changes at the component level.

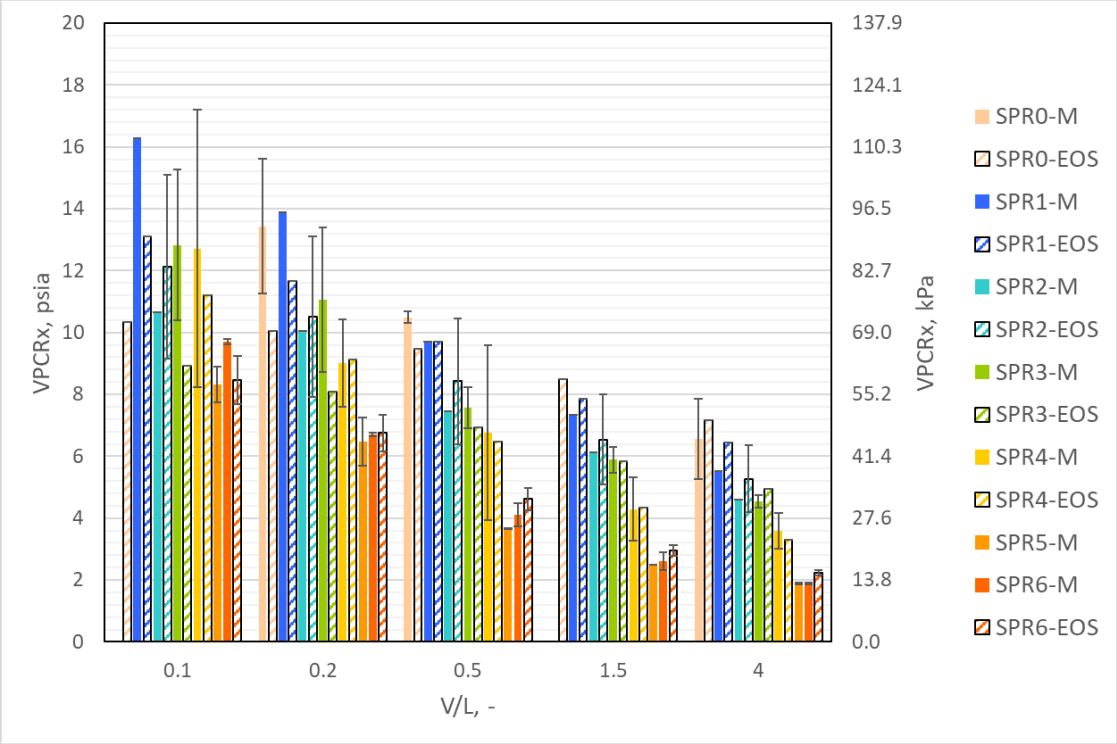

Figure F- 55: ASTM D6377-measured (solid) and EOS-modeled (cross-hatched) VPCRx(100°F) for SPR subsamples, exhibiting effects of unpressurized storage at Sandia.

F.4.1.1.4. Weathering Effects on PVT Relationship in Fireball Test Tank

The PVT conditions of the oil relevant to the fireball tank pre-conditioning process also changed because of the weathering of the SPR oil. Figure F- 56 shows pressures calculated for each of the SPR compositions, with the actual SPR and Texas Shale pressure measurements from the fireball test tank included for reference. The first SPR sub-sample composition taken at loading (SPR0, dashed purple line) showed a curve that was within the uncertainty of the Texas Shale measurement (solid yellow line). Successive samples gave progressively smaller pressures, which was expected for the loss of light ends. Eventually, the last two samples on the plot (SPR4, dashed yellow line; SPR6, dashed red line) lined up well with the actual test tank data (solid orange line). The weathering of the SPR oil caused greater separation in the test tank parameter space for the fireballs.

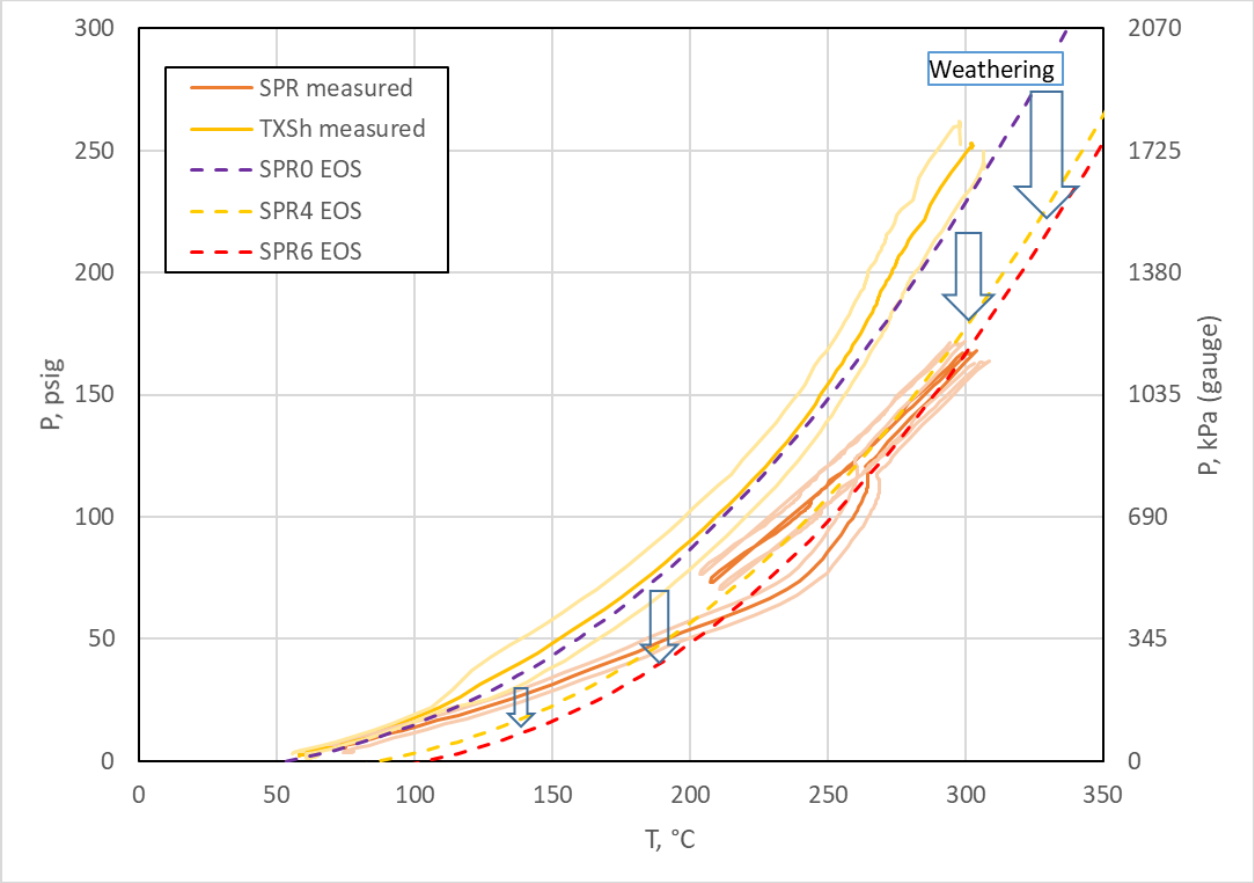

Figure F- 56: Pressure vs temperature measurements (solid lines) and EOS calculations (dashed lines) of the SPR subsamples by sampling event showing evolution of oil properties fireball test tank conditions due to weathering.

F.4.1.2. Texas Shale Oil Response to PSV Issue

As described in section F.2.2.4.2, the Texas Shale tanker experienced a pressure safety valve malfunction that caused the loss of a small amount of liquid oil during vapor-liquid compression process in December 2017 in advance of subsampling for the 5m pool fire test. The configuration of the failure--several gallons of liquid loss out of the top of the tank--suggested that the properties of the tanker contents would not be affected, but a review of the oil properties before and after the event is warranted. Primary concern was to maintain oil properties and composition representative of the loading condition, and while vapor-only losses deplete overall volatiles, liquid-only losses above the bubble point pressure should have no effect on the net properties in the remaining liquid. Measured $VPCR_4$(100°F) with time (days since loading) for subsamples pulled from the TX Shale tanker load is shown in Figure F- 57 The PSV failure occurred about 2 weeks after the tanker was loaded, and is annotated with a black vertical line between days 10 and 20. Comparing $VPCR_4$ associated with loading (Day 0) and for the 5m pool fire test (Day 48), the values agree to within ½ psia, which is within the 2σ error bars for method reproducibility. Similar behavior is observed for duration of pressurized storage at Sandia out to 310 days at the time of the final sample. Compositional data from the same sampling events are shown in Figure F- 58, fixed gases, and Figure F- 59, light ends. The PSV event occurred between loading (TXSh0) and subsampling for the 5m pool fire (TXSh1). C1 decreased from about 0.1 mole % to 0.07 mole % during this timeframe and remained stable throughout the remainder of the storage period. It is possible that this early change was due to the

PSV issue, though sample-to-sample uncertainty in methane is a persistent issue and difficult to associate with a specific factor or event. A slight reduction in mole % of C2-C5 is observed between TXSh0 and TXSh1, but TXSh3 returns to mirror the original loading values (TXSh0), indicating that no net change was evident, and the magnitude of changes observed fall within method uncertainty. The reader may wish to reference the SPR sample weathering results in section F.4.1.1, and Figure F-54 in particular, to calibrate what the effects of unpressurized sample handling and consequent loss of volatiles may look like for an oil monitored by the same analytical techniques. Ultimately, both Figure F- 58 and Figure F- 59 indicate that the fixed gas and light hydrocarbon compositions were stable within the resolution of the measurement methods, with no evidence of net loss of volatiles due to the PSV failure event or any other factors that may have affected the long-term storage of the sample.

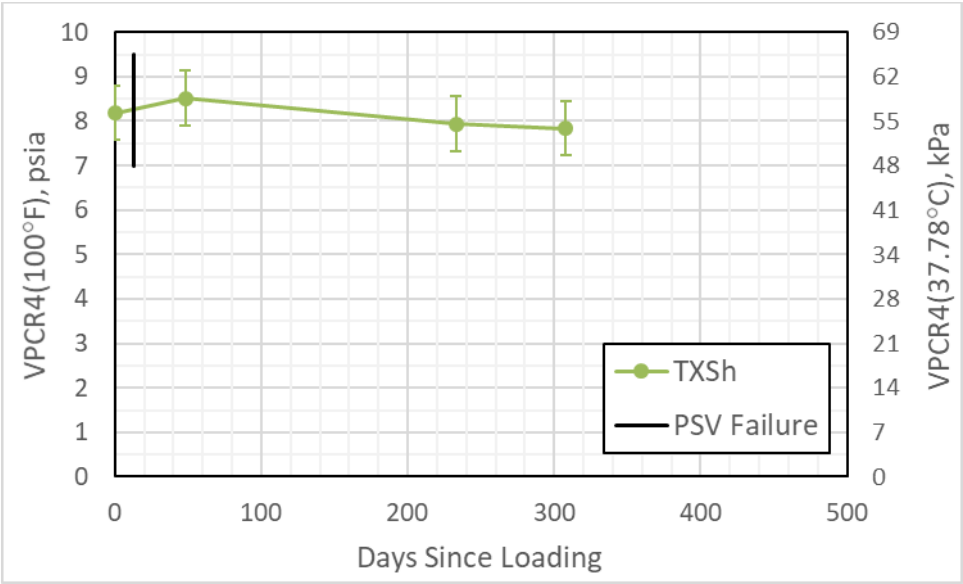

Figure F- 57: Measured VPCR4(100°F) versus days since loading for Texas Shale samples taken from Sandia tanker.

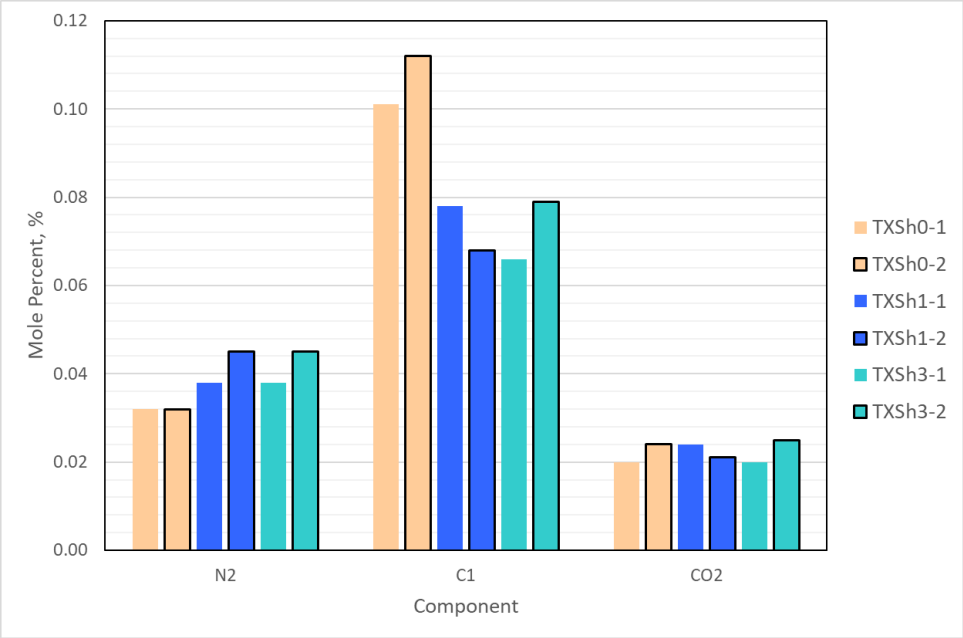

Figure F- 58: Measured fixed gas and methane compositions for TX Shale samples during storage in Sandia tanker.

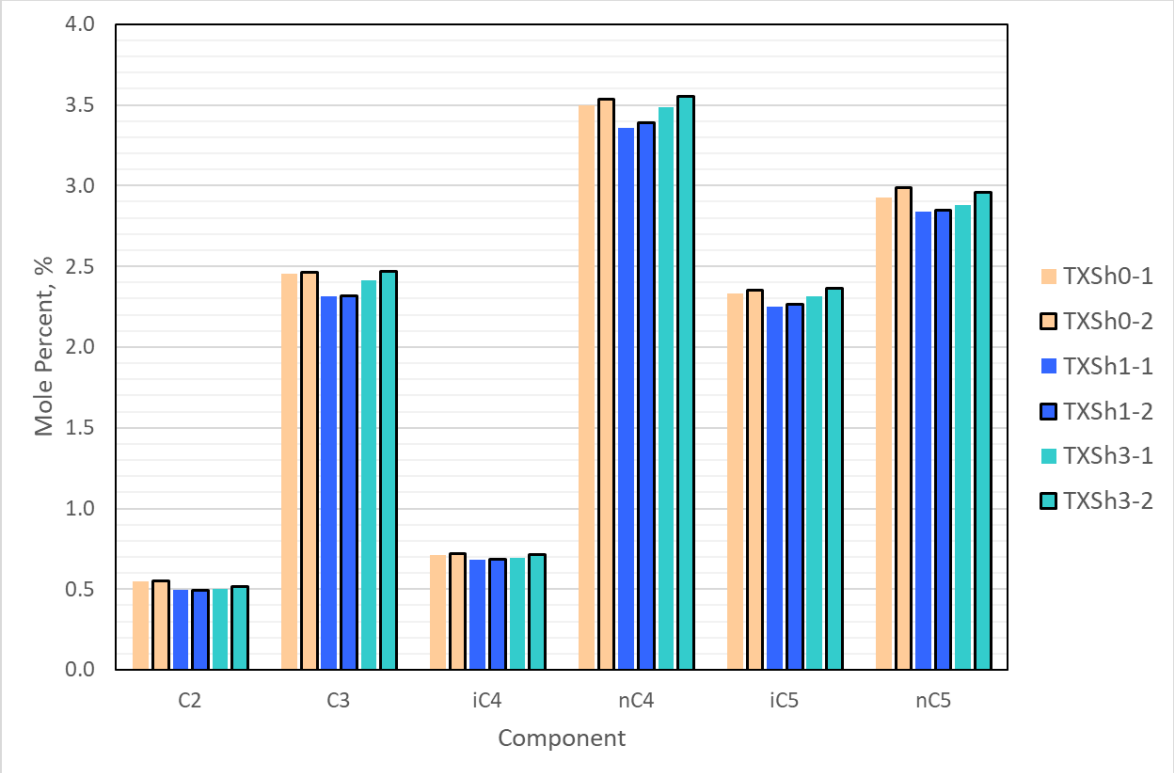

Figure F- 59: Measured light ends (C2-C5) for TX Shale samples during storage in Sandia tanker.

F.4.1.3. Bakken Oil Response to Fireball Tank Transfer

The Bakken oil was exposed to a unique handling sequence in August 2018 associated with a failed 400-gallon fireball test attempt (see section F.2.2.3.4) where 400 gallons of oil was transferred to the fireball tank on August 2, back into the tanker on August 16 after the failed fireball test, and once again back into the fireball tank on August 30 for what was the successful fireball test on September 5, 2018. The handling steps all utilized water drive under positive gauge pressure as described in section F.2.2.3.4, so no loss of volatiles or direct exposure to air was expected. Data available as of August 2018 from fireball tank temperature monitoring indicated that the oil was never exposed to high enough temperature to "crack" the oil (recall Figure F- 13), nor did it exhibit a pressure history inside the fireball tank that would suggest a physical change in properties during the pressure-temperature cycle of the failed test. Additional data on oil properties before and after the August transfers obtained from spot sampling in July and October are presented here.

Figure F- 60 shows measured $VPCR_4(100°F)$ for subsamples taken from the Bakken tanker taken throughout the duration of containment at Sandia. The August 2018 handling period is identified by the black rectangle between 300 and 400 days since loading. A ½-psi decrease in $VPCR_4$ was noted between the July (BKN4) and October (BKN5) subsampling, but this falls within the expected uncertainty of the sampling and analysis methods, so there was no evidence to suggest that the August 2018 handling period changed the measured $VPCR_4(100°F)$ value of the oil.

Figure F- 61 and Figure F- 62 show the fixed gas and light ends contents, respectively, for the BKN sampling events. The close overlay of the BKN4 and BKN5 data provide additional confirmation that the transfer operations and heating-cooling cycles did not affect any significant changes in base composition.

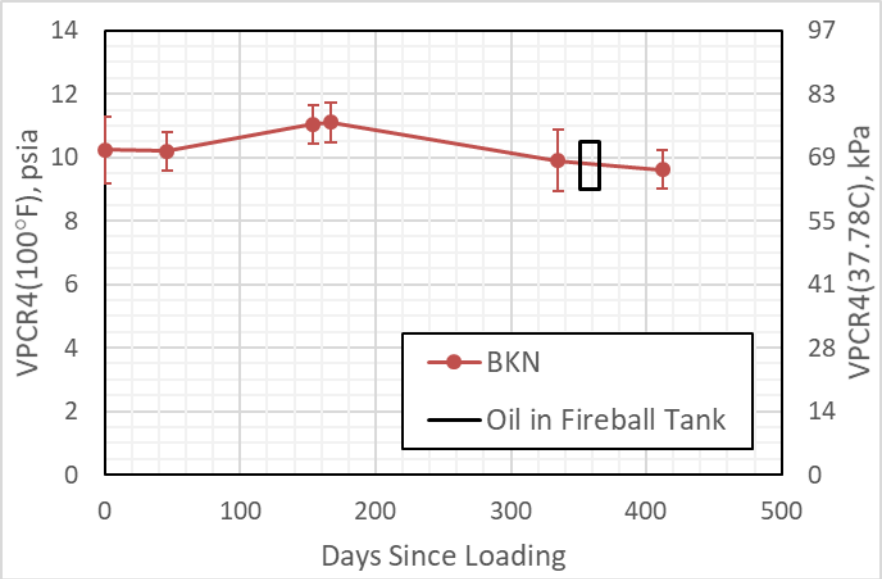

Figure F- 60: Measured VPCR4(100°F) versus days since loading for Bakken samples taken from Sandia tanker.

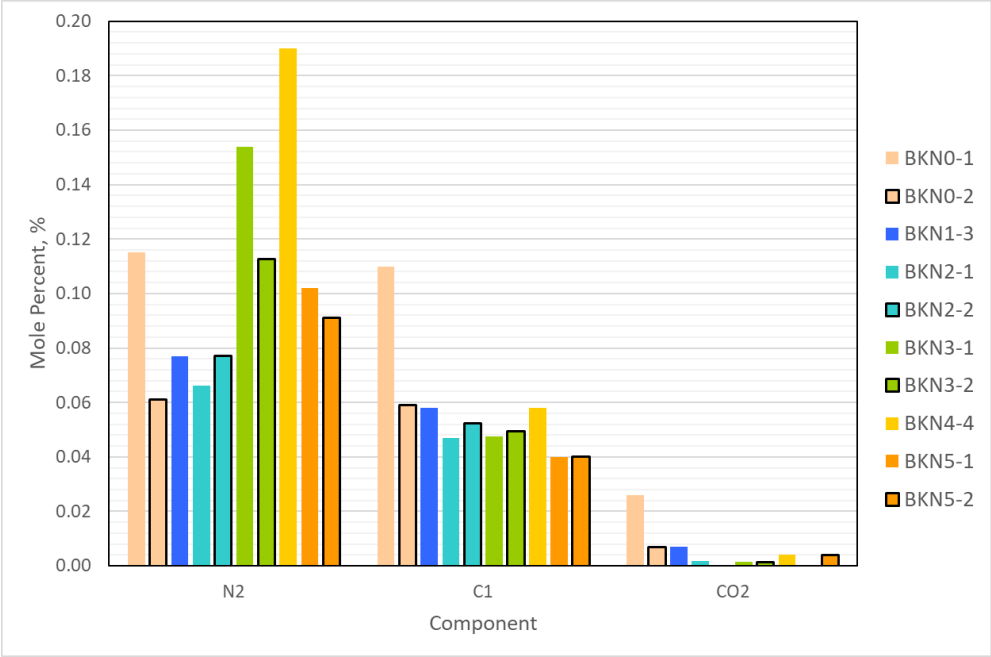

Figure F- 61: Fixed gas and methane concentration before (BKN4) and after (BKN5) the August 2018 fireball tank transfers.

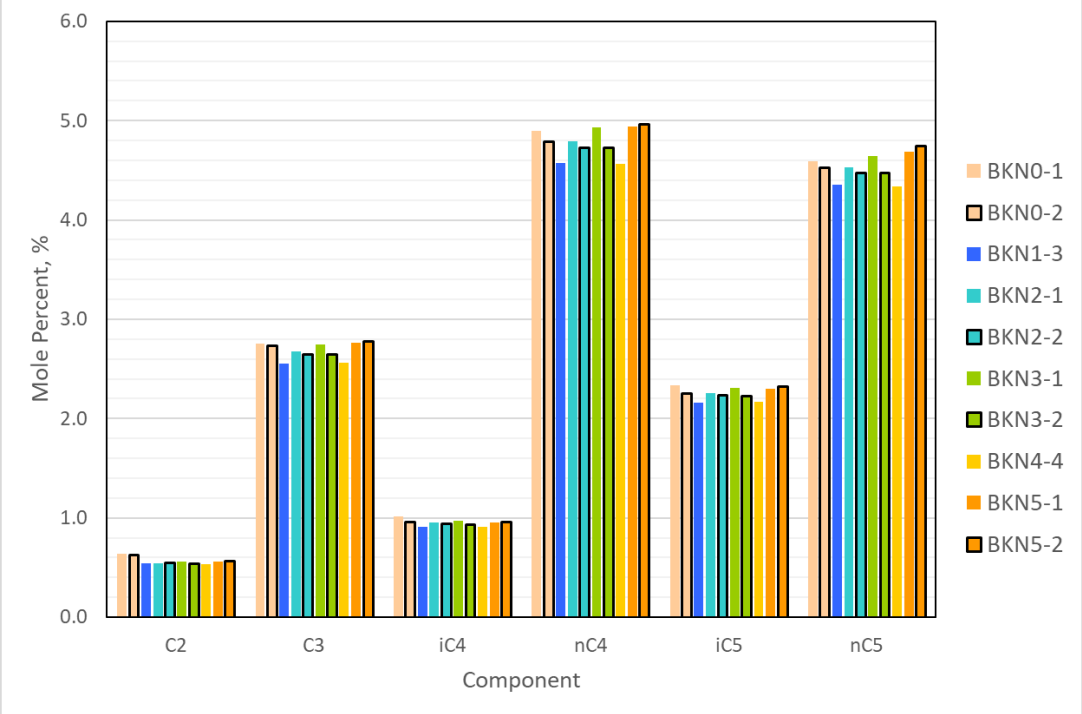

Figure F- 62: Light ends concentration before (BKN4) and after (BKN5) the August 2018 fireball tank transfers.

F.4.2. API Gravity vs VPCR

Some perspective on where the Task 3 oil properties fall relative to other oils in U.S. supply chain may be gained from reviewing a plot of $VPCR_4(100°F)$ versus API gravity (60°F), shown in Figure F- 63. Table F- 24 gives a brief summary of the sources of the data and the measurement methods used. This figure represents an update to a prior version presented in a 2015 literature survey for a range of SPR, NDPC , and PHSMA [88] data. New data from Task 2 [4] and Task 3 of this project have been added to the plot, along with available incoming commercial stream measurements at the SPR between 2015 and 2018. The data sources and measurement methods are summarized in Table F- 24. In the figure, ASTM D6377 measured $VPCR_x$ values (closed symbols) are shown where available. For systems where only compositional data were available, calculated $VPCR_x$ points (open symbols) are shown based on equation of state calculations. Note that PHMSA did not list individual API gravity values, so the mean $VPCR_4$ and 2 standard deviation (2σ) lines from that body of data were computed and added to the figure. The Crude Oil Characterization Research Study Task 2 data include values for samples of two types of oils taken in both summer and winter, across four different laboratories. The Task 3 sample measurements are represented as symbols connected by lines, showing the change in the oils over storage time.

As API gravities increase in the figure, larger $VPCR_4$ values were observed for incrementally lighter oils, with the exception of jet fuel, which was a specific cut of C9-C13 hydrocarbons with no light ends and no heavy ends. The SPR oil (purple diamonds with a line) started with $VPCR_4(100°F) = 6.5$ psia at loading (yellow star) and showed clear signs of weathering, as both VPCR and API gravity dropped. Contrast this to the Bakken and Texas shale oils that began and held constant at $VPCR_4(100°F)$ values clearly higher than the SPR oil. Had the shale oils been kept in unpressurized storage like the SPR oil, there would have been similar weathering into a region of the chart that may not be representative of crude oils in the associated supply chain. In general, the three Task 3 oils show a wide range of properties expected for crude oils, from shale oils with high $VPCR_4$ to the degassed SPR oil with low $VPCR_4$.

The Task 3 oils occupy interesting spots in the parameter space compared to other historical data. The Task 3 BKN oil hovered around the same VPCR and API as the NDPC, PHMSA, and Task 2 Bakken oils – $VPCR_4$ ranged from about 10-14 psia with a mean value around 12.5 psia. The Task 3 TXSh oil was denser than the Task 2 Eagle Ford oil, with a slightly lower $VPCR_4$. However, these two oils were sampled from different parts of the supply chain from different oilfields in Texas, so direct comparison is not as useful here. Interestingly, the incoming commercial oils to the SPR sat between the historical SPR data – mostly conventional crudes – and the Task 3 BKN oil. There is no clear information on the tight oil contents in the commercial streams, but the migration to higher API gravities through time is clear in this plot.

Table F- 24: Sources and methods for VPCR and API data in Figure F- 63 and Figure F- 64.

Plot Label	Source	VPCRx Method	API Method
SPR Sweet	SPR Database	Calculated	ASTM D5002
SPR Sour	SPR Database	Calculated	ASTM D5002
SPR Recent Commercial Receipts	SPR Database	Calculated	ASTM D5002
SPR Bakken	SPR Database	Calculated	ASTM D5002
NDPC Bakken Rail	[89]	ASTM D6377	ASTM D5002
NDPC Bakken Well	[89]	ASTM D6377	ASTM D5002
PHMSA Bakken	[88]	ASTM D6377	N/A
Task 2 – ND Bakken	[4]	ASTM D6377	ASTM D5002
Task 2 – ND Bakken Calculated	[4]	Calculated	ASTM D5002
Task 2 – TX Eagle Ford	[4]	ASTM D6377	ASTM D5002
Task 2 – TX Eagle Ford Calculated	[4]	Calculated	ASTM D5002
Task 3 – Jet A	This Report	ASTM D6377	ASTM D5002
Task 3 – SPR Load+Burn	This Report	ASTM D6377	ASTM D5002
Task 3 – BKN Load+Burn	This Report	ASTM D6377	ASTM D5002 or D4052[1]
Task 3 – TXSh Load+Burn	This Report	ASTM D6377	ASTM D5002

[1] ASTM D4052 used to measure API Gravity for BKN2 and BKN3 (collected under a different project)

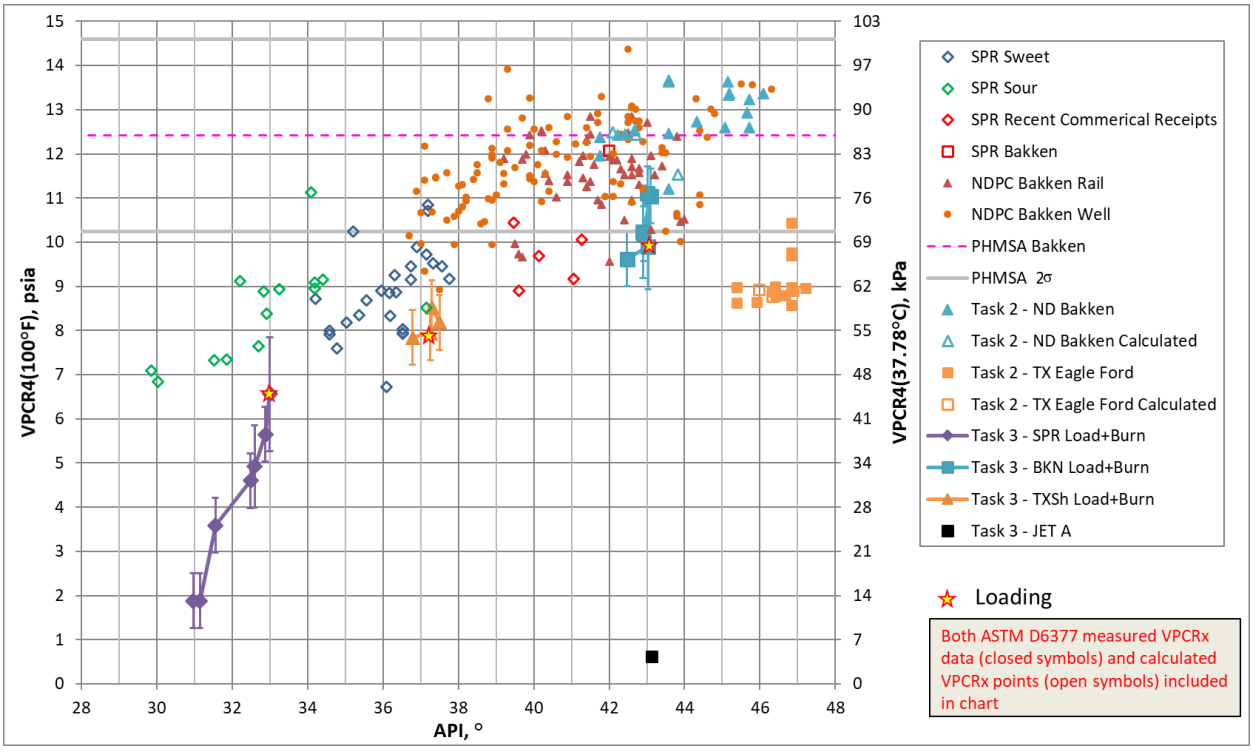

Figure F- 63: Overlay of SPR, PHMSA, and NDPC $VPCR_4$(100°F) vs. API Gravity with the fuels tested as part of this project

When considering the relevance to crude oil transportation, there is an understandable interest in measuring and reporting on VPCR at low vapor-liquid ratio (<< 1.0), because any practical transportation scenario is going to reduce the vapor volume to some small fraction of the liquid

volume in a closed container to maintain commercial viability of the shipping operation. To provide some perspective on lower VPCR, available data at $VPCR_{0.2}$(100°F) was processed and aggregated into the plot shown in Figure F- 64. $VPCR_{0.2}$ was selected, in part, because it corresponded well with independently measured bubblepoint pressure as described in the Task 2 technical report that evaluated analytical methods for applicability to this work.

Figure F- 64 shows API gravity versus $VPCR_{0.2}$(100°F) for recent SPR samples along with the fuels from the current study. Again, the Task 3 sample measurements are represented as symbols connected by lines, showing the change in the oils over storage time. Also, ASTM D6377 measured VPCRx values and calculated VPCRx points were represented by closed and open symbols, respectively. Scanning the figure from left to right, $VPCR_{0.2}$ increases with API gravity as would be expected for incrementally lighter oils, except for jet fuel. The Task 3 SPR, TXSh, and BKN oils occupied the same general regions of the chart as Figure F- 63, but with more scatter than the $VPCR_4$ measurements. This scatter was expected because uncertainty in nitrogen content has been shown to affect VPCR for V/L < 1 [4] and calculated bubblepoint pressure for hydrocarbon liquids [90]. Even so, the SPR oil showed a similar pattern of weathering with $VPCR_{0.2}$ as it did with $VPCR_4$ in Figure F- 63 (simultaneous decrease in both API and VPCR over time). The BKN oil showed more variability in $VPCR_{0.2}$ than it showed in $VPCR_4$, which is more sensitive to sample-to-sample N2 effects. Again, these three oils showed a range of properties that would be expected for crude oils, from shale oils with high $VPCR_{0.2}$ to degassed SPR oils with low $VPCR_{0.2}$.

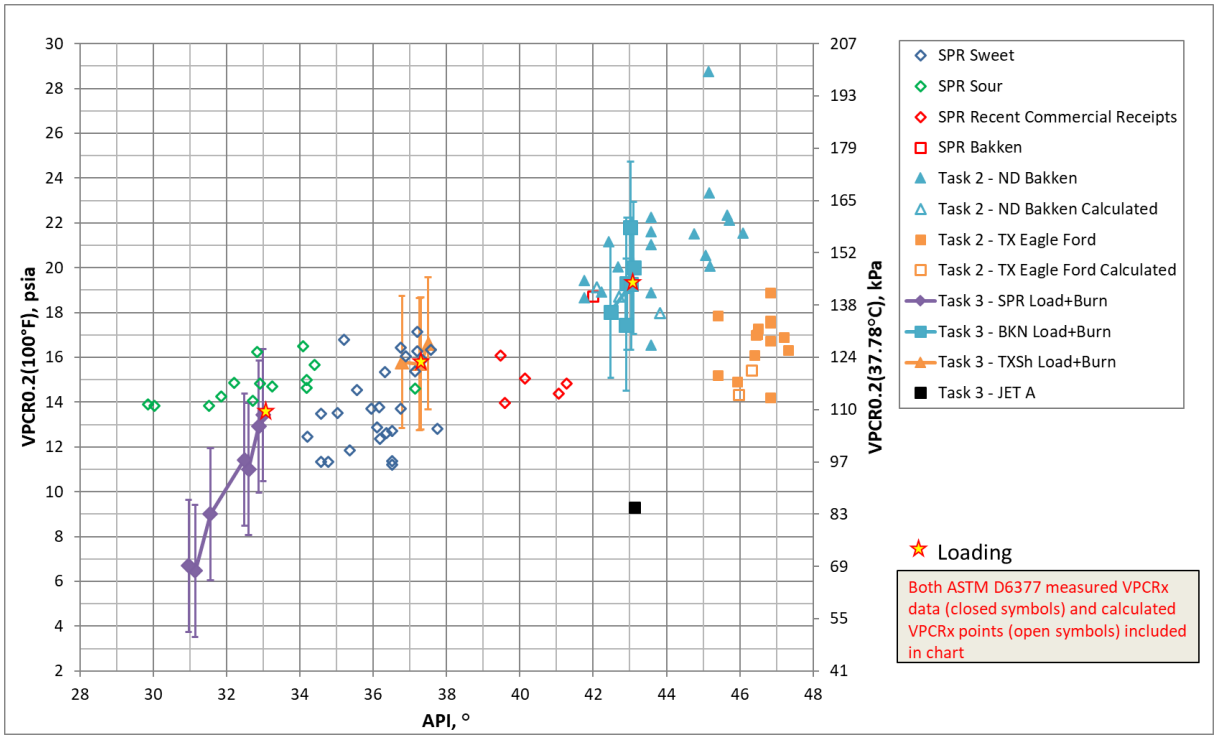

Figure F- 64: Overlay of SPR $VPCR_{0.2}$(100°F) vs. API Gravity with the fuels tested as part of this project

F.4.3. Post-Burn Solids Mass

Some solid residue was left in the pool fire pans after fire testing was complete, consistent with expectations outlined in [66]. A summary table of results is given in Table F- 25. SPR medium sour oil produced the most residue, with about 6% by mass (residue/feed) left after the 2m pool fire on 3/22/2017. The Bakken and TX Shale 5m tests produced only enough residue to create a powder coating on surfaces on or above the pan, and a total mass was not specifically determined, but estimated at less than 5 kg. Two Bakken pool fire tests run in January 2018 [77] with the same source Bakken oil made available here through sponsor sharing agreements generated about 0.3-0.4 % by mass residue to feed.

Table F- 25. Post-burn residue collected for selected pool fire tests.

Test Description	Test Oil	Test Date	Oil Feed	Oil Feed	Residue	Ratio (Residue/Feed)	Comment
			(gal)	(kg)	(kg)	(kg/kg)	
2m pool fire	SPR, cold	2/14/2017	25	82	N/A	N/A	boilover
2m pool fire	SPR, hot	3/22/2017	111.7	351	20	0.057	
5m pool fire	SPR, hot	4/6/2017	650.0	2045	N/A	N/A	
5m pool fire	SPR, ambient	8/15/2017	587.0	1936	N/A	N/A	boilover
5m pool fire	Bakken	10/9/2017	416	1277	< 5	< 0.01	
5m pool fire	TX Shale	1/15/2018	706	2248	< 5	< 0.01	boilover
2m pool fire*	Bakken	1/18/2018	82.5	253	0.7	0.003	
2m pool fire*	Bakken	1/31/2018	66	203	0.8	0.004	

* Additional information on the 2m Bakken pool fire tests are given in [77].

F.5. Tabular Listing of Compositional Data

F.5.1. Jet and SPR Compositional Data

F.5.1.1. Mole % and other properties

	Event Abbreviation	JetA	SPR0	SPR1	SPR2	SPR2	SPR3	SPR4	SPR6	SPR6
	Sampling Date	8/9/2017	1/24/2017	2/13/2017	3/20/2017	3/20/2017	4/5/2017	8/14/2017	10/2/2018	10/2/2018
	Sample Container		FPC	FPC	FPC	FPC	FPC	WD	FPC	FPC
	Cylinder Replicate	1	1	1	1	2	1	1	1	2
Composition (mol%)	H2S									
	N2+O2		0.03	0.10	0.12	0.11	0.06	0.18	0.13	0.12
	C1	0.00	0.01	0.00	0.01	0.00	0.00	0.03	0.00	0.00
	CO2		0.05	0.01	0.01	0.01	0.01	0.02	0.01	0.01
	C2	0.00	0.18	0.07	0.05	0.03	0.02	0.02	0.00	0.00
	C3	0.00	1.94	1.46	1.09	0.94	0.94	0.18	0.03	0.01
	iC4	0.01	0.89	0.78	0.70	0.61	0.64	0.28	0.07	0.06
	nC4	0.01	3.45	3.31	2.93	2.61	2.82	1.55	0.66	0.66
	iC5	0.01	2.40	2.49	2.25	1.94	2.19	1.75	1.29	1.29
	nC5	0.00	3.62	3.82	3.44	3.06	3.42	2.91	2.46	2.53
	iC6	0.01	1.37	1.75	1.65	1.44	1.25	1.75	1.75	2.15
	nC6	0.03	2.67	2.33	2.35	2.03	2.43	2.73	3.12	2.73
	iC8	0.07	0.04	0.04	0.05	0.04	0.04	0.04	0.05	0.04
	Ben	0.00	0.39	0.38	0.40	0.34	0.39	0.50	0.56	0.45
	C7	0.14	9.09	8.30	9.36	8.52	8.94	9.44	10.42	8.98
	Tol	0.08	1.52	1.41	1.52	1.63	1.55	1.65	1.77	2.84
	C8	0.48	9.24	8.98	10.03	9.80	8.98	9.09	9.79	9.48
	Etb	0.49	0.69	0.70	0.73	0.74	0.64	0.70	0.73	0.69
	Xyl		1.75	1.79	1.71	1.84	1.57	1.71	1.75	1.63
	C9	4.32	6.39	6.53	6.74	6.69	5.66	5.93	6.01	6.16
	C10	20.59	6.49	6.56	6.60	6.74	6.86	6.92	6.94	7.07
	C11	21.81	5.04	5.24	5.25	5.40	5.47	5.61	5.52	5.62
	C12	22.38	4.25	4.34	4.33	4.41	4.47	4.55	4.58	4.63
	C13	15.14	3.95	4.09	4.08	4.24	4.27	4.32	4.34	4.38
	C14	10.31	3.47	3.59	3.60	3.67	3.73	3.77	3.76	3.85
	C15	3.33	3.06	3.18	3.15	3.29	3.30	3.34	3.36	3.44
	C16	0.64	2.63	2.68	2.67	2.79	2.83	2.82	2.85	2.87
	C17	0.04	2.31	2.39	2.37	2.49	2.50	2.52	2.55	2.57
	C18	0.01	2.09	2.17	2.13	2.23	2.26	2.31	2.31	2.35
	C19	0.01	2.01	2.07	2.02	2.16	2.16	2.11	2.19	2.26
	C20	0.00	1.74	1.77	1.74	1.85	1.88	1.91	1.90	1.92
	C21	0.00	1.49	1.55	1.53	1.64	1.62	1.68	1.66	1.67
	C22	0.05	1.35	1.38	1.36	1.43	1.48	1.46	1.49	1.52
	C23	0.00	1.20	1.23	1.21	1.30	1.28	1.32	1.30	1.32
	C24	0.02	1.07	1.10	1.10	1.16	1.16	1.17	1.18	1.21
	C25	0.00	0.98	1.01	1.00	1.06	1.07	1.06	1.09	1.09
	C26	0.00	0.90	0.93	0.93	0.97	0.97	1.01	1.00	1.01
	C27	0.00	0.83	0.87	0.86	0.93	0.91	0.92	0.93	0.93
	C28	0.00	0.79	0.80	0.83	0.87	0.85	0.86	0.86	0.88
	C29	0.00	0.72	0.74	0.73	0.78	0.77	0.81	0.80	0.81
	C30+	0.00	7.92	8.08	7.39	8.23	8.64	9.08	8.81	8.77
Total	Specific Gravity at 60°F	0.81	0.86	0.86	0.86	0.86	0.86	0.87	0.87	0.87
	API Gravity at 60°F	43.12	33.84	33.79	33.70	32.31	32.99	31.97	31.34	31.32
	Molecular Weight	162.00	211.19	206.33	212.58	226.07	210.73	219.66	228.33	228.25
	Pounds per Gallon (in Vacuum)		7.14	7.14	7.14	7.20	7.17	7.22	7.24	7.25
	Pounds per Gallon (in Air)		7.13	7.13	7.13	7.19	7.16	7.21	7.24	7.24
	Cu. Ft. Vapor per Gallon @ 14.696 psia		12.82	13.13	12.75	12.09	12.92	12.47	12.04	12.05
C30+	Specific Gravity at 60°F		0.97	0.97	0.97	0.97	0.97	0.96	0.97	0.96
	API Gravity at 60°F		14.35	14.61	14.71	14.65	14.81	15.20	15.03	15.20
	Molecular Weight		586.32	583.11	575.07	577.01	582.79	591.71	577.59	580.96
	Pounds per Gallon (in Vacuum)		8.09	8.07	8.07	8.07	8.06	8.04	8.05	8.04
	Pounds per Gallon (in Air)		8.08	8.07	8.06	8.06	8.06	8.03	8.04	8.03
	Cu. Ft. Vapor per Gallon @ 14.696 psia		5.24	5.25	5.32	5.31	5.25	5.16	5.29	5.25
Total	Shrinkage Factor		0.99	0.99	0.99	0.99	0.99	0.99	0.99	0.99
	Flash Factor, Cu.Ft./STBbl.		18.77	4.63	22.73	14.12	3.34	14.43	14.12	14.46
	Color Visual		Crude	Crude	Crude	Crude	Crude	Crude	Crude	Crude
	API Gravity @ 60° F		33.11	32.88	32.60	32.60	32.49	31.67	30.97	30.97
	< C6 mass%	0.01	3.70	3.70	3.18	2.63	3.09	2.08	1.39	1.41

F.5.1.2. Mass %

	Event Abbreviation	JetA	SPR0	SPR1	SPR2	SPR2	SPR3	SPR4	SPR6	SPR6
	Sampling Date	8/9/2017	1/24/2017	2/13/2017	3/20/2017	3/20/2017	4/5/2017	8/14/2017	10/2/2018	10/2/2018
	Sample Container		FPC	FPC	FPC	FPC	FPC	WD	FPC	FPC
	Cylinder Replicate	1	1	1	1	2	1	1	1	2
Composition (mass%)	H2S									
	N2+O2		0.004	0.014	0.016	0.013	0.008	0.023	0.016	0.015
	C1	0	0.001	0	0.001	0	0	0.002	0	0
	CO2		0.01	0.002	0.002	0.001	0.001	0.003	0.001	0.001
	C2	0	0.025	0.01	0.007	0.004	0.003	0.003	0	0
	C3	0	0.404	0.312	0.226	0.184	0.196	0.036	0.005	0.002
	iC4	0.00465	0.245	0.22	0.192	0.156	0.177	0.073	0.017	0.016
	nC4	0.00478	0.95	0.933	0.802	0.672	0.778	0.41	0.169	0.168
	iC5	0.00518	0.819	0.871	0.763	0.62	0.751	0.575	0.407	0.409
	nC5	0	1.238	1.334	1.169	0.978	1.171	0.957	0.777	0.798
	iC6	0.00651	0.556	0.722	0.657	0.542	0.507	0.677	0.653	0.798
	nC6	0.01523	1.089	0.973	0.954	0.773	0.995	1.069	1.178	1.029
	iC8	0.05279	0.024	0.022	0.024	0.021	0.023	0.023	0.025	0.021
	Ben	0.00228	0.144	0.142	0.145	0.119	0.143	0.179	0.19	0.155
	C7	0.09044	4.157	3.888	4.26	3.652	4.094	4.144	4.391	3.795
	Tol	0.04525	0.663	0.629	0.657	0.664	0.677	0.691	0.713	1.148
	C8	0.3473	4.837	4.819	5.223	4.794	4.715	4.569	4.73	4.593
	Etb	0.36771	0.349	0.361	0.363	0.348	0.324	0.336	0.338	0.32
	Xyl		0.881	0.919	0.855	0.863	0.788	0.826	0.814	0.758
	C9	3.38516	3.836	4.014	4.018	3.75	3.403	3.419	3.326	3.422
	C10	17.8458	4.886	4.825	5.015	4.941	4.879	4.818	4.92	4.978
	C11	20.98126	4.173	4.236	4.385	4.348	4.272	4.295	4.298	4.343
	C12	23.21037	3.832	3.82	3.939	3.871	3.803	3.793	3.888	3.904
	C13	16.11638	3.852	3.897	4.015	4.026	3.937	3.9	3.988	3.994
	C14	12.2306	3.643	3.681	3.809	3.744	3.696	3.665	3.722	3.782
	C15	4.22122	3.443	3.493	3.568	3.597	3.502	3.477	3.552	3.614
	C16	0.84757	3.15	3.135	3.226	3.253	3.198	3.129	3.213	3.217
	C17	0.05617	2.938	2.974	3.046	3.085	3.004	2.969	3.061	3.06
	C18	0.01383	2.816	2.852	2.9	2.921	2.88	2.878	2.935	2.96
	C19	0.01043	2.85	2.872	2.893	2.98	2.896	2.774	2.933	3
	C20	0.00288	2.608	2.592	2.629	2.686	2.649	2.642	2.681	2.689
	C21	0.00416	2.333	2.369	2.424	2.506	2.396	2.443	2.46	2.456
	C22	0.09125	2.225	2.222	2.255	2.289	2.294	2.222	2.313	2.338
	C23	0	2.056	2.066	2.096	2.17	2.076	2.092	2.099	2.121
	C24	0.03803	1.916	1.922	1.992	2.014	1.962	1.945	1.998	2.019
	C25	0.00278	1.835	1.843	1.891	1.919	1.877	1.822	1.914	1.907
	C26	0	1.751	1.758	1.811	1.833	1.777	1.806	1.823	1.841
	C27	0	1.664	1.702	1.749	1.816	1.724	1.706	1.77	1.759
	C28	0	1.657	1.637	1.746	1.759	1.677	1.667	1.682	1.712
	C29	0	1.55	1.565	1.59	1.646	1.58	1.626	1.629	1.632
	C30+	0	24.59	24.354	22.687	24.442	25.167	26.316	25.371	25.226

F.5.2. Bakken Compositional Data

F.5.2.1. Mole% and other properties

	Event Abbreviation	BKN0	BKN0	BKN1	BKN2	BKN2	BKN3	BKN3	BKN4	BKN5	BKN5
	Sampling Date	8/17/2017	8/17/2017	10/2/2017	1/18/2018	1/18/2018	1/31/2018	1/31/2018	7/18/2018	10/4/2018	10/4/2018
	Sample Container	FPC	FPC	FPC					WD	FPC	FPC
	Cylinder Replicate	1	2	3	1	2	1	2	4	1	2
Composition (mol%)	H2S										
	N2+O2	0.12	0.06	0.08	0.07	0.08	0.15	0.11	0.19	0.10	0.09
	C1	0.11	0.06	0.06	0.05	0.05	0.05	0.05	0.06	0.04	0.04
	CO2	0.03	0.01	0.01	0.00	0.00	0.00	0.00	0.00	0.00	0.00
	C2	0.64	0.63	0.55	0.54	0.55	0.56	0.54	0.53	0.56	0.56
	C3	2.76	2.74	2.56	2.67	2.64	2.74	2.65	2.57	2.76	2.77
	iC4	1.01	0.96	0.91	0.95	0.94	0.97	0.94	0.91	0.95	0.96
	nC4	4.89	4.78	4.58	4.79	4.73	4.93	4.73	4.57	4.94	4.96
	iC5	2.34	2.25	2.16	2.26	2.23	2.31	2.23	2.17	2.30	2.33
	nC5	4.59	4.53	4.35	4.53	4.47	4.64	4.47	4.34	4.69	4.74
	iC6	2.45	2.97	3.60		0.00			2.95	2.47	3.23
	nC6	3.38	3.57	4.23	7.17	7.08	7.31	7.06	3.70	3.89	3.72
	iC8	0.10	0.10	0.12		0.00			0.10	0.11	0.10
	Ben	0.43	0.50	0.64	0.45	0.43	0.46	0.42	0.47	0.49	0.46
	C7	11.79	12.27	13.80	10.54	10.41	10.72	10.36	12.41	12.61	11.91
	Tol	1.01	1.08	1.33		0.00			1.06	1.08	2.14
	C8	12.33	12.23	12.97	11.50	11.36	11.68	11.30	12.27	12.00	11.56
	Etb	0.48	0.46	0.47		0.00			0.45	0.43	0.42
	Xyl	1.60	1.56	1.76		0.00			1.51	1.43	1.37
	C9	7.91	7.16	7.35	8.09	8.01	8.10	7.94	7.17	6.70	6.57
	C10	6.10	6.17	5.88	6.81	7.51	6.72	7.43	6.31	6.36	6.38
	C11	4.69	4.74	4.46	5.09	4.75	5.05	4.68	4.85	4.87	4.93
	C12	3.85	3.86	3.60	4.35	4.34	4.32	4.37	3.96	3.97	3.94
	C13	3.47	3.48	3.28	3.81	3.90	3.79	3.84	3.60	3.59	3.60
	C14	2.94	2.95	2.76	3.34	3.42	3.33	3.45	3.02	3.00	3.01
	C15	2.49	2.50	2.32	2.69	2.76	2.68	2.70	2.55	2.57	2.56
	C16	2.12	2.10	1.96	2.20	2.19	2.13	2.21	2.16	2.19	2.16
	C17	1.81	1.81	1.68	2.13	2.19	2.20	2.14	1.86	1.86	1.86
	C18	1.59	1.58	1.47	1.69	1.75	1.64	1.76	1.62	1.64	1.64
	C19	1.43	1.43	1.31	1.36	1.36	1.38	1.37	1.46	1.49	1.47
	C20	1.24	1.23	1.15	1.24	1.30	1.26	1.25	1.26	1.27	1.27
	C21	1.08	1.08	0.99	1.17	1.23	1.14	1.24	1.10	1.10	1.10
	C22	0.97	0.96	0.88	1.01	1.01	0.98	1.02	0.98	0.99	0.98
	C23	0.84	0.83	0.76	0.87	0.92	0.94	0.93	0.85	0.86	0.85
	C24	0.74	0.73	0.67	0.84	0.83	0.81	0.84	0.74	0.76	0.75
	C25	0.66	0.66	0.61	7.85	7.57	6.97	7.96	0.67	0.68	0.67
	C26	0.61	0.59	0.54					0.60	0.62	0.61
	C27	0.54	0.54	0.50					0.54	0.56	0.54
	C28	0.49	0.48	0.43					0.49	0.48	0.48
	C29	0.44	0.44	0.38					0.43	0.44	0.41
	C30+	3.96	3.93	2.86					3.52	3.15	2.87
Total	Specific Gravity at 60°F	0.80	0.80	0.80					0.80	0.80	0.81
	API Gravity at 60°F	44.54	44.84	45.18					44.67	44.65	44.29
	Molecular Weight	160.55	156.56	153.83					156.30	159.51	160.04
	Pounds per Gallon (in Vacuun	6.70	6.69	6.68					6.70	6.70	6.71
	Pounds per Gallon (in Air)	6.69	6.68	6.67					6.69	6.69	6.70
	Cu. Ft. Vapor per Gallon @ 14	15.84	16.22	16.47					16.26	15.93	15.91
C30+	Specific Gravity at 60°F	0.94	0.94	0.95					0.95	0.94	0.95
	API Gravity at 60°F	18.66	18.50	17.30					18.17	18.37	17.77
	Molecular Weight	548.66	550.07	537.56					544.56	539.48	529.73
	Pounds per Gallon (in Vacuun	7.86	7.87	7.93					7.88	7.87	7.90
	Pounds per Gallon (in Air)	7.85	7.86	7.92					7.87	7.86	7.89
	Cu. Ft. Vapor per Gallon @ 14	5.43	5.43	5.60					5.49	5.54	5.66
Total	Shrinkage Factor	0.99	0.99	0.99					0.99	0.99	0.99
	Flash Factor, Cu.Ft./STBbl.	2.11	7.10	15.27					5.74	16.36	24.45
	Simulated Flash Factor (69F)	2.30	0.50								
	Color Visual	Straw	Straw	Straw					Dark Amber	Crude	Crude
	API Gravity @ 60° F	42.52	42.55	42.76					42.51	42.35	42.60
	< C6 mass%	6.17	6.17	5.99	5.91	5.84	6.22	5.80	5.91	6.20	6.22

F.5.2.2. Mass %

	Event Abbreviation	BKN0	BKN0	BKN1	BKN2	BKN2	BKN3	BKN3	BKN4	BKN5	BKN5
	Sampling Date	8/17/2017	8/17/2017	10/2/2017	1/18/2018	1/18/2018	1/31/2018	1/31/2018	7/18/2018	10/4/2018	10/4/2018
	Sample Container	FPC	FPC	FPC					WD	FPC	FPC
	Cylinder Replicate	1	2	3	1	2	1	2	4	1	2
Composition (mass%)	H2S										
	N2+O2	0.02	0.011	0.014	0.0121384	0.0130419	0.0305522	0.0188317	0.034	0.018	0.016
	C1	0.011	0.006	0.006	0.0046185	0.0051768	0.0047993	0.0048524	0.006	0.004	0.004
	CO2	0.007	0.002	0.002	0.000483	0	0.00041	0	0.001	0	0.001
	C2	0.119	0.121	0.107	0.1005196	0.1010907	0.105407	0.0990823	0.102	0.106	0.106
	C3	0.757	0.771	0.733	0.7243024	0.7179634	0.7613178	0.7120735	0.724	0.763	0.764
	iC4	0.366	0.355	0.343	0.3399904	0.3351441	0.3560536	0.3317135	0.339	0.347	0.347
	nC4	1.771	1.776	1.729	1.7114308	1.6924121	1.8027675	1.6779412	1.698	1.798	1.801
	iC5	1.051	1.038	1.013	1.0014885	0.9915492	1.0482408	0.9818985	1.001	1.042	1.048
	nC5	2.063	2.086	2.04	2.0121613	1.9875193	2.1075014	1.9692603	2.003	2.12	2.137
	iC6	1.3	1.612	1.987					1.605	1.32	1.715
	nC6	1.812	1.964	2.37	3.700071	3.6618631	3.8658687	3.618648	2.042	2.101	2.002
	iC8	0.071	0.075	0.088					0.076	0.075	0.072
	Ben	0.211	0.247	0.326	0.2146273	0.2062713	0.223851	0.2025621	0.235	0.24	0.225
	C7	7.046	7.503	8.556	6.2149639	6.150073	6.4793094	6.0690649	7.604	7.562	7.126
	Tol	0.579	0.637	0.794					0.625	0.626	1.233
	C8	8.449	8.578	9.233	7.5578161	7.4819366	7.8660989	7.3835627	8.617	8.259	7.925
	Etb	0.314	0.31	0.326					0.303	0.283	0.276
	Xyl	1.058	1.06	1.212					1.026	0.949	0.909
	C9	6.227	5.775	5.997	6.0126815	5.9654825	6.1689068	5.8667444	5.79	5.303	5.181
	C10	5.566	5.58	5.746	5.6053286	6.1987503	5.6691923	6.0757199	5.746	5.96	6.118
	C11	4.699	4.701	4.782	4.6	4.2994225	4.6738002	4.1991748	4.853	5.012	5.19
	C12	4.207	4.175	4.209	4.3	4.2994225	4.3754725	4.2991552	4.311	4.455	4.52
	C13	4.102	4.078	4.147	4.1	4.1994359	4.1765874	4.0991945	4.249	4.357	4.467
	C14	3.736	3.72	3.758	3.9	3.9994628	3.9777023	3.9992141	3.83	3.924	4.027
	C15	3.393	3.368	3.383	3.4	3.49953	3.4804895	3.399332	3.47	3.59	3.67
	C16	3.083	3.02	3.048	3	2.9995971	2.9832767	2.9994106	3.129	3.271	3.294
	C17	2.789	2.764	2.778	3.1	3.1995702	3.2816044	3.099391	2.867	2.947	3.015
	C18	2.595	2.557	2.562	2.6	2.6996374	2.5855065	2.6994695	2.636	2.755	2.819
	C19	2.465	2.44	2.419	2.2	2.1997045	2.2871788	2.1995678	2.513	2.634	2.655
	C20	2.248	2.212	2.229	2.1	2.1997045	2.1877362	2.0995874	2.28	2.368	2.413
	C21	2.056	2.028	2.008	2.1	2.1997045	2.0882937	2.1995678	2.092	2.154	2.194
	C22	1.927	1.892	1.873	1.9	1.8997448	1.8894086	1.8996267	1.937	2.032	2.05
	C23	1.749	1.716	1.698	1.7	1.7997583	1.8894086	1.7996464	1.774	1.843	1.868
	C24	1.615	1.579	1.562	1.7	1.6997717	1.6905235	1.699666	1.603	1.697	1.715
	C25	1.497	1.479	1.473	24.1	23.296871	21.942731	24.295226	1.509	1.569	1.586
	C26	1.423	1.38	1.355					1.411	1.494	1.514
	C27	1.314	1.312	1.294					1.323	1.398	1.371
	C28	1.244	1.201	1.175					1.24	1.238	1.277
	C29	1.139	1.138	1.074					1.126	1.182	1.116
	C30+	13.921	13.733	10.551					12.27	11.204	10.233

F.5.3. TXSh Compositional Data

F.5.3.1. Mole % and other properties

	Event Abbreviation	TXSh0	TXSh0	TXSh1	TXSh1	TXSh3	TXSh3
	Sampling Date	11/28/2017	11/28/2017	1/19/2018	1/19/2018	10/3/2018	10/3/2018
	Sample Container	FPC	FPC	FPC	FPC	FPC	FPC
	Cylinder Replicate	1	2	1	2	1	2
Composition (mol%)	H2S	0.03	0.02				
	N2+O2	0.03	0.03	0.04	0.05	0.04	0.05
	C1	0.10	0.11	0.08	0.07	0.07	0.08
	CO2	0.02	0.02	0.02	0.02	0.02	0.03
	C2	0.55	0.55	0.50	0.49	0.50	0.52
	C3	2.46	2.46	2.32	2.32	2.42	2.47
	iC4	0.71	0.72	0.68	0.68	0.70	0.71
	nC4	3.50	3.54	3.36	3.39	3.49	3.55
	iC5	2.33	2.35	2.25	2.27	2.32	2.36
	nC5	2.93	2.99	2.84	2.85	2.88	2.96
	iC6	1.68	1.56	1.97	1.87	2.14	2.72
	nC6	1.57	1.47	1.62	1.59	2.17	2.03
	iC8	0.14	0.14	0.15	0.15	0.15	0.14
	Ben	0.97	0.94	0.83	0.88	1.23	1.11
	C7	11.86	11.86	11.27	11.81	13.44	12.48
	Tol	2.78	2.53	2.41	2.51	2.51	2.75
	C8	11.04	11.28	11.19	11.83	10.79	10.73
	Etb	1.46	1.47	1.47	1.63	1.32	1.28
	Xyl	1.48	1.53	1.58	1.77	1.20	1.26
	C9	6.18	6.34	5.78	6.51	5.45	5.76
	C10	6.10	6.03	6.25	5.92	6.28	6.14
	C11	4.87	4.81	4.96	4.79	4.89	4.79
	C12	3.76	3.76	3.88	3.71	3.83	3.76
	C13	3.89	3.86	3.98	3.81	3.87	3.80
	C14	3.22	3.24	3.32	3.16	3.28	3.21
	C15	2.79	2.76	2.88	2.76	2.83	2.78
	C16	2.25	2.26	2.31	2.21	2.28	2.25
	C17	2.42	2.43	2.49	2.38	2.09	2.06
	C18	1.61	1.63	1.68	1.60	2.00	1.98
	C19	1.82	1.78	1.87	1.76	1.80	1.77
	C20	1.42	1.44	1.47	1.40	1.44	1.42
	C21	1.25	1.23	1.29	1.23	1.29	1.27
	C22	1.14	1.15	1.17	1.12	1.15	1.13
	C23	1.00	1.01	1.03	0.98	1.02	1.01
	C24	0.89	0.89	0.93	0.88	0.92	0.90
	C25	0.82	0.83	0.85	0.81	0.83	0.82
	C26	0.77	0.76	0.77	0.74	0.75	0.74
	C27	0.71	0.71	0.74	0.70	0.72	0.71
	C28	0.66	0.66	0.69	0.66	0.64	0.64
	C29	0.61	0.61	0.62	0.58	0.57	0.58
	C30+	6.20	6.24	6.49	6.13	4.74	5.30
Total	Specific Gravity at 60°F	0.84	0.82	0.83	0.83	0.83	0.83
	API Gravity at 60°F	37.92	40.71	38.14	38.13	38.27	38.25
	Molecular Weight	180.30	179.31	178.01	181.15	177.52	180.01
	Pounds per Gallon (in Vacuun	6.96	6.85	6.95	6.96	6.95	6.95
	Pounds per Gallon (in Air)	6.96	6.84	6.95	6.95	6.94	6.94
	Cu. Ft. Vapor per Gallon @ 14	14.66	14.50	14.83	14.57	14.86	14.65
C30+	Specific Gravity at 60°F	0.95	0.93	0.95	0.96	0.96	0.96
	API Gravity at 60°F	16.76	19.96	16.88	16.58	15.88	16.18
	Molecular Weight	561.89	562.58	567.04	566.08	551.93	556.63
	Pounds per Gallon (in Vacuun	7.96	7.79	7.95	7.97	8.01	7.99
	Pounds per Gallon (in Air)	7.95	7.78	7.94	7.96	8.00	7.98
	Cu. Ft. Vapor per Gallon @ 14	5.37	5.25	5.32	5.34	5.50	5.45
Total	Shrinkage Factor	0.97	0.99	0.99	0.99	0.99	0.99
	Flash Factor, Cu.Ft./STBbl.	3.39	2.45	4.76	6.27	15.15	14.81
	Simulated Flash Factor (69F)	0.00	0.00	0.00	0.00		
	Color Visual	Crude	Crude	Crude	Crude	Crude	Crude
	API Gravity @ 60° F	37.20	37.22	37.53	37.06	36.91	36.66
	< C6 mass%	4.18	4.25	4.06	4.01	4.18	4.22

F.5.3.2. Mass %

	Event Abbreviation	TXSh0	TXSh0	TXSh1	TXSh1	TXSh3	TXSh3
	Sampling Date	11/28/2017	11/28/2017	1/19/2018	1/19/2018	10/3/2018	10/3/2018
	Sample Container	FPC	FPC	FPC	FPC	FPC	FPC
	Cylinder Replicate	1	2	1	2	1	2
Composition (mass%)	H2S	0.006	0.004				
	N2+O2	0.005	0.005	0.006	0.007	0.006	0.007
	C1	0.009	0.01	0.007	0.006	0.006	0.007
	CO2	0.005	0.006	0.006	0.005	0.005	0.006
	C2	0.091	0.092	0.084	0.082	0.085	0.086
	C3	0.601	0.606	0.574	0.564	0.6	0.604
	iC4	0.23	0.233	0.222	0.219	0.228	0.23
	nC4	1.127	1.146	1.097	1.088	1.141	1.147
	iC5	0.934	0.946	0.913	0.902	0.941	0.947
	nC5	1.172	1.201	1.15	1.135	1.17	1.185
	iC6	0.793	0.738	0.939	0.875	1.024	1.278
	nC6	0.748	0.704	0.784	0.758	1.052	0.973
	iC8	0.09	0.092	0.094	0.097	0.098	0.091
	Ben	0.418	0.408	0.363	0.38	0.542	0.482
	C7	6.191	6.233	5.97	6.144	7.087	6.499
	Tol	1.419	1.302	1.249	1.274	1.302	1.406
	C8	6.676	6.855	6.873	7.144	6.608	6.495
	Etb	0.861	0.873	0.876	0.953	0.791	0.757
	Xyl	0.869	0.905	0.944	1.034	0.719	0.744
	C9	4.297	4.435	4.038	4.477	3.851	4.012
	C10	4.98	4.904	4.952	4.866	5.408	5.233
	C11	4.372	4.302	4.314	4.326	4.626	4.486
	C12	3.68	3.661	3.678	3.648	3.95	3.836
	C13	4.116	4.07	4.08	4.06	4.321	4.19
	C14	3.668	3.679	3.671	3.617	3.94	3.819
	C15	3.407	3.35	3.409	3.383	3.638	3.537
	C16	2.93	2.921	2.915	2.892	3.124	3.045
	C17	3.338	3.339	3.326	3.31	3.049	2.964
	C18	2.348	2.374	2.382	2.357	3.08	3.01
	C19	2.804	2.739	2.787	2.737	2.926	2.854
	C20	2.295	2.327	2.305	2.286	2.466	2.4
	C21	2.129	2.089	2.123	2.099	2.315	2.248
	C22	2.038	2.044	2.027	2.01	2.163	2.107
	C23	1.87	1.877	1.866	1.841	2.013	1.959
	C24	1.736	1.719	1.744	1.73	1.881	1.826
	C25	1.653	1.673	1.675	1.64	1.769	1.722
	C26	1.623	1.587	1.573	1.572	1.66	1.619
	C27	1.557	1.554	1.569	1.549	1.651	1.617
	C28	1.492	1.499	1.515	1.499	1.522	1.505
	C29	1.423	1.428	1.411	1.38	1.409	1.411
	C30+	19.999	20.07	20.489	20.054	15.833	17.656

F.6. Tabular Listing of VPCRx Data

F.6.1. Jet VPCRx Data

	Event Abbreviation	JetA	JetA
	Sampling Date	8/9/2017	8/9/2017
	Temperature	100	100
	Sample Container		
	Cylinder Replicate	1	1
	Repeatability Replicate	a	b
	Sampling Temperature (F)		
	Sampling Pressure (psig)		
	Measured/Sim**U**lated	M	M
VPCRx (at these V/L)	0.0		
	0.05	15.15	15.24
	0.1	11.89	12.09
	0.2	9.28	9.34
	0.5	4.56	4.45
	1.0		
	1.5	1.53	1.52
	2.0		
	4.0	0.63	0.60

F.6.2. Bakken VPCRx Data

Direct measurements taken at 100°F

	Event Abbreviation	BKN0	BKN0	BKN1	BKN1	BKN1	BKN4	BKN4	BKN4	BKN4	BKN5	BKN5	BKN5	BKN5
	Sampling Date	8/17/2017	8/17/2017	10/2/2017	10/2/2017	10/2/2017	7/18/2018	7/18/2018	7/18/2018	7/18/2018	10/4/2018	10/4/2018	10/4/2018	10/4/2018
	Temperature	100	100	100	100	100	100	100	100	100	100	100	100	100
	Sample Container	FPC	FPC	FPC	FPC	FPC	MPC	MPC	MPC	MPC	MPC	MPC	MPC	MPC
	Cylinder Replicate	1	2	1	1	2	1	1	2	2	1	1	2	2
	Repeatability Replicate			a	b		a	b	a	b	a	b	a	b
	Sampling Temperature (F)	75		70	70	70								
	Sampling Pressure (psig)	148		45	45	45								
	Measured/Sim**U**lated	M	M	M	M	M	M	M	M	M	M	M	M	M
VPCRx (at these V/L)	0.0													
	0.05	18.53	18.10	27.71	28.00	26.61	22.64	23.56	20.75	21.49				
	0.1		17.40	19.78	19.95	21.50	22.33	22.32	19.66	19.82	19.18	18.99	19.02	19.01
	0.2	17.83	17.07	19.18	19.15	19.42	20.11	20.08	18.60	18.31	18.15	18.10	17.79	18.05
	0.5	15.70	15.40	16.09	16.04	16.21	16.23	16.56	15.22	15.37	15.25	15.25	15.30	15.40
	1.0													
	1.5		12.79	13.16	13.08	12.96	13.06	13.03	12.53	12.34	12.40	12.37	12.25	12.40
	2.0													
	4.0	9.87	10.61	10.18	10.23	10.18	10.10	10.38	9.54	9.58	9.58	9.68	9.58	9.65

Summary of measurements on shared Bakken sample from [77]

	Event Abbreviation	BKN2	BKN2	BKN2	BKN2	BKN2	BKN2	BKN2	BKN2	BKN3	BKN3	BKN3	BKN3	BKN3	BKN3	BKN3	BKN3
	Sampling Date	1/18/2018	1/18/2018	1/18/2018	1/18/2018	1/18/2018	1/18/2018	1/18/2018	1/18/2018	1/31/2018	1/31/2018	1/31/2018	1/31/2018	1/31/2018	1/31/2018	1/31/2018	1/31/2018
	Temperature	100	100	100	100	100	100	122	122	100	100	100	100	100	100	122	122
	Sample Container	FPC	FPC	FPC	FPC	FPC	FPC	FPC	FPC	FPC	FPC	FPC	FPC	FPC	FPC	FPC	FPC
	Cylinder Replicate	1	1	2	2	3	3	1	1	1	1	2	2	2	2	1	1
	Repeatability Replicate	a	b	a	b	a	b	a	b	a	b	a	b	c	d	a	b
	Sampling Temperature (F)																
	Sampling Pressure (psig)																
	Measured/Sim**U**lated	M	M	M	M	M	M	M	M	M	M	M	M	M	M	M	M
VPCRx (at these V/L)	0.0																
	0.05																
	0.1																
	0.2	20.00	19.99	19.97	19.97	19.93	19.93	24.03	24.03	22.66	22.64	21.86	21.84	21.03	21.03	25.09	25.06
	0.5	16.62	16.62	17.01	17.03	16.80	16.84	20.73	20.74	18.42	18.46	17.87	17.85	17.54	17.54	21.51	21.52
	1.0	14.68	14.69	15.19	15.19	14.74	14.74	18.57	18.55	15.88	15.87	15.56	15.56	14.98	14.99	19.03	19.03
	1.5	13.63	13.63	13.98	13.98	13.67	13.66	17.22	17.23	14.26	14.26	14.17	14.17	13.75	13.72	17.41	17.61
	2.0	12.84	12.84	13.10	13.11	12.88	12.89	16.36	16.38	13.42	13.40	13.27	13.29	12.93	12.92	16.71	16.72
	4.0	11.04	11.05	11.17	11.18	10.99	10.99	13.92	13.94	11.21	11.20	11.21	11.21	11.01	11.01	14.26	14.24

Values calculated from process simulator

	Event Abbreviation	BKN0	BKN0	BKN1	BKN2	BKN2	BKN3	BKN4	BKN5	BKN5
	Sampling Date	8/17/2017	8/17/2017	10/2/2017	1/18/2018	1/18/2018	1/31/2018	7/18/2018	10/4/2018	10/4/2018
	Temperature	100	100	100	100	100	100	100	100	100
	Sample Container	FPC	FPC	FPC	FPC	FPC	FPC	WD	FPC	FPC
	Cylinder Replicate	1	2	2	1	2	1	4	1	2
	Repeatability Replicate									
	Sampling Temperature (F)									
	Sampling Pressure (psig)									
	Measured/Sim**U**lated	U	U	U	U	U	U	U	U	U
VPCRx (at these V/L)	0.0	27.87	21.49	22.09	20.76	21.78	28.79	30.85	23.68	22.96
	0.05	25.73	20.31	20.66	20.22	20.37	27.62	27.70	21.97	21.41
	0.1	24.19	19.45	19.61	19.53	19.35	26.17	25.50	20.75	20.30
	0.2	22.06	18.24	18.18	17.41	17.95	21.85	22.58	19.10	18.78
	0.5	18.76	16.26	15.90	15.45	15.76	18.20	18.36	16.60	16.45
	1.0					14.04		15.49	14.70	14.66
	1.5	14.82	13.58	13.08	12.90	13.04	14.24	13.99	13.61	13.61
	2.0					12.32		12.99	12.83	12.86
	4.0	11.51	10.91	10.50	10.40	10.54	11.10	10.75	10.93	10.98

F.6.3. SPR VPCRx Data

Direct measurements at 100°F

	Event Abbreviation	SPR0	SPR0	SPR0	SPR0	SPR1	SPR1	SPR1	SPR1	SPR2	SPR2	SPR2	SPR2	SPR3	SPR3	SPR3	SPR3	SPR3	SPR3	SPR4	SPR4	SPR5	SPR5	SPR5	SPR5	SPR6	SPR6	SPR6	SPR6
	Sampling Date	1/24/2017	1/24/2017	1/24/2017	1/24/2017	2/13/2017	2/13/2017	2/13/2017	2/13/2017	3/20/2017	3/20/2017	3/20/2017	3/20/2017	4/5/2017	4/5/2017	4/5/2017	4/5/2017	4/5/2017	4/5/2017	4/5/2017	8/14/2017	8/14/2017	7/17/2018	7/17/2018	7/17/2018	7/17/2018	10/2/2018	10/2/2018	10/2/2018	10/2/2018
	Temperature	100	100	100	100	100	100	100	100	100	100	100	100	100	100	100	100	100	100	100	100	100	100	100	100	100	100	100	100
	Sample Container	FPC	FPC	FPC	FPC	FPC	FPC	WD	WD	FPC	FPC	WD	WD	FPC	FPC	FPC	FPC	FPC	FPC	WD	WD	MPC	MPC	MPC	MPC	MPC	MPC	MPC	MPC
	Cylinder Replicate	1	1	2	2	1	1	2	2	1	1	2	2	1	1	2	2	3	3	2	4	1	1	2	2	1	1	2	2
	Repeatability Replicate	a	b	a	b	a	b	a	b	a	b	a	b	a	b	a	b	a	b			a	b	a	b	a	b	a	b
	Sampling Temperature (F)	110	110	110	110	68	68	68	68	68	68	68	68	68	68	68	68	68	68	68	72								
	Sampling Pressure (psig)	145	145	145	145	22	22	22	22	22	22	22	22	23	23	23	23	23	23	2	2								
	Measured/SimUlated	M	M	M	M	M	M	M	M	M	M	M	M	M	M	M	M	M	M	M	M	M	M	M	M	M	M	M	M
VPCRx (at these V/L)	0.0																												
	0.05	22.74	22.30	22.08	22.39	19.52	19.82	17.44	17.53	15.30	15.24	17.05	17.30	15.89	15.50	17.73	17.76	17.47	17.47	33.63	17.47	17.65	17.57	17.53	17.81				
	0.1					16.12	16.43	14.25	13.92	10.74	10.55	16.01	15.72	13.14	12.99	13.70	14.11	11.42	11.60	11.13	14.30	8.41	8.64	8.07	8.15	9.61	9.84	9.65	9.68
	0.2	14.31	14.09	12.76	12.56	13.83	13.92	11.79	12.11	10.09	10.03	12.03	11.90	11.47	11.39	11.99	11.99	9.64	9.87	8.51	9.51	6.03	6.36	6.90	6.58	6.74	6.62	6.67	6.77
	0.5	10.54	10.57	10.34	10.52	9.59	9.79	9.89	9.36	7.44	7.49	8.22	8.26	7.81	7.74	7.71	7.75	7.15	7.20	5.77	7.77	3.71	3.62	3.71	3.59	3.97	3.98	4.17	4.30
	1.0																												
	1.5					7.30	7.35	7.52	7.42	6.10	6.17	6.57	6.46	6.10	6.03	5.88	5.99	5.64	5.65	3.93	4.65	2.49	2.50	2.50	2.49	2.49	2.50	2.65	2.75
	2.0																												
	4.0	7.04	6.99	6.10	6.10	5.54	5.52	5.80	5.74	4.59	4.59	5.33	5.17	4.62	4.58	4.52	4.64	4.35	4.48	3.39	3.79	1.89	1.89	1.87	1.87	1.87	1.91	1.87	1.87

Direct measurements taken at temperatures other than 100 °F for this project

	Event Abbreviation	SPR0	SPR0	SPR1	SPR1	SPR1	SPR1	SPR1	SPR1	SPR1	SPR1	SPR2	SPR2	SPR2	SPR2	SPR2	SPR2
	Sampling Date	1/24/2017	1/24/2017	2/13/2017	2/13/2017	2/13/2017	2/13/2017	2/13/2017	2/13/2017	2/13/2017	2/13/2017	3/20/2017	3/20/2017	3/20/2017	3/20/2017	3/20/2017	3/20/2017
	Temperature	68	68	68	68	68	68	122	122	122	122	68	68	68	68	122	122
	Sample Container	FPC	FPC	FPC	FPC	WD	WD	FPC	FPC	WD	WD	FPC	FPC	WD	WD	FPC	FPC
	Cylinder Replicate	1	1	1	1	2	2	1	1	2	2	1	1	1	1	1	1
	Repeatability Replicate	a	b	a	b	a	b	a	b	a	b	a	b	a	b	a	b
	Sampling Temperature (F)	110	110	68	68	68	68	68	68	68	68	68	68	68	68	68	68
	Sampling Pressure (psig)	145	145	22	22	22	22	22	22	22	22	22	22	22	22	22	22
	Measured/Sim**U**lated	M	M	M	M	M	M	M	M	M	M	M	M	M	M	M	M
VPCRx (at these V/L)	0.0																
	0.05	25.65	25.71	22.58	21.17	19.10	19.33	24.55	22.97	22.87	21.82	15.15	15.04	16.69	16.82	15.93	16.11
	0.1			10.86	10.70	12.25	11.95	21.17	20.91	19.04	19.37	7.90	7.44	7.78	7.48	14.73	14.60
	0.2	7.89	7.64	7.48	7.51	9.00	9.20	17.82	17.79	16.27	15.86	6.46	6.48	6.62	6.96	13.41	13.19
	0.5	6.42	6.54	5.58	5.59	5.91	5.96	12.99	13.02	12.76	12.79	4.84	4.84	4.59	4.82	10.47	10.29
	1.0																
	1.5			4.30	4.36	4.43	4.56	9.92	9.97	10.44	10.39	3.85	3.84	3.62	3.88	8.35	8.60
	2.0																
	4.0	4.59	4.67	3.42	3.42	3.46	3.42	7.48	7.54	8.57	8.32	3.03	3.06	2.88	2.91	6.52	7.00

Values calculated using a process simulator

	Event Abbreviation	SPR0	SPR1	SPR2	SPR2	SPR3	SPR4	SPR6	SPR6
	Sampling Date	1/24/2017	2/13/2017	3/20/2017	3/20/2017	4/5/2017	8/14/2017	10/2/2018	10/2/2018
	Temperature	100	100	100	100	100	100	100	100
	Sample Container	FPC	FPC	FPC	FPC	FPC	WD	FPC	FPC
	Cylinder Replicate	1	1	1	2	1	1	1	2
	Repeatability Replicate								
	Sampling Temperature (F)								
	Sampling Pressure (psig)								
	Measured/Sim**U**lated	U	U	U	U	U	U	U	U
VPCRx (at these V/L)	0.0	10.79	16.05	16.66	14.07	10.66	18.67	12.48	11.65
	0.05	10.53	14.28	14.57	12.26	9.62	15.44	10.21	9.54
	0.1	10.33	13.11	13.18	11.07	8.93	13.34	8.74	8.19
	0.2	10.04	11.65	11.44	9.60	8.07	10.76	6.96	6.54
	0.5	9.48	9.71	9.14	7.70	6.94	7.47	4.74	4.48
	1.0								
	1.5	8.49	7.86	7.05	6.02	5.85	4.80	3.02	2.90
	2.0								
	4.0	7.17	6.44	5.66	4.89	4.96	3.50	2.25	2.19

F.6.4. TXSh VPCRx Data

Direct measurements at 100°F

	Event Abbreviation	TXSh0	TXSh0	TXSh1	TXSh1	TXSh2	TXSh2	TXSh2	TXSh2	TXSh3	TXSh3	TXSh3	TXSh3
	Sampling Date	11/28/2017	11/28/2017	1/19/2018	1/19/2018	7/19/2018	7/19/2018	7/19/2018	7/19/2018	10/3/2018	10/3/2018	10/3/2018	10/3/2018
	Temperature	100	100	100	100	100	100	100	100	100	100	100	100
	Sample Container	MPC	MPC	MPC	MPC	MPC	MPC	MPC	MPC	MPC	MPC	MPC	MPC
	Cylinder Replicate	1	2	1	2	1	1	2	2	1	1	2	2
	Repeatability Replicate					a	b	a	b	a	b	a	b
	Sampling Temperature (F)	77	77										
	Sampling Pressure (psig)	40	40										
	Measured/SimUlated	M	M	M	M	M	M	M	M	M	M	M	M
VPCRx (at these V/L)	0.0												
	0.05	19.66	19.52	18.24	17.60	17.94	17.95	18.56	18.04				
	0.1	18.78	17.07	17.08	16.81	17.18	17.28	16.59	16.53	16.62	16.53	16.56	16.37
	0.2	17.49	15.74	15.73	15.75	15.95	15.89	15.40	15.56	15.66	15.82	15.94	15.70
	0.5	14.38	13.47	13.42	13.57	13.45	13.40	13.27	13.37	13.34	13.18	13.43	13.41
	1.0												
	1.5	10.99	11.17	11.03	10.78	10.57	10.52	10.67	10.66	10.39	10.48	10.45	10.44
	2.0												
	4.0	8.15	8.22	8.61	8.43	7.91	7.91	8.00	7.93	8.13	7.90	7.73	7.61

Values calculated using a process simulator

	Event Abbreviation	TXSh0	TXSh0	TXSh1	TXSh1	TXSh3	TXSh3
	Sampling Date	11/28/2017	11/28/2017	1/19/2018	1/19/2018	10/3/2018	10/3/2018
	Temperature	100	100	100	100	100	100
	Sample Container	FPC	FPC	FPC	FPC	FPC	FPC
	Cylinder Replicate	1	1	1	2	1	2
	Repeatability Replicate	a	b				
	Sampling Temperature (F)						
	Sampling Pressure (psig)						
	Measured/SimUlated	U	U	U	U	U	U
VPCRx (at these V/L)	0.0	18.60	18.48	17.58	17.79	17.74	19.32
	0.05	17.71	17.58	16.65	16.78	16.83	18.22
	0.1	17.03	16.91	15.96	16.05	16.15	17.40
	0.2	16.04	15.91	14.98	15.01	15.19	16.25
	0.5	14.28	14.16	13.30	13.29	13.55	14.34
	1.0						
	1.5	11.72	11.63	10.94	10.93	11.24	11.74
	2.0						
	4.0	9.16	9.10	8.59	8.61	8.92	9.23

APPENDIX G. BURN PROPERTY VS OIL PROPERTY PLOTS

G.1. Pool Fire vs Oil Properties

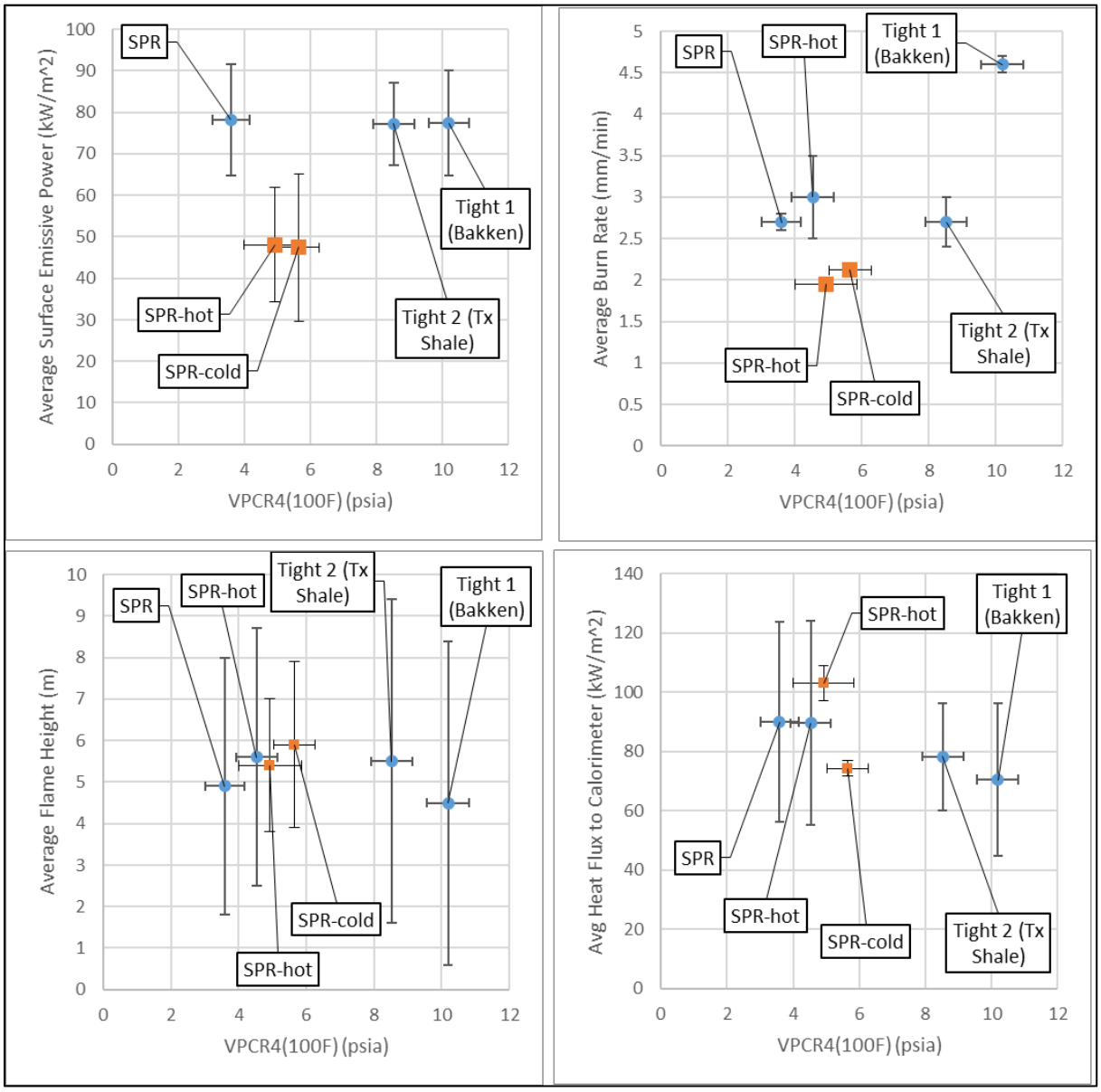

Figure G- 1: Oil property $VPCR_4(100°F)$ vs pool fire burn properties a) average surface emissive power, b) average burn rate, c) average flame height, and d) average heat flux to calorimeter for 2-m (orange squares) and 5-m (blue circles) pool fires

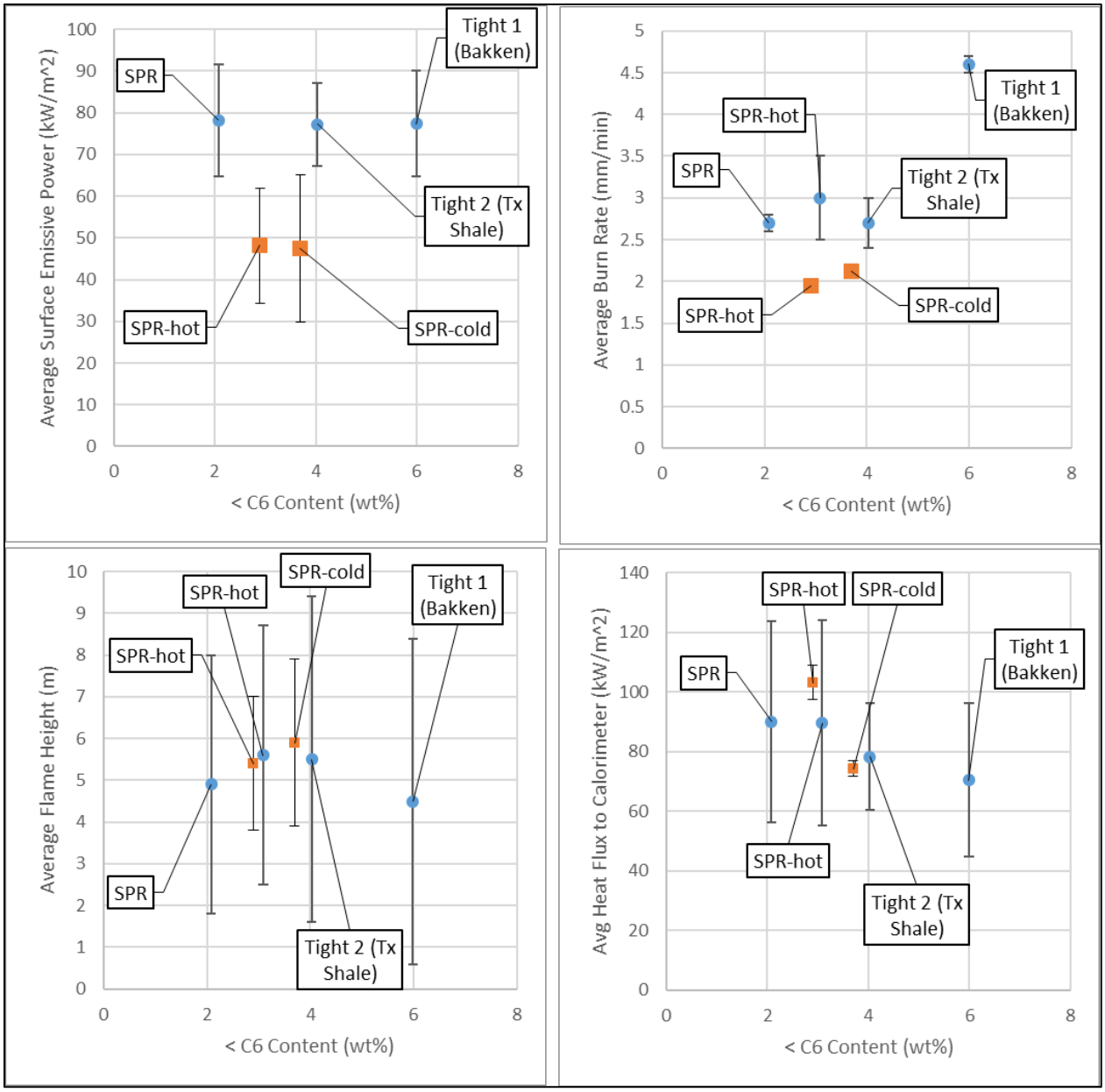

Figure G- 2: Oil property < C6 content (mass%) vs pool fire burn properties a) average surface emissive power, b) average burn rate, c) average flame height, and d) average heat flux to calorimeter for 2-m (orange squares) and 5-m (blue circles) pool fires

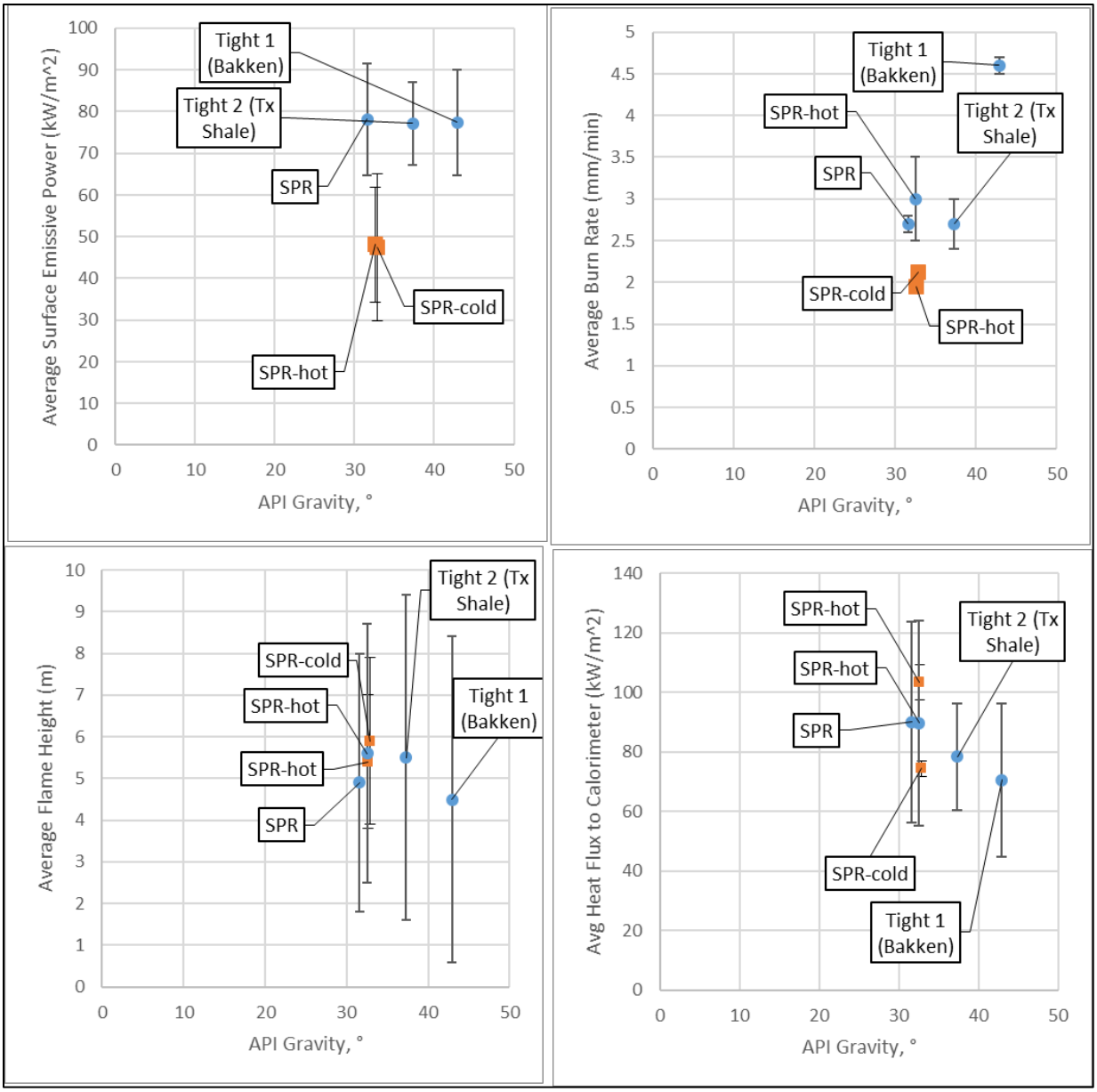

Figure G- 3: Oil property API gravity vs pool fire burn properties a) average surface emissive power, b) average burn rate, c) average flame height, and d) average heat flux to calorimeter for 2-m (orange squares) and 5-m (blue circles) pool fires

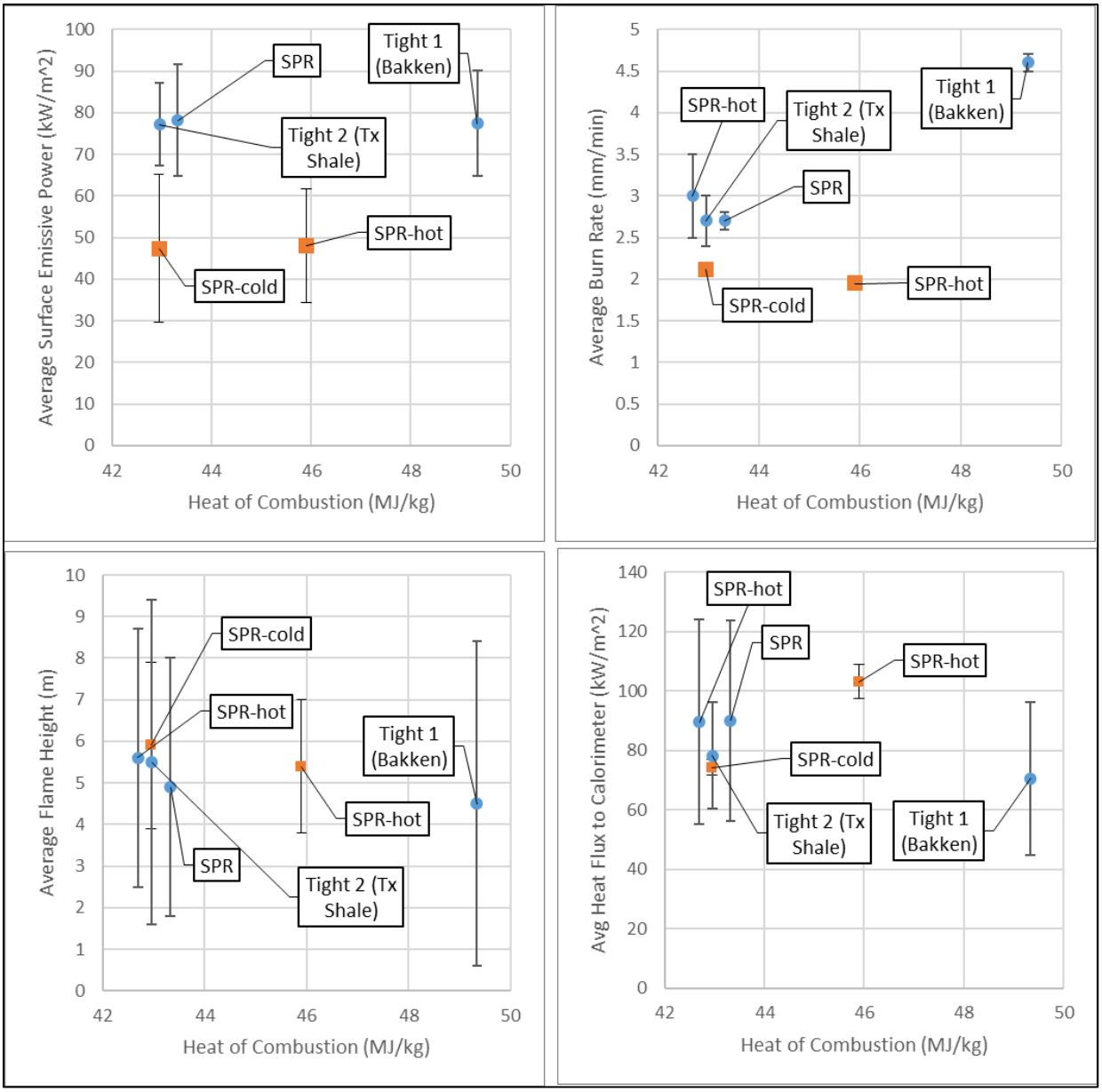

Figure G- 4: Oil property heat of combustion vs pool fire burn properties a) average surface emissive power, b) average burn rate, c) average flame height, and d) average heat flux to calorimeter for 2-m (orange squares) and 5-m (blue circles) pool fires

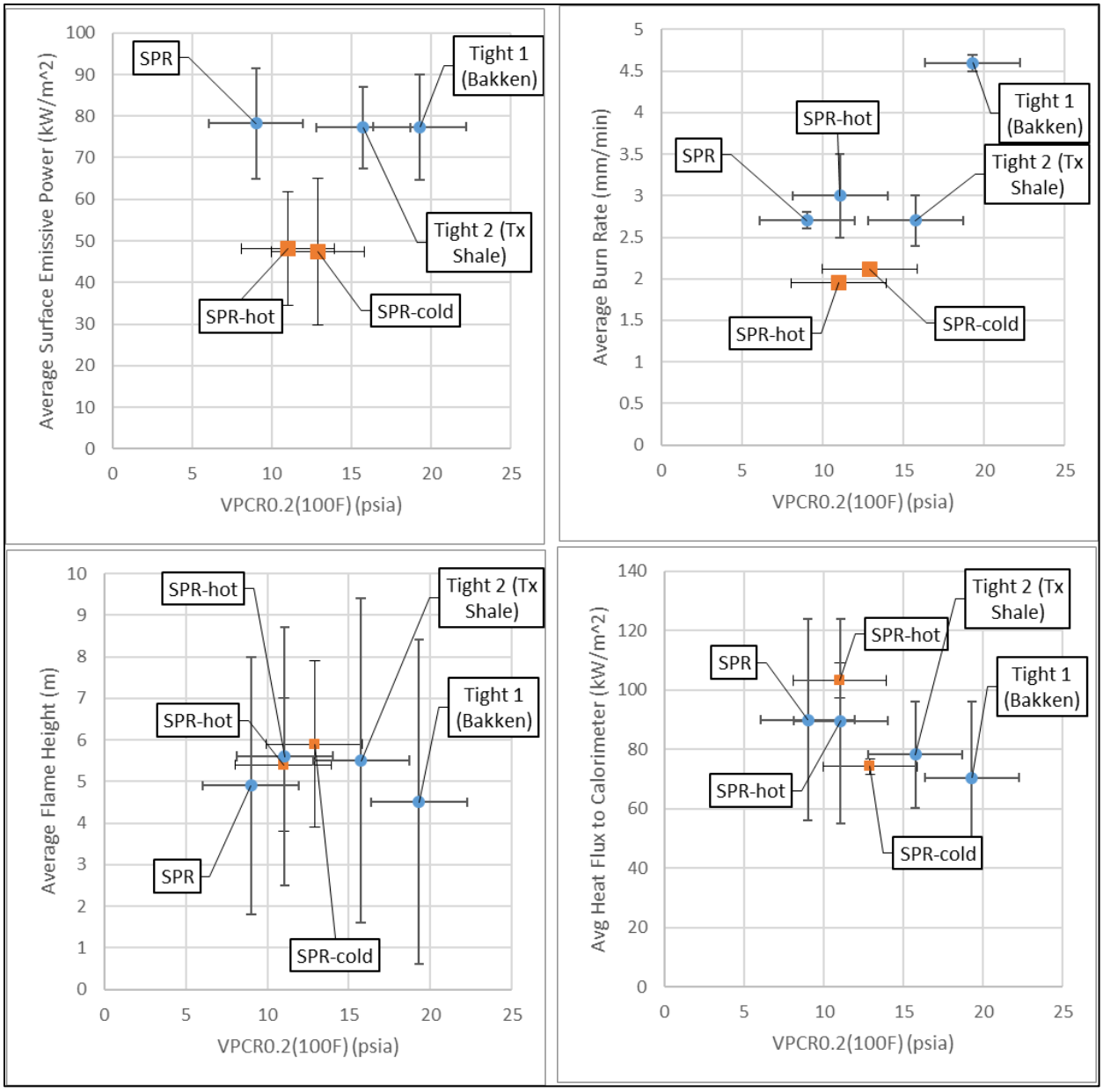

Figure G- 5: Oil property $VPCR_{0.2}$(100°F) vs pool fire burn properties a) average surface emissive power, b) average burn rate, c) average flame height, and d) average heat flux to calorimeter for 2-m (orange squares) and 5-m (blue circles) pool fires

G.2. Fireball vs Oil Properties

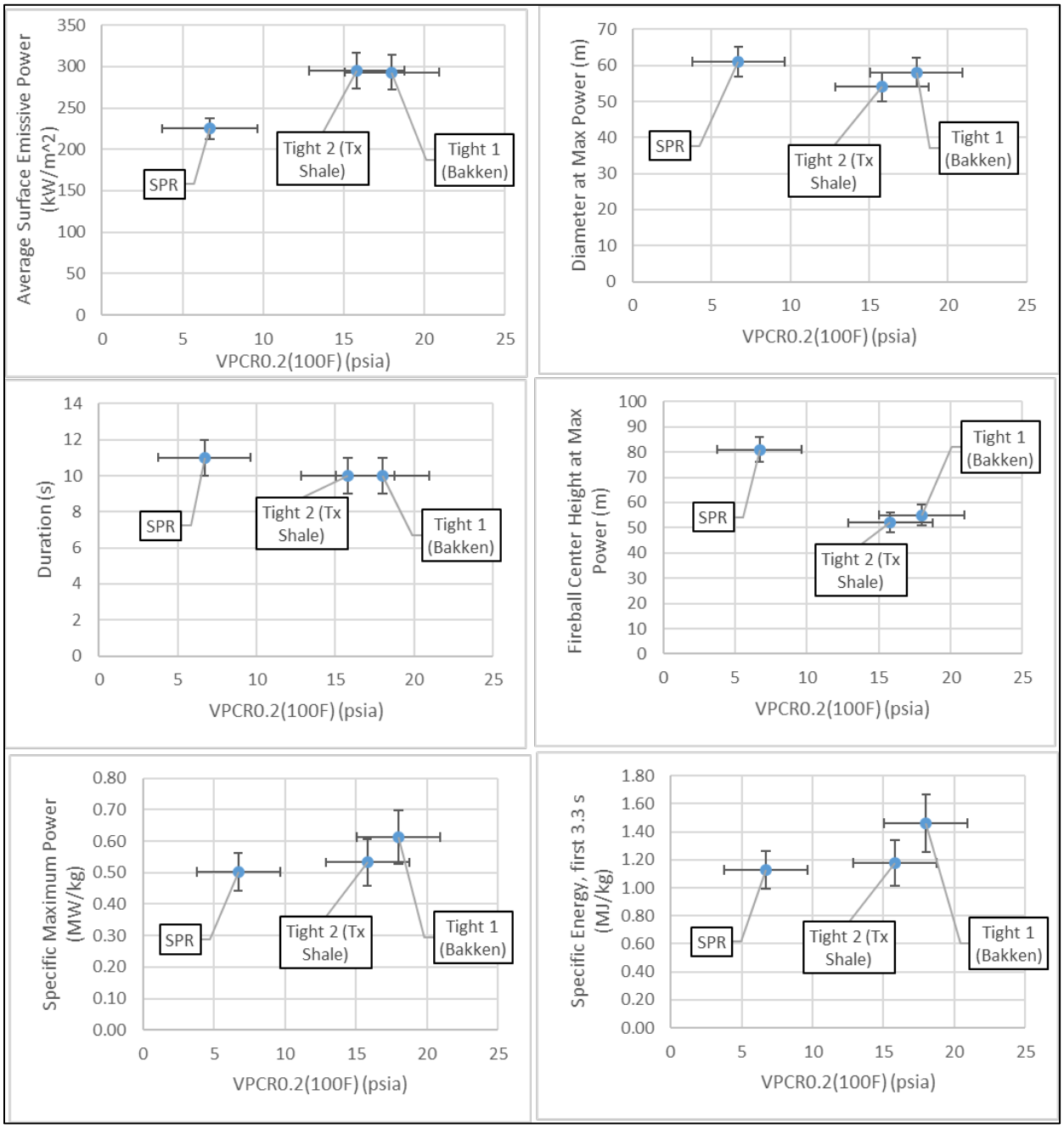

Figure G- 6: Oil property $VPCR_{0.2}(100°F)$ vs fireball burn properties a) average surface emissive power at max power, b) diameter at max power, c) duration, d) fireball center height at max power, e) specific maximum power, and f) specific energy from the first 3.3 s

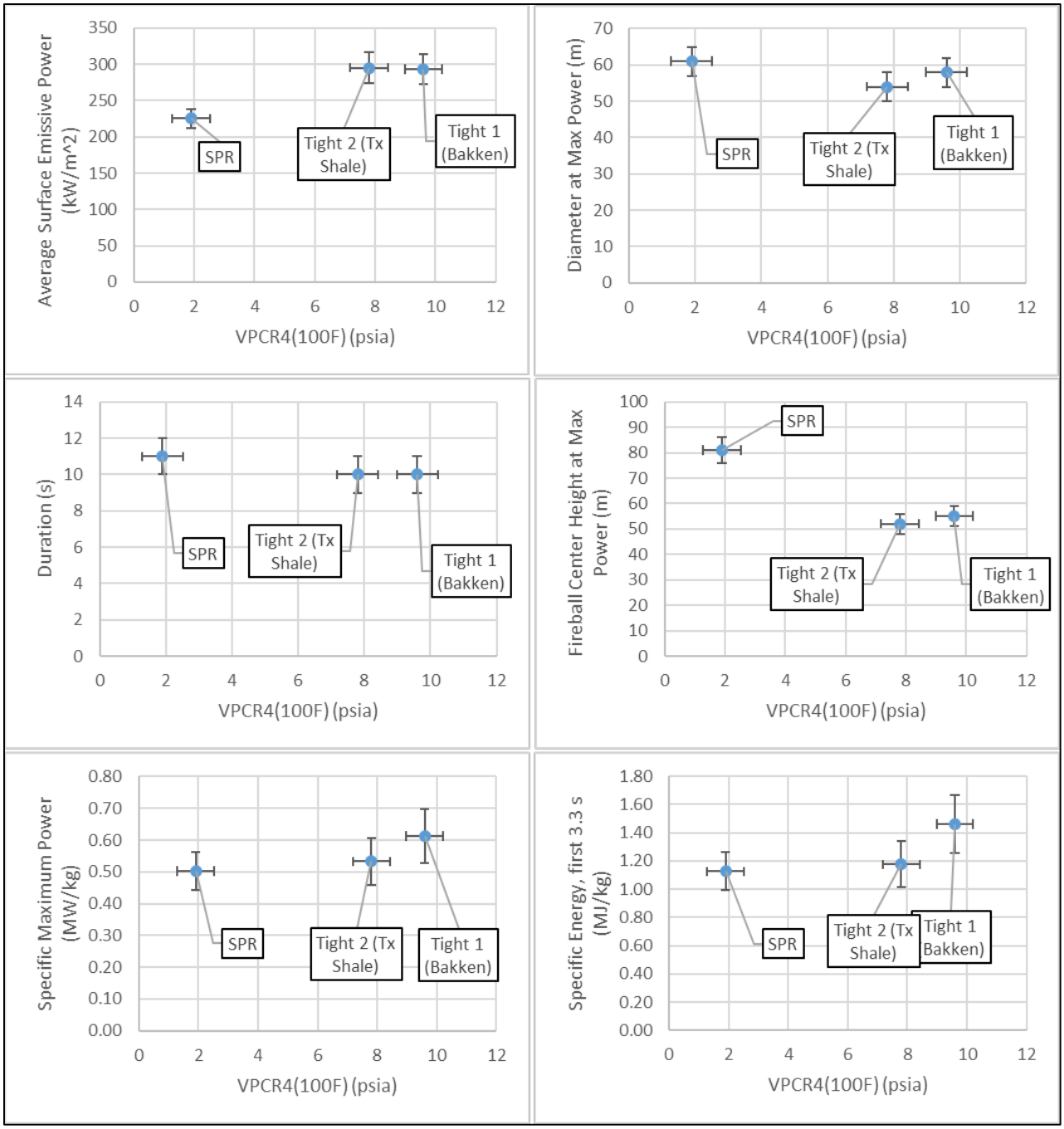

Figure G- 7: Oil property $VPCR_4(100°F)$ vs fireball burn properties a) average surface emissive power at max power, b) diameter at max power, c) duration, d) fireball center height at max power, e) specific maximum power, and f) specific energy from the first 3.3 s

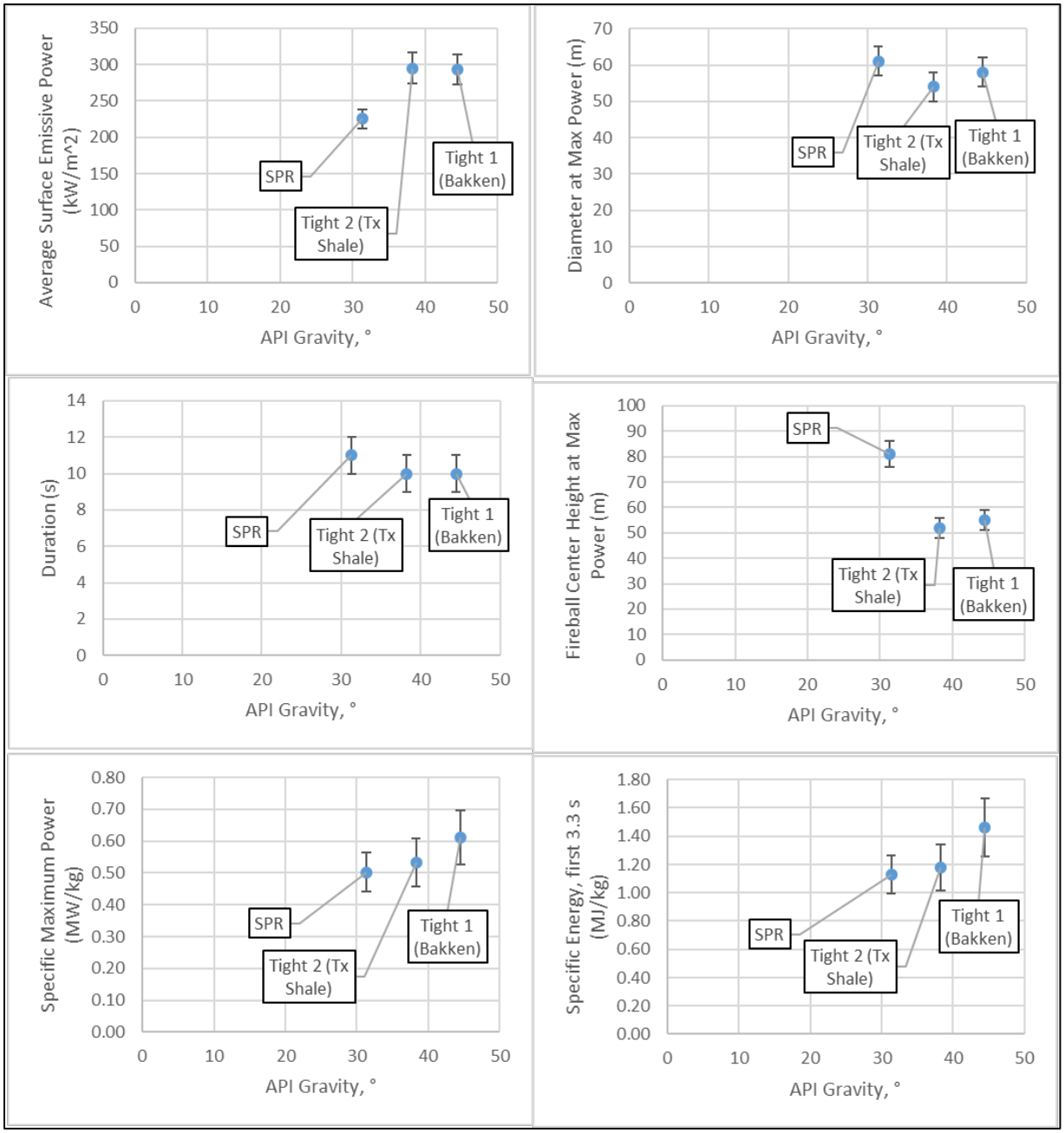

Figure G- 8: Oil property API gravity vs fireball burn properties a) average surface emissive power at max power, b) diameter at max power, c) duration, d) fireball center height at max power, e) specific maximum power, and f) specific energy from the first 3.3 s

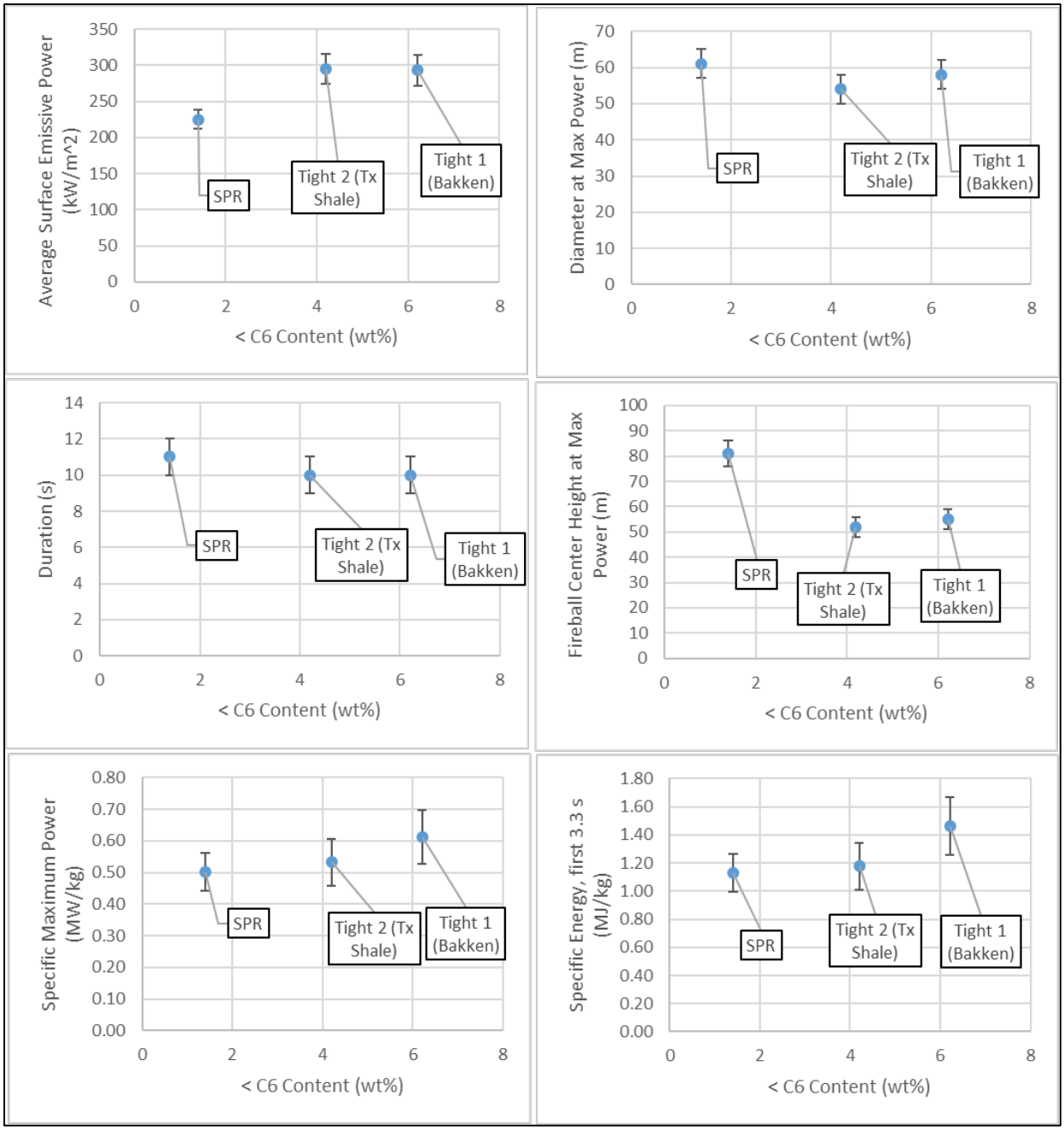

Figure G- 9: Oil property < C6 content (mass%) vs fireball burn properties a) average surface emissive power at max power, b) diameter at max power, c) duration, d) fireball center height at max power, e) specific maximum power, and f) specific energy from the first 3.3 s

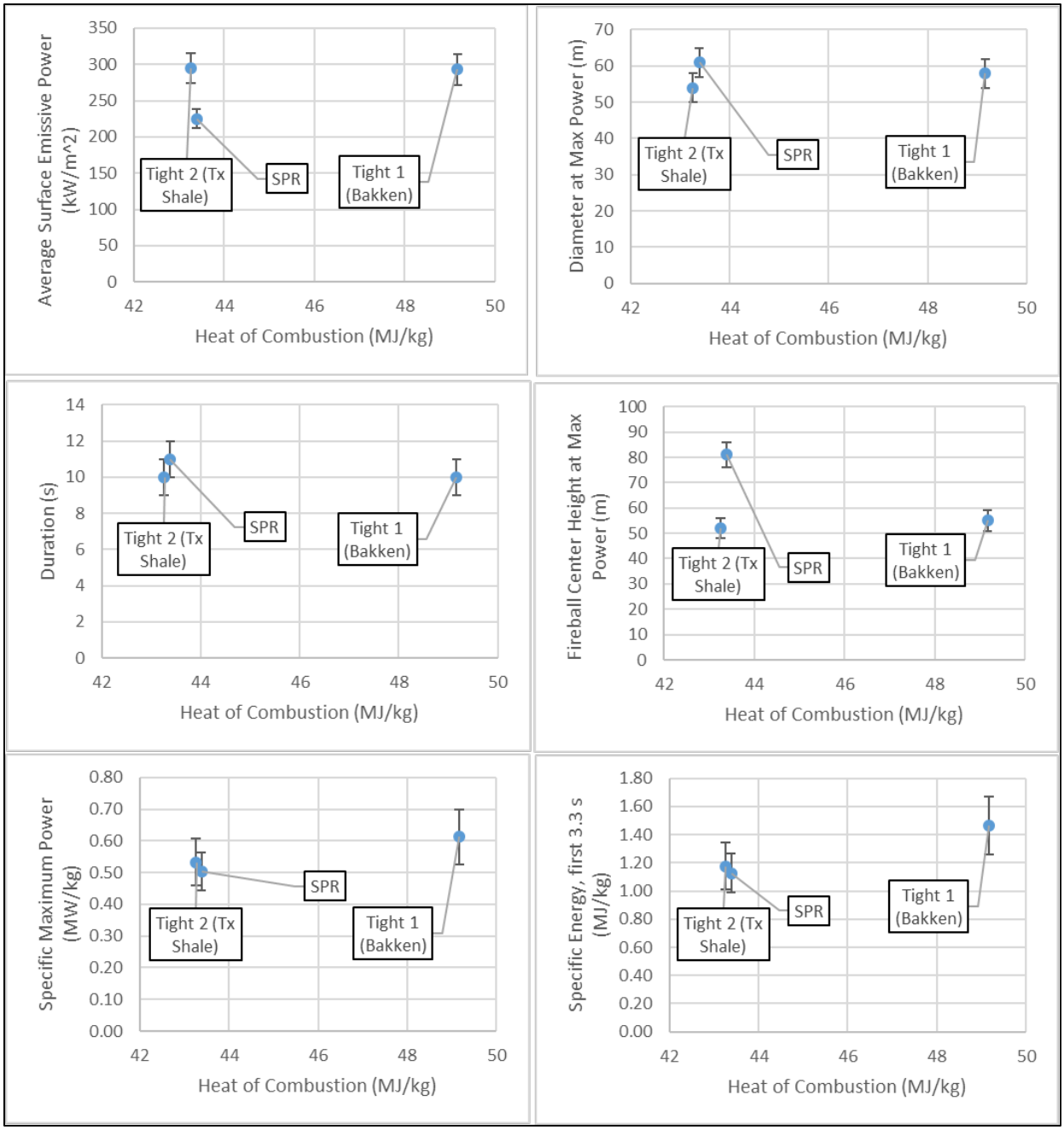

Figure G- 10: Oil property heat of combustion vs fireball burn properties a) average surface emissive power at max power, b) diameter at max power, c) duration, d) fireball center height at max power, e) specific maximum power, and f) specific energy from the first 3.3 s

DISTRIBUTION

Email - external

Name	Company Email Address	Company Name
Evan Frye	evan.frye@hq.doe.gov	Office of Oil & Natural Gas, U.S. Department of Energy, 1000 Independence Avenue, S.W., Washington D.C. 20585
Joseph Nicklous	joseph.nicklous@dot.gov	Office of Hazardous Materials Safety, Pipeline and Hazardous Materials Safety Administration, U.S. Department of Transportation, 1200 New Jersey Avenue, SE, Washington, D.C. 20590
Gina Solman	Gina.Solman@dot.gov	Volpe National Transportation Systems Center, U.S. Department of Transportation, 55 Broadway, Cambridge, MA 02142
Barbara Di Bacco	barbara.dibacco@tc.gc.ca	Transport Canada, Transportation of Dangerous Goods Directorate, 330 Sparks Street, Ottawa, Ontario, Canada K1A0N5

Email—Internal

Name	Org.	Sandia Email Address
Technical Library	9536	libref@sandia.gov

This page left blank

This page left blank

Sandia National Laboratories

Sandia National Laboratories is a multimission laboratory managed and operated by National Technology & Engineering Solutions of Sandia LLC, a wholly owned subsidiary of Honeywell International Inc. for the U.S. Department of Energy's National Nuclear Security Administration under contract DE-NA0003525.